Serviceability of Concrete Beams Reinforced with FRP and Concrete Prisms Prestressed with CFRP

BY

Hugues M. Vogel

A Thesis
Submitted to the Faculty of Graduate Studies of the
University of Manitoba in Partial Fulfillment of the
Requirements for the Degree of

DOCTOR OF PHILOSOPHY

Department of Civil Engineering
University of Manitoba
Winnipeg, Manitoba

ABSTRACT

Many researchers have identified the concern of steel corrosion in concrete. As a result, this thesis investigates the serviceability of concrete structures reinforced with Fiber Reinforced Polymer (FRP) reinforcement. The axial stiffness of some commercially available products can prevent the flexural stiffness of FRP reinforced concrete beams to comply with imposed serviceability limits. Although existing relationships for conventional steel have been modified to estimate deflection of concrete beams reinforced with FRP, they remain empirical and restricted to the properties of data used for calibration. The current thesis presents an alternate expression for effective moment of inertia that can be used to estimate the deflection of concrete beams reinforced with FRP. The derivation is achieved by considering material properties of the reinforcement and incorporating the effects of tension stiffening as well as concrete non-linearity in compression. The approach is more rational and does not include the empirical restrictions of relationships that have been previously developed. The accuracy and precision of the relationship is particularly accurate at higher loads with slight conservatism at lower loads.

Serviceability issues encountered with FRP reinforced concrete beam were also addressed by exploring an alternative reinforcing technique. Prestressed concrete prisms (PCPs) are small sections in which high strength concrete (HSC) is cast around a concentrically pre-tensioned FRP reinforcing bar. The technique enhances axial stiffness of the bare bar and flexural stiffness of concrete beams containing the reinforcement. However, prestress release causes transverse swelling of the bare bar in the anchorage zone and tensile splitting stresses within the relatively small cover. A linear elastic analysis was therefore performed to develop charts that can be used to select prestressing level for which damage of the cover is prevented and establish moment for which flexural stiffness remains enhanced. All samples in the thesis were designed with these charts to investigate the flexural performance of PCP reinforced beams subjected to repeated loading and thermal gradients. The flexural behaviour of PCP reinforced beams was found to be comparable to that of concrete beams prestressed to the same level with a bare reinforcing bar. The inclusion of dispersed fibers in the HSC of the PCP reinforcement was also found to provide enhancements to the post-cracking behavior of PCP reinforced beams.

TABLE OF CONTENTS

LIST OF TABLES

LIST OF FIGURES

LIST OF SYMBOLS

a= Parameter describing the influence of silica fume on the elastic modulus of concrete

A_c= Initial concrete area resisting tensile forces between adjacent cracks in a flexural member (at cracking)

A_{ce}= Effective concrete area resisting tensile forces between adjacent cracks in a tension member (at any load beyond cracking)

$A_{c,p}$= Concrete area in a composite reinforcement/prism

A_{cr}= Total reinforcing area at a crack transformed to concrete in a tension member

A_{cy}= Cross-sectional area of standard concrete test cylinder

A_g= Gross section area in tension members

A_m= Area of the material surrounding the bare reinforcement in a composite reinforcement/prism

A_{pr}= Equivalent area of the composite reinforcement/prism

A_R= Area of reinforcement

A_{Re}= Effective area of reinforcement that accounts for the effective concrete area

A_{tr}= Transformed section area for a flexural member

b= Rectangular beam width

b_w= Width of the web in a beam

c= Depth of neutral axis in an uncracked flexural member

c_c= Clear concrete cover

c_{cr1}= Depth of neutral axis in a cracked beam with the PCP reinforcement intact

c_p= Depth of neutral axis for beams with prisms assuming linear elastic behaviour of concrete in compression

c_{ts}= Depth of neutral axis that accounts for tension stiffening at any point along a flexural member

C= Concrete force in the compressive zone of flexural members

C_a= Elastic modulus correction factor that accounts for the influence of age on the trend with compressive strength (for 7 and 14 days of moist curing)

C_c= Concrete compressive force in a tension member due to prestressing

C_{ca}= Elastic modulus correction factor for the type of coarse aggregates in the mix

C_s= Elastic modulus correction factor for compressive strengths in excess of 90MPa at 28 days of moist curing

C'_s= Force in the compression reinforcement

d= Effective depth of reinforcement

d_b= Bar diameter

d'= Effective depth of compression reinforcement

D_f= Dispersed fiber diameter

E_c= Elastic modulus of concrete as defined in the CSA A23.3-04 design code

e_{tr}= Eccentricity of prestressed reinforcement for the transformed section

$E_{c,ACI363R(1992)}$= Elastic modulus of concrete as defined in the ACI 363R-92 design code

$E_{c,p}$= Elastic modulus of concrete in a composite reinforcement/prism

E_{c14D}= Elastic modulus of concrete after 14 days of moist curing

E_{c28}= ACI 363R-92 design code elastic modulus expression modified to account for 28 days of moist curing

$E_{c28,ca}$= ACI 363R-92 design code elastic modulus expression modified to account for the influence of coarse aggregate

E_{c28D}= Elastic modulus of concrete after 28 days of moist curing

$E_{c7,14}$= ACI 363R-92 design code elastic modulus expression modified to account for 7 and 14 days of moist curing

$E_{c,100}$= Elastic modulus of 100mm by 200mm standard concrete test cylinders

$E_{c,150}$= Elastic modulus of 150mm by 300mm standard concrete test cylinders

E_f= Elastic modulus of FRP reinforcement

E_m= Elastic modulus of the material surrounding the bare reinforcement in a composite reinforcement/prism

E_{pr}= Equivalent elastic modulus of the composite reinforcement/prism

E_R= Elastic modulus of reinforcement in the longitudinal direction

E_R^T= Elastic modulus of reinforcement in the transverse direction

E_s= Elastic modulus of steel (taken as 200GPa unless otherwise stated)

E_1= Elastic modulus of mortar

E_2= Elastic modulus of coarse aggregates

F= Nonlinear factor for effective moment of inertia

f_c= Average concrete tensile stress contribution beyond cracking

f_{CTOP}= Concrete stress at the extreme compressive fiber

$f_{c,p}$= Concrete stress in a tension member due to prestressing

f_{dp}= Concrete tensile strength when subjected to splitting stresses (relationship obtained from the double punch)

f_{dt}= Concrete strength in direct tension

f_{MID}= Stress at the middle of the effective concrete area surrounding the bare reinforcement when a flexural member reach cracking

f_o= Jacking stress applied to the reinforcement during prestressing

f_p= Stress level in the prestressed reinforcement

f_{PCP}= Average stress in the PCP reinforcement at a crack

f_{pe}= Effective stress level in the prestressed reinforcement, accounting for all losses

f_r= Modulus of rupture for concrete as defined in the CSA A23.3-04 design code

f_R= Reinforcement stress at a crack beyond cracking

f_{RC}= Reinforcement stress at a crack immediately after cracking

f_{sp}= Concrete tensile strength obtained from the split cylinder test

$f_{sp\ ACI363R(1992)}$= Split cylinder concrete tensile strength defined in the ACI 363R-92 design code

$f_{sp\ PROPOSED}$= Proposed expression for the split cylinder concrete tensile strength

$f_{sp\ Rashid(2002)}$= Split cylinder concrete tensile strength defined by Rashid et al. (2002)

f_t= Tensile stress applied to a tension member with dispersed fibers

F_T= Total force sustained by a standard concrete test cylinder

f_{to}= Ultimate strength in direct tension for a tension member with dispersed fibers

f_{TOP}= Stress at the top of the effective concrete area surrounding the bare reinforcement when a flexural member reach cracking

f_{tu}= Residual tensile strength of a tension member with dispersed fibers (corresponding to the ultimate tensile strain)

f'_c= Compressive strength of concrete

$f'_{c,100}$= Compressive strength of 100mm by 200mm standard concrete test cylinders

$f'_{c,150}$= Compressive strength of 150mm by 300mm standard concrete test cylinders

F_{Ni}= Bond force provided by mechanical interlock of the surface deformations introduced on the PCP reinforcement in the 3rd beam batch

F_1= Force sustained by the mortar in a standard concrete test cylinder

F_2= Force sustained by the coarse aggregates in a standard concrete test cylinder

g_1= Relative volume of the mortar in a standard concrete test cylinder

g_2= Relative volume of the coarse aggregates in a standard concrete test cylinder

h= Total height of the section for a flexural member

h_{ir}= Height of the idealized reinforcement/axial member

I_{cr}= Cracked Moment of inertia

I_{cr1}= Cracked moment of inertia for a beam with the PCP reinforcement intact

I_e= Effective moment of inertia for loads beyond cracking

I_g= Gross Moment of inertia

I_{ts}= Effective moment of inertia accounting for tension stiffening

j= Fraction of the effective reinforcement depth that characterizes the moment arm at the outermost crack from an adjacent set considered for bond performance (prestressed beams)

j_{cr}= Fraction of the effective reinforcement depth that characterizes the moment arm at the innermost crack from an adjacent set considered for bond performance (prestressed beams)

j_{cr1}= Fraction of effective reinforcement depth that characterizes the moment arm between the tensile force in the reinforcement and the compressive forces (PCP reinforced beams)

K= Stiffening factor for the tension stiffening factor in the CEB-FIP (1978) design code

K_R= Resistance factor for a PCP reinforced concrete beam

l_t= Transfer length of prestressed reinforcement

L= Beam span length (distance between the supports)

L_f= Dispersed fiber length

M= Applied/resisting moment

M_{app}= Moment applied to the flexural member during testing

M_c= Moment contribution from concrete in compression

M_{cr}= Cracking moment computed from gross section properties

$M_{cr,p}$= Moment required to cause cracking of the PCP reinforcement in a beam

$M_{cr,P/S}$= Moment required to cause cracking of a prestressed beam

M_{cr1}= Cracking moment of a beam when PCP reinforcement is intact

M_{cr2}= Moment in a beam when the PCP reinforcement reaches cracking

$M_{i\ app}$= Moment applied to the flexural member after release of prestress

$M_{P/S}$= Moment applied to the flexural member to remove initial camber

M_{sw}= Self weight moment applied to the flexural member after release of prestress

M_T= Moment contribution from the idealized reinforcement/axial member

M'_{app}= Moment applied to a flexural member adjusted to reflect the removal of effective prestressing

M'_{cr}= Cracking moment computed from gross section properties adjusted to reflect the removal of effective prestressing

M_1= Moment at the innermost crack from an adjacent set considered for bond performance

M_2= Moment at the outermost crack from an adjacent set considered for bond performance

n= Modular ratio for either steel or FRP reinforcement in normal strength concrete

n_c= Modular ratio for high strength concrete in normal strength concrete

n_n= Number of notches within a given distance away from the crack at midspan

n_p= Modular ratio for either steel or FRP reinforcement in high strength concrete

$\bar{n}$= Effective modular ratio that accounts for tension stiffening (equivalent to n/η)

N= Axial load applied to a tension member

N_{cr}= Cracking load of a tension member

$N_{cr,ir}$= Cracking load of the idealized reinforcement/axial member

$N_{cr,p}$= Cracking load of the composite reinforcement/prism

N_m= Axial load contribution from the material surrounding the bare reinforcement in a composite reinforcement/prism

N_R= Axial load contribution from the bare reinforcement in a composite reinforcement/prism

p= Pressure exerted by the reinforcement to the surrounding concrete due to differential swelling of the materials

P= Initial or effective prestressing force applied to a flexural member

P_a= Load applied to the samples at midspan

P_{app}= Load applied to the samples at midspan during intermediate static tests (2^{nd} beam batch)

P_C= Load applied to the specimen for bond tests performed in accordance with the CEB-FRP (1978) model code

P_{cr}= Load at midspan that causes cracking of the beam

P_e= Effective prestressing force applied to a flexural member accounting for total losses

P_i= Initial prestressing force applied to a flexural member accounting for initial losses, including elastic shortening

P_t= Axial load applied to a tension member during experimental testing

r= Radial distance from the center of the reinforcement in the linear elastic model for concrete cover stresses

r_R= Reinforcement radius (equal to $d_b/2$)

R= Modification factor for service level ratios

R_{cd}= Ratio of specimen width to bar diameter for the linear elastic model for concrete cover stresses

SF_{fr}= Silica fume content written as a fraction of the cementitious material in the mix

S_{bot}= Bottom section modulus based on transformed section properties

S_{top}= Top section modulus based on transformed section properties

S_{tr}= Section modulus (top or bottom) based on transformed section properties

S_1= Stiffness measured from the reference batch (1st PCP reinforced beam batch) at a given load beyond cracking

S_3= Stiffness measured from the investigated batch (3rd PCP reinforced beam batch) at a given load beyond cracking

T= Reinforcement force at a crack

T_{cr1}= Force in the reinforcement at the innermost crack from an adjacent set considered for bond performance

T_{cr2}= Force in the reinforcement at the outermost crack from an adjacent set considered for bond performance

T_1= Concrete tension force acting outside of the effective tension area

V_f= Fiber volume fraction in fiber reinforced concrete

w= Width and height of the PCP reinforcement

x= Distance away from the midspan crack

y_b= Distance from the neutral axis to the extreme tension fiber

α = Stress block factor (fraction of the concrete compressive strength)

α_b= Bond coefficient for $\kappa_{ACI\text{-}01}$

α_f= Fraction of the direct tensile strength of concrete representing the upper residual strength value in a tension member

α_1= Factor accounting for the bond characteristics of the reinforcement in the stress-strain model for fiber reinforced concrete

α_2= Factor accounting for the loading scheme in the stress-strain model for fiber reinforced concrete

β= Stress block factor (defines the centroid of resultant compressive force)

β_b= Tensioning stiffening factor for tension members (Bischoff and Paixao 2004)

β_{cd}= Factor accounting for the effects of concrete cover to bar diameter ratio when pressure is exerted at the interface between the reinforcement and concrete

β_f= Fraction of the cracking strain of concrete representing the strain value that corresponds to the upper residual strength value in a tension member

γ= Factor accounting for the relative distance of the idealized reinforcement with respect to the neutral axis

γ_c= Concrete mass density, typically ranging between 1500 and 2500kg/m^3

γ_f= Fraction of the cracking strain of concrete representing the strain value that corresponds to the ultimate tensile strain in a tension member

δ_f= Fraction of the cracking strain of concrete representing the strain value that corresponds to the lower residual strength value in a tension member

δ_{ms}= Midspan deflection recorded during intermediate static tests

Δ = Total axial displacement of standard concrete test cylinder for elastic modulus two-phase theoretical model (springs in series)

ΔM= Moment gradient between adjacent cracks

Δr_c= Displacement of the concrete surrounding the reinforcement in the radial direction

Δr_R= Displacement of the reinforcement in the radial direction

ΔT= Force transfer between the concrete and composite reinforcement/prism, including the contribution from surface deformations

ΔT_c= Force transfer to concrete from reinforcement between adjacent cracks

ΔT_R= Force transfer from reinforcement to concrete between adjacent cracks (equal to ΔT_C)

Δx= Average crack spacing

Δx_g= Distance from midspan to the gauge used to measure concrete strain during experimental testing

Δ_1 = Axial displacement of mortar in a standard concrete test cylinder for elastic modulus two-phase theoretical model (springs in series)

Δ_2 = Axial displacement of coarse aggregates in a standard concrete test cylinder for elastic modulus two-phase theoretical model (springs in series)

$\Delta\varepsilon$ = Applied strain in a standard concrete test cylinder

$\Delta\varepsilon_p$= Elastic shortening strain in the composite reinforcement/prism

ε= Axial strain applied to the composite reinforcement/prism

ε_c= Concrete tensile strain away from the crack at midspan

ε_{cg}= Concrete tensile strain measured 50mm away from the crack at midspan

ε_{cr}= Cracking strain in tension for either concrete or the material surrounding the bare bar in a composite reinforcement/prism

ε_{CTOP}= Concrete strain at extreme compressive fiber

ε_{c1}= Concrete tensile strain at the crack at midspan

ε_{c2}= Concrete tensile strain corresponding to full stress transfer away from the crack at midspan

ε_m= Average member strain in a tension member with dispersed fibers

ε_{MID}= Tensile strain at the middle of the effective concrete area surrounding the bare reinforcement when a flexural member reaches cracking

ε_o= Jacking strain applied to the reinforcement during prestressing

ε_R= Reinforcement strain at a crack

ε_{RM}= Average member strain in a tension member

ε_t= Tensile strain applied to a tension member with dispersed fibers

ε_T= Unrestrained lateral strain of the reinforcement at the interface of the concrete

ε_{tl}= Tensile strain at which the residual tensile strength in a tension member with dispersed fibers is reached

ε_{to}= Tensile strain corresponding to the ultimate stress applied to a tension member with dispersed fibers

ε_{TOP}= Tensile strain at the top of the effective concrete area surrounding the bare reinforcement when a flexural member reaches cracking

ε_{tu}= Ultimate tensile strain applied to a tension member with dispersed fibers

ε'_c= Strain at peak concrete compressive stress

ε_θ= Circumferential strain at the interface separating the reinforcement and concrete when pressure develops from differential swelling of the materials

η= Stiffness factor for the tension stiffening model in the CEB-FIP (1978) design code

η_o= Fiber orientation fiber for fiber reinforced concrete

κ= Reduction factor for effective moment of inertia

$\kappa_{ACI\text{-}01}$= ACI 440.1R-01 reduction factor for effective moment of inertia

$\kappa_{ACI\text{-}06}$= ACI 440.1R-06 reduction factor for effective moment of inertia

$\kappa_{YOST\text{-}03}$= Reduction factor for effective moment of inertia (Yost et al. 2003)

λ = Factor accounting for the density of concrete in the calculation of modulus of rupture

λ_f= Fraction of the direct tensile strength of concrete representing the lower residual strength value in a tension member

ν_R^{LT}= Poisson's ratio for the reinforcement that describes lateral strain due to loading in the longitudinal direction

ν_R^{TT}= Poisson's ratio for the reinforcement that describes transverse strain due to lateral pressure

ν_c= Poisson's ratio for concrete

ξ= Ratio of extreme compressive strain to strain at peak concrete compressive stress

ρ= Reinforcement ratio for beams containing any type of reinforcement

ρ_b= Balanced reinforcement ratio for FRP reinforced beams

ρ_{bm}= Balanced reinforcement ratio for PCP reinforced beams accounting for the transformation of bare reinforcement to high strength concrete

ρ_{frp}= Reinforcement ratio for FRP reinforced beams

ρ_p= Reinforcement ratio between reinforcement and concrete in idealized axial members embedded in the tension zone of flexural elements

ρ_R= Reinforcement ratio between reinforcement and concrete in the tension zone of flexural elements (equivalent to A_R/A_c)

ρ_s= Reinforcement ratio for steel reinforced beams

σ_r= Radial (compressive) concrete cover stresses

σ_θ= Circumferential (tensile) concrete cover stresses

$\sigma_{\theta,max}$= Maximum circumferential concrete cover stresses (at the interface)

τ= Bond stresses in the anchorage zone of prestressed members

$\tau_{b\text{-}actual}$= Actual distribution of bond stresses at the surface of the reinforcement between any set of adjacent cracks

$\tau_{b\text{-}average}$= Average bond strength

τ_d= Bond stress that can develop on the surface of dispersed fibers

$\tau_{PCP,average}$= Average bond strength between adjacent cracks for PCP reinforcement

$\tau_{PS,average}$= Average bond strength between adjacent cracks for PCP reinforcement

ϕ_{cr}= Curvature at a cracking in a flexural member

ϕ_{ts}= Curvature accounting for tension stiffening at any point along a flexural member

Ψ= Neutral axis stress block inclusion factor

ACKNOWLEDGMENTS

Firstly, I would like to acknowledge my advisor Dr. Dagmar Svecova for having gratefully shared her knowledge and provided the guidance necessary in reaching this final step in the fulfillment of my Doctorate degree. Despite all the hardships and obstacles encountered during what has rightfully become an adventure, I am eternally grateful for the trust as well as the faith she has placed in my abilities to achieve the goals we had mutually established for this project.

I would also like to thank Dr. Aftab Mufti for having given me the opportunity to work for the ISIS Canada Structural Health Monitoring Resource Center (SHMRC) and supporting me in the completion of my Doctorate degree. I am truly thankful for having had the chance to work alongside such skillful and knowledgeable individuals from which I have already learned more then I could ever imagine.

The Natural Sciences and Engineering Research Council (NSERC) is also thanked for their funding. In more specific terms, I am very appreciative of the council for having contributed to the ongoing efforts involved in providing a wider knowledge of and perspective on the uses of FRP as reinforcement in concrete structures. It forms the essence by which new ideas can flourish to improve the performance of civil infrastructure by using innovative materials.

I must also express my gratitude towards Mr. Chad Klowak for having shared his conceptual knowledge towards the fabrication and testing of all samples reported in this document. I would also like to thank Ms. Liting Han and Ms. Evangeline Murison for having patiently been the guiding stream in my initially blinded quest to tame the use of Data Acquisition (DAQ) systems as well as the instrumentation required for testing.

I would also like to thank my friends and family, which have been the driving force behind all of my accomplishments. I would especially like to thank my parents, who have always been there to guide me through the seasons of my life and who have always believed in all that I am and all that I have become. Their strength and wisdom will forever be a source of inspiration.

CHAPTER 1

INTRODUCTION

1.1 PROBLEM DEFINITION

The greatest threat to the durability of a concrete structure is corrosion of the reinforcement. Although for many years steel bars have consistently performed well as reinforcing materials, electrochemical corrosion has become a growing concern in civil infrastructure. There has been, in response to this issue, a rising interest to explore the feasibility of using alternative corrosion resistant materials among which Fiber Reinforced Polymer (FRP) has shown particular promise.

The composition of FRP reinforcement consists of synthetic or organic fibers embedded in a polymeric resin matrix. Many studies have observed and agreed that properties of the resulting composite material differ from that of steel reinforcement from a physical, mechanical and thermal point of view. These differences can compromise the compatibility of the material in a concrete environment and can be a significant obstacle to the interaction between the materials. Although some FRP reinforcing bars provide strengths that considerably exceed those for conventional steel and allow a reduction in the area required to achieve a given resistance, the gained advantage remains unfulfilled by relatively low elastic modulus values. More specifically, the combination of smaller area and lower elastic modulus prevent the flexural stiffness of FRP

reinforced beams to comply with imposed serviceability limits. Serviceability is further influenced by the wide range of surface preparations available for FRP reinforcement. Although bond of steel reinforcement primarily depends on mechanical interlock, the absence of surface deformations or lack of stiffness of the polymeric resin matrix causes the bond strength of FRP reinforcement to be governed by chemical adhesion and friction. These secondary mechanisms of force transfer to the surrounding concrete influence the distribution of cracks along the member and provide further uncertainties in achieving the required limitations on serviceability.

Although design guidelines and codes have been established to incorporate these proprietary differences to use FRP reinforcement in civil engineering applications, the documents present relationships that are adaptations from those used for steel reinforced elements. The expressions are empirical in nature, which brings sensitivity to conditions other than those from which they were derived and introduces a certain difficulty in reflecting the wider range of properties that exists for commercially available FRP products. Consequently, the performance of existing relationships remains vulnerable and compels the need for developing an approach that is capable of appropriately representing the mechanical and bond properties of the reinforcement.

Although more fundamental approaches to the estimation of deflection exist, the serviceability issues encountered with FRP reinforced concrete structural members remain. Larger reinforcing areas can be used to improve the condition but the modification conceals the advantages arising from using the reinforcement's higher strength. It can also significantly increase material costs beyond that required for members that are designed on the basis of resistance. Conventional prestressing of concrete with FRP reinforcement can offer a convenient solution to the issue of serviceability for which the strength of the reinforcement can be more appropriately utilized. However, situations where sections are designed with higher geometrical complexity and draped tendons can cause the application of prestress to become cumbersome as well as costly. An alternate solution consists of embedding the reinforcement in a second material for which load-sharing concepts maintain axial load with reductions in axial strain. This composite reinforcement does not forestall cracking of the beam as observed for prestressed concrete but the material surrounding the bare reinforcement can be chosen to remain intact beyond the cracking stage to ensure flexural stiffness is maintained within appreciable levels.

The choice of material becomes important in the design process of the composite reinforcement and must have stronger tensile resistance than the surrounding concrete. Specialized materials can reach relatively high costs and the behavior of reinforced concrete in direct tension is very well documented. Consequently, the choice of high strength concrete as the stiffness enhancing material is one that can be more convenient from a design perspective. Although the use of the material in structural applications has strongly increased over the last decades, design code relationships were originally intended to establish the properties of a material with lower strength. As a result, the reliability of existing relationships must be carefully investigated to ensure an adequate estimation of the composite reinforcement's performance can be reached. Also, the ability of the reinforcement to enhance flexural stiffness relies on a transfer of forces, which depends on the bond performance of high strength concrete in a normal strength concrete environment. The performance is critical to the behavior of concrete reinforced with such material and has strong influence on the serviceability conditions of the elements. Design codes provide relationships for establishing the bond strength of composite sections, but the interface between high and normal strength concrete in applications using the composite reinforcement is generally free of transverse reinforcement. The interaction must therefore be investigated in fuller detail.

Pre-compressing the concrete can also delay cracking of the composite reinforcement and extend the load range for which flexural stiffness is enhanced. The ensuing components are referred to as prestressed concrete prisms (PCPs) in the literature, for which the prestressing level primarily depends on and is mainly limited by a phenomenon called the Hoyer effect. The Hoyer effect is a wedge-shaped expansion of the reinforcing bar in the anchorage zone of the pre-compressed element when prestressing is released. Differential transverse swelling of the reinforcing bar and concrete in this region will produce a state of radial as well as circumferential stresses within the cover. Being tensile, circumferential stresses hold the potential for initiating cracks within the concrete cover. If the prestressing force is sufficiently high, the stresses will cause a propagation of cracks through the cover until complete splitting of the envelope occurs. Damage within the concrete cover can significantly influence the bond interaction between reinforcement and concrete in the PCP reinforcement. The phenomenon must therefore be thoroughly investigated to ensure adequate performance of the PCP reinforcement in the structural elements is achieved.

1.2 RESEARCH BACKGROUND

In spite of the issues presented in the previous section, the use of FRP reinforcement in civil infrastructure continues to show promise. Although some fibers are susceptible to the high pH of concrete, their resistance to the corrosion process affecting conventional steel is a key property to the development of infrastructure having superior long-term performance. Previous research on FRP reinforced concrete elements should therefore be reviewed in order for the current project to suggest possible improvements on existing relationships used to estimate their behavior as well as present solutions to address issues with serviceability for the reinforcement.

1.2.1 Serviceability of Steel Reinforced Concrete Elements

The serviceability of steel reinforced concrete members has been widely studied. The extent of this research has strong relevance and can serve as a possible guide to solve some of the issues encountered with the serviceability of concrete structures reinforced with FRP. The research includes short-term as well as long-term deflections of non-composite reinforced, composite reinforced and prestressed concrete beams. Branson (1968) provided detailed design procedures for computing the deflection of such beams by including the use of multipliers for creep and shrinkage as well as compression steel in ordinary reinforced beams and non-tensioned steel in prestressed beams. The paper was intended to broaden the use of the effective moment of inertia relationship presented in earlier work (Branson 1963) and adopted by ACI Committee 318 (1966). It also served as a supplement to handbooks involved with the design of steel reinforced concrete structures (ACI 340-67, ACI 317-65). The efforts were consequences of the fact that our knowledge of a reinforced concrete section's stiffness is far less certain than our knowledge of its strength, especially when time-dependent deformations are sought.

The observation was also made obvious by Gilbert (1983) who emphasized that the estimation of long-term behavior had several fundamental weaknesses. Although many practical situations may require an approximation with the use of only a simple deflection multiplier, it was observed that in certain cases a more accurate prediction of deflection may be necessary and a more fundamental approach is needed. In his earlier work, results enforced the fact that most

reinforced concrete slabs fall completely outside the limits of Branson's study (Branson 1963) and that the use of the effective moment of inertia expression may not be reliable for long-term estimates of deflections. As a result, a technique was presented in which the stiffness of the tensile reinforcement after cracking is adjusted to consider an area of concrete that is effective in providing additional axial stiffness at the level of the steel. The concept accounts for the average contribution of concrete in the tension zone between the cracks and was initially proposed by Rao and Subrahmanyam (1973). The method was shown to produce accurate and computationally efficient results (Gilbert 1983).

Although research by Gilbert (1983) brought clarity to the limitations of Branson's equation, it was impeded by the growing concern of corrosion in civil infrastructure and the rising interest of FRP reinforcement as a replacement to conventional steel in reinforced concrete. Researchers started to focus their projects on establishing differences in the properties of both reinforcing materials. Based on their observations, researchers emphasized that the design sequence for concrete structures reinforced with conventional steel may not be appropriate for that involving the use of FRP products as the reinforcing material. Differences in elastic modulus and bond performance for these products over conventional steel reinforcement suggest that it is stiffness rather than strength that usually governs the final choice of section. The difference was significant and brought an adjustment to research performed on the serviceability of reinforced concrete structures. Researchers concentrated their efforts on short-term deflections for which modifications to the effective moment of inertia initially proposed by Branson (1963) were considered in favor of the effective concrete area concept initially sought out by Rao and Subrahmanyam (1973) for concrete structures reinforced with conventional steel.

1.2.2 Serviceability of FRP Reinforced Concrete Elements

When FRP products were first considered as reinforcement for concrete structures, the tensile properties were thoroughly studied. Design guidelines for reinforcing concrete structures with FRP published by ISIS Canada (ISIS Design Manual No.3, 2001) provide the designing engineer with properties gathered from a broad range of manufacturers. Values in this manual are vastly detailed and provide a strong basis for selecting reinforcement based on mechanical as well as

thermal properties. On a similar note, values reported by ACI Committee 440.1R (2001) for the design and construction of concrete reinforced with FRP bars provide an adequate summary for the properties of commonly used FRP products that are listed in ISIS Design Manual No.3 (2001). The summary suggests that the tensile strength and elastic modulus values reported by the manufacturers are generally lower for Glass FRP (GFRP) reinforcement than they are for Carbon FRP (CFRP) reinforcement. Moreover, the manual emphasizes the wide range of properties existing for commercially available FRP reinforcement. Since the properties of conventional steel are well known and fixed, the condition underlines the importance as well as the difficulty of including the influence of these properties in establishing relationships that are capable of estimating the performance of structures reinforced with the material.

The bond performance of FRP reinforcement in concrete was the first extensively studied parameter after the tensile properties were established. Benmokrane et al. (1996) emphasized the importance and lack of experimental data for the bond behavior of FRP reinforcing bars in concrete. The behavior is one of the main traits of a reinforced concrete structure, which controls critical design parameters such as development length and crack spacing. These parameters govern deflection and the research became an initial step towards developing a relationship capable of estimating the deformation of concrete structures reinforced with FRP.

From the perspective of lower costs, Benmokrane et al. (1996) decided to study the bond performance of GFRP reinforcement in comparison to conventional steel. Several surface finishes were added to the smooth bar by helically winding the same kind of fibers and applying an additional coating of thermosetting resin with a dispersion of sand particles. Since larger bar sizes provide greater surface area and therefore lower bond stresses to transfer the load from the reinforcement to the surrounding concrete, a total of four bar diameters were investigated in the study. For each of the bar diameters, a total of five concrete beam tests were carried out to determine the average bond strength in accordance with that shown in Figure 1.1(a). The specimens are generally believed to realistically simulate the stress conditions of reinforced concrete elements subjected to bending. As illustrated in the figure, they consist of two rectangular concrete blocks joined at the top by a steel ball joint and at the bottom by the reinforcement to be tested for bond with concrete. As illustrated in Figure 1.1(b), the main

conclusion arising from the research stated that the bond strength of GFRP reinforcing bars were consistently lower than that measured for steel reinforcing bars at any of the bar diameters considered. Wider crack spacing and different load-deflection behavior can therefore be expected in beams reinforced with GFRP products as opposed to conventional steel.

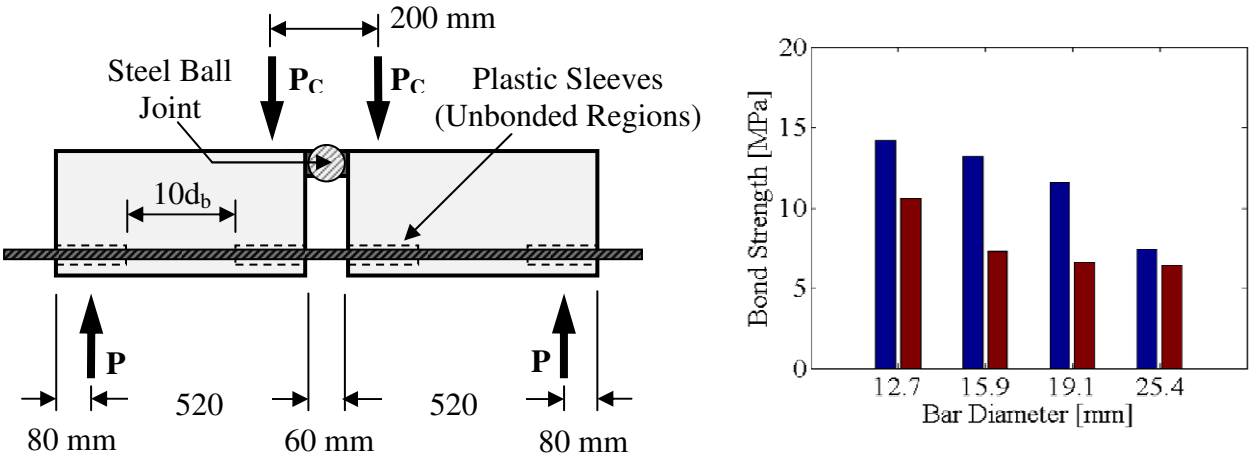

(a) Concrete Beam Specimen (b) Average Bond Strength Results

Figure 1.1 – **Average Bond Strength of GFRP Reinforcement**

Tighiouart et al. (1998) extended the research conducted by Benmokrane et al. (1996) on bond performance by considering an additional type of GFRP reinforcing bar. The additional GFRP reinforcing bar contained surface deformations achieved by thoroughly wrapping the rod with a resin impregnated strand prior to the polymerization process of the resin. The surface finish for this reinforcing bar is also deformed but the end result is distinctly different from that observed for rebars investigated by Benmokrane et al. (1996).

In order to ensure continuity with research performed by Benmokrane et al. (1996), bond tests were performed using the same concrete beam specimens and loading scheme as that illustrated in Figure 1.1(a). The same set of bar diameters as those chosen by Benmokrane et al. (1996) were considered. The overall trend observed in the results suggested that the manufacturing process for the bars used by Tighiouart et al. (1998) provided superior bond strength than that observed for rebars studied by Benmokrane et al. (1996). The observation implied that the bond performance of GFRP reinforcement is highly dependent on the manufacturing process and surface finish adopted. The result had strong implications for the behavior of concrete structures

reinforced with FRP since it reflects the wide range of properties that are commercially available for the material. If adequate documentation for these properties is not provided by the manufacturer, the serviceability of FRP reinforced concrete elements will be difficult to estimate if an adaptation of the design guidelines for conventional steel is used. Any adaptation therefore remains vulnerable unless a fundamental approach is taken to properly document and incorporate the bond performance of commercially available FRP products.

The bond performance of FRP reinforcement in concrete was also documented and compared to that of conventional steel in research conducted by Katz and Berman (2000). The researchers performed pullout tests on four distinct types of GFRP reinforcement. As in previous research, each bar was selected to represent a different bond mechanism to concrete. The surface of the bars was either molded with deformations similar to that of steel reinforcement or wrapped with a thin braid of fibers on the surface and fine sand particles evenly distributed on the surface. The last two types of rebar were wrapped using a braid of fibers with varying widths. Pullout tests were performed at various temperatures with the use of a heating jacket wrapped around the sample. Unlike research performed by Tighiouart et al. (1998), results obtained from Katz and Berman (2000) for three of the four rods revealed average bond strengths comparable to that of conventional steel. The average bond strength for the remaining bar was considerably lower than that achieved with the other reinforcing bars of the research due to inadequate hardening of the outer polymer holding the sand particles. The result was, once again, a clear indication that the bond strength of FRP reinforcement greatly varies over the range of commercially available surface preparations. It also confirmed that the lack of standardized properties for the material can lead to issues with quality control.

The main focus, however, of research conducted by Katz and Berman (2000) was to investigate the pullout load-slip behavior of each reinforcing bar. Results indicated higher slip values for the GFRP rods at the peak average bond stress. The observation suggests that although satisfactory average bond strength values can be achieved with FRP reinforcement, higher slip measurements can occur for which the deflection of reinforced concrete structures can be affected through larger curvatures and crack widths.

The high variability in bond characteristics for FRP reinforcing bars as well as their direct relationship with development length and crack spacing can strongly influence the deflection of a member. In addition to the lower modulus of the reinforcement, research from Benmokrane et al. (1996) indicated that the bond performance of the reinforcement could cause Branson's equation to overestimate the effective moment of inertia of concrete beams reinforced with FRP. In fact, research from Gao et al. (1998a) revealed that a modified expression for the effective moment of inertia was required to account for the lower elastic modulus and different bond behavior of the reinforcement. The revised expression was adopted and recommended by ISIS Design Manual No.3 (2001) as well as ACI 440.1R (2001). The modification consisted of applying a factor to reduce the contribution of the uncracked portions of the beams to flexural stiffness. The portion of the factor accounting for the distinct bond characteristics of FRP reinforcement was described as a bond-depend coefficient. It was fixed at a value of 0.5 and derived on the basis of simply supported tests performed on a total of 62 GFRP reinforced beams with various reinforcement ratios, concrete strengths and beam geometries. Further research was however recommended by ACI 440.1R (2001) to investigate the reliability of the bond-dependent coefficient for other types of FRP reinforcement and various bond characteristics.

In more recent work, Yost et al. (2003) provided further insight on the empirical form of Branson's model and its sensitivity to conditions other than those from which it was derived. The authors emphasized that the relationship had been derived from experimental data characterizing the behavior of steel reinforced concrete beams with a nonlinear transition from the properties of a gross section to that of a fully cracked section. The sensitivity of Branson's relationship for effective moment of inertia brought the research to stress the requirement for evaluating FRP deflection models on the basis of a database containing a significant amount of experimental data. Based on experimental data from 48 simply supported concrete beams reinforced with GFRP, the research alluded to the fact that the transition between gross and cracked section properties was more abrupt than that observed with the use of conventional steel. The result is consistent with an overestimation in effective moment of inertia (Benmokrane et al. 1996) and was found to be particularly true for beams having ratios of gross to cracked section properties ranging from four to eight times that of hypothetical steel reinforced samples. Yost et al. (2003) clarified that this abrupt transition causes the modified effective moment of inertia expression

suggested by Gao et al. (1998a) to overestimate the parameter, especially for lightly reinforced beams. For larger reinforcing areas, the research found that the error in the effective moment of inertia relationship adopted by ACI 440.1R (2001) decreased. The observation brought Yost et al. (2003) to consider and propose a bond-dependent coefficient that was no longer fixed but reliant on the reinforcing area chosen in the design process. More specifically, the coefficient was written in terms of the ratio of actual to balanced reinforcement ratio as well as the ratio of elastic modulus for FRP reinforcement and conventional steel. It was found to vary linearly between 0.15 and 0.3 for reinforcement ratios ranging between 0.35 and 2.7 times that for the balanced condition. However, Yost et al. (2003) recommended a maximum average value of 0.25 for reinforcement densities ranging between 1.2 and 2.7.

In later publications, a similar modification was proposed by ACI 440.1R (2006) in which a fifth of the ratio of actual to balanced reinforcement ratio was suggested to be more accurate than that presented in earlier publications by the committee (ACI 440.1R-01). Unlike that presented in earlier research (Gao et al. 1998a, Yost et al. 2003), the modification deliberately discarded the influence of modulus on flexural stiffness transition. This choice can be significant, especially in the case of GFRP reinforcement. It should be noted that the lower elastic modulus for this type of reinforcement can have considerable impact on crack widths and therefore serviceability of concrete elements reinforced with the material.

Although modifications presented by Gao et al. (1998a) and Yost et al. (2003) appropriately incorporate the influence of elastic modulus on deflection, the relationships remain empirical in nature and include the influence of bond only through the use of a factor that is fixed or dependent on the reinforcing area. The sensitivity of the relationships to the conditions for which they were derived is inherent and earlier research on the mechanical properties as well as the bond characteristics of FRP reinforcement is not being appropriately incorporated in the derivation. In accordance with this observation, Bischoff and Paixao (2004) indicated the need for re-evaluating Branson's equation and developing a rational approach capable of estimating deflections equally well for all reinforcing materials used in civil infrastructure.

The research conducted by Bischoff and Paixao (2004) was thoroughly involved with studying the combined influence of elastic modulus, bond performance and reinforcing area on the serviceability of concrete elements reinforced with steel as well as FRP material. Although the elastic modulus primarily affects crack width, the bond performance and reinforcing area affect crack spacing by controlling the ability of the reinforcement to transfer tensile forces to the surrounding concrete. The transfer of forces stiffens the behavior of the bare reinforcing bar by sharing some of the load carried by the reinforcement at a crack with the surrounding concrete. The concept is called tension stiffening and was comprehensively studied in the research carried out by Bischoff and Paixao (2004). The corresponding relationships provide a more fundamental approach by which the bond performance of the reinforcement can be included to establish the serviceability of elements reinforced with either steel or concrete.

Unfortunately, the concept of tension stiffening is rarely investigated on flexural elements but rather on specimens subjected to direct tension. Results can however be adapted to idealize the behavior of the reinforcement in the tension zone of flexural components with an averaged contribution of concrete between the cracks. Bischoff and Paixao (2004) performed their investigations on concentrically reinforced tension specimens and ensured continuity with previous research by selecting the use of GFRP reinforcement in their samples. A total of three bar diameters were considered in the research and the corresponding responses were compared to that obtained from a specimen with similar geometry and reinforced with a steel bar. Member deformation was measured over a pre-defined gauge length using two displacement transducers placed at opposite sides of the specimens. The parameter was divided by the gauge length to establish average member strain and evaluate the average tensile force resisted by the concrete between the cracks over the length of the member. This force was intended to be a measure of concrete contribution and its ability to stiffen the response of the bare FRP bar.

More specifically, Bischoff and Paixao (2004) derived the contribution of concrete beyond cracking by subtracting the bare bar response from the measured member response using average member strains recorded during the tests. The contribution was further divided by the concrete area surrounding the reinforcement to evaluate the average tensile stress carried by the cracked concrete. Bischoff and Paixao (2004) expressed the result as a declining fraction of the cracking

strength and plotted the parameter as a function of the average member strain. The parameter was referred to as a tension stiffening factor, which was observed to vary between 1 at cracking and 0 in the absence of bond. The authors suggested that the trend was attributed to a decrease in the contribution of concrete beyond cracking due to the progression of cracking and loss of bond.

Aside from establishing the tension stiffening factor, Bischoff and Paixao (2004) verified the adequacy of relationships provided in the CEB-FIP model code (1978) for estimating the response of concrete members reinforced with GFRP bars. The method proposed by the code consisted of a theoretical approach that uses the tension stiffening factor to establish member response using an effective or average bar stiffness accounting for the additional contribution of concrete between cracks. The estimate was found to be more accurate than the corresponding property defined in the ACI 224.2R (1986) report for steel reinforced concrete members subjected to direct tension. The researchers further stressed that the method proposed by ACI 224.2R (1986) was empirical and that, although it is well suited for design, it can only provide a reasonable prediction of axial deformation over a limited range of reinforcement ratios. The CEB-FIP model code (1978) therefore provides a more fundamental as well as reliable method by which the behavior of the reinforcement in a cracked flexural member can be idealized with the contribution of concrete between cracks.

The performance of relationships provided in the CEB-FIP model code (1978) was further confirmed by research conducted by Sooriyaarachchi et al. (2005) on GFRP reinforced concrete members tested in direct tension. The researchers investigated two grades of concrete as well as two bar diameters for concrete specimens with square cross-sections. Based on the concrete strengths and bar diameters considered, the research confirmed that the method proposed by ACI 224.2R (1986) grossly overestimated the tension stiffening response of the members. The result was particularly true for lower reinforcing ratios achieved in the research. Sooriyaarachchi et al. (2005) thereby indicated that relationships in the CEB-FIP model code (1978) provided a better understanding of tension stiffening. Conclusions are similar to those brought forward by Bischoff and Paixao (2004), which suggests that the expressions form a strong basis for developing equations that are more accurate in estimating the deflection of FRP reinforced concrete members.

1.2.3 Alternate Reinforcement for Concrete Structures

Research performed on the mechanical properties and bond characteristics of FRP reinforcement indicates that serviceability can play a significant role in the design of concrete beams reinforced with the material (Yost et al. 2003). Although existing modifications to Branson's effective moment of inertia equation for conventional steel can provide satisfactory results, they remain empirical and sensitive to the properties of the experimental data from which they were derived. As discussed, tension stiffening concepts can provide a fundamental approach for which these empirical forms of sensitivity can be eliminated from estimating the deflection of FRP reinforced beams. Nonetheless, alternate forms of reinforcement are also available to improve the properties of bare FRP reinforcing bars and provide flexural stiffness that eliminates the potential for violating serviceability limits imposed by design codes and guidelines.

Early research by Evans and Parker (1955) suggested the use of prestressed concrete units as reinforcement in floors and decks of fairly short span concrete bridges. In their investigations, the authors observed that composite beams did not exhibit sudden changes in strain or deflection when the cracking moment of the composite construction was reached. Experimental load-deflection curves showed stiffness transitions that were much more gradual than that observed for either reinforced or prestressed concrete beams. More importantly, some of the specimens showed only minute changes in flexural behavior and the researchers emphasized the difficulty involved in detecting as well as measuring crack widths at this stage. The authors clarified that the stage corresponded to a condition for which the pre-compressed units were still intact. The observations lead to the conclusion that the additional contribution of concrete provided the reinforcement with superior stiffness and that the use of prestressing delayed cracking of the units such that two distinct cracking moments were apparent for the beams. The researchers suggested that the concept was an attempt to lower the costs involved with normal prestressed concrete design while retaining the advantages of that type of construction. The savings were based on eliminating the need for unstressed concrete that has the required quality for prestressed applications as well as the added advantage from using the units as permanent forms for the composite construction.

Evans and Parker (1955) were primarily concerned with the bond performance of the units in the unstressed concrete environment. More specifically, they studied the influence of differential shrinkage and creep on bond interaction between the two types of concrete used in the composite construction. Three sets of beams were tested in the research, each of which made use of a different shape for the prestressed component. The research found that stresses induced by differential shrinkage and creep influenced the cracking load of the composite sections but did not show evidence of issues with bond performance between the prestressed and unstressed concrete.

Early research by Mikhailov (1958) also suggested the use of prestressed concrete units but as reinforcement in the walls of a water retaining concrete structure. The units were placed at the extremities of the structure and also served as formwork, which alleviated the cost of timber as well as the cost of labor for assembly. The models tested were regarded as strips from the wall that served the purpose of investigating the interaction between the precast prestressed components and the surrounding unstressed concrete. Although Mikhailov (1958) further noticed the difficulty in detecting crack widths in the wall when the prestressed units remained intact, the higher control over flexural cracking was limited by the small prestressing levels used for the elements placed in the tension and compression zones. Mikhailov (1958) stressed the requirement for additional investigation in which higher prestressing levels are considered and where the use of such elements is extended to structures other than those intended for massive hydraulic buildings.

Based on this statement, Hanson (1969) reported further work in which smaller pre-compressed concrete elements were introduced as reinforcement in the deck of continuous bridges. The prestressed prisms were intended to reinforce the deck concrete for continuity and control flexural cracking in the negative moment regions. Moreover, the restraining effect on cracking of the cast-in-place concrete surrounding the prestressed prisms caused the specimens to behave as though they were prestressed. Although post tensioning of the negative moment region had been widely used in Europe to develop continuity and eliminate cracking, the complexity and cost had been given as reasons for which the method had not become widely used in North America.

The research performed by Hanson (1969) considered three sets of T-beams, each of which presented a different section geometry as well as reinforcing scheme. In each set, the width and height of the flange were designed to accommodate the required amount of prisms. All prestressed prisms were singly prestressed. All specimens were tested in negative moment bending over a central support and experimental results did not show evidence of bond or anchorage failure of the concrete prisms. More importantly, the author closely monitored crack widths during each test to investigate continuity over the central support. Crack widths in the specimens reinforced with prestressed prisms were observed to be consistently smaller at any given moment than those observed for control beams reinforced with conventional deformed steel. Results from the research suggested that the new technique was ready for trial in the field.

Mirza et al. (1971) also discussed advantages of establishing continuity of precast, prestressed girders by placing prestressed concrete prisms in the cast-in-place deck across interior supports. As initially observed by Evans and Parker (1955), researchers emphasized the restraining effect of the prisms on the surrounding concrete and the fact that higher cracking moments in the negative moment regions provided better control of flexural cracking and superior levels of continuity. Mirza et al. (1971) further stated that previous studies had been limited to static tests and that the fatigue behavior of the composite section needed to be evaluated for the reinforcing technique to be usable and acceptable for developing the concept of continuity in highway bridge construction.

A total of two control beams were however tested under static loading conditions by Mirza et al. (1971) to determine the cracking and ultimate loads based on the material properties and section geometries chosen for the project. All beams were designed with a rectangular cross-section and were reinforced with a single prestressed concrete prism. The cracking strength of elements containing the prisms was found to be 58% higher than the cracking load of beams reinforced with conventional steel. Fatigue tests were also performed on beams tested over a central support, with the objective of determining the long-term behavior of sections reinforced with prestressed prisms under loading conditions similar to those at continuity connections in a highway bridge. In the first set of fatigue tests, repeated loads were chosen to peak at 50 to 100% of the cracking load for the prisms. Intermediate static tests were performed on the specimens at

a predetermined number of cycles to establish the variation in beam stiffness from the load-deflection curve. The load for these intermediate tests never exceeded the magnitude of the repeated load and results did not reveal any appreciable changes in the flexural stiffness for the composite beams. In the second and final set of fatigue tests, Mirza et al. (1971) subjected the beams to a repeated load 40% larger than that corresponding to cracking of the prisms. The beams were found to display a noticeable variation in flexural stiffness over the course of intermediate static tests.

The applicability of research performed by Hanson (1969) and Mirza et al. (1971) on the possible improvement of continuity across the interior supports of bridges was limited by the test setup selected. Consequently, Zia et al. (1976) improved the setup to consider the influence of prestressed prisms on moment redistribution away from the negative region. The setup extended the idea of a central support to that of two span continuous beams with an intermediate support centered between two end supports. Furthermore, the specimens cast for the research consisted of composite T-beams whose web was fabricated from two rectangular precast prestressed concrete stems with continuity over the intermediate support. The continuity was developed through a combination of prestressed prisms and conventional reinforcing bars introduced in a flange that was later cast in the laboratory above of the stems. A diaphragm reinforced with deformed steel bars was also cast at the intermediate support to connect the two precast prestressed stems. The shear resistance as well as the composite action of the T-beams was achieved by extending steel rebars through the stem into the flange.

The prestressed prisms were tensioned with a single tendon having similar properties as those used by Mirza et al. (1971). A total of two specimens, one for each of the prestressing loads selected, were tested under static conditions to establish the behavior of the composite sections at the cracking and ultimate stages. Moment redistribution from the negative region to the positive region was also monitored during the tests and showed a distinct deviation from elastic theory. A maximum moment redistribution of 34% was observed for beams reinforced with prisms having the highest prestressing load. Conversely, beams reinforced with prisms having the lowest prestressing level revealed a maximum moment redistribution of 36%. The results did not suggest any noticeable trend in moment redistribution with prestressing load in the prisms.

Fatigue tests in the research were divided into three sets. The first and second sets consisted of testing three composite beams at repeated load cycles having different peak loads. The peak load for the first fatigue test in each set was chosen to remain below the cracking stage for the prisms. Peak loads for the fatigue tests performed on the second and third beams in each set were chosen to reach and exceed the cracking load, respectively. Results from intermediate static tests indicated a gradual redistribution of moment as the number of cycles increased for both types of prisms considered in the research. The load-deflection response midway between each span was also used to establish the variation in flexural stiffness during these tests. In opposition to that observed for moment redistribution, the influence of peak loads over the set of selected fatigue cycles were shown to have a stronger influence on the variation of flexural stiffness. Larger residual deflections at midspan and lower flexural stiffness values were observed during the intermediate tests when larger peak loads were adopted for the cycles. The outcome was already observed by Mirza et al. (1971) and also held true for beams reinforced with prisms having a lower prestressing load. Zia et al. (1976) also confirmed that peak loads below the cracking stage did not appreciably influence the level of moment redistribution as well as the variation in flexural stiffness with increasing number of cycles.

Mirza et al. (1971) were the first to advise that maintaining service loads below the cracking strength of the prestressed prisms could also allow the crack-free zone around the strands to provide an adequate protection against corrosion. The concept was also pointed out in research performed by Chen and Nawy (1994), which suggested that the use of prestressed prisms could be extended to applications in offshore, marine or similar structures prone to corrosion in an environment where on-site prestressing may prove to be difficult and expensive. In light of recent developments in the area of high strength concrete, the researchers considered the use of concrete reaching compressive strengths in excess of 1.5 times that considered in previous research for prestressed prisms. The elements were designed with various cross-sectional geometries and prestressing levels. The number of prisms provided in the tension zone also varied and the primary focus of the research was to investigate the use of composite construction in reducing material costs and improving serviceability behavior. Simply supported four-point bending tests were performed on the composite beams and special considerations were given to study the influence of providing varying amounts of conventional steel deformed bars on the

flexural stiffness of the composite beams beyond the cracking stage of the prisms. Experimental load-deflection results revealed that the higher prestressing levels provided larger moments for which the flexural stiffness was enhanced by the presence of the prisms. Similar conclusions were reached when a larger number of prisms were provided in the tension zone but the condition reduced the space necessary to provide additional deformed steel bars. As a result, the reduction in flexural stiffness observed when the prisms reached their cracking stage was found to be larger without the additional contribution of deformed steel. The presence of steel in the tension zone was also found to provide higher ductility and warning of impending failure.

Although Chen and Nawy (1994) emphasized the added advantages of using a combination of deformed steel bars and prestressed prisms, enhancements to the serviceability of the beams was limited by the use of concrete with similar compressive strength than the prisms. The authors continued to use a similar approach in later research involved with further investigations on moment redistribution and continuity of precast sections over interior supports of bridge constructions (Nawy and Chen 1998). The authors considered two-span continuous T-beams loaded between the supports. The research mainly considered the influence of reinforcing schemes along the beam spans on the degree of moment redistribution and its significance on controlling flexural cracking over the interior support. For beams having similar prism reinforcing configurations over the intermediate support, higher steel reinforcing areas in the positive moment regions were found to cause a state of moment redistribution away from the negative moment regions. An opposite state of redistribution was observed for beams containing lighter steel reinforcing schemes in the positive moment regions. The condition was mainly attributed to the relatively lower flexural stiffness of the beams at the loading point regions and was also found to cause larger crack widths over the intermediate support. Unlike previous research, the result underlined the importance of providing sufficient stiffness along the beam spans to reach the desired improvements on continuity when using prisms over the interior supports.

The gradual introduction of FRP as reinforcement in civil infrastructure eliminated the need for introducing prestressed prisms to protect strands against corrosion. The lower elastic modulus values of some commercially available FRP bars, however, lead Svecova and Razaqpur (2000)

to extend the concept of prisms to improve the axial stiffness of the reinforcement in the tension zone. The main priority of the research was to provide a condition for which the full strength of FRP reinforcement could be utilized in design without the need for larger reinforcing areas to satisfy serviceability issues that arise from the lower flexural stiffness of concrete structures containing the reinforcement. In opposition to previous research, the authors considered the use of a polymer concrete for the prestressed units that was capable of reaching relatively higher strengths in direct tension. All beams were simply supported and tested under four-point bending. Over the range of jacking loads considered, the authors concluded that an increase in the level of prestress causes a reduction in deflection for beams reinforced with prestressed prisms. Based on results from their experimental program, Svecova and Razaqpur (2000) also emphasized that deflections were four times smaller than that corresponding to similar beams reinforced with the same amount and type of CFRP bar. As mentioned by Evans and Parker (1955) as well as Mikhailov (1958) for conventional steel strands, Svecova and Razaqpur (2000) also observed that the use of prestressed prisms with CFRP reinforcement had considerable restraint on the appearance and development of cracks beyond the initial cracking stage of the beams. The cracks are hairline and the behavior has considerable promise on the improvement of serviceability for concrete structures reinforced with FRP.

Experiments performed by Davoudi and Svecova (2008) elaborated on previous research to consider the use of prestressed prisms to preserve continuity in members with continuous spans. The researchers used an 8mm diameter CFRP reinforcing bar with the same properties as that used by Svecova and Razaqpur (2000) and fabricated geometrically similar prestressed prisms. For economical reasons, the research considered the use of high performance concrete for the prisms in opposition to polymer concrete. The ten prisms cast over the course of the project were used to reinforce the flange as well as the web of two continuous T-beams. While prisms in the flange were placed at the interior support, the remaining prestressed units were used to reinforce the web of the beams to investigate the combined influence of continuity and flexural stiffness enhancement within the spans.

All tests were performed using a servo-hydraulic testing machine from which the applied load was converted to two point loads on either side of the intermediate support. Loading was applied

monotonically until failure and paused at predefined intervals to monitor the development of cracks during the course of each test. While deflections were monitored at midpsan as well as below the point of load, the reactions were measured from load cells placed under each of the three supports. Support reactions were used to establish the distribution of moment along the length of the beam during the tests. Any observed deviations from elastic theory were attributed to a redistribution of moment between the negative and positive moment regions of the beam. A total moment redistribution of 6.4% was observed for beams reinforced with prestressed prisms. The result was lower than that measured in companion steel reinforced T-beams, which suggested higher continuity when using prestressed prisms as reinforcement in continuous bridge construction. The opposite condition was observed when considering the companion CFRP reinforced beams. The result was attributed to the higher reinforcing area needed for CFRP reinforcement to achieve the required moment resistance for beams in the study. Researchers stressed that the requirement for larger areas with bare CFRP reinforcing bars was an economical incentive to extend the use of prestressed prisms in civil infrastructure and reduce production costs. Hairline cracks monitored prior to the cracking stage for the prestressed prisms continued to show the considerable restraint of the units on the development of cracks in flexural members. According to the authors, the observation presented an additional advantage by which the onset of prism cracking can cause sufficient reduction in flexural stiffness to provide similar warning of impending failure as that achieved with steel reinforced beams. The safety margin would, however, depend on the level of prestress used in the fabrication of the prisms.

1.2.4 Transverse Swelling of FRP Reinforcement

The use of polymer concrete by Svecova and Razaqpur (2000) has considerable implications on the performance of prestressed prisms with FRP reinforcement. The higher strength of the material was originally intended to increase the direct tensile strength of the units as well as the cracking moment but had stronger impact on the resistance of the concrete cover to lateral expansion of the reinforcement when prestress was released. The condition was also observed by Davoudi and Svecova (2008), which emphasized the consequent restriction placed on the level of prestressing that can be applied to the prisms when considering the use of FRP reinforcement. The potential for damage in the concrete cover of prestressed concrete elements is characteristic

of the reinforcing bar's attempt to regain its original shape in the transverse direction upon release. As discussed in earlier sections, the wedge shaped expansion of the prestressing element in the anchorage zone is better known as the Hoyer effect, which can generate a state of radial and circumferential stress within the concrete cover. It is illustrated in Figure 1.2 and can be more pronounced for FRP reinforcement than conventional steel strands fabricated from a helical twisting of wires that have restrictive influence on lateral expansion.

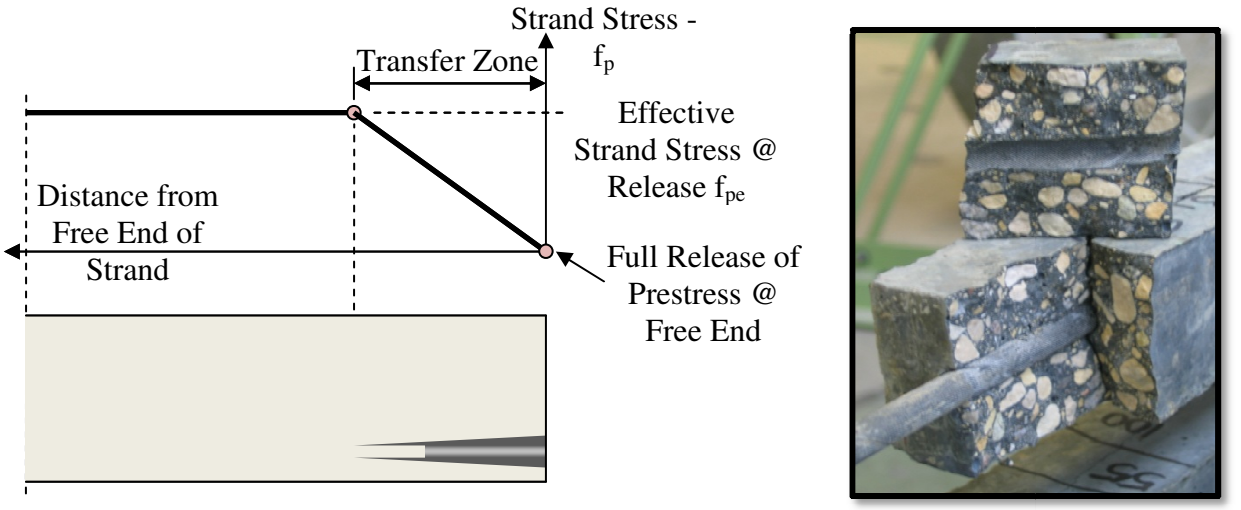

(a) Relationship with Transfer Zone (b) Prism Cover Splitting Failure

Figure 1.2 – **Lateral Expansion of Reinforcement in Transfer Zone** [Hoyer Effect]

Davoudi and Svecova (2008) also noticed that the alignment of fibers in the axial direction will bring thermal properties of FRP reinforcing materials to vary with orientation. More specifically, the properties in the longitudinal direction will be significantly influenced by the presence of the fibers while the resin will have a noticeable effect on those in the transverse direction. Due to the little moderating effect of fibers in the transverse direction, the transverse CTE of FRP reinforcement will be mainly affected by considerable swelling of the resin matrix under thermal action. As emphasized in earlier work by Aiello (1999), the CTE values of several FRP reinforcing bars can reach up to eight times that of concrete, which causes transverse swelling of both materials to be relatively different when considering temperature gradients. As a consequence of thermal loading, the incompatibility can generate additional stresses within the concrete cover and increase the likelihood of damage around the reinforcing bar.

Since circumferential stresses are tensile, the transverse swelling differential between FRP reinforcement and concrete will cause damage through initiation and development of cracks within the cover of structural elements. As the prestressing level or temperature increases, these longitudinal cracks will propagate away from the reinforcement towards the external surface of the elements until complete splitting of the cover occurs. The splitting phenomenon has been widely analyzed for traditional steel reinforced concrete members where bond interaction creates a wedging action of the reinforcement's surface deformations within the surrounding concrete during loading. Studies concerned with this mechanism of stress transfer have suggested that the development of longitudinal cracks within the cover can cause an abrupt drop in bond strength followed by a brittle bond failure (Aiello 1999).

1.2.4.1 Linear Elastic Representation of Transversely Induced Stresses

Rahman et al. (1995) was the first to thoroughly investigate transversely induced stresses and the main parameters affecting their development. The stresses investigated in the study were caused by thermal swelling of FRP reinforcement in a concrete environment. The research clearly identified the anisotropic nature of FRP reinforcement and found that the modulus of elasticity and CTE of the material in the transverse orientation were the key properties affecting thermal stresses within the cover. Establishing these properties on the basis of experimental work and confirming with theoretical estimates, the research incorporated differential transverse swelling of the reinforcement in a linear elastic axisymmetric formulation that was initially developed by Timoshenko and Goodier (1970) to investigate thermal stresses within the cover of concrete cylinders surrounding the reinforcement. The analysis concluded that thermal stresses arising from typical temperature gradients in the Canadian climate could instigate cracking in concrete elements reinforced with FRP, possibly leading to reductions in bond strength.

Aiello (1999) further investigated the development of thermal stresses within the cover of concrete elements reinforced with FRP by conducting a similar analysis. The analysis was carried out by defining possible failure mechanisms of the concrete cover and removing axisymmetric assumptions from the thermal stress problem previously assumed by Rahman et al. (1995). Assuming linear elastic material behaviour, the analytical procedure consisted of

dividing the concrete cover into triangular elements and determining the thermal loading at splitting on the basis of limiting strength conditions. The model presented by Aiello (1999) was verified with an experimental program consisting of concrete members reinforced with aramid FRP (AFRP) reinforcement at various depths to investigate the influence of concrete cover provisions. The specimens were subjected to thermal gradients inside a furnace until longitudinal cracks appeared on the external surface. For the two levels of concrete compressive strengths considered in the research, it became apparent that the model was in agreement with experimental results for small concrete cover values corresponding to concrete cover to bar diameter ratios below 2.0. However, for concrete cover to bar diameter ratios beyond 2.0, the critical temperature observed during the experiments was consistently lower than that predicted by the analytical model.

Aiello (1999) attributed the divergence between experimental and theoretical results to the presence of nonlinear phenomena. The concept was not considered in the model and was thought to create a redistribution of stresses between the concrete and reinforcement. The concluding remarks of the research stressed the need for improvement of the theoretical model by incorporating nonlinear phenomena and evaluating its effect on concrete cover failure of FRP reinforced concrete structures subjected to thermal loading.

1.2.4.2 Non-Linear Elastic Representation of Transversely Induced Stresses

In light of conclusions obtained from the use of linear elastic thermal stress expressions, de Schutter et al. (1997) examined a two-dimensional non-linear finite element analysis of thermal incompatibility between FRP reinforcement and concrete. The research was specifically concerned with the high transverse CTE of AFRP reinforcement and thermal stresses that subsequently develop within the cover. Prestressed prisms with equal sides were considered in the analysis to investigate the additional influence of prestress release. The added source of transverse expansion was introduced as an equivalent thermal loading in the research.

It was clear from the finite element analysis that transverse thermal expansion of FRP reinforcement had a considerable influence on the concrete cover required to prevent the

occurrence of the splitting phenomenon. The researchers recognized the importance of considering the Hoyer effect by noting a 50% increase in the concrete cover required to prevent splitting under a simultaneous temperature increase of 60^{o}C. However, the research noticed that the concrete tensile strength had a considerable effect on and strong potential in preventing the development of cracks within the cover. More specifically, the Hoyer effect on critical concrete cover was found to reduce by 27% when increasing the compressive strength from 45 to 90MPa. The result justifies the use of polymer concrete by Svecova and Razaqpur (2000) as well as the requirement for higher compressive strength concrete in prisms that are prestressed with FRP reinforcement.

1.3 PROPOSED RESEARCH

1.3.1 Deflection of Concrete Beams Reinforced with FRP

Based on past research and previous discussions, it is clear that the empirical form of Branson's equation has limitations from which the long-term deflection of certain steel reinforced concrete structures cannot be accurately estimated. The mechanical and bond properties of FRP reinforcement are distinctly different from that of conventional steel and the limitations of Branson's expression also apply to the estimation of short-term deflection in concrete elements reinforced with the product. Although numerous modifications have been suggested to improve the relationship and provide more accurate estimations of deflection for concrete reinforced with FRP, their form remains empirical and sensitive to the properties of data from which they were established.

In accordance with this observation, the first portion of this thesis will consider recent research to assess Branson's work and establish a more fundamental approach for estimating deflection of concrete elements reinforced with FRP. The assessment will adapt tension stiffening concepts to adjust the behavior of reinforcement in the tension zone of flexural elements and account for the average contribution of concrete between cracks. The technique will allow the derivation of a new expression for effective moment of inertia and is comparable to stiffening the response of the bare bar by considering an effective area of concrete at the level of the tension reinforcement.

It is an attempt to mend earlier research involved with improving the estimation of long-term deflection in steel reinforced concrete beams and recent research concerned with the accuracy of estimating deflections for FRP reinforced concrete.

Since tension stiffening concepts are based on theoretical derivations that include the distinctive properties of the reinforcement, they provide a more rational approach to the estimation of deflection. With the additional consideration for material non-linearity at higher service loads, the expression for effective moment of inertia developed for this project will finally be compared to existing modifications for Branson's effective moment of inertia expression. The comparison will be achieved by undertaking a statistical analysis on a database containing the load-deflection response of beams reinforced with various types of FRP products.

1.3.2 Prestressed Concrete Prism Reinforcement

Previous discussions have also shown that it is the distinct bond performance and relatively smaller modulus values of FRP reinforcement over conventional steel that prevent the full strength of the material to be exploited through smaller reinforcing areas in the design process. As suggested in more recent research, the condition can be improved by introducing the use of prestressed prisms as reinforcement in concrete structures containing FRP materials. The concept restrains cracking and provides an enhancement to flexural stiffness that allows the use of smaller reinforcing areas and provides better means for utilizing the reinforcement's strength. Unfortunately, the wide range of material properties available for FRP reinforcement complicates the selection process for concrete and prestressing level if the desired behavior of the pre-compressed unit is to be successfully achieved.

In accordance with this situation, the current project will provide a detailed outline on the influence of each material on the behavior of the prestressed prisms. A strong emphasis is intended to be placed on considering the influence of the Hoyer effect and its potential for damaging the concrete cover of the prisms in the transfer region when prestress is released. Based on an analytical formulation of concrete stresses available in the literature, the thesis will establish the extent of prestressing that can be achieved without a degradation of bond that would

arise from the occurrence of cracks within the cover. The process will allow critical design charts to be developed from which a given combination of prestressing level and prism geometry can be selected. One of the charts is shown in Figure 1.3(a) for illustrative purposes as well as for a given concrete compressive strength. The charts will be elaborated to consider the mechanical properties for a wide range of concrete mix designs and extended to account for thermal swelling of the reinforcement in its environment.

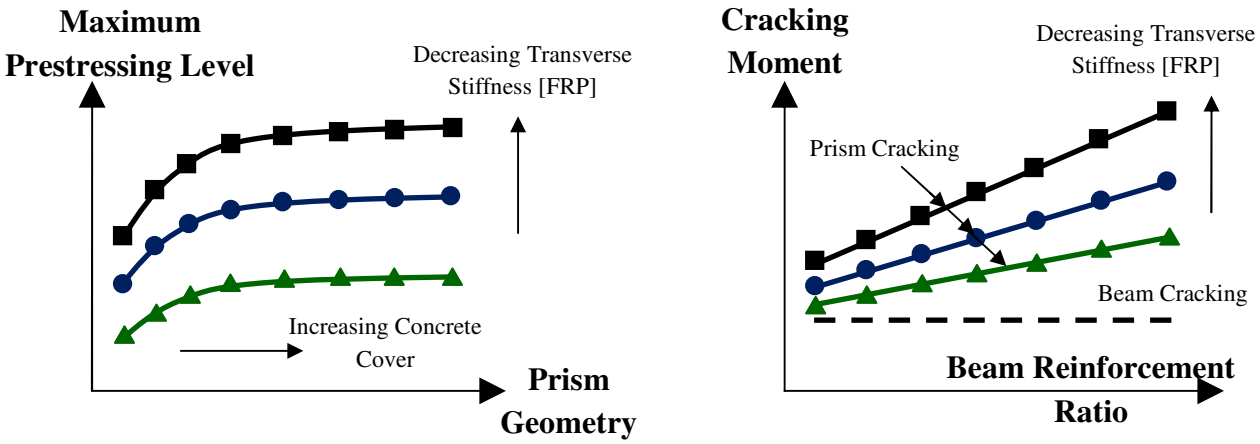

(a) Critical Prestressing Level & Geometry

(b) Cracking Moment & Reinforcing Area

Figure 1.3 – **Design Charts for Prestressed Prism Reinforcement**

Based on results obtained from these charts as well as recommendations from the CSA S806-02 code for the design and construction of building components with FRP, an additional set of design charts will be developed for the designing engineer. The charts will consider an optimum prism geometry that prevents damage of the concrete cover and provide the designing engineer with a set of tools to establish the range of moments for which the flexural stiffness of the reinforcement is enhanced by the prestressed prism concept. As illustrated in Figure 1.3(b), the range corresponds to the difference between the moment for which the beam cracks and the moment for which the prisms reach their cracking stage. Results will be extended for the selection of a reinforcement ratio that allows the desired range of moments under service conditions to be achieved for beams containing prestressed prisms.

1.3.3 Experimental Program

Prior to the introduction of FRP as reinforcement in concrete structures, the use of prestressed concrete prisms had been widely studied with conventional steel strands. As discussed in earlier sections, the pre-compressed elements were initially considered for economical reasons but researchers gradually developed the concept around the discovery of additional advantages. Their restraint on flexural cracking was rapidly found to improve the corrosion protection of the bare reinforcement and provided a means for ensuring continuity at the interior supports of bridge construction. Subsequent research on the concept was therefore aimed at investigating the use of prestressed prisms over continuous supports, which prevented researchers from fully studying their potential on improving deflection in the positive moment regions.

Although some researchers have studied the influence of either steel or FRP prestressed prisms on the flexural stiffness in positive moment regions, the extent of experimental data available in the literature is restricted. The condition stresses the need for more research with extended details on serviceability. The experimental program of this thesis firstly addresses the issue by extending previous research and investigating the response of beams reinforced with FRP prestressed prisms in their positive moment regions. Based on suggestions from earlier work, the program will also be extended to compare the performance of these beams to those prestressed with a bare FRP reinforcing bar.

As anticipated, the bond performance of the prisms will depend on a concrete-to-concrete interface and special attention will also be brought to studying the stabilized crack pattern and establishing estimates for average bond strength. In light of optimizing axial stiffness as well as cracking strength for the prestressed prisms, the project enforced the use of concrete with higher compressive strength than that used for the beam. Since higher strength concrete is employed, the average values of bond strength will be used to confirm or suggest revisions to estimates presented in the CSA A23.3-04 design code for composite construction consisting of normal strength concrete elements cast at separate times. Additional instrumentation will also be provided in the vicinity of cracks to investigate the optimum bond performance of the high strength concrete in its normal strength environment.

Based on previous sections, it is strongly suggested that FRP reinforcement has the potential to initiate and develop cracks within its surrounding when prestress is being released and thermal gradients considered. To optimize prestressing level and performance, prisms in this research were designed without allowance for thermal gradients. Since concrete cover damage from thermal weathering can create a state of stress relief around the reinforcement followed by deterioration of the bond between the materials, a portion of the prisms in this research will be subjected to thermal gradients expected in the Canadian climate. The gradients will be applied to the prisms in their embedded state within the beams to investigate the influence of confinement provided by the presence of stirrups and surrounding concrete. The weathering process will be followed by flexural tests to evaluate the influence of thermal action on flexural response. Any conceivable deviation in the response will be attributed to a loss in the performance of the prestressed prisms, which depends on and will be related to the degree of thermal compatibility between the FRP reinforcement and high strength concrete.

Previous discussions have also suggested that the performance of prisms prestressed with FRP reinforcement has not been investigated under repetitive loading conditions. The current study will therefore be extended to consider the fatigue performance of beams containing the elements with cycles selected from information and conclusions that evolved from previous research. In the final stages of the research, an effort will be made to enhance the performance of prestressed prisms with the inclusion of surface deformations on the sides of the elements as well as the addition of dispersed fibres in the high strength concrete mix. While surface deformations will improve the bond performance of the prisms and influence the post-cracking behaviour of the beams, the addition of fibres will increase the cracking load of the elements and increase the service loads for which the flexural stiffness is enhanced. Static tests performed in this final stage of the experimental program will be accompanied by a detailed investigation on improvements achieved for the flexural stiffness at and beyond the cracking stage.

1.4 RESEARCH OBJECTIVES

The objectives of the research were established using arguments presented in previous sections and are more concisely stated below. They include goals set out for the deflection analysis of

beams reinforced with FRP reinforcement, the detailed outline on factors influencing the behavior of prestressed prisms and the experimental program of the project.

[1] Consider tension stiffening concepts to establish a more fundamental as well as rational relationship for effective moment of inertia that describes the gradual reduction in flexural stiffness beyond cracking for beams containing FRP reinforcement.

[2] Provide a thorough analysis of stresses arising from the differential swelling of FRP reinforcement in a concrete environment, from which design charts can be established for the use of prestressed prisms as reinforcement in concrete structures.

[3] Conduct an experimental program to provide insight on the performance of beams with prestressed prisms and establish bond performance of the units in a concrete environment subjected to the potentially damaging effects of thermal gradients and repeated loading.

1.5 RESEARCH SCOPE

The tension stiffening concepts used in the derivation process of the effective moment of inertia relationship for beams reinforced with FRP reinforcement will be based on expressions presented by Bischoff and Paixao (2004) for reinforced concrete members subjected to direct tension. Their inclusion will serve as an idealization of the reinforcement in the tension zone of flexural elements where an additional area of concrete is effective in resisting a portion of the load beyond cracking. The model accounts for the additional contribution of concrete between cracks along the length of flexural members loaded beyond the cracking stage. The influence of material non-linearity for concrete in compression will also be factored into the derivation to overcome the under-estimation of deflection at larger service loads. The ability of the relationship to incorporate the behavior of the reinforcement in a concrete environment will finally be tested by considering a database containing the load-deflection response of GFRP, CFRP as well as AFRP reinforcing bars. The database allows a wide range of mechanical properties and surface preparation for FRP reinforcement to be considered.

The analysis of concrete stresses to prevent cover damage of the prisms after prestress release and thermal loading will be based on expressions presented by Rahman et al. (1995). The formulation is based on a linear elastic axisymmetric formulation that was initially developed by Timoshenko and Goodier (1970) to investigate radial as well as circumferential stresses within the cover of a concrete cylinder surrounding the reinforcement. In establishing design charts for the optimum combination of prism geometry and prestressing level, the analysis will incorporate the influence of such a biaxial state of stress on the tensile strength and the initiation of cracks within the concrete cover.

The experimental program will consider CFRP as the prestressing reinforcement. The high strength concrete for the prestressed prisms will be based on a design developed by the Portland Cement Association (PCA) Research and Development Bulletin RD104T (1992) with the required chemical admixtures. Both prestressed beams and beams reinforced with prestressed prisms will be tested under a third-point loading scheme to achieve a comparative measure of flexural stiffness improvements in positive moment regions. The behavior of control specimens will be thoroughly evaluated with respect to the response of beams subjected to a combination of repeated loading as well as thermal cycles ranging between $-30^{o}C$ and $+40^{o}C$, which are typical extremes of temperature expected in the Canadian climate. Based on the design philosophy of prestressed prisms in this research, any deviations in the behavior will be associated with performance loss of the reinforcing alternative and related to the fatigue behavior of prestressed prisms as well as the degree of thermal incompatibility of FRP reinforcement in concrete.

CHAPTER 2

DEFLECTION OF CONCRETE BEAMS REINFORCED WITH FRP

2.1 GENERAL

The current chapter will provide a review on the response of reinforced concrete flexural members. The review will shed light on the gradual decline in flexural stiffness that is typically observed beyond cracking and present code relationships for effective moment of inertia that are used to describe this reduction. The limitations of these expressions in estimating the deflection of concrete beams reinforced with Fiber Reinforcement Polymer (FRP) will be discussed and addressed by proposing a more rational expression for effective moment of inertia. The development of the relationship (Vogel and Svecova 2008, Vogel and Svecova 2009) relies on the consideration of tension stiffening concepts that account for the declining contribution of concrete surrounding the reinforcement in the tension zone. The chapter will establish the accuracy of the proposed expression using a database that contains experimental load-deflection records from glass FRP (GFRP), carbon FRP (CFRP) and aramid FRP (AFRP) reinforced concrete beams tested by other researchers. As an added advantage over code expressions, the database will also be used to improve the accuracy of the relationship by providing calibration factors that account for the influence of concrete non-linearity in compression.

2.2 RESPONSE OF REINFORCED CONCRETE MEMBERS

The response of reinforced concrete members subjected to flexure can be divided into two stages. The first stage describes the uncracked response of the member for which the flexural stiffness is highest. If the moment is increased sufficiently, cracks will initiate at the extreme tension fibers where the tensile strength of concrete is reached. The condition marks the onset of the second stage, which describes the cracked response of the member. Once this stage has been reached, the absence of tensile resistance from concrete at the cracks will require loads to be entirely carried by the reinforcement. The flexural stiffness of the reinforced concrete member is greatly reduced within this stage but the cracked response remains well above that of a member that is fully cracked. The phenomenon arises from the ability of the reinforcement to bond and transfer some of the tension to its surroundings, which leads to the contribution of concrete between individual cracks. With further loading, stresses within the concrete on either side of a crack increase until the tensile strength is once more reached, causing the development of additional cracks. The process continues until crack spacing is insufficient to bring tensile stresses within the concrete to initiate new cracks. The resulting crack pattern is referred to as the stabilized crack pattern where additional load widens existing cracks with limited effects on flexural stiffness. The behavior is graphically described in Figure 2.1(a) through the use of a flexural member's load-deflection response.

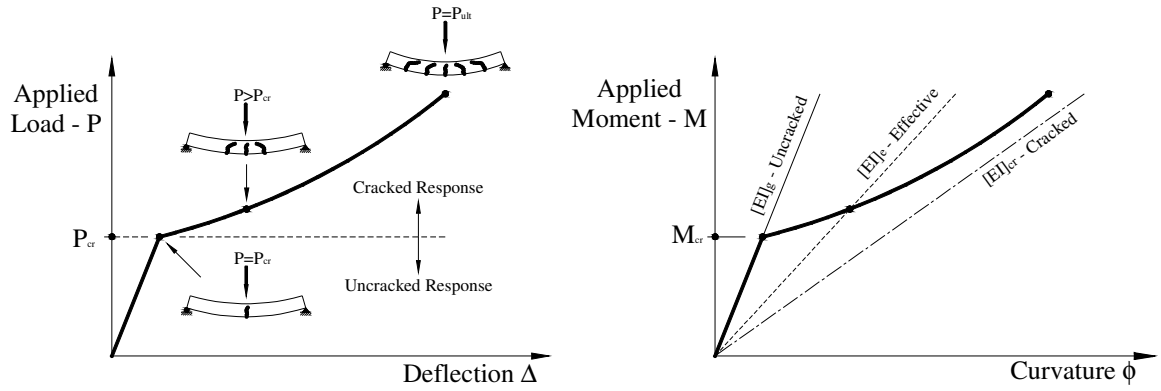

(a) Load-Deflection (b) Moment-Curvature

Figure 2.1 **- Flexural Response of Reinforced Concrete Members**

The figure clearly shows stiffer flexural behavior prior to the formation of cracks and emphasizes the gradual reduction of stiffness beyond the cracking stage. Figure 2.1(b) further illustrates the reduction as being representative of a transition from the flexural stiffness of a gross section E_cI_g to that of a section for which the element is fully cracked E_cI_{cr}. Although transformed section properties reflect the exact behavior of uncracked elements, code relationships typically use gross section properties when approximating the deformation of beams prior to and after cracking. The properties are more easily calculated and provide smaller uncracked flexural stiffness for conservative estimates of deflection.

2.2.1 Existing Code Relationship

Code equations used to determine the effective flexural stiffness of reinforced concrete elements within the transition range of Figure 2.1(b) are developed to reflect a softening effect on moment of inertia. More specifically, the ACI 318 (1966) building code requirements as well as the CSA A23.3-04 design handbook provide a common expression for establishing the parameter in analyzing the deflection of concrete beams reinforced with steel.

$$I_e = \left(\frac{M_{cr}}{M}\right)^3 I_g + \left(1 - \left(\frac{M_{cr}}{M}\right)^3\right) I_{cr} \qquad \text{EQ2.1}$$

In this equation, I_e is the effective moment of inertia, M_{cr} is the cracking moment computed from gross section properties, M is the applied moment, I_g is the gross moment of inertia and I_{cr} is the cracked moment of inertia. As emphasized by Yost et al. (2003), the cubic form of EQ2.1 was intended to represent the nonlinear characteristics of the transition for which the contribution of concrete declines between the cracks. The expression is based on work presented by Branson (1963) and was derived from experimental data of concrete beams reinforced with conventional steel. Researchers agree, however, that the empirical nature of Branson's research brings sensitivity to the

relationship for conditions other than those for which it was derived (Yost et al. 2003, Bischoff and Paixao 2004).

2.2.2 Limitations of Code Relationship

One of the main limitations of Branson's equation arises from the fact that it was calibrated from experimental data using gross section properties. As opposed to the cracked moment of inertia, the gross moment of inertia does not account for the axial stiffness and, more specifically, for the density of reinforcement in the tension zone. Consequently, the contribution of uncracked segments along the length of a cracked flexural member does not alter when considering sections having different reinforcement ratios.

When lower reinforcement ratios are considered, the larger crack widths as well as the larger curvatures arising from the requirement of force equilibrium at any given applied moment should cause a faster transition in flexural stiffness. Conversely, the larger force that each bar is required to sustain will also increase crack spacing to prevent the average shear stress at the surface of the reinforcement to exceed the bond strength. Unlike the condition for crack width and curvature, an increase in crack spacing suggests higher contributions of the uncracked segments along the length of the member and therefore a slower transition in flexural stiffness. According to the results of Figure 2.2, Branson's expression (EQ2.1) suggests that the influence of crack width and curvature is more influential than crack spacing such that a faster transition in effective moment of inertia, and therefore flexural stiffness, should prevail for decreasing reinforcement ratios. The figure shows that the result is valid for loads ranging from 40 to 80% of ultimate.

It is also apparent from the figure that the moment of inertia remains consistently farther from the fully cracked condition as lower reinforcement ratios are considered. Although this observation has been shown to be accurate for the range of properties studied by Branson (1963), it should be noted that the outcome can be moderated if transformed section properties were used to account for reductions in reinforcement ratio. The

relationship proposed by Branson to estimate deflection of steel reinforced concrete beams can therefore find itself limited by the use of gross moment of inertia values. The limitation has been documented in the literature and it is generally shown that the flexural stiffness transition provided by the expression is excessively soft and that member deformation is underestimated for relatively low reinforcement ratios corresponding to ratios of gross to cracked moment of inertia exceeding 4 (Bischoff and Paixao 2004). Although significant in the design of steel reinforced concrete, the limitation can reach stronger relevance when considering the use of alternate reinforcing materials for which different mechanical properties prevail.

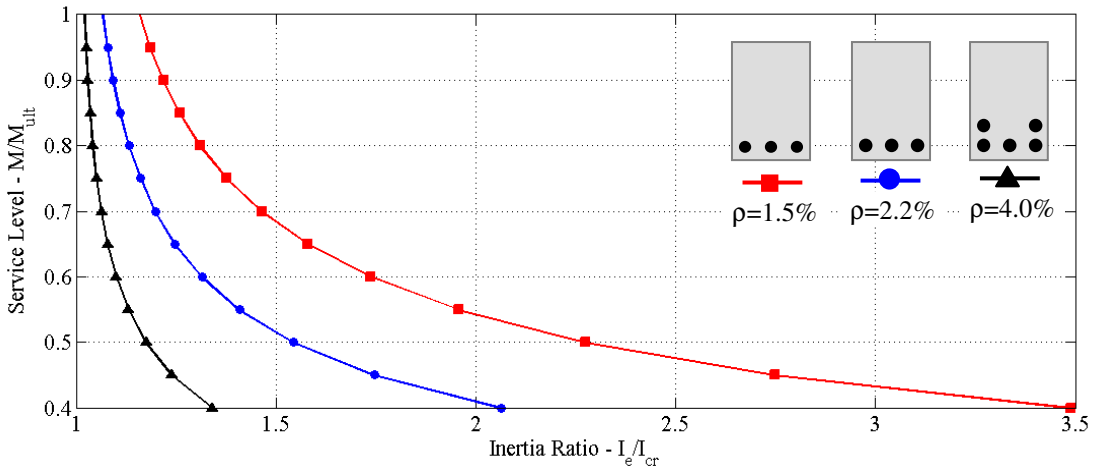

Figure 2.2 **– Effective Moment of Inertia Transition**

2.2.3 Code Relationship Modifications for Alternate Reinforcement

The use of FRP as reinforcement in concrete structures has greatly increased over the last decade due to concerns with corrosion of conventional steel. The resulting interest in FRP reinforcement has lead many researchers to recognize that properties can differ significantly from that of steel reinforcement. This is more clearly illustrated in Figure 2.3 (ACI 440.1R-01) where tensile properties of CFRP as well as GFRP reinforcement are outlined with respect to conventional steel.

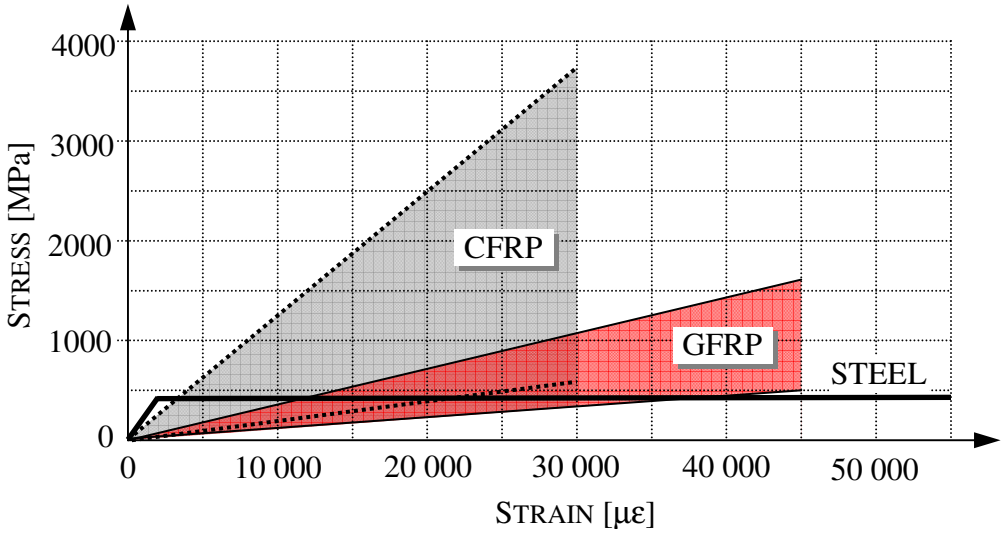

Figure 2.3 **- Mechanical Properties of FRP Reinforcement**

In particular, the figure illustrates that a wide range of mechanical properties exist for FRP reinforcement and that tensile strengths typically exceed the yield strength of steel. These relative magnitudes indicate that lesser FRP reinforcing areas are required to achieve resistances that are similar to those obtained from sections reinforced with steel. These areas can potentially fall below those for which Branson's effective moment of inertia is applicable. Unfortunately, codes and guidelines for the design of concrete structures with FRP products generally emphasize the non-ductile behavior of the reinforcement for which rupture can cause sudden as well as catastrophic failures in flexural members. It is therefore commonly recommended for the reinforcement ratio to be increased beyond that required for the balanced condition such that higher warning of impending failure is exhibited through plastic deformation of concrete in compression (ACI 440.1R-01). Due to the higher ultimate strength and strain values of FRP reinforcing bars, the balanced reinforcement ratio of FRP reinforced members still remains persistently lower than that for steel reinforced members. The result is particularly true for FRP materials of higher strength. Thus, although it is commonly agreed for compression failures to be more desirable for FRP reinforced concrete structures (Nanni 1993b), the higher reinforcement ratio requirement can still maintain the possibility of violating the limitations set out by Branson's equation.

Early modifications of Branson's equation did not account for the effect of reinforcing area. Instead, work by Gao et al. (1998a) attributed Branson's overestimation of flexural stiffness for concrete beams reinforced with FRP to the relatively low elastic modulus values of the reinforcing material. It was also recognized that the surface roughness or deformations of commercially available FRP products did not possess characteristics that were inherent to conventional steel (Tighiouart et al. 1998). Research from Gao et al. (1998a) therefore proposed a reduction factor κ that would not only compensate for the lower elastic modulus but also for the different bond performance of the material in a concrete environment.

$$I_e = \kappa\left(\frac{M_{cr}}{M}\right)^3 I_g + \left(1-\left(\frac{M_{cr}}{M}\right)^3\right) I_{cr} \qquad \text{EQ2.2}$$

$$\kappa_{ACI\text{-}01} = \alpha_b\left(\frac{E_f}{E_s}+1\right) \qquad \text{EQ2.3}$$

While E_f and E_s are the respective elastic modulus values for FRP and steel, α_b was defined as a bond coefficient. The modification, denoted $\kappa_{\text{ACI-01}}$, was initially proposed by Gao et al. (1998a) and later adopted by ACI Committee 440 (2001) as well as by ISIS Design Manual 3 (2001). It was clearly stated in each document, however, that the suggested bond coefficient value of 0.5 could be used for all types of FRP reinforcement but that additional data was required for a more comprehensive evaluation of the parameter.

Since the proposal of this parameter, researchers have noticed that the softening effect of the bond coefficient proposed by Gao et al. (1998a) was not fully sufficient in estimating the flexural transition, and therefore deflection, of beams reinforced with FRP material. Although research suggests reasonable agreement of the coefficient with experimental data of highly over-reinforced beams, under-reinforced beams continue to compel the need for considering the effects of reinforcement density (Yost and Goodspeed 2001).

Yost et al. (2003) investigated an extensive population of 48 beams to maintain an acceptable level of reliability in the results while providing a detailed evaluation of the effect of reinforcement density. The research provided a modification to Branson's equation in which the reinforcement density relative to a balanced strain design was incorporated (EQ2.4). The modification factor replaced the bond coefficient but continued to consider the effect of relative elastic modulus values on effective moment of inertia. A similar approach was also adopted by ACI Committee 440 (2006) but the possible effects of elastic modulus on the transition of flexural stiffness beyond cracking were discarded (EQ2.5).

$$\kappa_{YOST\text{-}03} = \left(0.064\frac{\rho_{frp}}{\rho_b} + 0.13\right)\left(\frac{E_f}{E_s} + 1\right) \qquad \text{EQ2.4}$$

$$\kappa_{ACI\text{-}06} = \frac{1}{5}\frac{\rho_{frp}}{\rho_b} \qquad \text{EQ2.5}$$

2.3 REVISED APPROACH TO FLEXURAL STIFFNESS TRANSITION

Although numerous researchers have established the limitations of Branson's relationship for effective moment of inertia, the empirical nature of the modifications presented in the preceding section remain constricted by the properties of the experimental database chosen for statistical analysis. Researchers have continuously emphasized the need to re-evaluate Branson's work for developing a rational approach capable of predicting member deformation for concrete members containing reinforcement other than steel (Bischoff and Paixao 2004). Extensive research has been performed to study the behavior of reinforced concrete elements beyond the cracking stage and theoretical concepts found in the literature can be adapted to describe the cracked response of flexural members. An effective moment of inertia relationship developed on the basis of these concepts can improve statistical stability as well as accuracy for estimating the deformation of a wider range of beams that have material as well as geometric properties lying outside of that considered in previous research.

2.3.1 Factors Influencing Deflection of Reinforced Concrete Members

Previous sections have outlined parameters that are essential in describing the deformation of concrete members reinforced with either steel or FRP material. These parameters arise from extensive research and their contribution to the softening in flexural stiffness beyond cracking have been established to calibrate Branson's equation for estimating deflection of concrete members reinforced with FRP. It should also be noted from the discussion of Section 2.2.2 that the development of cracking along the length of a concrete member is a primal contribution to this gradual transition in stiffness. Before a revised approach to flexural stiffness transition can be initiated, the distribution of cracking in a flexural member should be studied to confirm the influence of parameters established in earlier research.

For this purpose, Figure 2.4 illustrates a flexural member loaded beyond the cracking stage. At the location of cracks, tensile forces are solely carried by the reinforcement and crack widths are governed by the elastic modulus of the reinforcement. The relatively low elastic modulus values of Figure 2.3 suggest that larger strains, and therefore crack widths, are expected in concrete elements reinforced with FRP reinforcement than in those reinforced with steel. The higher curvatures arising from these larger crack widths will strongly influence deflection, which suggests the need for including elastic modulus to calculate the effective moment of inertia. The requirement was confirmed by Gao et al. (1998a) as well as Yost et al. (2003). Each researcher brought modifications to the gross section properties of Branson's equation in which elastic modulus was originally not considered.

In order to identify the remaining factors influencing the deflection of reinforced concrete members, we need to investigate the stress condition between adjacent cracks. Between these cracks, tensile forces are gradually transferred to the concrete through shear stresses at the surface of the reinforcement. The actual shear stress distribution is shown in Figure 2.4, but an average value is typically used to describe the force transfer between the materials. The total force transferred to the concrete is equivalent to the difference in

tensile forces between adjacent cracks. By allowing a reduction in tensile force between the cracks, the contribution of concrete stiffens the response of the reinforcement. The concept is called tension stiffening and has significant influence on the spacing of cracks.

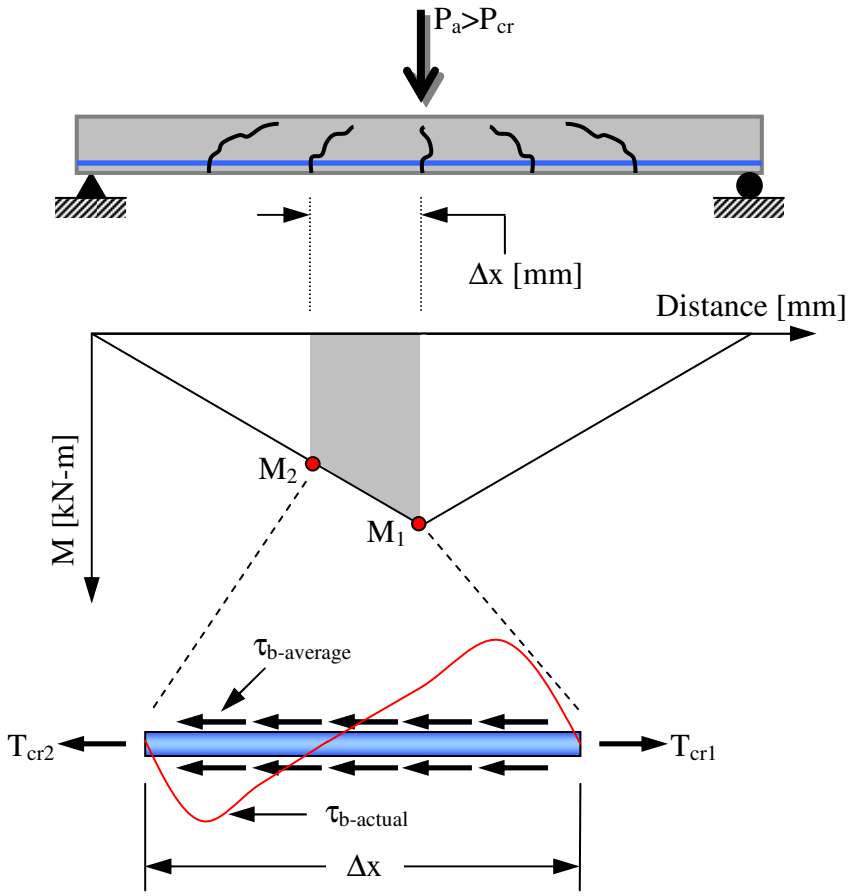

Figure 2.4 **- Bond Performance of Tension Reinforcement**

This average crack spacing Δx can be established by considering force equilibrium of the bar segment shown in Figure 2.4 between adjacent cracks. The requirement will give an expression that relates average bond stress $\tau_{b\text{-}average}$ to the total force transferred from the reinforcement ΔT_R (EQ2.6) to the concrete. In this equation, the circumference of the bar has been expressed in terms of the reinforcing area A_R. Furthermore, the total force transferred to and resisted by the concrete ΔT_C cannot exceed that which will cause cracking. If a given concrete area A_c is assumed to contribute between the cracks, the

maximum transferable tensile force can be written in terms of the concrete tensile strength f_r (EQ2.7).

$$\Delta T_R = \left(\frac{4A_R}{d_b} \Delta x \right) \tau_{b\text{-}average} \qquad \text{EQ2.6}$$

$$\Delta T_C = A_c f_r \qquad \text{EQ2.7}$$

Equilibrium requirements between the reinforcement and concrete are met when forces transferred from one medium to the other are equal. As a result, EQ2.6 and 2.7 can be combined to determine the average crack spacing (EQ2.8). The parameter is related to the average bond stress as well as the ratio of area between reinforcement and concrete ρ_R.

$$\Delta x = \frac{f_r d_b}{4\tau_{b\text{-}average}\rho_R} \qquad \text{EQ2.8}$$

According to the relationship of EQ2.8, the crack spacing will decrease if the concrete or reinforcement provides superior bond performance. Larger reinforcement ratios will have the same effect on crack spacing since each reinforcing bar is required to carry smaller tensile forces at any given moment. Ultimately, the relationship confirms the choice of Gao et al. (1998) and Yost et al. (2003) to include effects of bond performance as well as reinforcement density in their modifications to Branson's equation. Although highly documented in the literature through tests conducted on FRP reinforced elements tested in direct tension, their effect on crack spacing and deflection has conceptual complexity.

More specifically, the narrower crack spacing arising from higher bond performances should indicate a more rapid force transfer between the reinforcing material and concrete. Although larger concrete contribution is theoretically expected, the larger number of cracks along the length of the member will suggest a physical behavior that is closer to that of a fully cracked member. A similar form of contradiction holds for lower bond performances, where the smaller number of cracks arising from larger crack spacing and

smaller concrete contribution suggests a behavior that is closer to that of an uncracked member. The condition was already discussed in earlier sections when the softening effect of Branson's equation was presented in Figure 2.2. Although the impact of these parameters on the concrete area that is effective in resisting tension along the length of a flexural member can be as significant as their complexity, relationships in the literature are available to consider them in any deflection analysis such as the one performed in this thesis. The expressions will be presented in the following sections to develop a procedure that is more rational than Branson's equation for establishing the effective moment of inertia of beams containing reinforcement with properties other than steel.

2.3.2 Effective Concrete Area in Tension

Analytical studies concerned with the post-cracking behavior of reinforced concrete beams or slabs are mostly aimed at modeling the contribution of concrete between cracks (Gilbert 1983). Branson (1963) has initially considered this contribution by suggesting a model in which a portion of the concrete surrounding the reinforcement remains effective in resisting tensile forces beyond the cracking stage. The effective concrete area concept is illustrated in Figure 2.5(a) for a singly reinforced concrete beam after cracking. The area contributes to the gradual loss in flexural stiffness after cracking and its breadth mainly depends on the magnitude of the moment applied. As a result, relationships for the contribution of concrete were developed to reduce the effective concrete area with an increase in applied moment. As illustrated in Figure 2.5(b), the relationship proposed by Branson (1963) and later studied by Clark and Spears (1978) as well as Warner and Pulmano (1980) reflects this concept by incorporating the ratio of cracking moment to applied moment (EQ2.9). The expression also includes the reinforcement ratio ρ_s as well as the modular ratio n, which accounts for the ratio of elastic modulus between the reinforcement and concrete. The relationship also accounts for section geometry in terms of the width of the web b_w and the depth of reinforcement d.

$$A_{ce} = b_w d\left(0.21 - n\rho_s\right)\left(\frac{M_{cr}}{M}\right)^2 \qquad \text{EQ2.9}$$

Figure 2.5(b) also shows that, for lower reinforcing ratios, the concrete area proposed by Branson (1963) reduces at higher rates with applied moments. It is also apparent that values immediately after cracking are lower for larger reinforcement ratios, which is explained by the reduced amount of concrete that surrounds denser reinforcing schemes in the tension zone. Values for effective concrete area are also shown to become negative when the ratios exceed a given value. Reinforcement ratio values for which this condition is true are given by EQ2.10. The expression was developed from EQ2.9 by ensuring that the transformed reinforcement ratio $n\rho_s$ remains smaller than 0.21. The relationship is a function of the concrete strength f'_c as well as the elastic modulus of the bar. It places an upper bound on the reinforcement ratio in addition to the possibility of a lower bound for which Branson's effective moment of inertia was already sensitive. Although the smaller elastic modulus of FRP reinforcement will increase the limitation to higher reinforcement ratios, concrete sections reinforced with the material are generally reinforced with ratios exceeding that for the balanced condition (ACI 440.1R-01). A risk of breaching the restriction set out by EQ2.10 therefore still remains.

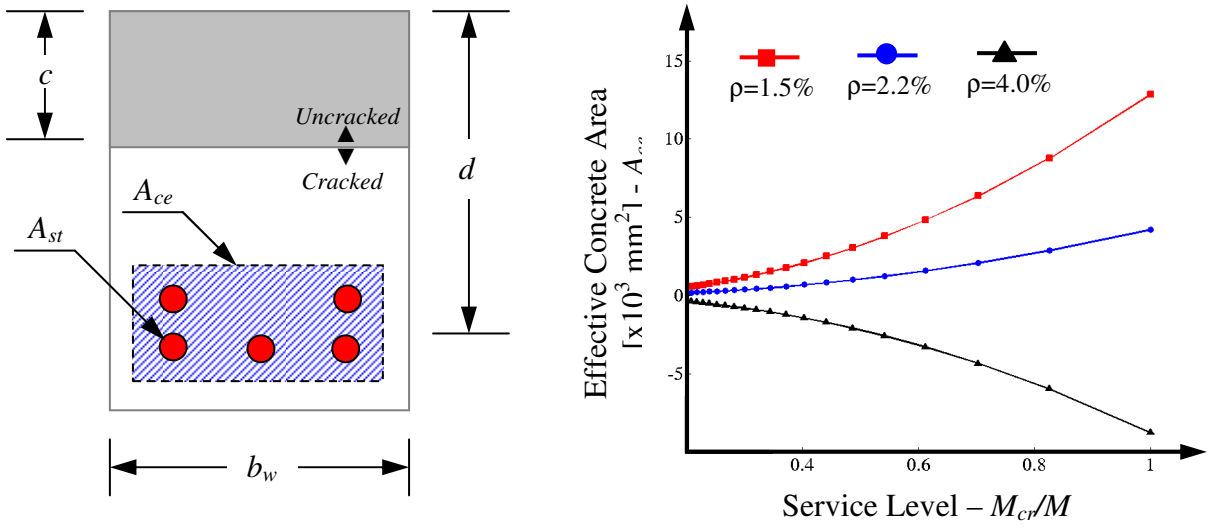

(a) Geometric Representation (b) Service Level Trend

Figure 2.5 **- Effective Concrete Area beyond Cracking**

$$\rho_s < \frac{945\sqrt{f'_c}}{E_R} \qquad \text{EQ2.10}$$

Furthermore, the nature of EQ.2.9 remains empirical and was calibrated using data that is limited to the behavior of concrete elements reinforced with steel (Gilbert 1983). It includes the effects of reinforcement ratio as well as elastic modulus for the reinforcement, but the absence of bond performance can restrict the accuracy of the relationship in estimating the post-cracking behavior of flexural elements reinforced with FRP. An alternate approach capable of incorporating all of these parameters for FRP should therefore be considered in establishing the effective concrete area. The approach should serve as a platform from which the effective concrete area as well as the post-cracking behavior can be established for elements that are reinforced with materials having properties different from that of conventional steel.

2.3.3 Alternate Relationships for Effective Concrete Area

Several other relationships for effective concrete area have been proposed since the initial concept was suggested by Branson (1963). The first is analogous to the approach adopted by ACI Committee 318 (2002) for effective moment of inertia and has been adopted by ACI Committee 224 (1986) for tension members reinforced with steel.

$$A_{ce} = \left(\frac{N_{cr}}{N}\right)^3 A_g + \left(1 - \left(\frac{N_{cr}}{N}\right)^3\right) A_{cr} \qquad \text{EQ2.11}$$

In this equation, N_{cr} is the cracking load of the tension member, N is the axial load applied to the member, A_g is the area of the gross section and A_{cr} is the total reinforcing area transformed to concrete. The expression was modified by Aiello et al. (2003) to fit the behavior of concrete members reinforced with CFRP. The modification consisted of applying a softening coefficient to the uncracked contribution, which implies that limitations of the expression are similar to those encountered with Branson's equation for effective moment of inertia. Although providing good predictions, the research concluded that a more extensive set of experimental data was required to validate the modification. It was later confirmed by Sooriyaarachchi et al. (2005) that the code model highly overestimated tension stiffening and lacked conservatism in estimating the deformation

of concrete members reinforced with GFRP. The conclusion prevailed despite the introduction of a modification factor by Sooriyaarachchi et al. (2005) that accounted for the bond performance and elastic modulus of the composite reinforcement.

Sooriyaarachchi et al. (2005) also concluded that the model presented in the CEB-FIP model code (1978) was more accurate in predicting tension stiffening when considering the appropriate factor for bond performance. The code introduces a method in which the effective concrete area is modeled using an average strain of the reinforcement in the tension zone for a given load after cracking (EQ2.12).

$$\varepsilon_{RM} = \varepsilon_R \left(1 - K \left(\frac{f_{RC}}{f_R} \right)^2 \right) \qquad \text{EQ2.12}$$

In this expression, the contribution of concrete beyond the cracking stage is modeled by stiffening strains in the reinforcement at a crack ε_R on the basis of a stiffening factor K. The stiffening process also considers the ratio of reinforcement stress at a crack immediately after cracking f_{RC} to reinforcement stress at a crack beyond cracking f_R. This ratio is equivalent to that relating cracking moments to applied moments in Branson's equations for effective moment of inertia and effective concrete area. Consequently, it allows a gradual transition in average strain from that in which concrete is still efficient in resisting tension to that in which the load is solely being carried by the reinforcement.

This strain-based relationship can be established by idealizing reinforcement and concrete as an axial member sharing the load in the tension zone of a flexural member. The added contribution of concrete can be used to represent an averaged influence of the material along the length of the flexural member. More specifically, the complete load N resisted by this idealized reinforcement can be written as the sum of the contribution for the concrete N_c and reinforcement N_R. While the concrete contribution is expressed as the product of the concrete area surrounding the reinforcement and average concrete tensile stress contribution beyond cracking, the reinforcement contribution can be expressed as the product of the member strain and corresponding axial stiffness.

$$N = \beta_d f_{dt} A_c + \varepsilon_{RM} E_R A_R \qquad \text{EQ2.13}$$

In this equation f_{dt} is the concrete tensile strength in direct tension, A_R is the cross-sectional area of reinforcement, β_d is a tension stiffening factor, ε_{RM} is the axial member strain defined by EQ2.12 and A_c is the concrete area surrounding the reinforcement. As presented by work from Bischoff and Paixao (2004) on the behavior of steel reinforced concrete members tested in direct tension, the concrete contribution can be obtained by subtracting the reinforcement contribution from the axial member's response. Once this average concrete tensile load is determined for a given average strain, it is divided by the concrete area to establish the average concrete tensile stress contribution f_c in the portion that remains uncracked.

A concrete stress-strain response should be obtained, which comprises a post-cracking descending branch after the tensile strength is reached. The average concrete tensile stress contribution beyond cracking is written in terms of the tension stiffening factor β_d that varies in accordance with the material properties, bond characteristics and ability of the reinforcement to transfer load to the surrounding concrete.

Several modifications can be brought to the relationship of EQ2.13. The ratio of reinforcement area to concrete area can be defined as the reinforcement ratio ρ_p for the idealized axial member that resists forces in the tension zone. This will account for the distribution of reinforcement in the tension zone of the flexural member. The concrete tensile strength can also be related to the reinforcement stress at a crack immediately after cracking. The expression can be established by considering force equilibrium of the member at cracking and writing the cracking load N_{cr} in terms of stresses and areas. As before, the modular ratio n is taken as the ratio of elastic modulus from the reinforcement and concrete.

$$\frac{f_{dt}}{\rho_p} = \frac{f_{RC}}{1 + n\rho_p} \qquad \text{EQ2.14}$$

Incorporating these modifications into EQ2.13 provides the expression presented by the CEB-FIP model code (1978) for modeling the tension stiffening effect (EQ2.15). It should be noted that, in the derivation of this expression, the axial member was expressed as the product of reinforcement strain ε_R and axial stiffness $[EA]_R$ at a crack.

$$\varepsilon_{RM} = \varepsilon_R \left(1 - \frac{\beta_d}{1 + n\rho_p} \left(\frac{f_{RC}}{f_R} \right) \right) \qquad \text{EQ2.15}$$

It was suggested and confirmed by research from Rao (1966) that the tension stiffening factor could be taken as the ratio of reinforcement stresses immediately before and after cracking. The additional modification justifies the application of a second power to the ratio of stresses in EQ2.12 and allows the stiffening factor to be expressed in terms of the modular ratio and reinforcement ratio (EQ2.16). These additional inclusions allow EQ2.12 to account for various reinforcing schemes as well as a wide range of elastic modulus values for FRP reinforcement. The result should serve as an improvement to the fixed value of 0.5 used by Sooriyaarachchi et al. (2005).

$$K = \frac{1}{1 + n\rho_p} \qquad \text{EQ2.16}$$

2.3.4 Deformation Response of Idealized Reinforcement

The main advantage arising from the use of EQ2.15 relates to its ability of encompassing the main factors that influence stiffness as well as deformability of concrete structures reinforced with materials having physical and mechanical properties that are different from that of conventional steel. Before it can be applied to estimate the deflection of flexural members, the relationship must be expanded to describe the load-deformation response of an idealized form of reinforcement in the tension zone. The step consists of introducing the tension stiffening factor simplification suggested by Rao (1966) and multiplying both sides of the equation by the axial stiffness of the bare bar.

$$N = \varepsilon_{RM} E_R \frac{A_R}{\left(1 - \frac{1}{1 + n\rho_p}\left(\frac{f_{RC}}{f_R}\right)^2\right)} \qquad \text{EQ2.17}$$

The stiffness factor in the denominator of this expression can be simplified by writing stresses in the reinforcement at a crack in terms of the product of applied load and cross-sectional area (EQ.2.18). This allows the stress ratio to be conveniently replaced by the member surcharge ratio N_{cr}/N.

$$\eta = 1 - \frac{1}{1 + n\rho_p}\left(\frac{N_{cr}}{N}\right)^2 \qquad \text{EQ2.18}$$

The factor increases the area of the bare reinforcement to that which accounts for the declining contribution of concrete beyond cracking. This concept of effective reinforcing area A_{Re} (EQ2.19) is analogous to that of an effective concrete area originally presented by Branson (1963).

$$A_{Re} = A_R / \eta \qquad \text{EQ2.19}$$

The concept can now be used to establish an effective moment of inertia that includes the averaged influence of concrete in the tension zone of any flexural member. In order to calculate deflection using conventional equations, this area should be constant along the complete length of the flexural member. Since the axial load in the reinforcement varies along this length, a section must be strategically chosen to determine the required magnitude of the effective reinforcing area. To avoid an overestimation of the effective axial stiffness for the idealized reinforcement, the area should be calculated at the point of maximum moment. This critical section will provide an effective axial stiffness that can be applied to the remaining portions of the member for which axial loads and strains are reduced while maintaining a constant flexural stiffness. The concept is illustrated in Figure 2.6 where the deformation response of EQ2.17 is plotted for the idealized

reinforcement at the critical section. Effective sections are also shown in the figure at the corresponding load stages.

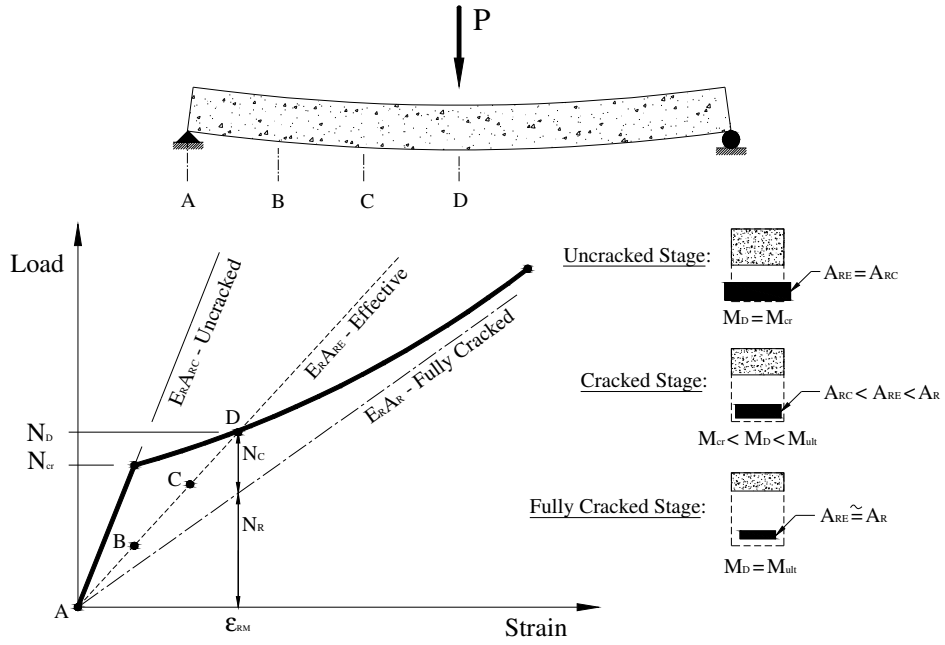

Figure 2.6 **– Deformation Response of Idealized Reinforcement at Critical Section**

2.3.5 Effective Concrete Area of Idealized Reinforcement

Before the load-deformation relationship of EQ2.17 can be used to describe the behavior of tension reinforcement in flexural members, an initial concrete area A_c should be delimited to represent the idealized reinforcement for which tension stiffening principles apply. At such a stage, it becomes important for the delimited area to fully represent the portion of concrete that contributes to resisting tensile forces within the section once it has reached the cracking stage. It should represent an area of concrete influenced by the presence of the reinforcement and its influence on the development of cracks along the member. The area was therefore delimited in accordance with crack control requirements presented in the CSA A23.3-04 design code. The concept is illustrated in Figure 2.7 and was chosen on the basis of its simplicity and potential for reducing the complexity of incorporating tension stiffening in deflection calculations. The figure also contains the

strain profile immediately before cracking that will be used to determine the cracking load of the idealized reinforcement in the tension zone.

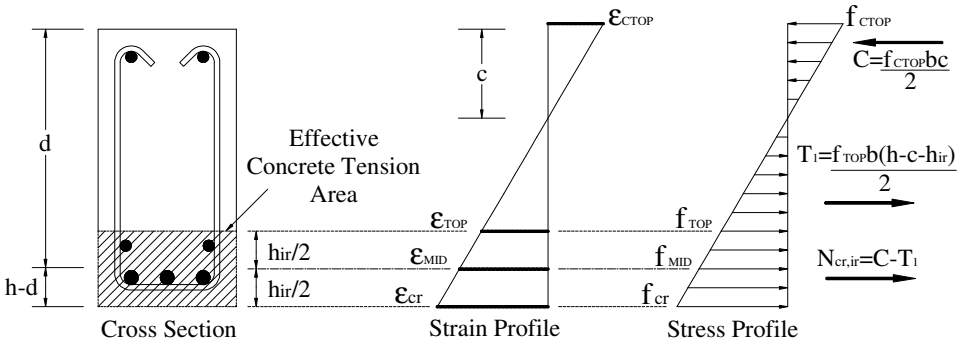

Figure 2.7 **- Effective Concrete Area at the Cracking Stage**

2.3.6 Cracking Load of Idealized Reinforcement

The cracking load is another requirement for establishing the effective stiffness of the idealized reinforcement beyond cracking. Its presence in EQ2.18 indicates that it is an important parameter in estimating the tensile contribution of concrete in cracked flexural members. As illustrated in Figure 2.7, the stress gradient can be used to establish a relationship for the cracking load of the idealized reinforcement. More specifically, the parameter is determined by considering force equilibrium in the section and evaluating the difference between compressive and tensile forces outside the effective concrete area when the extreme tension fiber reaches the cracking strain ε_{cr}. The analogy can be extended for beams with various reinforcement sizes and multiple reinforcing layers.

The compressive and tensile forces required for the analysis can be written in terms of the curvature at cracking, height of idealized reinforcement and geometric properties of the section. The relationships are obtained by integrating the stress profile over the member area and assuming that the stress-strain relationship for concrete in compression behaves linearly at the onset of cracking.

$$C = \frac{\varphi_{cr} E_c}{2} bc^2 \qquad \text{EQ2.20}$$

$$T_1 = \frac{\varphi_{cr} E_c}{2} b h_{ir}^2 \gamma \qquad \text{EQ2.21}$$

$$\varphi_{cr} = \frac{\varepsilon_{cr}}{h - c} \qquad \text{EQ2.22}$$

$$\gamma = \left(\frac{h - c}{h_{ir}} - 1 \right)^2 \qquad \text{EQ2.23}$$

In these equations as well as in Figure 2.7, C is the concrete force in the compressive zone, b is the width of the section and T_1 is the concrete tensile force acting outside of the effective tension area. Furthermore, E_c is the elastic modulus of concrete, c is the depth of neutral axis of the uncracked section, h_{ir} is the height of idealized reinforcement, h is the total depth of section. Lastly, ϕ_{cr} is the curvature at cracking, ε_{cr} is the cracking strain of concrete in tension and γ is a factor accounting for the relative distance of the idealized reinforcement with respect to the neutral axis. Finally, the difference between the contributions in compression (EQ2.20) and tension T_1 (EQ2.21) provides the relationship that is required to establish the cracking load of the idealized reinforcement $N_{cr,ir}$.

$$N_{cr,ir} = \frac{\varphi_{cr} E_c}{2} b \left(c^2 - h_{ir}^2 \gamma \right) \qquad \text{EQ2.24}$$

2.3.6.1 Force Equilibrium Relationships for Neutral Axis Depth

Now that all of the parameters required to describe the load-deformation response of idealized reinforcement in the tension zone have been established, force equilibrium must be considered to achieve an expression for the neutral axis depth. This will require the appropriate expressions for concrete compressive force to be derived. Once these final expressions have been established, the moment M and curvature ϕ_{ts} at the critical section can be determined. Beyond the cracking stage, these parameters can be used to calculate

the effective moment of inertia I_{ts} (EQ2.25) for deflection analysis while accounting for the effects of tension stiffening.

$$I_{ts} = \frac{M}{E_c \varphi_{ts}} \qquad \text{EQ2.25}$$

Since deflections are generally calculated at service conditions where concrete stresses remain within the linear elastic range, a triangular stress distribution similar to the one illustrated in Figure 2.7 can be adopted to determine the compressive force in concrete at any point beyond the cracking stage. The assumption remains valid for concrete stresses no greater than 30 to 40 percent of the compressive strength (MacGregor and Bartlett, 2000).

$$C = \frac{f_{CTOP}}{2} b c_{ts} \qquad \text{EQ2.26}$$

In this equation, f_{CTOP} is the concrete stress at extreme compressive fiber and c_{ts} is the depth of neutral axis that accounts for the effects of tension stiffening. Once the stresses exceed the linear elastic threshold, the compressive force is determined on the basis of an alternate stress-strain relationship that accounts for non-linearity. The parabolic model used in this thesis is taken from MacGregor and Bartlett (2000). The model is illustrated in Figure 2.8 and expressed in EQ2.27 in terms of stresses and strains. Integrating the curve when stresses at the extreme compressive fiber exceed the linear-elastic range of concrete allows the compressive force (EQ2.28) to be expressed in simpler form through the use of stress block factors (EQ2.29).

$$f_{CTOP} = f'_c \left\{ 2 \frac{\varepsilon_{CTOP}}{\varepsilon'_c} - \left(\frac{\varepsilon_{CTOP}}{\varepsilon'_c} \right)^2 \right\} \qquad \text{EQ2.27}$$

$$C = \alpha f'_c \beta c_{ts} b \qquad \text{EQ2.28}$$

$$\alpha\beta = \frac{\varepsilon_{CTOP}}{\varepsilon'_c} - 1/3\left(\frac{\varepsilon_{CTOP}}{\varepsilon'_c}\right)^2 \qquad \text{EQ2.29}$$

In these equations, the stress block factors are expressed as α and β while ε_{CTOP} is the strain at extreme compressive fiber for service conditions, ε'_c is the strain at peak compressive stress.

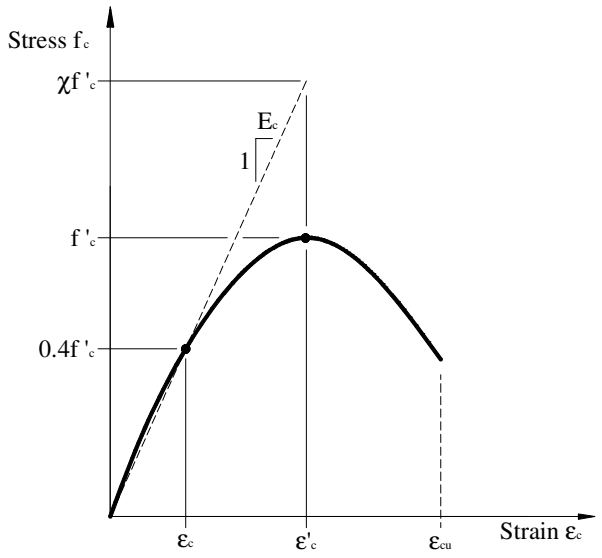

Figure 2.8 **– Parabolic Model for Concrete in Compression**

A total of two equations for neutral axis should result from the consideration of force equilibrium, depending on the behavior of concrete in compression. The first expression corresponds to linear elastic behavior and the second corresponds to non-linear behavior. For the linear elastic behavior, the concrete compressive force given by EQ2.26 should be in equilibrium with the tensile force of EQ2.17. The concrete stress at extreme compressive fiber and axial strain in the flexural reinforcement can be written in terms of the strain at extreme compressive fiber to simplify the force equilibrium expression and establish the required quadratic equation. The solution to this equation can be expanded to the form shown in EQ2.30.

$$c_{ts} = d\left(-\overline{n}\rho + \sqrt{(\overline{n}\rho)^2 + 2\overline{n}\rho}\right) \qquad \text{EQ2.30}$$

As before, the depth of reinforcement is written as d in this equation, while ρ is the reinforcement ratio of the beam under consideration and $\overline{n}$ is the modular ratio modified to take into account the axial stiffness of the reinforcement enhanced by the additional contribution of concrete in tension. This last variable is the main difference from what is given in the literature for cracked sections of reinforced concrete structures (MacGregor and Bartlett 2000). In more specific terms, it is an effective modular ratio (EQ2.31) that accounts for the stiffness factor η from EQ2.18. The factor reaches its minimum when cracking initiates within the idealized reinforcement and its maximum at the ultimate state of the beam when axial strains in the reinforcement are highest.

$$\overline{n} = \frac{E_R}{E_c \eta} \qquad \text{EQ2.31}$$

Since the effective modular ratio depends on the stiffness factor, the axial load resisted by the idealized reinforcement must be established in order to calculate the depth of neutral axis. It can be determined by substituting the appropriate strain limitations in EQ2.17 for flexural reinforcement at service conditions (ISIS Design Manual 3 2001).

When concrete in compression reaches a state of non-linearity, additional steps are required to replace the compressive strength of concrete by the elastic modulus and extreme compressive fiber strain. The substitution will simplify the compressive force expression and allow force equilibrium to give an expression for neutral axis depth that is similar in form to that described by EQ2.30. The first step consists of noticing that elastic modulus values used in practice are typically calculated using a secant modulus that passes through the stress-strain curve at approximately $0.4f'_c$ (Collins and Mitchell, 1997). The procedure is illustrated in Figure 2.8 and setting the concrete stress f_{CTOP} of the parabolic model to 40% of the compressive strength allows the strain ratio (EQ2.32) to be expressed in quadratic form (EQ2.33).

$$\xi = \frac{\varepsilon_{CTOP}}{\varepsilon'_c} \qquad \text{EQ2.32}$$

$$\xi^2 - 2\xi + 0.4 = 0 \qquad \text{EQ2.33}$$

Two solutions for strain ratio can be obtained from this expression. While the first solution corresponds to 1-√3/√5 and a strain ratio below unity, the second corresponds to 1+√3/√5 and a ratio exceeding unity. Based on the parabolic model, the first solution relates the strain at extreme compressive fiber to the required stress level of $0.4f'_c$. Retaining this solution and using similar triangles in Figure 2.8 provides an expression for compressive strength in terms of elastic modulus and strain ratio (EQ2.34).

$$f_c^{'} = \frac{5(1-\sqrt{3/5}\,)E_c\varepsilon_{CTOP}}{2\xi} \qquad \text{EQ2.34}$$

Completing the substitution of this relationship in the force equilibrium expression allows the neutral axis depth (EQ2.35) to be expressed in terms of the strain ratio as well as a factor accounting for the stress block factors (EQ2.36).

$$c_{ts} = \frac{d}{2\psi}\left\{-\overline{n}\rho\xi + \sqrt{(\overline{n}\rho\xi)^2 + 4\overline{n}\rho\xi\psi}\right\} \qquad \text{EQ2.35}$$

$$\psi = \frac{5(1-\sqrt{3/5}\,)}{2}\alpha\beta \qquad \text{EQ2.36}$$

Although EQ2.35 is simple in form, an iterative procedure is required to determine the neutral axis depth. The procedure is a requirement that arises from the fact that the strain ratio (EQ2.32) and the stress block factor (EQ2.36) depend on the neutral axis depth. In similarity with the case of linear elastic behavior of concrete in compression, the iterative procedure starts with the selection of a strain limitation (ISIS Design Manual 3 2001) that is used to establish the tensile force in the idealized reinforcement and effective modular ratio. The strain value is also used to calculate the extreme compressive fibre strain, provided the neutral axis is known. Once the compressive strain is established on the

basis of this neutral axis estimate and strain in the idealized reinforcement, the strain ratio and stress block factor can be calculated to determine an alternate value for neutral axis depth from EQ2.35. The alternate value becomes the estimate and the process is repeated until both values remain unchanged. It should be noted that the iterative procedure also requires and is preceded by the determination of cracking load for the idealized reinforcement in the tension zone.

2.4 STATISTICAL ANALYSIS OF BEAM DATABASE

Although service conditions usually reflect a linear-elastic behavior of concrete in compression, the complexity of the iterative procedure discussed in the previous section remains a considerable disadvantage from the perspective of the designer when higher load levels need to be considered. As a result, the following sections will show that the procedure was not intended for direct application but rather used to calibrate a proposed expression for effective moment of inertia that accounts for the effects of tension stiffening and that is similar in form to the cracked moment of inertia. A beam database created for this thesis was therefore firstly analyzed using this expression and the iterative procedure for neutral axis depth with concrete non-linearity (EQ.2.35). The deflection analysis was also successfully used to simplify the tension stiffening factor by including a ratio for moment as opposed to a ratio of axial load in the idealized reinforcement. A second deflection analysis was then performed without the consideration for non-linearity and the requirement for iteration to calculate the depth of neutral axis (EQ2.30). Results from both analyses were finally compared to develop a non-linearity factor that can be applied to the proposed expression for effective moment of inertia and relieve the requirement for iteration when establishing the neutral axis depth. Eventually, a third deflection analysis was undertaken to evaluate the performance of the effective moment of inertia expression in comparison with relationships that exist in the literature.

2.4.1 Properties and Management of the Database

The database considered for deflection estimation contains a total of 192 beams. Of these concrete beams, a total of 139 are reinforced with GFRP reinforcement while a total of 48 are reinforced with CFRP. The remaining 5 beams are reinforced with AFRP, which are included for information purposes only until further data is gathered to reach superior statistical significance.

The database includes information pertinent to the research involved in testing the beams considered for the analysis. The researcher's name, year of the study as well as the label of each beam is included in the database such that the load-deflection behavior of specific members can be extracted and individually studied. Material properties include those of the concrete and reinforcing material while the geometric properties allow the database to consider the analysis of doubly reinforced T-beams with multiple layers of reinforcement. Finally, information pertaining to the span length and positioning of load can be used to analyze various loading schemes for simply supported beams.

2.4.2 Service Load Level

As illustrated in previous sections, the ratio of cracked moment to applied moment is typically chosen to describe the gradual reduction in moment of inertia beyond the cracking stage. The ratio is generally more practical to use for establishing service load levels than the ratio of cracking load to applied load in the idealized reinforcement. Consequently, the first database analysis was aimed at eliminating the requirement for calculating axial loads and providing an approach that is more common to the designer.

The ratios of axial load in the reinforcement were plotted against the ratios of moment for every beam in the database. The step is illustrated in Figure 2.9 for a beam that was arbitrarily selected from the database (Thériault and Benmokrane 1997). The relationship remained close to linear for all beams in the database but the slope of the trend line shown in the figure was found to reach values ranging from as low as 0.6 to as high as

1.1. The variation is attributed to the fact that changes in section geometry can influence the behavior of the beam but not necessarily the behavior of the idealized reinforcement. More specifically, changes that affect the reinforcement ratio for the overall section might not affect that which corresponds to the idealized reinforcement. The observation confirms the reason for which section properties were considered by Branson's effective reinforcement area concept (EQ2.9).

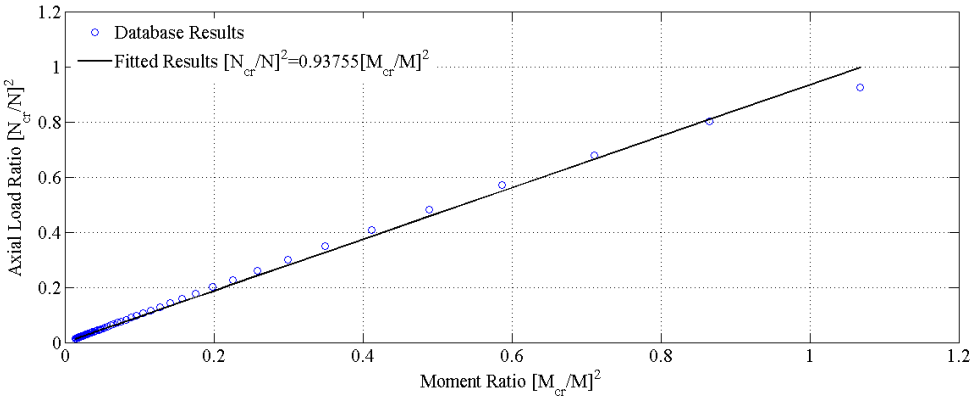

Figure 2.9 - **Service Level Ratio Relationship**

If reductions in both section height and reinforcement depth are specifically considered for a given reinforcing area, the reinforcement ratio of the idealized reinforcement will remain unchanged but that of the overall section will increase. For small reinforcement ratios, the suggested changes in height and depth will cause a higher reduction in the cracking moment than in the resisting moment. For any given ratio of axial load in the reinforcement, an increase in reinforcement ratio will correspond to a reduction in the moment ratio and an increase in the slope of Figure 2.9.

With further reductions in height and depth, reinforcement ratio values continue to increase and are accompanied with gradually increasing curvatures to maintain force equilibrium within the section. The larger compressive strains and the parabolic nature of the stress-strain relationship of concrete in compression (EQ2.27) will cause the stress block factors (EQ2.29) to plateau. As a result, the neutral axis depth becomes the only variable that can be adjusted to maintain equilibrium within the section. At this point, reductions in the moment arm as well as the resisting moment become more pronounced.

Furthermore, the higher ratio of reinforcement within the section reduces the extreme tension fibre distance sufficiently to produce smaller reductions in cracking moment. The combination eventually brings the moment ratio to increase and the slope of Figure 2.9 to reduce. The variation in slope for the complete database is therefore expected to follow a second-degree curve that gradually increases until a given reinforcement ratio is reached. Once this value is exceeded, the slope gradually reduces such that the result of Figure 2.10 is obtained for what is referred to as the modification factor for service level ratios *R*. In order to incorporate the relative behavior of the beam and the idealized reinforcement, the results were plotted in terms of a factor that relates the reinforcement ratio for the section ρ to the reinforcement ratio for the idealized reinforcement ρ_p.

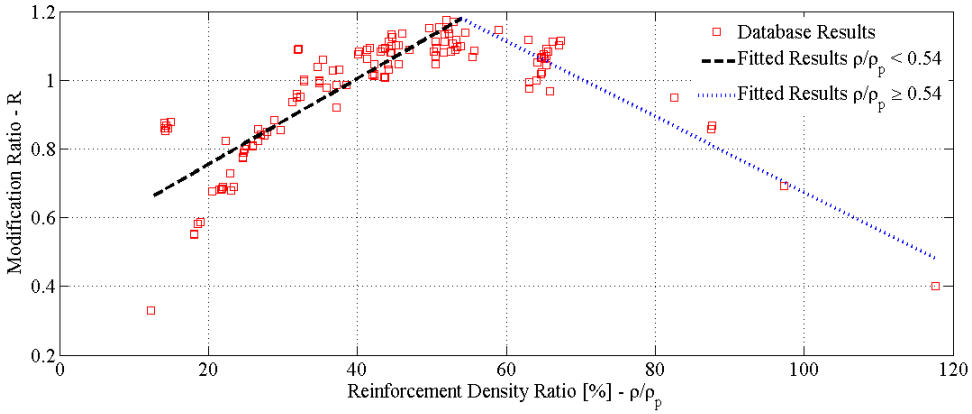

Figure 2.10 **- Modification Factor for Service Level Ratios** [Complete Database]

For simplicity, the variation in the modification ratio illustrated in Figure 2.10 was approximated with two straight lines. The slope and intersection point of these lines were determined on the basis of a regression analysis for which the root mean squared error (RMSE) was minimized over the range of reinforcement density ratios considered. The procedure allows a more accurate estimation of the modification factor for the range of properties in the database. While the slope of each line represents the intensity by which the modification factor varies, the intersection point defines the reinforcement density ratio for which the variation alters from an increase to a reduction in the factor. The parameters are expressed in EQ2.37 such that the stiffness factor can now be expressed in terms of the modification factor and moment ratio (EQ2.38).

$$R = \begin{cases} 1.25\,\rho/\rho_p + 0.51 & \rho/\rho_p < 0.54 \\ -1.10\,\rho/\rho_p + 1.77 & \rho/\rho_p \geq 0.54 \end{cases} \qquad \text{EQ2.37}$$

$$\eta = 1 - \frac{R}{1 + n\rho_p}\left(\frac{M_{cr}}{M}\right)^2 \qquad \text{EQ2.38}$$

The effective moment of inertia was also recorded for all of the beams in this first database analysis. The values were evaluated using an expression derived using EQ2.25. The moment in this equation can be written as the sum of the contributions from the idealized reinforcement (EQ2.39) and concrete in compression (EQ2.40). The concrete contribution includes the neutral axis depth defined by EQ2.35.

$$M_T = \varepsilon_{RM} E_R \frac{A_R}{\eta}(d - c_{ts}) \qquad \text{EQ2.39}$$

$$M_c = \frac{f_{CTOP}}{3} b c_{ts}^2 \qquad \text{EQ2.40}$$

These relationships were obtained by taking moments about the neutral axis. In these expressions, the concrete compressive stress as well as the strain in the idealized reinforcement can be written in terms of the concrete strain at extreme compressive fibre. The curvature at the critical section can also be written as a ratio of this strain value and the neutral axis depth from EQ2.35. These modifications as well as the sum of moments from individual contributions allow the effective moment of inertia of EQ2.25 to be expressed in a form that can be directly used in deflection calculations (EQ2.41). It is as simple as the cracked moment of inertia expression, with the additional advantage of including the effects of tension stiffening and material non-linearity.

$$I_{ts} = \frac{b c_{ts}^3}{3} + \overline{n} A_R (d - c_{ts})^2 \qquad \text{EQ2.41}$$

2.4.3 Non-Linearity of Concrete in Compression

Although EQ2.41 greatly simplifies the proposed model to a form that is more commonly used by the practicing engineer when estimating deflections, it does not eliminate the requirement for iteration when non-linear behavior of concrete in compression is reached. The second database analysis therefore consisted of evaluating the influence of concrete non-linearity on effective moment of inertia values evaluated from EQ2.41. Accordingly, the complete database was analyzed using neutral axis depths that assume linear-elastic behavior of concrete in compression (EQ2.30). Effective moment of inertia values obtained from both analyses were then tabulated and compared with the intent of establishing a non-linearity factor that can eliminate the need for iteration when evaluating the neutral axis depth for effective moment of inertia in EQ2.41.

Results are illustrated in Figure 2.11 for a specific beam in the database (Zhao et al. 1997). The non-linearity factor F is conveniently plotted against the moment ratio. The factor (EQ2.42) represents the ratio of effective moment of inertia obtained from the non-linear analysis to that obtained from the linear-elastic analysis.

$$F = \frac{I_{ts/non-linear}}{I_{ts/linear-elastic}} \qquad \text{EQ2.42}$$

More specifically, it corresponds to the amount by which the effective moment of inertia for linear elastic conditions needs to be adjusted to account for non-linear considerations. The figure illustrates that effective moment of inertia values from both analyses are in close agreement for a wide range of applied moments. Small variations in the non-linearity factor can be observed for applied moments ranging from the cracking moment (M_{cr}/M=1.0) to five times the cracking moment (M_{cr}/M=0.2). Beyond this stage, the degree of non-linearity increases such that the effective moment of inertia values that account for material non-linearity deviate considerably from and decrease more rapidly than those evaluated with linear-elastic assumptions. Part of the second database analysis was therefore aimed at establishing this transition point with the intent of obtaining an

appropriate representation for the complete range of beams in the database. Results will be particularly useful to moderate the probability of under-estimating deflections when using EQ2.41 at higher load levels.

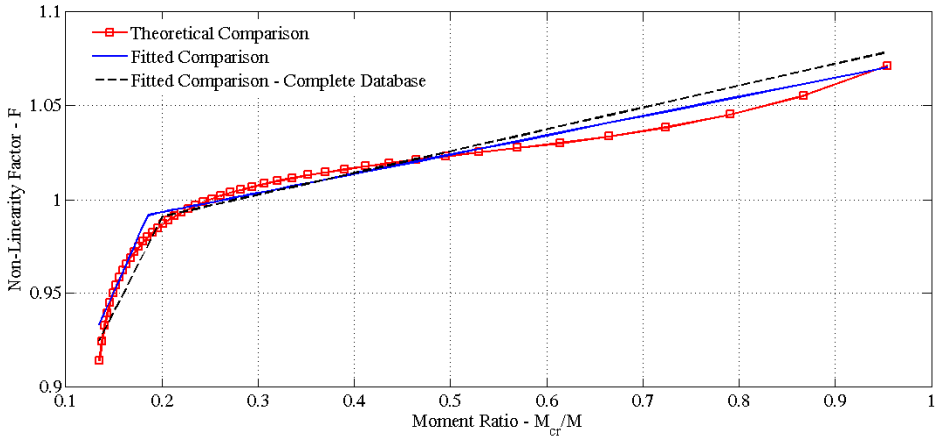

Figure 2.11 **- Non-Linearity Correction Factor**

As illustrated in Figure 2.11, results were fitted with two distinct lines whose intersection point represents the moment ratio that best defines the transition point from linear-elastic to non-linear behavior of concrete in compression. The first set of lines in the figure establishes the intersection by minimizing the root mean squared error (RMSE) over the complete range of moment ratios for the specified beam. The procedure provides a fitted comparison for which an average error of ±0.0013 is anticipated with a transition point of 0.18 for the moment ratio. The slope of each line segment was also determined in the minimization process.

The process was repeated for all beams in the database and a distribution was obtained for moment ratios that most appropriately define the transition point. Results are shown in Figure 2.12 in the form of a boxplot. Figure 2.12(a) shows the different components of the boxplot, which comprise the lower quartile, the median and the upper quartile. These parameters correspond to values below which 25%, 50% and 75% of the data lies, respectively. The range of values between the lower and upper quartiles is typically referred to as the inter-quartile range, which encompasses 50% of the data. The whiskers extending from each end of the box show the extent of the rest of the data and do not extend more than 1.5 times the inter-quartile range. Any values beyond this point are

marked by a point and referred to as outliers. Outliers are individual data points that are inconsistent with the statistical nature of the bulk of the data and are typically excluded from the analysis. The boxplot of Figure 2.12(b) contain outliers that lie beyond the extent of the upper whisker. All of these values were, however, kept in the distribution because they were found to represent over-reinforced beams for which the failure is governed by concrete crushing with noticeable non-linearity. Furthermore, the points are relatively close to the inter-quartile range.

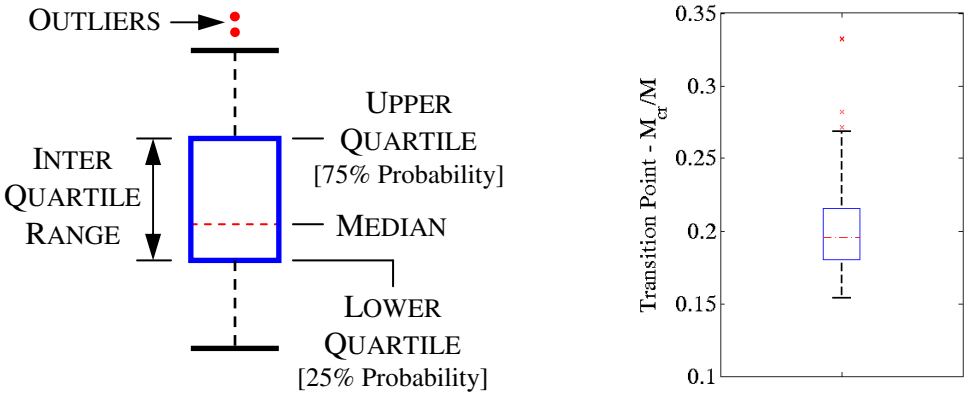

(a) Boxplot (b) Database Results

Figure 2.12 **- Distribution for Moment Ratio at the Transition Point**

The average transition point from this distribution was calculated as 0.21. This ratio defines the onset of non-linearity for applied moments that exceed 4.78 times the cracking moment. The ratio was applied to the complete database a final time to establish the slopes of each line segment through minimization of the non-linearity factor's RMSE over the full range of moment ratios considered. From the analysis, an average slope of 1.00 was obtained for the line segment spanning the range of moment ratios that define non-linear behavior. For the linear-elastic segment corresponding to moment ratios beyond 0.21, the slope of the line was found to average 0.12 with the non-linearity factor exceeding unity. These fitted results from the complete database were also plotted in Figure 2.11 for comparative purposes. It should be noted, however, that non-linearity factors exceeding unity will increase effective moment of inertia values when applied to EQ2.41. Since the result leads to an under-estimation of deflection, a non-linearity factor of 1.0 was suggested for moment ratios beyond 0.21 (EQ2.43).

$$F = \begin{cases} 1.0 & M_{cr}/M > 0.21 \\ 1.00\,M_{cr}/M + 0.79 & M_{cr}/M \leq 0.21 \end{cases} \qquad \text{EQ2.43}$$

The non-linearity factor defined by this expression brings the suggested simplification for effective moment of inertia to completion (EQ2.44). The result can be applied to the complete database and its performance can be established against other methods that exist in the literature.

$$I_{ts} = F\left\{\frac{bc_{ts}^3}{3} + \overline{n}A_R\left(d - c_{ts}\right)^2\right\} \qquad \text{EQ2.44}$$

2.4.4 Comparative Results and Discussion

A total of two relationships from the literature were studied to establish the performance of the model suggested in EQ2.44. The relationships are based on modifications brought to Branson's equation (EQ2.1) for effective moment of inertia of steel reinforced concrete beams. The modifications were proposed by ACI committee 440 (2006) and obtained from research presented by Yost et al. (2003).

Effective moment of inertia values from these modifications were used to establish ratios of estimated to experimental deflections at load levels ranging from 25 to 80% of ultimate. Ratios were obtained on the basis of elastic modulus and cracking moment values computed from code equations and calculated using compressive strengths listed in the database. Results are listed in Table 2.1 for the complete database and compared to those obtained from all relationships considered in this thesis. Results are also shown in Figure 2.13 for the complete database as well as separately for the GFRP and CFRP reinforced concrete beams.

When analyzing the complete database, results from the suggested model as well as those from ACI 440.1R (2006) and Yost et al. (2003) compare well at the load levels considered. The average of deflection ratios for the complete database fluctuates close to

unity, which indicates that the three methods are reliable in estimating deflection of concrete beams reinforced with GFRP as well as CFRP products. However, results from the modification factor proposed by ACI 440.1R (2006) continue to underestimate deflections with ratios below unity for the complete range of load levels. The modification proposed by Yost et al. (2003) also underestimates deflection but only for load levels beyond 45% of ultimate since for most of the lower load levels, the modification provides a conservative estimate of deflection. The suggested model follows a similar trend but with a smaller degree of underestimation at higher load levels and conservative estimates for all load levels below 60% of ultimate.

Table 2.1 - **Average Deflection Ratios** [Complete Database]

LOAD LEVEL [%]	ACI 440.1R (2006)	YOST et al (2003)	SUGGESTED (EQ2.48)
25	0.93	1.02	0.99
30	0.93	0.99	0.98
35	0.95	1.01	1.03
40	1.00	1.03	1.02
45	0.98	1.00	1.02
50	0.98	0.99	1.02
55	0.98	0.98	1.00
60	0.96	0.93	0.98
65	0.95	0.92	0.97
70	0.94	0.90	0.96
75	0.93	0.88	0.94
80	0.91	0.87	0.93

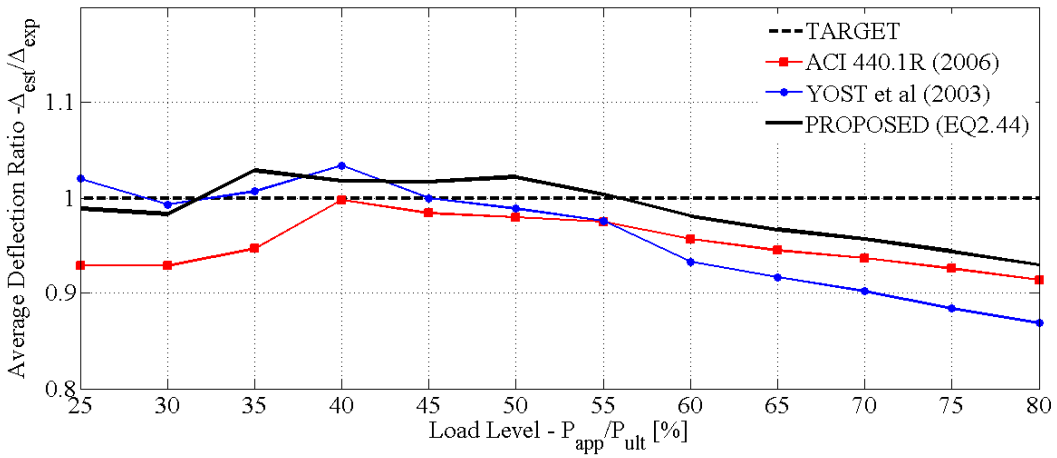

(a) Complete Database [192 Beams]

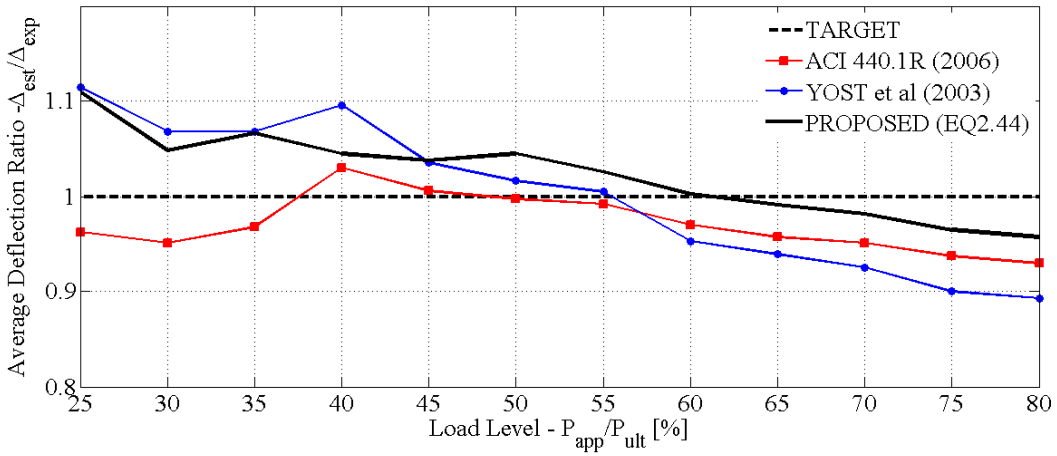

(b) GFRP Reinforcement [139 Beams]

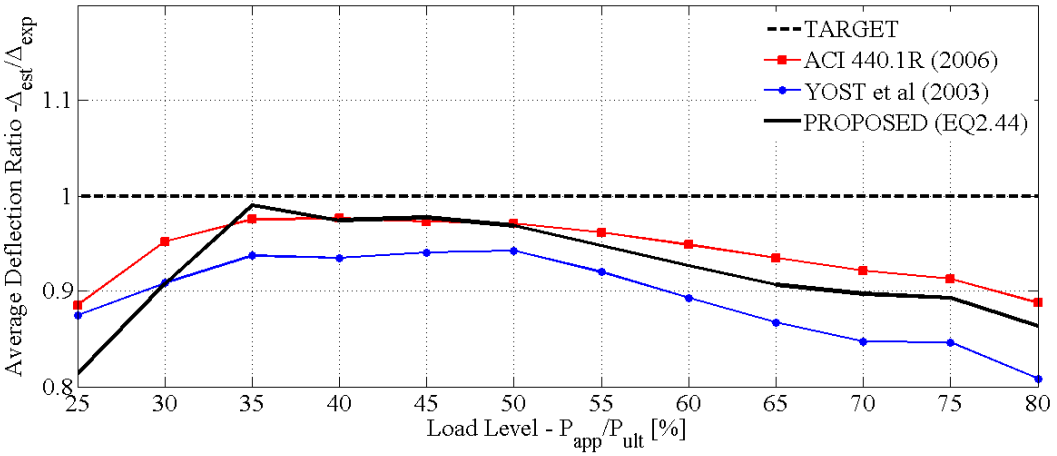

(c) CFRP Reinforcement [48 Beams]

Figure 2.13 **- Estimated Average Deflection Ratios**

It can also be concluded from Figure 2.13 that deflection ratios for beams reinforced with GFRP reinforcement are closer to or beyond unity for all load levels considered and those for beams reinforced with CFRP reinforcement are well below unity. The outcome holds true for all methods considered and reflects the lack of conservatism in estimating deflections for beams reinforced with CFRP reinforcement particularly at load levels below 35 and beyond 50% of ultimate. The result can be attributed to the fact that methods consider the softening in flexural stiffness beyond cracking to be more sensitive to the reinforcing area provided than the elastic modulus of the reinforcement.

It should also be noted from Figure 2.13 and results from the complete database that the suggested model is more accurate in estimating deflections at higher load levels. The result arises from the added advantage of considering non-linearity for concrete in compression. However, results from the suggested relationship for effective moment of inertia continue to underestimate deflection for load levels beyond 55% of ultimate. The ratio of 0.21 relating cracking to applied moment in EQ2.43 is therefore not an adequate transition point for which the non-linearity factor comes into effect. The observation is further illustrated in Figure 2.14 for which most of the moment ratios at the 80% load level exceed the value of 0.21. The transition point was therefore increased such that the non-linearity factor of EQ2.45 encompasses moment ratios that more adequately describe load levels ranging from 60 to 80% of ultimate. Figure 2.14 also illustrates that the procedure ensures the selected transition point includes only a minimal amount of beams at the 55% load level. Results at this level should not be affected by the modification since they are conservative and do not appear to be influenced by non-linear behavior of concrete in compression. The modification brought to the non-linearity factor is described in EQ2.45.

$$F = \begin{cases} 1.0 & M_{cr}/M > 0.27 \\ 1.64\,M_{cr}/M + 0.55 & M_{cr}/M \le 0.27 \end{cases} \qquad \text{EQ2.45}$$

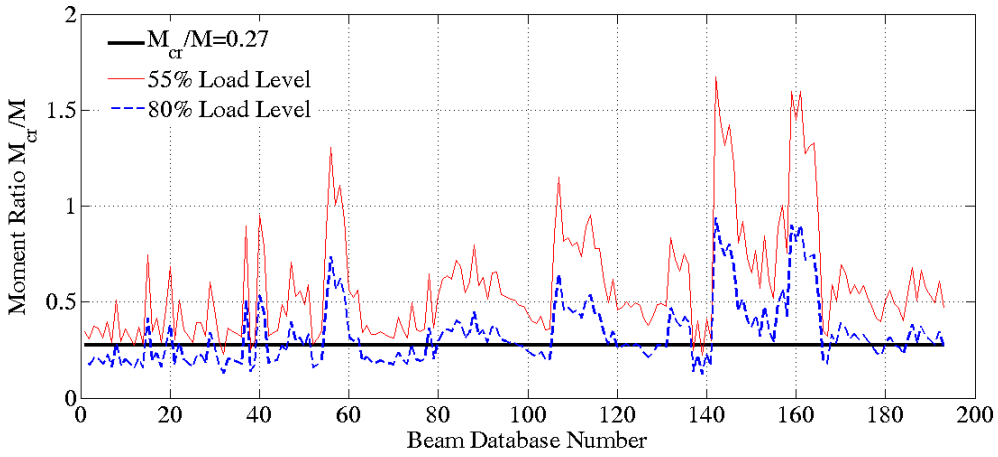

Figure 2.14 - **Moment Ratios at Specified Load Levels**

Average deflection ratios reflecting this modification are listed in Table 2.2 and shown in Figure 2.15. While maintaining similar results at load levels below 50% of ultimate, the revised ratios obtained from the suggested model show an improvement at load levels between 60 and 80% of ultimate.

Table 2.2 – **Revised Average Deflection Ratios** [Complete Database]

LOAD LEVEL [%]	ACI 440.1R (2006)	YOST et al (2003)	SUGGESTED (EQ2.48)
25	0.93	1.02	0.98
30	0.93	0.99	0.98
35	0.95	1.01	1.03
40	1.00	1.03	1.02
45	0.98	1.00	1.02
50	0.98	0.99	1.03
55	0.98	0.98	1.01
60	0.96	0.93	1.00
65	0.95	0.92	0.99
70	0.94	0.90	0.99
75	0.93	0.89	0.98
80	0.92	0.87	0.97

The advantage of including non-linearity beyond a moment ratio of 0.27 is further illustrated in Figure 2.16(a) for a beam selected from the database (Zhao et al. 1997). The figure also emphasizes that the suggested model produces an immediate increase in deflection after cracking. The result arises from the sudden loss of concrete around the idealized reinforcement and the corresponding increase in curvature at this stage. An effective moment of inertia response is also plotted in Figure 2.16(b) to provide further comparison between the suggested model and that from modification factors considered in this thesis. For completeness, load-deflection estimates for all beams in the database are provided in Appendix A of this thesis.

2.4.5 Estimating with Confidence

Confidence intervals are used to establish the influence of standard deviation on the distribution of observations about the mean. For a chosen level of confidence and a given

load level, larger standard deviations will strongly increase the probability of incorrectly estimating deflection. The outcome is valid even for results in Figure 2.13 where deflection ratios at any load level are reliably close to unity. In order to determine whether the standard deviations shown in Figure 2.17 are sufficiently small to reduce this probability, intervals with 95% confidence were established for every load level considered. The intervals enclose 95% of the deflection ratios that were calculated over the complete database. This translates to a 95% probability of estimating deflections within the interval for any of the methods considered in this thesis. If the standard deviation is within tolerance, the intervals will be sufficiently small to inspire confidence in the estimations that were established in the previous section.

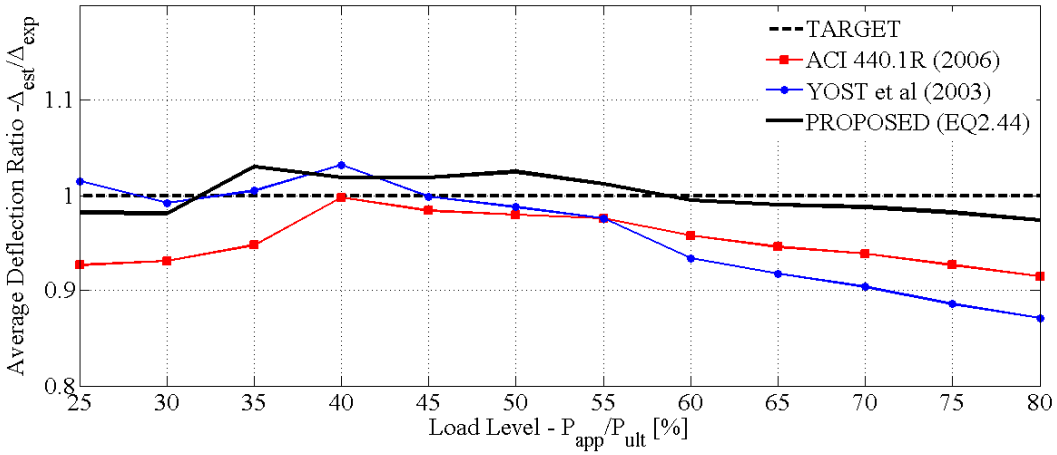

(a) Complete Database [192 Beams]

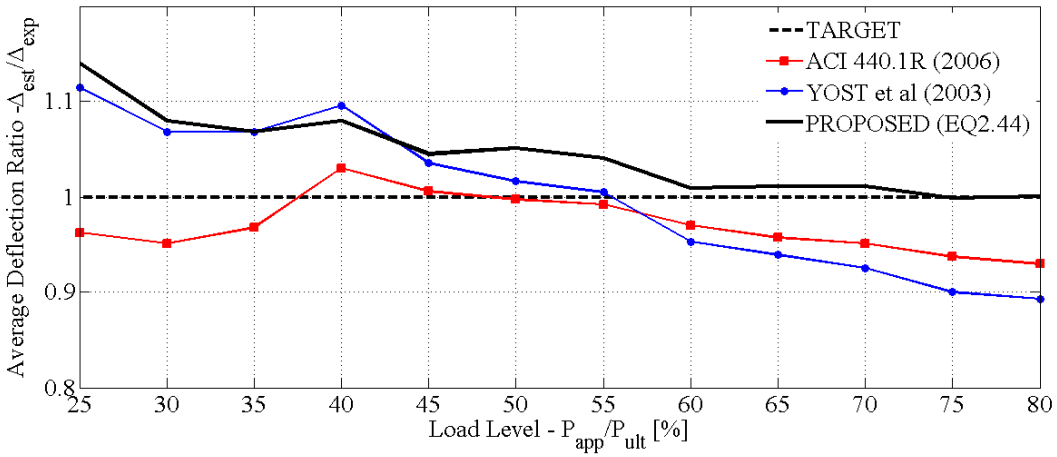

(b) GFRP Reinforcement [139 Beams]

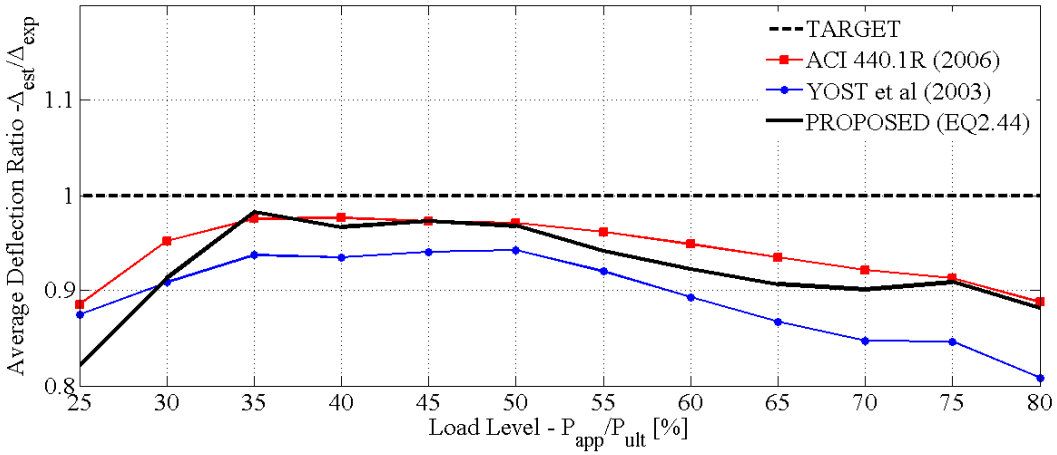

(c) CFRP Reinforcement [48 Beams]

Figure 2.15 **- Revised Estimation of Average Deflection Ratios**

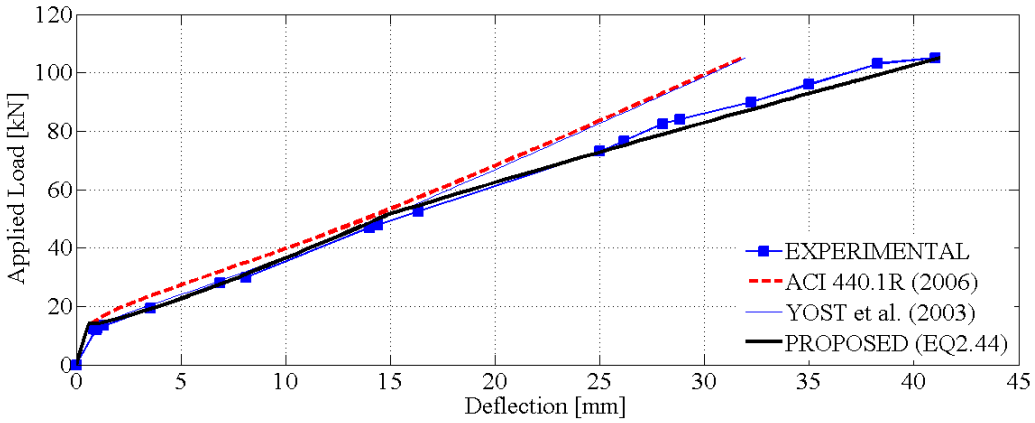

(a) Load-Deflection Response Estimate

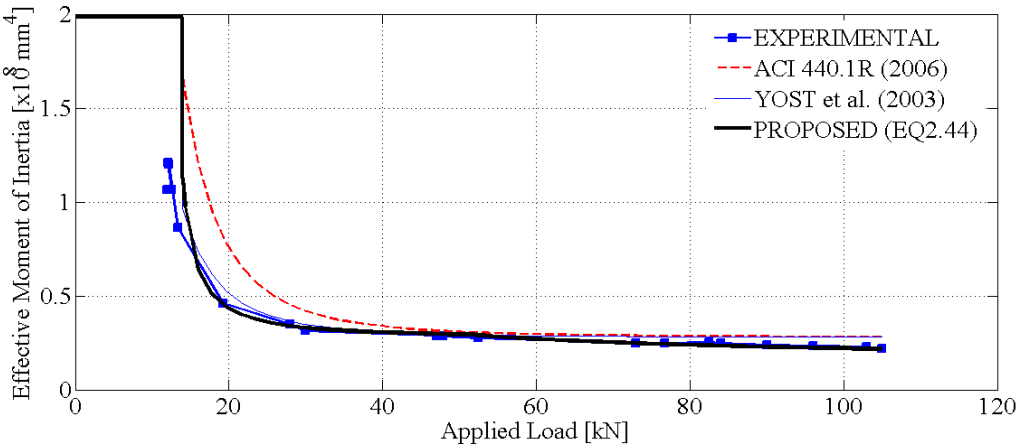

(b) Inertial Moment Response

Figure 2.16 **- Typical Flexural Response from Database**

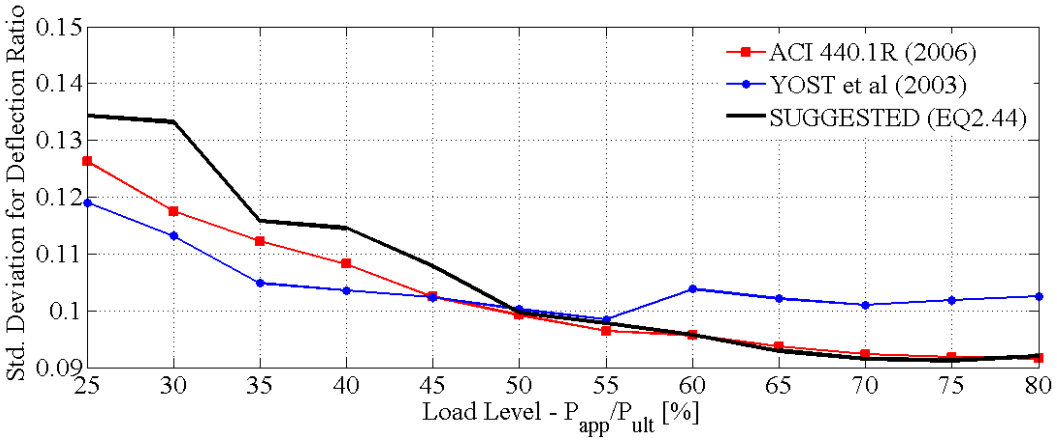

Figure 2.17 **- Standard Deviation of Deflection Ratios** [Complete Database]

The limits of the interval represent estimates that are 1.96 standard deviations below and above the mean. Their distance from the mean is called the margin of error, which is listed in Table 2.3 for all load levels and methods considered. Shaded cells in this table represent the minimum values for margin of error at each load level. Results indicate that estimates of the deflection ratio are within reasonable margins of the average for all methods.

Table 2.3 - **Margin of Error** [Complete Database]

LOAD LEVEL [%]	ACI 440.1R (2006)	YOST et al (2003)	SUGGESTED (EQ2.48)
25	0.25	0.23	0.26
30	0.23	0.22	0.26
35	0.22	0.21	0.23
40	0.21	0.20	0.22
45	0.20	0.20	0.21
50	0.19	0.20	0.20
55	0.19	0.19	0.19
60	0.19	0.20	0.19
65	0.18	0.20	0.18
70	0.18	0.20	0.18
75	0.18	0.20	0.18
80	0.18	0.20	0.18

Although values for margin of error can vary from as low as 18% (±0.18), they can vary from as high as 26% (±0.26) from the averages listed in Table 2.1. This restrictive level of confidence can be attributed to the fact that different types of reinforcement are considered within the database, for which a variation in performance, and therefore

estimation, exists. The result is more clearly shown in Figure 2.13, where methods either underestimate deflection for beams reinforced with CFRP or overestimate deflection for beams reinforced with GFRP.

CHAPTER 3

PRESTRESSED CONCRETE PRISM REINFORCEMENT

3.1 DEFLECTION OF CONCRETE BEAMS REINFORCED WITH FRP

The rising interest from the industry to overcome the detrimental effects of corrosion in civil infrastructure has lead research within the last decades to study the use of FRP reinforcement as a replacement to conventional steel. As a result, the previous chapter was aimed at incorporating the properties of FRP reinforcement in a relationship that is capable of estimating deflection of beams with equal accuracy to what is obtained for steel reinforcement. In doing so, the chapter established that most FRP reinforcing bars have an elastic modulus relatively lower than what is inherent to steel reinforcement (Yost et al. 2003). The relative magnitude suggests that the inferior flexural stiffness of FRP reinforced concrete beams can govern the design when considering the compliance to imposed deflection limits (Yost et al. 2003).

The previous chapter also emphasizes the fact that FRP products have higher tensile strength than conventional steel. Smaller reinforcing areas can therefore be used to achieve a given resistance. This will cause further reductions in flexural stiffness, but the linear elastic behavior of FRP reinforcement and the absence of plastic deformation prior to failure will restrict warning of impending failure. It is therefore typical for concrete sections reinforced with FRP to be reinforced with ratios exceeding that for the balanced

condition (ACI 440.1R-01, Nanni 1993b). Although the recommendation can lead to improvements in deflection at service conditions, it overshadows the advantage from which smaller reinforcing areas can be used to reduce costs in civil infrastructure. The current chapter will consider a method in which the higher strength of FRP material can be used with smaller reinforcing areas that satisfy the required limits on serviceability.

3.2 CONCRETE PRISMS PRESTRESSED WITH FRP REINFORCEMENT

For a given area, the reinforcement's axial stiffness is governed by the elastic modulus. The relatively low elastic modulus value of FRP products is the main parameter that can reduce axial stiffness of the reinforcement and prevent deflection limitations to be met. Load-sharing concepts can be used to overcome this effect. More specifically, the reinforcement can be embedded in a second material that reduces the tensile force being carried by the bare reinforcing bar. The second material sustains the load that is being relieved from the reinforcement and reductions in the applied strain will provide an increase in the axial stiffness at any given load. The analogy is shown in Figure 3.1.

At any given strain, the figure illustrates that the total response can be written as the sum of the contribution from each material. Both of these contributions can, in turn, be written in terms of the applied strain and the fundamental assumption in flexural theory is required for this step if the element is to be used as reinforcement. It states that plane sections taken normal to the beam axis before loading remain plane after the beam is subjected to bending. The assumption implies that normal strains are proportional to the distance from the neutral axis and, more importantly, are equal for all of the materials at the reinforcing level. The contributions from the reinforcement (EQ3.1) and surrounding material (EQ3.2) can therefore be written as the product of the same applied strain at the reinforcement level as well as the axial stiffness of the corresponding material.

$$N_R = \varepsilon[EA]_R \qquad \text{EQ3.1}$$

$$N_m = \varepsilon [EA]_m \qquad \text{EQ3.2}$$

In these equations, N_R is the contribution from the reinforcement and N_m is the contribution from the surrounding material. Furthermore, ε is the axial strain applied to the composite element, $[EA]_R$ is the axial stiffness of the reinforcement and $[EA]_m$ is the axial stiffness of the material surrounding the reinforcement. If these contributions are added and the applied strain factored from the total response, the load-deformation relationship of EQ3.3 can be expressed in terms of the axial stiffness of the composite reinforcement, which can be referred to as a prism, prior to cracking $[EA]_{pr}$ (EQ3.4).

$$N = \varepsilon [EA]_{pr} \qquad \text{EQ3.3}$$

$$[EA]_{pr} = [EA]_R + [EA]_m \qquad \text{EQ3.4}$$

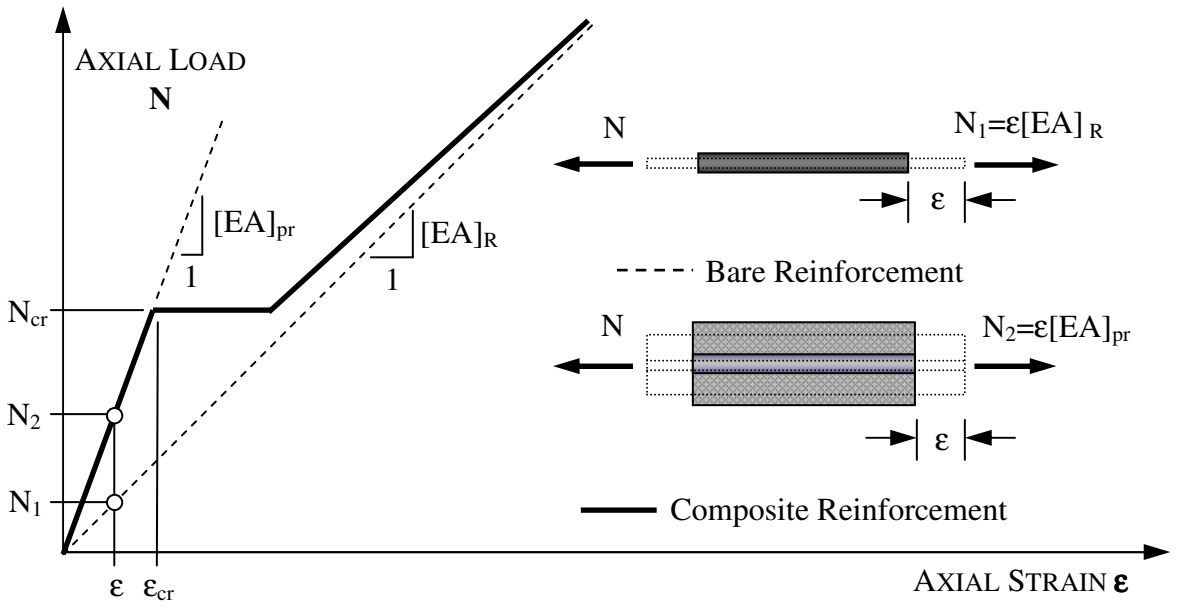

Figure 3.1 **- Load-Deformation Response of Composite Reinforcement**

As illustrated in Figure 3.1, it is apparent that the tensile strength of the stiffness enhancing material is not required to match that of the bare reinforcement. This arises

from the fact that deflection limitations for flexural members must be satisfied at service conditions alone and that higher axial stiffness for the reinforcement is only required at load levels spanning this stage. The load at which the material reaches its tensile strength corresponds to the cracking load for the composite reinforcement. The parameter is denoted N_{cr} and leads to the development of transverse cracks along the length of the composite member. It can be expressed as the product of axial stiffness for the composite member and cracking strain for the material surrounding the reinforcement.

$$N_{cr} = \varepsilon_{cr}\left[EA\right]_{pr} \qquad \text{EQ3.5}$$

The cracking strain in this equation is denoted ε_{cr} and can be written in terms of the elastic modulus E_m and direct tensile strength f_{dt}, which arises from testing the material in pure axial tension (EQ3.6). The relationship assumes linear-elastic behavior in tension.

$$\varepsilon_{cr} = \frac{f_{dt}}{E_m} \qquad \text{EQ3.6}$$

Beyond the cracking stage, a fully developed crack pattern develops along the length of the composite member and most of the load is being carried by the reinforcement. The axial stiffness decreases and the load-deformation response becomes almost parallel to that of the bare bar. Since the second material continues to contribute to axial load between the cracks, the response remains well above that of the bare bar. The result is well known and illustrated in Figure 3.1. It was observed as early as 1899 from tests performed on mortar prisms reinforced with steel wires (Considère 1899).

The behavior of reinforced concrete members subjected to pure axial loads has been widely documented in the literature (Bischoff and Paixao 2004, Aiello et al. 2003, Collins and Mitchell 1997). As a result, the use of concrete as the stiffness enhancing material presents a choice that is familiar to many and has its benefits from a design perspective. In order for flexural members to maintain adequate rigidity and meet deflection requirements under service conditions, concrete chosen for the application must remain

intact beyond the cracking stage of the beam. The condition will provide corrosion protection for the reinforcement and concrete with higher strength can be used for the purpose. Higher compressive strengths will improve direct tensile strength and elastic modulus, which respectively lead to an increase in cracking load as well as axial stiffness for the alternate reinforcement.

The performance of the composite reinforcement can be improved by considering prestressing in addition to the use of higher strength concrete. Since prestressing involves stretching of the reinforcing bar, a shortening strain in the concrete and reinforcement will occur at release. The strain will cause a reduction in the reinforcement's prestressing force, which is balanced by a compressive force that develops within the concrete portion of the composite member. Forces arising from this elastic shortening process are self-equilibrating, which allows the use of force equilibrium to determine the shortening strain (EQ3.7).

$$\Delta\varepsilon_p = \varepsilon_o \frac{[EA]_R}{[EA]_R + [EA]_{c,p}} \qquad \text{EQ3.7}$$

In this equation, $\Delta\varepsilon_p$ is called the elastic shortening strain, ε_o is the jacking strain applied to the reinforcement during the prestressing application and $[EA]_{c,p}$ is the axial stiffness of the high strength concrete surrounding the reinforcement. An important observation is that the elastic shortening strain must be removed from the composite reinforcement before any tensile stresses develop within the concrete portion. As a result, the strain must be applied to the composite reinforcement in addition to the cracking strain in order for the cracking load to be reached. The cracking load increases in accordance with this requirement, which improves the serviceability range for which higher axial stiffness of the composite reinforcement prevails. The revised cracking load is denoted $N_{cr,p}$ and is defined by EQ3.8. Figure 3.2 illustrates the effects of prestressing more clearly by using the appropriate strains that arise from the prestressing application as well as a direct tension test performed on the composite reinforcement.

$$N_{cr,p} = (\Delta\varepsilon_p + \varepsilon_{cr})[EA]_{CR} \qquad \text{EQ3.8}$$

It should be noted at this stage that the load-deformation response of the composite reinforcement will start at the elastic shortening strain. The condition arises from the fact that concrete is initially compressed to that strain when prestress has been released. The reinforcing bar, on the other hand, is not subjected to the same level of strain. It is not compressed but rather stressed in tension by an initial strain that corresponds to the jacking strain adjusted to account for elastic shortening losses.

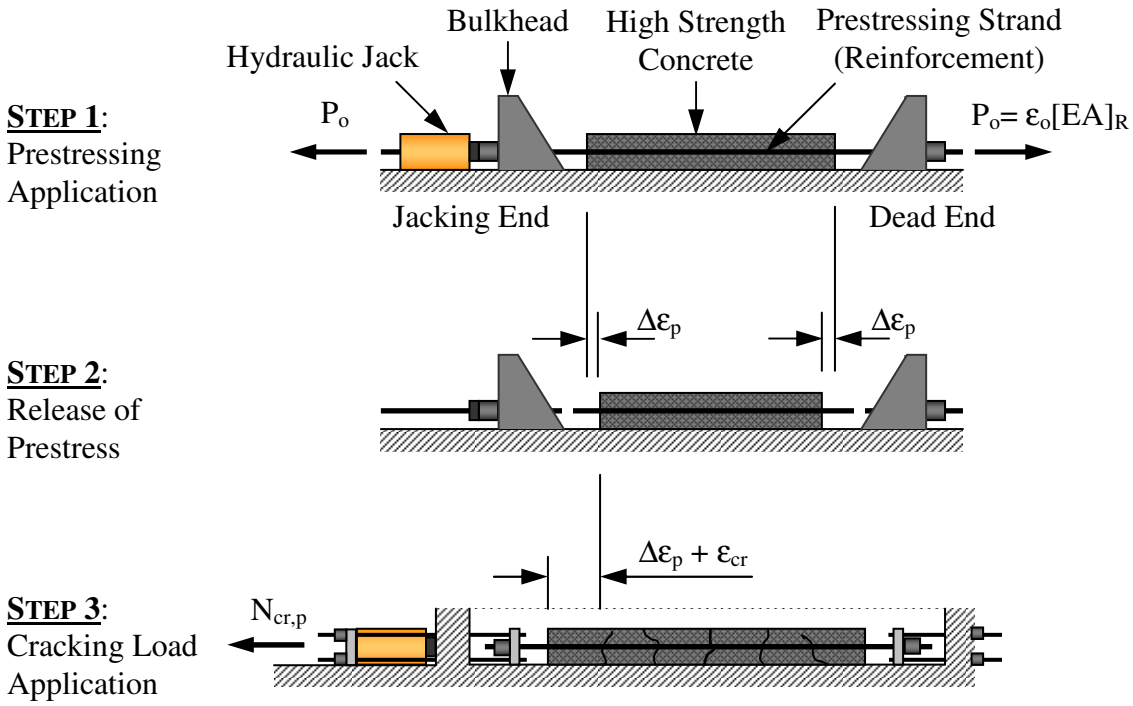

Figure 3.2 - **Prestressing and Load Application of Composite Reinforcement**

Both materials in the composite reinforcement will therefore start at different strains when subjected to axial loading. They will, however, be subjected to identical changes in deformation such that the axial stiffness remains the same as that obtained for the non-prestressed element shown in Figure 3.1. The load-deformation response of EQ3.3 can therefore be used to estimate the behavior of the prestressed composite reinforcement in tension, provided that it is offset to account for the initial strain that arises from elastic shortening. The outcome is illustrated in Figure 3.3 and plotted alongside the response of

the non-prestressed member as well as the bare reinforcement. The figure clearly shows the advantage of considering prestressing to increase cracking load. As discussed earlier, the parameter is vital in providing the largest possible serviceability range and greatly depends on the direct tensile strength and elastic modulus of the high strength concrete mix.

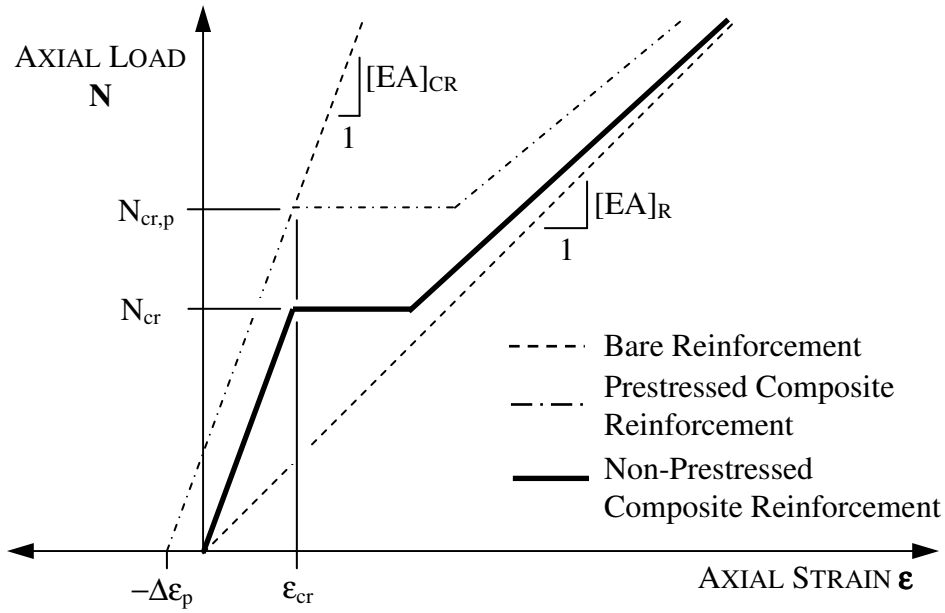

Figure 3.3 - **Load-Deformation Response of Prestressed Composite Reinforcement**

Other researchers have studied the use of prestressed composite reinforcement in concrete beams. They are referred to as Prestress Concrete Prisms (PCPs) and were initially used for reinforcing concrete pavements (Kommandigesellschaft 1963). Since then, several researchers have discussed the advantages of PCP reinforced concrete and suggested the advantage of using the concept in environments for which corrosion protection is essential (Hoppe 1963, Zia et al. 1976). The environments include water tanks, pressured pipes and roads. More recent work has considered the use of PCPs as reinforcement in continuous concrete T-beams, which can provide higher dowel resistance and reduce moment redistribution to the interior spans beyond the cracking stage (Chen and Nawy 1998, Davoudi and Svecova 2008). However, the research has been limited to PCPs with steel reinforcement and little research has been done with FRP

reinforcement. The distinctive properties of the reinforcement can significantly influence the design and behavior of FRP PCPs and more attention must be attributed to the subject.

3.3 DIFFERENTIAL SWELLING OF FRP IN PRESTRESSED CONCRETE

During the prestressing operation, elongations in the longitudinal direction are typically accompanied by contractions of the reinforcement in the lateral direction. Upon release, the amount of material surrounding the reinforcement at the ends of the component is insufficient to resist the complete prestressing force. A transfer length is required for the concrete to achieve a compressive force that is capable of establishing equilibrium with the reinforcement. Bond stresses between the materials will dissipate within this length such that gradual increases in compressive force will shrink concrete to the elastic shortening strain. Longitudinal strains in the reinforcement will steadily reduce and since they are typically accompanied by contractions in the lateral direction, the condition will provide a wedge shaped expansion of the reinforcing bar within the anchorage zone. The concept is illustrated in Figure 3.4 and is called the Hoyer effect.

The wedge shaped expansion of the reinforcement in the anchorage zone is critical at the extremities of prestressed concrete elements. The absence of shear resistance from the concrete at this location will cause a complete release of prestress, which provides the reinforcement with the potential of regaining its original shape in the lateral direction. This lateral recovery of the reinforcement will cause the surrounding concrete to withstand internal pressure such that a state of radial as well as circumferential stress will develop within the concrete cover. While radial stresses are compressive, circumferential stresses are tensile. If these stresses exceed the tensile strength, splitting cracks will develop within the cover and cause stress relief and potential deterioration of the bond between the materials.

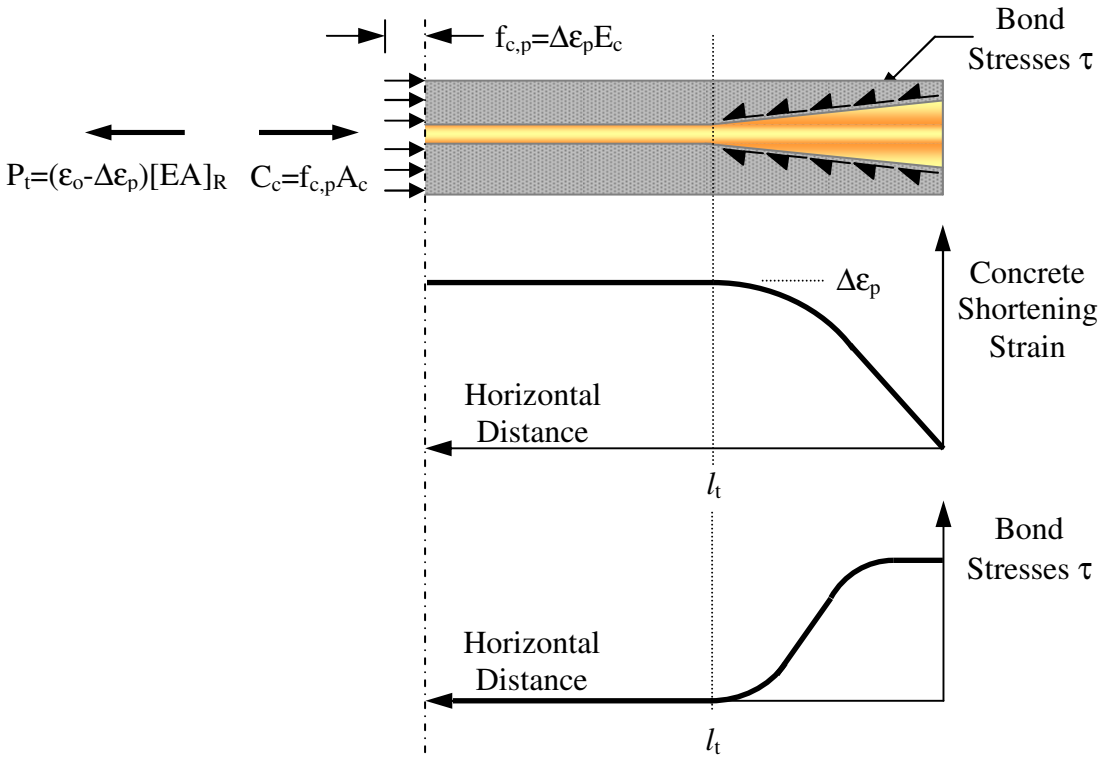

Figure 3.4 – **Transfer of Prestress** [Hoyer Effect]

3.4 LINEAR ELASTIC MODEL FOR CONCRETE COVER STRESSES

The closed-form solution for a thick-walled cylinder subjected to internal pressure presented by Timoshenko and Goodier (1970) can be used to describe the biaxial state of stress developing in the concrete cover. The linear elastic solution has been considered by several researchers (Rahman et al. 1995, Gentry and Hussain 1999, Aiello 1999) to analyze stresses that arise from excessive thermal swelling of reinforcement in a concrete environment. The solution was modified for the case of a unidirectional composite rod embedded in a concrete cylinder with different thermoelastic properties. Although the fabrication of PCPs in this thesis will be eased by the use of square formwork, the diameter of the concrete cylinder can be extended to the extremities of the cover for the analysis. The surplus of concrete in the corners of the PCP can alleviate stresses that develop along the shorter dimensions of the cover but neglecting its effect will allow the analysis to be conservative in selecting the critical prestressing level.

Figure 3.5(a) represents the adaptation of the linear elastic model to describe the Hoyer effect in PCPs. In this figure, c_c is the clear concrete cover, d_b is the bar diameter and r is the radial distance extending from the center of the reinforcement. Based on the convenient choice of geometry for the model, Timoshenko and Goodier (1970) were able to make axisymmetric assumptions in the derivation of circumferential (EQ3.9) and radial (EQ3.10) stress components that are represented in Figure 3.5(b). More specifically, the assumption implies that the distribution of stresses within the concrete cover remains unchanged when rotating about the longitudinal axis of the reinforcement. Furthermore, the sum of the stress components is constant through the concrete cover, which produces a uniform extension or contraction of individual elements along the radial direction. The condition creates a condition of plane stress for which cross-sections perpendicular to this axis remain plane and absent of shear stresses.

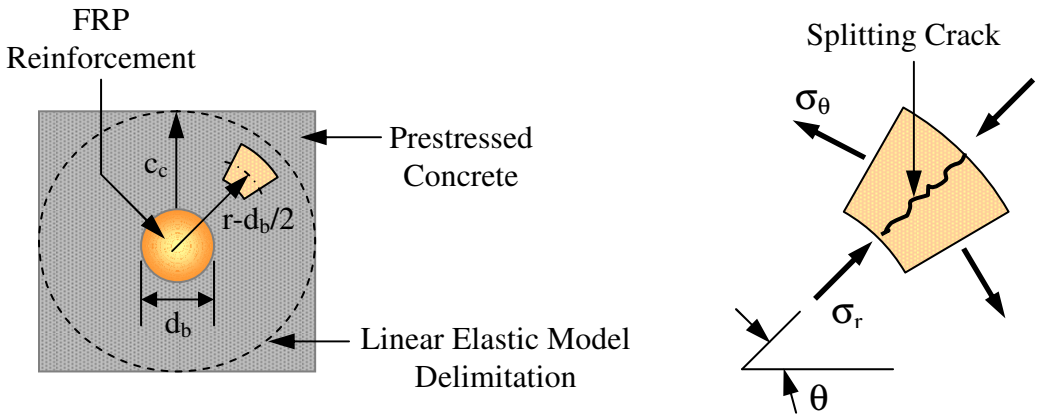

(a) Model Representation (b) Biaxial Stress State

Figure 3.5 – **Linear Elastic Model Adaptation for PCPs**

$$\sigma_\theta = \frac{1}{R_{cd}^2 - 1}\left(1 + 0.25R_{cd}^2 \frac{d_b^{\,2}}{r^2}\right)p \qquad \text{EQ3.9}$$

$$\sigma_r = \frac{1}{R_{cd}^2 - 1}\left(1 - 0.25R_{cd}^2 \frac{d_b^{\,2}}{r^2}\right)p \qquad \text{EQ3.10}$$

$$R_{cd} = 2^{c_c}/_{d_b} + 1 \qquad \text{EQ3.11}$$

Aside from being a function of geometry, stresses generated by the linear elastic model are directly related to the pressure p exerted by the reinforcement on the surrounding concrete. A typical distribution of radial and circumferential stresses obtained from these relationships is illustrated in Figure 3.6(a) for an internal pressure of 5.74MPa, a clear concrete cover of 20mm and bar diameter of 8mm. Stresses are plotted along the complete concrete cover of the linear elastic model. The figure suggests that both stresses reach their maximum level at the surface of the reinforcement and that they dissipate with radial distance from the interface.

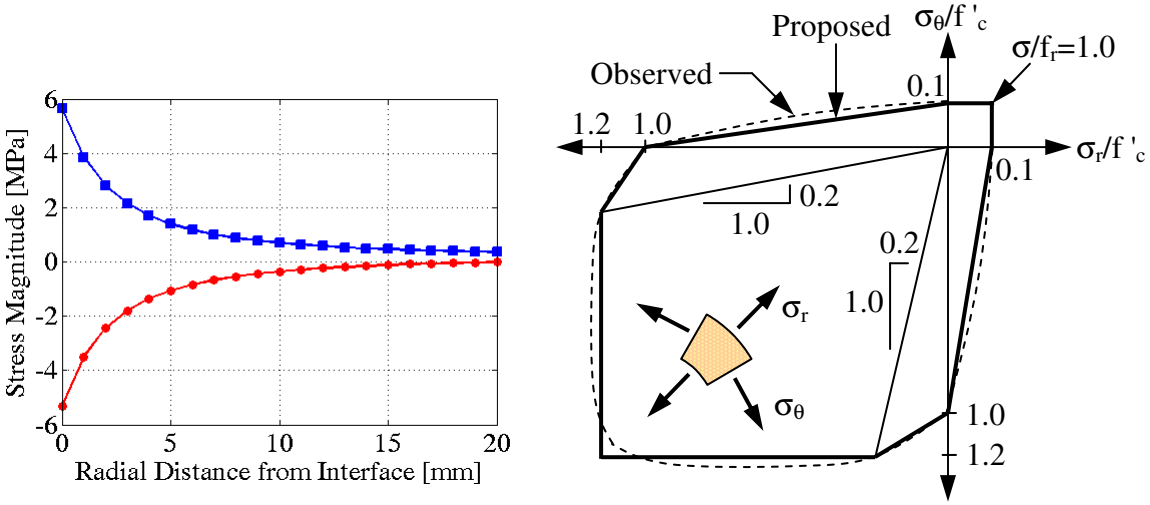

(a) Distribution (b) Failure Stress Envelope

Figure 3.6 – **Concrete Cover Biaxial Stress State**

Although the tensile strength of concrete is relatively lower than its compressive strength, circumferential stresses are not necessarily the primary interest in the analysis. As indicated by research from Kupfer et al. (1969), biaxial states of stress can have a strong influence on the strength of concrete. While the biaxial tensile strength of concrete is nearly equal to its uniaxial tensile strength, the strength of concrete in biaxial compression is greater than its uniaxial compressive strength by up to 27% (Pillai, S.U. 1999). The tensile strength of concrete can however be reduced when compressive

stresses on a perpendicular plane are present. The result is commonly illustrated using biaxial concrete strength envelopes as the one shown in Figure 3.6(b). The figure contains the envelope measured by Kupfer et al. (1969) as well as a proposed approximation to the envelope suggested by Tasuji et al. (1978). The envelopes suggest that the combination of tensile and compressive stresses is the most undesirable stress condition in concrete. The combination of circumferential and radial stresses within the concrete cover of the linear elastic model should therefore be considered rather than ignored. Their magnitude is primarily influenced by the mechanical properties of the materials in the linear model, which are accounted by the relationship for pressure. The relationship is established by satisfying compatibility of radial displacements at the interface separating the concrete and reinforcement (EQ3.12).

$$\Delta r_R = \Delta r_c \qquad \text{EQ3.12}$$

Here, Δr_c and Δr_R are the respective radial displacements of concrete and reinforcement at the interface. When the prestress is released, the process by which the reinforcement expands laterally and attempts to regain its original shape at the extremities of the member is restrained by the presence of concrete. The restrictive effect of concrete on this unrestrained lateral displacement can be used to establish a relationship for the radial displacement of the reinforcement at the interface (EQ3.13). More specifically, the displacement can be written in terms of the unrestrained lateral displacement reduced to account for the effects of pressure exerted by the concrete on the reinforcement.

$$\Delta r_R = r_R \varepsilon_T - r_R \frac{p}{E_R^T}(1 - \nu_R^{TT}) \qquad \text{EQ3.13}$$

In this equation, ε_T is the unrestrained lateral strain of the reinforcement, r_R is the reinforcement radius and $E_R{}^T$ is the elastic modulus of the reinforcement in the transverse direction. Also, $\nu_R{}^{TT}$ is Poisson's ratio that accounts for lateral strains that arise from transverse pressure loading from the concrete on the reinforcement. The radial displacement of the concrete can be obtained by considering circumferential strain at the

interface. Although the value represents a ratio of change in circumference to initial circumference, the relationship is equivalent to establishing radial strain (EQ3.14) at the interface.

$$\varepsilon_\theta = \frac{\Delta r_c}{r_R} \qquad \text{EQ3.14}$$

Both stresses in the concrete cover will contribute to this strain. While circumferential stresses directly contribute to this strain, radial stresses will be related to it by using Poisson's ratio for concrete. Multiplying radial stresses at the interface by this ratio and subtracting the result from the circumferential stresses at the interface allows a relationship for radial displacement of concrete to be developed once it is divided by the elastic modulus of concrete and multiplied by the radius of the reinforcement (EQ3.15).

$$\Delta r_c = \frac{r_R p}{E_c}\left[\beta_{cd} + \nu_c\right] \qquad \text{EQ3.15}$$

$$\beta_{cd} = \left(\frac{R_{cd}^2 + 1}{R_{cd}^2 - 1}\right) \qquad \text{EQ3.16}$$

In these expressions, the modulus of elasticity of concrete is denoted E_c and Poisson's ratio is defined as ν_c. The factor β_{cd} includes the effects of clear concrete cover to bar diameter ratio. Finally, substituting the results from EQ3.13 and EQ3.15 for the radial displacements of reinforcement and concrete in the compatibility requirement of EQ3.12 gives an expression for internal pressure at the interface of the linear elastic model (EQ3.17).

$$p = \frac{\varepsilon_T}{(\beta_{cd} + \nu_c)/E_c + (1 - \nu_R^{TT})/E_R^T} \qquad \text{EQ3.17}$$

The relationship explicitly defines pressure as a function of the reinforcement's unrestrained lateral strain. As seen for the case of circumferential and radial stresses, it also considers the influence of clear concrete cover to bar diameter ratio. Finally and most importantly, internal pressure is the parameter that allows the mechanical properties of each material to be incorporated in the analysis. It therefore controls the sensitivity of the linear elastic model to changes in the properties of the reinforcement and high strength concrete used in the fabrication of PCPs.

3.4.1 Sensitivity of Internal Pressure Formulation

The objective of the sensitivity analysis is to determine the influence of each property on the behavior of the linear elastic model. Considering a variation in the properties having the highest influence can provide a significant impact on selecting a prestressing level that optimizes cracking load while preventing crack development within the concrete cover. The analysis should be performed over the range of material properties that define and control the internal pressure defined by EQ3.17.

3.4.2 Material Properties for Analysis

One of the requirements arising from the use of PCPs as reinforcement in concrete structures is to ensure that the composite reinforcement maintains its axial stiffness beyond the cracking stage of the beam. As discussed in earlier sections, the condition requires the concrete surrounding the reinforcement in the composite reinforcement to have higher strength than that selected for the beam. Based on past research aimed at achieving sufficient tensile strength, the sensitivity analysis will consider concrete compressive strengths in excess of 80MPa. The higher strength will affect the modulus of elasticity, which can be determined on the basis of Clause 8.6.2 of the CSA A23.3-04 design code for concrete strengths in excess of 40MPa.

$$E_{c,p} = (3300\sqrt{f_c'} + 6900)\left(\frac{\gamma_c}{2300}\right)^{1.5} \qquad \text{EQ3.18}$$

The relationship is empirical in nature and was determined from test results on concrete with a mass density γ_c ranging from 1500 to 2500kg/m^3. For normal density concrete, the mass density of concrete is typically taken as 2400kg/m^3. Higher strength concrete typically exhibits higher permeability to water and chlorides, which arises from the lower porosity of the paste structure and composition (PCA Research and Development Bulleting RD104T 1992). The mass density for higher strength concrete should therefore be larger than that anticipated for normal density concrete and values ranging between 2400 and 2500 kg/m^3 can be expected. A value of 2450 kg/m^3 was used to represent this range and define elastic modulus values from EQ3.18 and the range of concrete strengths considered in the sensitivity analysis.

Unlike the elastic modulus, Poisson's ratio for concrete does not vary with compressive strength. The parameter can vary from about 0.11 to 0.21 and usually falls in the range 0.15 to 0.20 (MacGregor and Bartlett 2000). Since the concrete cover of the linear elastic model is subjected to a combination of tensile and compressive stresses, the biaxial stress tests conducted by Kupfer et al. (1969) can be used to refine the range of Poisson's ratio within 0.18 to 0.20.

Research conducted by Rahman et al. (1995) emphasizes that there is no existing standard method for determining the transverse elastic modulus of FRP reinforcement. The research also emphasized that further work on developing a suitable test method for determining the parameter was required. Since fibers are only aligned along the axis of the reinforcement, values for the parameter are mainly influenced by the elastic modulus of the resin and are generally smaller than elastic modulus values prevailing in the longitudinal direction. Due to air entrapment in the resin, Rahman et al. (1995) confirmed that experimental values obtained for the parameter were lower than those calculated on the basis of theoretical expressions. Values used for the sensitivity analysis of this thesis

were chosen to reflect those reported in the literature, which can range from as low as 3100MPa (Rahman et al. 1995) to as high as 6200MPa (Gentry and Hussain 1999).

Since the transverse material properties of FRP reinforcement differ from those in the longitudinal direction, the material is referred to as being transversely isotropic. Such a material has three independent ratios for Poisson's effect, which include ν_R^{LT}, ν_R^{TT} and ν_R^{TL}. The first superscript denotes the direction of loading and the second denotes the direction of lateral strain where L and T indicate the longitudinal and transverse directions, respectively. For longitudinal loading, the ratio ν_R^{LT} is controlled by that of the fibers and is typically taken as 0.2. For transverse loading, the ratio ν_R^{TT} is governed by that of the resin and is generally taken as 0.35. These values were suggested in work presented by Rahman et al. (1995) and were also used in the linear elastic analysis presented by Gentry and Hussain (1999). Since the pressure is derived using the compatibility of transverse strains between reinforcement and concrete, the ratio ν_R^{TL} is not required for the linear elastic analysis.

3.4.3 Analysis Results

The sensitivity analysis was performed by investigating the variation of internal pressure over the range of material properties outlined in the previous section. Since the prestressing level is unknown at this stage and highly dependent on the outcome of this analysis, results shown in Figure 3.7 represent internal pressure values that were normalized with respect to the unrestrained transverse strain of the reinforcement. In more specific terms, the normalized parameter was determined over the range of possible values for transverse elastic modulus of the reinforcement as well as for each material's Poisson's ratio. For each of these variables, the result was expanded to consider the complete range of compressive strengths that can be used for PCP reinforcement. Results were expressed in the form of a scalogram, for which the vertical axis corresponds to the compressive strength and the horizontal axis corresponds to the variable under consideration. For each possible combination of values between the compressive strength and selected variable, the corresponding magnitude of normalized pressure is associated

to a relative degree of shading and plotted. The progression of shading and its direction can be used to establish which of the two variables have prevailing influence on internal pressure for a specific prestressing level. It should be noted that variables other than the one being considered were kept fixed at the central value of their respective range such that results from each scalogram are centered about the same value.

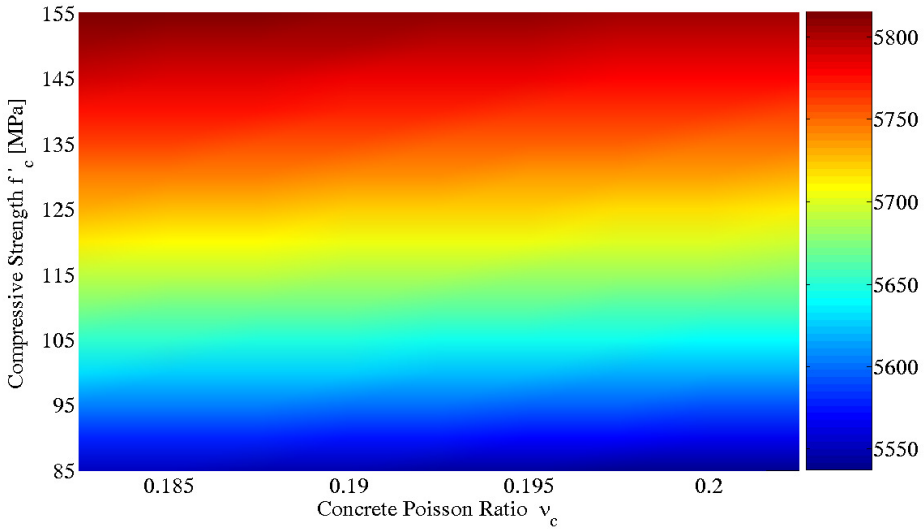

(a) Concrete Poisson Ratio [E_R^T=4500 MPa & ν_R^{TT}=0.35]

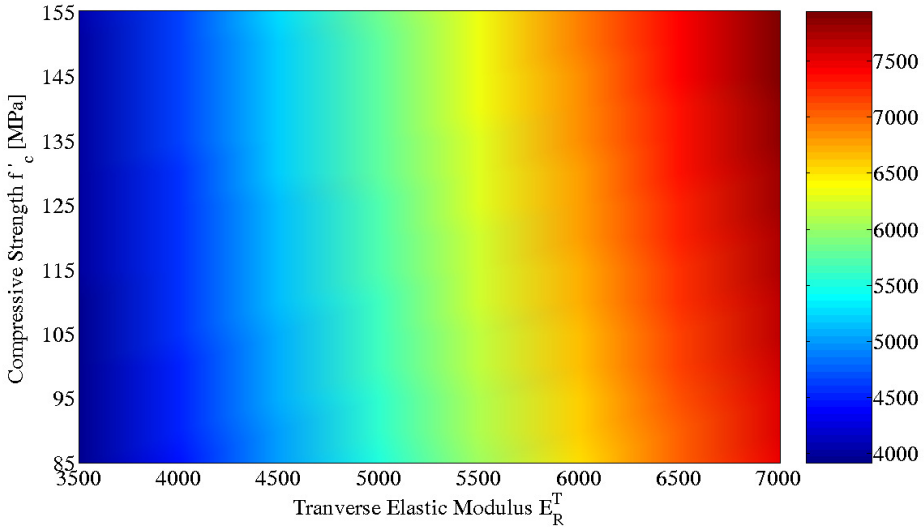

(b) Transverse Elastic Modulus [ν_c=0.19 & ν_R^{TT}=0.35]

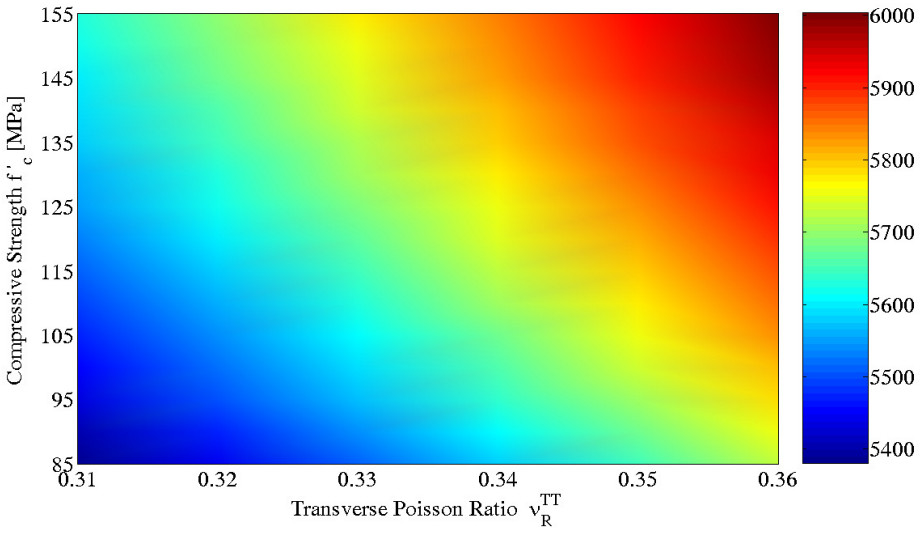

(c) Transverse Poisson Ratio [ν_c=0.19 & E_R^T=4500 MPa]

Figure 3.7 - **Sensitivity Analysis Results for Normalized Internal Pressure**

Figure 3.7(a) indicates that the variation of shading is predominant in the vertical direction. The result suggests that stronger changes in the magnitude of the normalized parameter are attributed to a change in the compressive strength. The degree of variation in shading is much less noticeable in the horizontal direction and the linear elastic model is therefore more sensitive to a change in compressive strength than in Poisson's ratio for concrete. The result can be expanded to Figure 3.7(b) where the change in normalized pressure was investigated over the possible range of concrete compressive strengths and transverse elastic modulus for the reinforcement. In this case, however, the variation in shading is predominantly in the horizontal direction, which indicates that the model is more sensitive to changes in transverse elastic modulus than changes in compressive strength.

In opposition to results illustrated in previous figures, Figure 3.7(c) does not show a distinct progression of shading in either horizontal or vertical directions. Instead, the figure illustrates a diagonal variation in shading over the range of concrete compressive strengths and transverse Poisson's ratio for the reinforcement. The result suggests that the linear elastic model is equally sensitive to each of these variables. The interpretation is

further justified by observing that the variation of shading, and therefore pressure magnitude, is similar in both directions when considering identical locations along each axis.

Based on results from the sensitivity analysis, it is apparent that the linear elastic model is most sensitive to changes in the transverse elastic modulus of the reinforcement. Figure 3.7(b) confirms that normalized pressure values obtained for this parameter can vary from as low as 4000×10^{-6} to as high as 7500×10^{-6}MPa/με, which represents the highest range arising for the sensitivity analysis. The compressive strength of concrete and transverse Poisson's ratio for the reinforcement are next in the ranking and represent variables for which the model has equal sensitivity. Finally, Poisson's ratio for concrete is the variable for which the model demonstrates the least amount of sensitivity.

Unfortunately, it is not possible to establish the full extent of variation in internal pressure from the results of Figure 3.7 since each scalogram keeps material properties other than those under consideration unchanged. However, since the linear elastic model is most sensitive to the transverse elastic modulus of the reinforcement, the range of normalized pressure values obtained from changing this parameter is a good indication of the amount of variation. If the complete set of possible combinations among the variables of interest is considered, the maximum normalized pressure should occur when the denominator of EQ3.17 is minimum. For this, Poisson's ratio for concrete should be the smallest in its range and Poisson's ratio for the reinforcement as well as elastic modulus values for all materials should be the greatest in their respective ranges. The opposite holds true for getting the minimum normalized pressure. In this case, the largest possible Poisson's ratio for concrete and the minimum Poisson's ratio for reinforcement will maximize the denominator of EQ3.17 with the smallest elastic modulus values. Maximum and minimum normalized pressure values are plotted in Figure 3.8 over the range of possible concrete compressive strengths for the project.

While Figure 3.8(a) suggests minimum values varying between 3790×10^{-6}MPa/με for a compressive strength of 80MPa and 3910×10^{-6}MPa/με for a compressive strength of

150MPa, Figure 3.8(b) specifies maximum values for the parameter ranging between 7690×10^{-6}MPa/με and 8200×10^{-6}MPa/με. For the complete range of variables considered in this thesis, the extent of variation for normalized internal pressure can therefore be taken to vary between 3790×10^{-6} to 8200×10^{-6}MPa/με.

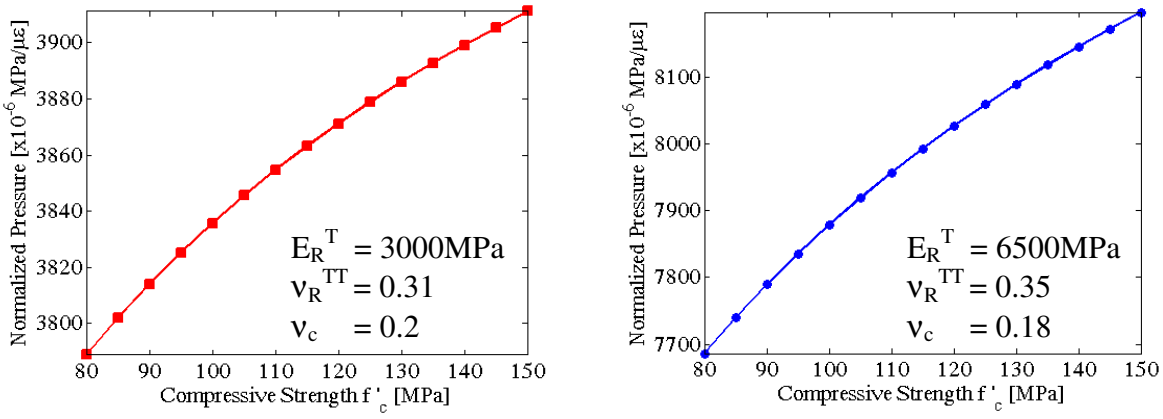

(a) Minimum Pressure (b) Maximum Pressure

Figure 3.8 - **Extreme Normalized Internal Pressure Values**

3.4.4 Influence of Concrete Cover

Results from Figure 3.6(a) suggest that the clear concrete cover can have a significant impact on the distribution of stresses around the reinforcement. More specifically, the figure demonstrates that stresses concentrate and rapidly dissipate near the interface between the materials. Most of the stresses are therefore being resisted in this region and the tendency suggests that increasing the clear concrete cover beyond a certain value will have a negligible influence on the magnitude of stresses that develop in proximity of the reinforcement. For a given unrestrained transverse strain and clear concrete cover, larger bar diameters cause larger differential movement between the materials and create higher stress levels around the reinforcement. The clear concrete cover to bar diameter ratio c_c/d_b therefore becomes a prevailing parameter for which more than the internal pressure is influenced. The sensitivity of the linear elastic model to this parameter must therefore be investigated using the complete formulation for circumferential stresses.

The development of cracks within the concrete cover can lead to significant stress relief and deterioration of the bond between the materials used in the fabrication of PCP reinforcement. To prevent cracks from initiating within the concrete cover, the maximum circumferential stress should remain below the tensile strength of concrete. In accordance with Figure 3.6(a), such a stress occurs at the interface between the reinforcement and concrete. Its magnitude is obtained by using EQ3.9 and substituting half the bar diameter as the radial distance from the center of the reinforcement (EQ3.19).

$$\sigma_{\theta,max} = \beta_{cd}\, p \qquad \text{EQ3.19}$$

The sensitivity of this parameter with respect to the c_c/d_b ratio is illustrated in Figure 3.9 for the range of concrete compressive strengths and reinforcement transverse elastic modulus values considered for the linear elastic analysis. As previously stated, Poisson's ratio for concrete varies over a relatively small range that is confined between 0.18 and 0.2. The parameter has little influence on the behavior of the linear elastic model and an average representative value of 0.19 was selected for the purpose of establishing sensitivity of the model to concrete cover. Since Poisson's ratio for the reinforcement in the transverse direction is mainly influenced by the resin, the commonly accepted value of 0.35 (Rahman et al. 1995, Gentry and Hussain 1999) was selected as a representative value for FRP products and used to establish the results of Figure 3.9. The range of concrete cover to bar diameter ratios considered in this figure was chosen in accordance with that recommended by manuals concerned with the design of concrete structures reinforced with FRP products (ISIS Canada 2001). The lower limit for the ratio corresponds to the highest possible bar diameter of 35mm associated with the smallest recommended clear concrete cover value of 20mm (c_c/d_b=0.5). Conversely, the upper limit for the ratio corresponds to the smallest possible bar diameter of 8mm associated with the largest recommended clear concrete cover value of 40mm (c_c/d_b=6.5).

For similar reasons as those chosen for establishing the sensitivity of internal pressure to material properties, the circumferential stress values of Figure 3.9 were normalized with respect to the unrestrained transverse strain of the reinforcement. Results from this figure

indicate that the linear elastic model is noticeably sensitive to c_c/d_b ratios between 0.5 and 2.5. In fact, a strong reduction in circumferential stresses at the interface can be achieved when increasing the c_c/d_b ratio within this range. Beyond a value of 2.5, increasing the ratio has negligible influence on the linear elastic model since reductions in the tensile stresses at the interface are insignificant. The ability of these ratios to prevent the formation of cracks within the concrete cover is therefore greatly diminished and larger prestressing levels are achieved with increasing difficulty.

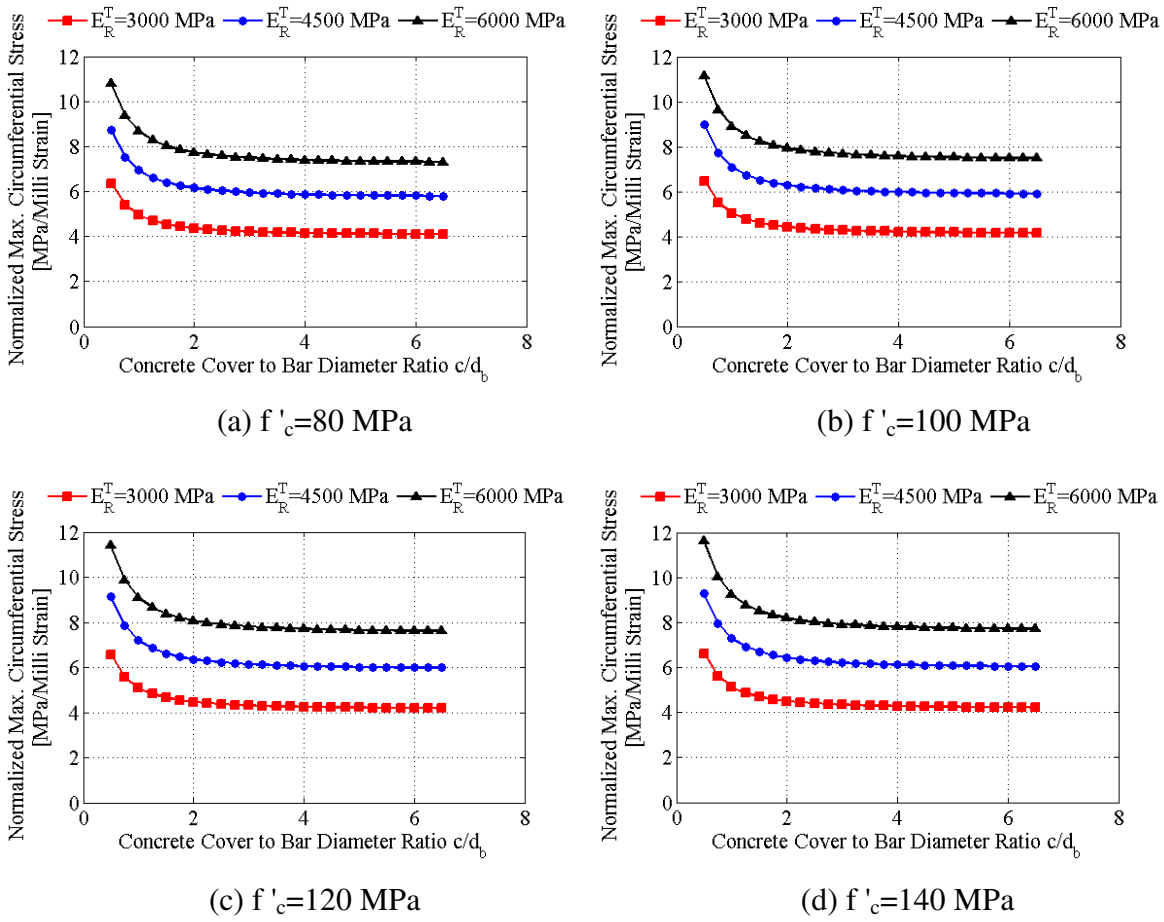

(a) f '$_c$=80 MPa (b) f '$_c$=100 MPa

(c) f '$_c$=120 MPa (d) f '$_c$=140 MPa

Figure 3.9 – **Sensitivity Analysis for Normalized Maximum Circumferential Stresses**

Despite this limitation, the results of Figure 3.9 can be modified to establish the maximum prestressing level as well as the corresponding c_c/d_b ratio that will prevent the occurrence of cracks within the cover. The first step consists of writing the unrestrained transverse strain of the reinforcement in terms of the initial prestressing strain. Since

prestressing is completely released at the ends of the PCP reinforcement, the unrestrained transverse strain is equivalent to the product of the initial prestressing strain and Poisson's ratio for the reinforcement ν_R^{LT} (EQ3.20). In turn, the initial prestressing strain can be calculated by dividing the initial prestressing stress f_o in the reinforcement and the elastic modulus of the reinforcement in the longitudinal direction (EQ3.21).

$$\varepsilon_T = \nu_R^{LT} \varepsilon_o \qquad \text{EQ3.20}$$

$$\varepsilon_o = \frac{f_o}{E_R} \qquad \text{EQ3.21}$$

The second step consists of substituting the expression for unrestrained transverse strain in the relationship for internal pressure. The maximum initial prestressing strain for which crack initiation is prevented within the concrete cover (EQ3.22) can then be determined by ensuring that the maximum circumferential stress from EQ3.19 remains below the tensile strength of concrete.

$$\varepsilon_o = \frac{f_{dp}}{\nu_R^{LT} \beta_{cd}} \left[(\beta_{cd} + \nu_c)/E_c + (1 - \nu_R^{TT})/E_R^T \right] \qquad \text{EQ3.22}$$

The third and last step consists of selecting a concrete tensile strength f_{dp} that appropriately reflects the biaxial state of stress in the concrete cover of the linear elastic model. The double punch test is an indirect tension test that can reproduce the required state of stress of Figure 3.6(b). It presents an alternative to the split-cylinder test and was introduced by Chen (1970). The test consists of concentrically loading a concrete cylinder at the extremities with two cylindrical steel punches. Two conical fragments develop beneath the steel punches and penetrate within the concrete cylinder during the test (Marti 1990). Collins and Mitchell (1997) suggest that the tensile strength from the double punch test is approximately 93% of the splitting tensile strength (EQ3.23).

$$f_{dp} = 0.551\sqrt{f'_c} \qquad \text{EQ3.23}$$

The maximum prestressing strains of EQ3.22 are plotted in Figure 3.10. The same range of material properties as those used for the sensitivity analysis of the linear elastic model to c_c/d_b ratios was selected for developing the diagrams in this figure. Results indicate that changing the c_c/d_b ratio between 0.5 and 2.5 has a strong influence on the prestressing level sustained by the PCP reinforcement without the occurrence of cracking within the cover. Noticeably higher prestressing levels can be achieved when increasing the ratio within this range, which is inherent to the findings of Figure 3.9 where strong reductions in interfacial stresses can be reached. Conversely, results from Figure 3.9 also indicate that reductions in these stresses are negligible when the c_c/d_b ratio is increased beyond a value of 2.5. Figure 3.10 confirms this aspect of the analysis by indicating that the maximum prestressing level is not influenced by these ratios. The result implies that increasing the c_c/d_b ratio beyond 2.5 will not allow higher prestressing levels to be achieved without having the possibility of cracks developing within the concrete cover. The result deters the use of larger proportions for the composite reinforcement and the dimensional ceiling can serve as an advantage when considering the use of PCP reinforcement in flexural members with relatively thin webs. The result also prevents higher cracking loads from being reached but higher prestressing levels can still be achieved by altering the mechanical properties of the concrete or bare reinforcing bar for which the linear elastic model was found to be highly sensitive.

3.5 DESIGN CHARTS FOR SERVICE MOMENT

From the sensitivity analysis of the previous section, it is apparent that a c_c/d_b ratio of 2.5 marks a transition point for establishing the optimum prestressing level in PCP reinforcement. While c_c/d_b ratios below this value greatly reduce the level of prestress that can be achieved, ratios beyond the value have limited influence on the parameter. For the case of a concrete beam reinforced with PCP reinforcement, the ratio can be used to determine the largest service moment for which the concrete cover of the reinforcement remains intact and maintains the enhanced level of flexural stiffness. This upper limit on

service moment can be expanded to develop design charts that consider various material properties, geometries and reinforcement ratios for the beam as well as the PCP reinforcement. The procedure will require the consideration of force equilibrium when the PCP reinforcement has reached the cracking stage as well as several modifications to simplify the use of the charts for the designer. As a starting point, stress and strain profiles at the onset of the stage are examined in Figure 3.11 along with the cross sectional properties of the reinforcement.

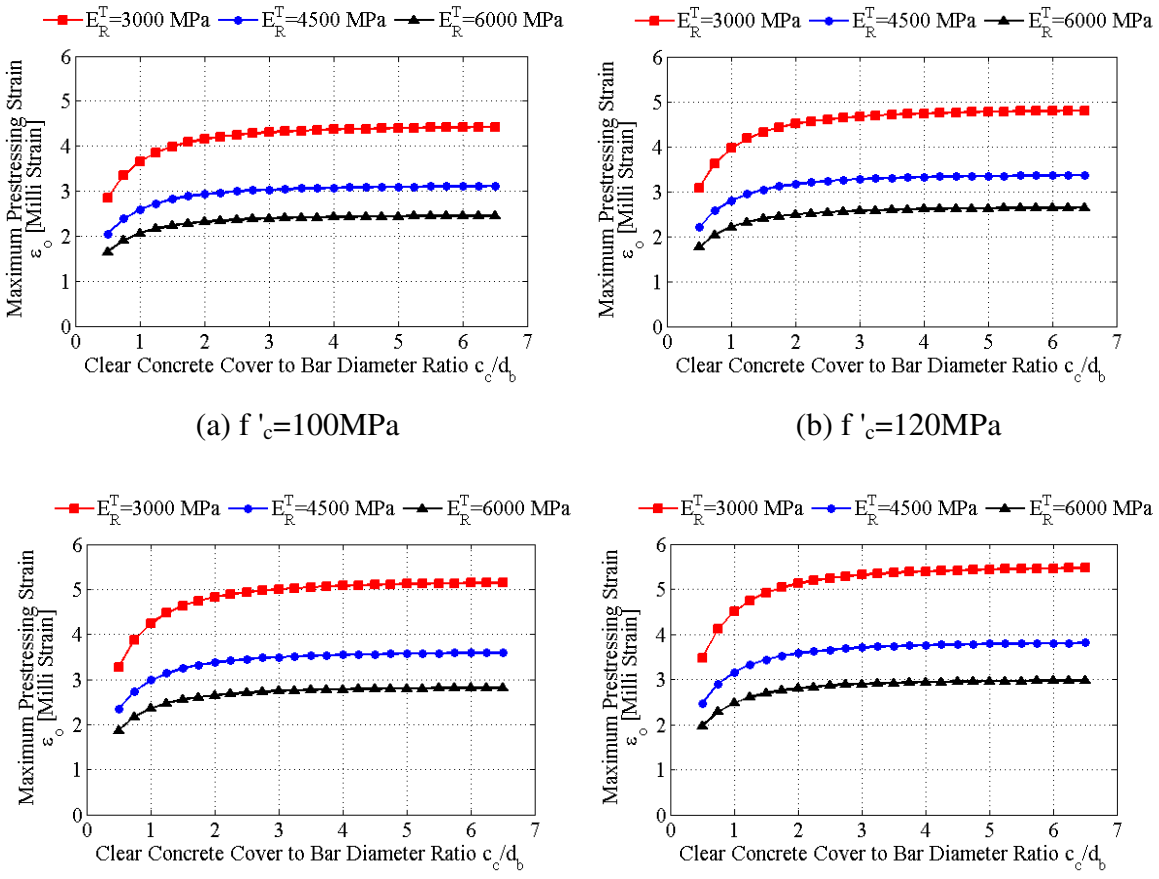

(a) f '$_c$=100MPa (b) f '$_c$=120MPa

(c) f '$_c$=140MPa (d) f '$_c$=160MPa

Figure 3.10 – **Maximum Allowable Prestressing Level**

When the PCP reinforcement reaches its cracking stage, the unstressed and lower strength concrete surrounding the reinforcement has already cracked and does not contribute to tensile resistance. Although a portion of the concrete remains uncracked below the neutral axis, the contribution can be ignored in moment calculations since it is

small and relatively close to the neutral axis. The complete tensile force can therefore be taken as the PCP reinforcement's cracking load and the maximum service moment resisted by the section at the onset of cracking can be written as shown in EQ3.24.

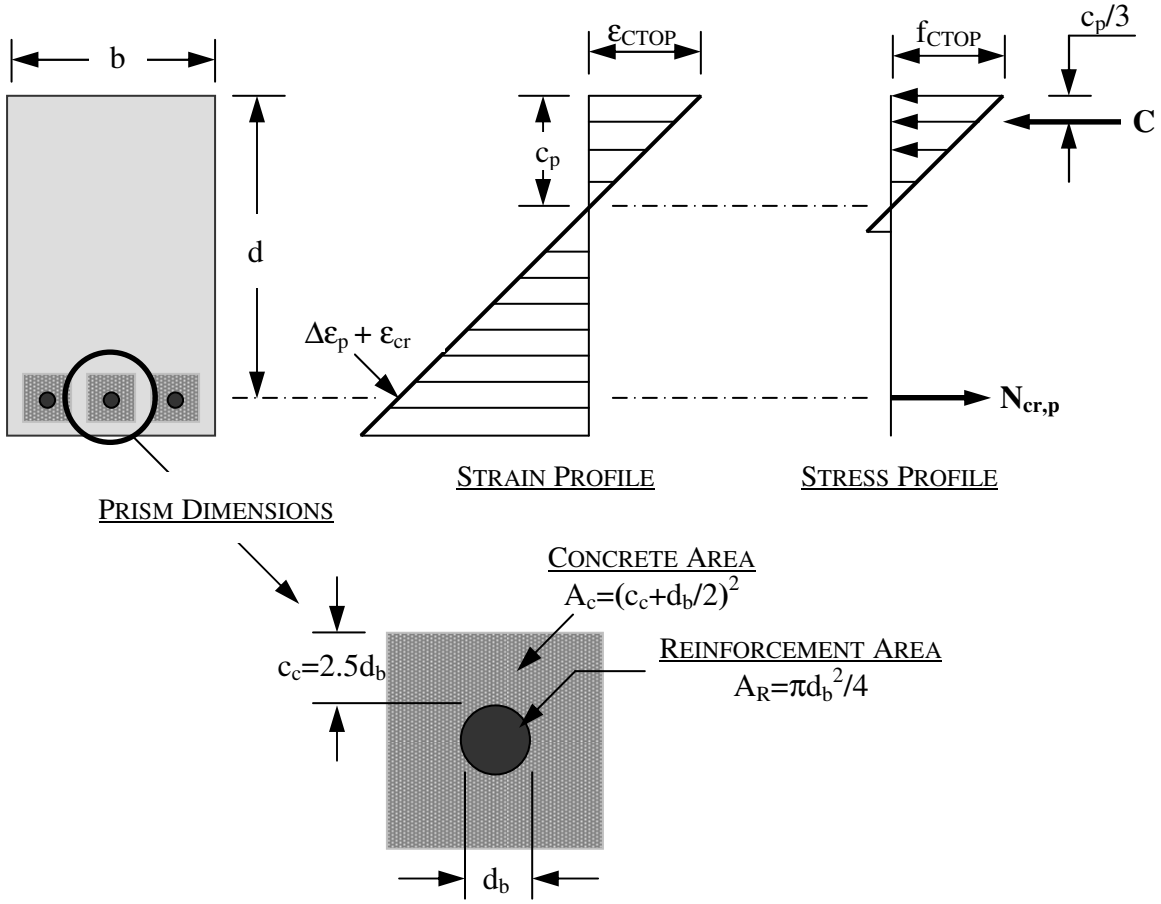

Figure 3.11 – **Cracking of PCPs in Reinforced Concrete Beams**
[Stress and Strain Conditions]

$$M_{cr,p} = N_{cr,p}(d - c_p/3) \qquad \text{EQ3.24}$$

In this equation, the maximum service moment $M_{cr,p}$ is taken about the point of application of the compressive force. The effective depth of reinforcement is denoted d and the depth of neutral axis is denoted c_{na}. Since the stress and strain profiles of Figure 3.11 represent service conditions, linear elastic behavior of concrete in compression has been assumed to prevail and the force acts at one third of the neutral axis depth. The cracking load in the equation can be determined on the basis of EQ3.8 but several

substitutions are required to ease the inclusion of geometry and material properties. Firstly, the expression can be modified to include the reinforcement ratio of the bare reinforcement in the beam (EQ3.25) as well as in the PCP reinforcement (EQ3.26).

$$\rho = \frac{A_R}{bd} \qquad \text{EQ3.25}$$

$$\rho_p = \frac{A_R}{A_c} \qquad \text{EQ3.26}$$

From EQ3.25, the reinforcing area A_R can be written as the product of the reinforcement ratio ρ, beam width b and effective depth of reinforcement. Similarly, EQ3.26 can be used to write the area of concrete in the PCP reinforcement A_c as the ratio of reinforcing area A_R to prism reinforcement ratio ρ_p. Substituting this rearrangement of terms in the relationship for axial stiffness of the PCP reinforcement (EQ3.4) and factoring the elastic modulus of concrete gives a revised form for the expression (EQ3.27).

$$[EA]_{pr} = \rho\left(n_p + \frac{1}{\rho_p}\right)E_{c,p}bd \qquad \text{EQ3.27}$$

In this equation, n_p is the modular ratio for the PCP reinforcement. It corresponds to the ratio of elastic modulus for the bare reinforcement to elastic modulus for the high strength concrete $E_{c,p}$ (EQ3.28). The substitutions can also be used to write the elastic shortening strain (EQ3.7) in terms of the prism reinforcement ratio. The adjustment is shown in EQ3.29 and does not include the beam reinforcement ratio since the prestressing effect, and therefore elastic shortening, is relevant to the PCP only.

$$n_p = \frac{E_R}{E_{c,p}} \qquad \text{EQ3.28}$$

$$\Delta\varepsilon_p = \varepsilon_o\left(\frac{n_p}{n_p + 1/\rho_p}\right) \qquad \text{EQ3.29}$$

From the revised formulation for axial stiffness (EQ3.27) as well as the altered expression for elastic shortening strain (EQ3.29), the cracking load of the PCP reinforcement can be re-written as shown in EQ3.30. The modified expression no longer depends on a specific area for the bare reinforcing bar or surrounding concrete. The reinforcement ratio is selected in the design process and the prism reinforcement ratio can be written in terms of the selected proportions of concrete cover to bar diameter. More specifically, the expressions from Figure 3.11 for reinforcing area as well as concrete area can be substituted in EQ3.26 with the aim of writing the prism reinforcement ratio in terms of the transition c_c/d_b ratio (EQ3.31).

$$N_{cr,p} = \left[\varepsilon_o\left(\frac{n_p}{n_p + 1/\rho_p}\right) + \varepsilon_{cr}\right]\rho\left(n_p + \frac{1}{\rho_p}\right)E_{c,p}bd \qquad \text{EQ3.30}$$

$$\rho_p = \frac{\pi}{4R_{cd}^2} \qquad \text{EQ3.31}$$

Before EQ3.30 can be substituted in the expression for maximum service moment, an equation for the depth of neutral axis must be established by ensuring force equilibrium is maintained within the section. A relationship for the concrete compressive force is required for the purpose. The force can be calculated by integrating the linear stress profile of Figure 3.11 over the area of concrete in the compression zone (EQ3.32).

$$C = f_{CTOP}\frac{bc_p}{2} \qquad \text{EQ3.32}$$

For equilibrium, the compressive force of EQ3.32 is equated to the cracking load of EQ3.30 and the resulting relationship can be simplified by expressing the extreme compressive fiber stress f_{CTOP} as the product of elastic modulus and extreme compressive

fiber strain ε_{CTOP}. Similar triangles in the strain profile of Figure 3.11 can then be used to write the strain in terms of that sustained by the PCP reinforcement at the onset of cracking (EQ3.33). Re-organizing and grouping terms will translate the force equilibrium requirements to a quadratic expression from which EQ3.34 is the non-negative solution for neutral axis depth that needs to be retained.

$$\varepsilon_{CTOP} = (\Delta\varepsilon_p + \varepsilon_{cr})\left(\frac{c_p}{d - c_p}\right) \qquad \text{EQ3.33}$$

$$c_p = d\left[\sqrt{(n_c\rho_{bm})^2 + 2n_c\rho_{bm}} - n_c\rho_{bm}\right] \qquad \text{EQ3.34}$$

In this equation, n_c is the modular ratio for the PCP reinforced beam. It corresponds to the ratio of elastic modulus for concrete in the composite reinforcement to elastic modulus for the concrete in the beam E_c (EQ3.35). The reinforcement ratio for the beam ρ_{bm} is obtained by dividing the transformed area of the composite reinforcement by the product of beam width and effective depth of reinforcement (EQ3.36). The expression was simplified by the substitution of reinforcement ratios for areas.

$$n_c = \frac{E_{c,p}}{E_c} \qquad \text{EQ3.35}$$

$$\rho_{bm} = \rho\left(n_p + \frac{1}{\rho_p}\right) \qquad \text{EQ3.36}$$

The relationships for cracking load (EQ3.30), neutral axis depth (EQ3.34) and beam reinforcement ratio (EQ3.36) can now be substituted in the equation for maximum service moment (EQ3.24). To achieve a more general form, the expression can be normalized with respect to the dimensions of the beam (EQ3.37).

$$\frac{M_{cr,p}}{bd^2} = K_R \qquad \text{EQ3.37}$$

$$K_R = \left[\varepsilon_o \left(\frac{n_p}{n_p + 1/\rho_p} \right) + \varepsilon_{cr} \right] \left(1 - \frac{\sqrt{(n_c \rho_{bm})^2 + 2n_c \rho_{bm}} - n_c \rho_{bm}}{3} \right) \rho_{bm} E_{c,p} \qquad \text{EQ3.38}$$

Results from EQ3.37 are illustrated in Figure 3.12 for reinforcement ratios beyond the balanced condition. The figure can be used as a design chart for which the required beam reinforcement ratio can be chosen to achieve a given service moment without significant loss in flexural stiffness. The charts were determined for a maximum prestressing strain that corresponds to the recommended c_c/d_b ratio of 2.5 as well as for the range of material properties investigated during the sensitivity analysis. As expected, results from the figure indicate an increasing trend with reinforcement ratio. From the results of Figure 3.10, the maximum prestressing strain increases for lower transverse elastic modulus values, and the resulting trend in service moment is more pronounced.

Figure 3.12 also includes a horizontal line representing the initial cracking moment for the beam. The moment defines the stage for which cracking is initiated within the concrete surrounding the PCP reinforcement. Results emphasize the range of service moments that can be applied to the beam without sacrificing the enhanced flexural stiffness provided by the use of PCP reinforcement. The initial cracking moment was calculated using gross concrete section properties and Clause 9.8.2.3 of CSA A23.3-04 (EQ3.39).

$$M_{cr} = \frac{f_r I_g}{y_t} \qquad \text{EQ3.39}$$

In this equation, y_t is the distance from the neutral axis of the gross section to the extreme tension fiber. It can be taken as half of the beam height. The modulus of rupture f_r can be determined in accordance with Clause 8.6.4 of CSA A23.3-04 (EQ3.40) where λ is a

factor accounting for the density of concrete. Since most designs use normal density concrete, the factor can be taken as 1.0. Finally, the gross moment of inertia is a function of the width and height of the element (EQ3.41).

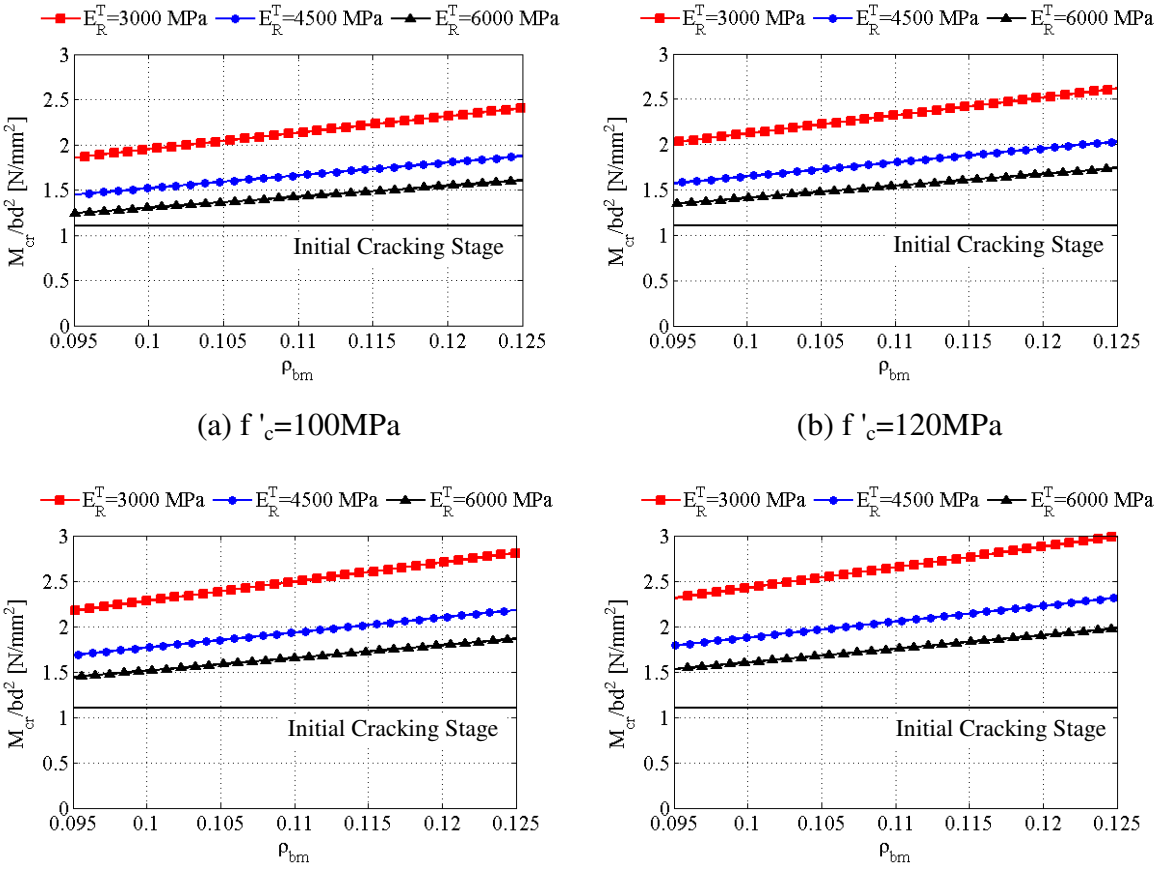

(a) f '$_c$=100MPa (b) f '$_c$=120MPa

(c) f '$_c$=140MPa (d) f '$_c$=160MPa

Figure 3.12 - **Design Charts for Max. Service Moment** [f′$_c$=50MPa, E_R=171,962MPa]

$$f_r = 0.6\lambda\sqrt{f_c'} \qquad \text{EQ3.40}$$

$$I_g = \frac{bh^3}{12} \qquad \text{EQ3.41}$$

These last two relationships allow the initial cracking moment to be normalized with respect to the geometry of the section (EQ3.42). However, the design process generally

involves the use of effective depth as opposed to section height. For beams reinforced with a single layer of reinforcement, the depth can range from 80 percent of the height for shallow sections to 97 percent of the height for deeper sections. A value of 80 percent was used as a conservative estimate (EQ3.43) such that the range of service moments beyond the initial cracking moment are slightly larger than those shown in Figure 3.12 if deeper sections are used.

$$\frac{M_{cr}}{bh^2} = \frac{f_r}{6} \qquad \text{EQ3.42}$$

$$\frac{M_{cr}}{bd^2} = \frac{f_r}{3.84} \qquad \text{EQ3.43}$$

CHAPTER 4

PROPERTIES OF THE HIGH STRENGTH CONCRETE MIX

4.1 HIGH STRENGTH CONCRETE FOR PCP REINFORCEMENT

The previous chapter established that high strength concrete (HSC) can be used to improve the axial stiffness of PCP reinforcement. The higher compressive strengths enhance the direct tensile strength and elastic modulus of the material, which can increase the cracking load as well as the axial stiffness of the PCP reinforcement. Higher tensile strengths can also improve the resistance of concrete to stresses that arise from lateral expansion of the reinforcement in the transfer region once prestressing is released. Design charts in Chapter 3 were developed to consider the mechanical properties of HSC and allow the selection of prestressing levels that can optimize cracking load of the PCP reinforcement while preventing the concrete cover from splitting in the transfer region. Since codes are generally developed for the design of elements with normal strength concrete, the current chapter will evaluate the adequacy of code relationships for the estimation of properties inherent to HSC. This will ensure that the behavior and serviceability of structures reinforced with PCPs can be successfully estimated. The chapter also investigates the introduction of dispersed fibers in the mix for enhanced tensile performance as well as the investigation of mortar properties for the development of theoretical models for elastic modulus.

4.2 CONCRETE MIX DESIGN

The concrete mix used in this project was selected from the PCA Research and Development Bulletin RD104T (1992). The report presents engineering properties of commercially available HSC obtained from six separate mixes over a period of three years. The mix with the highest strength gain was selected since the project involves prestressing of concrete elements and requires the earliest release date to minimize relaxation losses within the tendon. The mix has the highest silica fume content out of the six designs proposed by the report, which provides the lowest permeability to chlorides as well as the lowest water absorption rate. The advantages are significant when considering protection of the reinforcement to environments that are susceptible to entice deterioration.

4.2.1 Mix Proportions and Gradation of Aggregates

The proportions of the mix are listed in Table 4.1. Aside from including the use of silica fume, the low water-cement ratio of the mix requires the use of a High Range Water Reducer (HRWR) to achieve an acceptable level of workability during each cast. A retarder was also included in the mix to maintain workability and allow sufficient time to cast the elements before reaching the set time. The weight of silica fume is in terms of its dry weight and the maximum size of aggregate was chosen as 12.5 mm.

Table 4.1 – **Concrete Mix Proportions**

Parameters [/m^3]	Quantity
Cement Type I [kg]	564
Silica Fume [kg]	89
Coarse Aggs. SSD [kg]	1068
Fine Aggs. [kg]	593
HRWR Type F [L]	20.11
Retarder Type D [L]	1.46
Water [kg]	144
Water:Cement Ratio	0.26

To ensure sufficient strength was achieved from the mix design, coarse and fine aggregates were sieved in accordance with the requirements of ASTM Standard C33-03. Table 4.2 lists the grading limits in terms of sieve specification as well as in terms of percentage and weight of aggregate retention.

Table 4.2 – **Aggregate Grading Limits**

Sieve Specification	Fine Aggs. Retained		Coarse Aggs. Retained	
	%	Weight [kg/m^3]	%	Weight [kg/m^3]
12.5 mm [½ in.]	-	-	45	480.60
4.75 mm [No. 4]	2.5	14.83	55	587.40
1.18 mm [No.16]	30	177.90	-	-
600 με [No.30]	25	148.25	-	-
300 με [No.30]	25	148.25	-	-
150 με [No.30]	12.5	74.13	-	-
PAN < 150 με	5	29.65	-	-
Total Weight [kg]	593		1068	

4.2.2 Moisture Absorption of Coarse Aggregates

The total amount of water added to a concrete mix can greatly influence the development of compressive strength. It is therefore important to notice that the porosity of coarse aggregates can lead to moisture absorption and consequently reduce the amount of water available for reaction with cement in the mix. In order to account for this and control the total amount of water in the mix, coarse aggregates are required to be in a saturated surface dry (SSD) condition. The moisture absorption capacity of coarse aggregates used in this project was therefore tested on the basis of ASTM Standard C127-04. A total of six test samples were completely dried with an oven capable of maintaining a uniform temperature of 110 ± 5^{o}C and subsequently immersed in water at room temperature. After having removed each sample from the water and dried the surface with a large absorbent cloth, weight differences with the dried condition were computed. From these results, an average 1.46% increase in the weight of coarse aggregate was observed and attributed to water absorption with a standard deviation of 0.18%. A trial batch was cast by adding water to compensate 1.4% absorption from the fully dried coarse aggregates introduced in the mix. Based on mechanical properties obtained from this batch, the first set of PCPs

was cast by compensating for lower water absorption from the coarse aggregates. The 0.7% compensation produced the desired properties from the mix and was therefore kept for all subsequent sets of PCPs.

4.3 MECHANICAL PROPERTIES

Cylindrical concrete specimens were tested in accordance with ASTM Standard C39/C39M-04a, C496/C496M-04 and C469-02 for determining the compressive strength, splitting tensile strength and elastic modulus, respectively. All tests were performed with a 1350kN TestMark hydraulic testing machine. The test setup is shown in Figure 4.1(a) for compressive tests and in Figure 4.1(b) for splitting tensile tests.

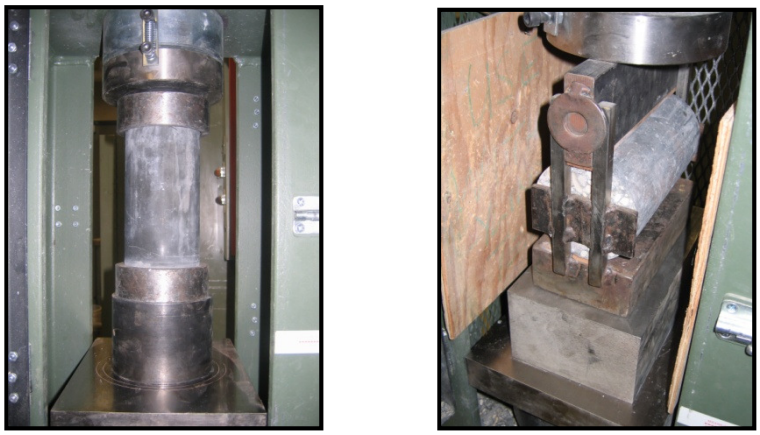

(a) Compressive Strength (b) Tensile Strength

Figure 4.1 – **Cylindrical Concrete Test Setup**

The load was applied such that the required rate of 14.4±6MPa/min and 1.05±0.35MPa/min was maintained during all compressive and tensile strength tests, respectively. Although peak load rates were exceeded during the initial stages of each test, the process was achieved in a controlled manner and in accordance with the standards until approximately 5% of the ultimate load was reached. The procedure ensured specimens were not subjected to shock loading. As allowed by the standard for compressive tests, a gradual reduction in the load rate was observed but not prevented during the final loading stages. The reduction is attributed to the formation and

development of cracks within the samples, which contribute to gradual loss in stiffness arising from material non-linearity.

4.3.1 Compressive Strength Development

A total of 3 specimens with a diameter of 100mm and a height of 200mm were tested in compression at approximately 3, 7, 14 and 28 days. In order to maintain similar moisture content during all compressive tests, specimens were consistently taken out of the curing room 24 hours prior to testing. The procedure was considered on the basis of work presented by Li (2004), which suggests that water absorbed in the pores of concrete specimens lead to transverse bursting stresses that can greatly influence the compressive strength of cylindrical specimens and therefore consistency in the results.

Compressive strengths recorded from each test were averaged for each testing day and each of the three sets of 50mm by 50mm by 2450mm PCPs cast in this project. Results are shown in Table 4.3 and further illustrated in Figure 4.2 along with those obtained from the trial batch as well as those reported by the PCA Research and Development Bulletin RD104T (1992) for the corresponding mix. The figure suggests that the strength of concrete reported by the bulletin and obtained from the trial batch are distinctly lower than those achieved for the three batches of PCPs. The result is a direct consequence of the higher water content used to achieve SSD conditions for coarse aggregates in the trial batch. It can also be observed from the figure that the first batch of PCPs exhibits higher compressive strengths than that obtained from subsequent batches. The first set of prisms was cast at a temperature of 28^{o}C with the laboratory overhead door open while the remaining batches were cast at an approximate temperature of 19.5^{o}C. There is a strong possibility that higher local temperature and air circulation within the laboratory during the first concrete pour reduced the water content in the mix, thereby increasing the concrete's compressive strength. These results suggest a significant sensitivity of the mix to water content. Nevertheless, compressive strengths at 28 days are consistent among all PCP batches and vary within 6.5% of each other.

Table 4.3 – **Compressive Strength Development**

TRIAL BATCH		PCP SET #1		PCP SET #2		PCP SET #3	
Age [Days]	Strength [MPa]	Age [Days]	Strength [MPa]	Age [Days]	Strength [MPa]	Age [Days]	Strength [MPa]
3	75.7	4	98.7	3	85.6	3	83.1
7	94.4	8	123.8	7	110.8	9	112.4
14	114.7	14	131.9	13	122.1	14	122.5
28	-	28	139.2	28	133.5	28	130.8

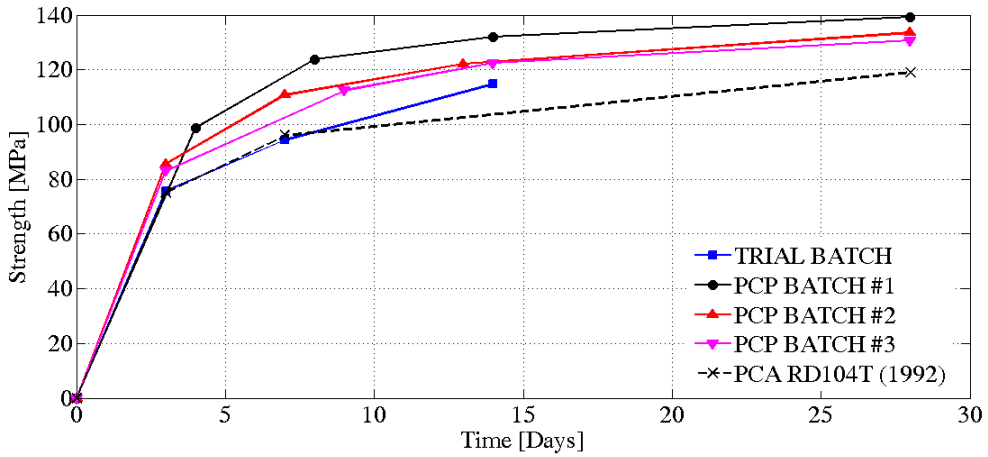

Figure 4.2 - **Compressive Strength Development with Age**

4.3.2 Tensile Strength Development

At each of the days selected for compressive strength testing, an additional 3 specimens were set aside to determine and investigate splitting tensile strength. In order to control the effects of moisture on strength, specimens intended for tensile tests were also taken out of the curing room 24 hours prior to testing. Results in terms of age at testing are shown in Table 4.4 and graphically illustrated in Figure 4.3(a). Reported values do not include those for the first set of PCPs. The omission is attributed to an over-estimation of tensile strength caused by the presence of imperfections in the bearing strips and the difficulty in transferring load to the samples. Material for these strips was altered for subsequent batches and average tensile strengths obtained from concrete cylinders cast with all remaining sets of PCPs were considered and reported. Concrete from the trial batch was not tested for tensile strength at 3 days since the concrete mix was not

anticipated to reach the required value for prestress release within the first few days of curing when using SSD conditions for coarse aggregates (Burg & Ost 1992).

Table 4.4 **– Tensile Strength Development**

TRIAL BATCH		PCP SET #2		PCP SET #3	
Age [Days]	Strength [MPa]	Age [Days]	Strength [MPa]	Age [Days]	Strength [MPa]
3	-	3	5.5	3	5.4
7	5.4	7	6.2	9	6.4
14	6.3	13	6.4	14	6.7
28	-	28	7.1	28	6.8

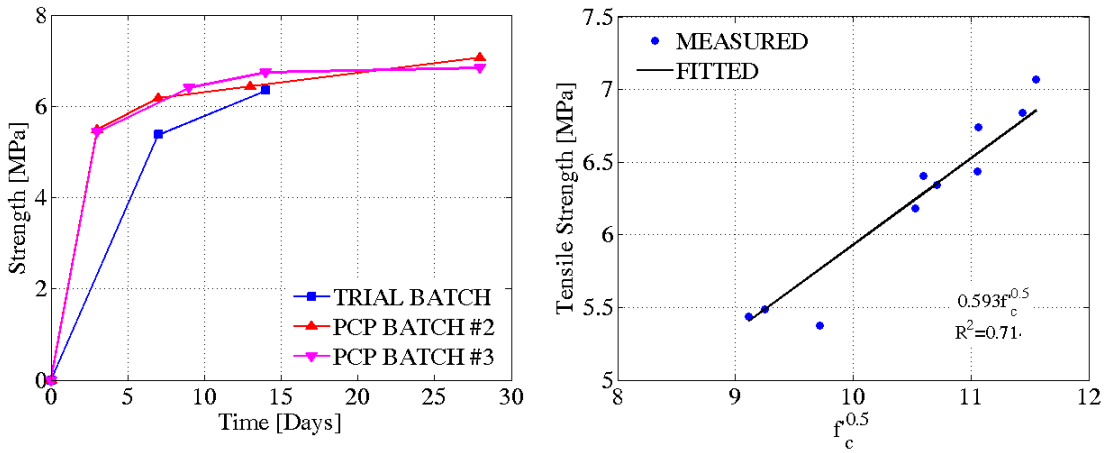

(a) with Age (b) with Compressive Strength

Figure 4.3 **–Tensile Strength Development**

Tensile strength values typically display a linear trend with the square root of the compressive strength (MacGregor and Bartlett 2000). This statement is graphically shown in Figure 4.3(b). A relationship describing this trend was obtained by fitting a linear model to the measured data on the basis of a least squares method. It is expressed in EQ4.1 and has a correlation coefficient of 0.71, which suggests a strong relationship with the linear model explaining 71% of the variation in the measured values about the mean.

$$f_{sp} = 0.593\sqrt{f_c'} \qquad \text{EQ4.1}$$

The splitting tensile strength is mainly used in the design of structural lightweight concrete members to evaluate shear resistance provided by concrete and to determine the development length of reinforcement (ASTM C496/C496M-04). Consequently, results from the splitting tensile test cannot be directly used to determine the cracking strength of PCP reinforcement in this project. The same applies for describing the tensile strength of the concrete cover when subjected to circumferential stresses that arise from transverse swelling of the reinforcement in the transfer region. However, some approximate relationships exist that can be used to correlate values obtained from the splitting tensile test to those required for the project (Collins and Mitchell 1997).

According to Collins and Mitchell (1997), the direct cracking strength of concrete can be taken as 65% of the strength obtained from a splitting tensile test. Applying this relationship to the fitted results of EQ4.1 allows an expression to be established for describing the direct tensile strength of concrete selected for this project (EQ4.2). The expression correlates quite well with that suggested by the reference, which relates direct tensile strength to 33% of the square root of the compressive strength.

$$f_{dt} = 0.385\sqrt{f_c'} \qquad \text{EQ4.2}$$

As discussed in Chapter 3, the double punch test is an indirect tension test that creates a state of stress comparable to what develops in the transfer region of prestressed concrete elements due to lateral expansion of the reinforcement upon release. Collins and Mitchell (1997) suggest a relationship in which the tensile strength from the double punch test can be written as approximately 93% of the splitting tensile strength. As before, this relationship can be applied to the fitted results of EQ4.1 to establish an expression that describes the tensile resistance of the concrete cover to transverse differential swelling of the reinforcing bar.

$$f_{dp} = 0.551\sqrt{f_c'} \qquad \text{EQ4.3}$$

4.3.3 Elastic Modulus and Poisson's Ratio

The elastic modulus and Poisson's ratio were measured during 14 and 28day compressive tests for all sets of PCPs. Values at 14 days are relevant in establishing the adequacy of the HSC mix in sustaining stresses induced at release. Similarly, those at 28 days are typically reported by design codes and relevant for describing properties of the material that are required for establishing the performance of concrete beams reinforced with PCP reinforcement in the design process. From each set of compression tests, two cylindrical concrete specimens were instrumented with a bonded 90^{o} cross electrical resistance strain gauge. As required by the standard for the test, the effective length of gauge line was 60mm, which represents more than three times the maximum aggregate size of 12.5mm. The sensor was also capable of measuring longitudinal as well as transverse strains to the nearest millionth. Elastic modulus values shown in Table 4.5 were determined by fitting a linear trend through diagrams relating compressive stress to the corresponding longitudinal strain. The results for Poisson's ratio displayed in Table 4.6 were obtained by evaluating the relationship between transverse and longitudinal strains with an approach similar to that used for estimating elastic modulus. As illustrated in Figure 4.4, the linear regression analyses were performed for a longitudinal strain range extending from 50 millionths to that corresponding to a stress of 40% of ultimate. The regression algorithm is based on a least squares method that fits a line through the data by minimizing the summed squared of residuals between measured values and the predicted model.

Table 4.5 **– Elastic Modulus Development with Compressive Strength**

Age [Days]	PCP SET #1		PCP SET #2†		PCP SET #3	
	Strength [MPa]	Modulus [MPa]	Strength [MPa]	Modulus [MPa]	Strength [MPa]	Modulus [MPa]
14	129.4	46 409	123.8	46 336	122.9	43 411
	135.1	44 897	129.7	46 423	128.8	46 595
28	142.7	44 009	137.3	44 134	129.8	46 581
	137.1	47 716	136.7	44 531	125.6	43 716

† 14day tests were performed at 13 days

Table 4.6 – **Poisson's Ratio**

Age [Days]	PCP SET #1	PCP SET #2†	PCP SET #3
14	0.25	0.25	0.24
	0.23	0.25	0.24
28	0.22	0.24	0.25
	0.23	0.23	0.22

†14day tests were performed at 13 days

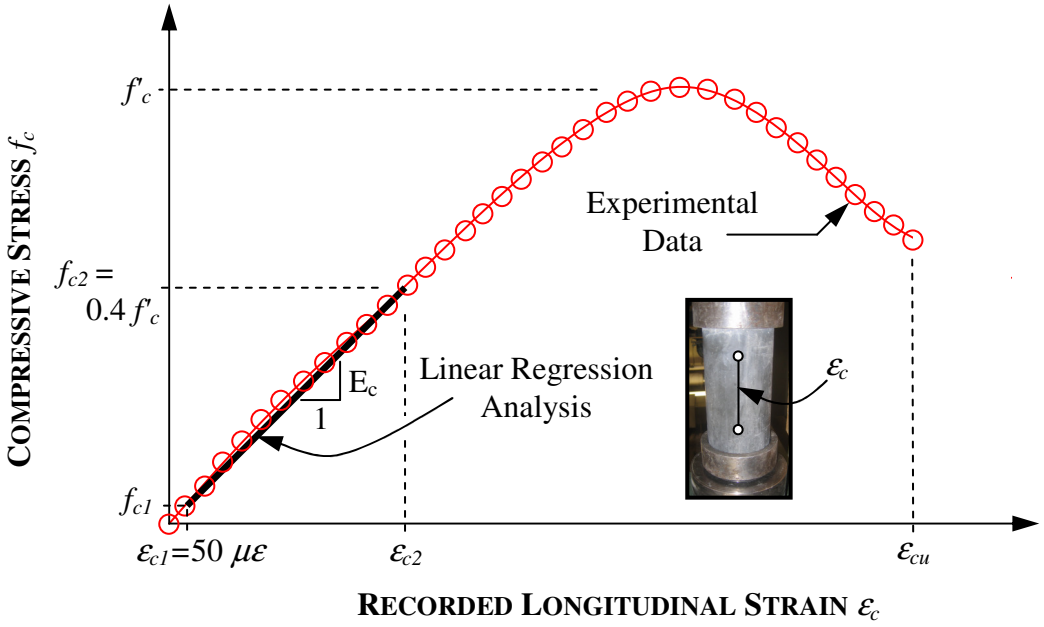

Figure 4.4 - **Elastic Modulus Determination**

As expected, the results of Table 4.5 indicate that elastic modulus values for concrete tend to increase with compressive strength. Conversely, values for Poisson's ratio are found to remain consistent over the complete range of ages considered for testing. The ratios appear to fluctuate between 0.22 and 0.25 with a respective mean and standard deviation of 0.24 and ±0.01. The mean of this distribution was found to vary within a margin of error of ±0.006 at a 95% confidence level.

4.3.3.1 Empirical Approach to Elastic Modulus Development

Past research and building code standards have often empirically correlated the properties of concrete with compressive strength (MacGregor and Bartlett 2000). The correlation of elastic modulus values in Table 4.5 should therefore be evaluated and compared with existing relationships to verify their applicability in estimating the parameter for higher concrete strengths as those achieved in this project. Several relationships exist for determining the elastic modulus of normal-weight concrete. For concrete strengths exceeding 40MPa, the CSA Standard A23.3-04 states that the elastic modulus in compression can be taken as defined by EQ4.4. The relationship accounts for the influence of coarse aggregates by incorporating the density of concrete γ_c, which can range between 1500 and 2500kg/m^3. As illustrated in Figure 4.5, the expression consistently overestimates the stiffness of concrete used in this project for the average density of 2479kg/m^3 measured by weighing cylindrical specimens prior to each compressive test. The outcome suggests that the code equation is not calibrated to estimate stiffness of concrete with density and strengths comparable to those obtained for the HSC mix in this thesis.

$$E_c = \left(3300\sqrt{f_c'} + 6900\right)\left(\frac{\gamma_c}{2300}\right)^{1.5} \qquad \text{EQ4.4}$$

Carrasquillo et al. (1981) recommend the use of an alternate equation for elastic modulus, which is similar in form to that presented by the CSA A23.3-04 code (EQ4.5) and was later adopted by ACI Committee 363R (1992). The relationship does not account for the density of concrete but agrees well with the upward trend in secant modulus values that were measured during compressive tests performed at 28 days for the first three sets of PCPs cast in this project. The observation is confirmed by Figure 4.5, where experimental results for elastic modulus are plotted against the square root of compressive strength. It should also be noted that EQ4.4 and 4.5 were derived to represent elastic modulus at 28 days. When compared to earlier stages, the internal structure of concrete has stabilized at this age and reached a state in which strength gain over time has greatly decreased.

Although 28day test results are shown and analyzed separately in Figure 4.5(b), Figure 4.5(a) indicates that the relationships remain in reasonable agreement with values obtained from tests performed after only 14 days.

$$E_{c\ ACI363R(1992)} = 3320\sqrt{f_c'} + 6900 \qquad \text{EQ4.5}$$

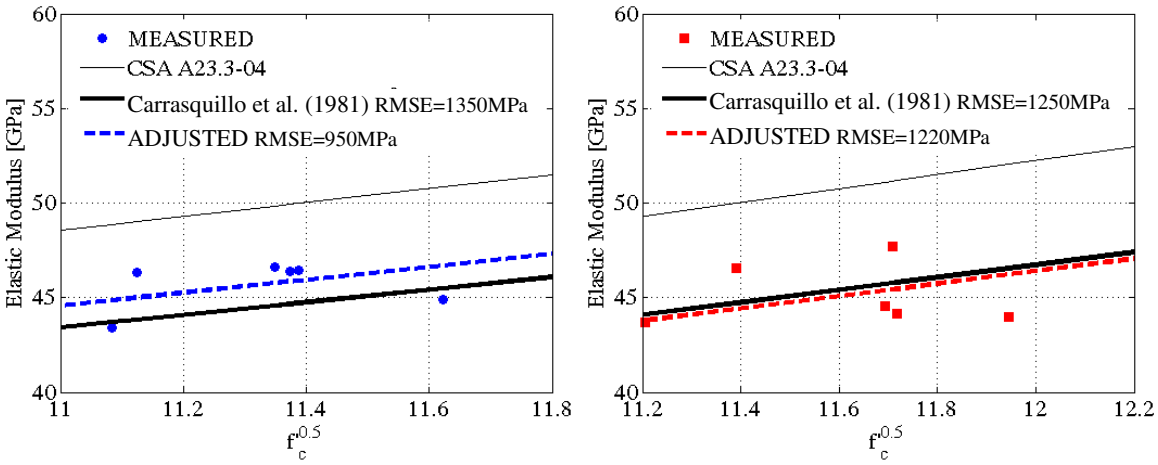

(a) 14 Days (b) 28 Days

Figure 4.5 - **Elastic Modulus Estimation**

The figure also emphasizes the relatively low correlation between experimental data and the relationship recommended by Carrasquillo et al. (1981). The Root Mean Squared Error (RMSE), which represents the average error that can be expected when evaluating elastic modulus over the range of compressive strengths considered, was found to vary between ±1356MPa for tests conducted at 14 days and ±1250MPa for tests performed at 28 days. The result for this error is a consequence of the strong variation in values recorded for elastic modulus, which can be attributed to fluctuations in strength, varying distribution of aggregates as well as inconsistent compaction among samples at the time of casting. Nevertheless, the slope of the relationship can be adjusted to reflect this variability more accurately and provide an improvement to the goodness of fit of the linear model. The adjustments are also presented in the figure and described by EQ4.6 for the 14day tests and EQ4.7 for the 28day tests. They improve the RMSE by approximately

30% for the 14day tests and 2.4% for the 28day tests over the range of compressive strengths considered for the regression analyses.

$$E_{c\,14D} = 3425\sqrt{f_c'} + 6900 \qquad \text{EQ4.6}$$

$$E_{c\,28D} = 3292\sqrt{f_c'} + 6900 \qquad \text{EQ4.7}$$

4.3.3.2 Theoretical Approach to Elastic Modulus Development

As discussed in earlier sections, empirical models express the modulus of elasticity as a function of the compressive strength alone. As mentioned in work presented by Rashid et al. (2002), the higher variability of compressive strength for HSC increases uncertainty and decreases confidence in the expressions for elastic modulus. Although a relationship remains apparent between elastic modulus and compressive strength, it can be attributed to the fact that both properties depend on the nature of the aggregates and the quantity of pozzolanic materials present in the mix design. More importantly, the elastic modulus depends on the relative stiffness of the mortar and coarse aggregates. In light of these observations, many researchers have been involved with the development of theoretical models in which elastic modulus is estimated using two-phase structures that incorporate the interaction between coarse aggregates and hydrated cement (Illston et al. 1987).

As reported by Hansen (1965), the two most fundamental models were conceived on the premise that the constituents are either supposed to carry the same strain or develop the same stress. The first of these models is called the Voigt model in which the hydrated cement and coarse aggregates share the applied load as a set of springs in parallel. The second approach is referred to as the Reuss model in which each constituent has to sustain the applied load as a set of springs in series. The models are graphically interpreted in Figure 4.6, where E_1 is the elastic modulus of the mortar, E_2 is the elastic modulus of the coarse aggregates, g_1 is the relative volume of the mortar in the sample and g_2 is the relative volume of the coarse aggregate.

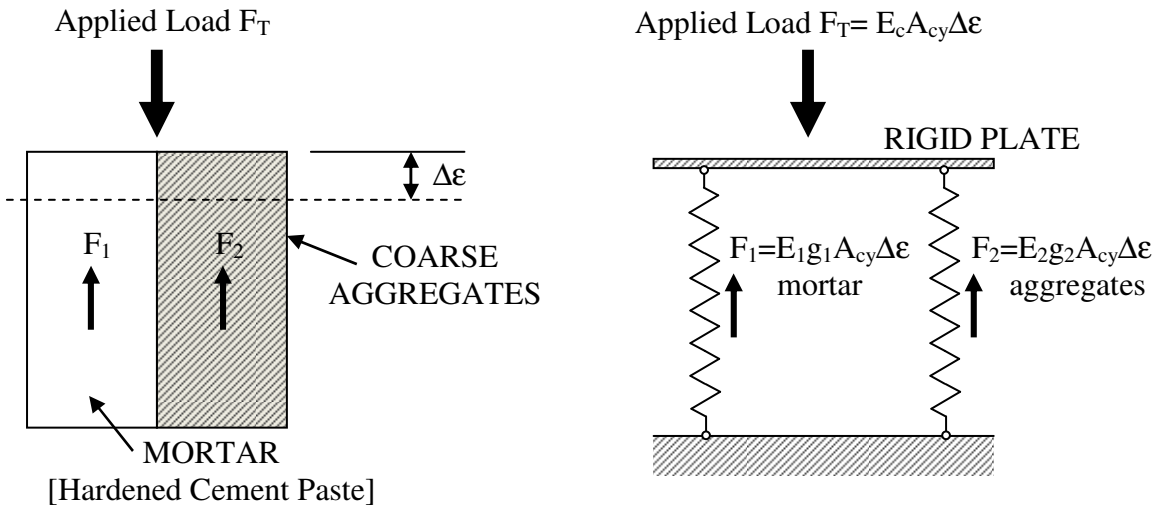

EQUIVALENT STRAIN (Springs in Parallel): $E_c = E_1 g_1 + E_2 g_2$

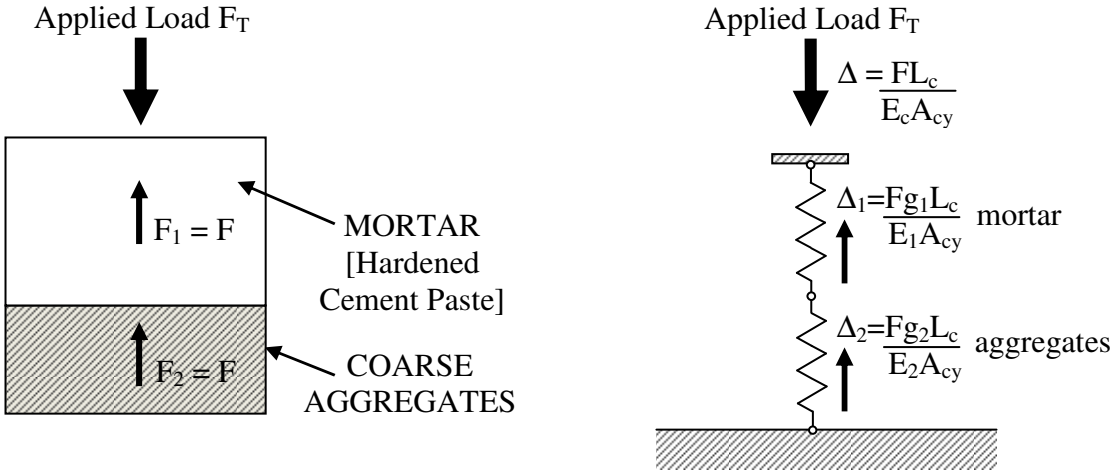

EQUIVALENT STRESS (Springs in Series): $1/E_c = g_1/E_1 + g_2/E_2$

Figure 4.6 - **Fundamental Models for Elastic Modulus**

Researchers (Hirsch 1962, Popovics and Erdey 1970) have observed that the Voigt model represents an upper bound and that the Reuss model represents a lower bound for the estimation of elastic modulus. As an attempt to reach higher accuracy, their research suggested a compromise in which the composition and behavior of concrete elements could be described from a combination of the fundamental models. Despite these efforts, Baalbaki et al. (1992) concluded based on the results of two series of experimental results that it still remained unreliable to estimate the elastic modulus of HSC solely from the

relative volumes as well as the modulus of mortar and coarse aggregates. With further research, Baalbaki (1996) eventually proposed a model similar to that presented by Hirsch (1962) as well as Popovics and Erdey (1970) in which the nature of the aggregate and the inclusion of silica fume was incorporated with the use of an additional parameter denoted *a*. The parameter allows for a more adequate representation of the interaction between the mortar and coarse aggregates as well as their mutual sharing of the applied load. The model remains a combination of the fundamental models and is illustrated in Figure 4.7 (Baalbaki 1996). When the parameter takes a value of zero, elastic modulus estimations represent the upper bound given by the Reuss model. Furthermore, when the parameter takes a value of one, elastic modulus estimations represent the lower bound given by the Voigt model.

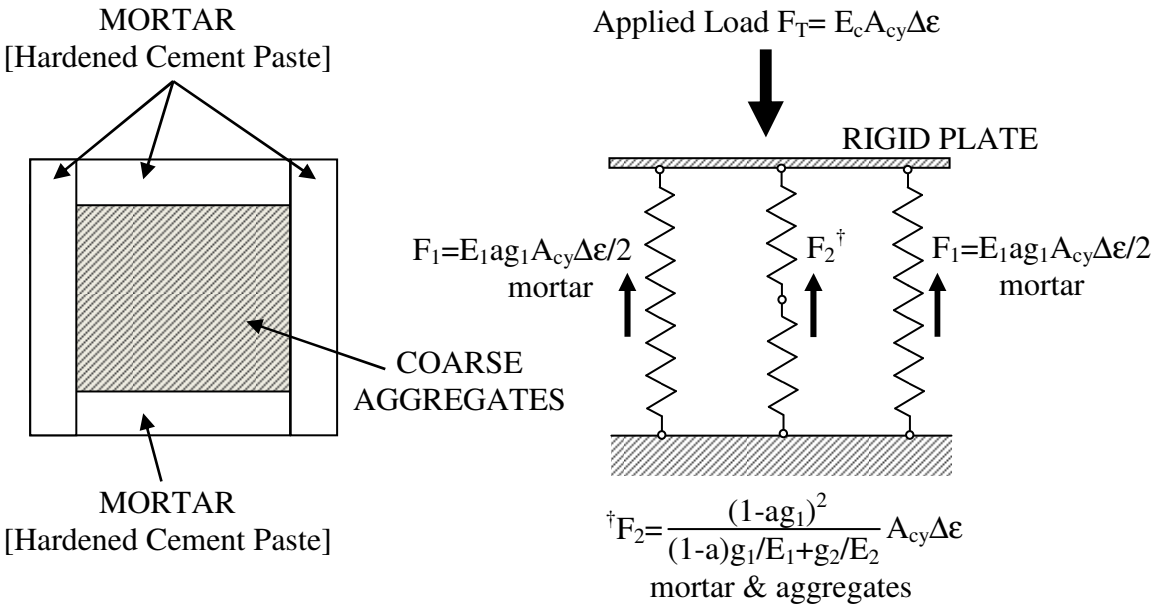

REFINED MODEL (Springs in Series & Parallel): $E_c = ag_1E_1 + (1-ag_1)^2/[(1-a)g_1/E_1 + g_2/E_2]$

Figure 4.7 - **Refined Elastic Modulus Model**

In order to investigate the model proposed by Baalbaki (1996) and provide a relationship for the parameter *a* that best describes the influence of constituents and proportions chosen for concrete used in this project, a total of four silica fume contents were selected for investigation. At each of these selected contents, a total of two mortar cylinders and three concrete cylinders were cast and tested in compression after 28 days to estimate

elastic modulus. Table 4.7 lists the results obtained from these tests. The average values shown for each set of tests indicate a gradual increase in elastic modulus with silica fume followed by a slight decrease once the optimum content is reached.

Table 4.7 – **Compression Test Results for Mortar**

Label†	Silica Fume Content [kg/m^3]	Elastic Modulus [GPa]	Average Elastic Modulus [GPa]	Strength [MPa]	Average Strength [MPa]
M-SF0-1	0	33.7	33.6	118.0	119.7
M-SF0-2	0	33.5		121.4	
C-SF0-1	0	42.1	42.6	97.2	97.4
C-SF0-2	0	43.0		97.4	
C-SF0-3	0	42.6		97.5	
M-SF30-1	30	37.2	37.2	133.8	134.3
M-SF30-2	30	37.1		134.7	
C-SF30-1	30	42.4	43.0	99.6	103.6
C-SF30-2	30	43.5		105.2	
C-SF30-3	30	43.1		105.9	
M-SF75-1	75	32.6	36.9	132.5	127.7
M-SF75-2	75	41.2		122.8	
C-SF75-1	75	41.8	42.9	114.0	112.2
C-SF75-2	75	44.1		112.5	
C-SF75-3	75	42.8		110.2	
M-SF89-1	89	35.5	35.4	125.0	123.8
M-SF89-2	89	35.3		122.5	
C-SF89-1	89	42.0	42.7	112.9	115.1
C-SF89-2	89	43.4		116.3	
C-SF89-3	89	42.7		116.0	

†M=Mortar, C=Concrete, SF=Silica Fume Content

As illustrated in Figure 4.8(a), the trend in elastic modulus is more pronounced for the mortar samples than it is for the concrete samples, due to the attenuating influence of coarse aggregates. The trend for parameter a is shown in Figure 4.8(b) and can be derived from these results as well as the relationship shown in Figure 4.7. A fitted expression for the parameter (EQ4.8) is also shown in the figure. The relationship should allow for a more suitable estimation of the model for elastic modulus presented by Baalbaki (1996) at each of the silica fume contents considered. The relative volume fractions g_1 for the

mortar and g_2 for the coarse aggregates have been determined using the volume of the concrete cylinders as well as the measured density of coarse aggregates and concrete. Also, the average elastic modulus of coarse aggregates has been taken as 50.5GPa based on that reported in past research (Giaccio et al. 1992, Baalbalki et al. 1992).

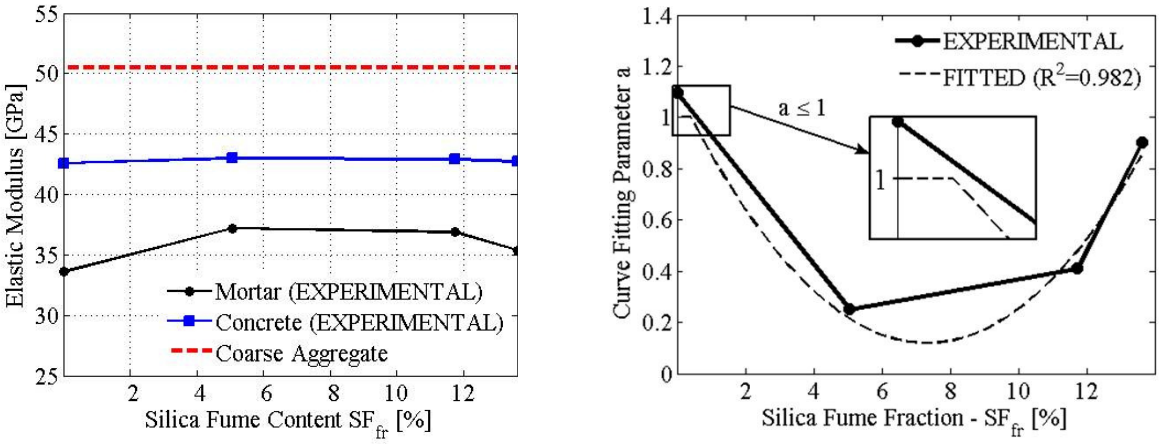

(a) Elastic Modulus Trend (b) Curve Fitting Parameter

Figure 4.8 **– Elastic Modulus of Mortar, Concrete and Coarse Aggregates**

$$a = 0.02SF_{fr}^2 - 0.27SF_{fr} + 1.11 \le 1.0 \qquad \text{EQ4.8}$$

In this equation, SF_{fr} is the amount of silica fume represented as a percentage of the cementitious content in the concrete mix. As discussed previously, the parameter should not exceed unity, which represents the upper bound for elastic modulus. The higher level of accuracy achieved with the parameter expressed in EQ4.8 is shown in Table 4.8 along with that achieved from the fundamental models.

Table 4.8 – **Fitted Results for Elastic Modulus**

Silica Fume Content [kg/m^3]	Avg. Elastic Modulus [MPa]	Reuss Model [MPa] (a=0)	Voigt Model [MPa] (a=1)	Estimated [MPa] (a EQ4.8)
0	42,568	40,404	42,104	42,104
30	43,003	42,875	43,886	42,981
75	42,914	42,670	43,733	42,975
89	42,705	41,651	42,985	42,617

4.4 STATISTICAL ANALYSIS OF HSC DATABASE

It should be noted at this stage that design provisions contained in the major building code standards are limited to tests that are conducted on normal strength concrete (NSC). Although research, such as the one presented in the previous sections, is progressively moving towards the development of expressions capable of estimating the mechanical properties of HSC, the statistical relevance of relationships are limited by the extent of experimental data considered for analysis. It is for this reason that a database containing information that pertains to the key properties of HSC for design has been created from the results published by various researchers.

4.4.1 Research Background on the Properties of HSC

Rashid et al. (2002) were the first to gather results from various researchers to provide expressions that allow the performance of HSC having compressive strengths as high as 120MPa to be estimated with a level of confidence similar to that achieved with NSC having compressive strengths as low as 10MPa. Within this range of compressive strengths, Rashid et al. (2002) as well as Iravani (1996) concluded that expressions from different standards and codes of practice tend to overestimate elastic modulus for HSC. The splitting tensile strength was also found to display an inverse S-curve relationship with compressive strength and larger scatter of test data was observed for HSC. The results emphasized the difficulty involved in developing expressions that define concrete properties with an accuracy level that is consistent over the full range of commercially produced concrete. Research from Rashid et al. (2002) showed that code relationships start diverging noticeably from experimental data for compressive strengths beyond approximately 90MPa. When comparing results with NSC, Rashid et al. (2002) attributed the higher variability in results for HSC to the fact that strength relies to a larger extent on the compressive strength of coarse aggregates in the mix. Since any adjustment to code relationships lead to a reduction in the accuracy for NSC, modifications presented in the previous sections as well as the current section are intended to be used for a narrower

range of compressive strengths that reflect more accurately the properties of HSC similar to those used for this project.

It should also be noted that code relationships for NSC are generally developed from tests performed at or beyond the age of 28 days (Iravani 1996). At this point, curing has reached a stage in which the structure of concrete has stabilized to a form that is more typical of service conditions. The relationships are therefore not well suited to estimate the mechanical properties of concrete at the time of prestress release when its ability to resist splitting stresses must be determined. Based on this observation, experimental data should be analyzed separately such that adjustments can provide a global expression that allows the progression of mechanical properties to be estimated for curing stages up to and beyond 28 days. Although experimental data prior to 28 days of curing is limited when considering records from tests performed in this project or even from past research, it is more extensive when considering results beyond this stage of curing. Nevertheless, the analyses performed in the following sections can serve as an initial step towards the development of relationships that allow the performance of concrete to be estimated at prestress release or any other critical stages of construction.

4.4.2 Properties and Management of the Database

As shown in Table 4.9, the database created for this project contains a total of 327 data points from a total of 13 researchers, which includes experimental results for splitting tensile strength, elastic modulus and Poisson's ratio. The database contains information pertaining to the researchers, year of research, type of coarse aggregates used in the concrete mix as well as the age of concrete at testing. The compressive strengths in the database range from 90MPa to 160MPa, as required by the project. Cylinders in the database were moist cured for at least the first 7 days and all the tests were performed between 7 and 1085 days of curing.

Table 4.9 – **Database Properties**

Researcher	Coarse Aggregate	No. Data Points		
		Splitting Tensile Strength	Elastic Modulus	Poisson's Ratio
Aitcin & Mehta (1990)	Granite/Limestone	-	2	-
Baalbaki et al. (1992)	Granite/Limestone Sandstone Quartzite	-	12	-
Burg & Ost (1992)	Dolomite	1	7	-
Tighiouart et al. (1994)	Granite/Limestone Sandstone	-	17	-
Khayat et al. (1995)	Dolomite	8	6	-
Iravani (1996)	Sandstone	6	11	11
Wee et al. (1996)	Granite/Limestone	-	4	-
de Larrard & Belloc (1997)	Granite/Limestone	-	1	-
Mansur et al. (1999)	Granite/Limestone		2	-
Rashid et al. (2002)	Granite/Limestone	38	43	20
Mostofinejad & Nozhati (2005)	Granite/Limestone Andesite Quartzite	-	39	-
Vogel et al. (2008)	Granite/Limestone	13	18	16
Davoudi (2009)	Granite/Limestone	16	11	11
Vogel & Svecova (2009) †	Granite/Limestone	-	12	-
TOTAL NO. DATA POINTS		82	185	58

†Document under preparation for publication

As emphasized by Rashid et al. (2002), design procedures contained in the various standards and codes of practice for structural concrete make use of 150mm by 300mm cylinders. Most of the tests performed on HSC are, however, typically performed using smaller 100mm by 200mm cylinders since most testing facilities do not have equipment with sufficient loading capacity to reach the required compressive strengths. Since the smaller size specimens provide higher compressive strength and elastic modulus values,

the database must provide correction factors to allow comparison of experimental results. Research from Rashid et al. (2002) provides the following relationships for converting the strength and modulus of larger cylinders to that of smaller sizes used in most of the experiments of the database.

$$f'_{c,100} = 1.04 f'_{c,150} \qquad \text{EQ4.9}$$

$$E_{c,100} = 1.32 E_{c,150} - 8.36 \qquad \text{EQ4.10}$$

In these equations, $f'_{c,100}$ and $E_{c,100}$ are the compressive strength and elastic modulus of 100mm by 200mm cylinders, respectively. Similarly, $f'_{c,150}$ and $E_{c,150}$ are the compressive strength and elastic modulus of 150mm by 300mm cylinders, respectively. Finally, the concrete mixes considered for use in the database contain silica fume content similar to that used for concrete in this project, which allows for a water-cementitious ratio ranging between 0.20 and 0.30.

4.4.3 Elastic Modulus Development

In order to remain consistent with existing relationships for elastic modulus, the expressions proposed in this thesis preserve the intercept from the relationship adopted by ACI Committee 363R (1992). The modifications are provided to the slope using a least squares method that minimizes the summed square of residuals to fit linear models to the experimental data. The first modification considered for the database analysis will account for elastic modulus of concrete with compressive strengths in excess of 90MPa.

$$E_{c28} = 3{,}320 C_s \sqrt{f'_c} + 6900 \qquad \text{EQ4.11}$$

In this equation, E_{c28} is the elastic modulus of HSC at and beyond 28 days of curing and C_s is the correction factor that can be taken as 1.03 for compressive strengths in excess of

90MPa at 28days. The adjustment was found to improve the RMSE by approximately 2.3% with respect to the ACI Committee 363R (1992) expression and 20.8% with respect to the CSA A23.3-04 expression. Since the statistical parameter represents the average error in elastic modulus over the range of compressive strengths considered, the adjustment provides a noticeable improvement on the goodness of fit of the linear model.

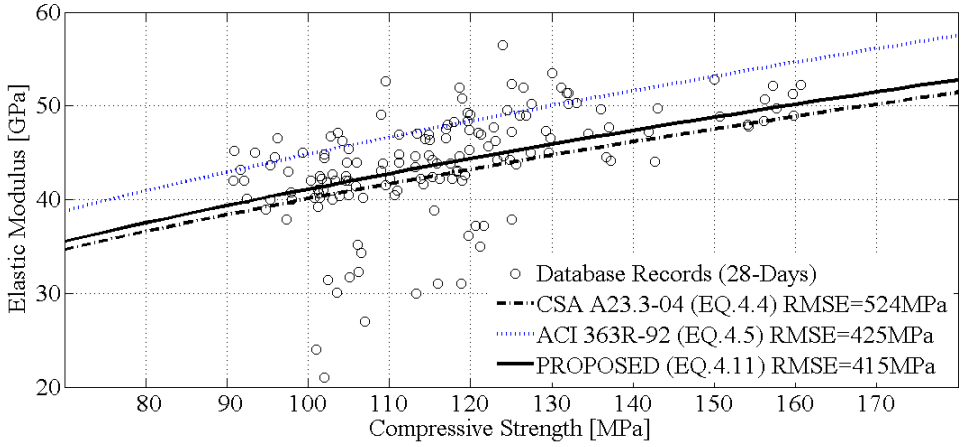

Figure 4.9 **– Elastic Modulus Trend with Compressive Strength** [≥28 Days Curing]

Figure 4.9 also confirms the observation made by Rashid et al. (2002), which stated that significant variability in the experimental results is noticeable when considering the range of compressive strengths in the database. The variability can be attributed to slight differences in the size and shape of specimens in the batches, varying distribution of aggregates within the samples as well as inconsistent compaction among the samples during casting. These sources are, however, also present for NSC and cannot account for the additional variability that is typically observed for HSC. Since the influence of curing regime, concrete age, and chemical admixture have been accounted for in the selection criteria for the database, the factor creating scatter in the results of Figure 4.9 must be attributed to one or more of the materials composing the mix.

Mansur et al. (1994) confirmed with later emphasis by Iravani (1996) that one of the most significant contributions to scatter of data for elastic modulus is the type of coarse aggregates. A total of six aggregate types have been recorded within the database listed in Table 4.9. Figure 4.10 illustrates that granite and limestone have similar influence on the trend of elastic modulus with compressive strength. However, research from Aïtcin and

Mehta (1990) has revealed that differences between the modulus of elasticity of granite and limestone can arise. Some granite aggregates contain laumonite, which is known to cause trans-granular fractures due to its instability under moist environments. Ultimately, the fractures contribute to a weakening of compressive strength and elastic modulus for concrete mixes containing the aggregates. The result was not present in the database records but should be kept in mind when using the relationships developed in this paper.

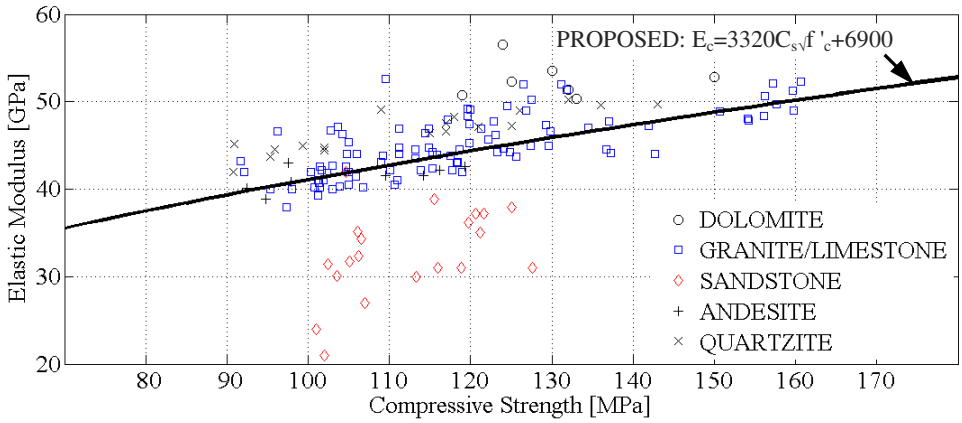

Figure 4.10 **– Elastic Modulus Trend with Compressive Strength & Aggregate Type**

Results from Figure 4.10 also indicate that the use of dolomite as the coarse aggregate provides higher elastic modulus values while sandstone restricts the property to lower levels. Finally, the use of quartzite as coarse aggregate suggests elastic modulus values that follow the upper bound of results obtained for concrete with granite and limestone. Conversely, the use of andesite suggests values of elastic modulus that follow the lower bound. In order to account for a larger portion of scatter in the data, the demarcation of Figure 4.10 with respect to the influence of coarse aggregates can be used to refine the relationship of EQ4.11 for elastic modulus. In addition to the inclusion of a modification factor for compressive strengths in excess of 90MPa, a modification factor for coarse aggregates can be added to the expression if the type used in the mix is known.

$$E_{c28,ca} = 3{,}320 C_s C_{ca} \sqrt{f_c'} + 6900 \qquad \text{EQ4.12}$$

In this equation, $E_{c28,ca}$ is the elastic modulus of HSC at and beyond 28 days of curing with a modification factor C_{ca} for the type of coarse aggregates used in the concrete mix. A total of six values of the factor were obtained, each of which corresponds to one of the aggregate types found in the database. Results are shown in Table 4.10 along with the RMSE values obtained from the least squares fit as well as the extent of experimental data considered for each type of aggregate. As anticipated, the largest values of the factor are for dolomite and quartzite. The value for granite and limestone lies between that for quartzite and andesite with the lowest values obtained for sandstone aggregates. Results also indicate larger RMSE values for sandstone, which suggests larger scatter of data for the aggregate. Results for concrete with dolomite and andesite should be interpreted with care due to the relatively low number of data points for the aggregates.

Table 4.10 – **Modification Factor for Coarse Aggregates**

Coarse Aggregate	Modification Factor C_{ca}	RMSE [MPa]	No. Data Points
Dolomite	1.17	971	7
Granite/Limestone	1.03	259	94
Sandstone	0.71	1028	20
Andesite	0.98	464	8
Quartzite	1.10	296	18

The remaining data from the database consists of experimental values obtained from tests performed on standard cylinders prior to 28 days of curing. The data was plotted in Figure 4.11 and analyzed to incorporate a final modification factor to the elastic modulus relationship. The modification factor is introduced in EQ4.13. It broadens the scope of the relationship by accounting for the influence of early age on elastic modulus. It should be noted that the correction factor for coarse aggregates was not included in this expression since data is insufficient to reach statistical significance for each of the aggregate types at these curing stages.

$$E_{c7,14} = 3{,}320 C_s C_a \sqrt{f_c'} + 6900 \qquad \text{EQ4.13}$$

In this expression, $E_{c7,14}$ is the modulus of elasticity at 7 or 14 days of curing and C_a is a modification factor that accounts for the influence of age on the trend with compressive strength. According to the least squares method used to establish a linear fit for elastic modulus with compressive strength, the factor can be taken as 1.06 at 7 days of curing as well as 1.00 at 14 days of curing and beyond. The result indicates that HSC gains stiffness at a higher rate with compressive strength during the early stages of curing with a stabilization reached after 14 days of curing.

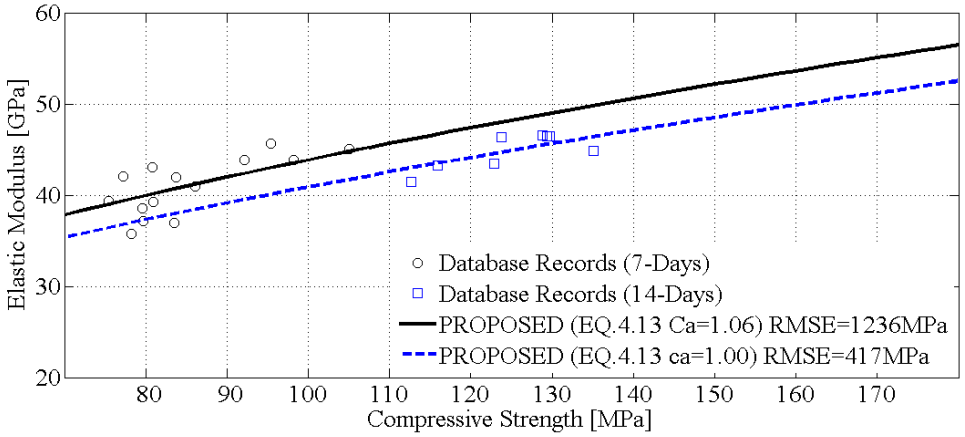

Figure 4.11 **– Elastic Modulus Trend with Compressive Strength at Early Age**

4.4.4 Tensile Strength Development

The ACI Committee 363R (1992) report on HSC states that the splitting tensile strength can be taken as that given in EQ4.14 for normal-weight concrete with compressive strengths between 21MPa and 83MPa. The result is in close agreement to that previously reported for the trial batch as well as the second and third batches of PCP reinforcement cast in this project.

$$f_{sp\,ACI363R(1992)} = 0.59\sqrt{f_c'} \qquad \text{EQ4.14}$$

In this expression, $f_{spACI363R(1992)}$ is the splitting tensile strength as defined by the ACI Committee 363R (1992) report on HSC. The expression is based on moist cured specimens tested at the ages of 7, 28 and 95 days. The relationship covers the range of

curing stages that are required in the estimation of performance for PCP reinforcement at release and under service conditions. According to Iravani (1996), the relationship is capable of estimating the splitting tensile strength within ten percent of the measured data for HSC with or without supplementary cementitious materials and compressive strengths that reach 120MPa after 28 days. The performance of the relationship was tested further by Rashid et al. (2002) on a larger dataset, which included additional data for normal weight concrete tested between 28 and 91 days. The researchers suggested that the splitting tensile strength did not necessarily have to be expressed as the square root of the compressive strength.

$$f_{sp\ Rashid(200\ 2)} = 0.47 f_c'^{0.56} \qquad \text{EQ4.15}$$

In this equation, $f_{sp\ Rashid(2002)}$ is the splitting tensile strength of concrete tested between the ages of 28 and 91 days. The researchers derived EQ4.15 with the intent of approximating what was suggested to be an inverse S-curve relationship for splitting tensile strength with compressive strength. However, when investigating compressive strengths beyond those considered in their research, it becomes apparent that the trend could have been the result of wider scatter in data for HSC. In fact, results from Figure 4.12 show that the rate of increase in splitting tensile strength decreases with compressive strengths in excess of 110MPa. The increase suggested by Rashid et al. (2002) therefore causes EQ4.15 to over-estimate the splitting tensile strength of HSC for compressive strengths in excess of 110MPa. To overcome this problem, an alternate expression was derived and presented in this thesis with a higher coefficient and a lower exponent.

$$f_{sp\ PROPOSED} = 0.72 f_c'^{0.42} \qquad \text{EQ4.16}$$

In this equation, $f_{sp\ PROPOSED}$ is the splitting tensile strength of concrete that accounts for any curing stages ranging between 7 and 434 days. The expression preserves the accuracy achieved from that presented by Rashid et al. (2002) for the lower compressive strengths in the database and converges to the results obtained with the ACI 363R (1992) expression for compressive strengths in excess of 110MPa. The RMSE values are

comparable among all the expressions considered but the correlation coefficients were found to suggest that the proposed relationship is capable of explaining 74.9% of the variation in the results about the mean compared to 69.8% for the ACI 363R (1992) method and only 22.4% for the method proposed by Rashid et al. (2002).

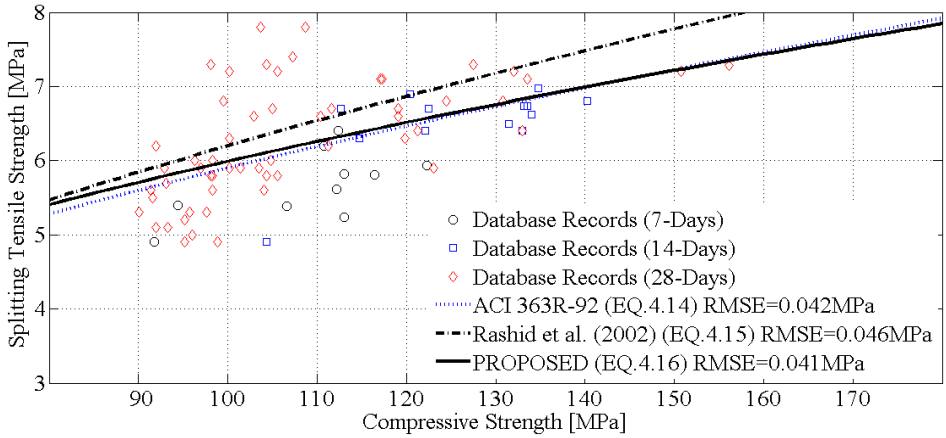

Figure 4.12 **– Splitting Tensile Strength Trend with Compressive Strength**

4.4.5 Poisson's Ratio

According to MacGregor and Bartlett (2000), Poisson's ratio can vary from about 0.11 to 0.21 and usually falls within the range 0.15 to 0.20 for NSC. Results presented by Iravani (1996) as well as Rashid et al. (2002) confirm the lower bound to this range but suggest an upper bound reaching 0.25. Both investigations reported an average of 0.20 for the parameter over a range of compressive strengths extending from 20MPa to 125MPa. Figure 4.13 shows the variation in the parameter over the range of compressive strengths in the database and for tests performed between 7 and 540 days of moist curing. The figure contains a total of 58 data points and does not show influence arising from the time of test. It also confirms results obtained from the first three batches of PCP reinforcement cast in this project where the ratios fluctuate between approximately 0.16 and 0.25. The measured data was found to average 0.21 with a standard deviation of ±0.02. Although an average value is generally appropriate for describing Poisson's ratio for NSC, the results in Figure 4.13 suggest a gradual increase in the parameter with compressive strength. It is

therefore expected for Poisson's ratio to display a slight increase with compressive strength when HSC is considered.

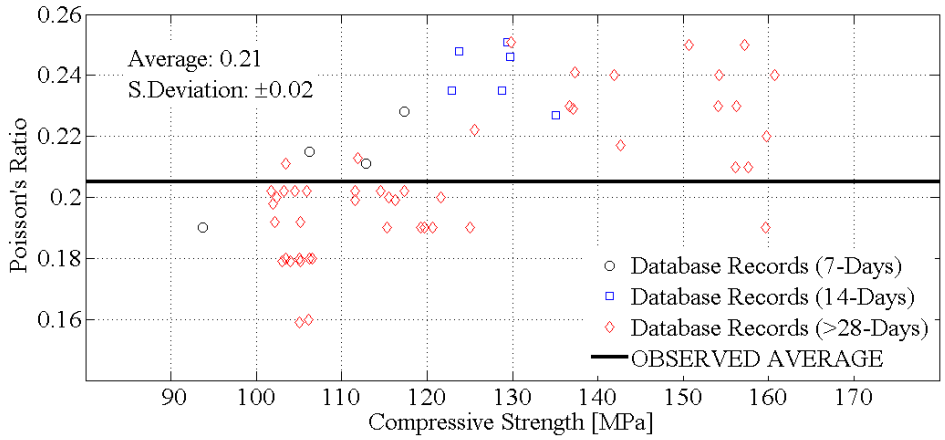

Figure 4.13 **– Poisson's Ratio Variation with Compressive Strength**

4.5 FIBER REINFORCED CONCRETE

Based on results presented in the previous section, the higher strength concrete used in this thesis provides a significant gain in tensile strength from what is typically achieved with normal strength concrete. Although the result was intentional as well as desirable for the design of PCPs as reinforcement in concrete structures, it should be noted that the tensile strength only increases as a function of the square root of the compressive strength and therefore requires a considerable increase in the compressive strength. Based on results from the last two sets of PCPs, the average compressive strength of 131.2MPa represents a 165% increase from a normal 50MPa compressive strength concrete but only provides a 65% increase in splitting tensile strength when considering the measured average of 6.95MPa.

These results underline the weakness of concrete in tension as well as the difficulty of enhancing the property for structural applications such as the one suggested in this thesis. The addition of short discontinuous fibers can, however, play a significant role in the improvement of mechanical properties for concrete in compression but more importantly in tension (Bencardino et al. 2008). It has been shown by previous research (Banthia

1997) that the main advantage arising from the dispersion of fibers in the cement paste of a concrete mix lies in its restraining effect on crack growth and subsequent reduction in crack width in a stressed state. Debonding and pull out of individual fibers traversing a crack require additional absorption of energy, which results in a substantial increase in toughness and fracture resistance of the material to cyclic as well as dynamic loads (Bencardino et al. 2008). The behavior of Fiber Reinforced Concrete (FRC), however, greatly depends on the synergistic interaction of each component, which is influenced by their relative characteristics as well as their proportions in the mix.

4.5.1 Stress-Strain Behavior of FRC

The influence of adding fibers to plain concrete has been observed to have similar effects to the stress-strain behavior in tension than it has in compression. As a result, the stress-strain relationship of FRC in tension described by EQ4.17 and suggested by Lok and Xiao (1999) is very similar to that proposed by Soroushian and Lee (1990) for the behavior of FRC in compression. The similarity arises from the fact that fibers share the same ability to control crack initiation and subsequent growth in both loading conditions.

$$f_t = \begin{cases} f_{to}\left[2\left(\frac{\varepsilon_t}{\varepsilon_{to}}\right) - \left(\frac{\varepsilon_t}{\varepsilon_{to}}\right)^2\right] & whenever \quad \varepsilon_t \le \varepsilon_{to} \\ f_{to}\left[1 - \left(1 - \frac{f_{tu}}{f_t}\right)\left(\frac{\varepsilon_t - \varepsilon_{to}}{\varepsilon_{t1} - \varepsilon_{to}}\right)\right] & whenever \quad \varepsilon_{to} \le \varepsilon_t \le \varepsilon_{t1} \\ f_{tu} & whenever \quad \varepsilon_{t1} \le \varepsilon_t \le \varepsilon_{tu} \end{cases} \qquad \text{EQ4.17}$$

The stress-strain behavior defined by EQ4.17 is shown in Figure 4.14 where ε_t is the strain at any applied tensile stress f_t. Furthermore, f_{to} is the ultimate strength in direct tension, ε_{to} is the corresponding strain and ε_{t1} is the strain at which the residual tensile strength f_{tu} is reached. The residual strength is sustained until the ultimate tensile strain ε_{tu} is achieved. The residual tensile strength and corresponding strain can be determined on

the basis of EQ4.18 and 4.19, which are expressions that were developed by Lok and Pei (1988).

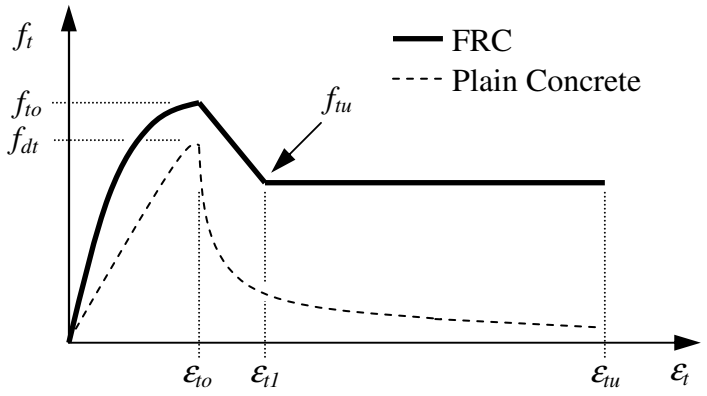

Figure 4.14 - **Stress-Strain Relationship for FRC in Direct Tension**

$$f_{tu} = \eta_o V_f \tau_d L_f / D_f \qquad \text{EQ4.18}$$

$$\varepsilon_{t1} = \frac{\tau_d}{E_s} L_f / D_f \qquad \text{EQ4.19}$$

In similarity to the case of stress-strain in compression (Soroushian and Lee 1990), the softening branch is enhanced with a residual tensile strength and strain that are a function of fiber content as well as fiber length L_f to diameter D_f ratio. They are also a function of the fiber volume fraction V_f, maximum bond stress that can be developed on the surface of the fibers τ_d as well as a fiber orientation factor η_o, which accounts for the distribution of fibers in the cement paste. According to Lok and Xiao (1999), there are two probabilistic models that can be used to determine the fiber orientation factor. Based on work presented by Hannant (1978) as well as Soroushian and Lee (1990), the factor can be taken as 0.405 for beams and 0.5 for slabs. The higher value for slabs arises from the relatively smaller thickness of the structural component for which the boundaries allow the fibers to be oriented in a direction that is optimal in controlling crack initiation.

When fibers are not introduced in the mix, the stress-strain response of concrete in uniaxial tension is nearly linear up to cracking (Collins and Mitchell 1997). Although the cracking strain of Figure 4.14 remains unchanged in the presence of fibers, plain concrete will crack at a lower stress and the post-cracking tensile resistance can only be detected with relatively stiff testing machines. Nevertheless, the stress-strain response of FRC in tension remains considerably higher than that observed for plain concrete. The outcome is advantageous to the use of PCP reinforcement, since the higher contribution of the concrete mix beyond the cracking stage will allow a larger percentage of axial stiffness to be maintained at higher loads.

4.5.2 Compressive and Tensile Strength Development

A total of three batches were cast to study the influence of fibers on the compressive and tensile strength of HSC used in this project. The first batch did not contain fibers and served as a basis for comparing strengths obtained from subsequent batches. The two remaining batches were based on the same mix design and contained an additional fiber content of 600 and 1800g/m^3 of concrete, respectively. The synthetic reinforcing material was obtained from Grace MicroFiber^{FM} and consisted of 19mm long polypropylene fibers in a microfilament form. With a diameter of approximately 82microns and a corresponding specific gravity of 0.91, the fiber content added to the second and third batches corresponds to 0.07 and 0.2% by volume of concrete, respectively. Although relatively small when compared to what is typically used in FRC research, these values represent the limits of a range that is recommended by the manufacturer. Moreover, the HSC mix used in this project has limited workability and fiber contents in the vicinity of 0.2% were found to appreciably reduce the ease with which concrete can be poured in the relatively small formwork.

Each of the two FRC batches was cast in the same concrete mixer as that used for the first batch. For optimum dispersion in the mix, fibers were added during the mixing process and mixed for a minimum of 70 revolutions as recommended by the manufacturer as well as Hannant (1978). A total of 3 cylindrical specimens with a diameter of 100mm and a

height of 200mm were tested in compression as well as in tension at 7 and 14 days to monitor strength development for the period preceding the release of prestress. In order to limit the influence of transverse bursting stresses that arise from the presence of moisture, specimens were once again consistently taken out of the curing room 24 hours prior to testing.

Compressive and tensile strengths recorded from each test were averaged for each testing day and each of the three batches cast in this stage of the project. Results are shown in Table 4.11 with tensile strengths illustrated in Figure 4.15 as a function of fiber content. Average compressive strength values are consistent among all batches, although slightly higher for the second batch. Nevertheless, results indicate a 21.2% increase in the splitting tensile strength after 7 days of moist curing as well as a comparable 21.1% increase after 14 days of moist curing between the first and third batches. The trend in tensile strength is linear with fiber content although slightly tapered for tests performed after 14 days of moist curing.

Table 4.11 – **FRC Strength Development**

AGE [Days]	BATCH #1 [CONTROL]		BATCH #2 [$V_f = 0.07\%$]		BATCH #3 [$V_f = 0.2\%$]	
	COMP. [MPa]	TENS. [MPa]	COMP. [MPa]	TENS. [MPa]	COMP. [MPa]	TENS. [MPa]
7	98.4	5.66	100.9	6.06	98.7	6.86
14	113.6	6.11	117.2	6.69	115.5	7.40

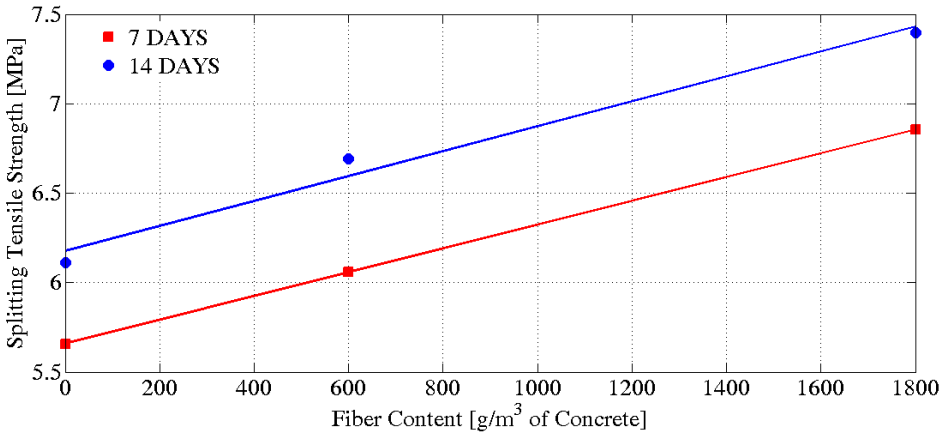

Figure 4.15 **–Tensile Strength Development** [FRC]

Based on the optimum fiber content of 1800g/m^3 in Figure 4.15, an additional three batches of PCP reinforcement were cast to investigate the added performance of using fibers in the HSC mix. More specifically, the fourth and sixth batches were intended to investigate the influence of fiber reinforced PCP reinforcement on the flexural behavior of beams. The fifth batch was intended to investigate the influence of fibers on the performance of PCP reinforcement in direct tension. Results from standard cylinder testing for these additional batches are shown in Table 4.12. These results indicate an increase in splitting tensile strength that ranges from 14.0% at 14 days of moist curing for the fifth batch to 29.2% at the time of test for the fourth batch. Although some variability is apparent in the results with slightly higher increases at the time of test as well as for the fourth batch, the range represents an average increase of 21.6% in tensile strength. The increase is consistent and in close agreement to that obtained from the trial batch.

Table 4.12 – **Final PCP Batch Strength Development**

(a) Without Fibers

AGE [Days]	PCP SET #4		PCP SET #5		PCP SET #6	
	COMP. [MPa]	TENS. [MPa]	COMP. [MPa]	TENS. [MPa]	COMP. [MPa]	TENS. [MPa]
14	118.5	5.8	112.7	6.7	-	-
Time of Test (>28)	129.9	5.5	133.0	6.2	-	-

(b) With Fibers

AGE [Days]	PCP SET #4		PCP SET #5		PCP SET #6	
	COMP. [MPa]	TENS. [MPa]	COMP. [MPa]	TENS. [MPa]	COMP. [MPa]	TENS. [MPa]
14	120.4	7.1	115.6	7.6	112.7	7.1
Time of Test (>28)	134.8	7.2	128.8	7.4	132.7	6.5

4.6 PERFORMANCE OF PCP REIFNORCEMENT IN DIRECT TENSION

In light of results obtained for the splitting tensile strength of FRC, a total of four PCPs were cast and tested to investigate the influence of fibers on the performance of HSC in direct tension. Two of these PCPs were cast without fibers to establish a reference with the remaining two samples containing fibers. Based on results obtained for strength gain and workability during the trial batches, a fiber content of 1800g/m^3 was selected for addition to each of the PCPs. Results from these tests are intended to provide information pertaining to the load-strain response of PCP reinforcement, its cracking load as well as the post-cracking contribution of the HSC in direct tension.

4.6.1 Load-Strain Response

As shown in Figure 4.16, the load-strain response of each PCP was established using a 1000kN capacity MTS testing machine as well as a Linear Variable Displacement Transducer (LVDT) placed at the top and bottom of the sample, respectively. Data was recorded with a 24-channel data acquisition (DAQ) system. The average strain along the length of the sample during each test was obtained by subtracting the bottom LVDT reading from the top reading and dividing the result by the clear length separating the sensors. The samples were designed to a length of 1800mm between the extremities of the concrete in order to accommodate for the allowable clearance and stroke provided by the testing frame.

As shown in Figure 4.16, the cross-section of the samples was chosen as 50mm by 50mm using the design charts developed in Chapter 3 and the design requirements for PCP reinforcement discussed more fully in Chapter 5. Figure 4.16 also illustrates that the tensile force is transferred to the specimens using high-pressure steel pipes bonded to the ends of the FRP reinforcement. The geometric characteristics of these pipes were chosen in accordance with Annex B of CSA S806 (2002) and were anchored using wedges in a conical base that bore on a set of steel plates at the extremities of the testing machine.

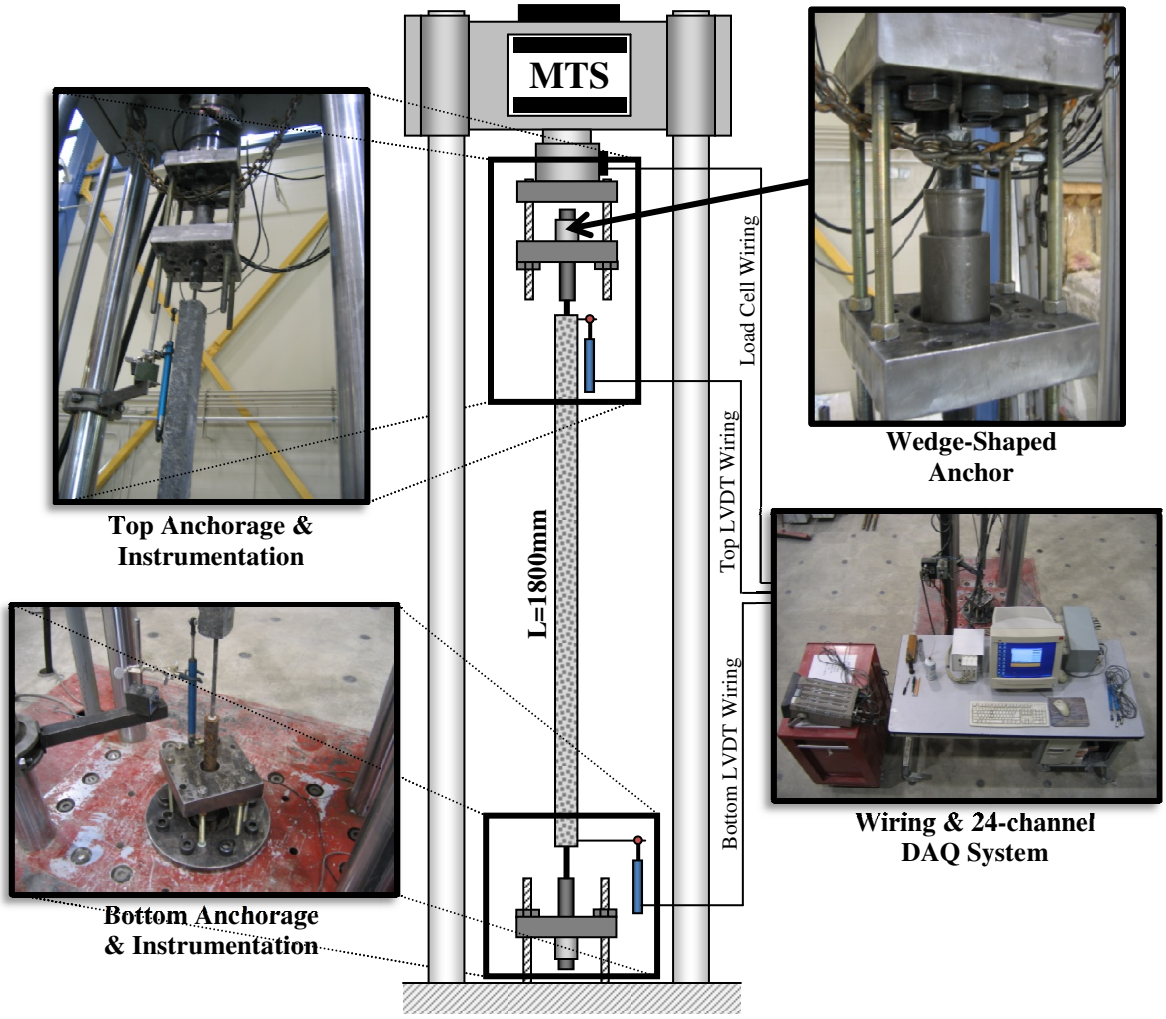

Figure 4.16 **– Direct Tension Test Setup**

The load-strain responses from each test have been comparatively combined in Figure 4.17 for analysis. Several conclusions can be drawn from this figure, the first of which relates to the higher cracking load observed for PCP reinforcement with dispersed fibers. The samples also revealed higher uncracked stiffness than those without fibers. Since all specimens were designed to have the same cross-sectional area and length, the increase was associated to the higher elastic modulus values observed for FRC in tension. The result is concurrent with those illustrated in Figure 4.14, which present the stress-strain relationships for FRC and conventional concrete.

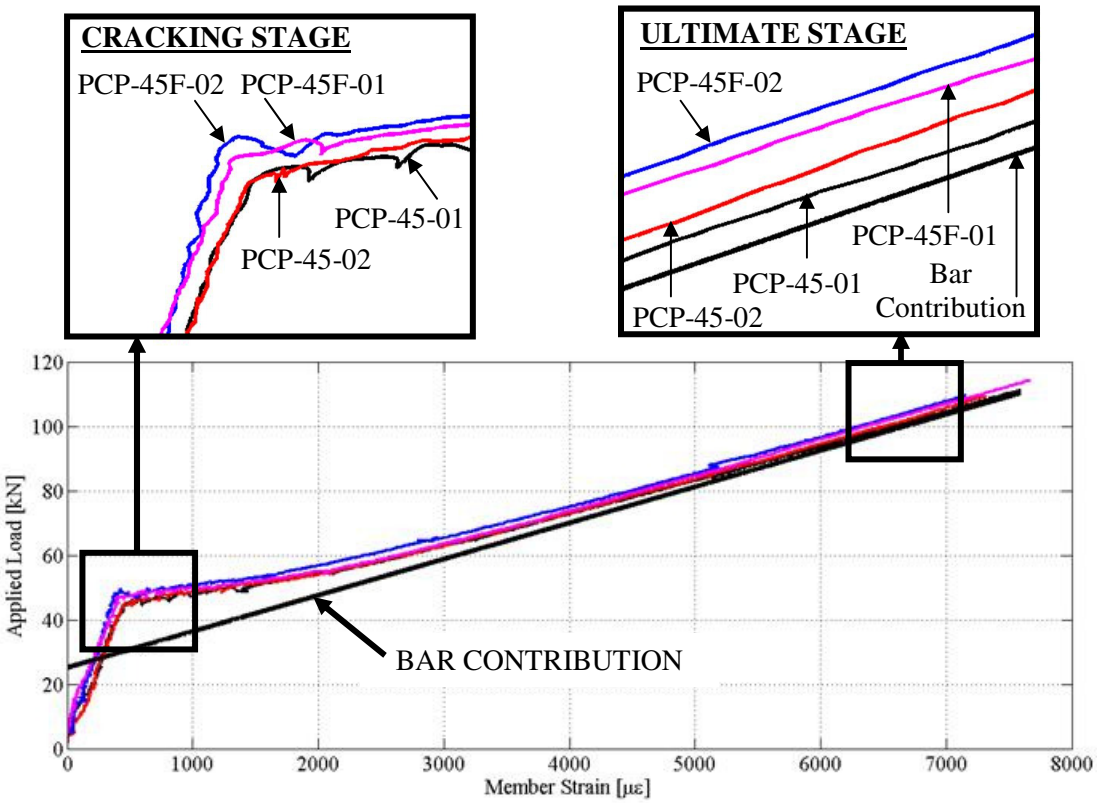

Figure 4.17 **– Load-Strain Response**

The cracking loads were recorded for each of the samples using the results presented in Figure 4.17 and tabulated in Table 4.13 for further analysis. These values were found to represent an average increase of 6.7% in tensile strength compared to the 21% increase observed from standard cylinder testing. The distinction can firstly be attributed to the difference in stress conditions encountered during split cylinder tests and direct tension tests.

Table 4.13 – **Cracking Strength of PCP Reinforcement**

LABEL	Cracking Load [kN]	Applied Strain @ Cracking [με]
PCP-45-01	45.6	486.5
PCP-45-02	45.2	458.3
PCP-45F-01	49.4	430.1
PCP-45F-02	47.4	436.5

The difference can also be attributed to the lower applied strains at cracking observed for specimens with dispersed fibers. The condition is illustrated in the first highlighted segment of Figure 4.17 at the cracking stage. The applied strains at this stage correspond to the removal of elastic shortening ε_{sh} and the application of the cracking strain of concrete in direct tension ε_{cr}. Since the concrete cracking strain is anticipated to be consistent for all samples tested in direct tension, the lower applied strains at cracking arise from lower elastic shortening and therefore lower effective prestressing levels at the time of test. The outcome is the result of higher losses, which eventually cause lower cracking loads to be recorded for samples with dispersed fibers. These additional losses can transpire from the lower workability of concrete with fibers and the higher potential for water entrapment beneath the reinforcing material. The ensuing voids lead to larger creep than anticipated. The values of applied strains at cracking listed in Table 4.9 indicate an 8.3% increase in losses for samples with dispersed fibers.

It is also apparent from the second highlighted segment of Figure 4.17 at the ultimate stage that the average strains incurred by the samples with fibers are consistently smaller than those for remaining samples until failure. Although the 6.7% increase in cracking load will provide limited improvements to the service range for beams with PCP reinforcement, the attenuation of strains beyond cracking should provide improvements to the post-cracking stiffness of beams with PCP reinforcement containing dispersed fibers.

4.6.2 Post-Cracking Contribution of Concrete

The attenuation of strains observed in Figure 4.17 for PCP reinforcement with dispersed fibers can be explained by additional contribution of FRC beyond cracking. In order to confirm this additional contribution, the load contribution of the bare bar was first subtracted from the total load. The resulting force can then be divided by the cross-sectional area of concrete, neglecting the reinforcing area. Since each response reported in Figure 4.17 approaches the bar contribution with increased strain, the stress arising from the division should provide a declining post-cracking contribution of concrete.

Results for all specimens are shown in Figure 4.18 and were normalized with respect to the direct tensile strength.

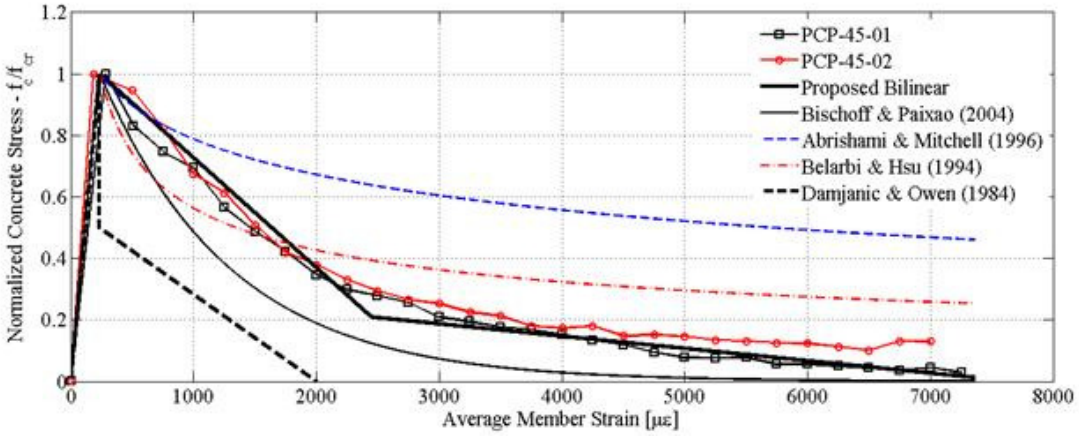

(a) Without Fibers

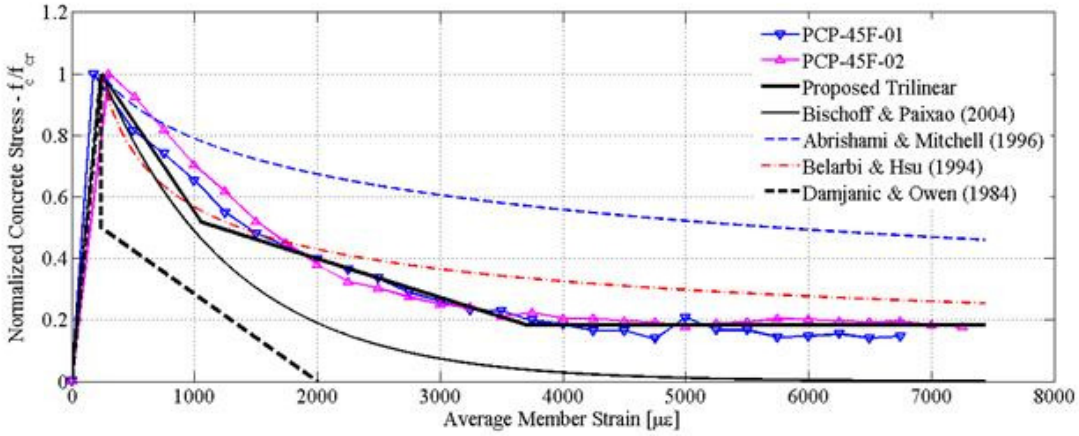

(b) With Fibers

Figure 4.18 **– Post-Cracking Contribution of Concrete in Direct Tension**

Figure 4.18(a) reveals that the post-cracking contribution of concrete for specimens without fibers gradually tapers towards a state without residual strength. The outcome indicates that sufficient slip eventually develops between the cracks to induce a behavior that is analogous to that of a bare bar without the contribution of concrete. Conversely, Figure 4.18(b) shows that the contribution of concrete beyond cracking for specimens with fibers tapers towards a residual strength. In this case, sufficient resistance is provided by the fibers through each crack to counteract the effect of slip that develops between the cracks.

As shown in Figure 4.18, several models have been proposed in the literature to describe the post-cracking contribution of concrete in direct tension. The earliest model considered for comparison with the experimental data was presented in work reported by Damjanic and Owen (1984). The relationship has two segments, the first of which is an immediate drop in concrete stress to half of the cracking strength. The second segment describes gradual crack development with a progressive reduction in concrete contribution until an average member strain of 15 times the cracking strain is reached. The model is the least accurate and most conservative of all methods.

Belarbi and Hsu (1994) also proposed a model to describe the post-cracking contribution of concrete. In their investigations, the researchers developed an expression (EQ4.20) that relates normalized concrete stresses to a power of the ratio of cracking strain to average member strain. Of all existing methods considered, the model has the most accuracy with respect to the experimental data with the least RMSE values.

$$\frac{f_c}{f_{dt}} = \left(\frac{\varepsilon_{cr}}{\varepsilon_m}\right)^{0.4} \qquad \text{EQ4.20}$$

In this equation, f_c is the average concrete stress along the member, f_{dt} is the cracking strength in direct tension, ε_{cr} is the strain at cracking and ε_m is the average member strain. In subsequent research, Abrishami and Mitchell (1996) elaborated on a tensile stress-strain relationship that had been originally suggested by Collins and Mitchell (1997) in which factors that relate to bond and loading scheme were considered.

$$f_c = \frac{\alpha_1 \alpha_2 f_{dt}}{1 + \sqrt{500\varepsilon_m}} \qquad \text{EQ4.21}$$

In this expression, α_1 is a factor accounting for bond characteristics of the reinforcement, equal to 1.0 for deformed reinforcing bars, 0.5 for plain bars, wires or bonded strands and 0 for unbounded reinforcement. Also, α_2 is a factor accounting for the loading scheme, equal to 1.0 for short-term monotonic loading and 0.5 for sustained or repeated loading. It

is apparent from the results of Figure 4.18 that the modification proposed by Abrishami and Mitchell (1996) is the least conservative of all methods considered. The final model considered herein was developed by Bischoff and Paixao (2004) for GFRP reinforced concrete tension elements. Although slightly conservative, the method approximates the shape of the post-cracking trend for specimens without fibers quite well.

$$\frac{f_c}{f_{dt}} = e^{[-1100(\varepsilon_m - \varepsilon_{cr})]} \qquad \text{EQ4.22}$$

In spite of these past efforts, a potential for improvement still exists for the models considered in the estimation of the post-cracking contribution of concrete in this research. It is for this reason that a bilinear model was developed for estimating the behavior of specimens without fibers and a trilinear model was introduced for the estimation of those with fibers. The models are presented in Figure 4.18 with observed ranges for critical parameters shown in Figure 4.19. The trilinear model was chosen for specimens with fibers because of its ability to incorporate residual strength more accurately than the bilinear model. The accuracy for each method is reported in Table 4.14 in terms of the RMSE. Results confirm the observations made previously and highlight the advantage of models presented in this thesis.

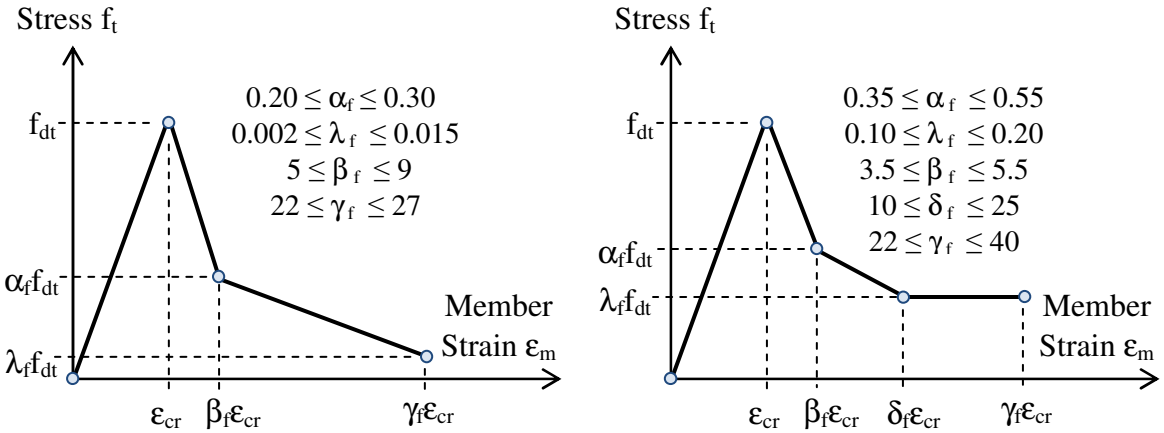

(a) Bilinear [No Fibers] (b) Trilinear [Fibers]

Figure 4.19 **– Proposed Models for Post-Cracking Contribution of Concrete**

Table 4.14 – **Accuracy (RMSE) of Models for Post-Cracking Concrete Contribution**

Specimen Label	Proposed Model	Bischoff & Paixao (2004)	Abrishami & Mitchell (1996)	Belarbi & Hsu (1994)	Damjanic & Owen (1984)
PCP-45-01	0.54†	0.64	1.27	1.04	1.61
PCP-45-02	0.55†	0.86	1.14	0.73	1.67
PCP-45F-01	0.57††	1.09	1.07	0.63	1.83
PCP-45F-02	0.40††	1.05	1.22	0.81	2.11

†Bilinear Model ††Trilinear Model

CHAPTER 5

EXPERIMENTAL PROGRAM: SERVICEABILITY & FATIGUE PERFORMANCE OF PCP REINFORCED CONCRETE BEAMS

5.1 GENERAL

In light of the conclusions reached during the deflection analysis performed in the first chapter of this thesis, the second and third chapters introduced the use of prestressed concrete prisms (PCP) as a reinforcing material in structural applications. The alternate reinforcement can improve the flexural stiffness of reinforced concrete elements under service conditions and preserve the advantages of Fiber Reinforced Polymer (FRP) reinforcement. An experimental program was designed and carried out to evaluate the performance, and most importantly the serviceability, of concrete beams reinforced with PCP reinforcement. The results were compared to those obtained from prestressed concrete beams, which can also improve the serviceability of FRP reinforced concrete elements through initial camber and higher cracking moment. To maintain an adequate basis for comparison, the PCP reinforcement and flexural specimens in this research were prestressed with the same type of reinforcing material and prestressing level.

The experimental program of this thesis was also aimed at evaluating the influence of temperature fluctuations within the Canadian climate. The influence was considered due to the presence of a wedge shaped expansion known as the Hoyer effect in the transfer region of prestressed elements combined with the higher potential of FRP reinforcement to swell under thermal gradients. Differential thermal swelling of reinforcement and concrete creates splitting stresses within the cover and the increased potential for cracking can lead to significant stress relief around the reinforcing bar and eventual loss of bond between the materials. The relatively small cross-section of PCP reinforcement increases the potential for concrete cover damage and the loss of bond can jeopardize the structural integrity required to achieve the desired improvements on serviceability.

While the static performance and thermal sensitivity were defining parameters for the first phase of the experimental program, the second phase of the program was designed to investigate the fatigue performance of beams with PCP reinforcement. The results were compared to those obtained from concrete beams prestressed with the same material and prestressing level as that used for PCP reinforcement. The influence of thermal gradients on fatigue performance was also studied by considering thermal gradients similar to those occurring in the Canadian climate. Results from this phase are intended to provide insight on the long term performance of PCP reinforcement under the combined effects of repeated loading and thermal weathering prior to its use in field applications.

The third and final phase of the experimental program consisted of investigating possible improvements to the performance of PCP reinforcement under service conditions. The inclusion of dispersed fibers in the High Strength Concrete (HSC) mix can improve the cracking strength of PCP reinforcement, thereby increasing the range of service loads for which the flexural stiffness of beams containing the reinforcement is enhanced. The inclusion of physical deformations on the surface can, additionally, improve the bond performance of PCP reinforcement. Results from the inclusion of dispersed fibers and the incorporation of surface deformations were closely analyzed to provide quantitative information on the serviceability improvement achieved with respect to specimens cast during the first phase of the program.

5.2 SECTION GEOMETRY AND TESTING PROCEDURE

As illustrated in Figure 5.1, all beams in this research were designed with a width of 125mm and a depth of 250mm. The reinforcement was centred at 50mm from the bottom of all beams in their casting position. Two 6mm diameter steel reinforcing bars were also provided at 30mm from the top of each beam to serve as compression reinforcement. The beams were 2550mm in length. Half the beams in the first two batches were pre-tensioned with a 9mm diameter Carbon FRP (CFRP) tendon while the remaining half was reinforced with 50mm high by 50mm wide PCP reinforcement. All of the beams in the third batch were reinforced with PCP reinforcement. The PCP reinforcement was also pre-tensioned with a 9mm diameter CFRP tendon. As shown in Figure 5.2, steel stirrups were used to tie the reinforcement in a cage and provide the required shear resistance during testing.

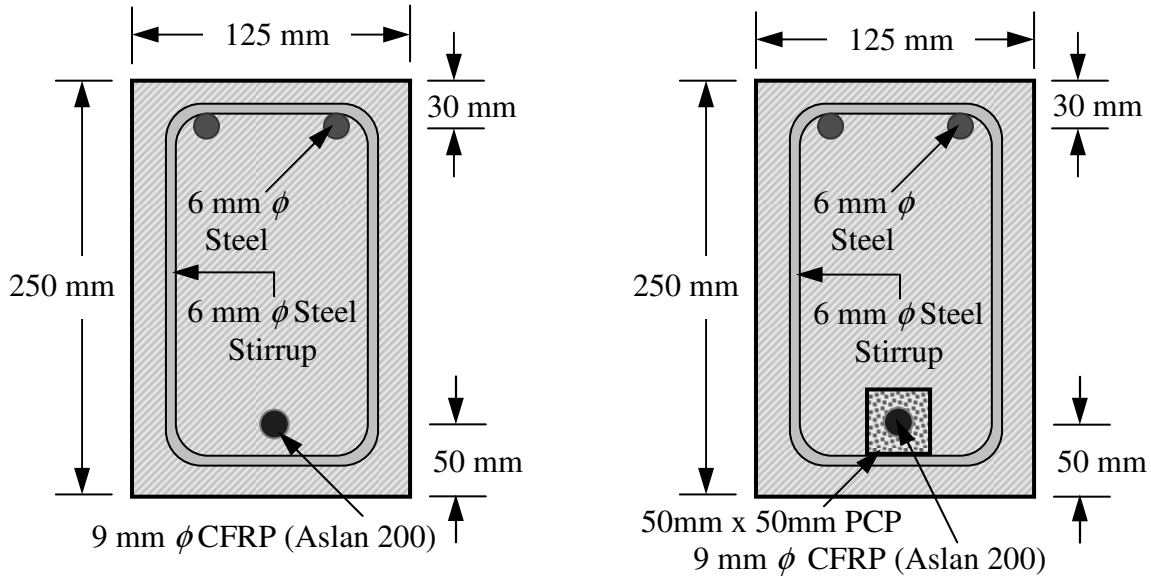

(a) CFRP Prestressed Beam (b) PCP Reinforced Beam

Figure 5.1 - **Beam Geometry**

As illustrated in Figure 5.3, all beams in this research were tested under three point loading with the load centered between the supports. The figure also shows that a 10 mm high by 10 mm wide notch was introduced at midspan to ensure the first crack initiates at

the point of maximum moment. The 100mm by 100mm grid pattern drawn on the beam made it easier to monitor the development of cracks and determine crack spacing.

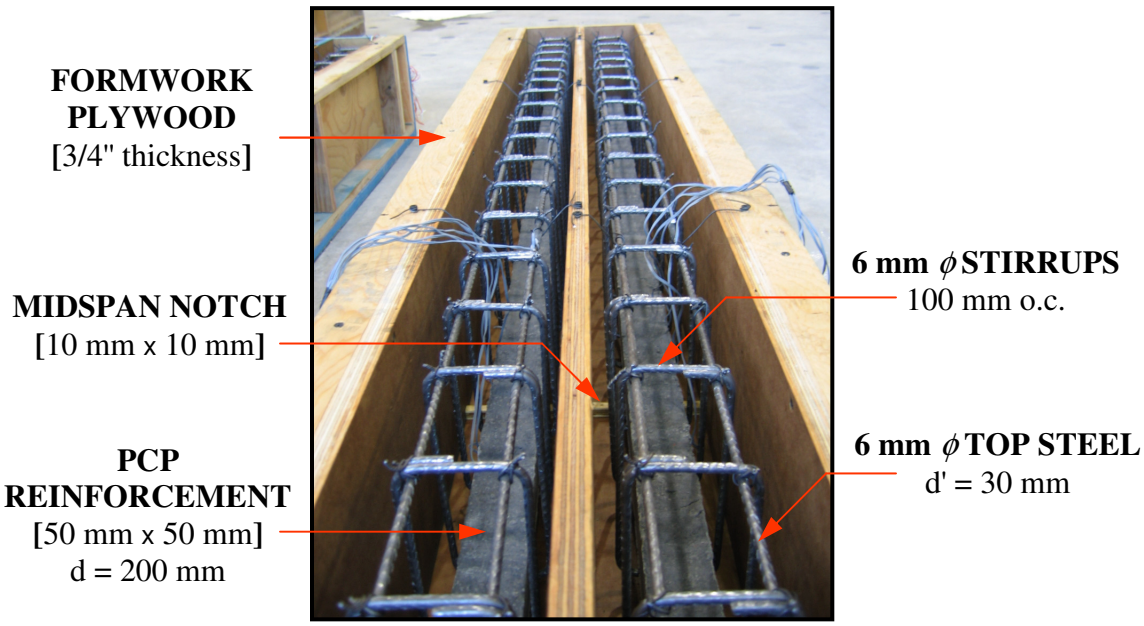

Figure 5.2 – **Reinforcing Cage inside Formwork**

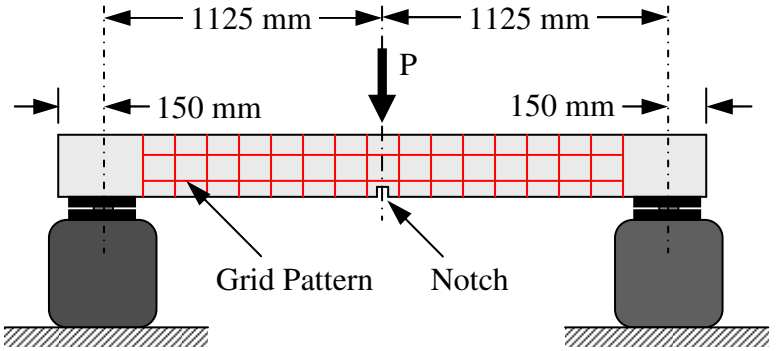

LOADING SCHEME

Before Casting [Inside Formwork]

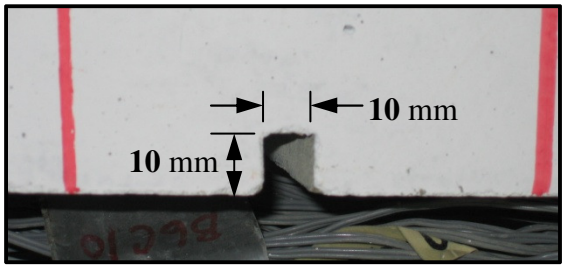

After Casting [Formwork Removed]

NOTCH SPECIFICATIONS

Figure 5.3 – **Testing Procedure**

5.3 APPLICATION OF PRESTRESS

Prestressing and casting of the specimens took place at the University of Manitoba McQuade Structures Laboratory in the month of October 2007. The prestressing force was applied to the reinforcement through the use of a hydraulic jack. A load cell was inserted between the jack and the bulkhead to determine the load applied to the tendons during the prestressing application. The prestressing bed was constructed during the summer of 2007 and mounted on the top flange of a W920x420 steel section. The width of the I-section allowed the bed to accommodate two rows and the length of the section allowed two specimens to be prestressed and cast in each row for a total of four. To ensure the reinforcing bars remained at the required depth along the bed, a thorough analysis was performed to ensure the supporting section had sufficient stiffness to resist the eccentric application of prestress and limit deflections along the length of the bed.

As illustrated in Figure 5.4, the bottom of the prestressing bed consisted of overlaid plyform supported on either side by a set of five threaded rods. The rods were bolted to the top flange of the supporting I-section, which allowed the prestressing bed to be adjusted for any reinforcing depth. For the PCP reinforcement, the sides of the formwork consisted of L51x51x6.4 steel angles assembled concentrically around the reinforcement prior to the application of prestress. For the prestressed beams, the sides and bottom of the formwork were assembled on the bottom of the bed around the reinforcement and the reinforcing cage prior to the application of prestress. Figure 5.5 illustrates the layout for the prestressed elements cast in this research.

During the application of prestress, a 6mm electrical resistance strain gauge from each specimen was connected to a 12-channel data acquisition (DAQ) system to monitor elongation in relation to the applied load. After the prestressing application, the end pieces of the formwork were adjusted to position the strain gauges at the appropriate locations along the length of the PCPs. In the case of the prestressed beams, the procedure was accomplished by shifting the complete formwork along the bed and subsequently introducing the end plates for casting the following day.

JACKING END

LOAD CELL

COUPLER MECHANISM

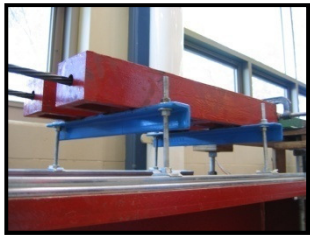

DEAD END

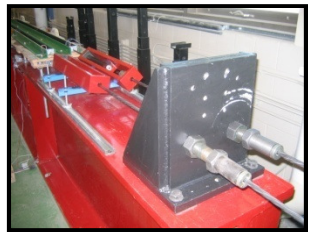

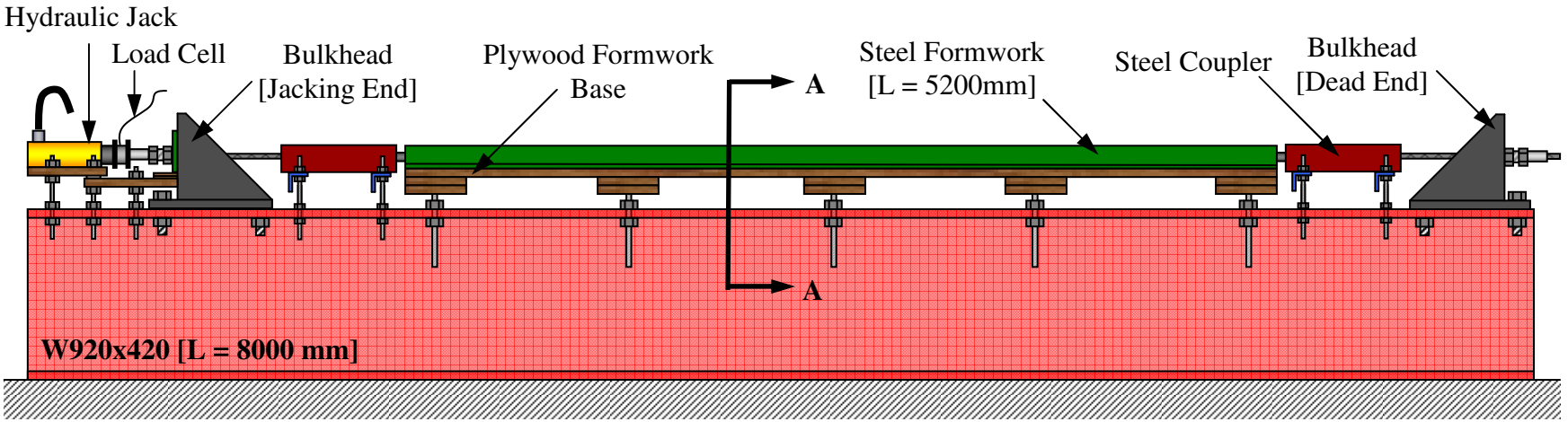

SECTION A-A DETAILS:

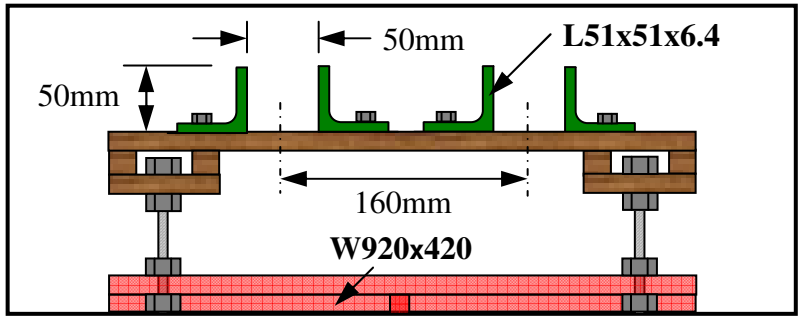

Figure 5.4 – **Prestressing Bed Details and Dimensions**

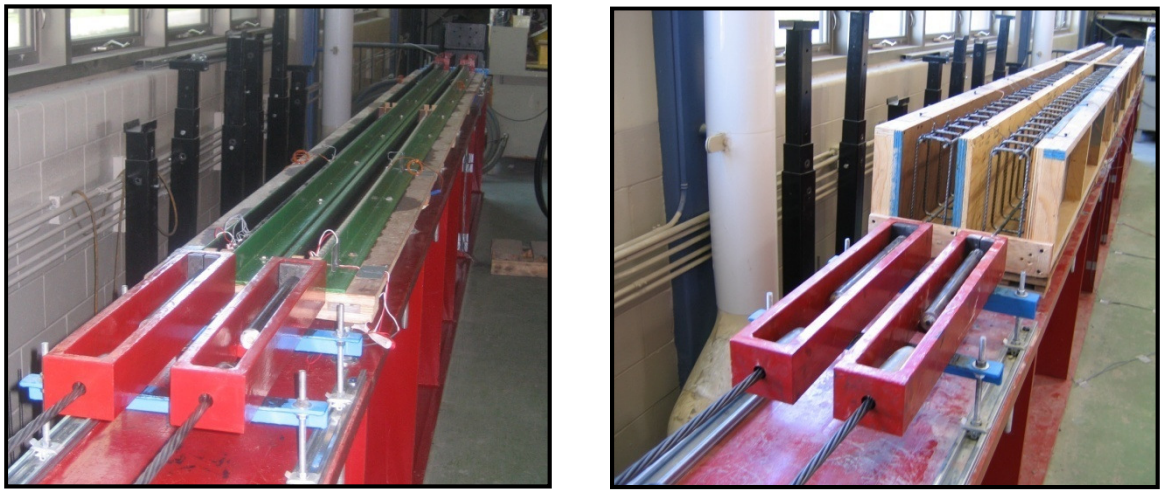

(a) PCP Reinforcement (b) Prestressed Beams

Figure 5.5 – **Prestressing Layout**

Due to the composition of FRP reinforcement and its frailty in the transverse direction, the use of chucks as those in prestressed steel applications was inadequate. A coupler mechanism was therefore used to transfer prestress to the reinforcement. Aside from having dimensions that accommodated the geometrical and mechanical properties of tendons used in the research, the mechanism is conceptually similar to that used in previous research involved with prestressing of FRP reinforcement at the University of Manitoba (Banthia 2003, Vogel 2005).

Each coupler consisted of two longitudinal steel plates welded to transverse steel plates at both ends. Each end was fitted with a hole, the first of which allowed the insertion of a 13mm diameter 7-wire low relaxation steel strand gripped with a steel chuck. The second hole allowed the introduction of a 35mm diameter anchor bonded to the end of the FRP reinforcement. A spacer was required and fabricated to prevent the anchor from sliding out of the second hole of the coupler during application of prestress. Figure 5.6 shows a detailed drawing and picture of the coupler assembly in the prestressing bed.

The coupler mechanism shown in Figure 5.6 was tested in previous research (Vogel, 2005) to ensure sufficient tensile strength was available for the application of prestress. Designed with a capacity exceeding the prestressing force required for the study, the

coupler was capable of sustaining a load of 156kN during the tension test. This load represents approximately three times the maximum prestressing force that is to be carried by the CFRP reinforcement in this research.

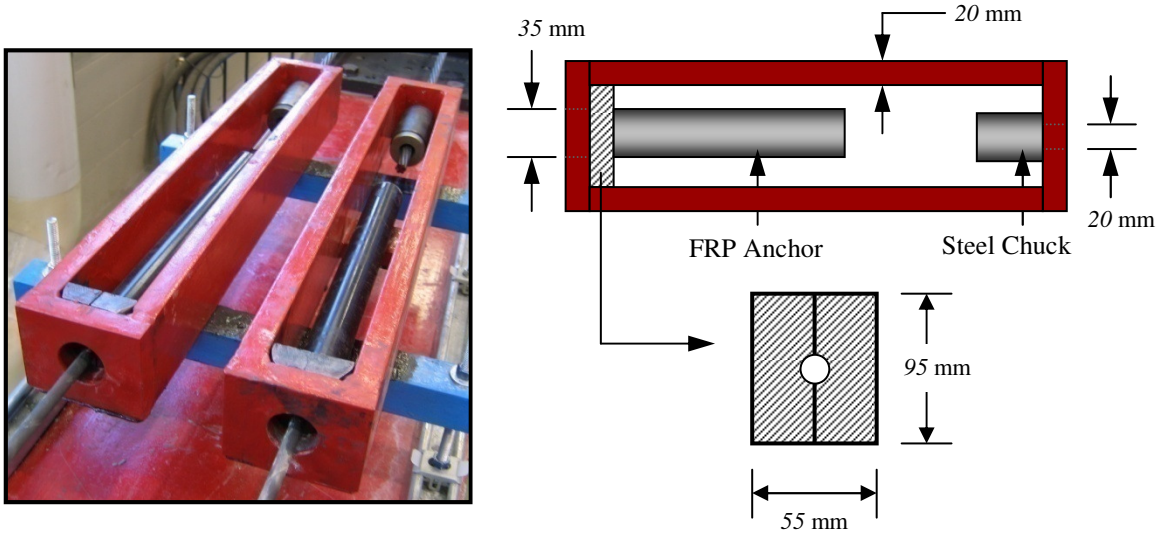

Figure 5.6 - **Coupler Mechanism and Assembly**

5.4 PRESTRESS LEVEL AND CORRESPONDING LOSSES

In order to evaluate the performance of PCPs as reinforcement in civil infrastructure, the same prestressing level was adopted for all beams in the project. The CFRP bars were stressed to 26 percent of their guaranteed tensile strength, which corresponds to a jacking strain of approximately 4000με. The level was primarily selected to ensure transverse differential swelling of the reinforcement does not cause tensile splitting of the concrete cover within the transfer region of the reinforcement. As illustrated in Figure 5.7(a), the design chart from Chapter 2 can be used for the purpose with an anticipated compressive strength of 120MPa for the HSC mix (PCA RD104T 1992) as well as a clear concrete cover to bar diameter ratio of 2.27 for the PCP reinforcement. Although slightly higher compressive and tensile strengths were obtained from the concrete mixed in this project at the time of test, the selected prestressing level is conservative and provides a safety clearance from the splitting phenomenon. The design chart in Figure 5.7(b) was also developed in Chapter 2 and can be used to establish the cracking moments of the PCP

reinforced beams on the basis of the optimum prestressing strains of Figure 5.7(a). Using a transverse elastic modulus of 3000MPa for the reinforcement, a reinforcing ratio ρ_{bm} of 0.1, a beam width b of 125mm and an effective reinforcement depth d of 200mm, the chart yields a cracking moment of approximately 5.75kN·m for the beam and 10.5kN·m once the PCP reinforcement reaches its cracking strength.

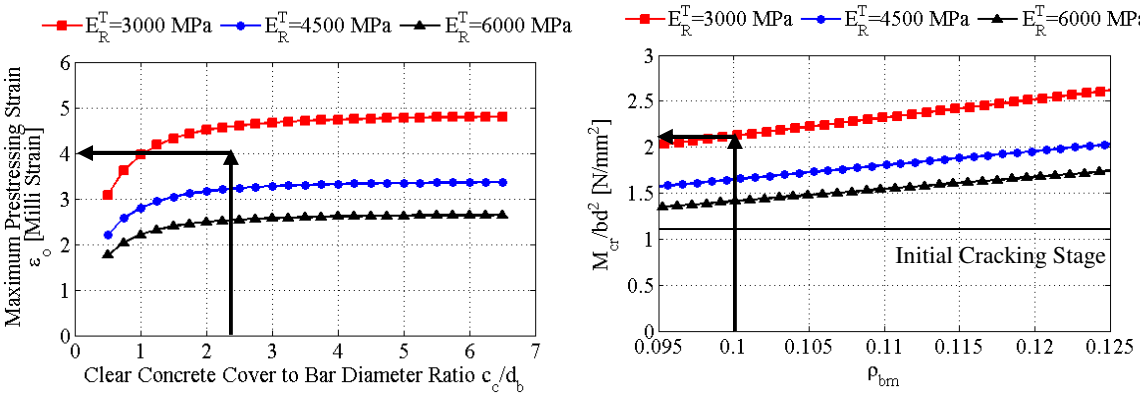

(a) Optimum Prestressing Level (b) Cracking Moments

Figure 5.7 - **Design Charts for Prestressing Level and Cracking Moments** [f'_c = 120MPa]

Prestress losses for the selected prestressing level were estimated on the basis of clause 10.6.2 of CSA S806 (2002) and are summarized in Table 5.1. They are primarily based on the mechanical properties of the high and Normal Strength Concrete (NSC) used in the project. The geometrical properties of the PCP reinforcement and prestressed concrete beams are also used in the determination of short term losses due to elastic shortening as well as long term losses due to creep and shrinkage. According to the results presented in this table, an initial loss of 10.6 and 3.3 percent immediately after transfer as well as a total loss of 31.9 and 20.2 percent was expected for CFRP bars in the PCP reinforcement and prestressed beams, respectively. Larger shortening and creep losses calculated for the bars in the PCP reinforcement mainly arise from the relatively small section size and higher compressive stresses being sustained by the surrounding concrete.

Prestressing was sustained during a total of 13 days for the PCP reinforcement and 15 days for the prestressed beams. The procedure allowed concrete to reach sufficient tensile strength to prevent splitting of the PCP reinforcement cover and excessive tensile stresses

to develop in the top fibres of the prestressed concrete beams. As opposed to cutting the steel strands at the end of the prestressing bed, the prestressing load was gradually released by tightening the nuts at the end of the hollow bolts that were inserted between the steel chucks and bulkheads. The mechanism is illustrated in Figure 5.8 and the procedure was primarily adopted to prevent impact loading of the PCP reinforcement and excessive tensile stresses to develop within the concrete cover.

Table 5.1 - **Estimated Prestress Losses** [MPa]

Source	Loss - Prism	Loss - Beam
Relaxation Prior to Transfer	7.8	7.8
Elastic Shortening	65.3	14.8
Time Dependent Losses		
Creep and Shrinkage	133.7	109.3
Relaxation	12.4	7.1
Total Losses	219.2	139.0

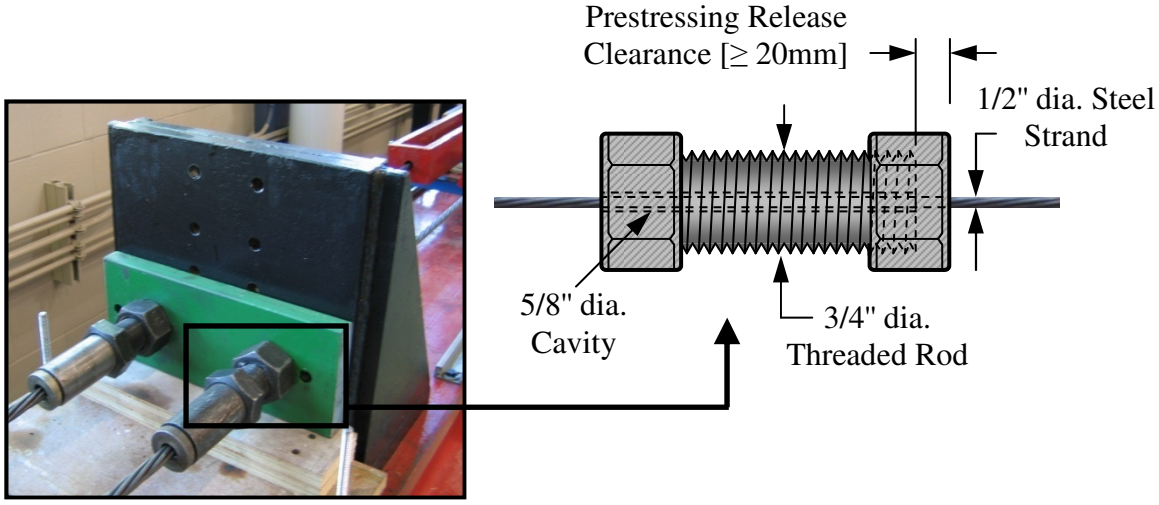

Figure 5.8 – **Prestress Release Mechanism** [Hollow Bolt and Nut Assembly]

Strains were also recorded prior to and at release of prestress to confirm the estimated losses arising from relaxation of the CFRP tendon as well as elastic shortening of concrete. The variation of strain in each prestressing row was averaged as shown in Figure 5.9(a) and plotted as a function of time elapsed after the application of prestress. Results are summarized in Table 5.2 and appear to be consistent among all prestressing rows. An average initial prestress loss of 8.8 and 2.6 percent were respectively measured

for the PCP reinforcement and prestressed beams immediately after release. Conversely, total prestress losses were measured on the basis of cracking moments recorded during the flexural tests. They respectively averaged 9.4 percent for the PCP reinforcement and 24.8 percent for the prestressed beams. Although initial losses for both prestressed elements are in close agreement with values predicted from clause 10.6.2 of CSA S806 (2002), total losses for the PCP reinforcement were noticeably and considerably lower than anticipated. More specifically, it is possible that creep and shrinkage modification factors presented in the CSA A23.3-04 reinforced concrete design code are not adapted for the higher strength concrete used in this research. Moreover, placing the PCP reinforcement in the curing room immediately after prestress release has lead to a reduction of time dependent losses attributed to the effects of creep and shrinkage.

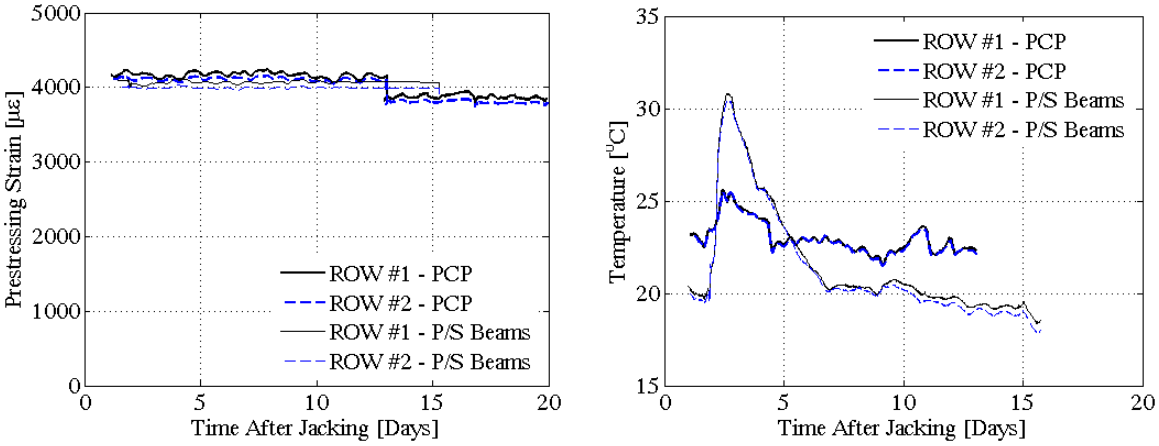

(a) Prestressing Strain (b) Temperature [°C]

Figure 5.9 – **Data Monitoring After Jacking** [Second PCP Batch]

Although the overall trend in prestressing strain was found to be decreasing, results from Figure 5.9(a) also show that localized fluctuations along the time domain exist. The effect is more noticeable for PCP reinforcement and is mainly attributed to the relatively small section geometry and the consequently strong sensitivity of the elements to temperature changes. Thermocouples placed on the surface of the reinforcing bars in the first prism and first row as well as in the first prism within the second row were used to convey the fluctuation of temperature prior to release. The sensors were placed in the vicinity of strain gauges used to monitor strains during and after jacking. Results presented in Figure

5.9(b) show a stronger thermal response and sensitivity of the PCP reinforcement to temperature fluctuations in the structures laboratory. The initial crowns observed in the temperature trends relate to heat generation during early age concrete curing.

Thermal gradients within the prestressed beams can also be observed in Figure 5.9(b) but the larger section geometry and concrete cover surrounding the reinforcement causes the fluctuations to be smoother and influenced to a lesser extent by changes in laboratory temperature. The figure also shows a larger increase in temperature than that observed in the PCP reinforcement within three days after casting. The observation is characteristic of the early stages of curing and the exothermic nature of the reaction between water and cement within the mix. Furthermore, the volume of concrete and thickness of the prestressed beams restrain the dissipation of temperature within the element, which explains the higher level of temperature measured at the surface of the tendon.

Figure 5.10 further suggests that a relationship exists between the fluctuation in strains after jacking and the temperature at the surface of the bare reinforcing bar. It should be noted that the longitudinal coefficient of thermal expansion (CTE) of CFRP reinforcement can range between –9 to 0με/^{o}C, depending on the manufacturer of the bar (ACI 440.1R-01). Since the thermal property for concrete is generally taken as 10με/^{o}C, the difference restrains free expansion of the tendon when considering the compatibility of longitudinal strains and assuming bond is preserved between the materials. The restraining effect is more pronounced once the concrete has hardened and developed larger stiffness at the approach of prestress release. Although results in Figure 5.10 were recorded during a period of 3 days prior to release, strains vary within 25με and suggest a definite contribution of temperature to strain fluctuations on the reinforcement. Although these strain fluctuations are small and recoverable, they can lead to a misinterpretation of elastic shortening when prestressing is released. The prestressing operation for PCP reinforcement should therefore be performed in a controlled environment where thermal variations are maintained within reasonable limits.

Table 5.2 - **Measured Prestress Losses** [MPa]

(a) PCP Reinforcement

Source	ROW #1 [PCP1 & PCP2]	ROW #2 [PCP3 & PCP4]
Relaxation Prior to Transfer	6.5	7.2
Elastic Shortening	56.3	56.2
Time Dependent Losses Creep, Shrinkage and Relaxation	3.6	5.3
Total Losses	66.4	68.7

(b) Prestressed Beams

Source	ROW #1 [PCB1 & PCB2]	ROW #2 [PCB3 & PCB4]
Relaxation Prior to Transfer	6.5	6.7
Elastic Shortening	11.7	11.4
Time Dependent Losses Creep, Shrinkage and Relaxation	151.5	157.3
Total Losses	169.7	175.4

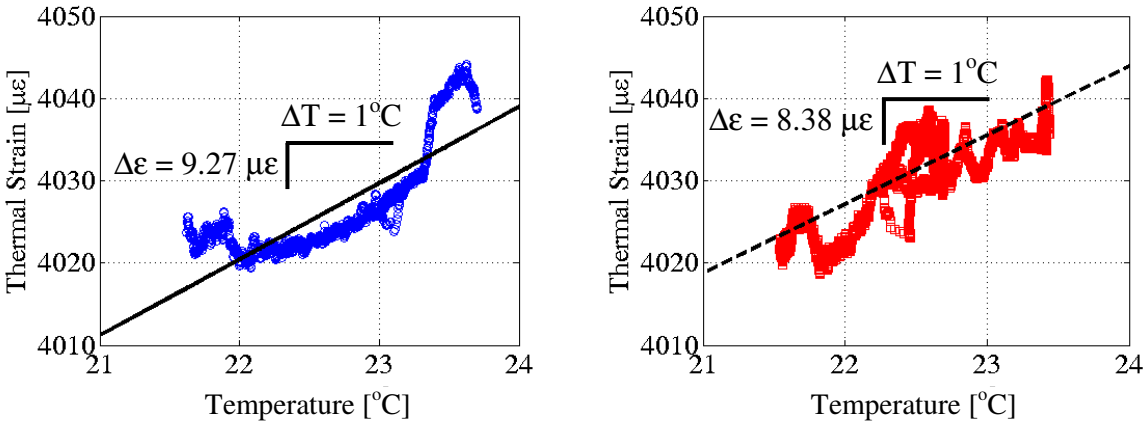

(a) ROW #1 [PCP1] (b) ROW #2 [PCP3]

Figure 5.10 – **Strain Variation with Temperature** [Days 10 through 14]

5.5 CRITICAL CONCRETE STRESSES

Concrete stresses occurring at the extreme fibers of the prestressed beams were calculated immediately after transfer and also after allowance for all losses. Originating from the prestressing effect and self-weight of the elements, these stresses were calculated by

means of transformed section properties and relationships that are illustrated in Figure 5.11.

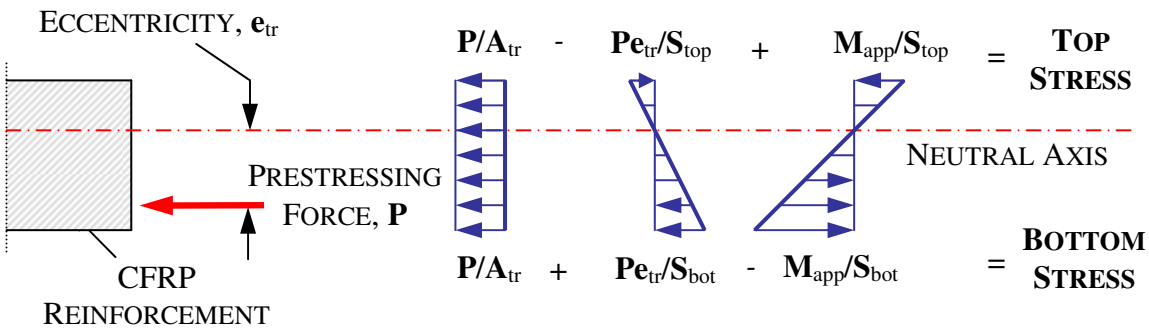

Figure 5.11 – **Calculation of Concrete Stresses due to Specified Loads**

Stresses were checked at all critical locations along the length of the beams, which includes the extremities of the flexural member as well as the midspan section. While stresses at the extremities of the member govern the design immediately after transfer, stresses at midspan control the design after allowance for all prestress losses. A summary of all concrete stresses can be found in Table 5.3. All values in this table are within the limits recommended by clause 10.4 of CSA S806 (2002). The section geometry is sufficient and bonded reinforcement in addition to what is already provided is not required.

Table 5.3 - **Critical Concrete Stresses** [MPa]

	RELEASE [$P = P_i$]				LONG-TERM [$P = P_e$]	
	Support		Midspan		Midspan	
	Top	Bottom	Top	Bottom	Top	Bottom
P/A_{tr}	1.33	1.33	1.33	1.33	1.03	1.03
Pe_{tr}/S_{tr}	-2.38	2.38	-2.38	2.38	-1.84	1.84
M_{sw}/S_{tr}	-	-	0.35	-0.36	0.35	-0.36
STRESSES	-1.05	3.71	-0.70	3.35	-0.46	2.51
ALLOWABLE	-2.74 ($-0.5f'_{ci}^{0.5}$)	18.00 ($0.6f'_{ci}$)	-1.36 ($-0.25f'_{ci}^{0.5}$)	18.00 ($0.6f'_{ci}$)	30 ($0.6f'_c$)	-3.54 ($-0.5f'_c^{0.5}$)
CHECK	**OK**	**OK**	**OK**	**OK**	**OK**	**OK**

5.6 MATERIAL PROPERTIES

In order to estimate the behaviour of beams presented in Figure 5.1, the properties of the concrete and reinforcement used in the research must be determined at the relevant stages of the project. Detailed properties of the HSC mix used in the PCP reinforcement are fully discussed in Chapter 3. Conversely, concrete with a compressive strength of 50MPa was selected for all beams cast in this research. Since the first two batches of beams were used to evaluate the performance of PCP reinforcement before as well as after thermal cycling, air content in the range of 6 to 8 percent was requested for the NSC mix summarized in Table 5.4.

Table 5.4 - **Concrete Mix Design**

COMPONENT	VALUE
Cement	407kg/m^3
Classified Sand	727kg/m^3
Water	147kg/m^3
10 mm Coarse Aggregate	1120kg/m^3
Water Reducing Admixtures	2L
Air Entraining Agent	33ml
Water:Cement Ratio	0.36
Density of Concrete	2401kg/m^3

On a similar note, the CFRP reinforcing bars used in the PCP reinforcement as well as in the prestressed concrete beams are manufactured by Hughes Brothers and carry the designation of Aslan 200. Table 5.5 lists the specifications provided by the manufacturer for the nominal bar diameter of 9mm. In order to confirm these nominal tensile properties for the reinforcement as well as the compressive and tensile strength of concrete for the beams in this project, experimental testing was performed at the University of Manitoba in accordance with the corresponding standards.

5.6.1 Reinforcement Tensile Properties

Tension was applied to the specimens through the use of steel anchors that were adapted to the grips of the testing machine. The anchors are high-pressure steel pipes commonly used in plumbing applications, bonded to the ends of the FRP reinforcement. Geometric characteristics are in accordance with Annex B of CSA S806 (2002) and are illustrated in Figure 5.12.

Table 5.5 - **Aslan 200 Reinforcement Specifications** [Hughes Brothers, Inc.]

PARAMETER	VALUE
Nominal Diameter [mm]	9
Sectional Area [mm^2]	65.2
Ultimate Strength in Tension [MPa]	2,068
Elastic Modulus [MPa]	124,000
Ultimate Strain [με]	16,677
Transverse CTE [με/^oC]	74 to 104
Longitudinal CTE [με/^oC]	-4 to 0
Maximum bond Stress [MPa]	8.45

A Bristar 100 expansive grout was used to cement anchors at the ends of all CFRP tension specimens. The interior wall of each anchor was cleaned using a steel wire brush. A washer was glued with Devcon 5-minute® epoxy gel at the bottom of each anchor to center the reinforcing bar within the steel pipe as well as to prevent leakage of the bonding agent. Anchors were subsequently cast in a vertical position using a suitable jig to maintain axial alignment with the FRP reinforcement. Specimens were kept in their vertical positions at least 12 hours and tested more than 24 hours after casting.

A 267kN (60kips) capacity testing machine was used for all tension tests. Specimens were instrumented with a longitudinal strain gauge to determine the modulus of elasticity while two specimens were instrumented with transverse strain gauges to evaluate Poisson's ratio. Load and strain was monitored and recorded using a 32-Channel DAQ System.

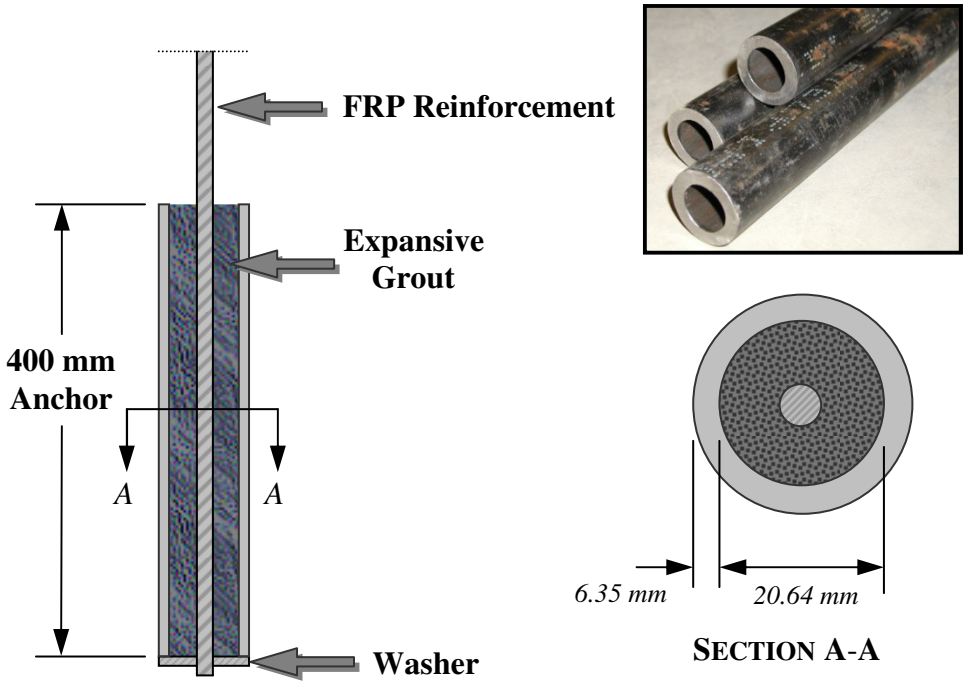

Figure 5.12 – **Anchor Geometric Properties**

All failures initiated with the sound of individual fibres fracturing followed by complete rupture of the specimen within the gauge length portion away from the anchors. The failure characteristic is illustrated in Figure 5.13(a) with averaged results from the complete set of tension tests summarized in Table 5.6. Figure 5.13(b) shows the stress-strain relationship obtained from a typical tension test performed on the reinforcing bars. Results in this figure emphasize the linear elastic behaviour of FRP reinforcement to failure.

5.6.2 Concrete Properties

The mechanical properties of concrete used for the beam batches cast during each of the three phases of this research were determined from tests performed on standard cylindrical concrete specimens. The concrete cylinders were cast simultaneously with the beams and kept in the same curing environment as the flexural elements at all times. ASTM standards C39/C39M-04a, C496/C496M-04 and C469-02 were used for determining the compressive strength, splitting tensile strength and elastic modulus,

respectively. As before, tests were performed with a 1350kN TestMark hydraulic testing machine using loading rates specified by the corresponding standards. The test setup for determining compressive and tensile strength is similar to that used for HSC cylinders tested during the fabrication of the prisms. Results are illustrated in Figure 5.14 up to 28 days of curing and presented in Table 5.7 up to the time of flexural test.

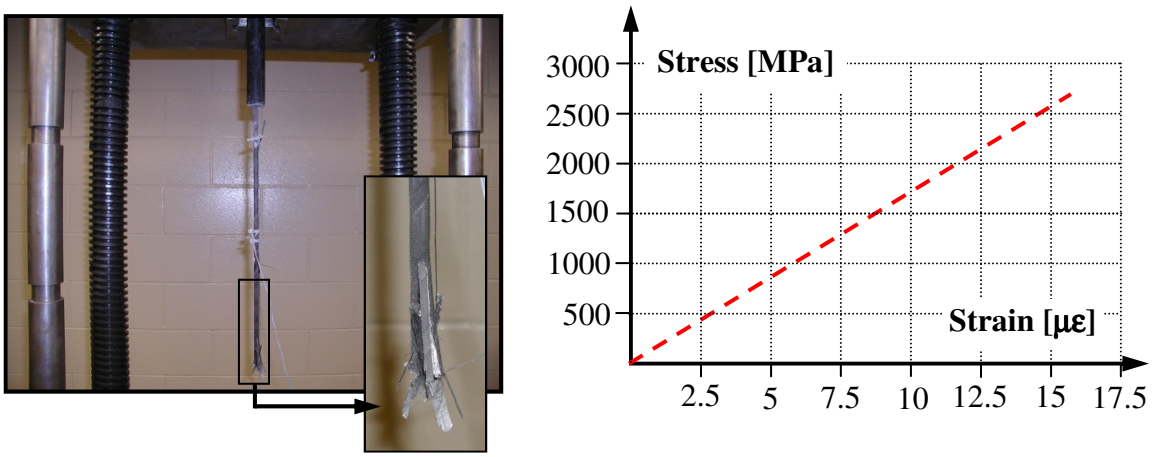

(a) Failure Characteristics (b) Stress-Strain Relationship

Figure 5.13 - **Tension Test Results** [Vogel, 2005]

Table 5.6 - **Tension Tests Result Summary**

PARAMETER	VALUE
Ultimate Strength in Tension [MPa]	2,563
Elastic Modulus [MPa]	171,962
Ultimate Strain [με]	14,472
Poisson's Ratio ν_f^{LT}	-0.35

To ensure sufficient strength was reached at critical stages during the curing process, compression and splitting tension tests were performed at the time of release for the prestressed beams as well as immediately after testing for the complete set of beams. To gain further awareness on the influence of thermal action on concrete strength, cylinders were placed within the chambers during the weathering process and also tested immediately after the flexural tests. Results from these additional tests are shown in parentheses in Table 5.7. Although compressive and tensile strengths at 180 days were

found to reduce from that measured after 28 days, the influence of temperature on strength is negligible for the 50 thermal cycles considered in this thesis.

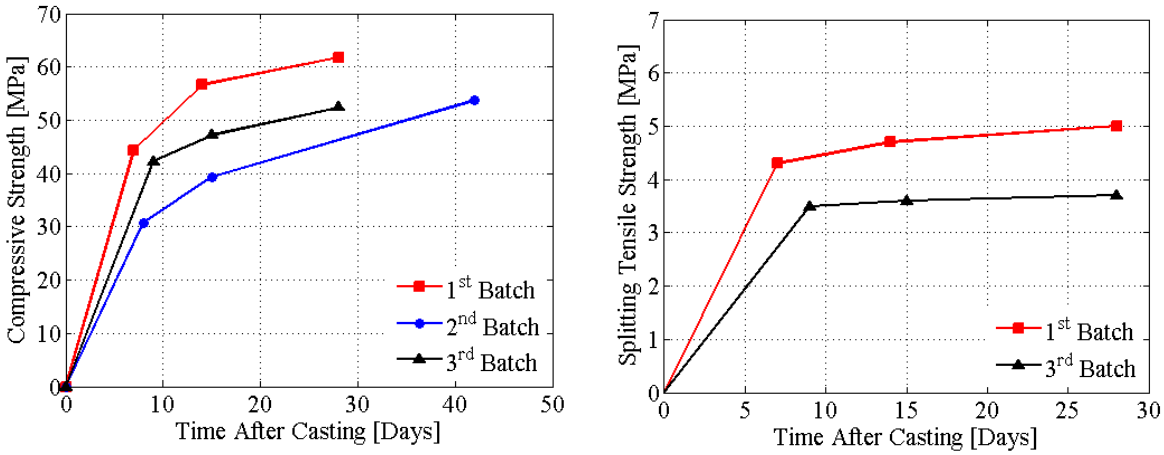

(a) Compressive (b) Splitting Tensile

Figure 5.14 - **Strength Development with Time**

Table 5.7 - **Concrete Strength Development** [MPa]

(a) Beam Batch#1 (First Phase)

Time of Test [Days]	Compressive Strength [MPa]	Split Cylinder Strength [MPa]
3	30.9	3.3
7	44.3	4.3
14 (Release of Prestress)	56.6	4.7
28	61.8	5.0
180 (Flexural Tests)	56.5 (54.3)	3.2 (3.1)

(b) Beam Batch#2 (Second Phase)

Time of Test [Days]	Compressive Strength [MPa]	Split Cylinder Strength [MPa]
4	25.3	-
8	30.8	-
15 (Release of Prestress)	39.3	-
42	53.7	-
133 (Flexural Tests)	54.3	4.6

(c) Beam Batch#3 (Third Phase)

Time of Test [Days]	Compressive Strength [MPa]	Split Cylinder Strength [MPa]
5	34.7	-
9	42.3	3.5
15 (Release of Prestress)	47.2	3.6
28	52.4	3.7
181 (Flexural Tests)	52.6	3.8

It should be noted at this stage that the second beam batch was cast during the month of December 2007 when the outside temperatures reached approximately -40^{o}C. The concrete truck was unable to enter the structures lab due to large scale testing obstructing the overhead door. As a consequence, a portion of the concrete batch froze in the mixer causing a shortage of standard concrete cylinders. It was therefore decided to preserve cylinders for estimating the strength at the critical stages for prestress release and flexural testing. Cylinders were therefore not placed in the environmental chamber to establish the loss of strength from thermal cycling, noting that it was found to be negligible from the first batch of tests. Similarly, standard concrete cylinders from the third beam batch were not placed in the environmental chamber since none of the samples were subjected to thermal cycles.

As illustrated in Figure 5.15(a), Young's modulus was determined by monitoring the contraction of the specimens with a dial gauge mounted between the top and bottom rings of a compressometer. The gauge was accurate to the nearest 100×10^{-6} in. and fitted within a gauge length of 75 mm. The dial gauge readings were converted to strain and plotted against applied stress, as shown in Figure 5.15(b) for a cylinder from the third batch of beams. A trendline was fitted through the results on the basis of a least squares method with a slope equivalent to the modulus of elasticity. Modulus tests for each batch were performed on a total of two standard concrete cylinders immediately after the flexural tests. Elastic modulus values were found to average 43,828MPa, 28,949MPa and 35,251MPa for the first, second and third beam batches, respectively.

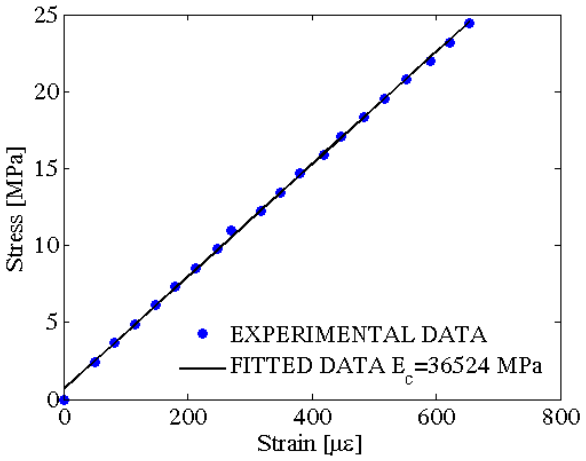

(a) Test Setup with Compressometer (b) Fitted Results [180 Days - Unweathered]

Figure 5.15 - **Evaluation of Young's Modulus**

5.7 WEATHERING PROCESS

5.7.1 Thermal Cycling

Standardized methods for evaluating the bond performance of PCP reinforcement or prestressed reinforcement in a concrete environment under the effects of service temperatures expected in the Canadian climate do not exist. It was therefore initially decided to subject half of the specimens from the first and second beam batches to temperature cycles ranging between +40°C and –40°C. Due to tardiness of the chamber in achieving temperatures of –40°C, specimens were cycled to a minimum temperature of –23°C as that required by ASTM E1512 (2001) for determining the bond performance of adhesive-bonded anchors under the effects of various factors including freezing and thawing action.

Based on the requirements of ASTM E1512 (2001), specimens intended for the thermal weathering process were subjected to a total of 50 cycles using a CONVIRON environmental chamber capable of reaching temperatures varying between +40°C and –40°C without humidity control. Beams were introduced in the chamber at room temperature and placed on several wooden blocks to prevent damage of the floor under excessive bearing stresses. Each cycle required 18 hours to reach completion for a total

of 38 days of thermal weathering. Temperature within the beams was monitored by means of a 32-channel DAQ system designed to acquire readings from thermocouples bonded to the surface of the bare reinforcing bar in both beams.

5.7.2 Temperature and Thermal Strain Readings

Temperature readings gathered from the thermocouples inside the beams are shown in Figure 5.16. The solid line in the figure represents data recorded from thermal sensors located inside the chamber. These readings represent temperature surrounding the beams at any time during the weathering process. As illustrated in the figure, extreme temperatures within the chamber were maintained during a total of five hours to achieve the temperatures required at the reinforcing level of the beams. Temperature readings from the samples were considered sufficiently close to those measured from the chamber sensors to confirm the aptness of the cycles to achieve the desired temperatures for the project.

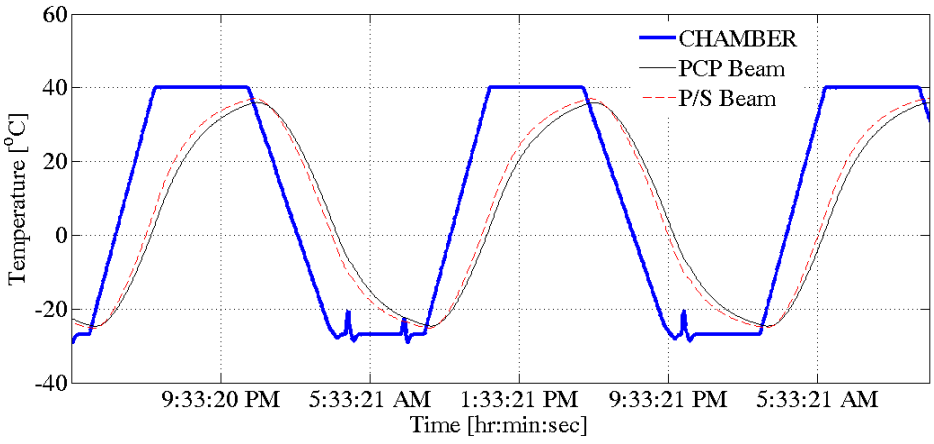

Figure 5.16 – **Temperature Fluctuation with Time** [January 21st & 22nd 2008]

The progression of strain under thermal gradients is expected to follow a similar trend as that observed for temperature during thermal loading within the chamber. Figure 5.17(a) illustrates the similarity by suggesting a linear relationship between thermally induced strains and temperature for beams in the first batch. The figure suggests that longitudinal strains (LSG) are less significant than those recorded in the transverse direction (TSG).

Consequently, the longitudinal expansion of the bare reinforcement under thermal action is negligible, leaving the transverse CTE as the major parameter affecting the development of bursting stresses within the concrete cover. Longitudinal strain readings were obtained from 6mm long strain gauges horizontally placed on the portion of the tendon extruding from the end of one of the prestressed beams. On the other hand, transverse strains were obtained from 2mm long strain gauges circumferentially mounted on the surface of the tendon. As illustrated in Figure 5.17(b), the external instrumentation was protected against moisture and the thermocouple was installed in close vicinity of the strain gauges to monitor temperature.

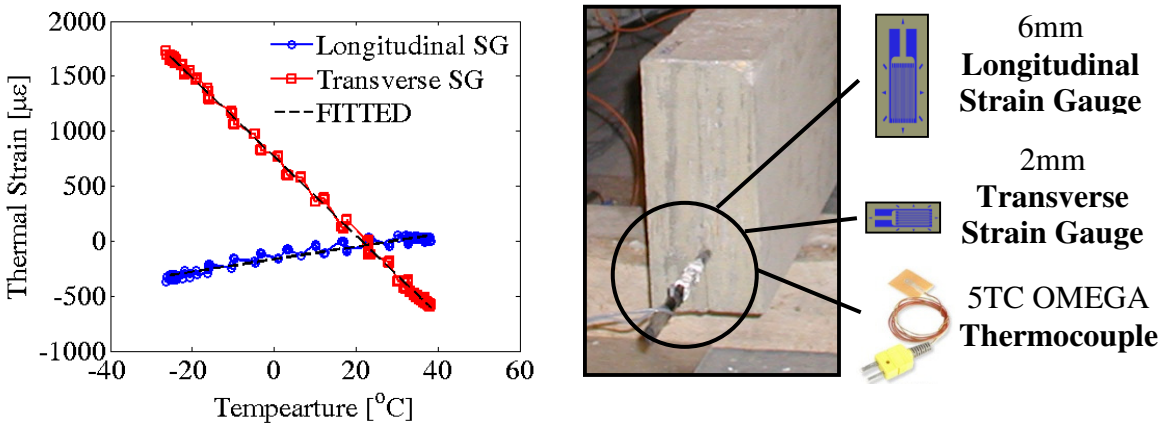

(a) Experimental Results (b) External Beam Instrumentation

Figure 5.17 – **Thermal Expansion Coefficient Determination**

A linear trend line was fitted to the data of Figure 5.17(a) with slopes recorded and averaged to give the longitudinal as well as transverse CTEs. Table 5.8 summarizes the results of this analysis and indicates that the CTE values for the CFRP reinforcement used in this research are different from that provided by the manufacturer. More specifically, the table indicates that the values have opposite sign from that listed by the manufacturer. It should be kept in mind, however, that values from the manufacturer are based on estimates provided by ACI 440.1R (2001). The estimates are generalized for a wide range of commercially available products and relate to carbon fibers alone as opposed to the composite nature of the reinforcement in the project, which also contains a polymeric resin matrix.

Table 5.8 **- Experimental Estimates for CTE** [First Beam Batch]

CTE	Manufacturer (Hughes Brothers, Inc.)	Thermal Strains (Experimental Data)
Longitudinal [με/^{o}C]	-9 to 0	6
Transverse [με/^{o}C]	74 to 104	-36

5.8 FLEXURAL TEST RESULTS AND DISCUSSION

In the sections that follow, beams will be referenced by their names. These names set apart three distinct features. The first part of the name identifies the reinforcing scheme for each beam, PCP-B for PCP reinforced beams and PC-B for prestressed concrete beams. The second part of the name identifies the batch of concrete being tested, which can range from 1 to 3 for this project. Finally, the third part identifies the sample number alone if the specimen was subjected to static loading, the sample number accompanied by a T if thermal weathering was considered and an F if repeated loading was considered. For the last batch of beams, the third part of the sample name was accompanied by an f if fibres were added to the HSC mix, an N if surface deformations were moulded onto the surface of the PCP reinforcement and the number 50 if the prestressing level was increased to 50kN. Table 5.9 provides a more elaborate description of the sample names with respect to their characteristics.

5.8.1 Moment-Curvature Response

The complete moment-curvature response for the PCP reinforced beams is shown in Figure 5.18(a). It was established using linear elastic theory prior to cracking and force equilibrium beyond cracking. The experimental response obtained for all beams tested in the first batch are also shown in the figure. As a basis for comparison, responses from the prestressed beams are illustrated in Figure 5.18(b). In spite of thermal weathering, experimental results from both types of beams compare very well with the theoretical

estimates. Moreover, the figure suggests that the flexural performance of PCP reinforced beams is equivalent to that obtained for prestressed beams at the same prestressing level.

Table 5.9 **– Experimental Program Details**

Beam Name	Loading Scheme	Weathering Conditions [^{o}C]	Reinforcing Scheme	Reinforcement Characteristics		
				Fibre Content [g/m^3]	Surface Finish	Jacking Level [kN]
PCP-B1-1T	Static	-25 to 40	PCP	0	Smooth	45
PCP-B1-2	Static	20	PCP	0	Smooth	45
PCP-B1-3T	Static	-25 to 40	PCP	0	Smooth	45
PCP-B1-4	Static	20	PCP	0	Smooth	45
PC-B1-1T	Static	-25 to 40	CFRP P/S	N/A	Deformed	45
PC-B1-2	Static	20	CFRP P/S	N/A	Deformed	45
PC-B1-3T	Static	-25 to 40	CFRP P/S	N/A	Deformed	45
PC-B1-4	Static	20	CFRP P/S	N/A	Deformed	45
PCP-B2-1T	Static	-25 to 40	PCP	0	Smooth	45
PCP-B2-2	Static	20	PCP	0	Smooth	45
PCP-B2-3TF	Fatigue	-25 to 40	PCP	0	Smooth	45
PCP-B2-4F	Fatigue	20	PCP	0	Smooth	45
PC-B2-1T	Static	-25 to 40	CFRP P/S	N/A	Deformed	45
PC-B2-2	Static	20	CFRP P/S	N/A	Deformed	45
PC-B2-3TF	Fatigue	-25 to 40	CFRP P/S	N/A	Deformed	45
PC-B2-4F	Fatigue	20	CFRP P/S	N/A	Deformed	45
PCP-B3-1f	Static	20	PCP	1800	Notch	45
PCP-B3-2Nf	Static	20	PCP	0	Notch	45
PCP-B3-3	Static	20	PCP	1800	Notch	45
PCP-B3-4N	Static	20	PCP	0	Notch	45
PCP-B1-1f50	Static	20	PCP	1800	Smooth	50
PCP-B1-2f50	Static	20	PCP	1800	Smooth	50
PCP-B1-3f50	Static	20	PCP	1800	Smooth	50
PCP-B1-4f50	Static	20	PCP	1800	Smooth	50

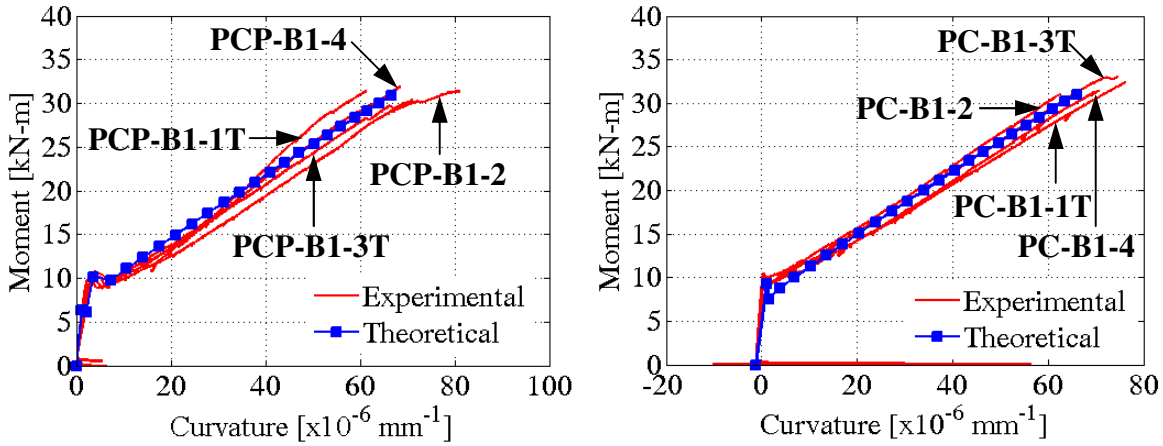

(a) PCP Reinforced Beams (b) Prestressed Beams

Figure 5.18 - **Moment-Curvature Response** [First Beam Batch]

As shown in Figure 5.19, the main difference in behavior occurs in the early loading stages when the beams are uncracked. The diagram shows two distinct cracking stages for beams containing PCP reinforcement, which arises from the additional presence of HSC around the bare reinforcing bar, and the effects of initial camber on curvature for the prestressed beams. The figure also suggests that the absence of initial camber in the PCP reinforced beams will cause a reduction in moment as well as an increase in curvature when the ultimate stage is reached. These parameters are illustrated in Figure 5.19 to provide a clearer emphasis on the difference in behavior between the two types of beams at the critical stages of loading.

Although initial camber will reduce deflections for the prestressed beams, the flexural stiffness provided by the PCP reinforcement remains comparable to that achieved with prestressed reinforcement. The result holds despite the stiffness loss incurred after the first cracking moment is reached for the PCP reinforced beams. Higher prestressing levels can also be achieved with the prestressed beams when considering the geometrical and mechanical properties of this research since extreme fiber stresses within the section were found to reside below the limits set by the CSA S806 (2002) design code. The higher levels can increase the cracking moment beyond that achieved with PCP reinforced beams and allow the uncracked stiffness to be maintained for a wider range of

loads. Nevertheless, the HSC mix was modified for the third batch of beams to increase the tensile strength and allow higher prestressing levels to be achieved in the PCP reinforcement without splitting of the cover. As will be discussed from the results of this batch, the higher strength and prestressing level can provide improvements to the cracking moment for beams containing the reinforcement.

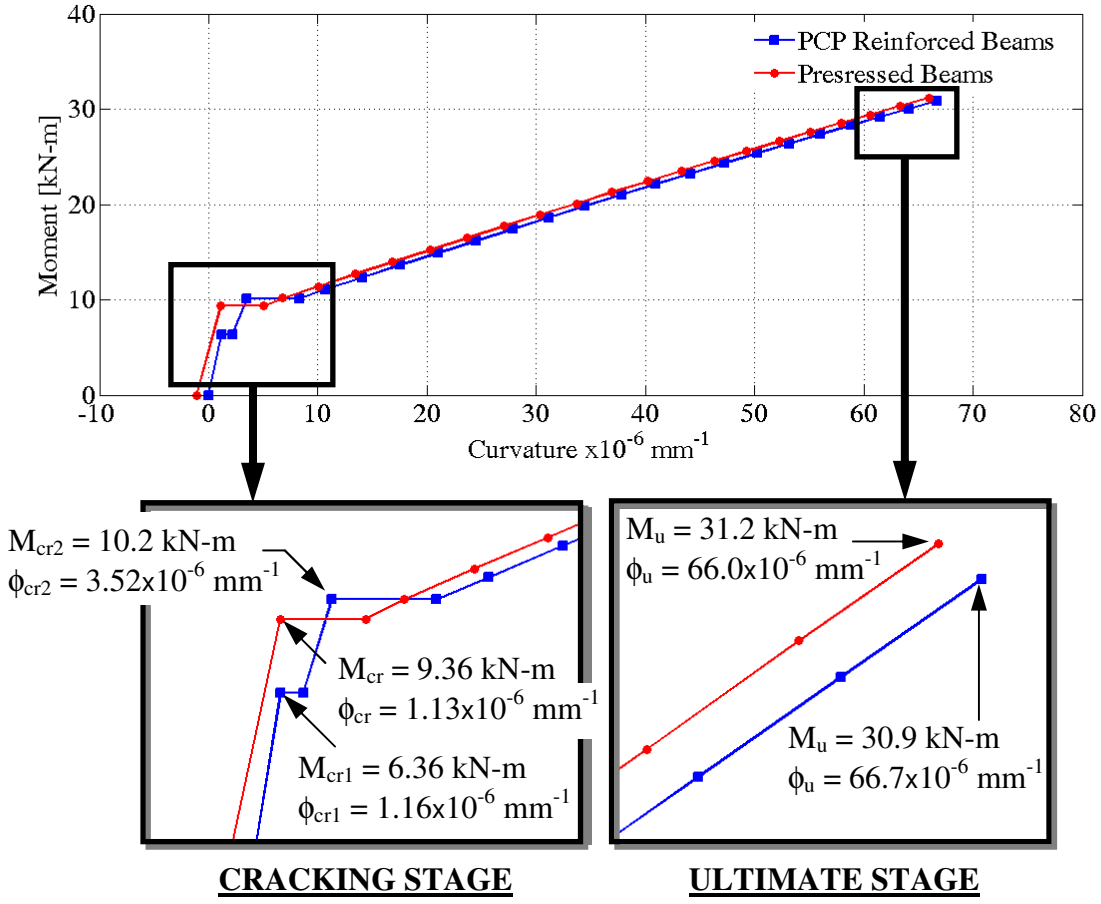

Figure 5.19 - **Theoretical Moment-Curvature Parameters** [First Beam Batch]

The theoretical moment-curvature response for beams in the second batch is shown in Figure 5.20 along with the experimental response obtained from all flexural samples. Beams in this batch were used to investigate the influence of temperature in combination with the fatigue performance of PCP reinforced beams. Results from prestressed beams were also considered for comparison purposes. It should also be noted that the results of Figure 5.20 were obtained from static tests performed after the completion of 2,000,000 cycles with loads ranging between 2kN and 15kN at midspan.

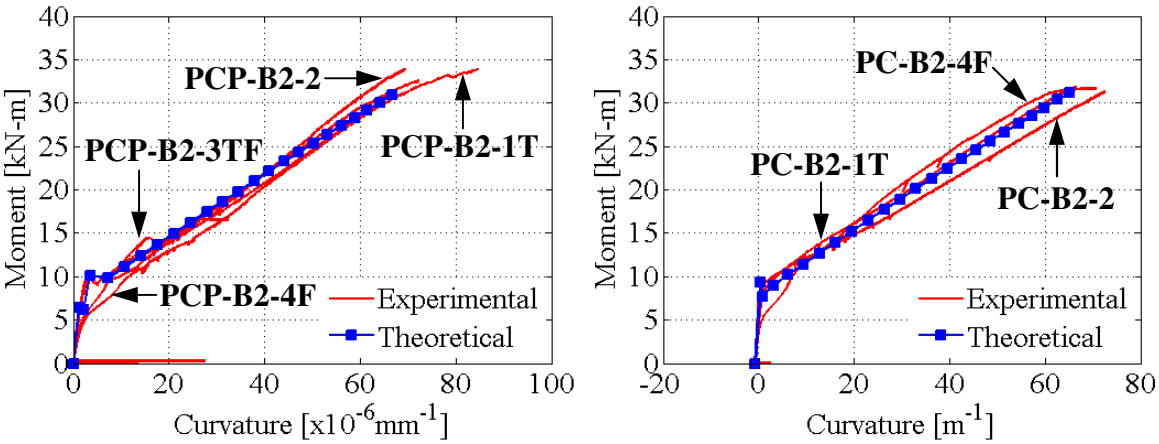

(a) PCP Reinforced Beams (b) Prestressed Beams

Figure 5.20 - **Moment-Curvature Response** [Second Beam Batch]

As with the first batch, experimental results from both types of beams in the second batch compare well with the theoretical estimates. The moment-curvature response continues to suggest that the flexural performance of PCP reinforced beams is highly comparable to that obtained for beams prestressed to the same level, with slight differences observed during the early stages of loading. As mentioned earlier, the PCP reinforced beams show two distinct cracking moments and the prestressed beams show smaller curvatures due to initial camber. Furthermore, results from beams subjected to repeated loading reveal a reduction in the flexural stiffness during the initial stages of loading. The result is associated with an increase in slippage of the reinforcement as the fatigue tests progress. If damage to the bond is maintained within tolerance, the amount of slippage that develops within the fatigue loading range is comparable to that which would occur at larger loads during a static test. The flexural response can therefore be restored once this load is reached during the final static tests. Figure 5.20 confirms this observation by illustrating a gradual convergence of the experimental and theoretical responses beyond the cracking stage. For the prestressed beams, Figure 5.20(b) reveals an additional feature. For beam PC-B2-4F, a gradual increase in curvature was observed under constant load at the ultimate stage. The increase indicates that, unlike PCP reinforcement, slippage in addition to what was incurred during the fatigue cycles was found to develop for the bare reinforcement in the closing stages of the test. Slippage continued until crushing of

concrete at the extreme compression fibre. It is also apparent from the results of Figure 5.20 that there is not sufficient evidence by which thermal gradients in the Canadian climate have influence on the fatigue performance of beams reinforced with PCP reinforcement or prestressed with CFRP reinforcement.

Finally, the theoretical moment-curvature response for the PCP reinforced beams in the third batch is shown in Figure 5.21 along with the experimental response obtained during each of the flexural tests. It should be noted that the beams in the third batch were not subjected to thermal weathering and that experimental results continue to be in good agreement with theoretical estimates, despite the introduction of notches along the length of the PCP reinforcement and fibres in the HSC mix. The result can be attributed to the fact that the moment-curvature response in the figure is localized to the midspan section and, as a consequence, cannot be used to represent the full influence of these additional parameters along the complete length of the beams. The result also indicates that the addition of fibres and the increase in prestressing level was not able to provide the anticipated improvements on cracking moment. As discussed in Chapter 4, the addition of fibres in the HSC mix was only found to provide a 6.7% increase in direct tensile strength. A slight increase in prestressing loss could, therefore, conceal the additional contribution provided by the use of fibres in the HSC mix and explain the results observed in Figure 5.21. The slightly lower flexural stiffness observed beyond the cracking stage in the figure confirms the larger prestressing losses suggested in this interpretation of the results. Chapter 4 suggested an additional 8.3% loss for PCP reinforcement containing dispersed fibers due to the lower workability of the concrete and the higher potential for water entrapment beneath the bare reinforcing bar.

Experimental estimates for moment at cracking and ultimate are listed in Table 5.10 for all beams tested. The PCP reinforced beams have two cracking moments. The first corresponds to cracking of the beam and the second corresponds to cracking of the PCP reinforcement. Moments at the critical stages agree with theoretical estimates provided in the first column of the tables. Additional losses and higher tensile strength of the concrete in the prisms has been considered for the theoretical estimates of the third beam batch.

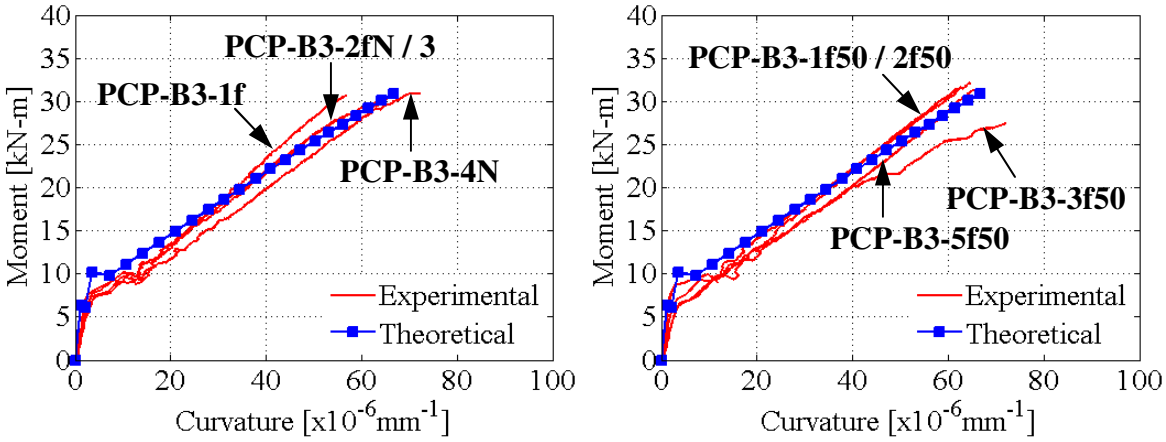

(a) PCP with Notches/Fibres (b) PCP with Fibres

Figure 5.21 - **Moment-Curvature Response** [Third Beam Batch]

Table 5.10 - **Flexural Moments at Critical Stages**

(a) First Beam Batch

Reinforcement	Beam Label	Cracking [kN-m]	Ultimate [kN-m]
Prestressed	PC-B1-1T	9.0	32.4
M_{cr}=9.9kN-m	PC-B1-2	10.6	31.1
M_u=31.2kN-m	PC-B1-3T	9.1	33.0
	PC-B1-4	10.2	31.4
PCP	PCP-B3-1T	6.6 / 10.1	31.4
M_{cr}=6.6 / 10.3kN-m	PCP-B3-2	6.8 / 10.0	31.4
M_u=31.2kN-m	PCP-B3-3T	7.9 / 10.2	30.4
	PCP-B3-4	5.3 / 10.5	31.9

(b) Second Beam Batch

Reinforcement	Beam Label	Cracking [kN-m]	Ultimate [kN-m]
Prestressed	PC-B2-1T	10.4	31.3
M_{cr}=9.8kN-m	PC-B2-2	10.3	31.9
M_u=31.1kN-m	PC-B2-4F	10.1	31.7
PCP	PCP-B2-1T	7.2 / 10.1	33.9
M_{cr}=6.5 / 10.3kN-m	PCP-B2-2	8.5 / 10.0	33.9
M_u=31.1kN-m	PCP-B2-3TF	6.2 / 10.7	32.5
	PCP-B2-4F	6.8 / 10.4	29.9

(c) Third Beam Batch

Reinforcement	Beam Label	Cracking [kN-m]	Ultimate [kN-m]
PCP M_{cr}=6.5 / 10.3kN-m (no fibers) / 9.9kN-m (fibers) M_u=31.0kN-m	PCP-B3-1Nf	7.4 / 9.7	31.5
	PCP-B3-2Nf	7.7 / 10.0	30.9
	PCP-B3-3N	7.8 / 10.2	31.0
	PCP-B3-4N	7.7 / 9.3	31.2
PCP M_{cr}=6.5 / 10.9kN-m M_u=31.0kN-m	PCP-B3-1f50	7.5 / 9.9	32.2
	PCP-B3-2f50	6.7 / 9.3	32.9
	PCP-B3-3f50	6.7 / 9.8	31.1
	PCP-B3-4f50	6.5 / 10.0	32.2

The experimental response in Figure 5.18, Figure 5.20 and Figure 5.21 was captured using PI-gauges mounted along the depth of the midspan section. The PI-gauges were tightened to a couple of screws that were glued to the surface of the elements using a Devcon 5-minute® epoxy gel. The screws maintain the required 200mm gauge length of the sensors prior to loading. Unfortunately, it is common for a crack to cause loss of readings from one of these sensors by propagating through the glued interface sealing the screw to the flexural element. For this reason, a total of 4 PI-gauges were mounted along the depth to provide sufficient data points to plot strain profiles with confidence throughout the test. Aluminum plates were also placed on the mounting screws between the sensors and the flexural component. The plates protect the sensors from the excessive widening of cracks traversing the gauge length. As illustrated in Figure 5.22, the first PI-gauge was placed at the same level as the top compression reinforcement, the second at the center of the section, the third at the same level as the tension reinforcement and the fourth at the bottom of the section. Readings from each sensor were plotted as a function of their location along the depth of the section and a line was fitted through the data using a least squares fitting method. The procedure was repeated at every load step and is illustrated in Figure 5.22 for two of the beams in the first batch. The strain profile for the PCP reinforced beam (PCPB1-4) is comparable to that for the prestressed beam (PCB1-1) at a load of 40kN. The reciprocal of the slope for each of these profiles represents the curvature, which was plotted in Figure 5.18, Figure 5.20 and Figure 5.21Figure 5.21 as a function of the applied moment. Strain profiles recorded during all tests are shown in

Appendix B of this thesis along with the readings from individual PI-gauges. Several beams show deviations in the strain profiles once cracks propagate through the anchorages for the PI-gauges.

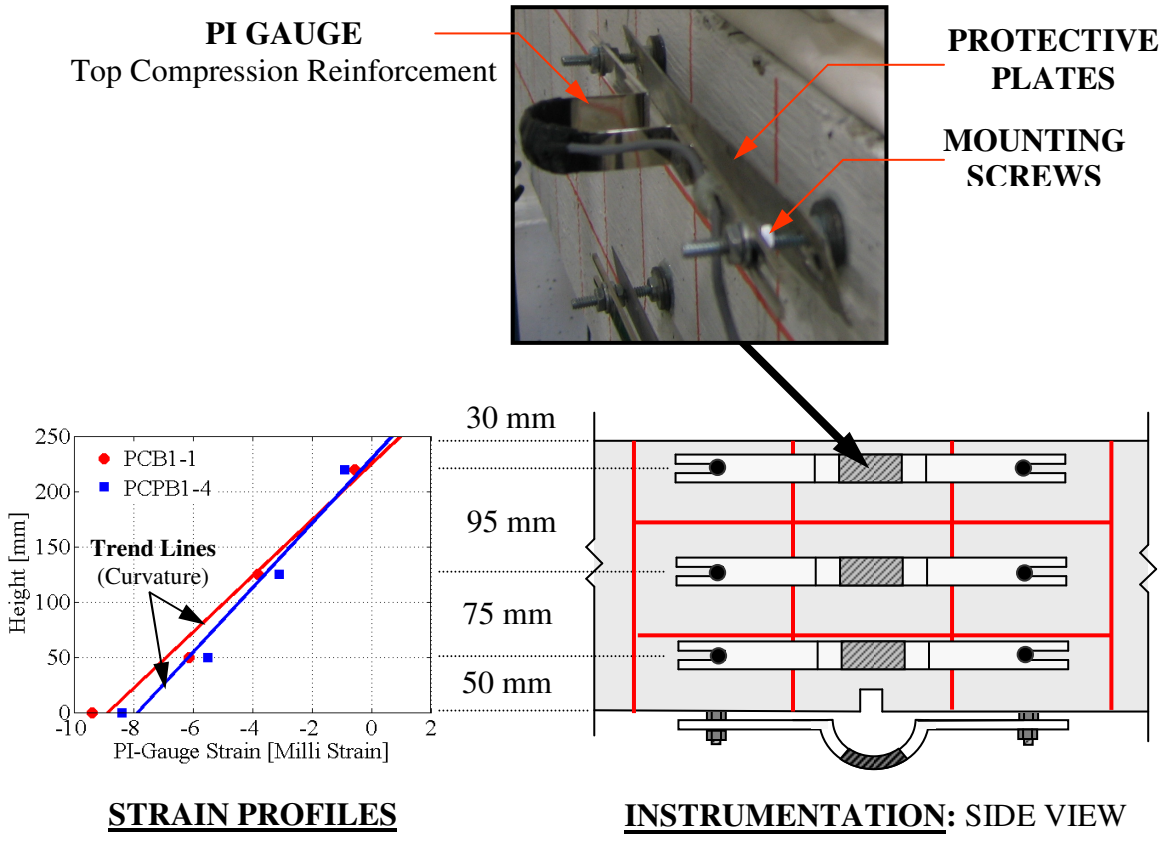

Figure 5.22 – **Strain Profile Fitting Procedure for Moment-Curvature**

5.8.2 Load-Deflection Response

The moment-curvature response in Figure 5.18 to Figure 5.21 gives valuable information on the resistance of the section to cracking and failure. Unfortunately, results from these figures are restricted to the midspan section and cannot describe the influence that the type of reinforcement has on flexural cracking along the length of each member during a test. When the cracking moment is reached, the loading scheme in this research will cause cracks to develop at midspan but portions of the beam where the applied moment is less than the cracking moment will remain uncracked. Although adjacent sections reach the cracking moment when the load increases, additional cracks will only develop at a

spacing that is governed by the bond performance of the reinforcement. Consequently, the uncracked portions of the beam will stiffen the behavior and maintain deflections below that of a fully cracked member. The concept, also referred to as tension stiffening in Chapter 2, indicates that the load-deflection response becomes a useful parameter in establishing the influence of reinforcing scheme on beam behavior beyond cracking. In light of this observation, the current section will investigate experimental load-deflection responses and establish the performance of each reinforcing scheme considered. Effective moment of inertia relationships presented in Chapter 2 for evaluating deflections will also be investigated to determine whether the behavior of beams in this research can be estimated with conventional methods.

It should be noted that the load-deflection response of a prestressed concrete beam is different than that of a reinforced concrete beam due to the presence of initial camber. Applied moments must therefore be adjusted to remove the influence of effective prestressing (EQ5.1) if deflections are to be estimated using the proposed approach as well as the relationships developed by Yost et al. (2003) and ACI 440.1R (2006). The procedure was presented by Branson and Trost (1982) for calculating the deflections of prestressed members with or without the presence of non-prestressed tension steel. The idealized load-deflection curve for applying the effective moment of inertia concept to prestressed beams is illustrated in Figure 5.23 along with the response of a reinforced concrete member.

$$M'_{app} = M_{app} - M_{P/S} \qquad \text{EQ5.1}$$

$$M_{P/S} = P_e e_{tr} \qquad \text{EQ5.2}$$

In these equations, M'_{app} is the applied moment adjusted by the removal of effective prestressing, M_{app} is the moment applied to the beam and $M_{P/S}$ is the moment required to remove the initial camber arising from effective prestressing. The latter is written as the product of effective prestressing force in the reinforcement P_e and eccentricity at which this force is applied to the member e_{tr}.

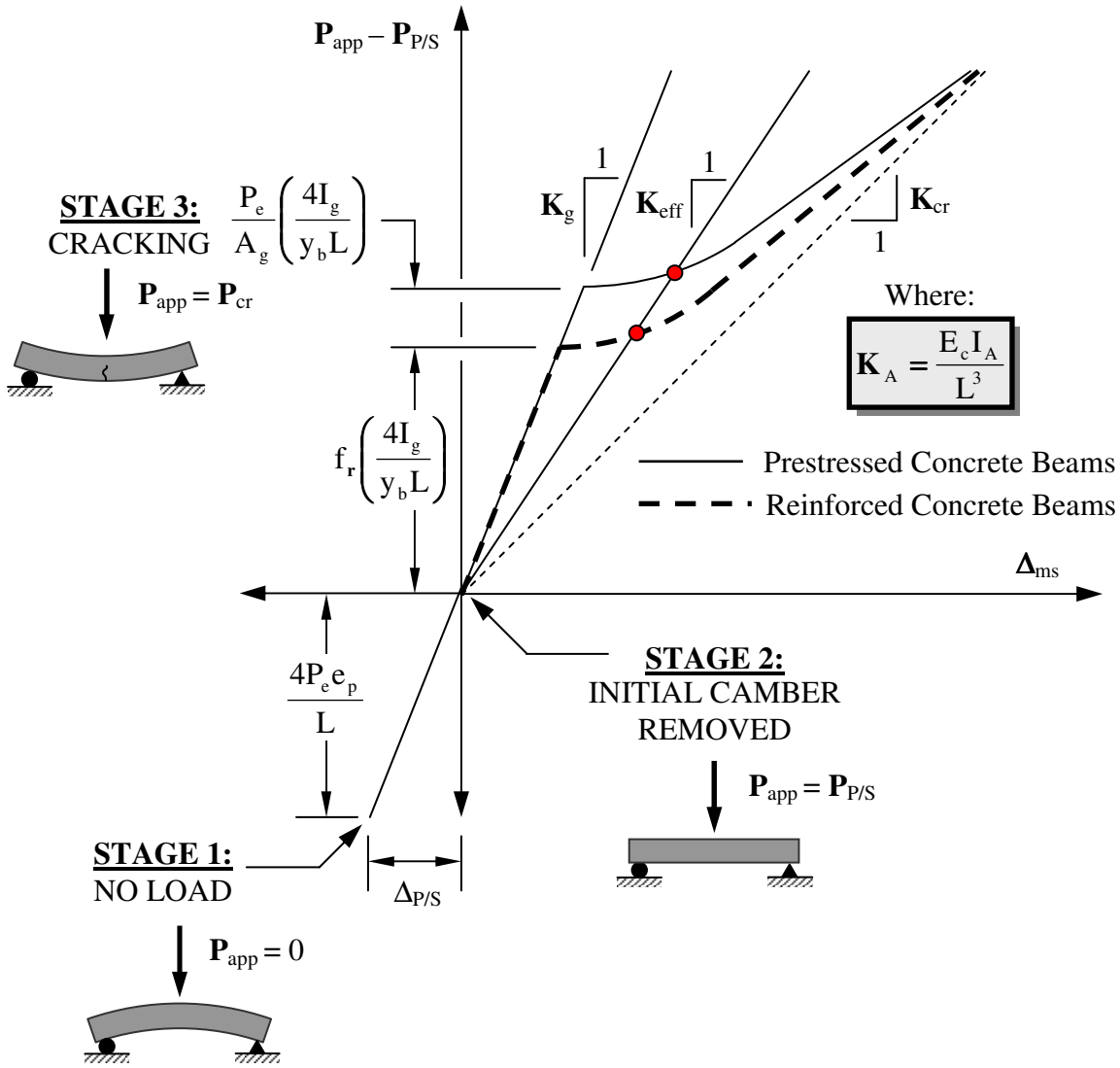

Figure 5.23 – **Prestressed Concrete Beam Effective Moment of Inertia Concept**

Since the relationships for effective moment of inertia are based on the moment applied to the member beyond cracking, the cracking moment for the beams in this research must also be adjusted to reflect the removal of prestress. The requirement is also shown in Figure 5.23 with the adjustment defined by EQ5.3.

$$M_{cr}^{'} = M_{cr,P/S} - M_{P/S} \qquad \text{EQ5.3}$$

$$M_{cr,P/S} = M_{P/S} + \frac{f_r I_g}{y_b} + \frac{P_e I_g}{A_g y_b} \qquad \text{EQ5.4}$$

In these expressions, M'_{cr} is the cracking moment adjusted to estimate deflections for prestressed beams on the basis of an effective moment of inertia approach and $M_{cr,P/S}$ is the cracking moment for the prestressed concrete beams. It should be reminded that the methods proposed by Yost et al. (2003) and ACI 440.1R (2006) use gross section properties for estimating deflections. As a result, I_g, A_g and y_b in EQ5.4 are gross section properties that do not account for the presence of the reinforcement. They respectively define the moment of inertia, cross sectional area and distance from the neutral axis to the extreme tension fibre. On the other hand, the relationship proposed in Chapter 2 to estimate the deflection of concrete members reinforced with FRP requires the use of transformed section properties to establish the effective moment of inertia. The approach, however, does not require the cracked moment of inertia to be calculated since it already consists of adjusting the parameter to include the effects of tension stiffening. Deflection estimates from these three methods are shown in Figure 5.24 and plotted along with the experimental data for the first batch of prestressed beams tested in this research.

The results indicate that the proposed approach is more efficient than the ACI 440.1R (2006) method in estimating the deflection of prestressed concrete beams in this research. It is also more conservative than the method proposed by Yost et al. (2003), which conveniently reduces the probability of under-estimating deflections. According to Figure 5.24, the outcome extends from the cracking stage to approximately 80% of ultimate. For loads beyond 85% of ultimate, the methods proposed by Yost et al. (2003) and ACI 440.1R (2006) start under-estimating deflections. The inclusion of concrete non-linearity in compression allows the effective moment of inertia relationship proposed in this thesis to estimate deflections with higher precision for loads approaching the ultimate stage. The deflection remains slightly under-estimated but, as discussed in Chapter 2, the result is a considerable improvement over existing methods. The trend in effective moment of inertia beyond cracking can be found in Appendix B of this thesis for all of the batches.

They are included to provide further insight on the performance of each method to estimate the parameter obtained from experimental data.

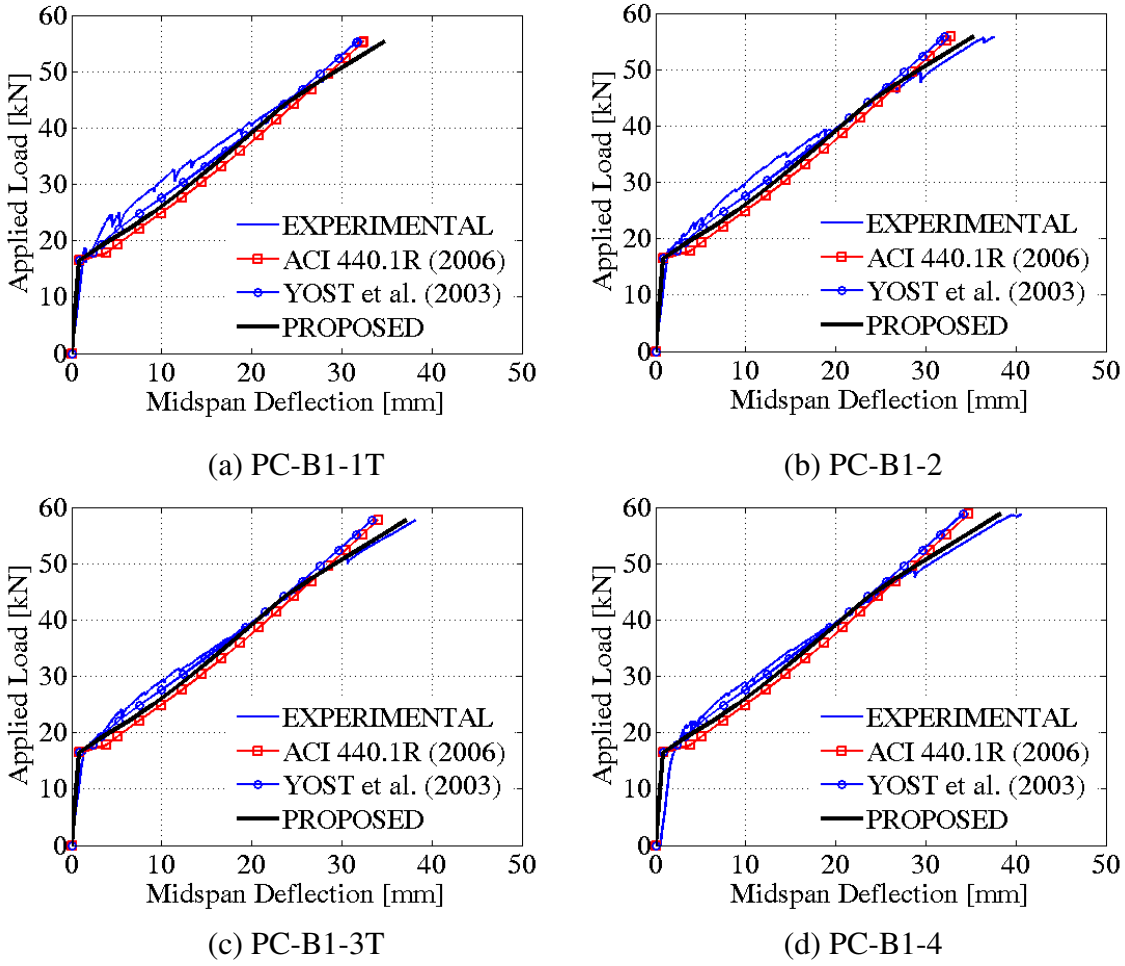

Figure 5.24 – **Load-Deflection Response** [First Batch Prestressed Beams]

The load-deflection behavior of PCP reinforced beams can also be estimated using the method outlined for prestressed concrete beams. Although not prestressed, the presence of an effective prestressing force in the bare bar allows the analogy of Figure 5.23 to be applied. Deflection estimates are shown in Figure 5.25 and demonstrate similar accuracy than that achieved for the prestressed concrete beams in this research. It should be noted that once the PCP reinforced beams have reached their first cracking moment, the moment of inertia drops considerably by approximately 54% at the cracked section. The load-deflection responses of Figure 5.25 show, in accordance to this fact, that the presence of a single crack at the point of maximum moment produces a noticeable

influence on the overall stiffness and moment of inertia of the flexural element. The estimated load-deformation response in the figure accounts for this observation by conservatively using a flexural stiffness that includes the moment of inertia of a section that is cracked but in which the PCP reinforcement is intact.

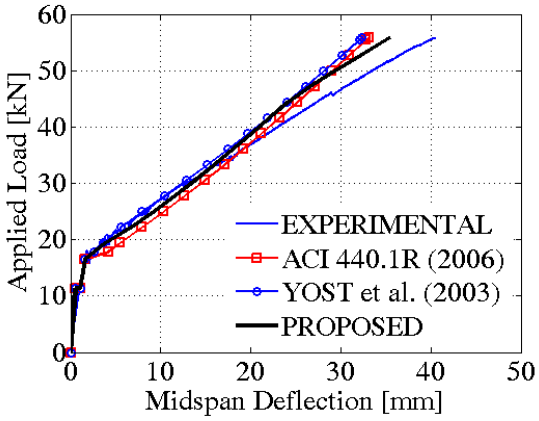

(a) PCP-B1-1T

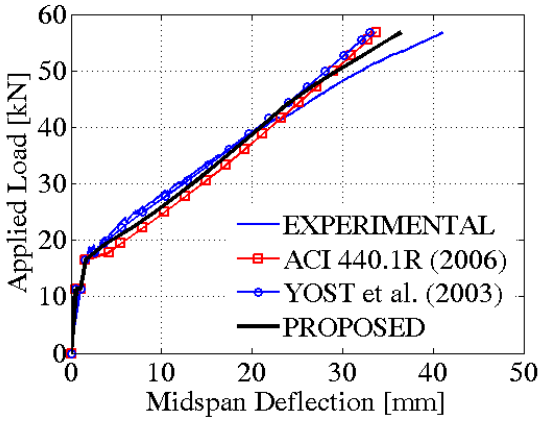

(b) PCP-B1-2

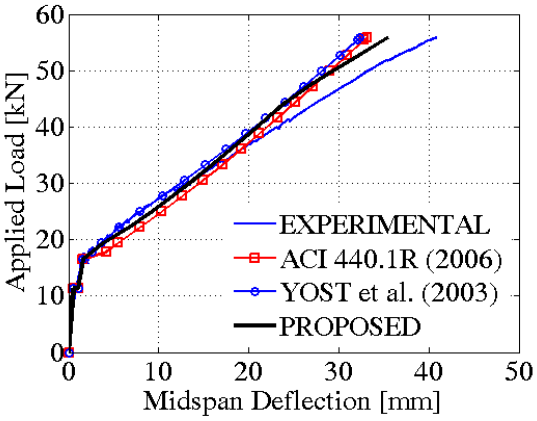

(a) PCP-B1-3T

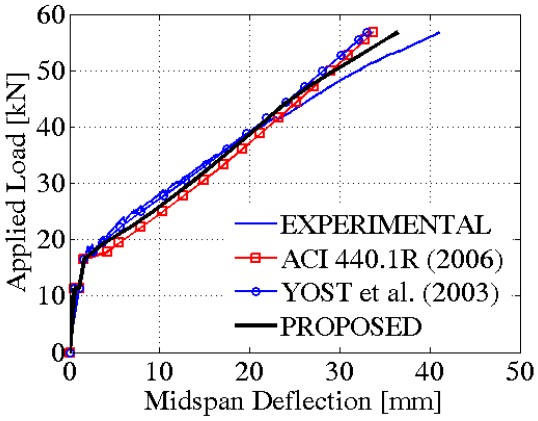

(b) PCP-B1-4

Figure 5.25 – **Load-Deflection Response** [First Batch PCP Reinforced Beams]

As before, results from Figure 5.25 indicate that the proposed approach is more efficient than the ACI 440.1R (2006) method in estimating the deflection of PCP reinforced beams in this research. The level of conservatism observed for the prestressed concrete beams is also preserved here when comparing estimates from the proposed approach to that obtained from the other two methods. However, the figure indicates that the method proposed by Yost et al. (2003) under-estimates deflection for loads beyond 60% of ultimate compared to 70% for the method developed by ACI 440.1R (2006). Although

the proposed approach lacks conservatism for loads beyond 65% of ultimate, the deflection estimates continue to be more accurate than the other methods due to the inclusion of material non-linearity in compression.

In order to summarize the ability of each method to estimate deflections beyond cracking, deflection ratios were computed for each beam at various load levels beyond cracking and averaged for each type of reinforcement. Results are shown in Figure 5.26. Deflection ratios beyond unity represent an over-estimation of deflection and ratios below unity represent an under-estimation of deflection.

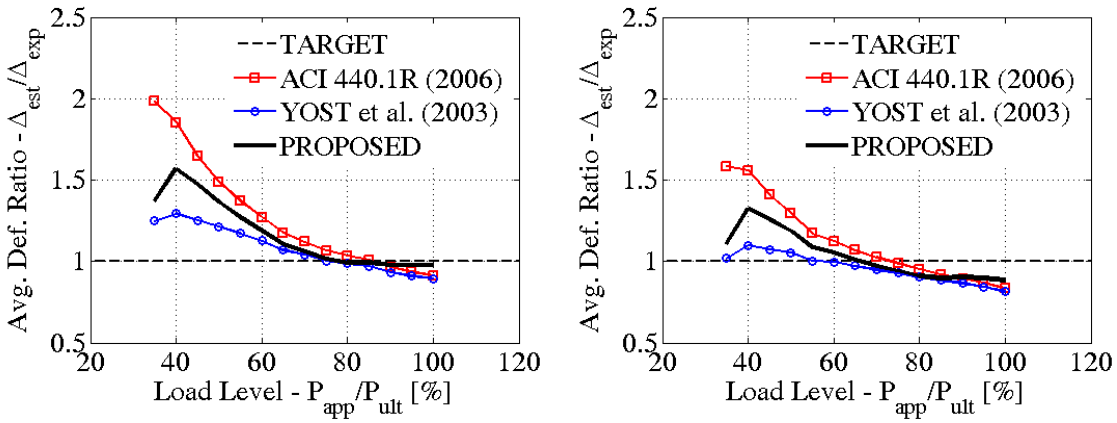

(a) Prestressed Beams (b) PCP Reinforced Beams

Figure 5.26 – **Average Deflection Ratios** [First Batch]

The load-deflection responses from the second batch of beams were also considered to investigate the influence of temperature and repeated loading on the ability of each method considered to estimate deflection. Deflection estimates from the three methods in Chapter 2 are shown in Figure 5.27 and plotted with the experimental data obtained from the prestressed beams. It should be noted that the response of samples evaluated for fatigue performance was obtained by performing a final static test after completion of repeated loading. The initial deflection observed at the beginning of each test corresponds to the residual value that accumulated during fatigue testing.

Despite residual deflections observed in Figure 5.27 for samples subjected to fatigue, the performance of all prestressed beams in the second batch is comparable beyond cracking.

The result confirms previous observations made using moment-curvature recorded at midspan and allows the deflection to be estimated using similar methods as those used for the first batch. Based on the estimates, it appears that the proposed approach remains more efficient than the ACI 440.1R (2006) method in evaluating deflection of prestressed concrete beams in this batch. It also continues to offer a higher level of conservatism than the method proposed by Yost et al. (2003) at all loads beyond cracking. As before, the proposed relationship for effective moment of inertia provides higher accuracy in estimating deflection for loads exceeding 90% of ultimate as opposed to 80% for beams in the first batch.

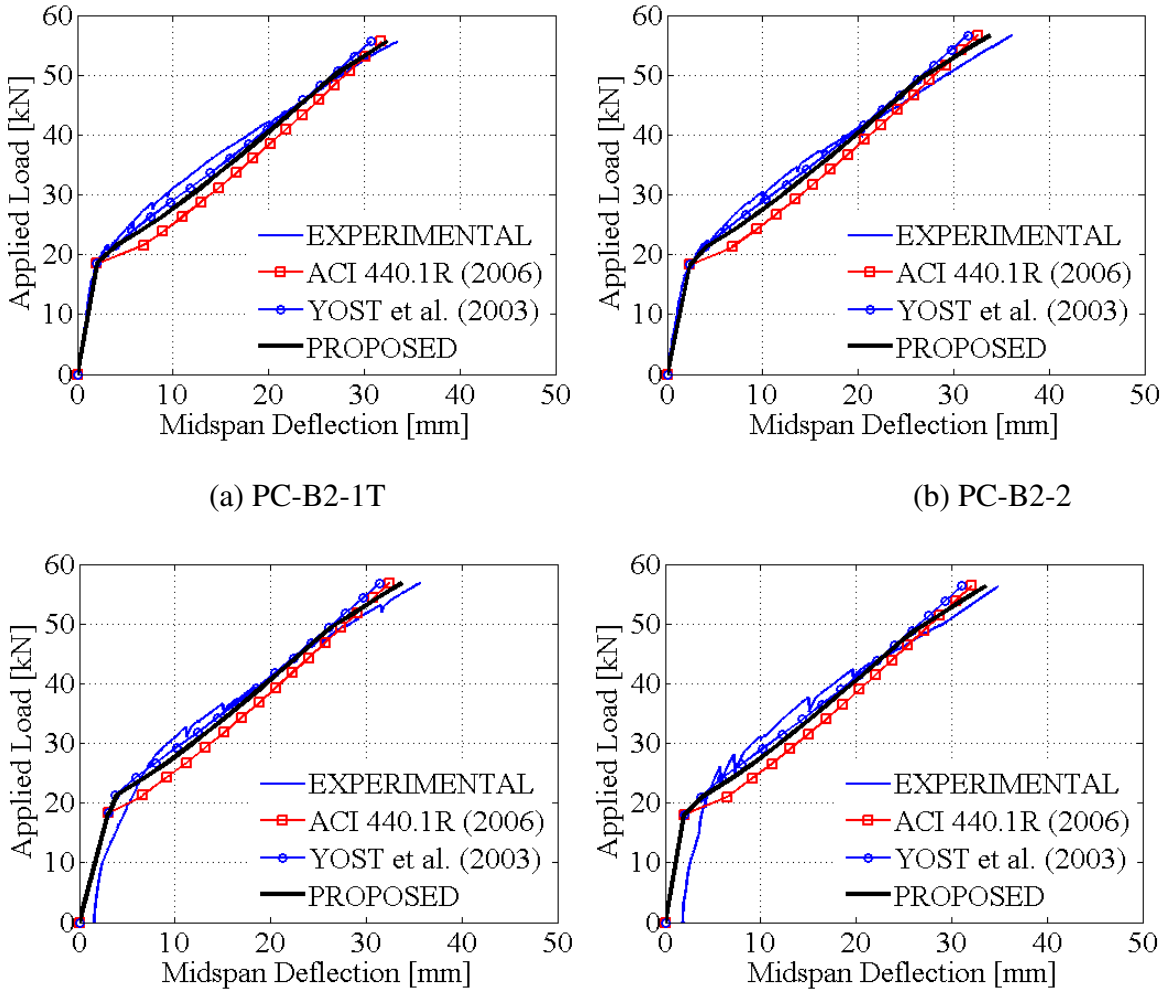

(a) PC-B2-1T

(b) PC-B2-2

(c) PC-B2-3TF

(d) PC-B2-4F

Figure 5.27 – **Load-Deflection Response** [Second Batch Prestressed Beams]

The load-deflection behavior for the PCP reinforced beams in the second batch is shown in Figure 5.28 along with the estimated response from each of the methods considered. A procedure similar to that used in the first batch of PCP reinforced beams was used to estimate deflections with the effective moment of inertia expressions considered. Results are in good agreement with those obtained from the first batch. The method from Yost et al. (2003) under-estimates deflection for loads beyond 70% of ultimate compared to 80% for the ACI 440.1R (2006) method. Beyond 75% of ultimate, Figure 5.28 suggests that the estimates of deflection from the proposed approach provide more accuracy than those obtained from other methods. The deflection ratios provided in Figure 5.29 confirm these observations as well as those made for the prestressed beams.

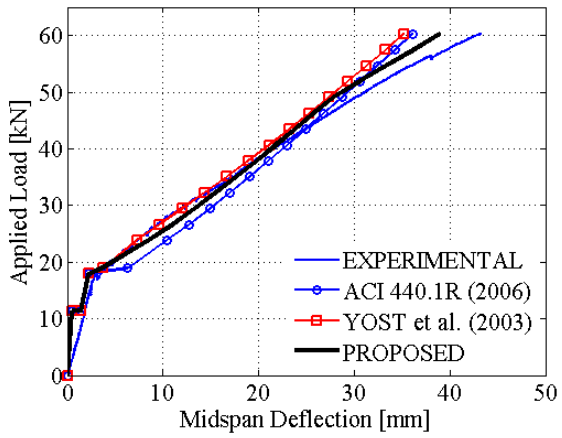

(a) PCP-B2-1T

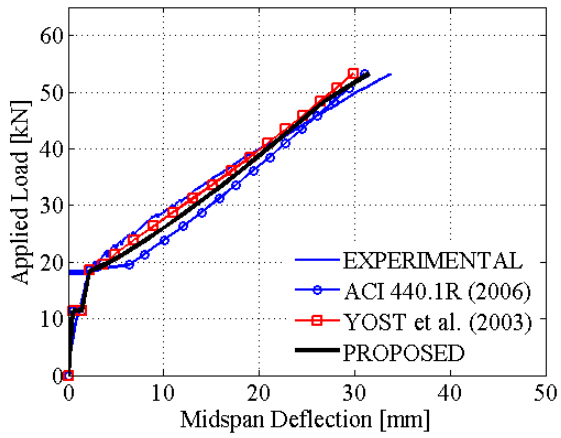

(b) PCP-B2-2

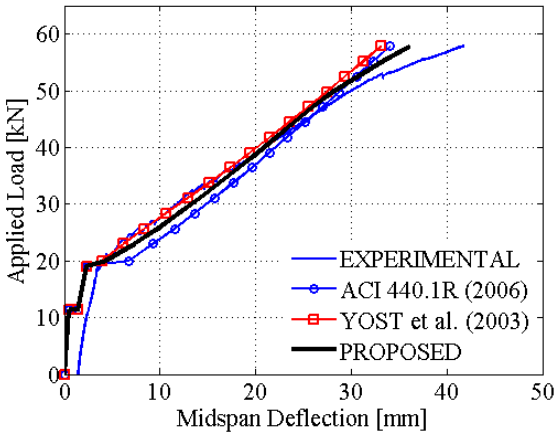

(c) PCP-B2-3TF

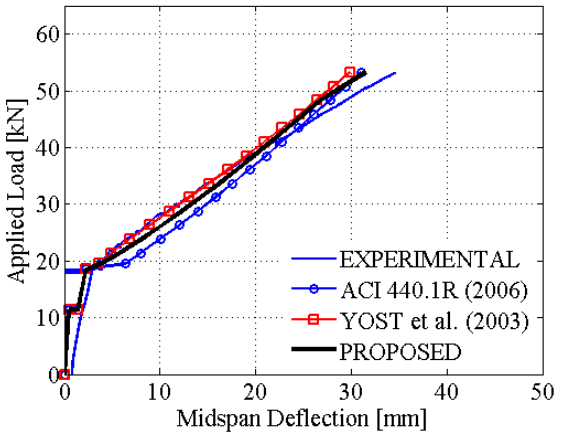

(d) PCP-B2-4F

Figure 5.28 – **Load-Deflection Response** [Second Batch PCP Reinforced Beams]

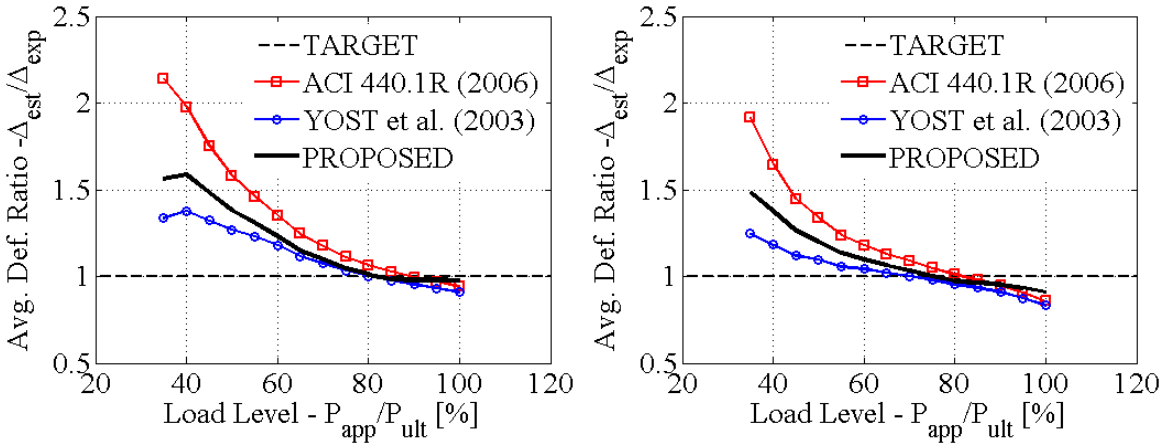

(a) Prestressed Beams (b) PCP Reinforced Beams

Figure 5.29 – **Average Deflection Ratios** [Second Batch]

The load-deflection responses from the third batch were also considered to investigate the introduction of deformations on the surface of PCP reinforcement as well as the introduction of fibres to enhance the strength of the elements in direct tension. The latter was considered to improve the bond performance of the reinforcement and the former was considered to achieve higher cracking moments. Combined, these parameters can improve the post-cracking behavior as well as the range of service loads for which the flexural stiffness is enhanced by the use of PCP reinforcement. In order to ensure this improvement can be adequately assessed in design, deflection estimates from the three methods considered in Chapter 2 are presented in Figure 5.30 along with experimental data. As observed for the first two batches, the estimation methods continue to under-estimate deflection for loads that approach ultimate. However, the lower post-cracking stiffness observed for beams without fibres (PCP-B3-3, PCP-B3-4N) cause the method developed by Yost et al. (2003) to start under-estimating deflection at loads beyond 50% of ultimate compared to 65% for the ACI 440.1R (2006) method and 60% for the proposed approach. The results suggest that beams with PCP reinforcement containing dispersed fibres exhibit smaller deflections than beams containing PCP reinforcement without dispersed fibres. The use of fibres in the PCP reinforcement therefore seems to have more benefit on the post-cracking behavior than on the range of service loads prior to cracking.

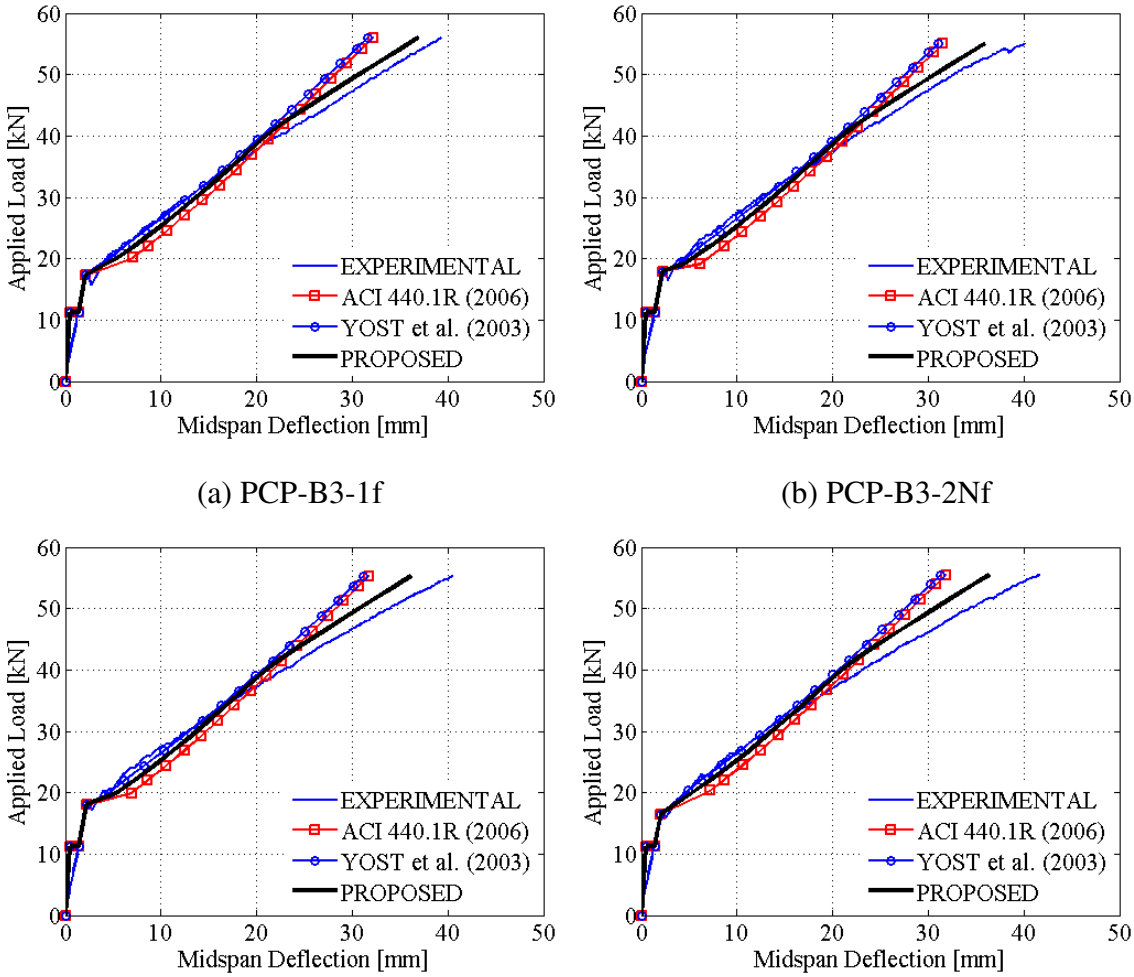

(a) PCP-B3-1f (b) PCP-B3-2Nf

(c) PCP-B3-3 (d) PCP-B3-4N

Figure 5.30 – **Load-Deflection Response** [Third Batch PCP with Notches / Fibres]

Dispersed fibres can also improve the resistance of concrete against splitting stresses in the concrete cover upon release of prestress. Consequently, the inclusion of fibres can also be used to achieve higher prestressing loads in the PCP reinforcement and enhance their strength in direct tension. Load-deflection responses of beams from the third batch that contain PCP reinforcement with a jacking load increased from 45 to 50kN are shown in Figure 5.31. Results suggest that the improvement on post-cracking behavior is more noticeable than that observed for beams containing PCP reinforcement with surface deformations alone.

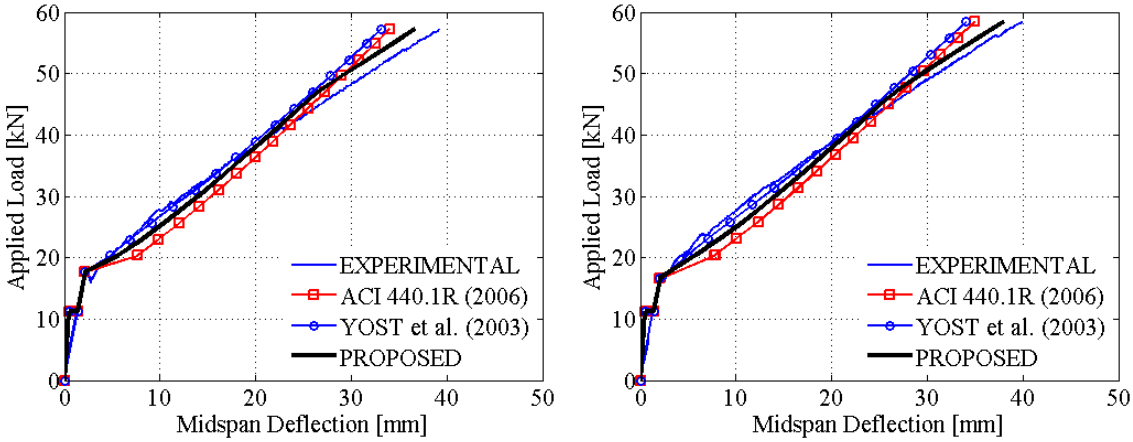

(a) PCP-B3-1f50 (b) PCP-B3-2f50

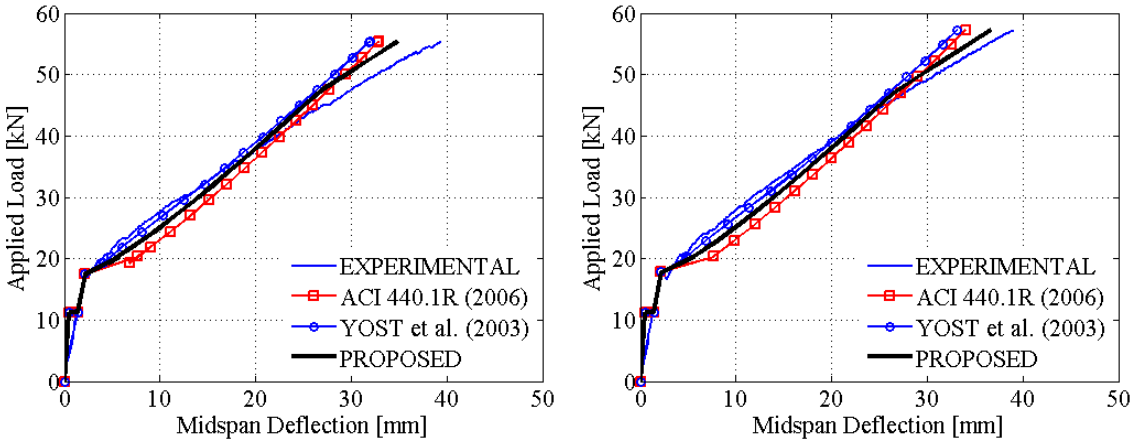

(c) PCP-B3-3f50 (d) PCP-B3-4f50

Figure 5.31 – **Load-Deflection Response** [Third Batch PCP with Fibres]

The accuracy obtained from deflection estimates in this figure also seems to be in closer agreement to those obtained for the first batch. The ACI 440.1R (2006) method starts under-estimating deflection for loads beyond 75% of ultimate compared to 70% for the proposed approach. Also, the method developed by Yost et al. (2003) stops providing conservative estimates at loads similar to those observed for the first batch. Deflection ratios in Figure 5.32 confirm this observation as well as those made for beams shown in Figure 5.30.

It is important to note from the load-deflection analysis performed in this section that the estimation methods for deflection do not contain provisions to include the influence of

fatigue loading or dispersed fibres in the PCP reinforcement. The accuracy achieved with the estimation methods considered mainly arose from the fact that fatigue loading did not appreciably influence the post-cracking behavior and that the inclusion of fibres, as well as the increase in prestressing, did not provide the anticipated enhancements on cracking moment. Improvements on the post-cracking stiffness were achieved but to an extent that is limited until further research is considered. Nevertheless, it should be reminded that the non-empirical nature of the proposed expression and its consideration for tension stiffening should promote its potential for estimating deflections if additional research is capable of providing further improvements and changes in the post-cracking behavior of beams containing PCP reinforcement.

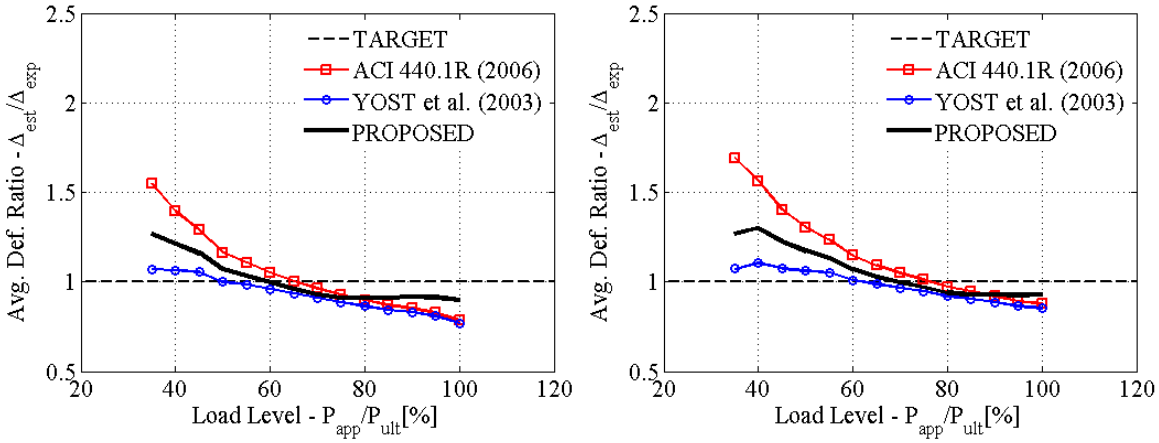

(a) PCP with Notches/Fibres (b) PCP with Fibres

Figure 5.32 – **Average Deflection Ratios** [Third Batch]

In order to provide more insight on the accuracy of each method, the average error that can be expected when evaluating deflections over the range of load levels considered is provided in Table 5.11 for each of the batches. The average error, evaluated using a root mean squared error (RMSE), was found to be smaller for the prestressed beams than for the PCP reinforced beams. The largest error was registered as ±1.17mm from the ACI 440.1R (2006) method (PC-B2-3TF) and the smallest error was evaluated as ±0.37mm from the method developed by Yost et al. (2003). The proposed approach had similar performance, with a minimum error recorded as ±0.38mm (PC-B1-1). It should be noted that, for the exception of five beams in Table 5.11, the proposed approach was capable of

achieving the smallest error for evaluating deflection over the range of loads considered. The shaded cells in the table represent the method that provides the smallest error in estimating deflections for each beam.

Table 5.11 – **Precision of Deflection Estimates**
[RMSE for all Beam Batches in mm]

Beam Name	ACI 440.1R (2006)	YOST et al. (2003)	PROPOSED
PCP-B1-1T	0.65	0.41	0.38
PCP-B1-2	0.85	0.49	0.60
PCP-B1-3T	0.67	0.47	0.40
PCP-B1-4	0.81	0.55	0.53
PC-B1-1T	0.84	0.94	0.70
PC-B1-2	0.85	0.96	0.72
PC-B1-3T	0.81	0.65	0.56
PC-B1-4	0.79	0.74	0.55
PCP-B2-1T	0.83	0.37	0.46
PCP-B2-2	0.76	0.52	0.47
PCP-B2-3TF	1.17	0.69	0.82
PCP-B2-4F	0.99	0.51	0.62
PC-B2-1T	0.80	0.83	0.51
PC-B2-2	0.89	0.69	0.52
PC-B2-3TF	0.74	0.42	0.46
PC-B2-4F	0.92	0.64	0.58
PCP-B3-1fN	0.77	0.89	0.69
PCP-B3-2N	0.82	0.92	0.74
PCP-B3-3fN	0.92	1.04	0.85
PCP-B3-4N	0.98	1.16	0.95
PCP-B1-1f50	0.69	0.75	0.53
PCP-B1-2f50	0.71	0.69	0.47
PCP-B1-3f50	0.80	0.85	0.68
PCP-B1-4f50	0.72	0.64	0.47

5.8.3 Performance of PCP Reinforcement under Repeated Loading

The second batch of beams was used to investigate the fatigue performance of PCP reinforcement. As a result, two of the four samples containing the reinforcement were subjected to repeated loading with intermediate static tests performed at 250,000 cycle intervals to evaluate changes in bond performance, crack width and flexural stiffness.

All samples tested for fatigue were subjected to a maximum load of 15kN during each cycle. At this load, the beam exceeds the first cracking stage but the HSC is sufficiently strong to remain intact and preserve the flexural stiffness. Such conditions are characteristic of the service state for PCP reinforced beams. The minimum load applied to the samples during each cycle was 2kN. The magnitude was chosen to minimize any movement at the bearing points as well as to prevent any delay in sensor response that generally occurs at the beginning of flexural tests. Loading was repeated for a total of 2,000,000 cycles, at which point a final static test was performed to establish the residual flexural performance of the samples. The total number of cycles was based on previous research in the area of PCP reinforced concrete (Zia et al. 1976). The intent was to achieve trends that are suitable for the evaluation of flexural performance under service conditions. It is, however, recommended that loads beyond the second cracking stage be investigated in future research to establish the extent of loading required to reach failure by fatigue.

5.8.3.1 Bond Performance Trend under Fatigue

The bond performance of flexural reinforcement plays a significant role in the behavior of reinforced concrete elements once the cracking stage has been reached. In reference to the discussion of Chapter 2, the concrete adjacent to a crack becomes an anchorage zone where tensile forces in the reinforcement are gradually transferred to the surrounding concrete. For the range of loads considered during fatigue testing, forces in the tension zone will be transferred through shear stresses that develop between the NSC of the beam and the HSC of the PCP reinforcement.

The bond performance was monitored through the use of 50mm long electrical resistance strain gauges instrumented on the surface of the beam at the reinforcement depth. The strain gauges were placed 50mm away from the first anticipated crack at midspan. Readings from these sensors give an indication of the stress that has been transferred from the reinforcement to the surrounding concrete.

Figure 5.33 illustrates this transfer of strain as well as the development length required to reach conditions for which strains can be computed using linear elastic assumptions for uncracked sections. If the bond performance of the reinforcement deteriorates over the course of testing, the transfer of strain will gradually stretch to that shown in the figure, and provide lower readings at the strain gauge location.

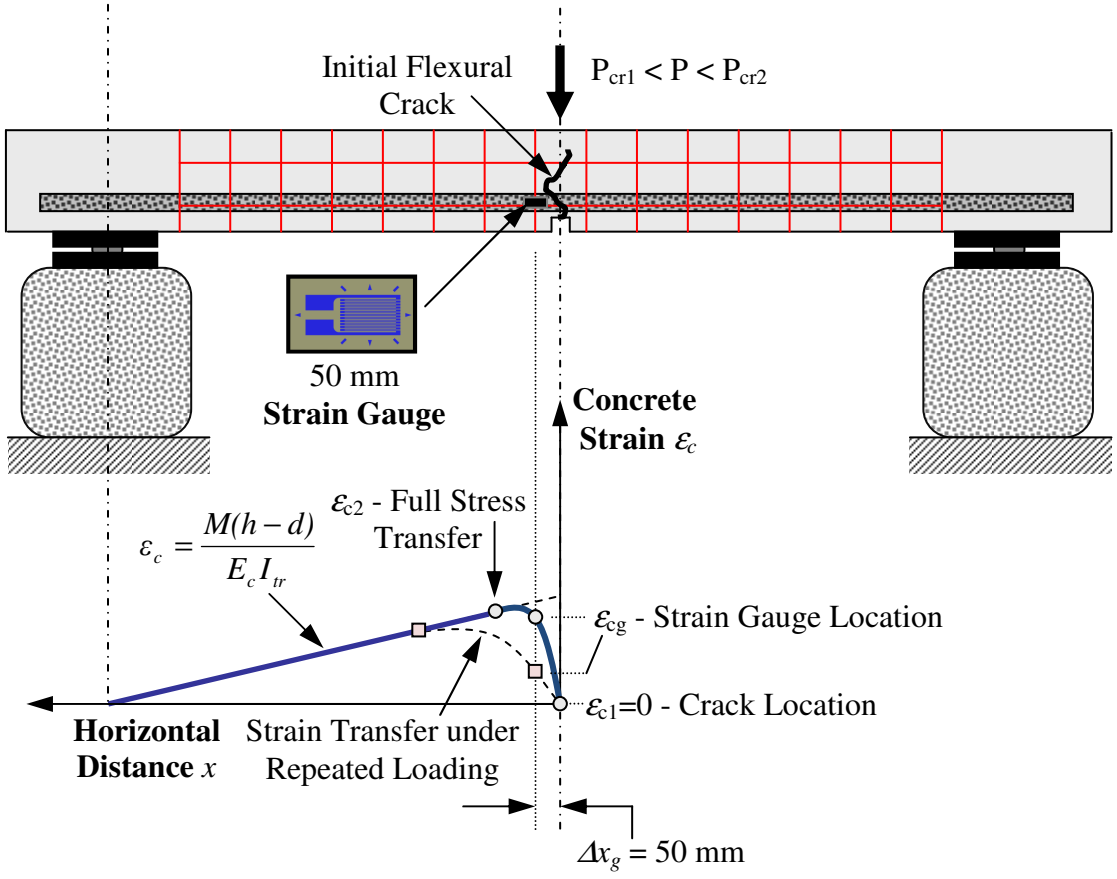

Figure 5.33 – **Concrete Strain Distribution beyond Cracking**

The progression in strain readings is shown in Figure 5.34(a) for the PCP reinforced beams. Results are plotted with respect to the number of cycles reached at each of the intermediate static tests. Results from the prestressed beams are shown in Figure 5.34(b) for comparison purposes. The level of deterioration ranges from 17% (PCP-B2-3TF) to 38% (PCP-B2-4F) for the PCP reinforced beams and from 14% (PC-B2-3TF) to 25% (PC-B2-4F) for the prestressed beams. These ranges suggest a higher level of uncertainty in bond performance for the PCP reinforcement than for the bare reinforcement used in the prestressed beams. The result is associated to the difficulty of achieving a surface finish that is as consistent for PCP reinforcement as it is for commercially available reinforcing bars. Material factors developed for the inclusion of PCP reinforcement in design should be adjusted to reflect these observations.

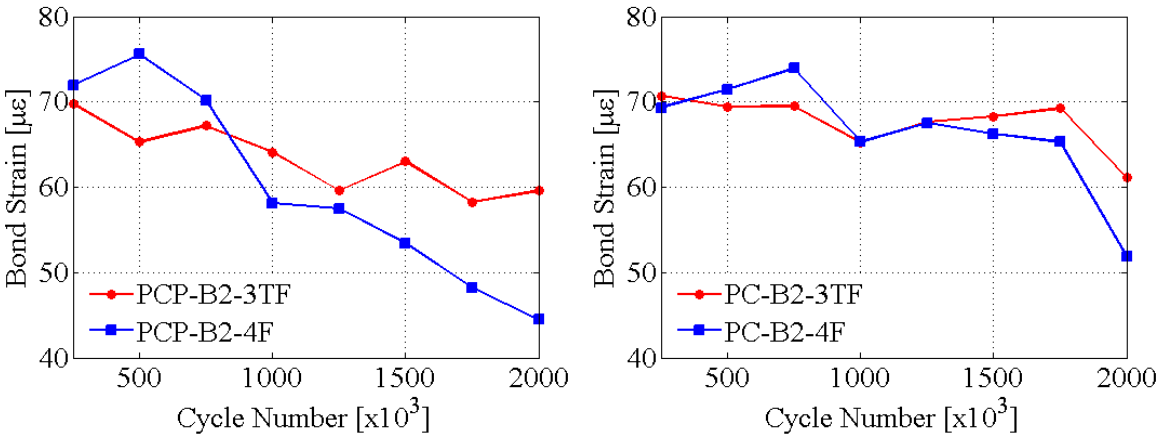

(a) PCP Reinforced Beams (b) Prestressed Beams

Figure 5.34 – **Concrete Strain Trend with Repeated Loading**

Results from Figure 5.34(a) also suggest that the PCP reinforced beam subjected to thermal weathering displays lower deterioration than the beam kept under ambient conditions. The same result was observed for the prestressed beams in Figure 5.34(b) but to a lesser extent. Additional testing should be performed to confirm this observation and reach a higher level of confidence in the results for thermal weathering.

Strain readings from the sensor placed on the surface of the PCP reinforced beams are shown in Figure 5.35 as a function of the applied load for each of the intermediate static

tests. The figure shows a progressive attenuation of strains as well as a bilinear behavior with applied load. Research presented by Lutz et al. (1968) on the mechanics of bond and slip of bars in concrete can explain this behavior. In the presence of surface deformations or roughness, the researchers revealed that during the initial stages of loading the bond strength in the vicinity of a crack is sufficient to allow the gradual development of a bar-to-concrete separation. When the separation is fully developed, it relieves a sufficient portion of the normal stress at the interface to reduce the ability of the reinforcement to transfer forces to the surrounding concrete. This transition stage causes strains recorded at the surface of the beam to increase at a lesser rate with applied load. Results in Figure 5.35 confirm that the effect is more pronounced for beams kept at ambient temperatures.

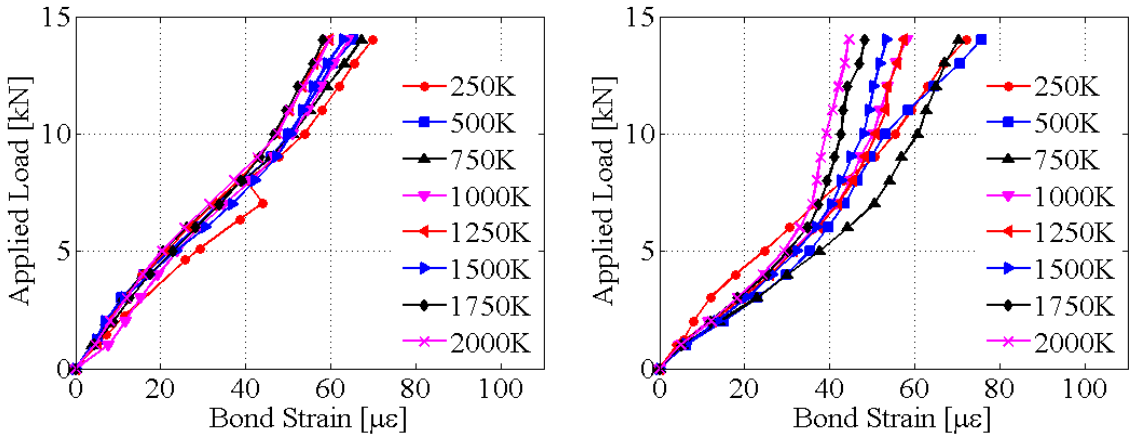

(a) PCP-B2-3TF (b) PCP-B2-4F

Figure 5.35 – **Surface Strains Trend with Applied Load** [Intermediate Static Tests]

5.8.3.2 Crack Width Trend under Fatigue

As mentioned in earlier sections, the progression of crack width plays a significant role in the design of FRP reinforced concrete. The parameter has strong significance in the assessment of serviceability, especially when the crack pattern has stabilized and concrete between individual cracks approaches its lowest contribution to deflection. Since design codes prevent loads from exceeding this stage by setting limitations on the parameter, the progression of crack width was investigated for loads that represent service conditions for the beams in this research.

The progression in crack width shown in Figure 5.36(a) for the PCP reinforced beams was recorded at the reinforcing level using a PI-gauge. Results are plotted with respect to the number of cycles at each of the intermediate static tests. As before, results from the prestressed beams are shown in Figure 5.36(b) for the purpose of comparison. The figures confirm the results obtained for bond performance, where progressively larger slip between the reinforcement and concrete produce an increase in crack width. Results also continue to suggest larger deteriorations in the parameter for the PCP reinforcement. The extent of deterioration ranges between 48% (PCP-B2-3TF) and 84% (PCP-B2-4F) for the PCP reinforced beams and up to 33% for each of the prestressed beams. As a consequence of the relationship with bond performance, results indicate higher variability in crack width for PCP reinforced beams subjected to repeated loading.

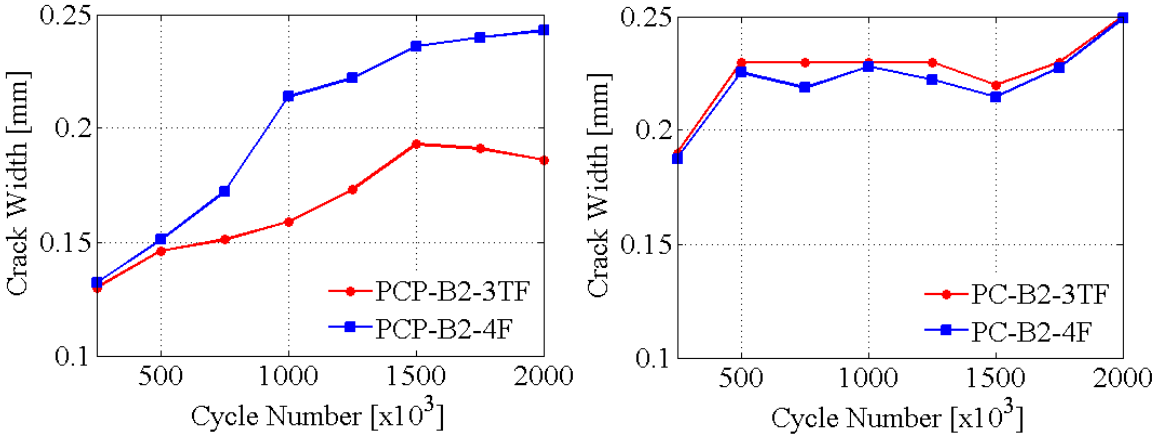

(a) PCP Reinforced Beams (b) Prestressed Beams

Figure 5.36 – **Crack Width Trend with Repeated Loading**

Figure 5.36 also suggests that the deterioration in crack width for the PCP reinforced beam subjected to thermal weathering (PCP-B2-3TF) was lower than for the one kept under ambient conditions (PCP-B2-4F). The result is consistent with that obtained from the analysis of bond performance but further research is required to confirm the trend. With this in mind, the prestressed beams show similar behavior despite the consideration of thermal weathering.

Crack width readings are shown in Figure 5.37 for the PCP reinforced beams. Results are plotted as a function of the applied load at each of the intermediate static tests. The figure

shows a progressive increase in crack width and, as in the case of bond performance, a bilinear behavior with applied load. The behavior can also be attributed to the progressive formation of a bar-to-concrete separation.

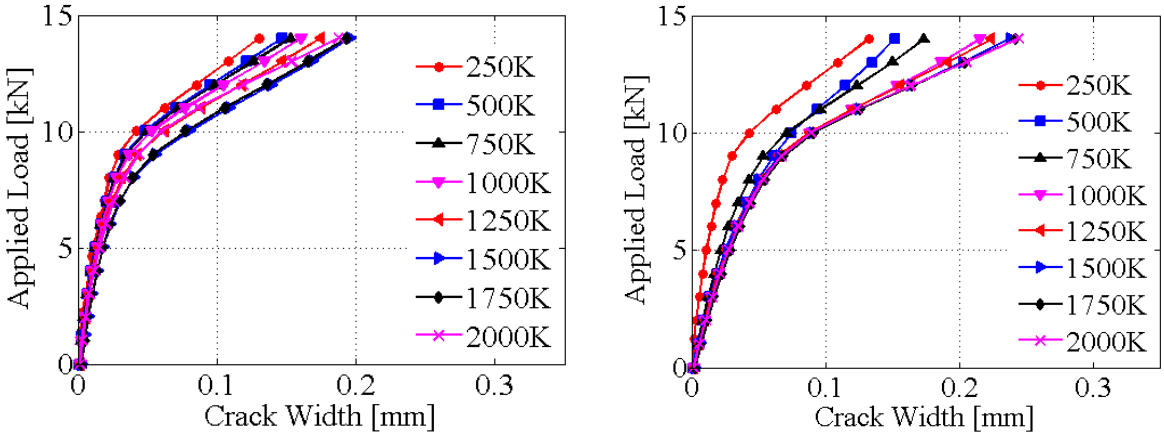

(a) PCP-B2-3TF (b) PCP-B2-4F

Figure 5.37 – **Crack Width Trend with Applied Load** [Intermediate Static Tests]

5.8.3.3 Midspan Deflection and Flexural Stiffness Trend under Fatigue

The progression of bond performance and crack width presented earlier was obtained from sensors providing measurements that are localized with respect to the section at midspan. However, the flexural stiffness of the member is influenced by the contribution of properties over the complete length of the member, which can provide a more global indication of the flexural performance over the service life of the member.

The procedure used for establishing the flexural stiffness of beams during fatigue testing is illustrated in Figure 5.38 using conceptual load-deflection responses at the intermediate static tests. The figure suggests a slight bilinearity, which is based on observations made during the evaluation of bond performance and crack width. A linear model based on a least squares regression method was fitted through the data to estimate an effective flexural stiffness at each of the intermediate tests.

The progression in flexural stiffness is shown in Figure 5.39(a) for the PCP reinforced beams with respect to the number of cycles reached at each of the intermediate static

tests. Results from the prestressed beams are shown in Figure 5.39(b) for comparison purposes. As expected, the deterioration in bond performance and crack width at the cracked location produces a gradual reduction in flexural stiffness with repeated loading. The deterioration in the parameter continues to be more pronounced for the PCP reinforcement. The amount of deterioration ranges from 29% (PCP-B2-3TF) to 32% (PCP-B2-4F) for the PCP reinforced beams and up to 16% (PC-B2-3TF) and 15% (PC-B2-4F) for the prestressed beams. Results from Figure 5.39 also suggest that the deterioration in flexural stiffness for both of the PCP reinforced beams and prestressed beams are similar despite the consideration of thermal weathering.

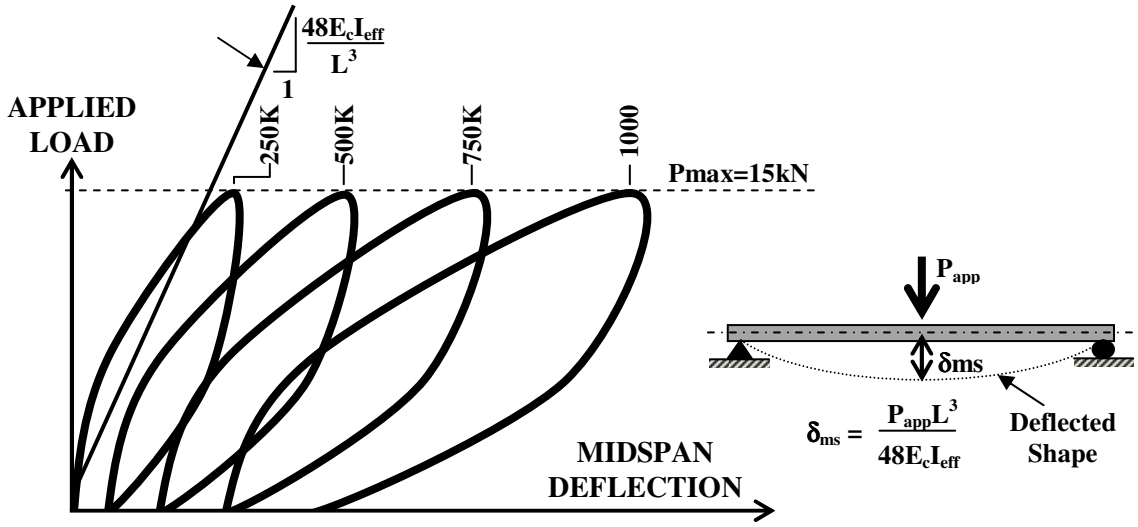

Figure 5.38 – **Linear Model for Flexural Stiffness Estimation**

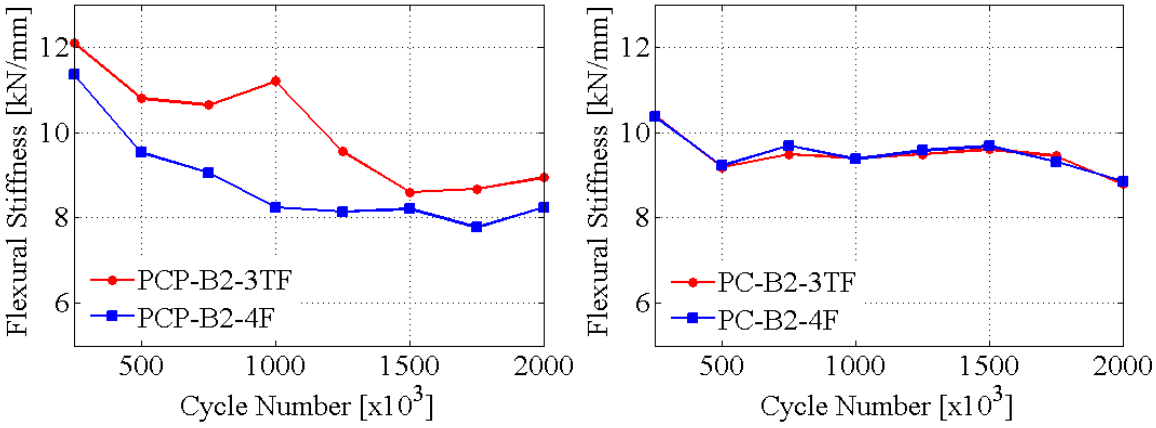

(a) PCP Reinforced Beams (b) Prestressed Beams

Figure 5.39 – **Flexural Stiffness Trend with Repeated Loading**

When considering the results presented in Figure 5.39 as well as those presented for bond performance and crack width, it is apparent that most of the deterioration for beams containing PCP reinforcement occurs within the first 1,000,000 cycles of testing. At this stage, the degree of deterioration for each of the investigated parameters tapers until the final 1,000,000 cycles are completed. The result was slightly different for the prestressed beams, with most of the deterioration taking place within the first 500,000 cycles of testing, followed by steadiness in the results and a dip during the final 500,000 cycles. Future research in the area should investigate whether this drop continues for the bare reinforcement when cycles in excess of 2,000,000 cycles are considered.

Deflection readings from the Linear Variable Displacement Transducer (LVDT) installed at midspan are shown in Figure 5.40 for the PCP reinforced beams as a function of the applied load at each of the intermediate static tests. The figure shows a progressive increase in deflection associated with the gradual reduction observed in flexural stiffness. The bilinear behavior conceptualized in Figure 5.38 and observed during the analysis of bond performance is also manifested in the figure.

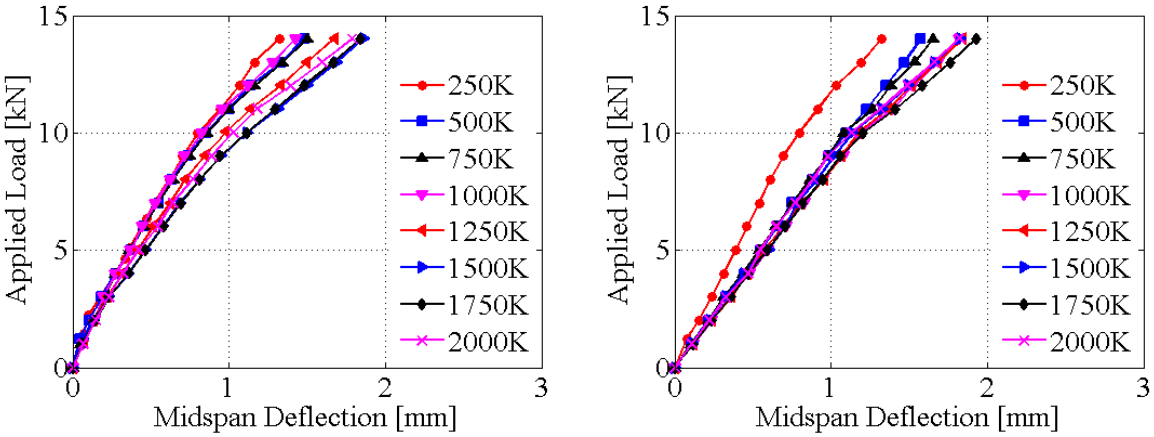

(a) PCP-B2-3TF (b) PCP-B2-4F

Figure 5.40 – **Load-Deflection Trend with Applied Load** [Intermediate Static Tests]

5.8.4 Performance of PCP Reinforcement with Fibres and Deformed Surfaces

The third batch of beams was cast to investigate the influence of deformations on the surface of PCP reinforcement as well as the influence of introducing dispersed fibres and

higher prestressing on flexural performance. Results from the load-deflection responses presented in Section 5.8.2 for the third batch of PCP reinforced beams suggest that the introduction of dispersed fibres and/or a higher prestressing level is more efficient in providing improvements on the post-cracking behavior than the introduction of surface deformations on the PCP reinforcement. The following sections will provide more insight on these observations.

5.8.4.1 Combination of Fibres and Deformed Surfaces

In the first set of four beams in the third batch, a fibre content of 1800g/m^3 was added to the PCP reinforcement. Among these four beams, a total of three contained PCP reinforcement with surface deformations. As shown in Figure 5.41, the deformations were introduced on the sides of the reinforcement using 12.5mm wide by 3mm thick steel plates welded to the sides of the formwork.

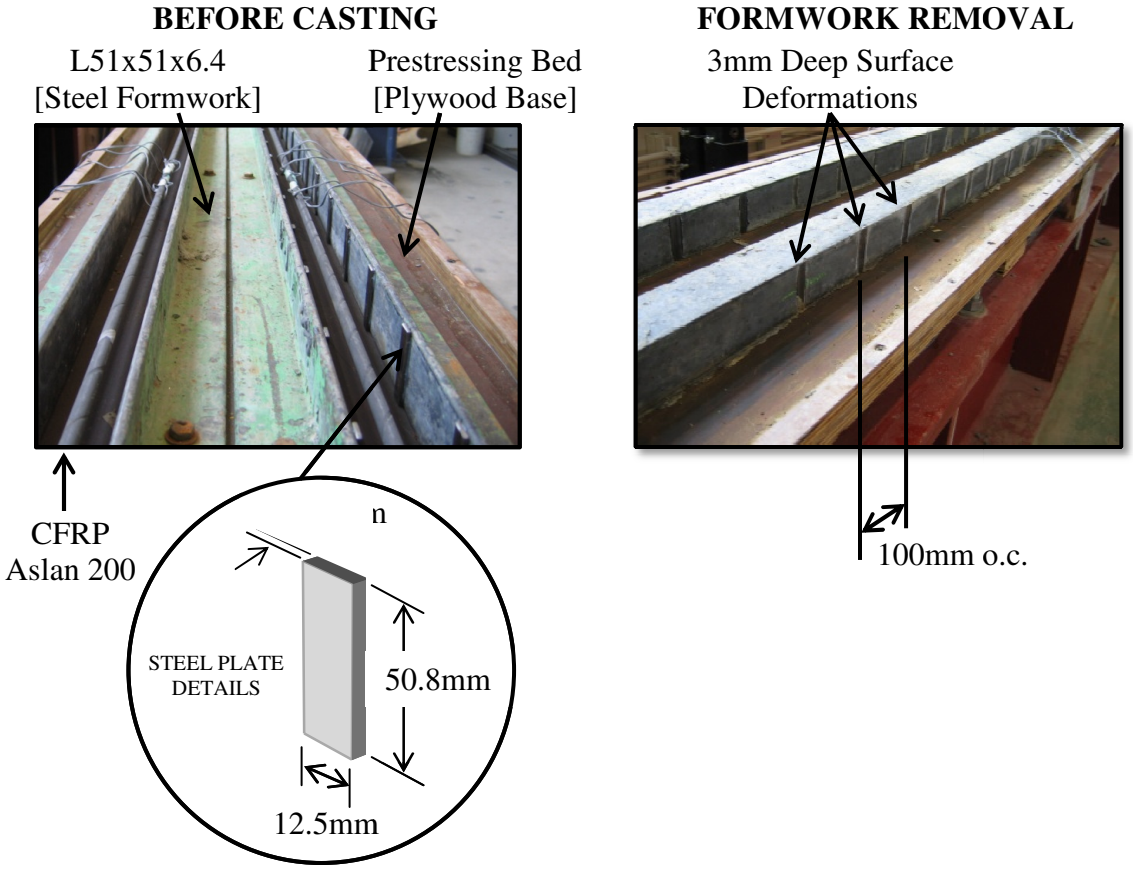

Figure 5.41 – **Formwork Modification for Surface Deformation** [PCP Batch#4]

After 14 days of curing, the formwork was removed for prestress release to reveal 3mm deep deformations on the side of the PCP reinforcement with a centre-to-centre spacing of 100mm. In order to assess the degree of influence on the post-cracking behavior, the load-deflection response from all beams was plotted in Figure 5.42 along with the beam labels and the average response obtained from the first beam batch (PCP-B1). The figure provides emphasis at several stages beyond cracking to illustrate the differences with respect to the first batch. Results indicate lower cracking loads but a gradual reduction in deflection until a load of approximately 65% of ultimate is reached. The improvement on flexural stiffness was then found to taper slightly until the ultimate stage was reached.

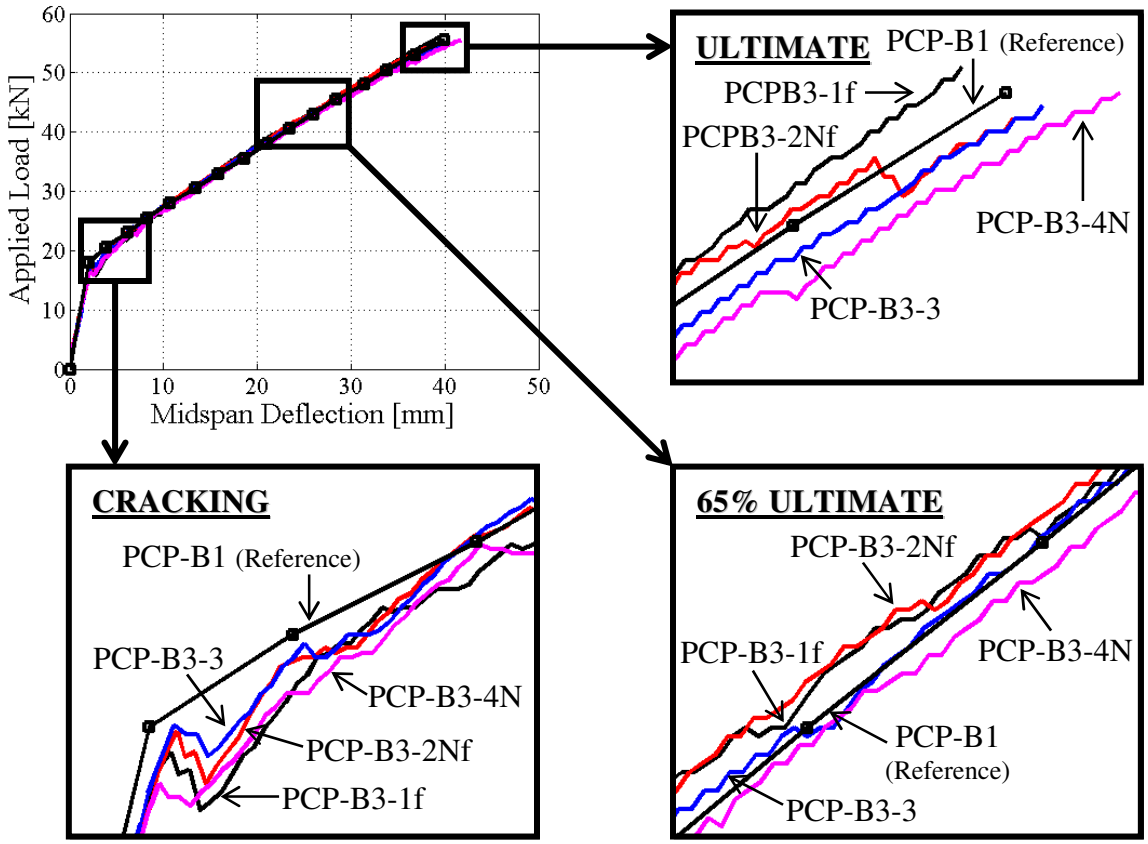

Figure 5.42 – **Load-Deflection Response Comparison** [Fibres & Deformed Surfaces]

Results from Figure 5.42 were used to quantify the difference in flexural stiffness between the third and first batch at loads ranging between the second cracking stage and ultimate. The procedure for evaluating the flexural stiffness is shown in Figure 5.43(a),

with the percent difference in the parameter plotted in Figure 5.43(b) for the first set of four beams in the third batch. Despite lower cracking loads, results in the figure reveal that the two beams containing PCP reinforcement with dispersed fibres (PCP-B3-1f, PCP-B3-2Nf) provide up to 5% of improvement on the post-cracking behavior when loads exceed approximately 50% of ultimate. Results from these beams also confirm that the presence of surface deformations does not improve the post-cracking behavior. The result is also valid for beams containing PCP reinforcement without fibres (PCP-B3-3, PCP-B3-4N).

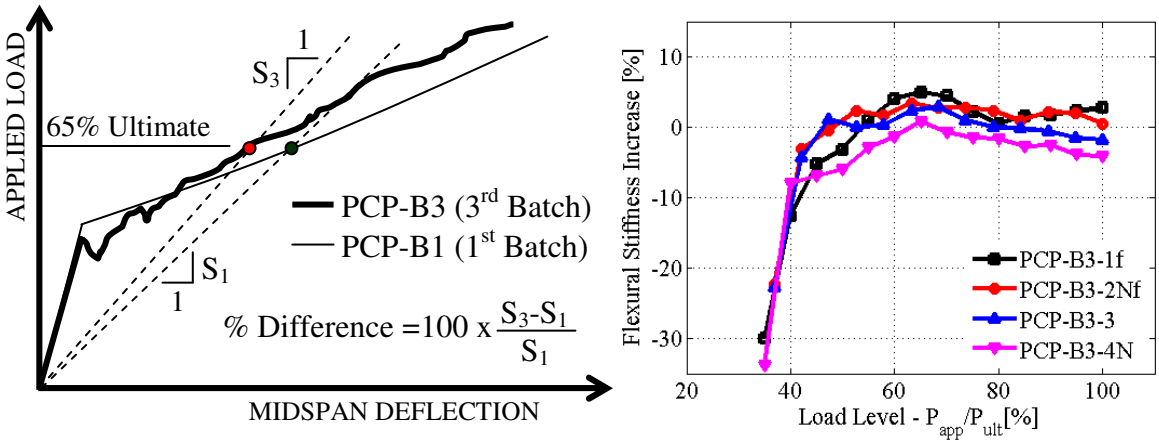

(a) Procedure (b) Results

Figure 5.43 – **Flexural Stiffness Improvement** [Fibres and Deformed Surfaces]

The lack of contribution from the surface deformations introduced on the PCP reinforcement in the third beam batch should be evaluated by examining the spacing chosen for the feature. The illustration provided in Figure 5.44 suggests that the spacing of the surface deformations has a significant impact on the contribution to bond performance. In the case of large spacing, the contribution of friction between the reinforcement and the concrete can dissipate sufficient tensile force from a crack before any form of mechanical interlock from the surface deformations is required. It is therefore believed from this observation and the results of Figure 5.43 that the 100mm spacing was excessive for the surface deformations and that a denser pattern should be considered in future research.

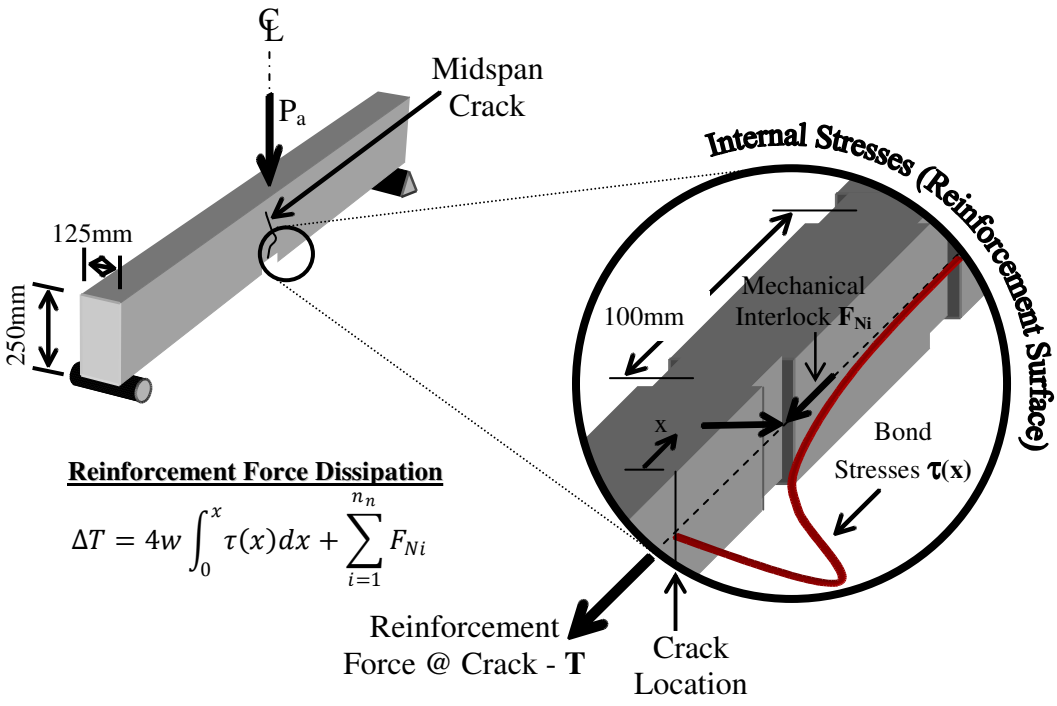

Figure 5.44 – **Bond Stresses for PCP Reinforcement with Deformed Surfaces**

5.8.4.2 Combination of Fibres and Higher Prestressing Force

A fibre content of 1800g/m^3 was also added to the PCP reinforcement for the second set of four beams in the third batch. The PCP reinforcement for these beams did not contain surface deformations but the jacking load was increased from 45kN, which was the level used for all preceding batches, to 50kN.

The load-deflection responses from these four beams are illustrated in Figure 5.45. The average response obtained from the first beam batch is also included in the figure for the purpose of comparison. The emphasized segments of the responses at cracking, 65% of ultimate and ultimate reveal that the improvements with respect to the first batch (PCP-B1) are more significant than those observed from the first four beams discussed in the preceding section. The results continue to suggest lower cracking loads but the reduction in deflection at 65% of ultimate and ultimate is more noticeable for all of these beams.

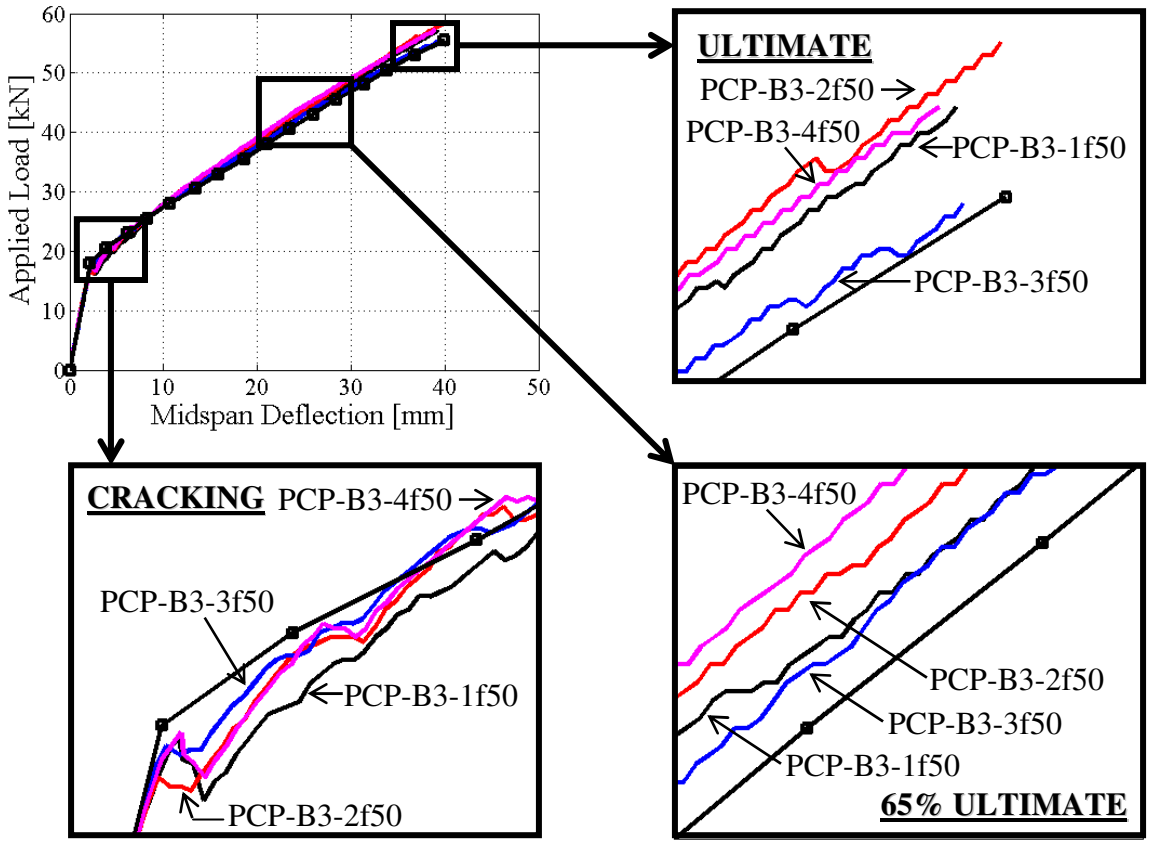

Figure 5.45 – **Load-Deflection Response Comparison** [Fibres & Higher Prestressing]

The differences in flexural stiffness associated with the smaller values of deflection recorded during the tests are shown in Figure 5.46 at loads ranging between the second cracking stage and ultimate. The figure reveals that all beams show improvements on the flexural stiffness once loads beyond 47% of ultimate are reached. An improvement ranging between 4% (PCP-B3-3f50) and 12% (PCP-B3-4f50) was observed at 65% of ultimate compared to 2% (PCP-B3-3f50) and 10% (PCP-B3-2f50) at ultimate. Results also confirm previous observations for which the first and third beams reveal a smaller improvement on flexural performance. The outcome is attributed to the casting sequence of PCP reinforcement and the higher potential for air and/or water entrapment that arises from the reduction of workability during the concrete pour.

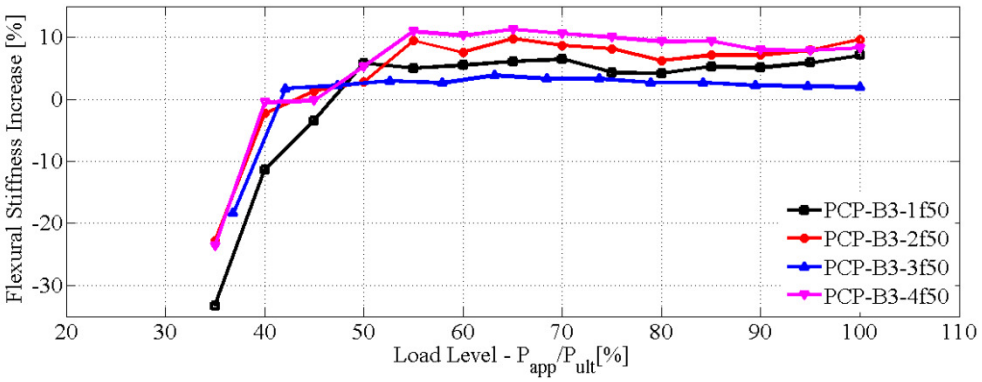

Figure 5.46 – **Flexural Stiffness Improvement** [Fibres and Higher Prestressing]

5.8.5 Bond Strength of PCP Reinforcement

As discussed in Chapter 2, tensile forces between cracks are transferred to the concrete through shear stresses at the surface of the reinforcement. These shear stresses vary along the length of the reinforcement, but an average value is generally used to describe the ability of the reinforcement to transfer forces in the surrounding concrete. The value is relevant to the design of reinforced concrete structures since it is more commonly used to establish parameters such as development length for the reinforcement. The average bond strength can be established by considering force equilibrium of the bar segment in Figure 2.4 of Chapter 2. The requirement gives an expression that relates the parameter to the total force transferred within the anchorage zone separating adjacent cracks.

$$\tau_{PCP,average} = \frac{\Delta T_R}{4w\Delta x} \qquad \text{EQ5.5}$$

Recalling from the relationship presented in Chapter 2, $\tau_{PCP,average}$ is the average bond strength, ΔT_R is the force transferred between adjacent cracks, w is the width of the PCP reinforcement and Δx is the crack spacing. The force transfer in this expression can be written as a function of the moment gradient between adjacent cracks and the moment arm separating the tensile force from the compressive forces.

$$\Delta T_R = \frac{\Delta M}{j_{cr1} d} \qquad \text{EQ5.6}$$

In this equation, ΔM is the increment in moment between adjacent cracks when the first cracking moment is reached at the outermost crack being investigated. Similarly, j_{cr1} is the fraction of effective reinforcement depth that characterizes the moment arm between the tensile force in the reinforcement and the compressive forces. The parameter remains constant between each set of adjacent cracks, provided that the concrete is in the linear-elastic range and that the PCP reinforcement remains intact at these locations. The derivation of the relationship is illustrated in Figure 5.47 along with the force diagram and properties of the cracked section.

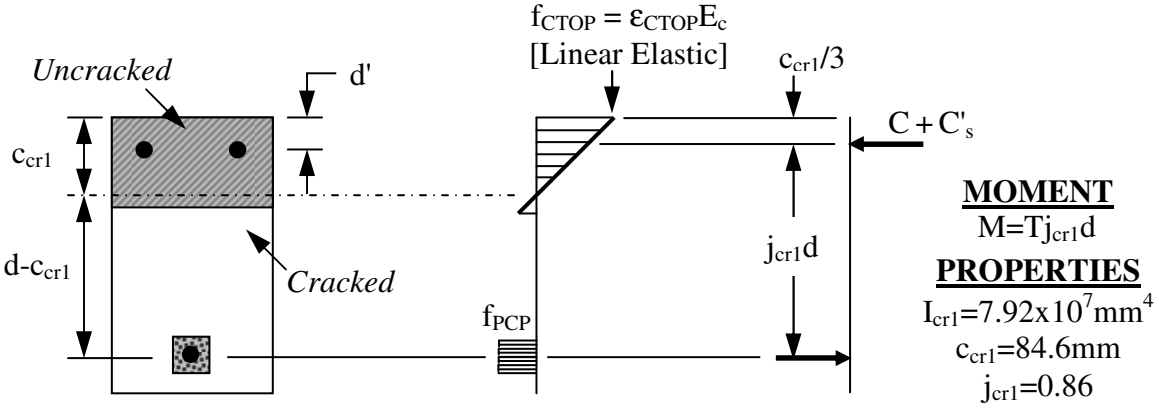

Figure 5.47 – **Cracked Section Properties and Moment Relationship** [$M_{cr1}<M<M_{cr2}$]

The crack spacing between each set of adjacent cracks can be evaluated using the stabilized crack pattern. The patterns for all beams tested in this research are shown in Table 5.12 along with the average crack spacing and the corresponding bond strength calculated using EQ.5.5. The values listed for the first batch of PCP reinforced beams show that the bond strength values average 0.22MPa. Clause 11.5.1 of the CSA A23.3-04 code for steel reinforced concrete provides an expression for estimating shear resisted by an interface separating concrete cast at different times. The estimate depends on the cohesion and friction maintained by the presence of reinforcement across the interface. In the absence of transverse reinforcement between the beam and the PCP reinforcement, the value of 0.25MPa provided in the code for cohesion at a concrete interface with non-intentional roughness is higher than the experimental average. Nevertheless, the values are close and suggest that PCP reinforcement has adequate bond to the NSC of beams in the study.

Table 5.12 – **Stabilized Crack Pattern and Average Bond Strength**

Label	Stabilized Crack Pattern	Average Crack Spacing [mm]	Average Bond Strength [MPa]
PCP-B1-4	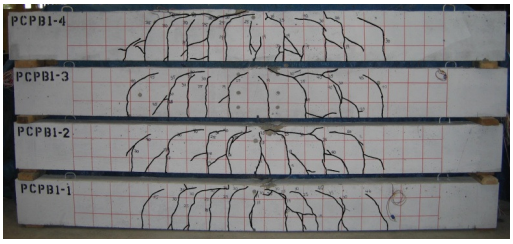	119.0	0.22
PCP-B1-3T		139.3	0.23
PCP-B1-2		112.1	0.21
PCP-B1-1T		105.9	0.21
PC-B1-4	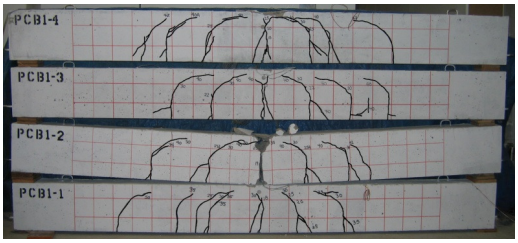	197.8	2.74
PC-B1-3T		208.0	2.64
PC-B1-2		248.4	2.81
PC-B1-1T		197.3	2.65
PCP-B2-4F	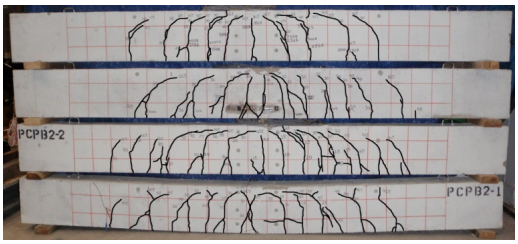	136.6	0.22
PCP-B2-3TF		127.0	0.22
PCP-B2-2		120.2	0.24
PCP-B2-1T		169.1	0.23
PC-B2-4F	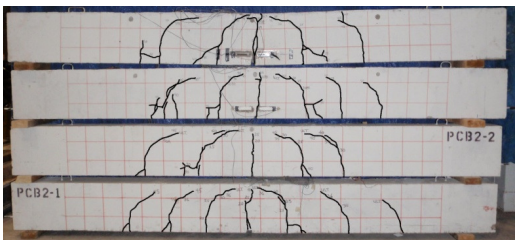	262.7	2.51
PC-B2-3TF		221.0	2.61
PC-B2-2		259.1	2.58
PC-B2-1T		245.4	2.98
PCP-B3-4N	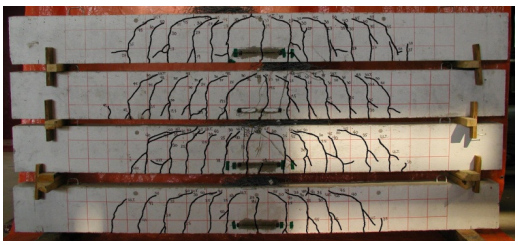	108.2	0.23
PCP-B3-3		113.3	0.23
PCP-B3-2Nf		101.4	0.24
PCP-B3-1f		102.7	0.22
PCP-B3-4f50	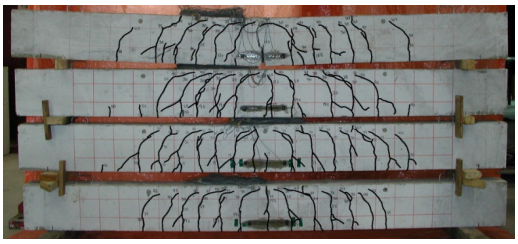	107.6	0.24
PCP-B3-3f50		103.9	0.24
PCP-B3-2f50		98.8	0.23
PCP-B3-1f50		137.4	0.24

The average bond strength for the prestressed beams in the first batch was evaluated using similar analogy as that used for the PCP reinforced beams. However, the properties of the cracked section for the prestressed beams are not constant due to the presence of effective prestressing strain in the reinforcement. The relationship for the variation in tensile force between adjacent cracks must therefore reflect this condition. The force diagram for the prestressed beams is the same as that shown in Figure 5.47 but the neutral axis, and therefore the moment arm, will change as the moment gradient increases between each set of adjacent cracks considered.

$$\Delta T_R = \frac{M}{jd} - \frac{M_{cr}}{j_{cr}d} \qquad \text{EQ5.7}$$

In this expression, M and M_{cr} are the moments at adjacent cracks when the beam reaches the cracking stage and j as well as j_{cr} are the corresponding fractions of the effective reinforcement depth that characterize the moment arm. The average bond strength of the bare reinforcing bar can be established from this expression as well as the crack spacing listed in Table 5.12.

$$\tau_{PS,avg} = \frac{\Delta T_R}{\pi d_b \Delta x} \qquad \text{EQ5.8}$$

In this relationship, d_b is the diameter of the reinforcing bar used to determine the surface area that resists bond stresses. In Table 5.12, results from this relationship were found to range from as low as 2.64MPa to as high as 2.81MPa with an average of 2.71MPa when the beam reaches cracking. Despite the relatively smaller surface area of the bare reinforcement, the larger crack spacing observed for the prestressed beams was not sufficient to reduce bond stress values below those observed for the PCP reinforcement. The range corresponds to 6% of the average compared to 9% for the PCP reinforcement. This suggests less variability for the prestressed beams, which continues to be associated with the higher difficulty of achieving a surface finish that is as consistent for PCP reinforcement as it is for commercially available reinforcement.

As indicated in Table 5.12, the bond strength of PCP reinforcement from the second beam batch was also evaluated to reflect the influence of repeated loading and thermal weathering. Results from individual specimens show that slightly larger crack spacing and smaller bond strength values can be expected for beams subjected to repeated loading. On the other hand, thermal weathering can be anticipated to produce a reduction in crack spacing and an associated increase in bond strength. The PCP reinforced beams tested under static loading are, however, an exception to this observation. Results from the second batch are in agreement with the data analysis performed during fatigue testing, where beams subjected to thermal weathering revealed less deterioration. Future research should consider a larger set of samples to confirm this result.

Finally, the average bond strength of PCP reinforcement used in the third beam batch was investigated to reflect the influence of adding dispersed fibres in the HSC mix and introducing surface deformations. Results show a slight reduction in crack spacing with respect to the first two batches of PCP reinforced beams. They also suggest that smaller crack spacing can be achieved when using PCP reinforcement with dispersed fibres only. The higher bond performance from which originates this smaller crack spacing occurs from the reduction in workability of HSC with 1800kg/m^3 of dispersed fibres. The condition causes an entrapment of air on the sides of the formwork during casting that can produce a network of smaller, more finely distributed voids on the surface of the PCP reinforcement. The higher bond performance arising from this denser network of surface roughness confirms earlier observations for which the addition of dispersed fibres provides higher levels of improvement on the post-cracking behavior in comparison to the inclusion of widely spaced surface deformations.

The average bond strength listed for beams PCP-B3-3 (0.23MPa) and PCP-B3-4N (0.23MPa) in Table 5.12 also indicate that the inclusion of surface deformations does not improve bond performance. Furthermore, results from beams PCP-B3-4N (0.23MPa) and PCP-B3-2Nf (0.24MPa) indicate that a 3.5% improvement in bond performance can be achieved with the addition of 1800kg/m^3 of dispersed fibres.

CHAPTER 6

CONCLUSIONS AND RECOMMENDATIONS

6.1 SUMMARY AND CONCLUSIONS

Several conclusions can be drawn from the results presented and discussed in this thesis. More specifically, the current section will present conclusions pertaining to each phase of the research. Through the use of tension stiffening concepts, the first phase includes the development of an effective moment of inertia relationship for estimating the deflection of Fiber Reinforced Polymer (FRP) reinforced concrete beams. The second phase of the research presents an alternate reinforcing technique, called Prestressed Concrete Prism (PCP) reinforcement, for which higher strength of FRP rebar can be more appropriately considered in design. Although the technique enhances the axial stiffness of the bare reinforcement, the increased potential for concrete cover damage that arises from transverse differential swelling of FRP rebar in the relatively small cross-section is thoroughly evaluated. Finally, the third phase of the project covers an experimental program that investigates the potential for this damage to influence the integrity of PCPs and the serviceability of concrete structures containing the reinforcement.

6.1.1 Deflection of Concrete Beams with FRP

[1] When examining the results from the complete database, the modification factor proposed by ACI 440.1R (2006) underestimates deflection with ratios below unity for the

full range of load levels considered. The modification proposed by Yost et al. (2003) also underestimates deflection but only for load levels beyond 45% of ultimate. For lower load levels, the modification provides a conservative estimate of deflection. A similar trend was observed for the suggested expression but with a relatively smaller degree of underestimation at higher load levels and conservative estimates for load levels below 60% of ultimate.

[2] It is apparent from the results of individual bars that the deflection ratios for beams reinforced with Carbon FRP (CFRP) are well below unity for all load levels and that those obtained for beams reinforced with Glass FRP (GFRP) are closer to or beyond unity. The outcome holds true for all methods considered and reflects the lack of conservatism in estimating deflections for beams reinforced with CFRP. The result can be attributed to the fact that the methods considered in this thesis have been primarily calibrated to estimate the deflection of beams containing rebar with properties similar to those of GFRP reinforcement.

[3] The margin of error of 95% confidence intervals has been shown to vary between 18% (±0.18) and 26% (±0.26) from the average for the load levels and methods considered in this thesis. These relatively low values enforce the precision with which the methods considered in this thesis can estimate deflection.

[4] When compared to other methods, the suggested expression for effective moment of inertia provides higher precision and accuracy at higher load levels. For the complete database, averages are significantly closer to unity and margins of error are the smallest at these conditions. The result arises from the inclusion of concrete non-linearity in compression and presents an advantage over existing methods since it attenuates the lack of conservatism at higher load levels.

6.1.2 Prestressed Concrete Prism Reinforcement

[1] According to the sensitivity analysis performed on the expressions describing the linear elastic model in this thesis, the material properties most susceptible to affect stresses and

damage within the concrete cover include the concrete compressive strength as well as the transverse elastic modulus and transverse Poisson's ratio for the reinforcement. While the model is most sensitive to the transverse elastic modulus, it has equal sensitivity to the concrete compressive strength and Poisson's ratio for the reinforcement.

[2] It is also clear from the analysis that the linear elastic model is also sensitive to changes in the ratio of concrete cover to bar diameter ratio c_c/d_b. However, charts for maximum circumferential stress show that increasing the c_c/d_b ratio beyond 2.5 does not appreciably alter the concentration of stress at the surface of the reinforcement. Unlike other parameters, increasing the c_c/d_b ratio beyond this value becomes inefficient in preventing the initiation of cracks within the cover. As a result, the maximum prestressing level for which cracks are prevented from initiating within the cover hardly increases with c_c/d_b ratios beyond 2.5.

[3] Critical service design charts used to establish service moments for which axial stiffness is enhanced by the use of PCP reinforcement were derived using a c_c/d_b ratio of 2.5 and the diagrams for maximum prestressing level. The service moments for which the PCP remains intact were found to increase linearly with an increase in concrete compressive strength as well as with a decrease in transverse elastic modulus for the bare bar. Since the charts are expressed in terms of a reinforcement ratio and the service moments normalized with respect to the section geometry, they provide a useful tool for the designing engineer and ease the conception of structures with PCP reinforcement.

[4] Experimental data for HSC with compressive strengths ranging from 90 to 170MPa was gathered from a total of 14 researchers and stored in a database containing data obtained from tests performed on the mix used for the PCP reinforcement in this thesis. The database was used to improve the relationship proposed by Carrasquillo et al. (1981) for elastic modulus at or beyond 28days of moist curing. The improvement consisted of providing a modification factor for compressive strengths exceeding 90MPa (C_s=1.04). The factor was found to reduce the Root Mean Squared Error (RMSE) by 2.3% with respect to the expression provided by ACI 363R (1992) and 20.8% with respect to the relationship provided by the CSA A23.3-04 design code.

[5] An additional factor denoted C_{ca} was also incorporated to the expression proposed by Carrasquillo et al. (1981) to improve accuracy and account for the influence of coarse aggregates on elastic modulus. A total of five aggregate types were identified in the database. While dolomite aggregates (C_{ca}=1.17) were found to provide the highest elastic modulus values, sandstone aggregates (C_{ca}=0.71) were held to account for the lowest elastic modulus values. After dolomite, quartzite aggregates (C_{ca}=1.10) were found to provide the highest elastic modulus values, followed by granite/limestone (C_{ca}=1.03) and andesite (C_{ca}=0.98).

[6] Since the properties of concrete are essential in determining the adequacy of concrete to sustain stresses arising from prestress release within the first 28-days of moist curing, an additional factor C_a was derived to account for the influence of age on elastic modulus. The factor was found to average 1.06 after 7days of moist curing and unity after 14days of moist curing.

[7] Splitting tensile strength values from the HSC database did not reveal any distinctive trends when considering the different stages of moist curing reported. The relationship fitted to the experimental data of the database is therefore capable of estimating splitting tensile strength for concrete between 7 and 434 days of moist curing. It is capable of explaining 74.9% of the variation about the mean compared to 69.8% for the relationship proposed by ACI 363R (1992) and 22.4% for the expression provide by Rashid et al. (2002). The inverse S-curve relationship of splitting strength with compressive strength originally suggested by Rashid et al. (2002) was attributed to higher scatter in the experimental data.

[8] Values of Poisson's ratio in the HSC database do not show influence arising from the time of test for compressive strengths in excess of 90MPa. For tests performed between 7 and 540 days of moist curing, the values were found to range between 0.16 and 0.25, which represents a wider spread than that observed for the first three batches of PCP reinforcement. The experimental data was also found to average a smaller value of 0.21 with a larger standard deviation of ±0.02.

[9] Tests performed on standard cylindrical samples of mortar and concrete have expanded the scope of the research to provide a theoretical expression for elastic modulus in which a parameter accounts for the influence of silica fume content in the concrete mix. The expression is theoretically modeled to account for the relative contribution of mortar and aggregates on the elastic modulus of concrete. The relationship is in good agreement with the experimental estimates.

6.1.3 Experimental Program

[1] Based on the results of static tests presented in this thesis, it is apparent that the CFRP prestressed reinforcement and the PCP reinforcement tested have excellent bond performance and flexural behaviour in a concrete environment that satisfies the minimum cover requirements of CSA S806 (2002). Performances do not show sufficient deviation to suggest the possibility of deterioration arising from thermal gradients expected in the Canadian climate.

[2] As a consequence of similarities between bond performance for each of the reinforcing techniques considered, the experimental load-deflection responses presented in this thesis are similar among prestressed and PCP reinforced beams. The outcome suggests that methods used for estimating the deflection of prestressed beams can also be used to estimate the deflection of beams reinforced with PCP reinforcement. The observation has considerable advantages from a design perspective.

[3] Based on the results from repeated loading, the deterioration in bond performance for the PCP reinforcement was found to range between 17 and 38% compared to 14 and 25% for the bare CFRP reinforcement used in the prestressed beams. The result suggests a higher level of uncertainty in bond performance for the PCP reinforcement, which is associated with the difficulty in achieving a surface finish that is as consistent as that achieved for commercially available reinforcement.

[4] The increase in crack spacing during repeated loading of the second beam batch ranges from 48 to 84% for the PCP reinforced beams compared with 33% for each of the

prestressed beams. The result confirms the higher variability observed in the bond performance for PCP reinforcement and also the higher level of deterioration observed in the parameter.

[5] A higher level of deterioration was also observed for midspan deflection and flexural stiffness of PCP reinforced beams subjected to repeated loading. While the prestressed beams revealed a deterioration of approximately 15%, it was found to range between 29 and 32% for the PCP reinforced beams. In similarity to that observed for bond performance and crack width, the trend in midspan deflection and flexural stiffness suggests that most of the deterioration for the PCP reinforced beams occurs within the first 1,000,000 cycles of testing with a taper until the remaining 1,000,000 cycles are completed. Most of the deterioration for the prestressed beams occurred within the first 500,000 cycles of testing, followed by steadiness in the results and a slight dip during the final 500,000 cycles.

[6] When comparing the load-deflection behaviour of beams from the third batch to those from the first batch, it can be shown that the inclusion of dispersed fibers in the PCP reinforcement enhances the post-cracking behaviour. When a jacking load of 45kN is applied to the PCP reinforcement, the additional contribution of the fibers through each crack can provide a reduction in deflection of up to 5% beyond the cracking stage of the beams. Conversely, when a jacking load of 50kN is considered for the PCP reinforcement with dispersed fibers, improvements of up to 12% were observed beyond the cracking stage.

[7] From the stabilized crack pattern of each PCP reinforced beams in the first batch, the average bond strength for the reinforcement was found to vary between 0.21 and 0.23MPa with an average of 0.22MPa. Although the value represents adequate bond of the reinforcement in a concrete environment, it is smaller than the 0.25MPa value listed by Clause 11.1.3 of the CSA A23.3-04 code for estimating shear resistance at the interface separating concrete cast at different times. The difference is mainly attributed to the fact that the code considers additional dowel resistance from transverse

reinforcement through the interface, which is absent when considering PCP in a concrete environment.

[8] The stabilized crack pattern of each prestressed beam in the first batch reveals average bond strength values for the CFRP bar that vary between 2.64 and 2.81MPa with an average of 2.71MPa. The average bond strength is larger than that calculated for the PCP reinforcement, in spite of the fact that the average crack spacing for the set of CFRP prestressed beams (212mm) is noticeably larger than that measured for the case of PCP reinforced beams (119mm). The range represents 6% of the average compared to 9% for the PCP reinforced beams. The result underlines the higher difficulty involved in achieving a surface finish that is as consistent for PCP reinforcement as it is for commercially available reinforcement.

[9] Results obtained from the stabilized crack pattern of beams in the second batch suggest an increase in crack spacing as well as a reduction in average bond strength when considering repeated loading. Conversely, thermal weathering was found to provide a slight increase in the parameter. More research is, however, required to confirm this observation.

[10] The stabilized crack pattern from the third beam batch did not reveal any improvement in bond strength for PCP reinforcement with surface deformations when comparing results to the first and second beam batches. On the other hand, the inclusion of dispersed fibers in the high strength concrete mix was found to provide slight improvements to the bond performance of PCP reinforcement. The outcome originates from the reduction in workability observed for high strength concrete with dispersed fibres. The condition causes an entrapment of air on the sides of the formwork during casting, which was found to produce a network of smaller, more finely distributed voids on the surface of the PCP reinforcement.

6.2 FUTURE RESEARCH

[1] Although expressions considered in Chapter 1 for estimating the deflection of beams with FRP are reliably accurate over the complete database, they continue to under-estimate deflection for CFRP reinforcement and over-estimate deflection for GFRP reinforcement. The result was initially unexpected since CFRP reinforcement is generally known to have larger elastic modulus values than GFRP reinforcement, which provides higher flexural stiffness for beams containing the reinforcement. However, the lower amount of CFRP reinforcement required to achieve compression failures suggests that existing methods weigh the influence of elastic modulus more highly than the influence of reinforcing area on flexural stiffness beyond cracking. The expression proposed in this thesis should be modified to account for this discrepancy by adjusting the tension stiffening factor β_d that was initially taken from research performed on conventional steel (Rao, 1966) for the case of FRP reinforcement.

[2] Results from the experimental program have shown that thermal weathering as well as repeated loading had slight influences on the residual static behaviour of PCP reinforced beams as well as prestressed beams. Future research should consider additional testing with longer periods of exposure as well as a wider range of repeated loading schemes to provide a more comprehensive evaluation of these conditions on the performance of samples considered in this thesis.

[3] Although the inclusion of dispersed fibers was efficient in improving the post-cracking behaviour of beams with PCP reinforcement, it was not successful in reaching the desired increases in cracking load and service range for which the flexural stiffness is enhanced. Based on literature reviewed in this thesis, future research should study the influence of various fibers on the cracking strength of PCP reinforcement and their relative influence on the post-cracking behaviour of PCP reinforced beams. The results should be documented with respect to the axial stiffness, length-to-diameter ratio as well as surface characteristics of the fibers.

APPENDIX A

LOAD-DEFLECTION RESULTS

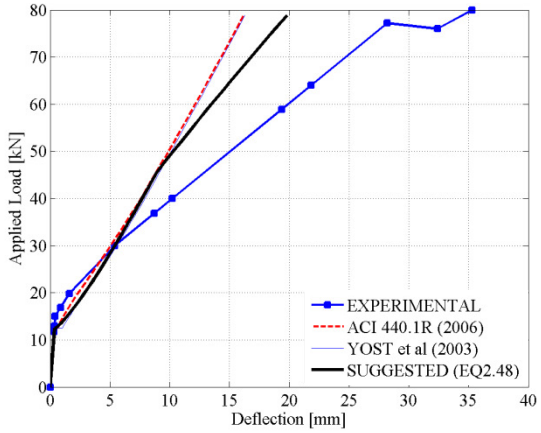

(a) Load-Deflection: BC4H

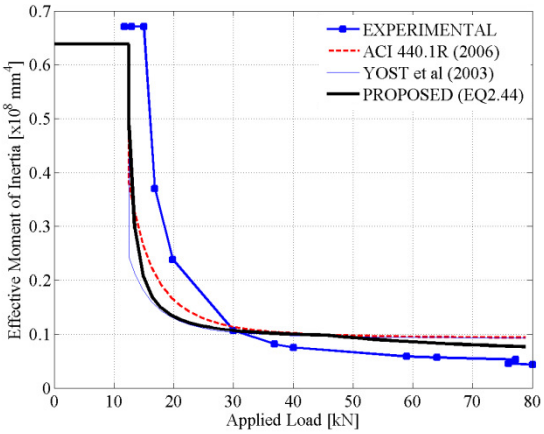

(b) Inertia: BC4H

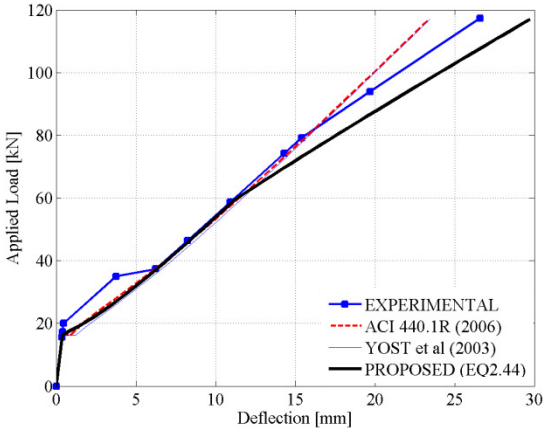

(c) Load-Deflection: BC4V

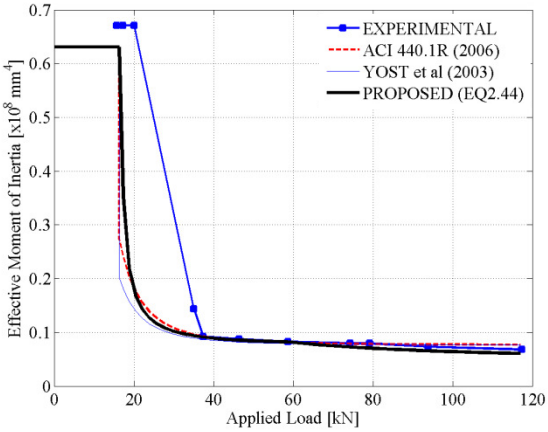

(d) Inertia: BC4V

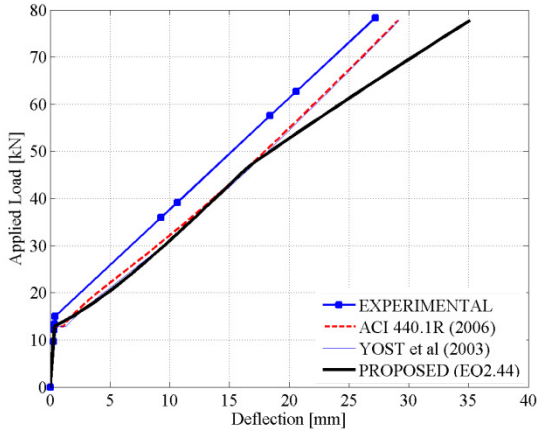

(e) Load-Deflection: BC2H

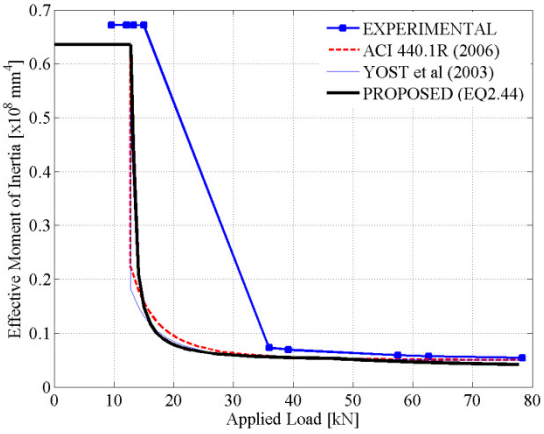

(f) Inertia: BC2H

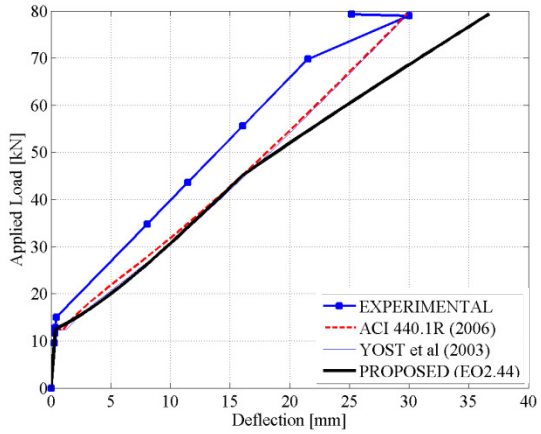

(g) Load-Deflection: BC2N

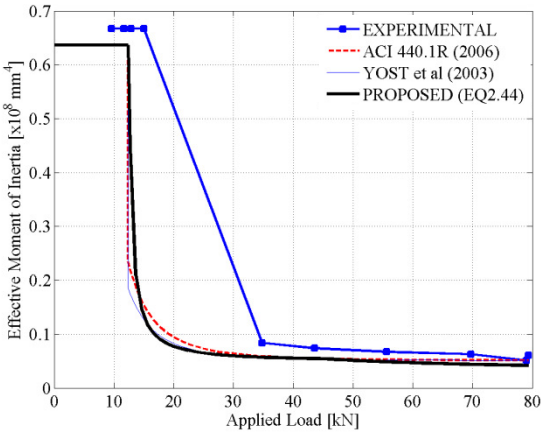

(h) Inertia: BC2N

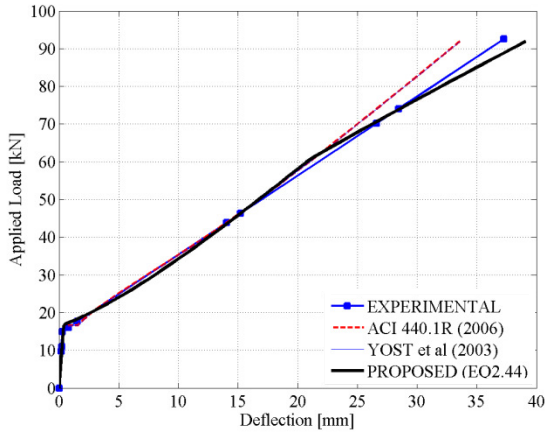

(i) Load-Deflection: BC2V

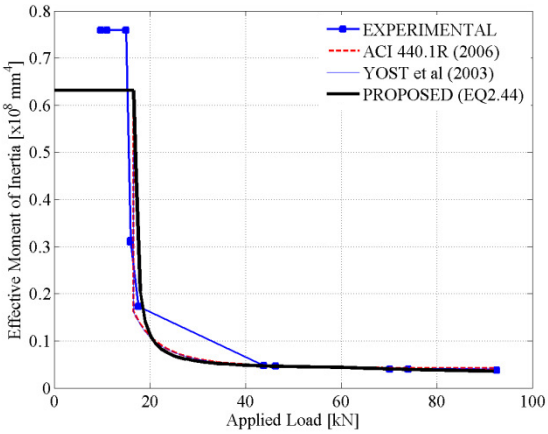

(j) Inertia: BC2V

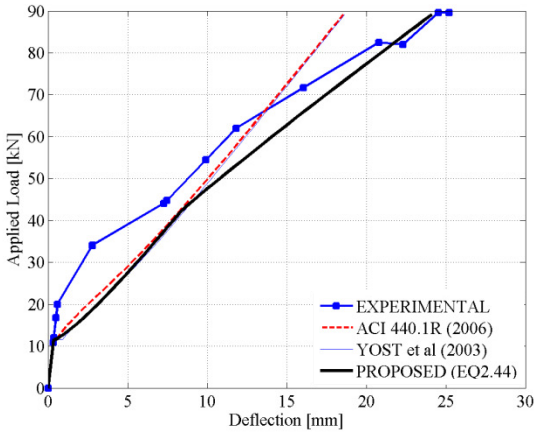

(k) Load-Deflection: BC4N

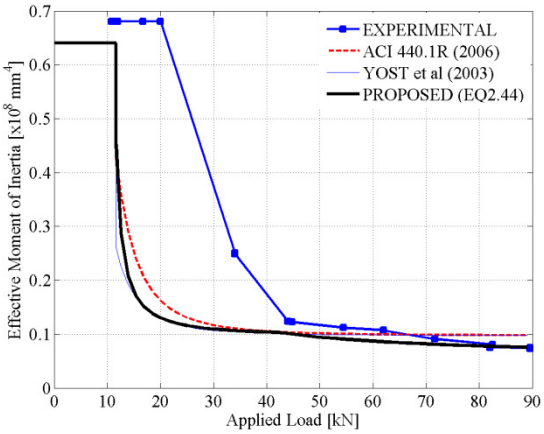

(l) Inertia: BC4N

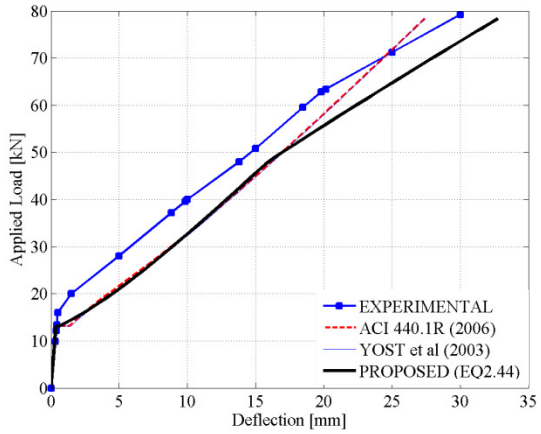

(m) Load-Deflection: BC2HA

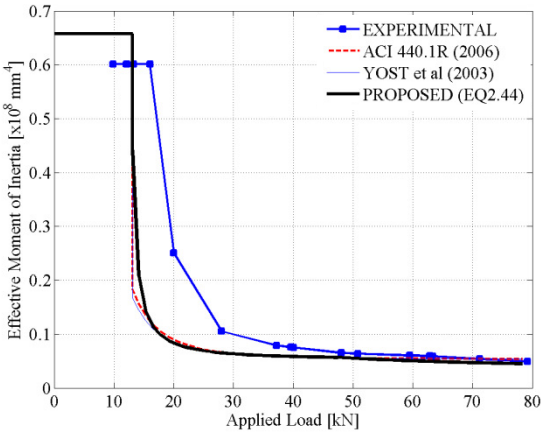

(n) Inertia: BC2HA

Figure A.1 **– Load-Deflection Estimates** [Benmokrane and Theriault 1997]

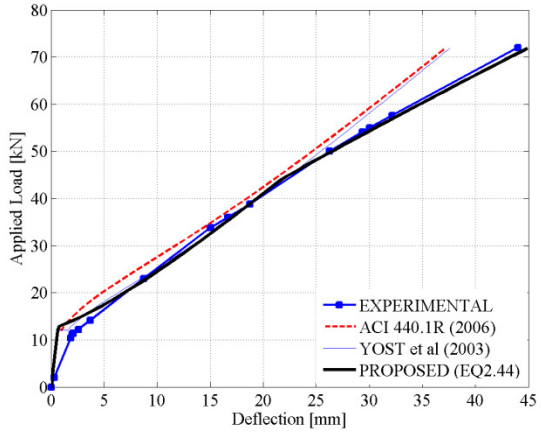

(a) Load-Deflection: COMP-00

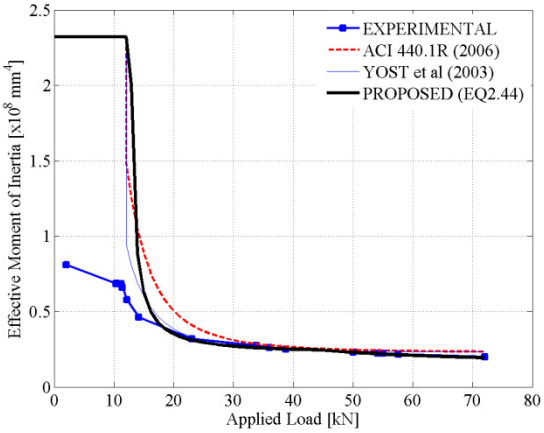

(b) Inertia: COMP-00

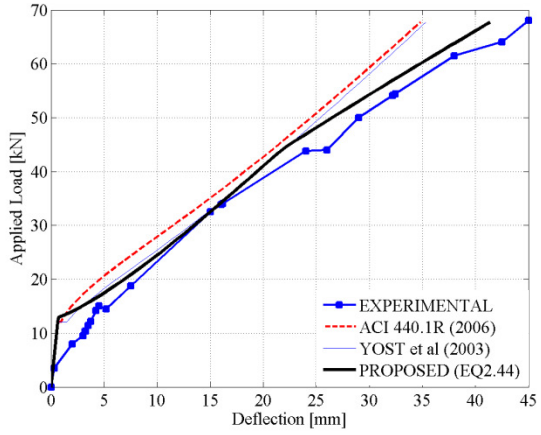

(c) Load-Deflection: COMP-25

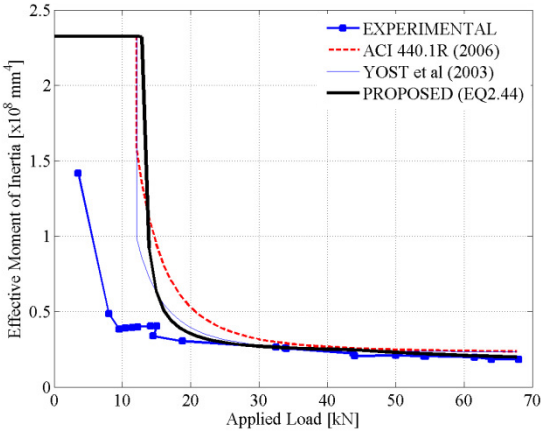

(d) Inertia: COMP-25

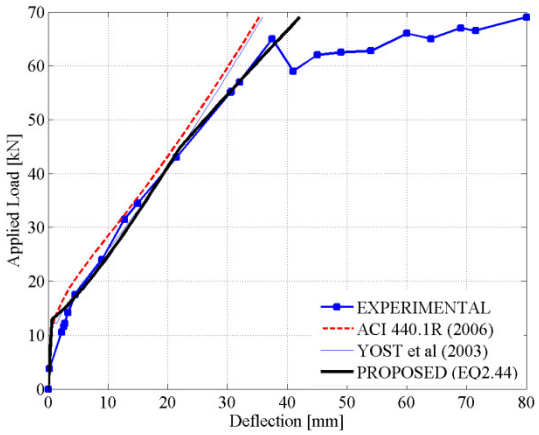

(e) Load-Deflection: COMP-50

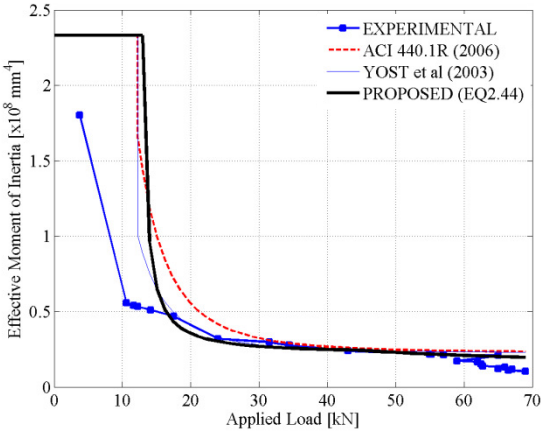

(f) Inertia: COMP-50

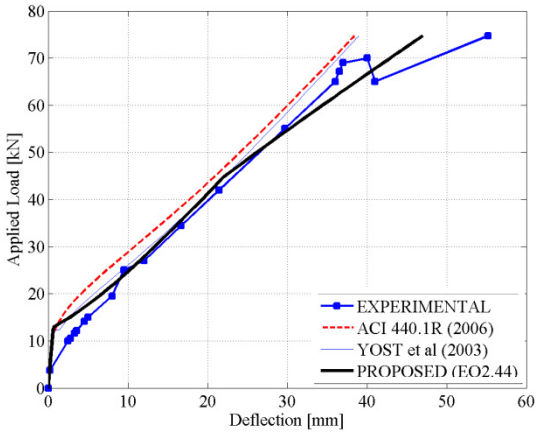

(g) Load-Deflection: COMP-75

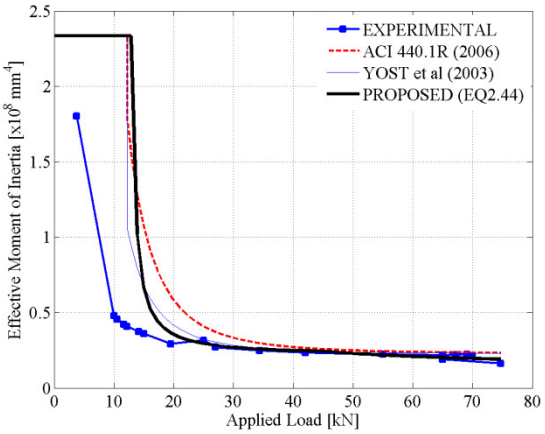

(h) Inertia: COMP-75

Figure A.2 **– Load-Deflection Estimates** [Almusallam et al. 1997]

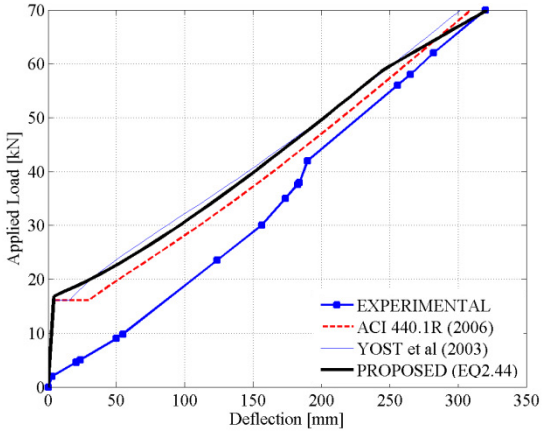

(a) Load-Deflection: C1

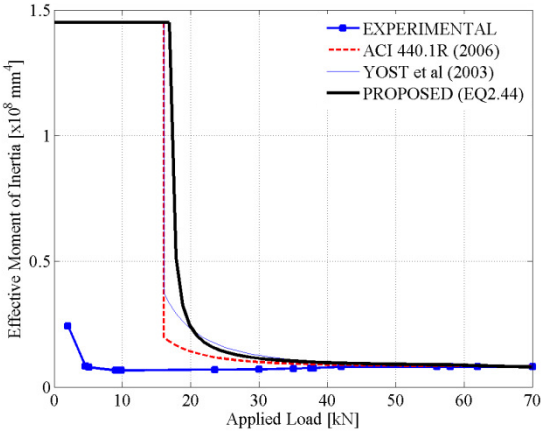

(b) Inertia: C1

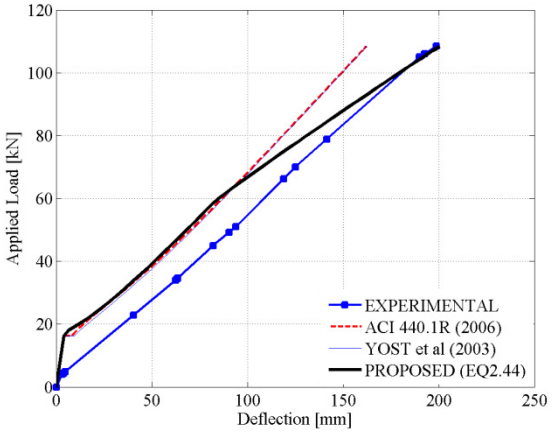

(c) Load-Deflection: C2

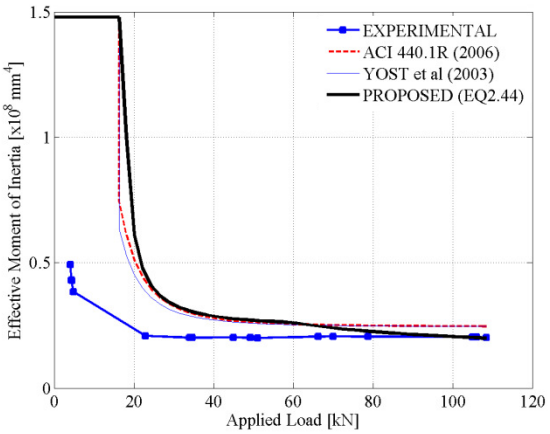

(d) Inertia: C2

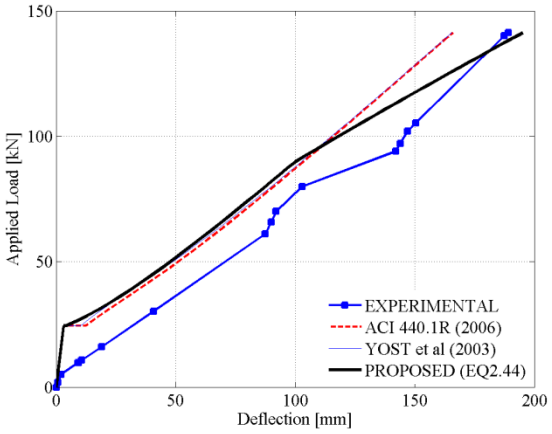

(e) Load-Deflection: C3

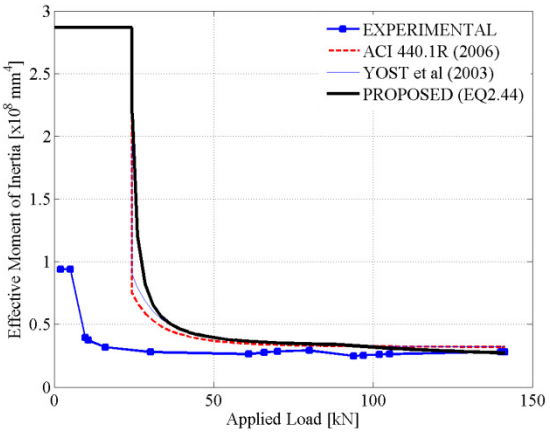

(f) Inertia: C3

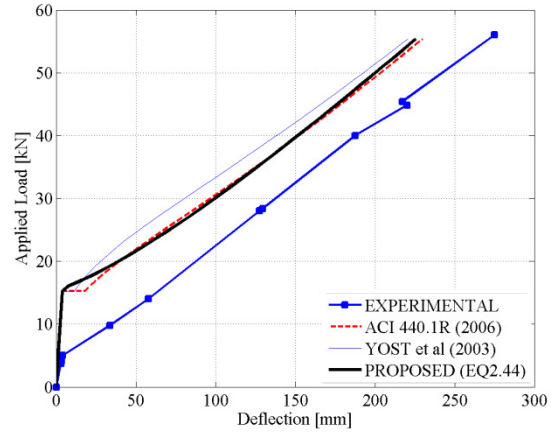

(g) Load-Deflection: CS

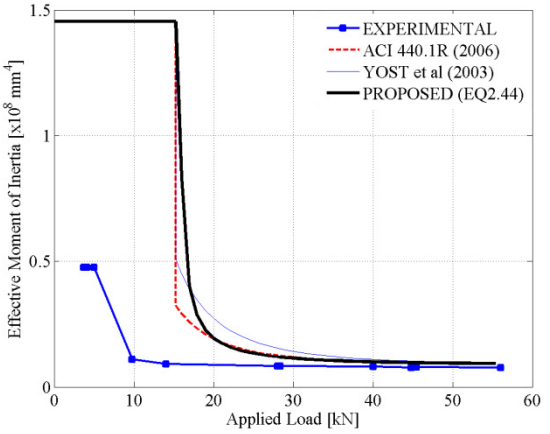

(h) Inertia: CS

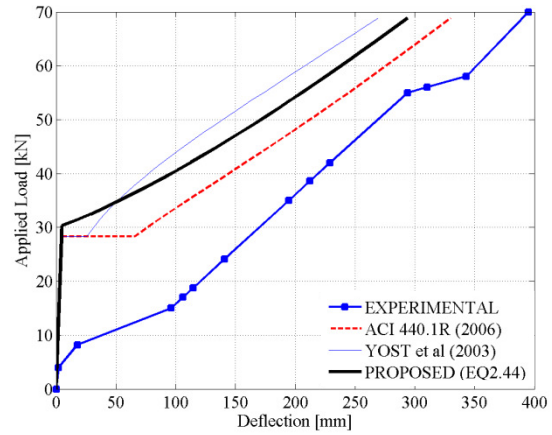

(i) Load-Deflection: H1

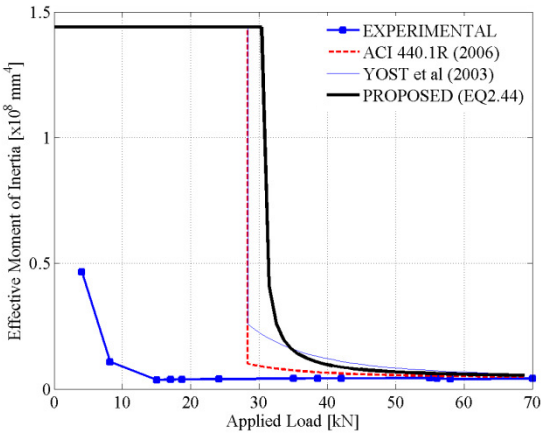

(i) Inertia: H1

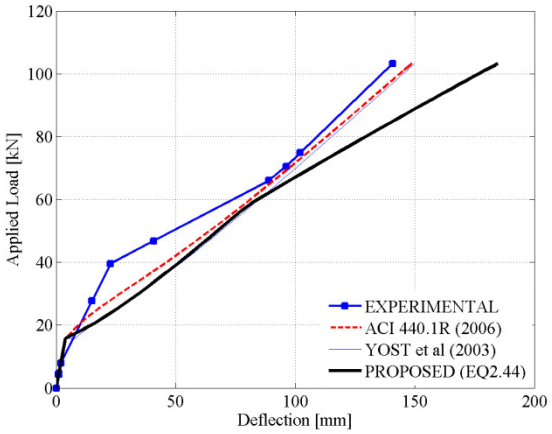

(k) Load-Deflection: H2

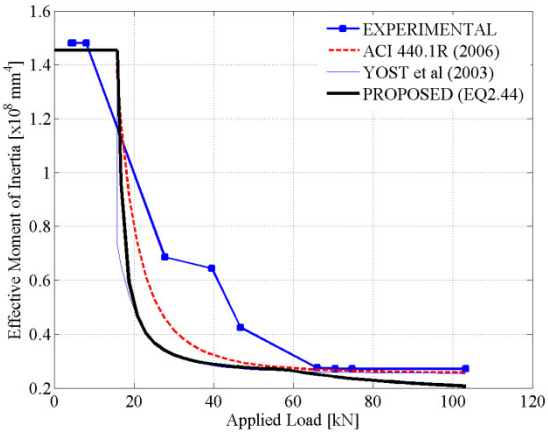

(l) Inertia: H2

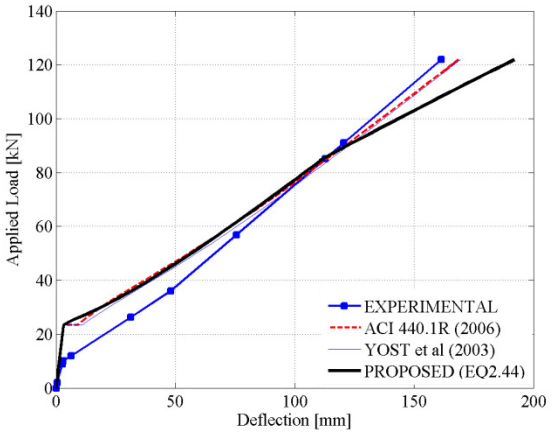

(m) Load-Deflection: H3

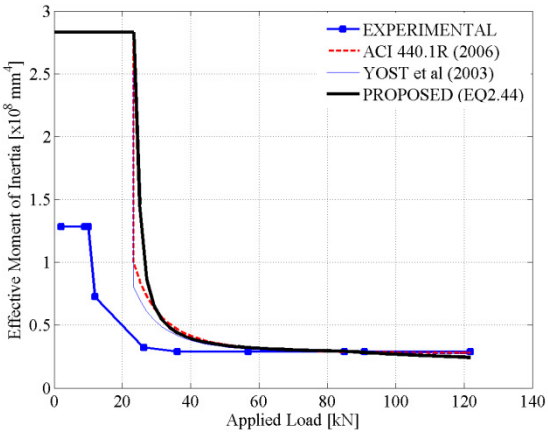

(n) Inertia: H3

Figure A.3 **– Load-Deflection Estimates** [Matthys and Taerwe 1995]

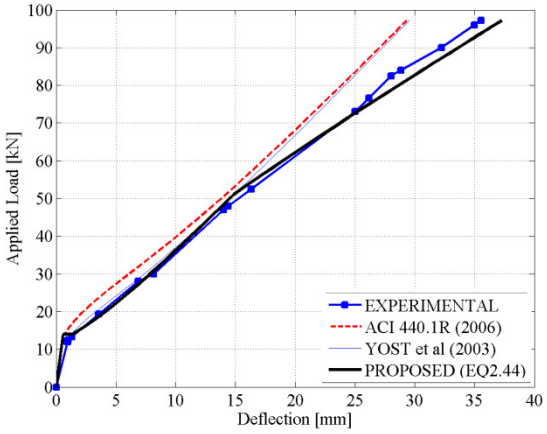

(a) Load-Deflection: GB5

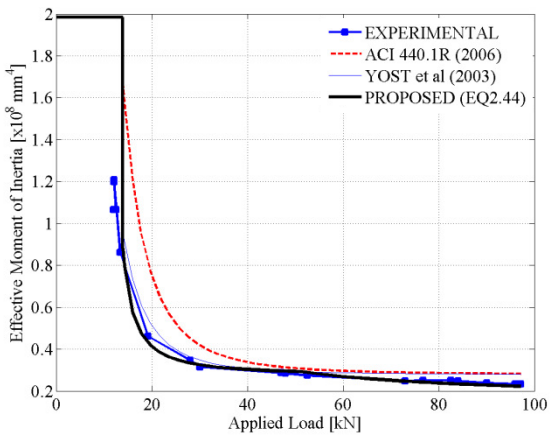

(b) Inertia: GB5

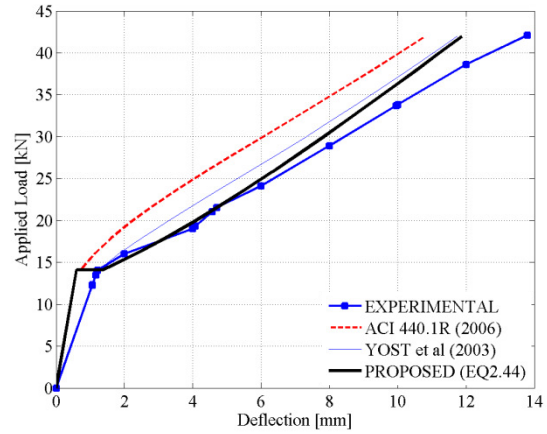

(c) Load-Deflection: GB6

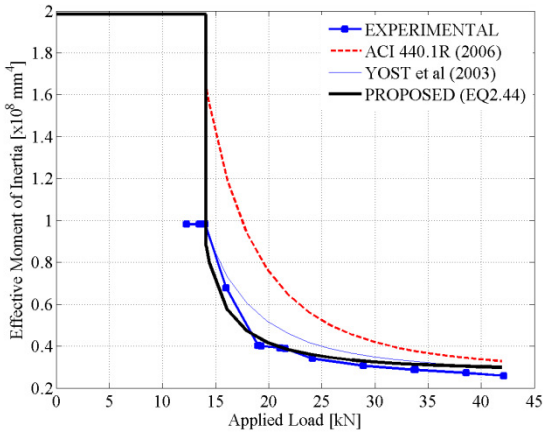

(d) Inertia: GB6

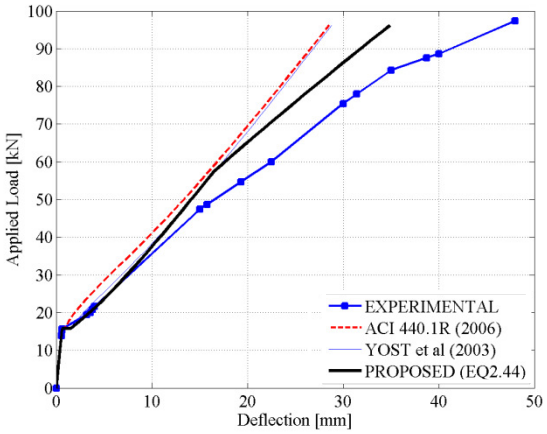

(e) Load-Deflection: GB11

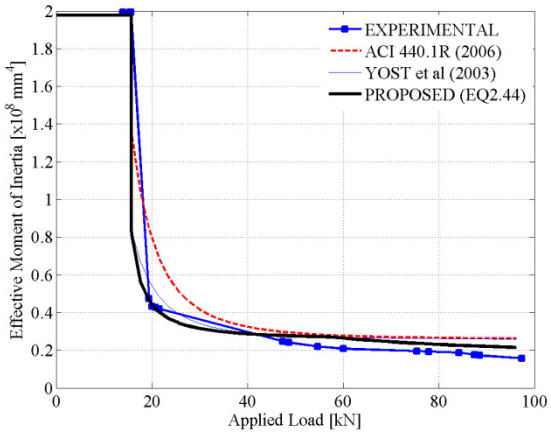

(f) Inertia: GB11

Figure A.4 **– Load-Deflection Estimates** [Zhao et al. 1997]

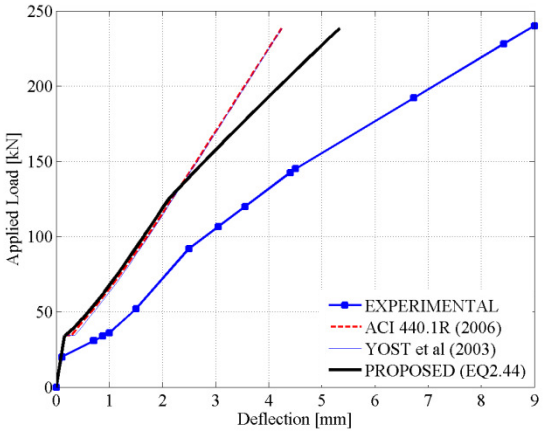

(a) Load-Deflection: NO.18

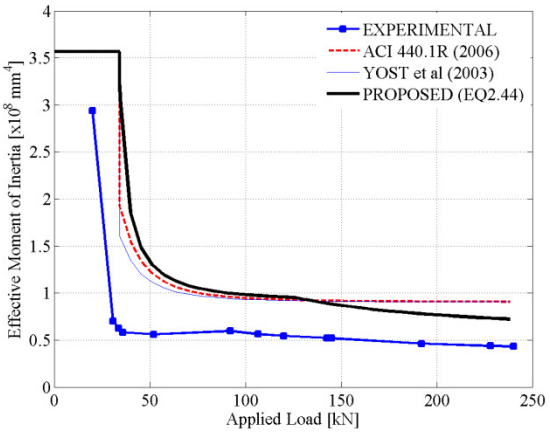

(b) Inertia: NO.18

Figure A.5 **– Load-Deflection Estimates** [Zhao and Maruyama 1995]

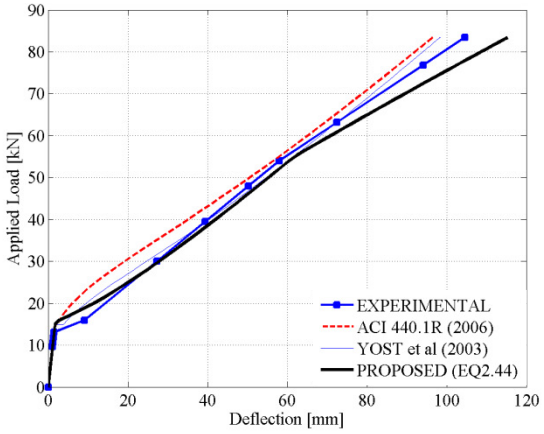

(a) Load-Deflection: C5

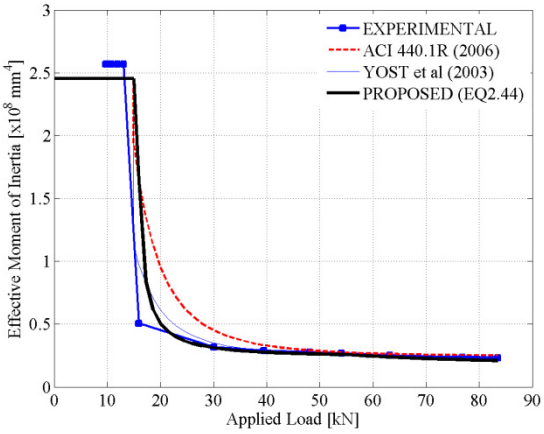

(b) Inertia: C5

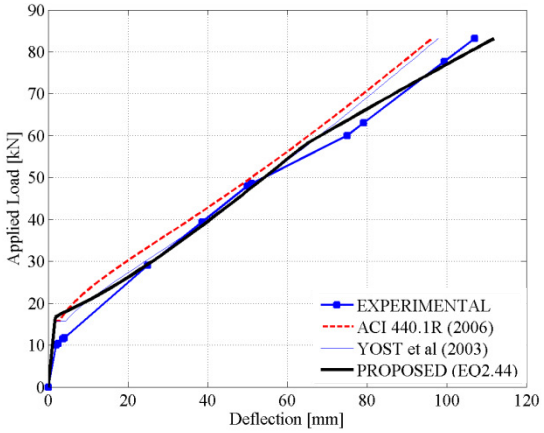

(a) Load-Deflection: F1

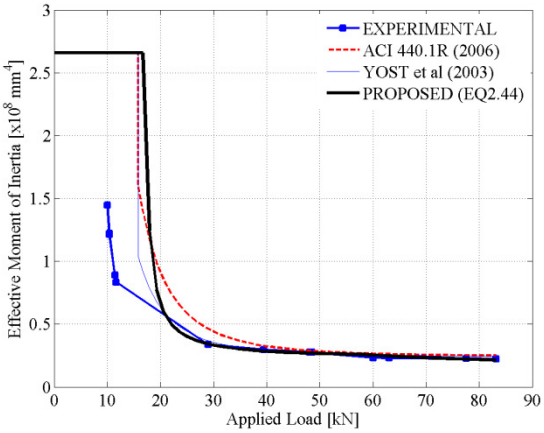

(b) Inertia: F1

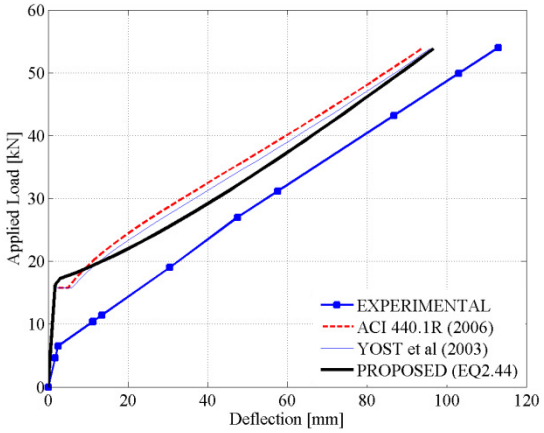

(c) Load-Deflection: F2

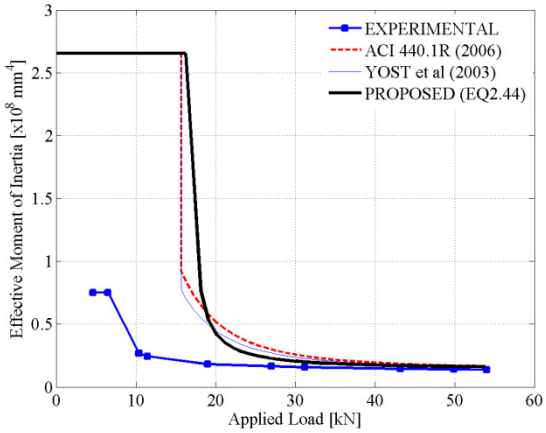

(d) Inertia: F2

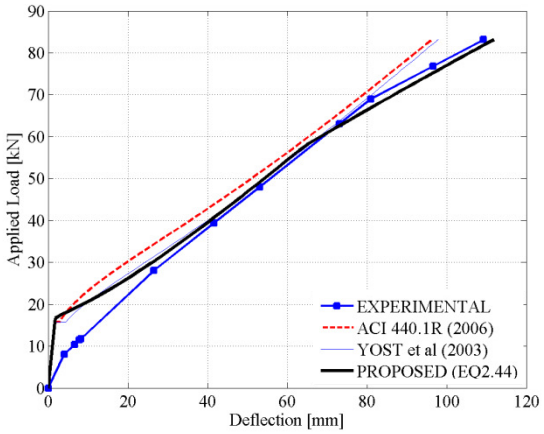

(e) Load-Deflection: F3

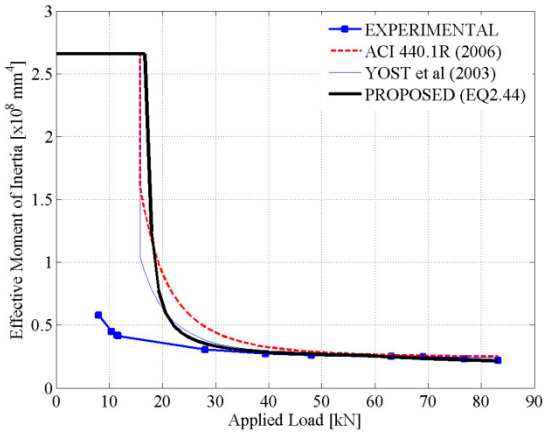

(f) Inertia: F3

Figure A.6 **– Load-Deflection Estimates** [Cosenza et al. 1997]

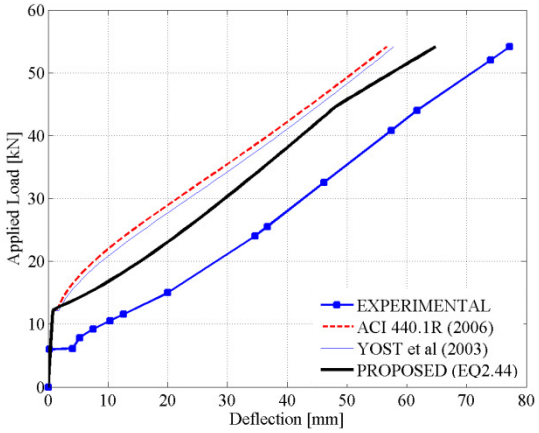

(e) Load-Deflection: C-120-M

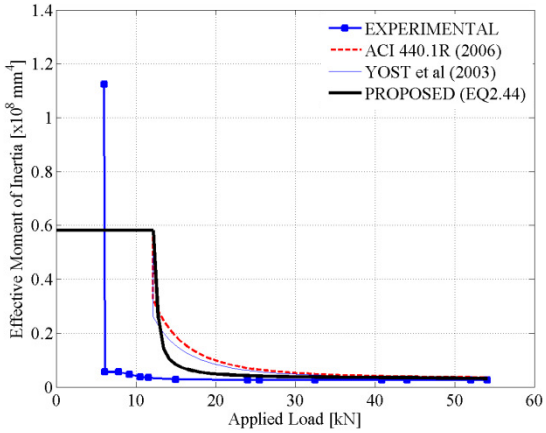

(f) Inertia: C-120-M

Figure A.7 **– Load-Deflection Estimates** [Kobayashi et al. 1997]

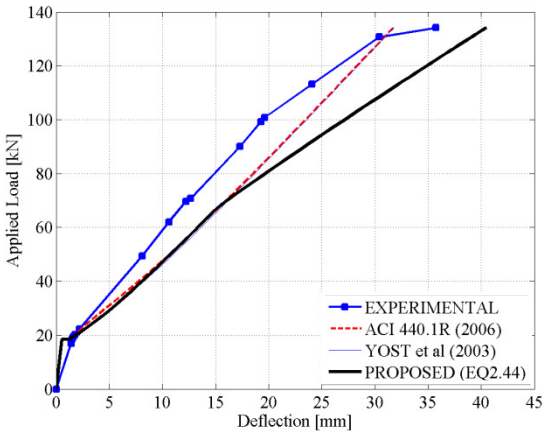

(a) Load-Deflection: F-1-GF

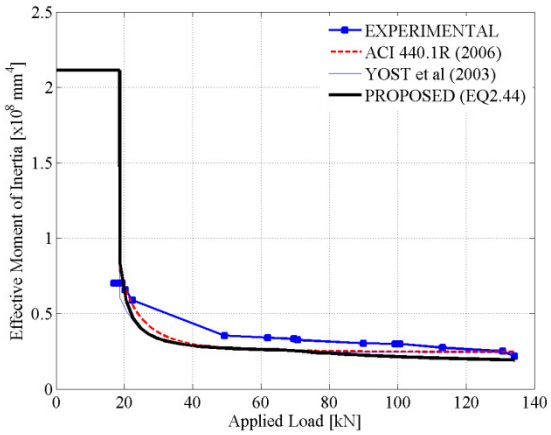

(b) Inertia: F-1-GF

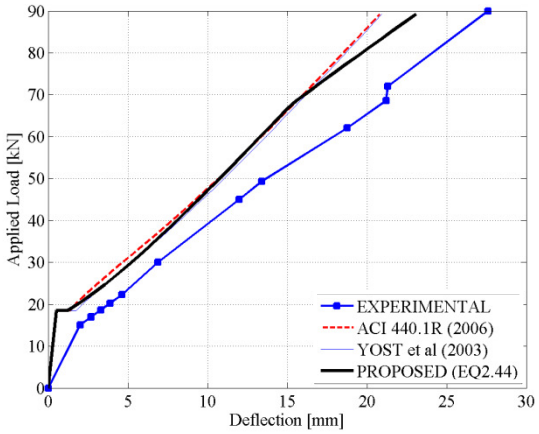

(c) Load-Deflection: F-2-GF

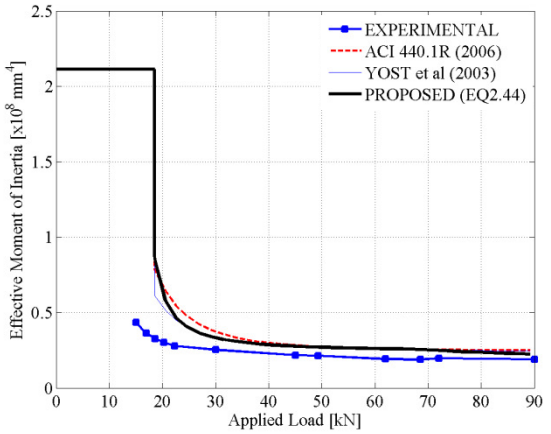

(d) Inertia: F-2-GF

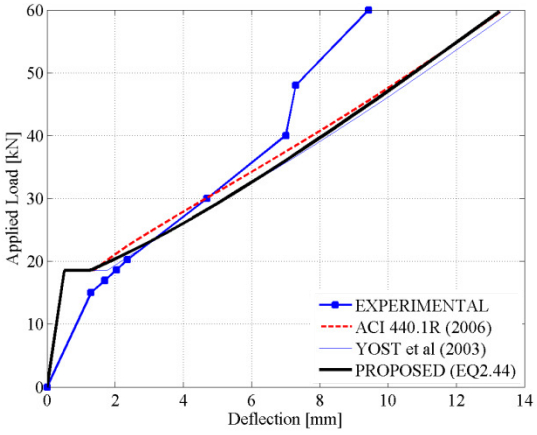

(e) Load-Deflection: F-3-GF

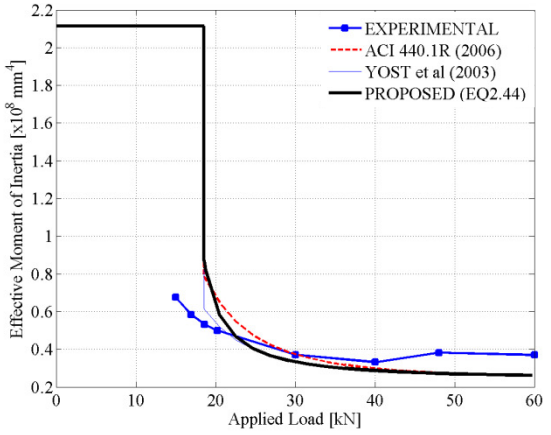

(f) Inertia: F-3-GF

Figure A.8 **– Load-Deflection Estimates** [Swamy and Aburawi 1997]

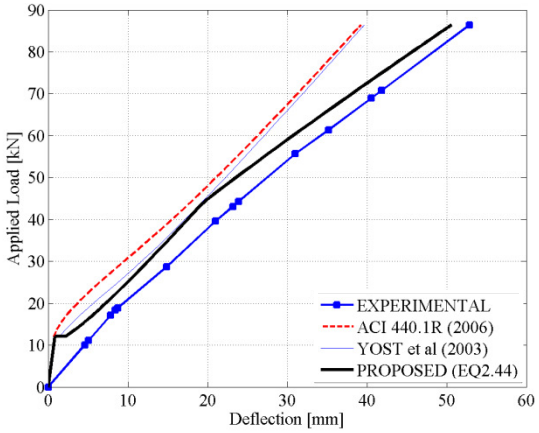

(a) Load-Deflection: BF9

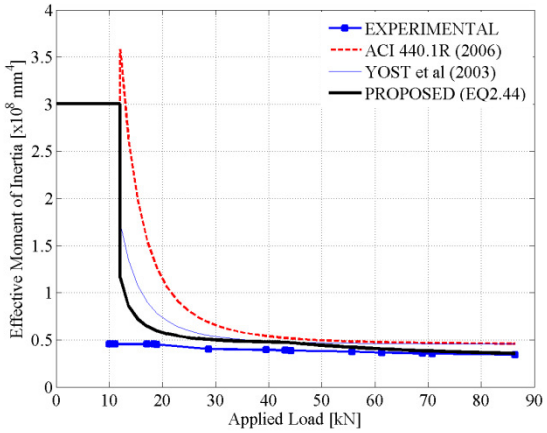

(b) Inertia: BF9

Figure A.9 **– Load-Deflection Estimates** [Nawy and Neuwerth 1997]

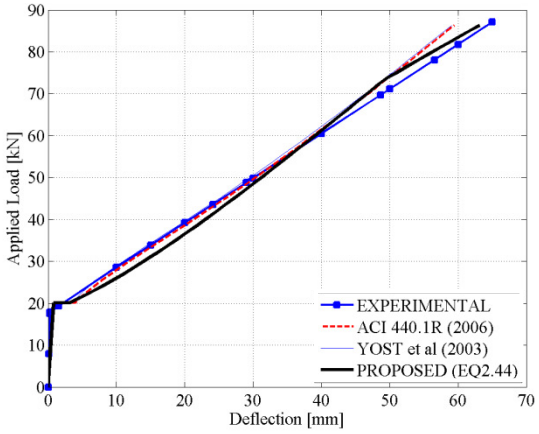

(a) Load-Deflection: CB2B

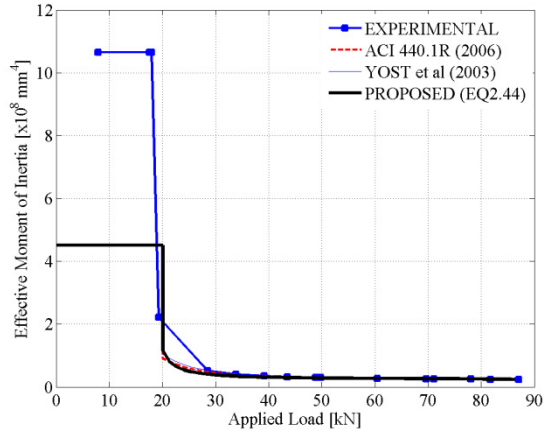

(b) Inertia: CB2B

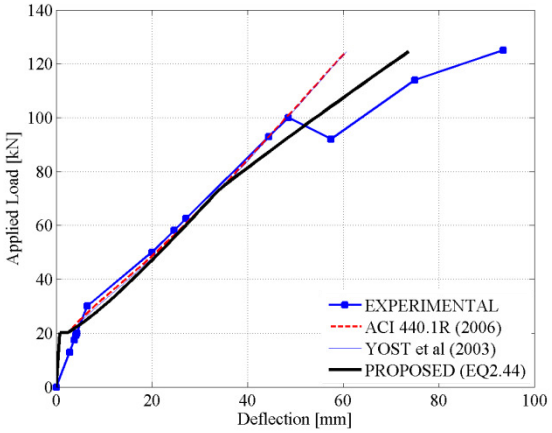

(c) Load-Deflection: CB3B

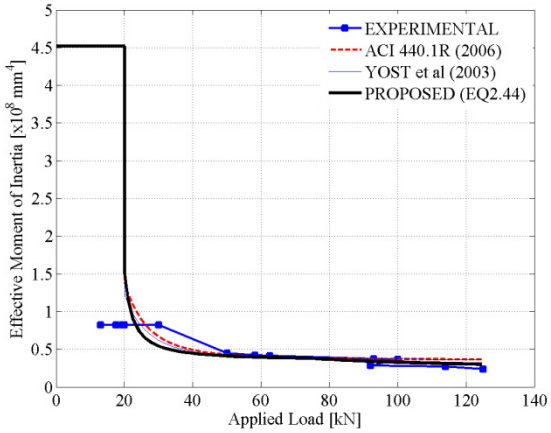

(d) Inertia: CB3B

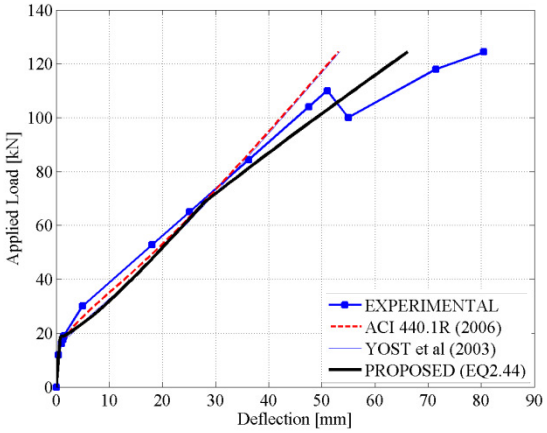

(e) Load-Deflection: CB4B

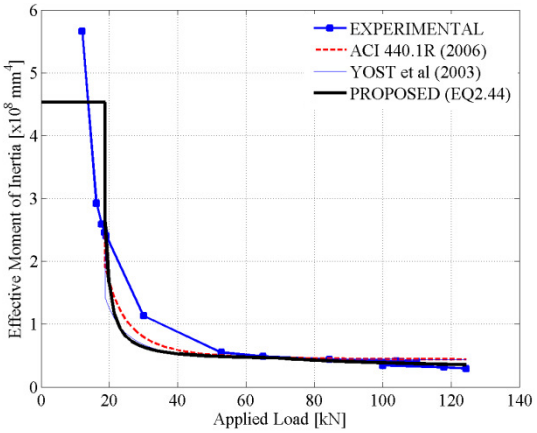

(f) Inertia: CB4B

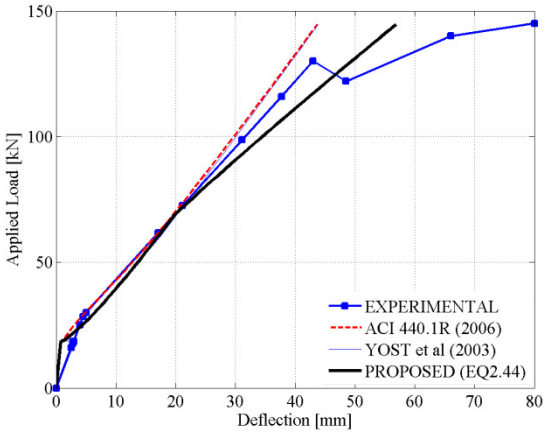

(g) Load-Deflection: CB6B

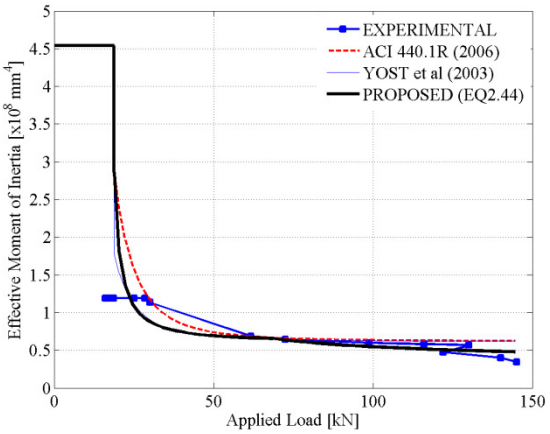

(h) Inertia: CB6B

Figure A.10 **– Load-Deflection Estimates** [Benmokrane and Masmoudi 1996]

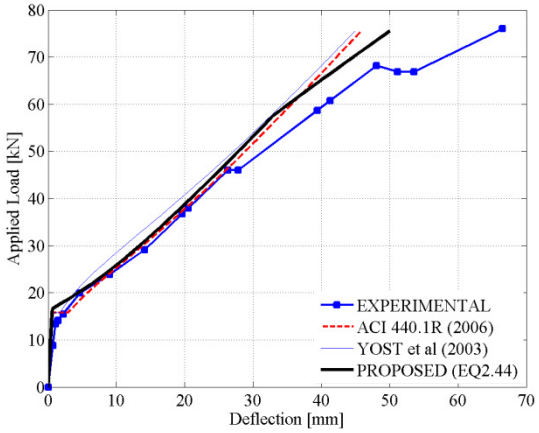

(a) Load-Deflection: FRP-1

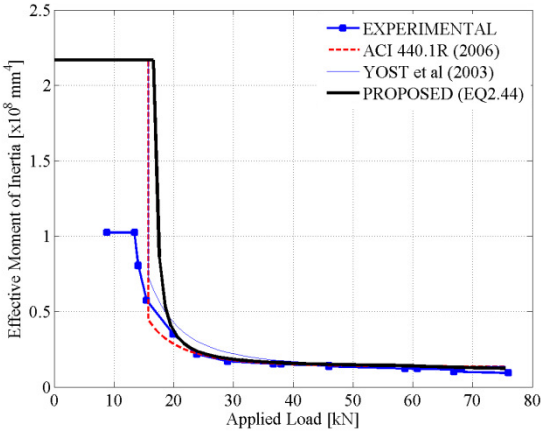

(b) Inertia: FRP-1

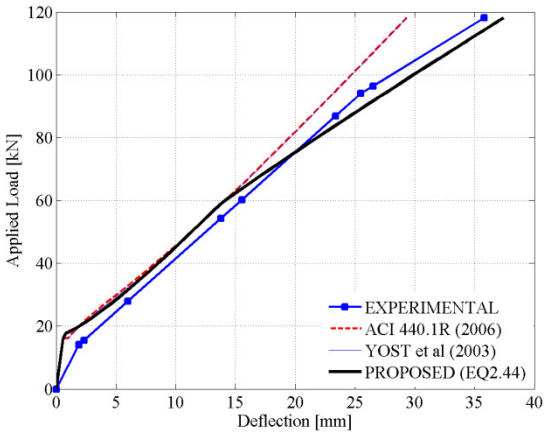

(c) Load-Deflection: FRP-3

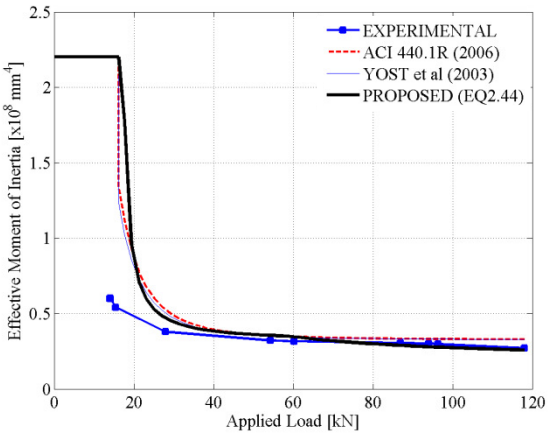

(d) Inertia: FRP-3

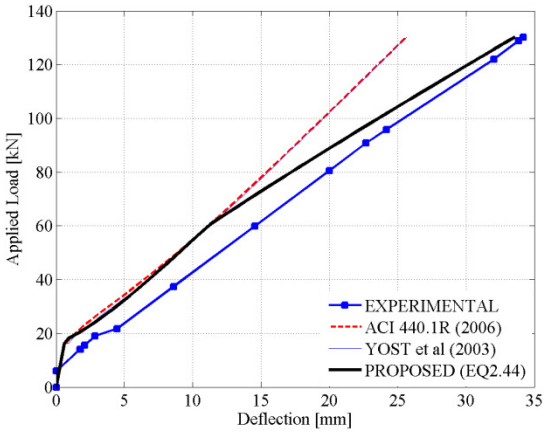

(e) Load-Deflection: FRP-4

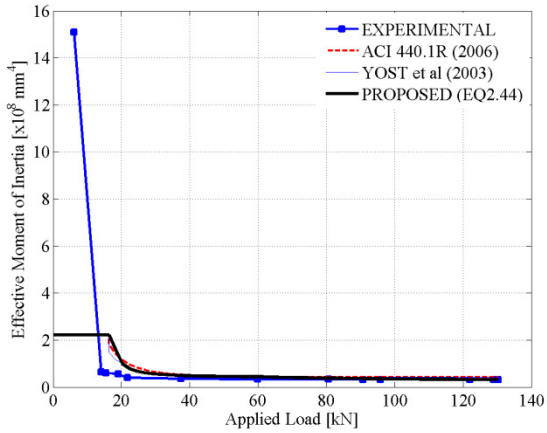

(f) Inertia: FRP-4

Figure A.11 **– Load-Deflection Estimates** [Svecova and Fernando 2001]

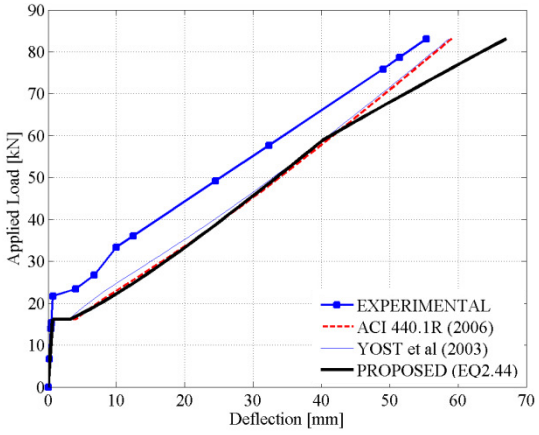

(a) Load-Deflection: GB1

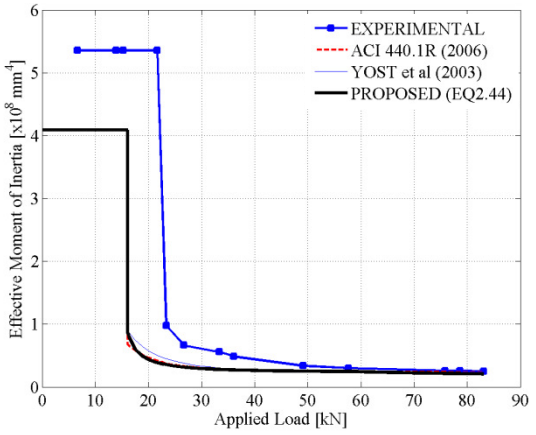

(b) Inertia: GB1

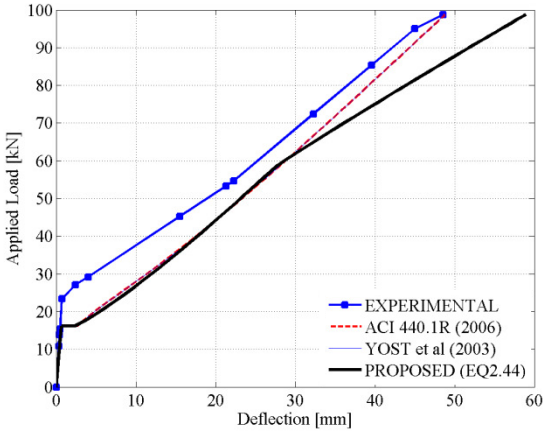

(c) Load-Deflection: GB2

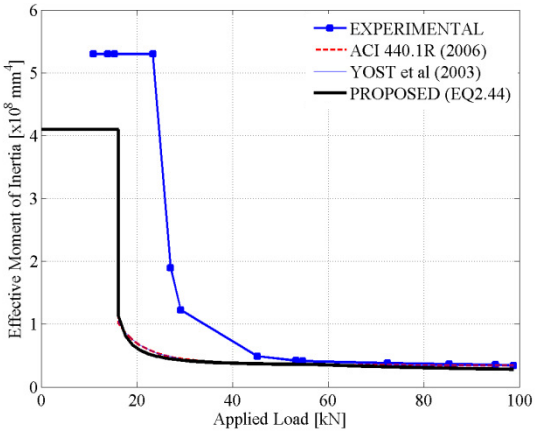

(d) Inertia: GB2

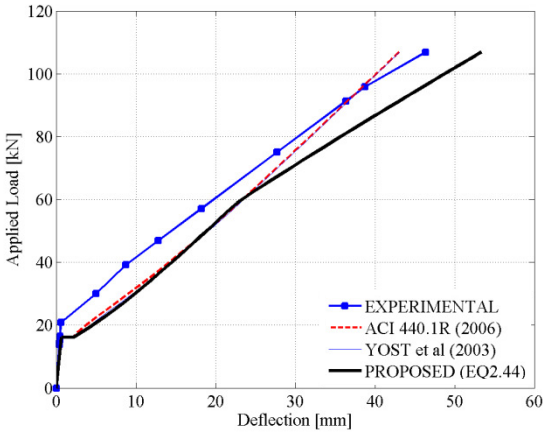

(e) Load-Deflection: GB3

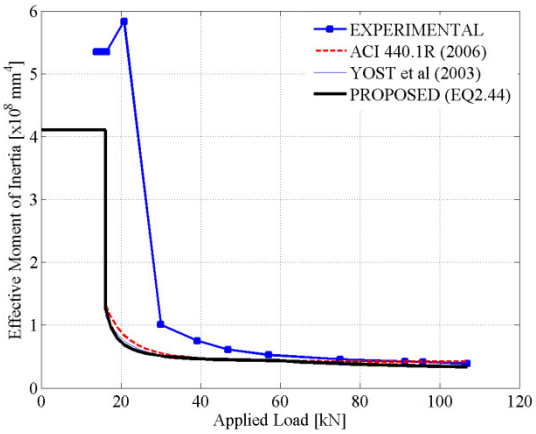

(f) Inertia: GB3

Figure A.12 **– Load-Deflection Estimates** [Toutanji and Saafi 2000]

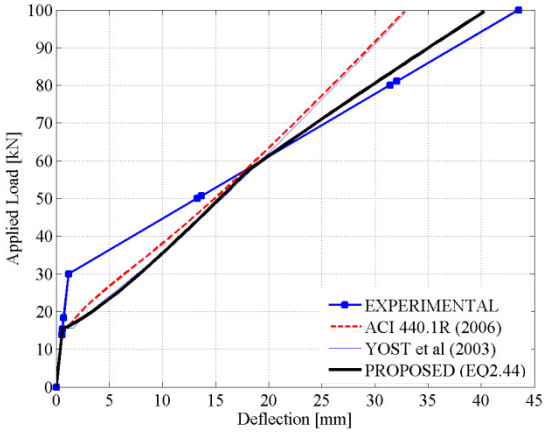

(a) Load-Deflection: GB10

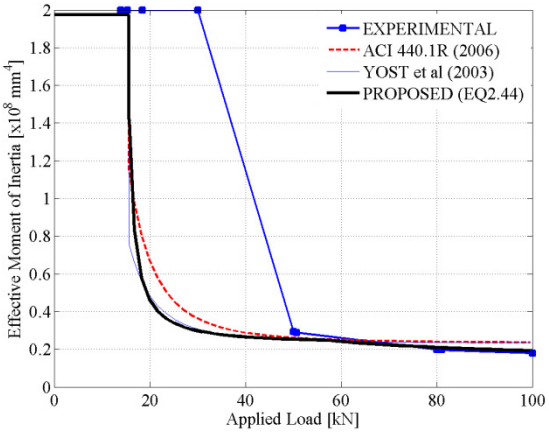

(b) Inertia: GB10

Figure A.13 **– Load-Deflection Estimates** [Duranovic et al. 1997]

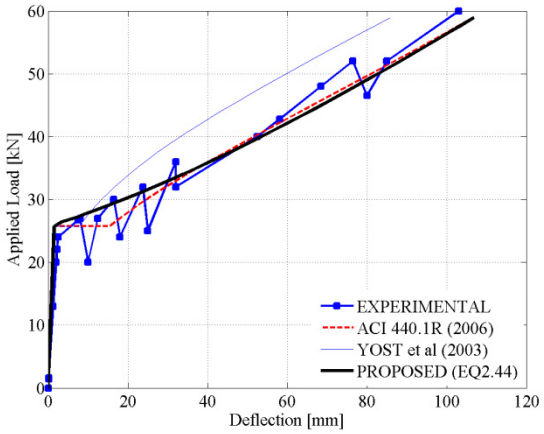

(a) Load-Deflection: I-150-A

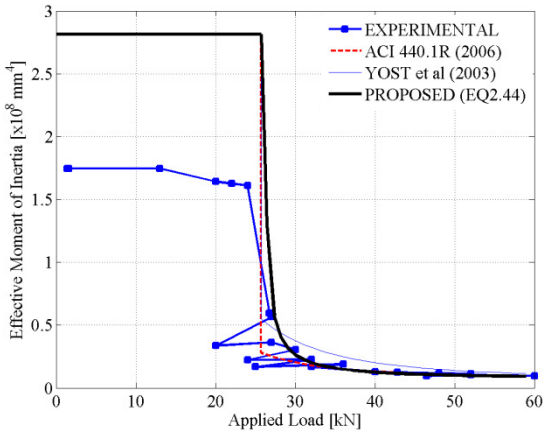

(b) Inertia: I-150-A

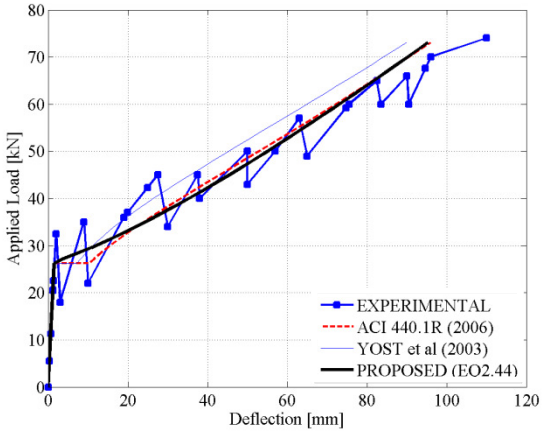

(c) Load-Deflection: I-150-B

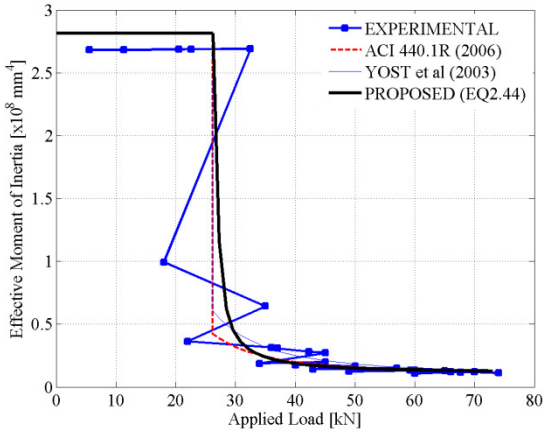

(d) Inertia: I-150-B

Figure A.14 **– Load-Deflection Estimates** [Abdalla and El-Badry 1996]

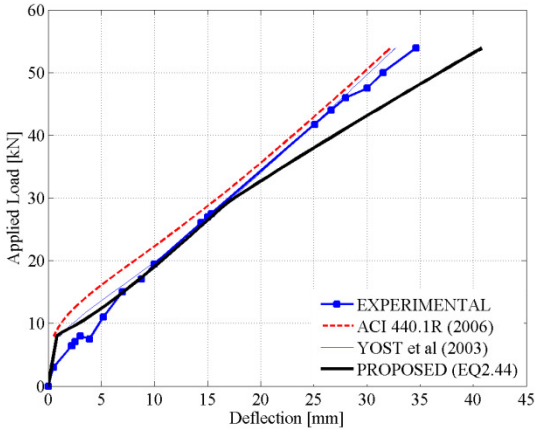

(a) Load-Deflection: II

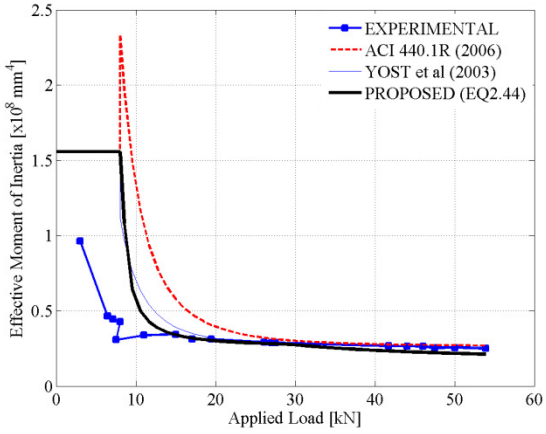

(b) Inertia: II

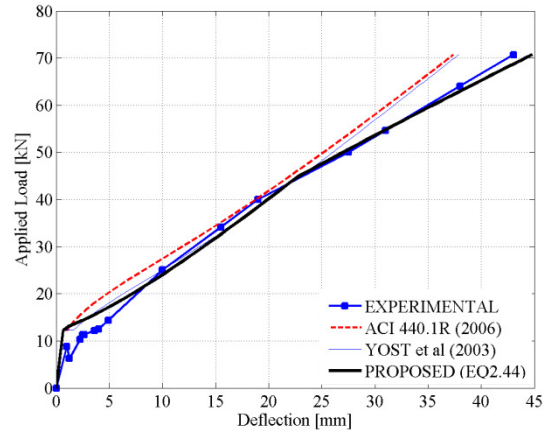

(c) Load-Deflection: III

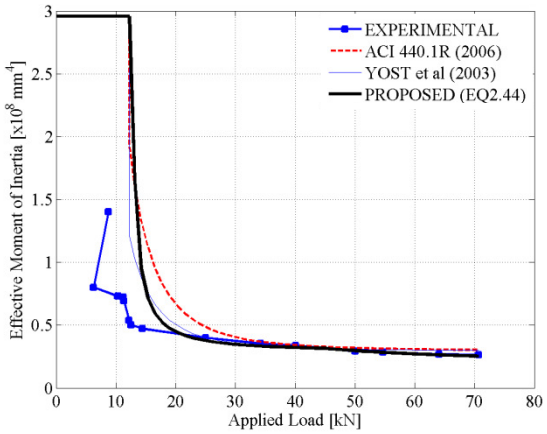

(d) Inertia: III

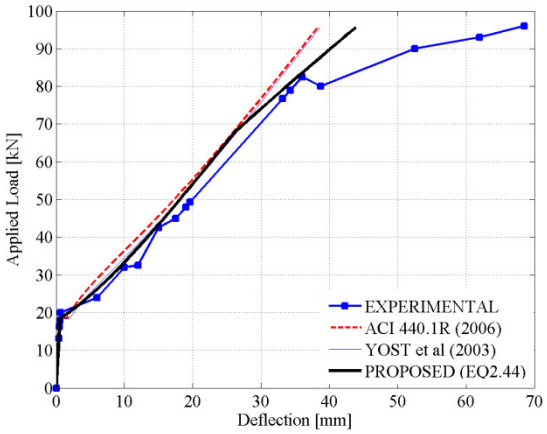

(e) Load-Deflection: IV

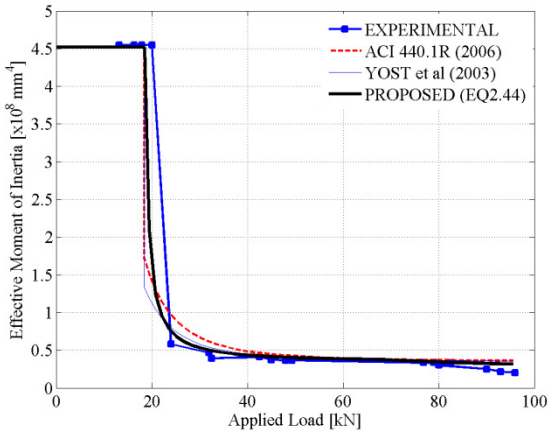

(f) Inertia: IV

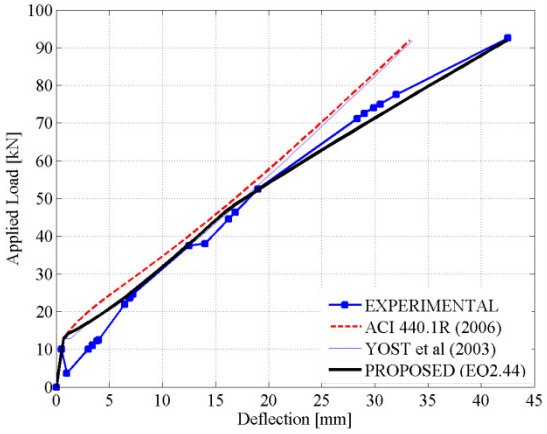

(g) Load-Deflection: V

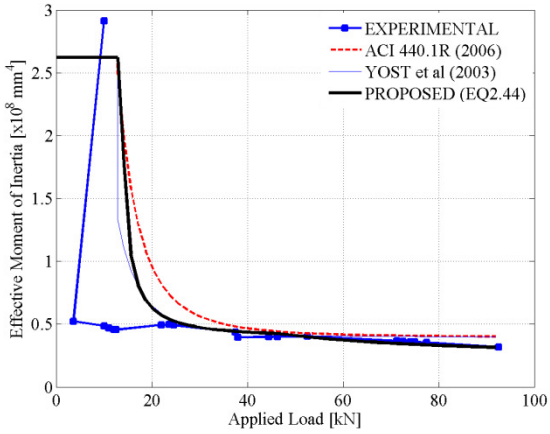

(h) Inertia: V

Figure A.15 **– Load-Deflection Estimates** [Al-Salloum et al. 1996]

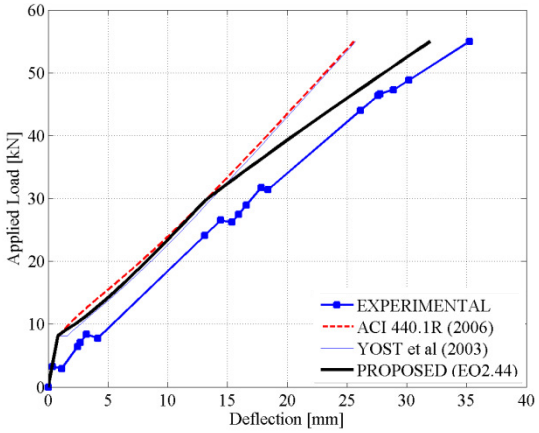

(a) Load-Deflection: Group II

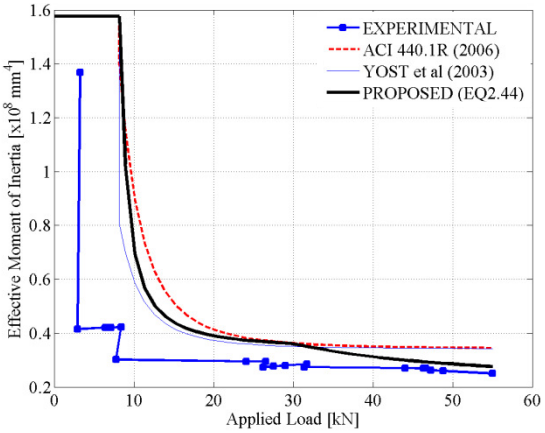

(b) Inertia: Group II

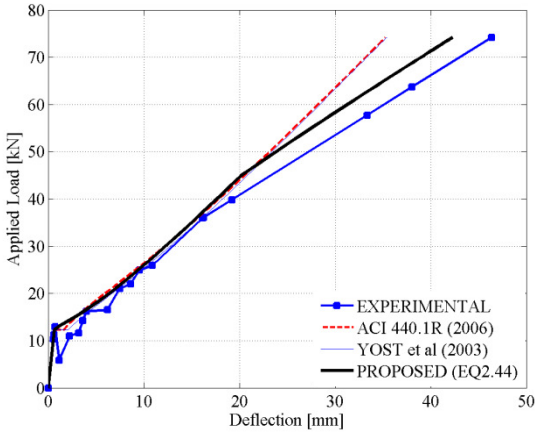

(c) Load-Deflection: Group III

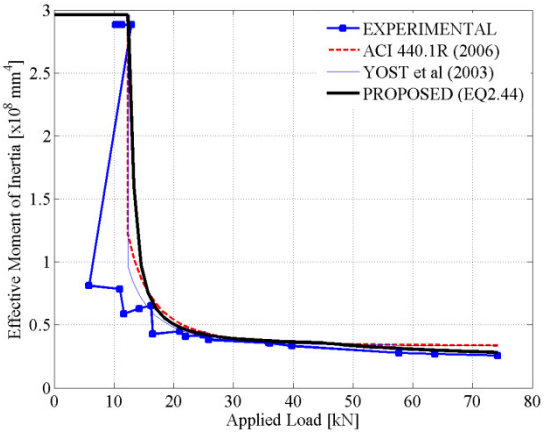

(d) Inertia: Group III

Figure A.16 **– Load-Deflection Estimates** [Alsayed et al. 1995]

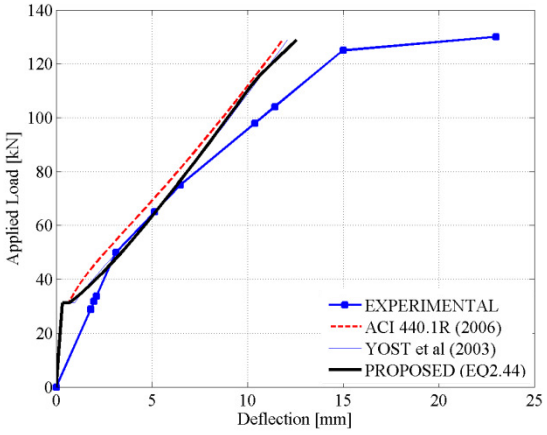

(a) Load-Deflection: Group B

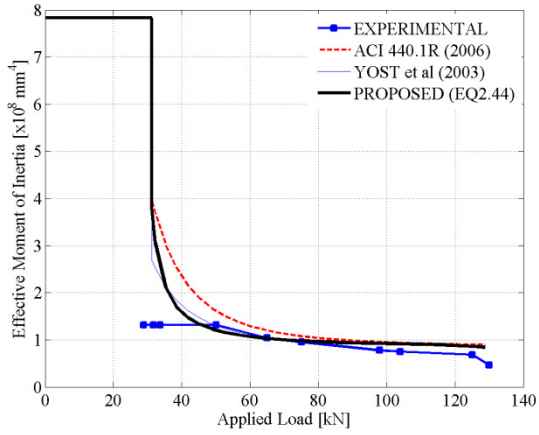

(b) Inertia: Group B

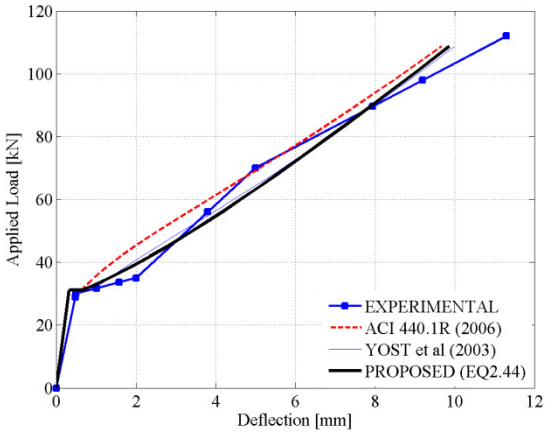

(c) Load-Deflection: Group D

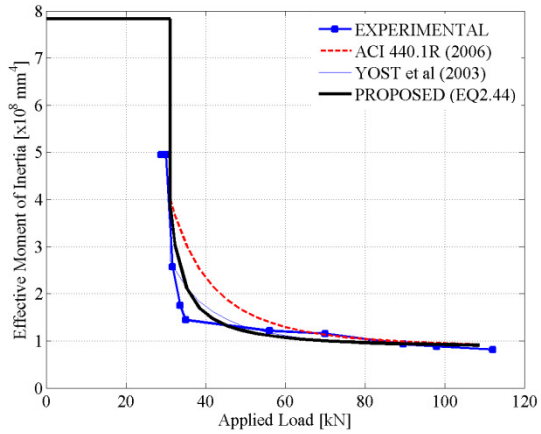

(d) Inertia: Group D

Figure A.17 **– Load-Deflection Estimates** [Alsayed et al. 1996]

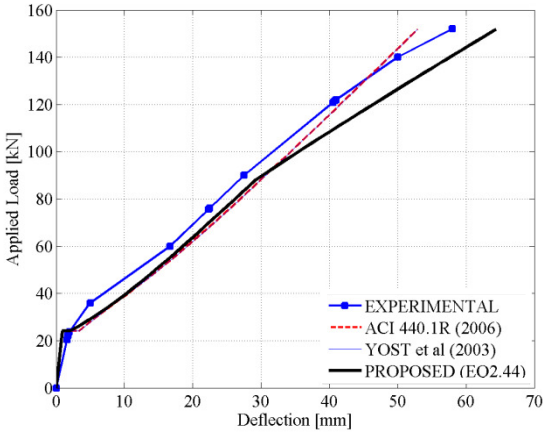

(a) Load-Deflection: ISO1-2

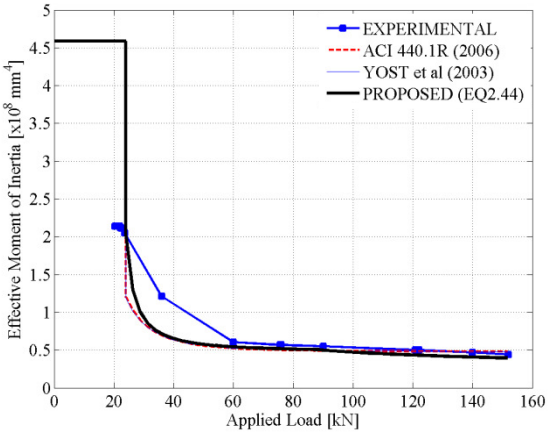

(b) Inertia: ISO1-2

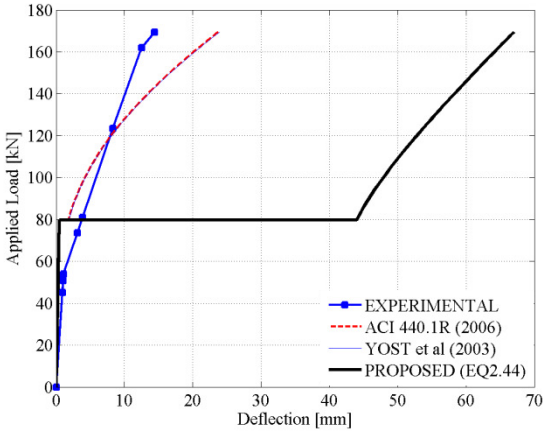

(c) Load-Deflection: ISO3-4

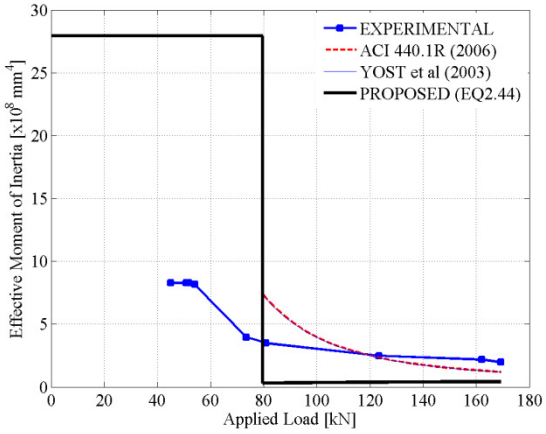

(d) Inertia: ISO3-4

Figure A.18 **– Load-Deflection Estimates** [Benmokrane et al. 1996]

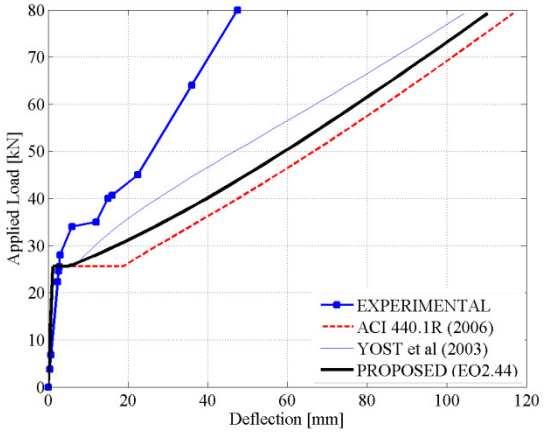

(a) Load-Deflection: LG0.5-1

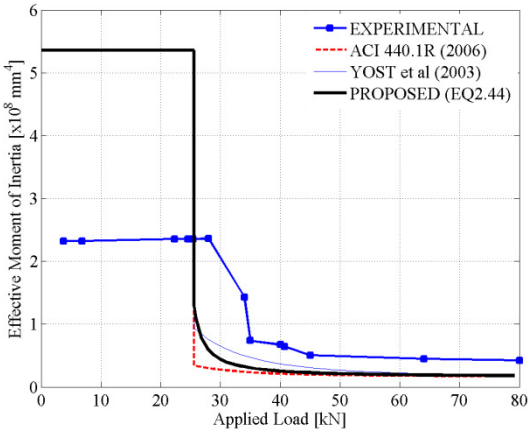

(b) Inertia: LG0.5-1

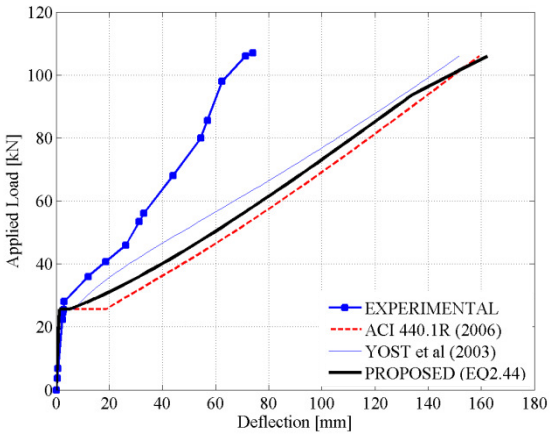

(c) Load-Deflection: LG0.5-2

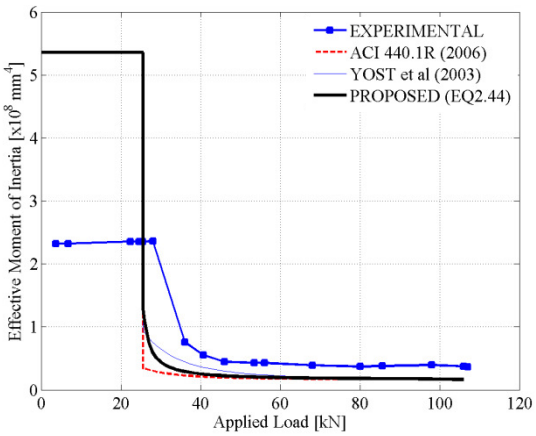

(d) Inertia: LG0.5-2

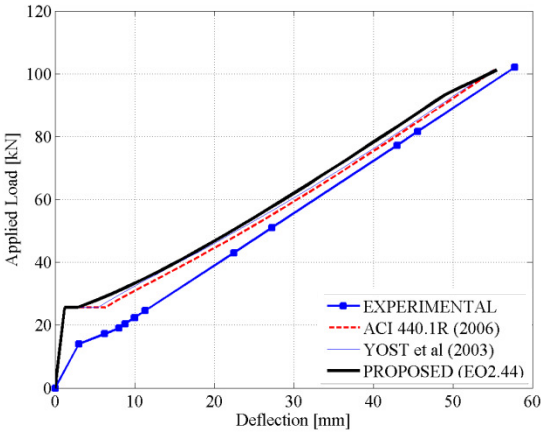

(e) Load-Deflection: LG1.5-1

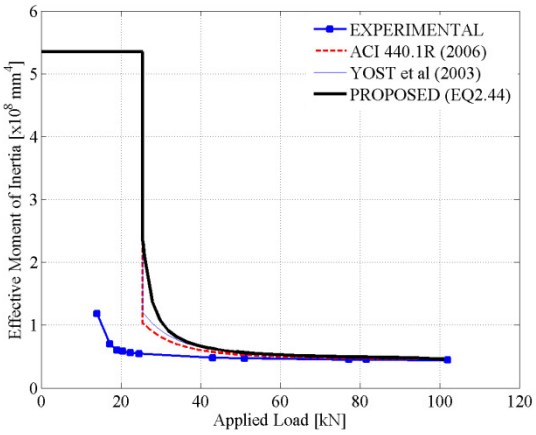

(f) Inertia: LG1.5-1

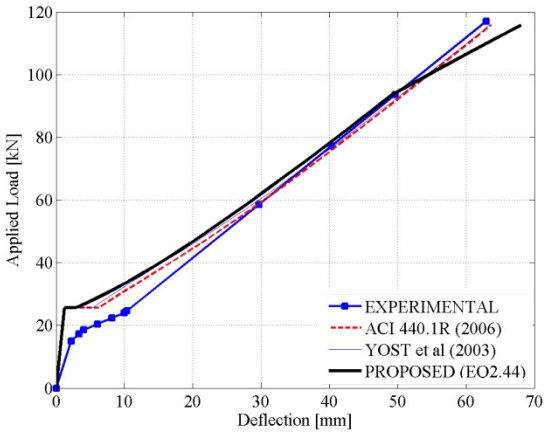

(g) Load-Deflection: LG1.5-2

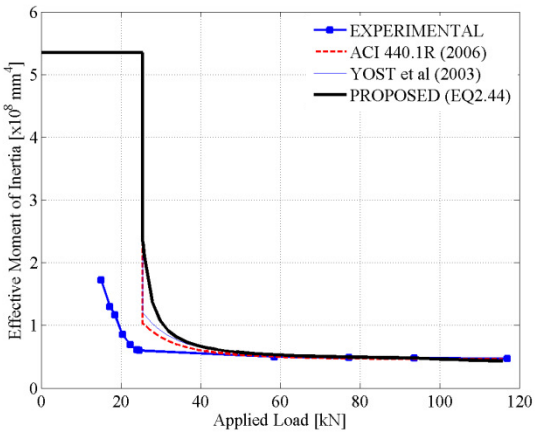

(h) Inertia: LG1.5-2

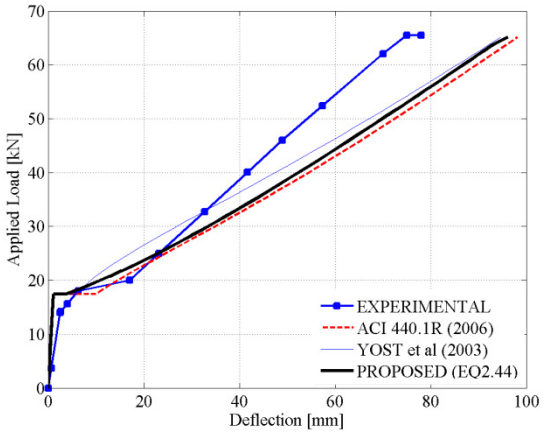

(i) Load-Deflection: NG0.5-1

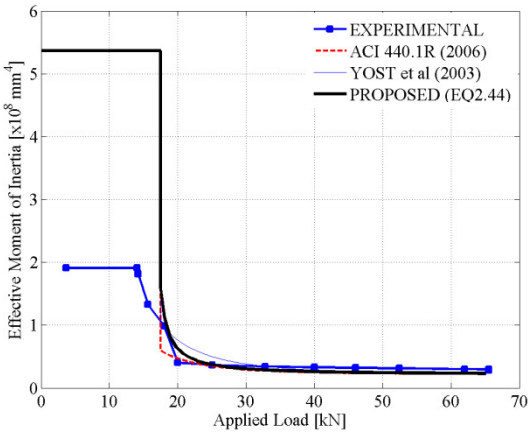

(j) Inertia: NG0.5-1

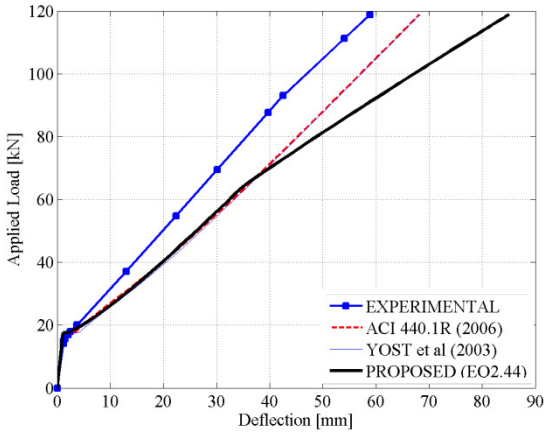

(k) Load-Deflection: NG1.5-1

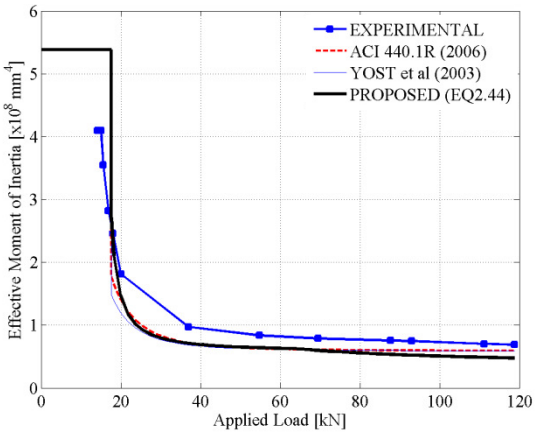

(l) Inertia: NG1.5-1

Figure A.19 **– Load-Deflection Estimates** [Jawara 1999]

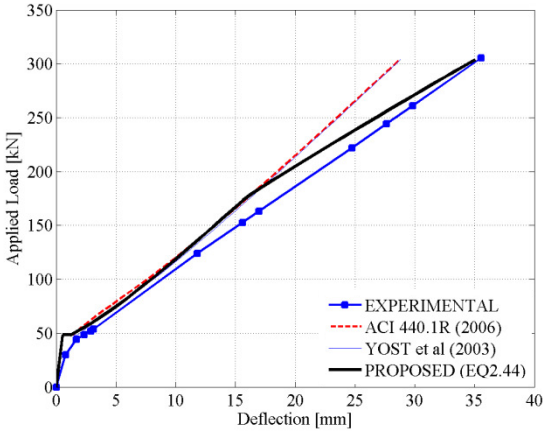

(a) Load-Deflection: D3#4

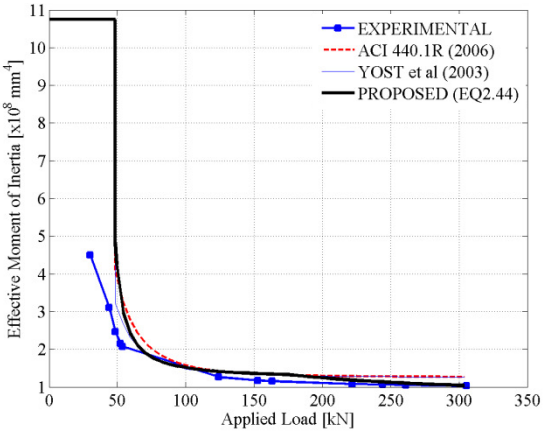

(b) Inertia: D3#4

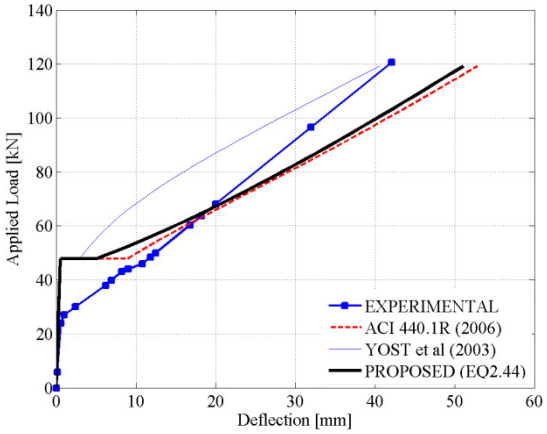

(c) Load-Deflection: D3#5

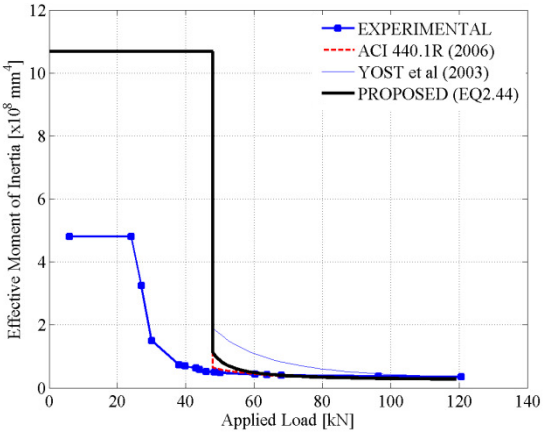

(d) Inertia: D3#5

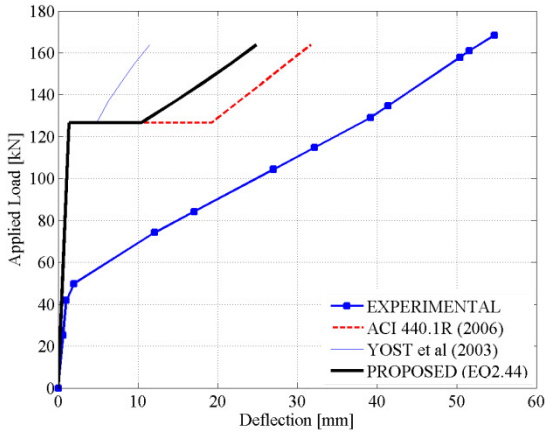

(e) Load-Deflection: 3A

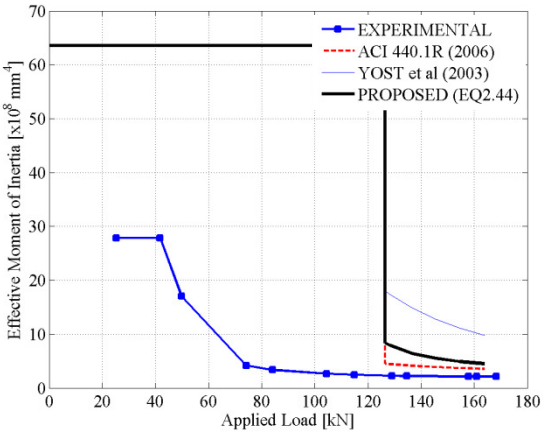

(f) Inertia: 3A

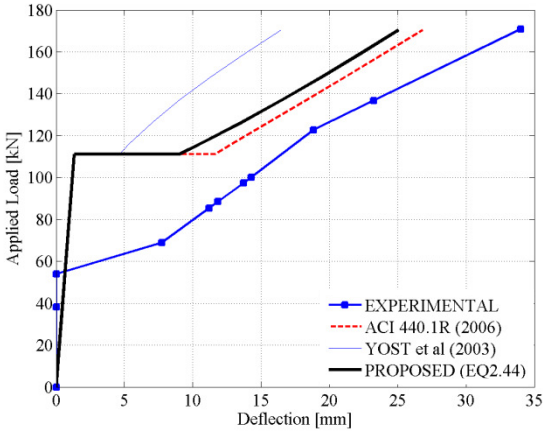

(g) Load-Deflection: 4L-A

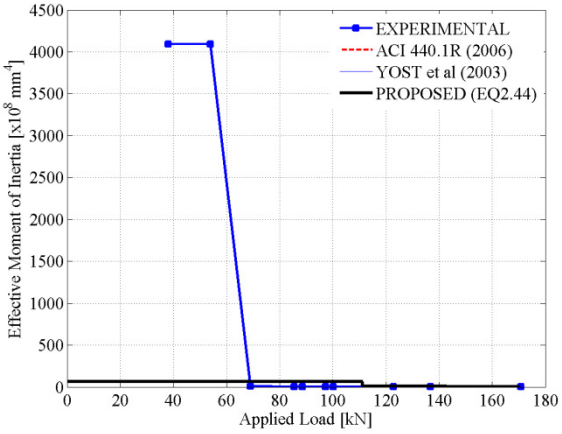

(h) Inertia: 4L-A

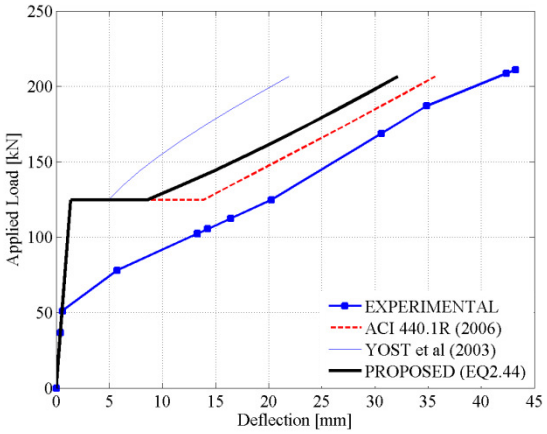

(i) Load-Deflection: 4L-B

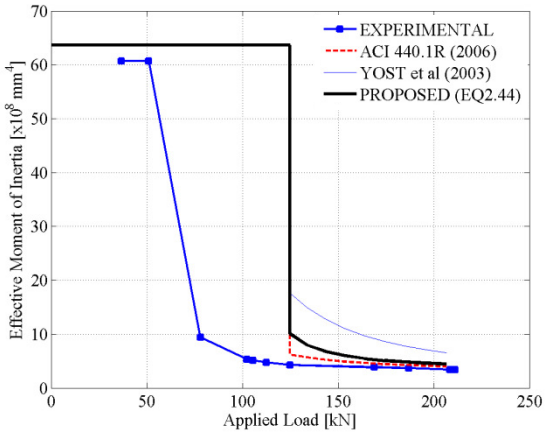

(j) Inertia: 4L-B

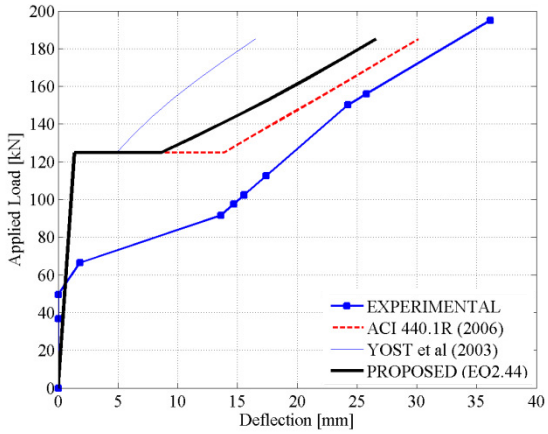

(k) Load-Deflection: 4L-C

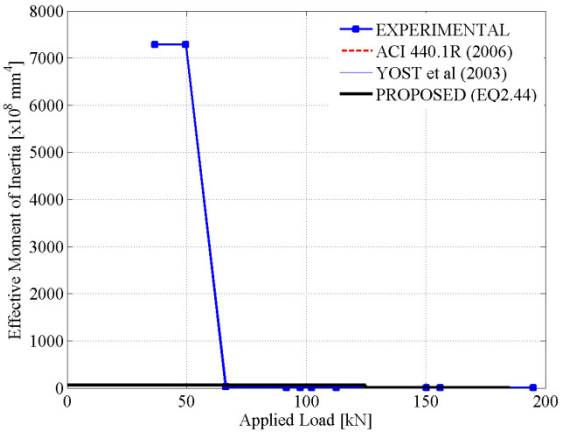

(l) Inertia: 4L-C

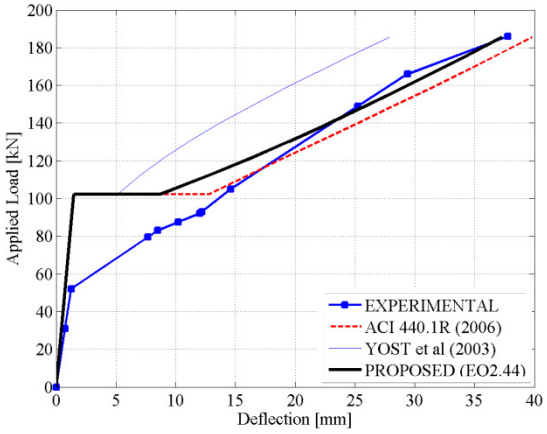

(m) Load-Deflection: 4L-D

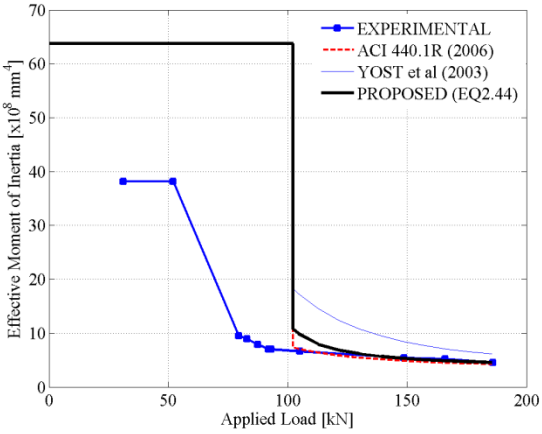

(n) Inertia: 4L-D

Figure A.20 **– Load-Deflection Estimates** [Mota 2004]

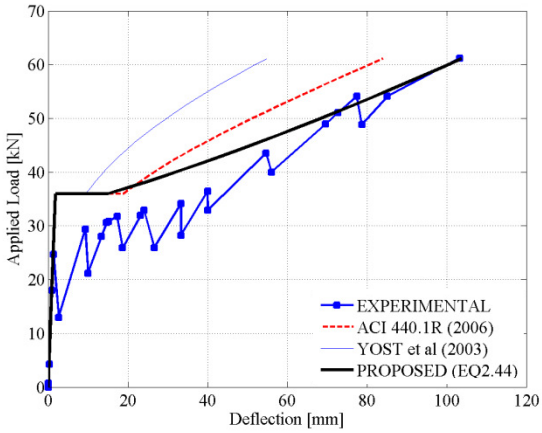

(a) Load-Deflection: I-150A

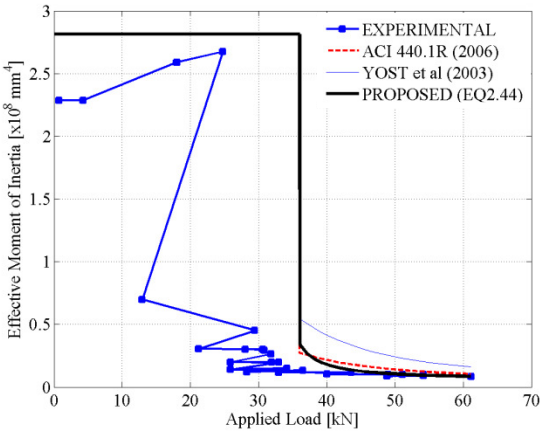

(b) Inertia: I-150A

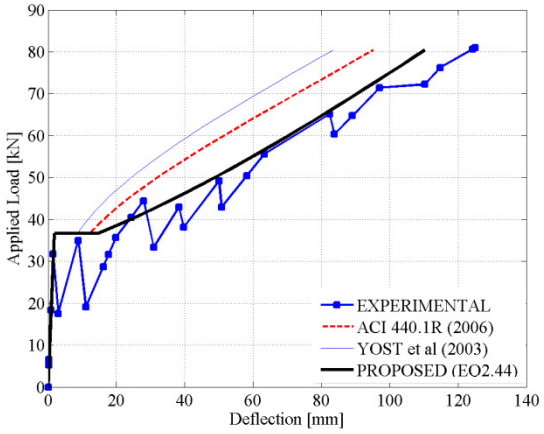

(c) Load-Deflection: I-150B

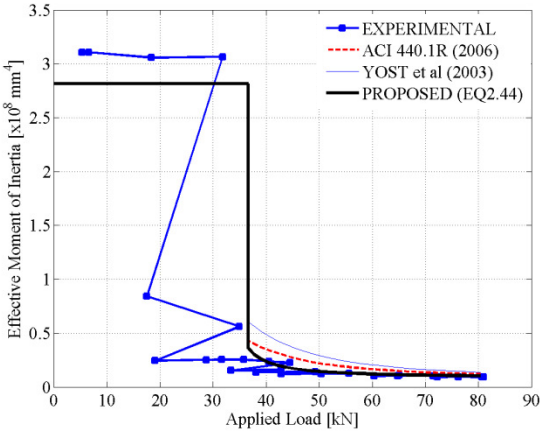

(d) Inertia: I-150B

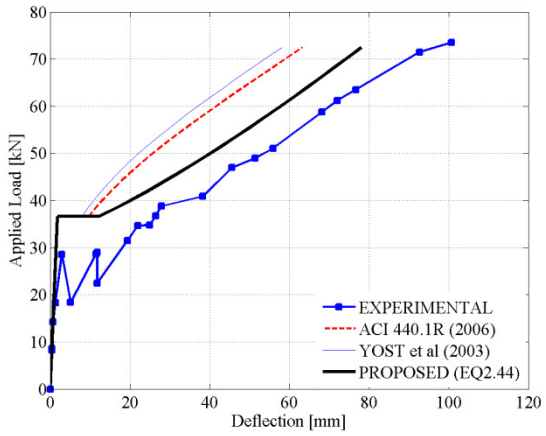

(e) Load-Deflection: I-150C

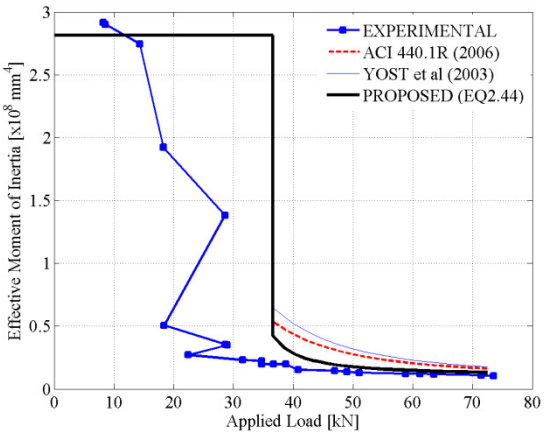

(f) Inertia: I-150C

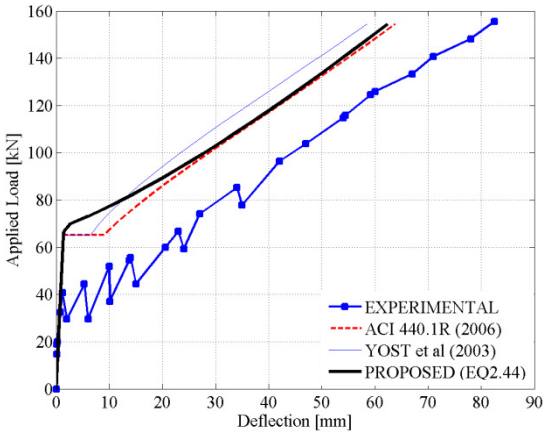

(g) Load-Deflection: I-200C

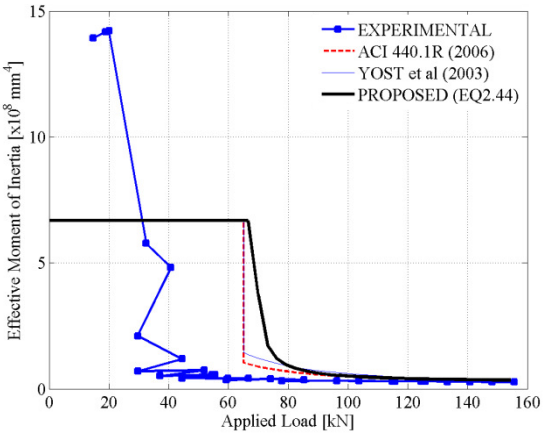

(h) Inertia: I-200C

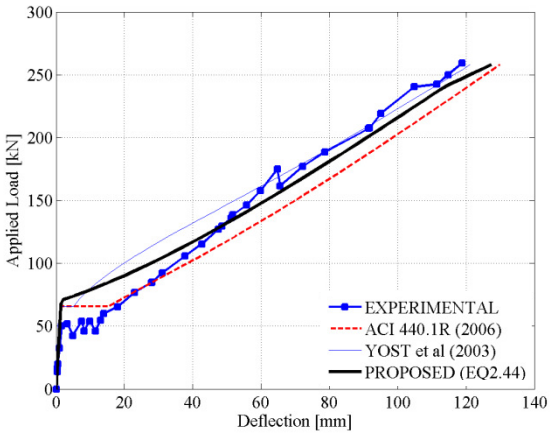

(i) Load-Deflection: LL-200C

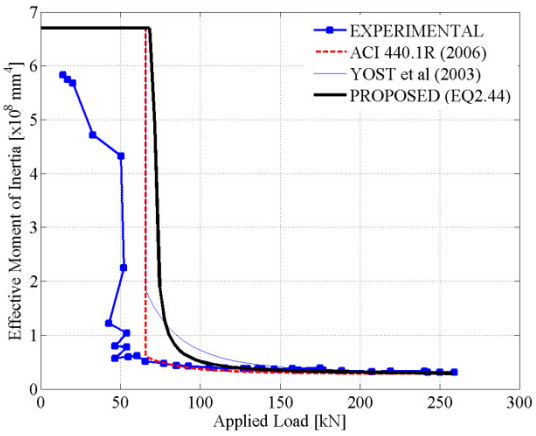

(j) Inertia: LL-200C

Figure A.21 **– Load-Deflection Estimates** [Michaluk 1995]

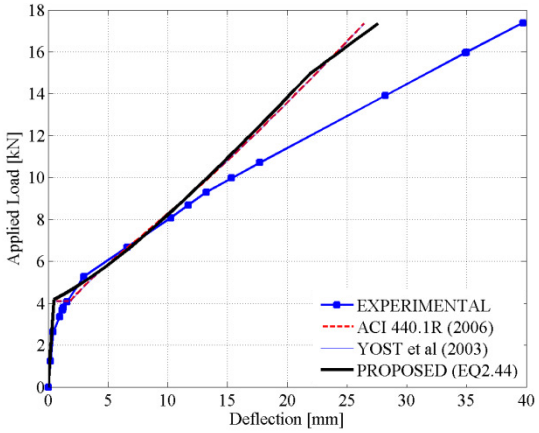

(a) Load-Deflection: D1

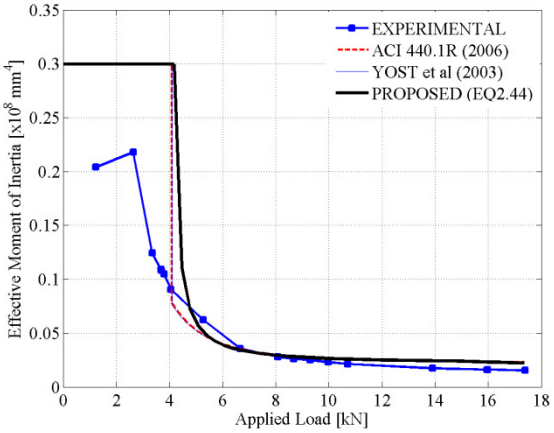

(b) Inertia: D1

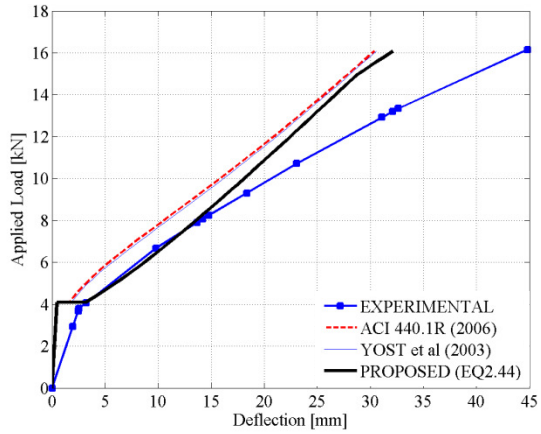

(c) Load-Deflection: D2

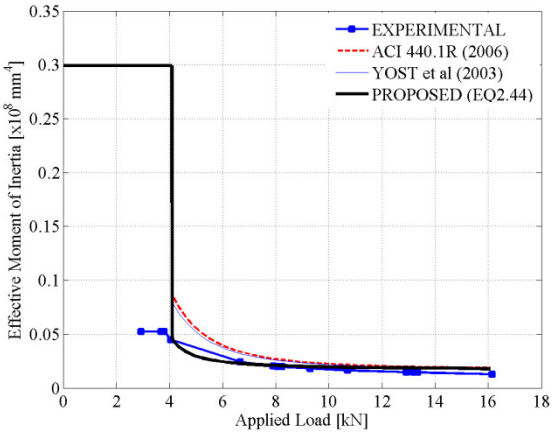

(d) Inertia: D2

Figure A.22 **– Load-Deflection Estimates** [Brown and Bartholomew 1996]

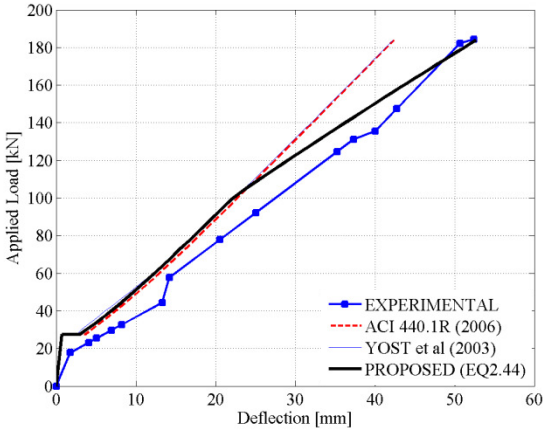

(a) Load-Deflection: IS-4

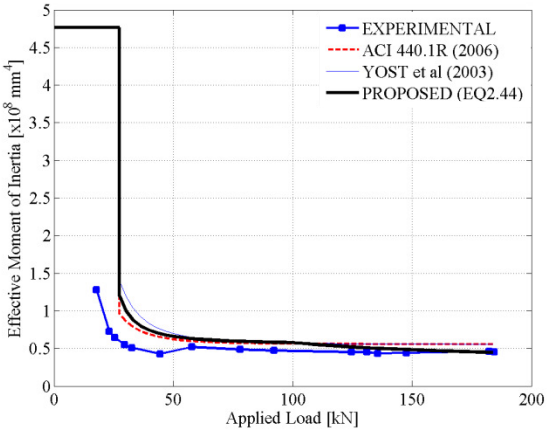

(b) Inertia: IS-4

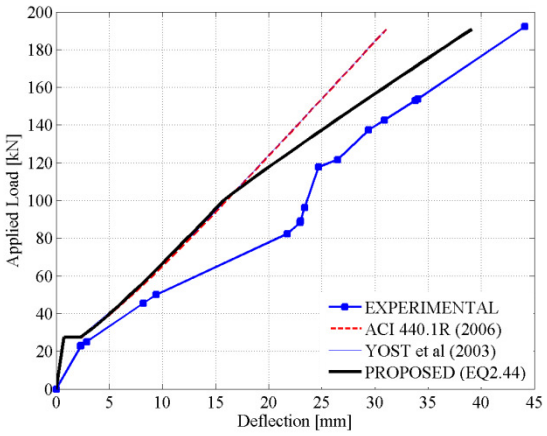

(c) Load-Deflection: IS-6

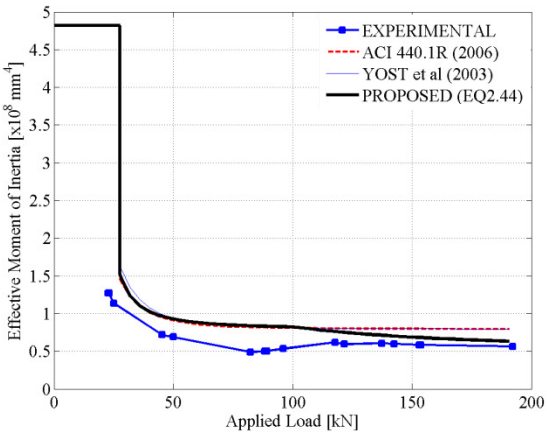

(d) Inertia: IS-6

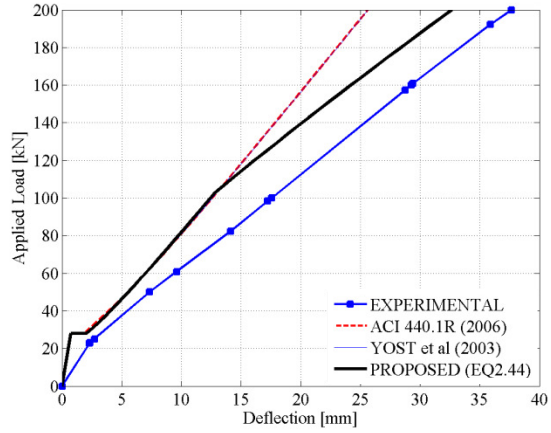

(e) Load-Deflection: IS-8

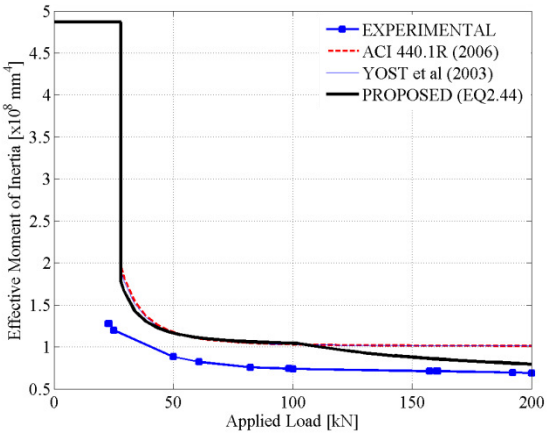

(f) Inertia: IS-8

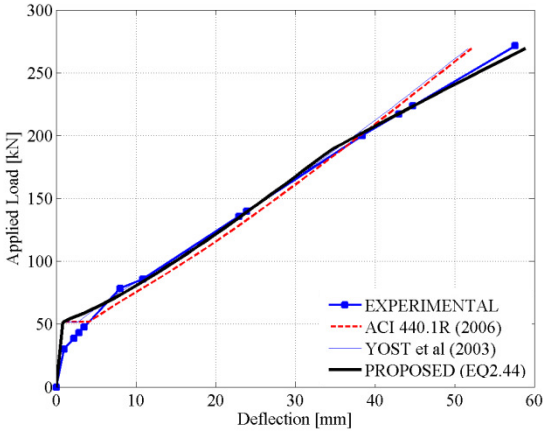

(g) Load-Deflection: S-C1

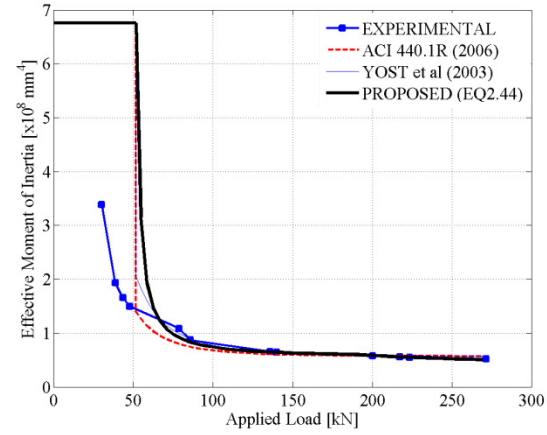

(h) Inertia: S-C1

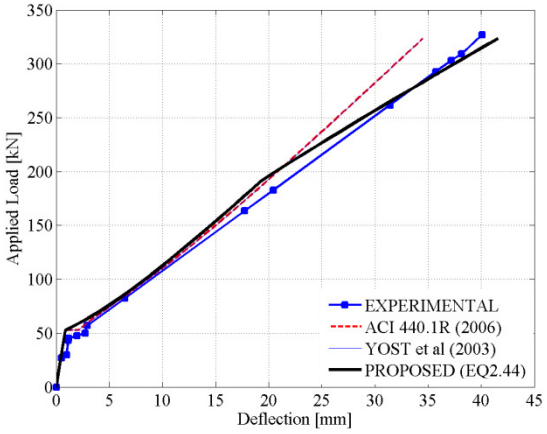

(i) Load-Deflection: S-C2B

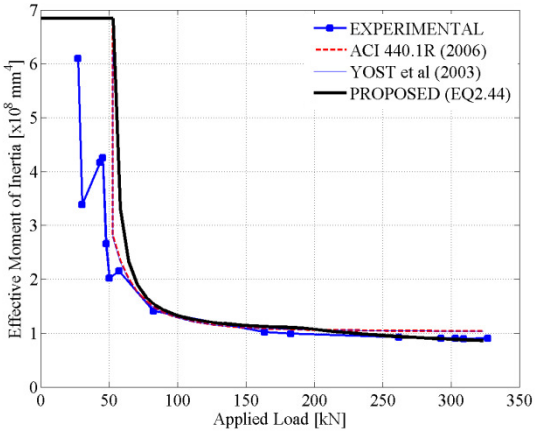

(j) Inertia: S-C2B

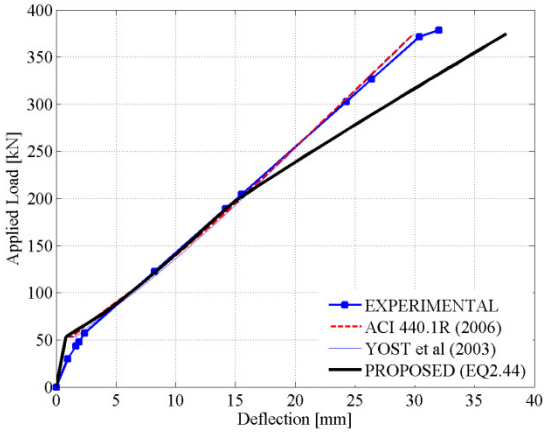

(k) Load-Deflection: S-C3B

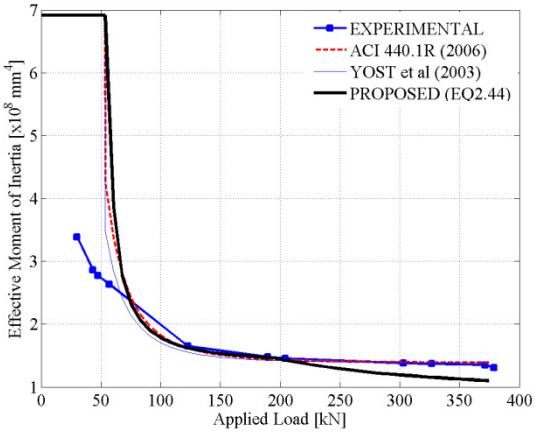

(l) Inertia: S-C3B

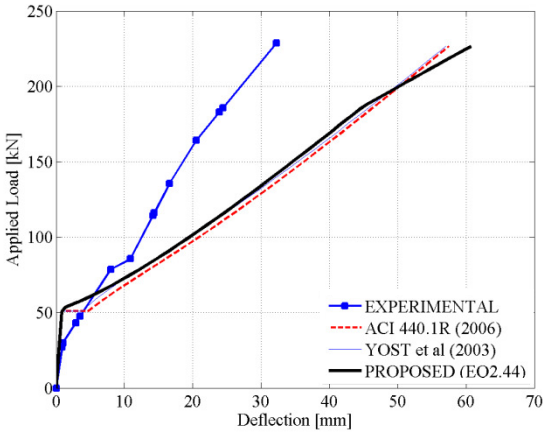

(m) Load-Deflection: S-G1

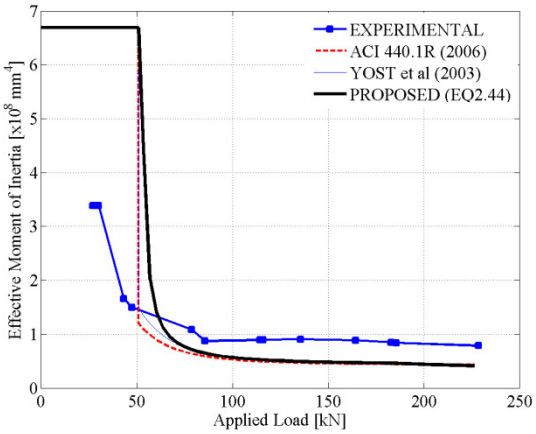

(n) Inertia: S-G1

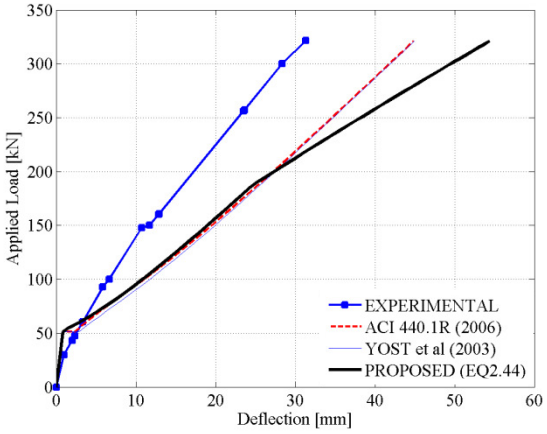

(o) Load-Deflection: S-G2B

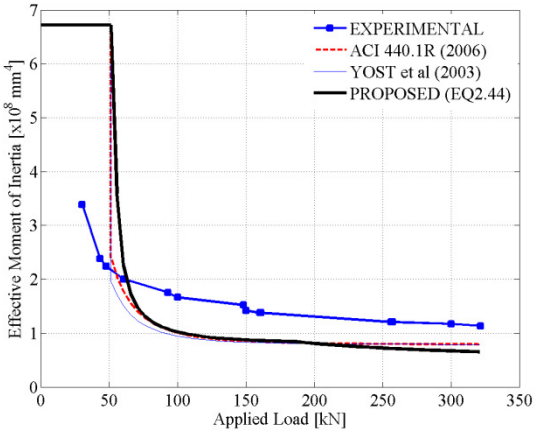

(p) Inertia: S-G2B

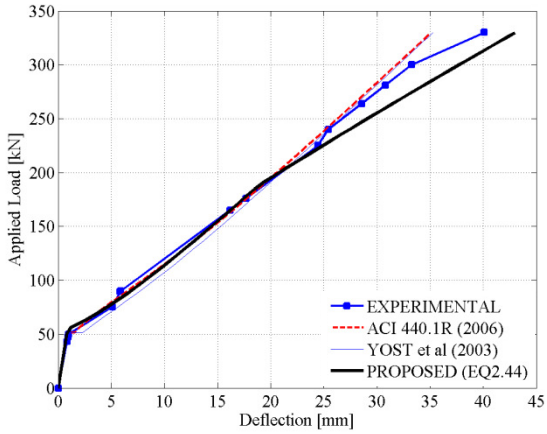

(q) Load-Deflection: S-G3B

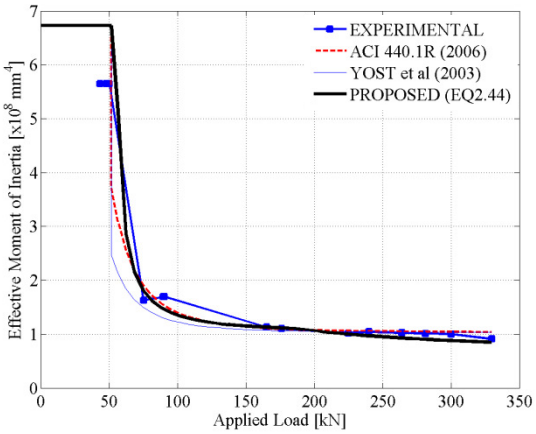

(r) Inertia: S-G3B

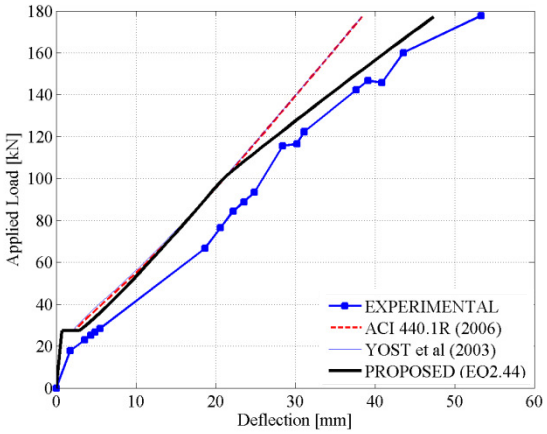

(s) Load-Deflection: CB-4

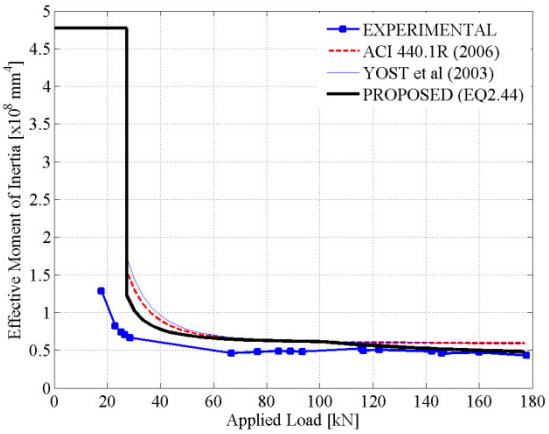

(t) Inertia: CB-4

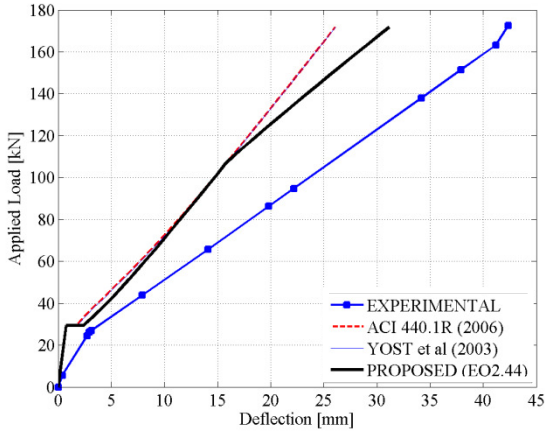

(u) Load-Deflection: CB-6

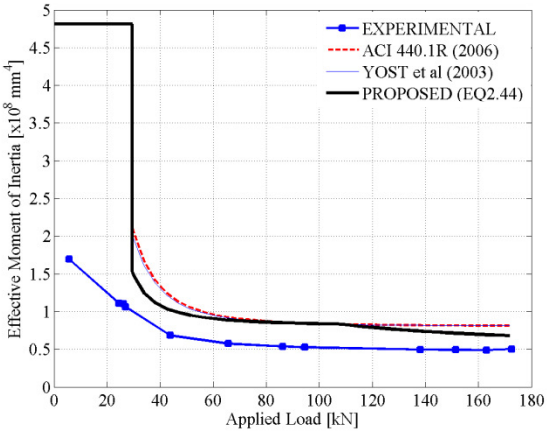

(v) Inertia: CB-6

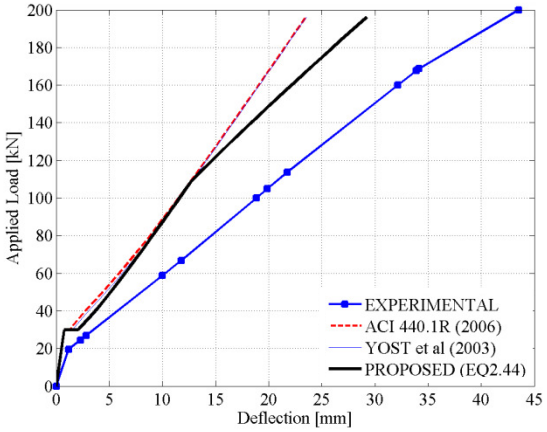

(q) Load-Deflection: CB-8

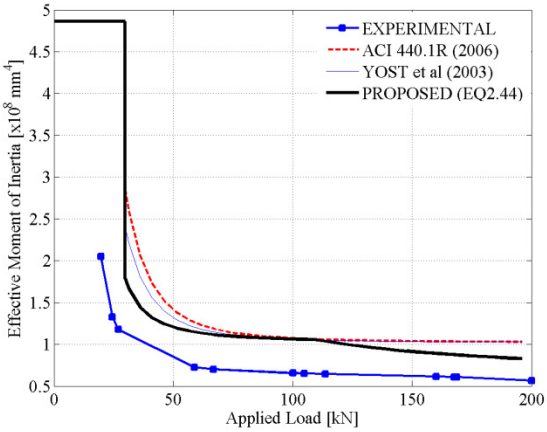

(r) Inertia: CB-8

Figure A.23 **– Load-Deflection Estimates** [El-Salakawy et al. 2003]

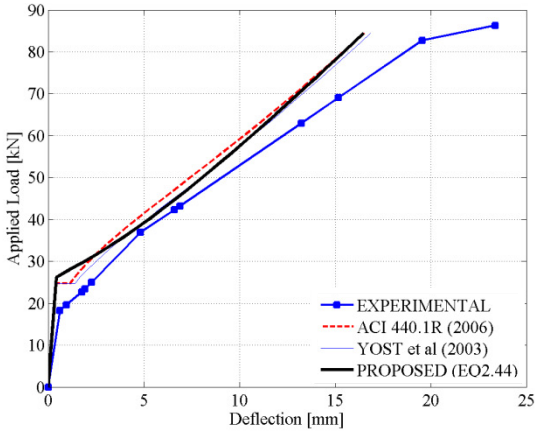

(a) Load-Deflection: 1a-NS

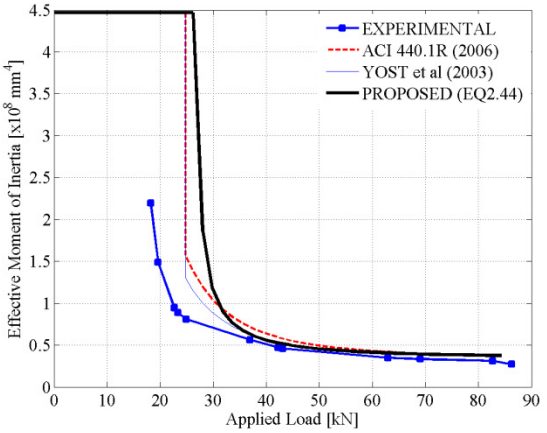

(b) Inertia: 1a-NS

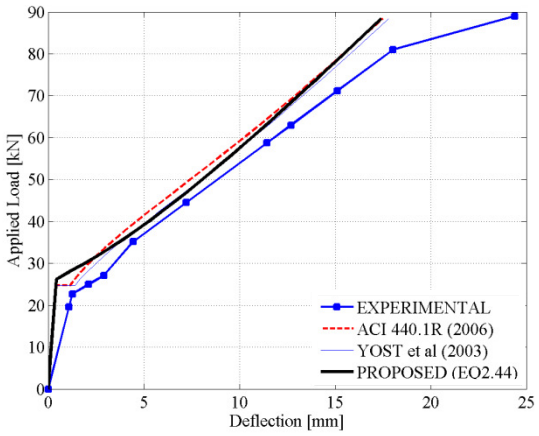

(c) Load-Deflection: 1b-NS

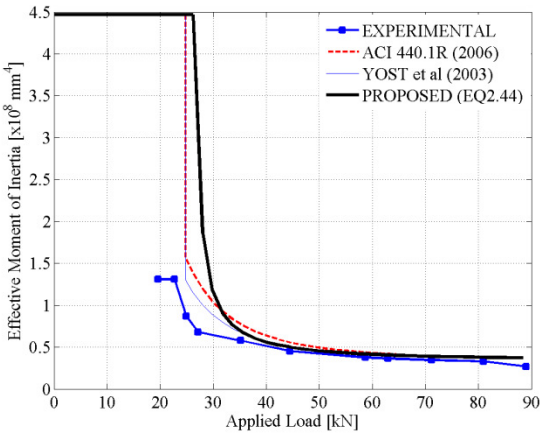

(d) Inertia: 1b-NS

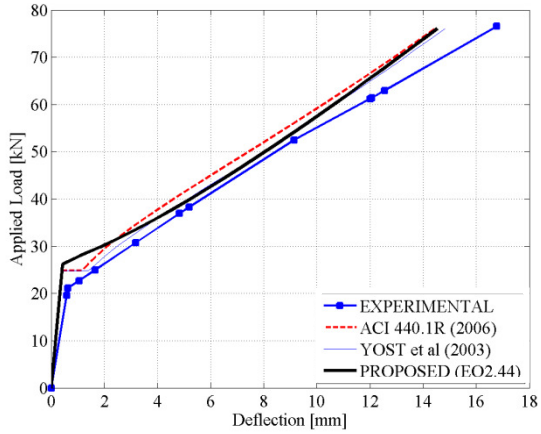

(e) Load-Deflection: 1c-NS

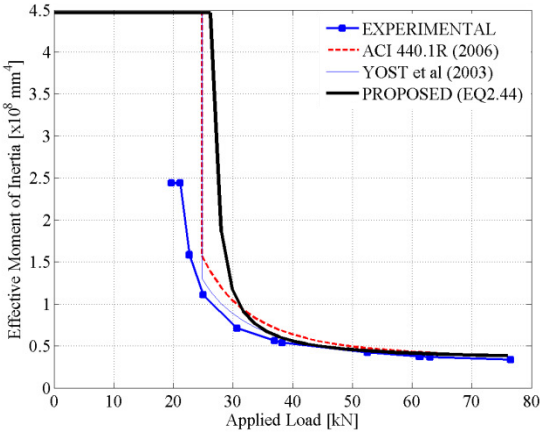

(f) Inertia: 1c-NS

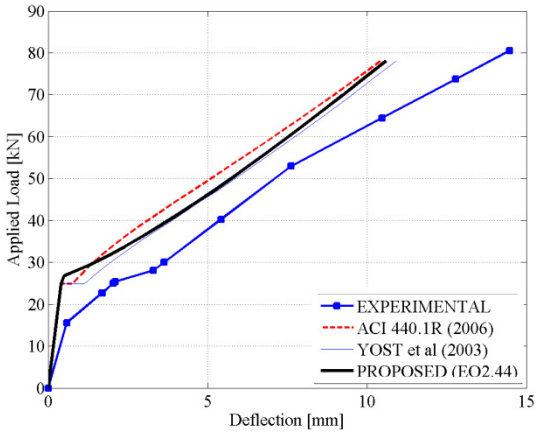

(g) Load-Deflection: 2a-NS

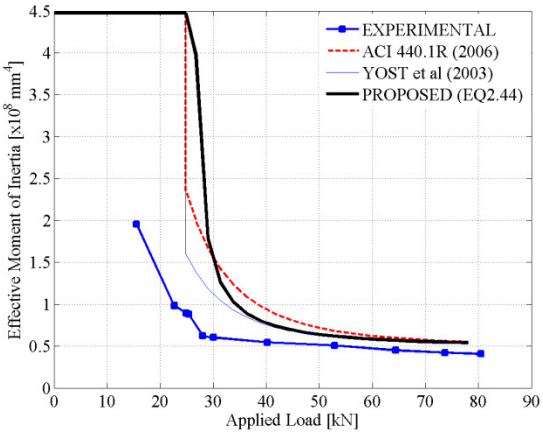

(h) Inertia: 2a-NS

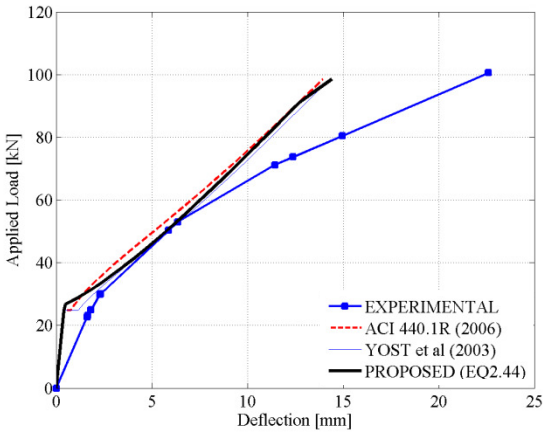

(i) Load-Deflection: 2b-NS

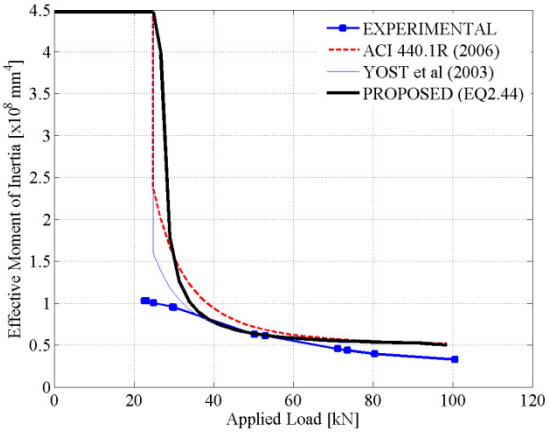

(j) Inertia: 2b-NS

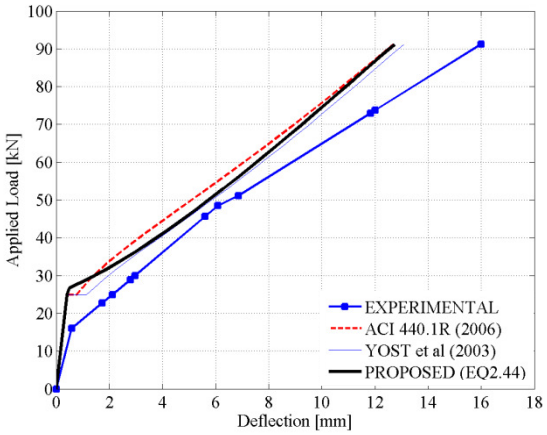

(k) Load-Deflection: 2c-NS

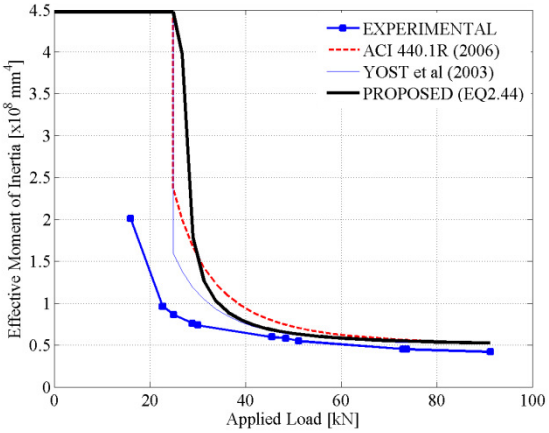

(l) Inertia: 2c-NS

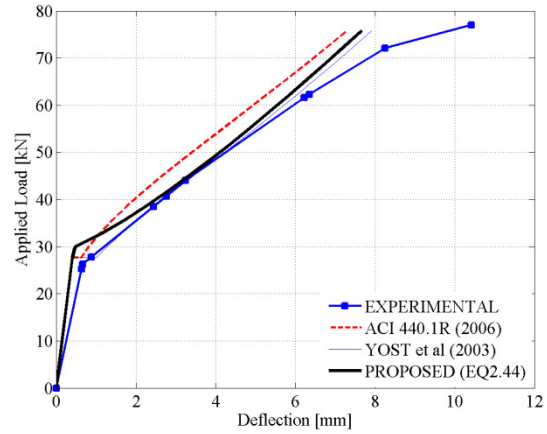

(m) Load-Deflection: 3a-NS

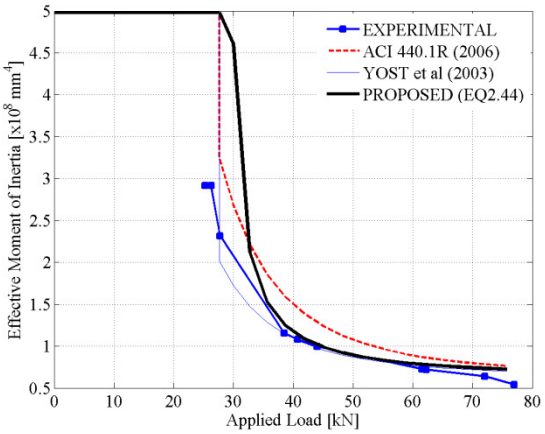

(n) Inertia: 3a-NS

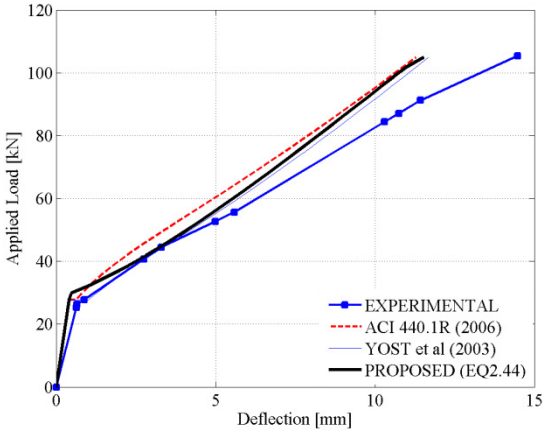

(o) Load-Deflection: 3b-NS

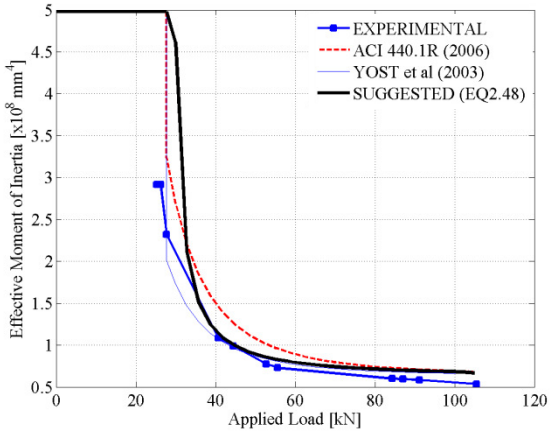

(p) Inertia: 3b-NS

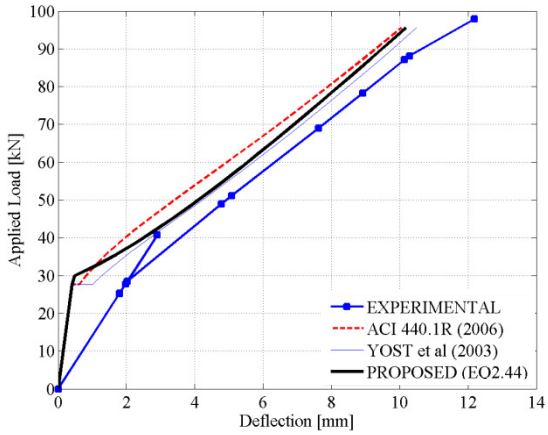

(q) Load-Deflection: 3c-NS

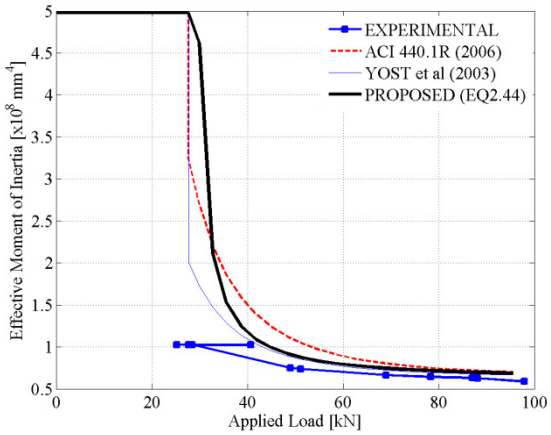

(r) Inertia: 3c-NS

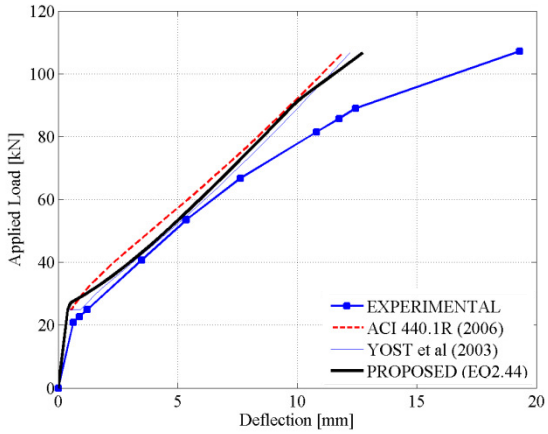

(s) Load-Deflection: 4a-NS

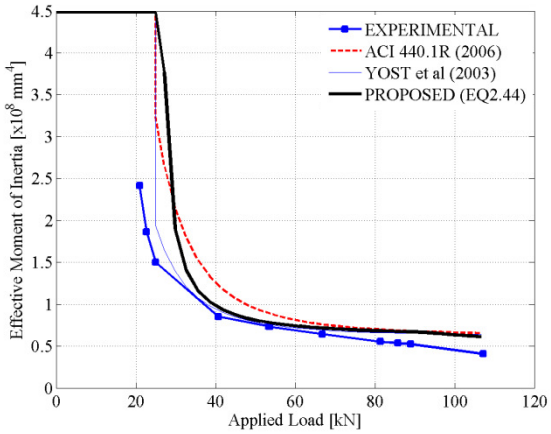

(t) Inertia: 4a-NS

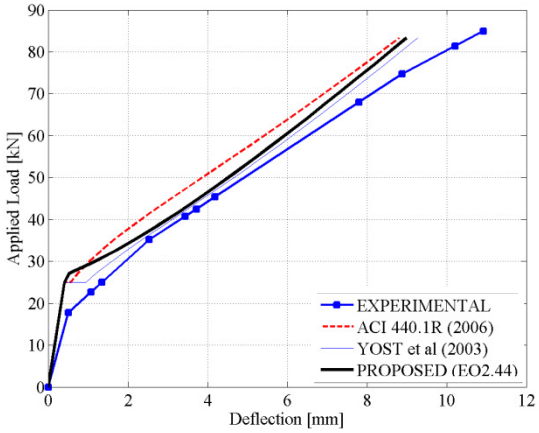

(u) Load-Deflection: 4b-NS

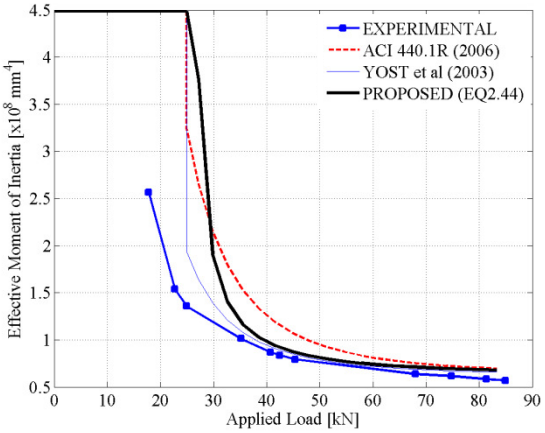

(v) Inertia: 4b-NS

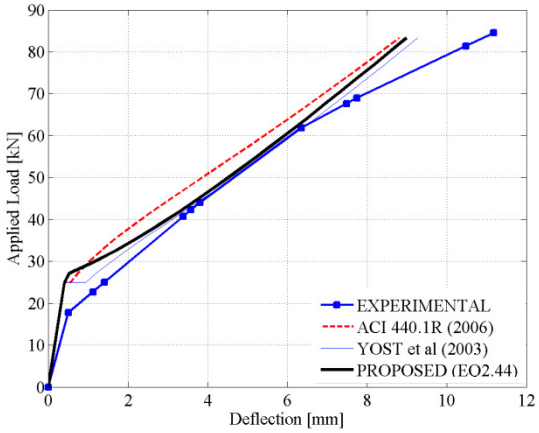

(w) Load-Deflection: 4c-NS

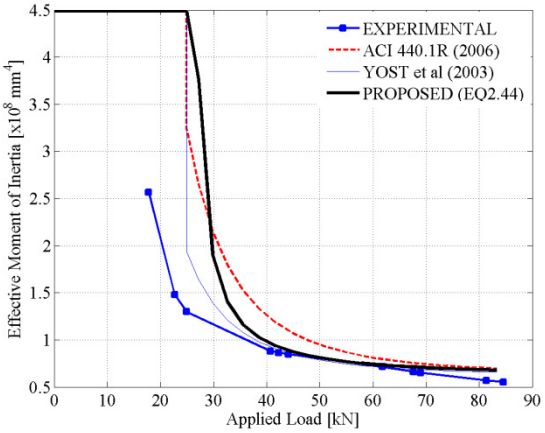

(x) Inertia: 4c-NS

Figure A.24 **– Load-Deflection Estimates** [Yost et al. 2003: NS Beams]

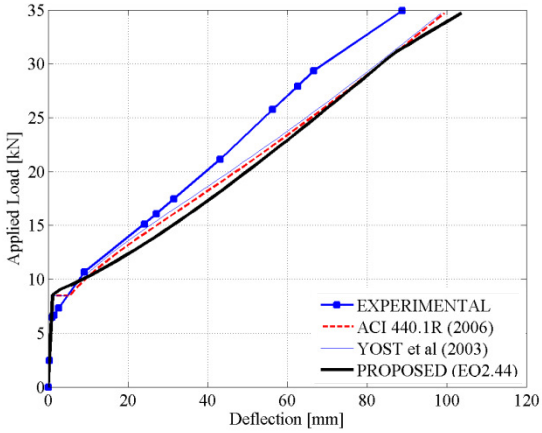

(a) Load-Deflection: 1a-NL

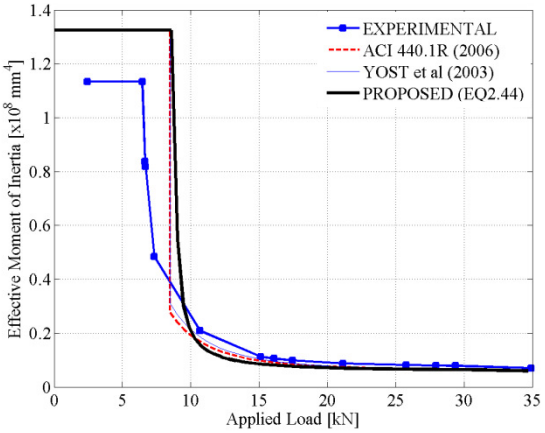

(b) Inertia: 1a-NL

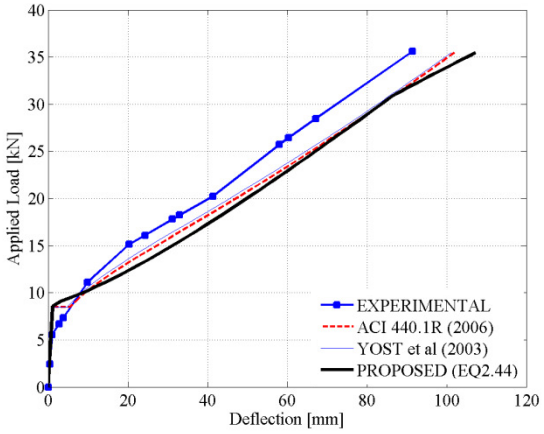

(c) Load-Deflection: 1b-NL

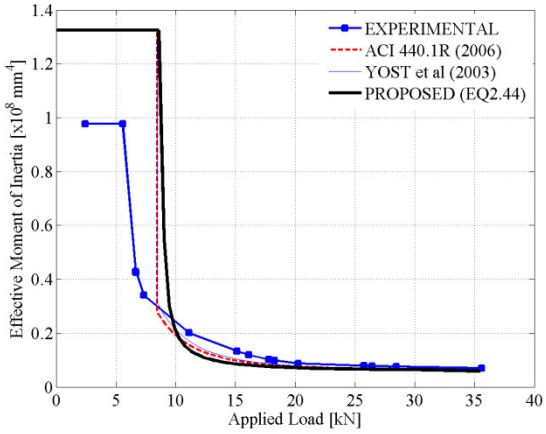

(d) Inertia: 1b-NL

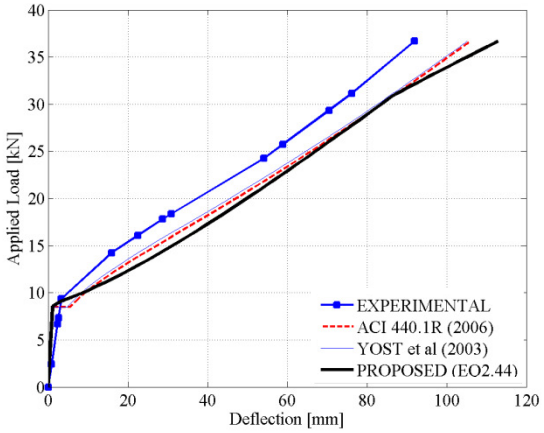

(e) Load-Deflection: 1c-NL

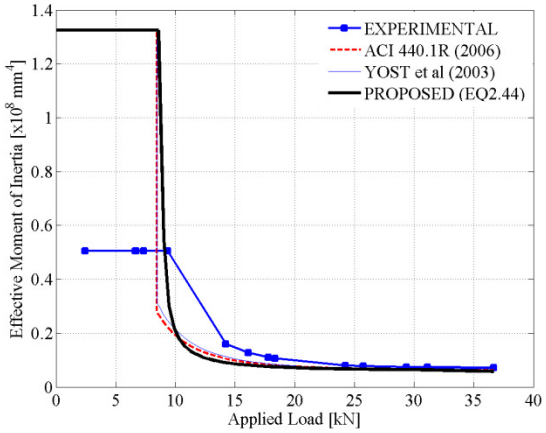

(f) Inertia: 1c-NL

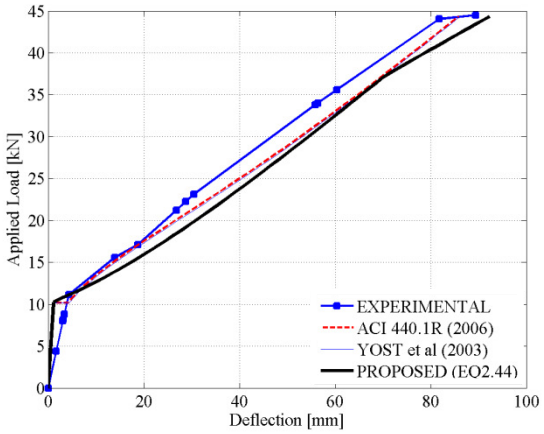

(g) Load-Deflection: 2a-NL

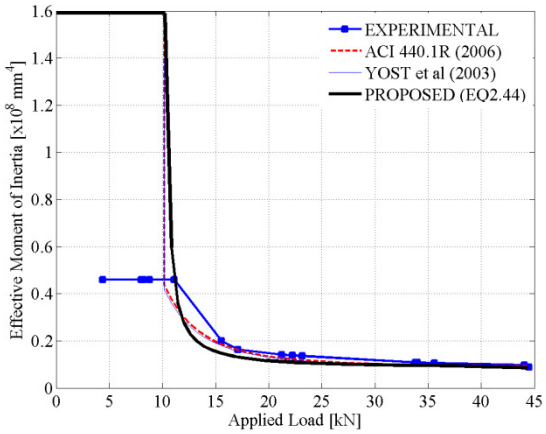

(h) Inertia: 2a-NL

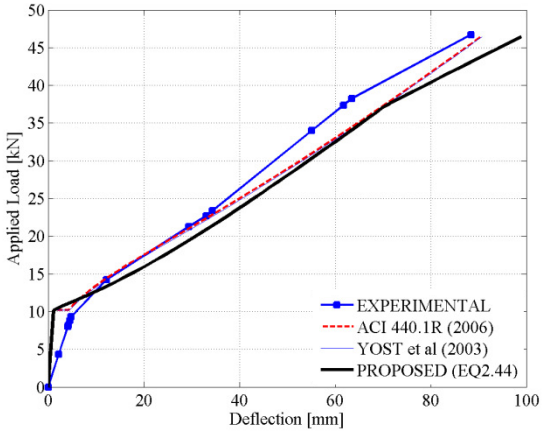

(i) Load-Deflection: 2b-NL

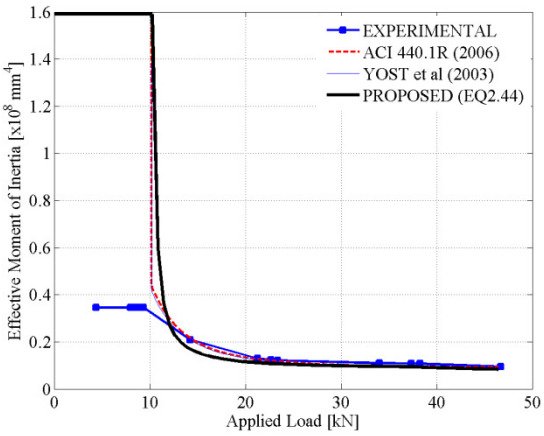

(j) Inertia: 2b-NL

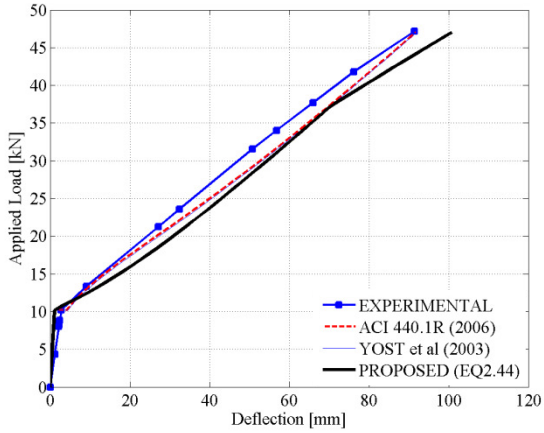

(k) Load-Deflection: 2c-NL

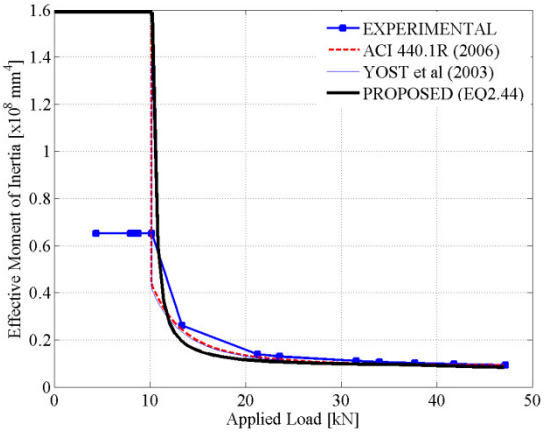

(l) Inertia: 2c-NL

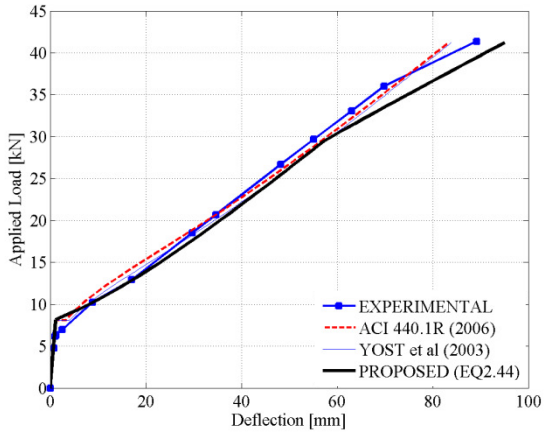

(m) Load-Deflection: 3a-NL

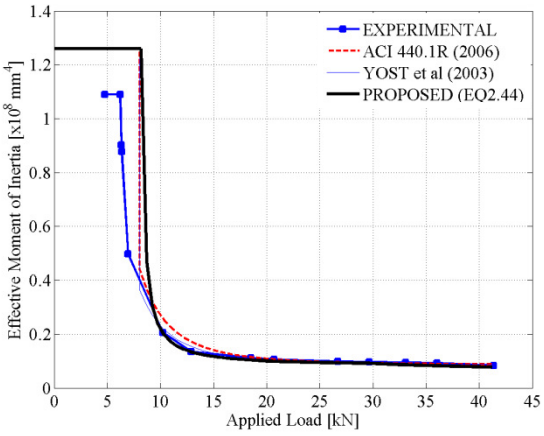

(n) Inertia: 3a-NL

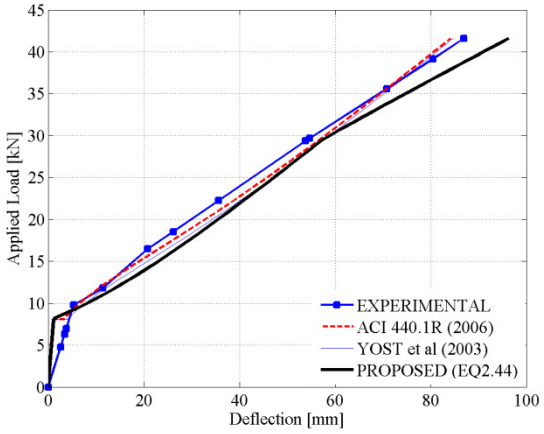

(o) Load-Deflection: 3b-NL

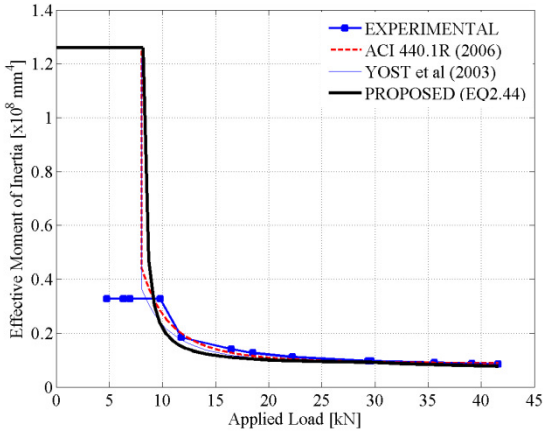

(p) Inertia: 3b-NL

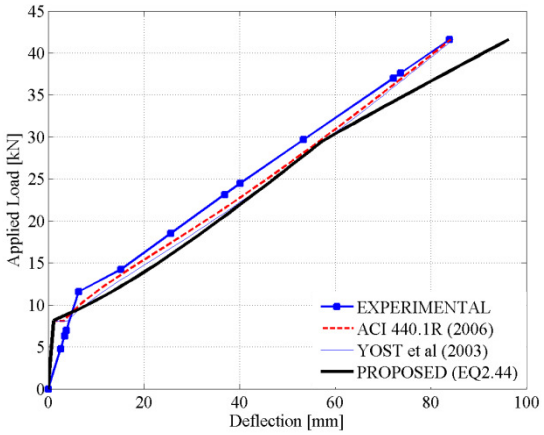

(q) Load-Deflection: 3c-NL

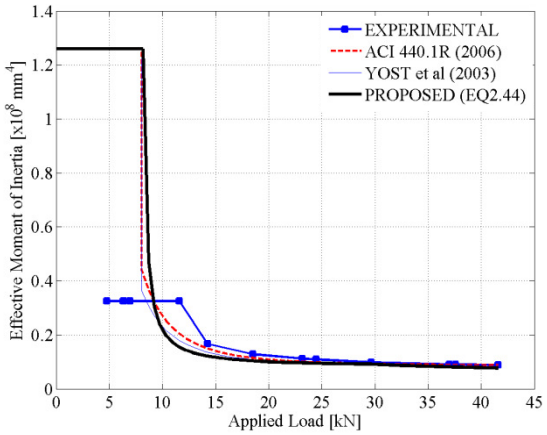

(r) Inertia: 3c-NL

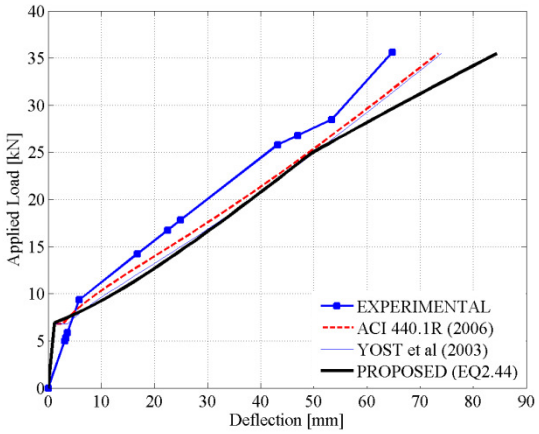

(s) Load-Deflection: 4a-NL

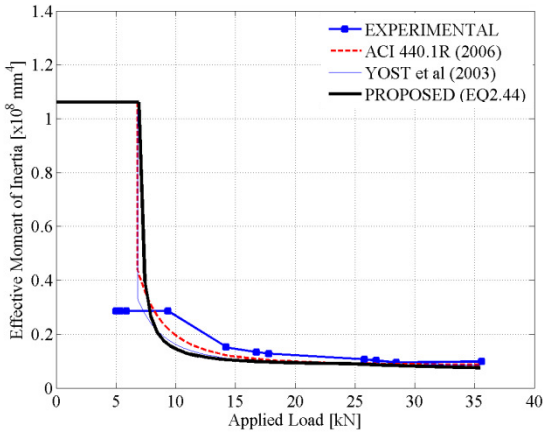

(t) Inertia: 4a-NL

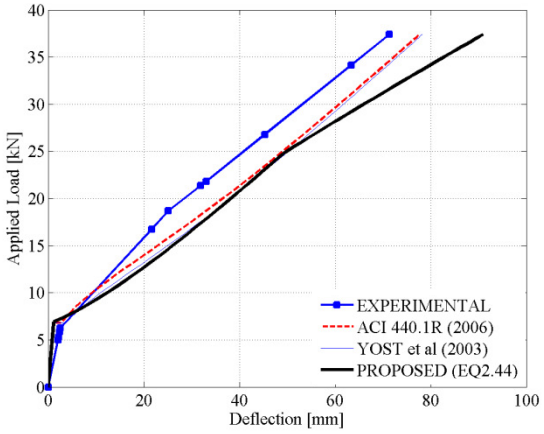

(u) Load-Deflection: 4b-NL

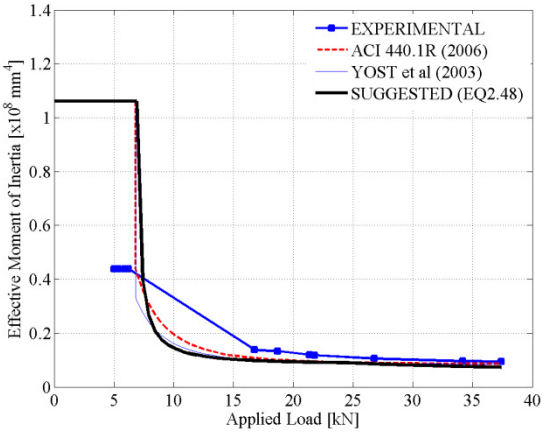

(v) Inertia: 4b-NL

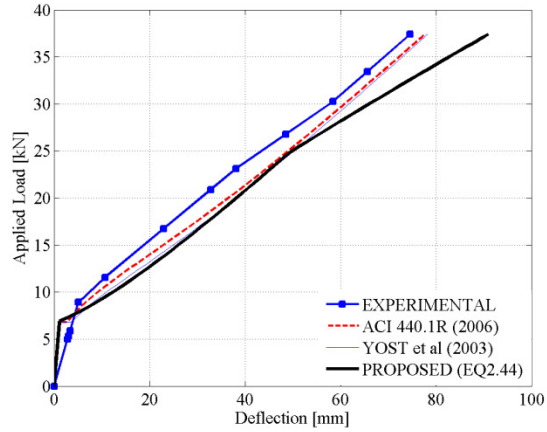

(w) Load-Deflection: 4c-NL

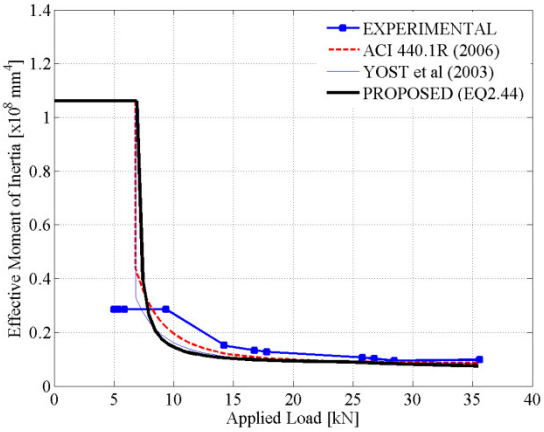

(x) Inertia: 4c-NL

Figure A.25 – **Load-Deflection Estimates** [Yost et al. 2003; NL Beams]

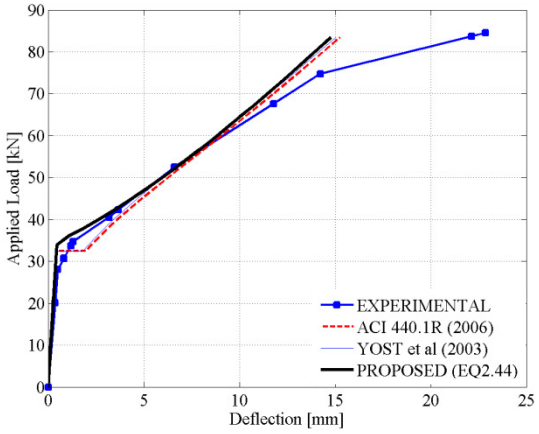

(a) Load-Deflection: 1a-HS

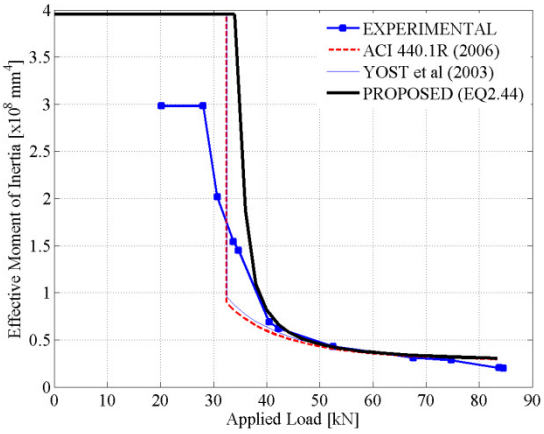

(b) Inertia: 1a-HS

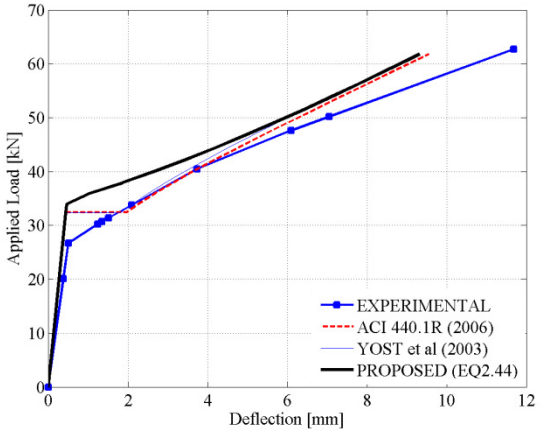

(c) Load-Deflection: 1b-HS

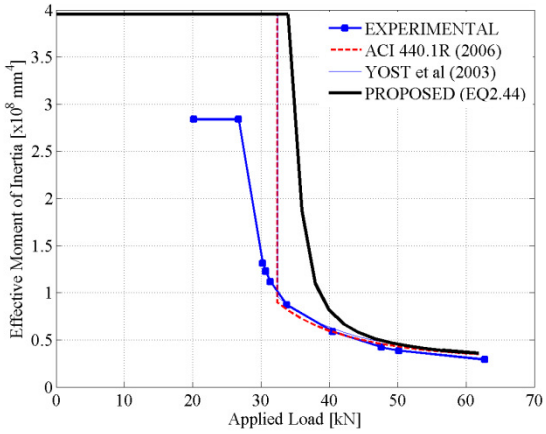

(d) Inertia: 1b-HS

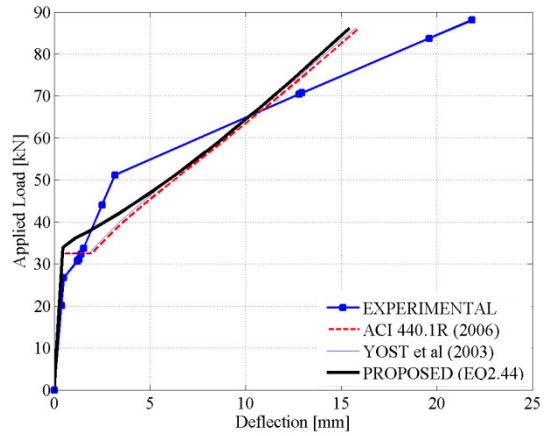

(e) Load-Deflection: 1c-HS

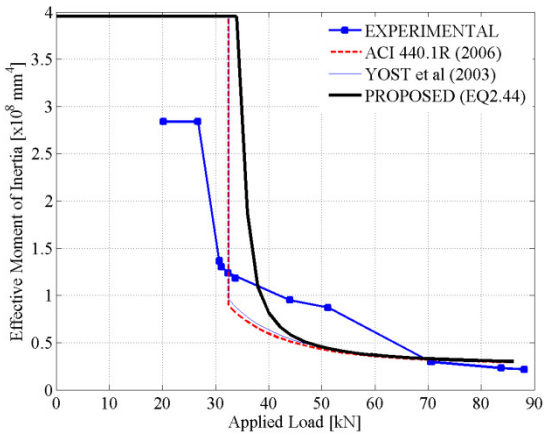

(f) Inertia: 1c-HS

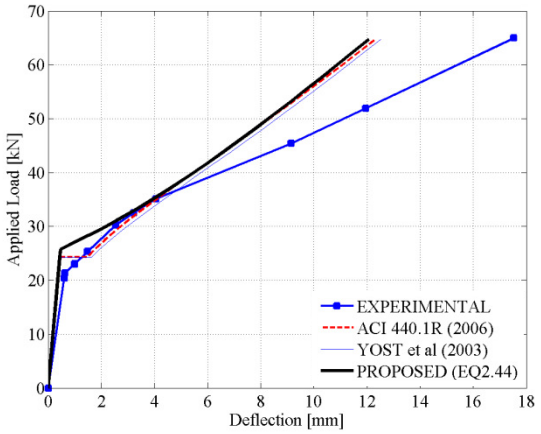

(g) Load-Deflection: 2a-HS

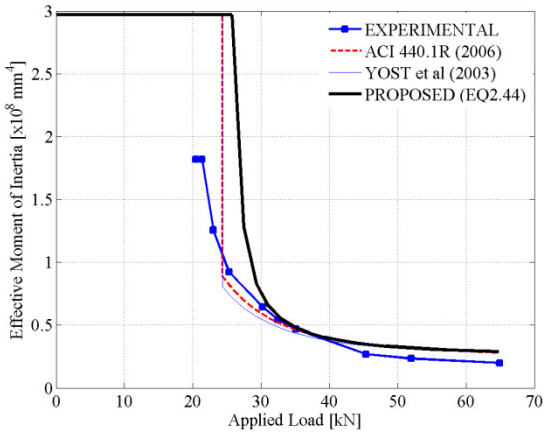

(h) Inertia: 2a-HS

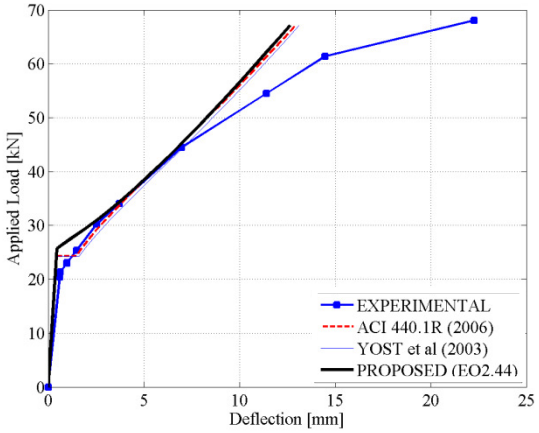

(i) Load-Deflection: 2b-HS

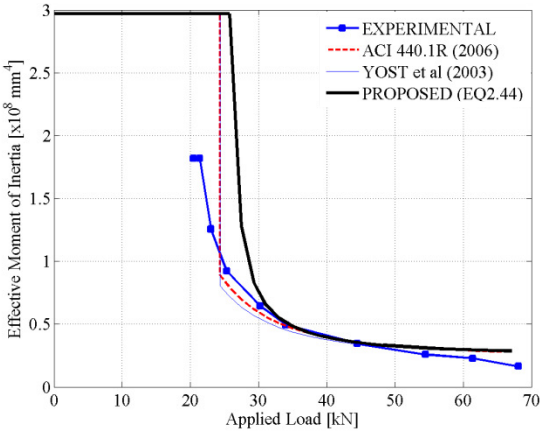

(j) Inertia: 2b-HS

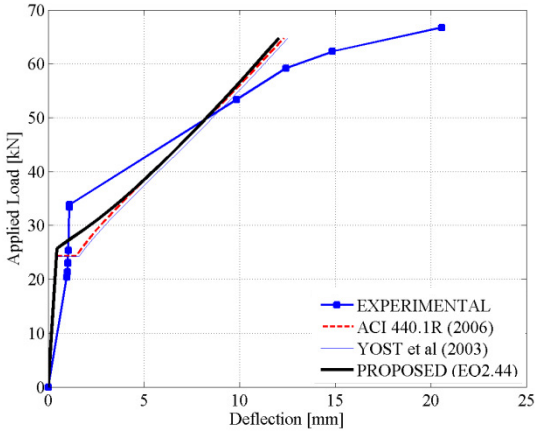

(k) Load-Deflection: 2c-HS

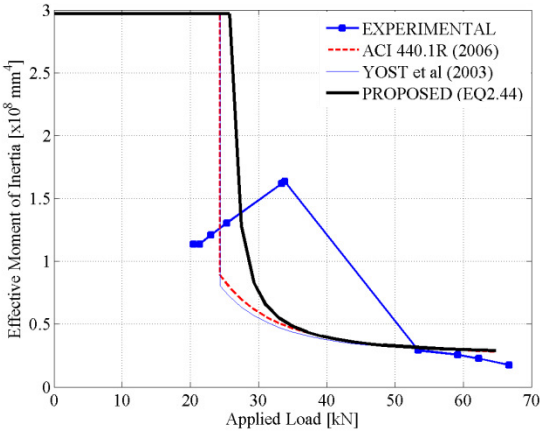

(l) Inertia: 2c-HS

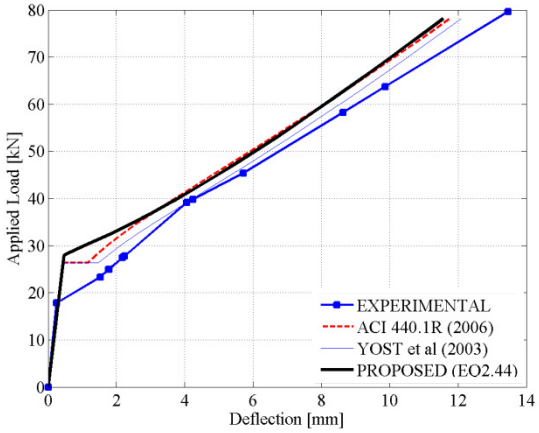

(m) Load-Deflection: 3a-HS

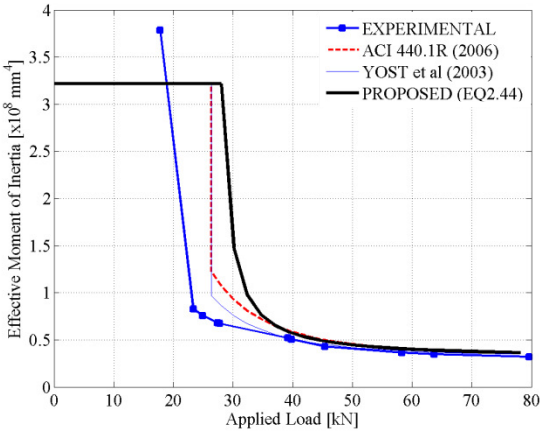

(n) Inertia: 3a-HS

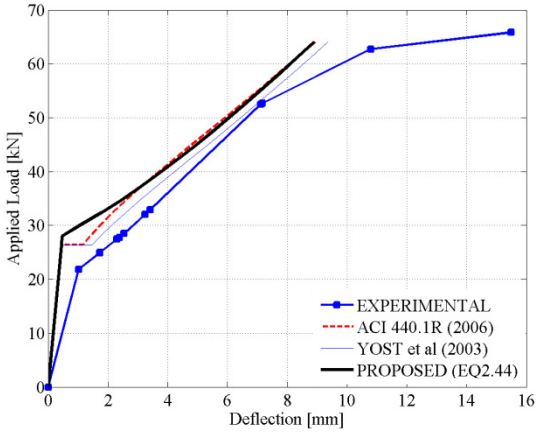

(o) Load-Deflection: 3b-HS

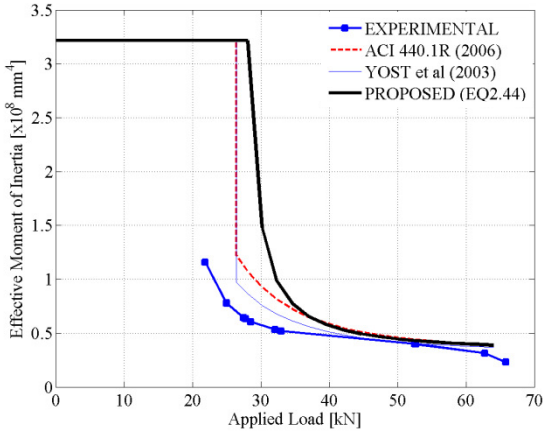

(p) Inertia: 3b-HS

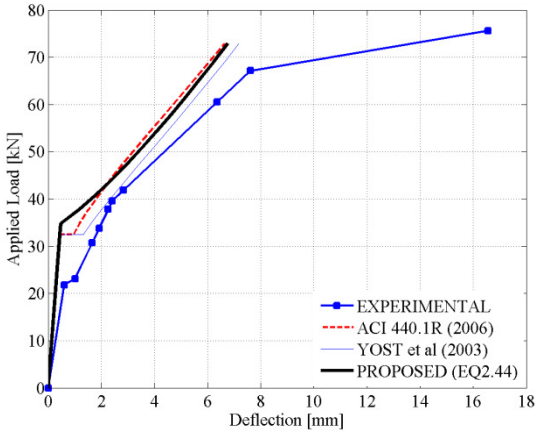

(q) Load-Deflection: 4a-HS

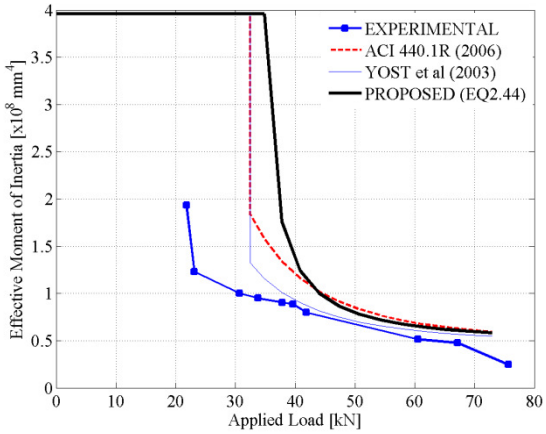

(r) Inertia: 4a-HS

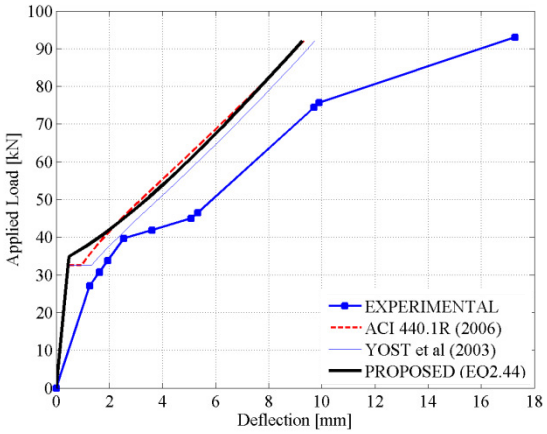

(s) Load-Deflection: 4b-HS

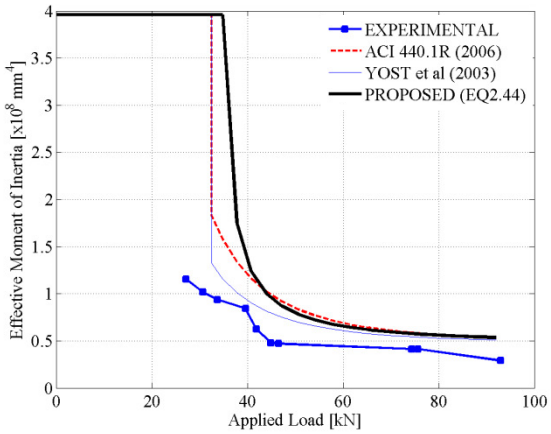

(t) Inertia: 4b-HS

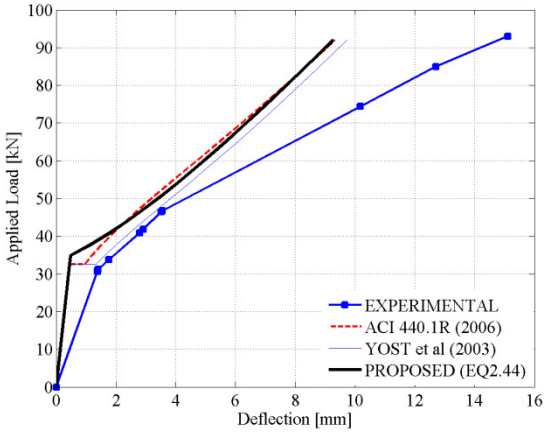

(u) Load-Deflection: 4c-HS

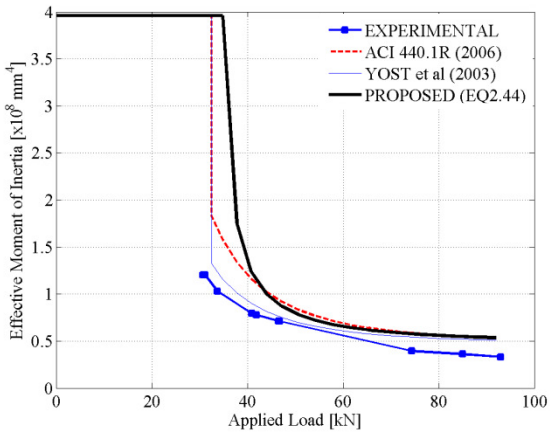

(v) Inertia: 4c-HS

Figure A.26 **– Load-Deflection Estimates** [Yost et al. 2003: HS Beams]

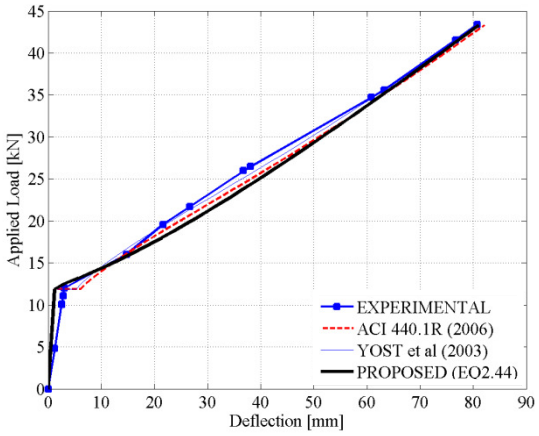

(a) Load-Deflection: 1a-HL

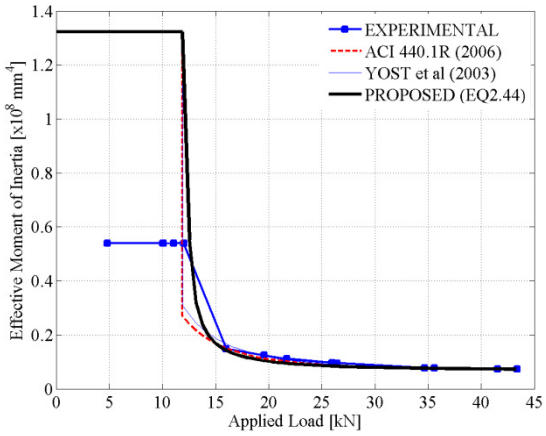

(b) Inertia: 1a-HL

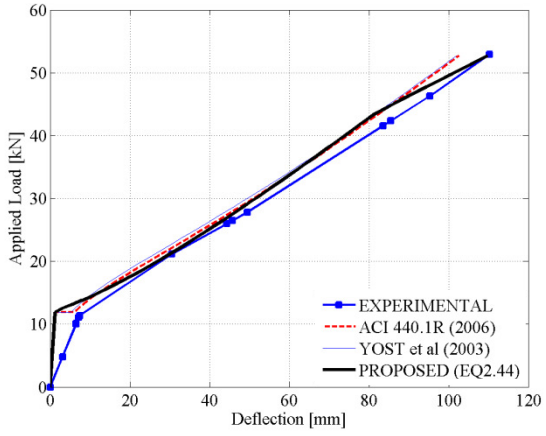

(c) Load-Deflection: 1b-HL

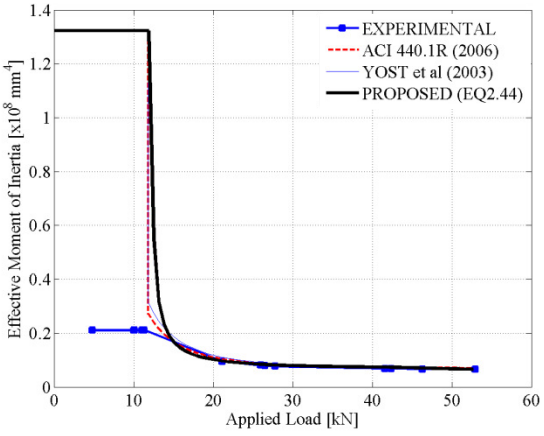

(d) Inertia: 1b-HL

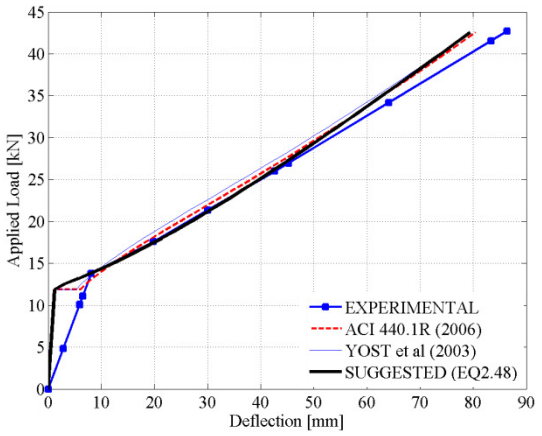

(e) Load-Deflection: 1c-HL

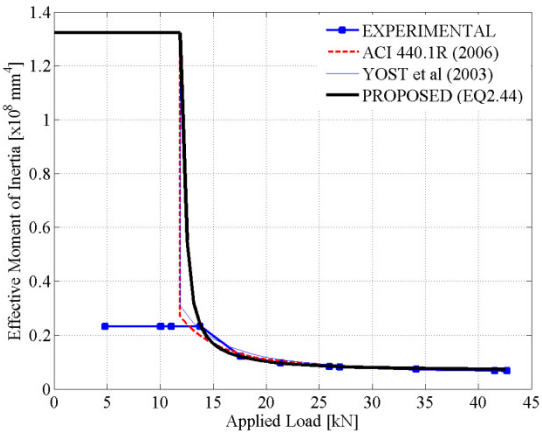

(f) Inertia: 1c-HL

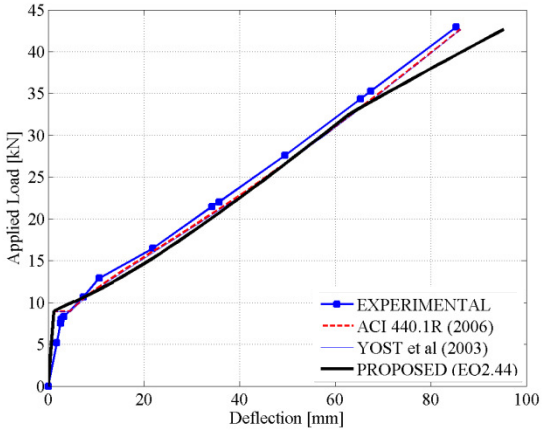

(g) Load-Deflection: 2a-HL

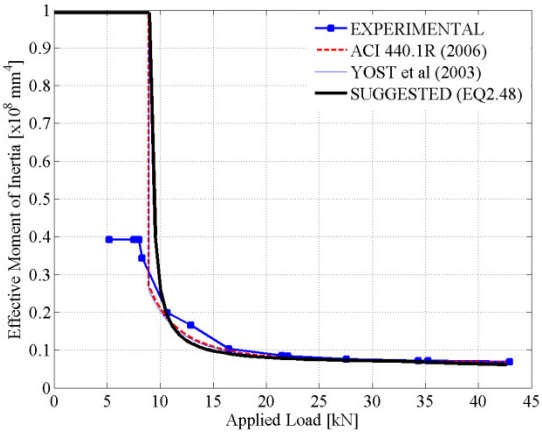

(h) Inertia: 2a-HL

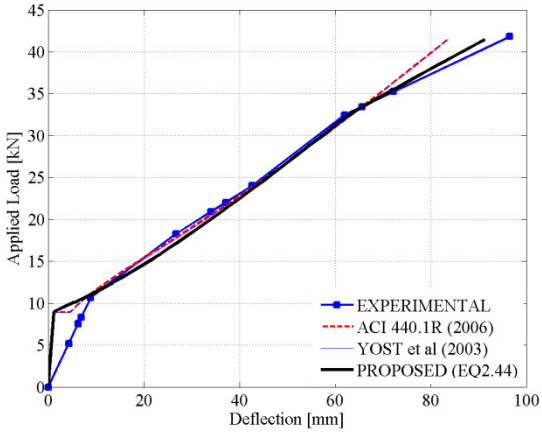

(i) Load-Deflection: 2b-HL

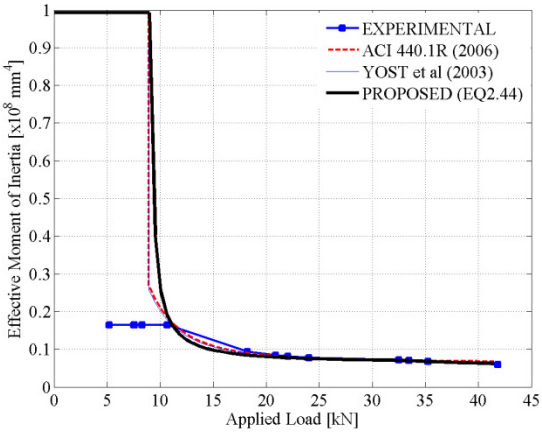

(j) Inertia: 2b-HL

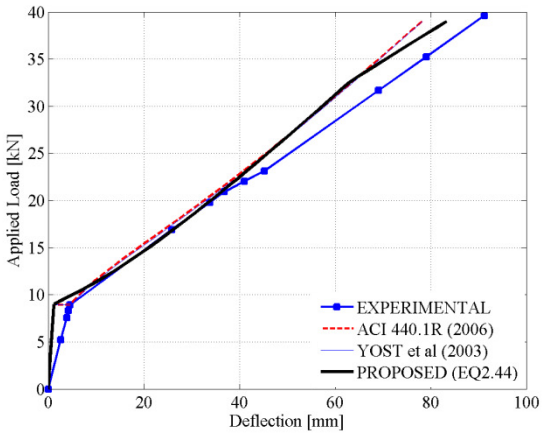

(k) Load-Deflection: 2c-HL

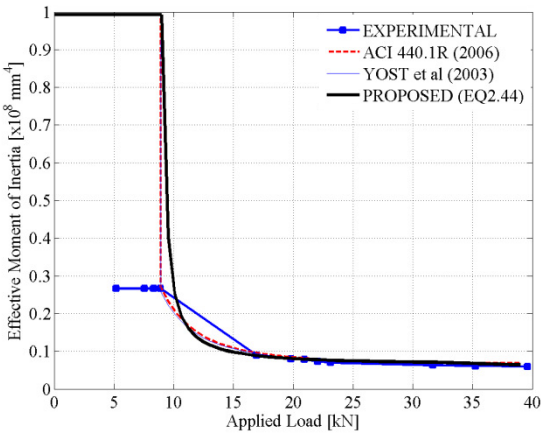

(l) Inertia: 2c-HL

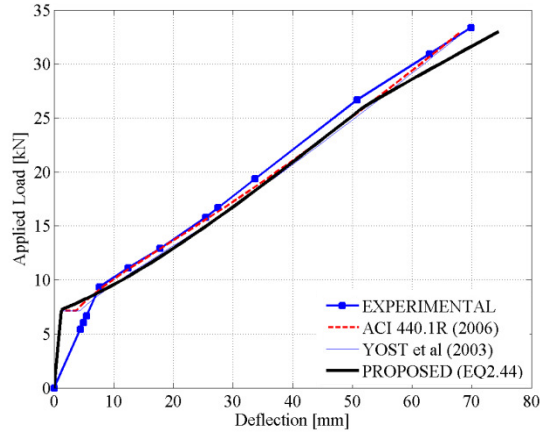

(m) Load-Deflection: 3a-HL

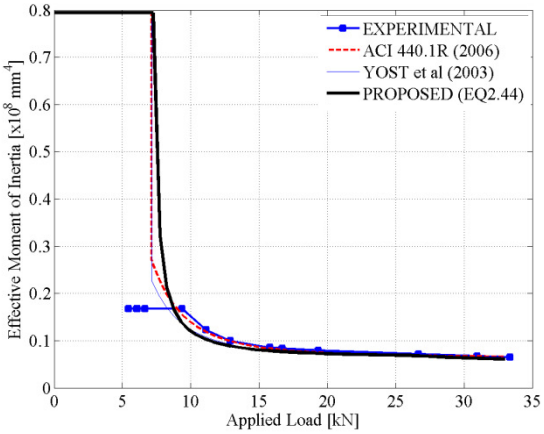

(n) Inertia: 3a-HL

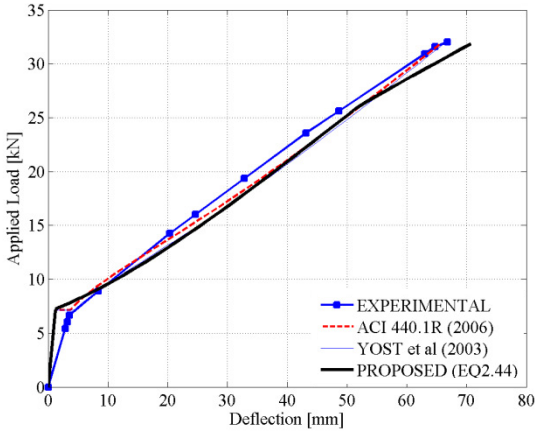

(o) Load-Deflection: 3b-HL

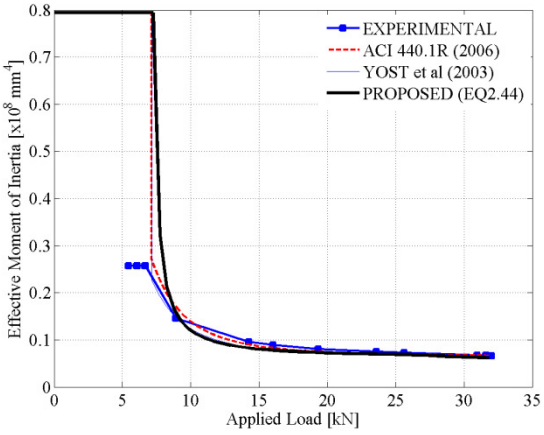

(p) Inertia: 3b-HL

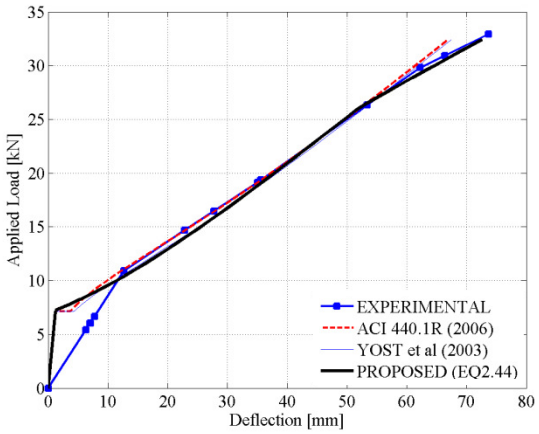

(q) Load-Deflection: 3c-HL

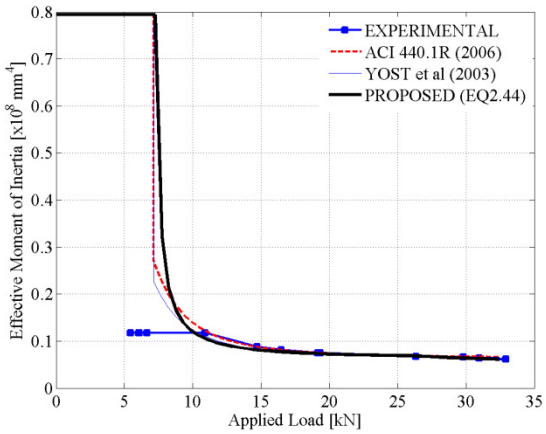

(r) Inertia: 3c-HL

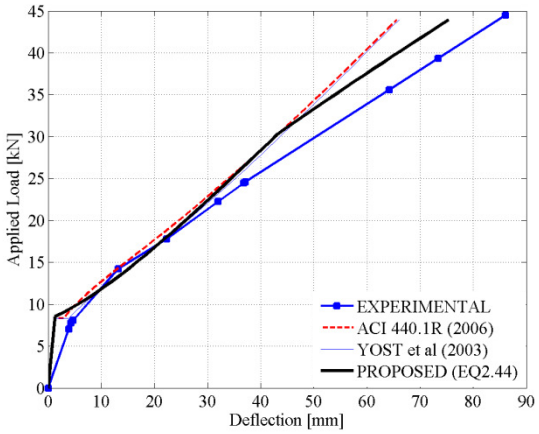

(s) Load-Deflection: 4a-HL

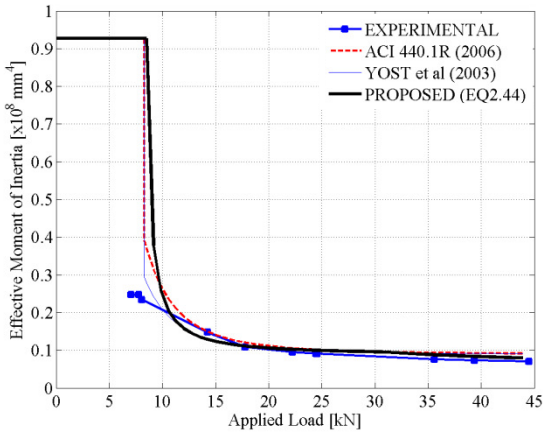

(t) Inertia: 4a-HL

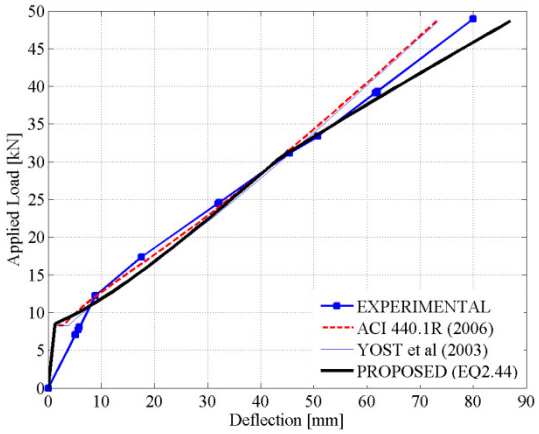

(u) Load-Deflection: 4b-HL

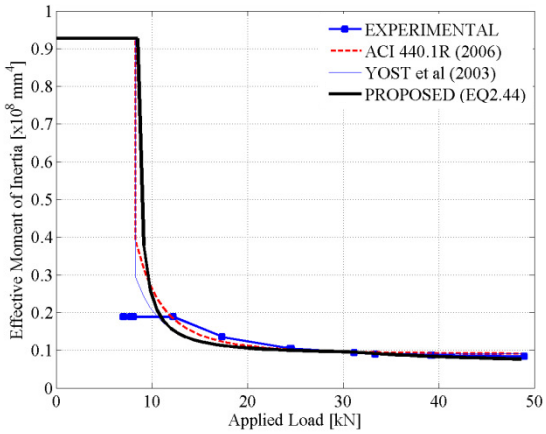

(v) Inertia: 4b-HL

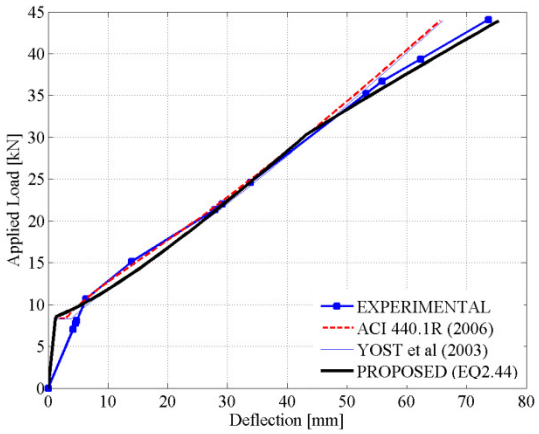

(w) Load-Deflection: 4c-HL

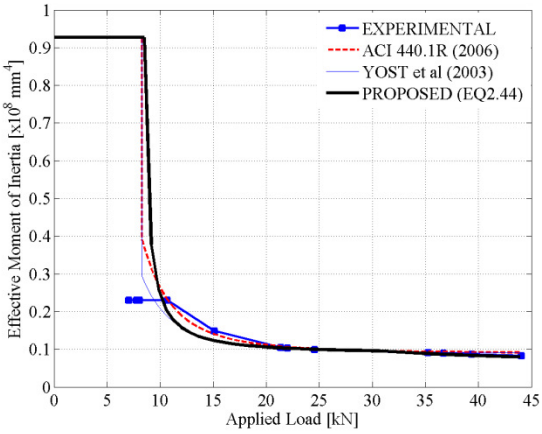

(x) Inertia: 4c-HL

Figure A.27 **– Load-Deflection Estimates** [Yost et al. 2003: HL Beams]

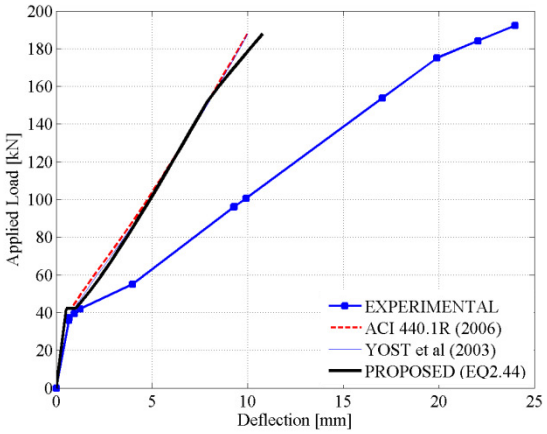

(a) Load-Deflection: BA1

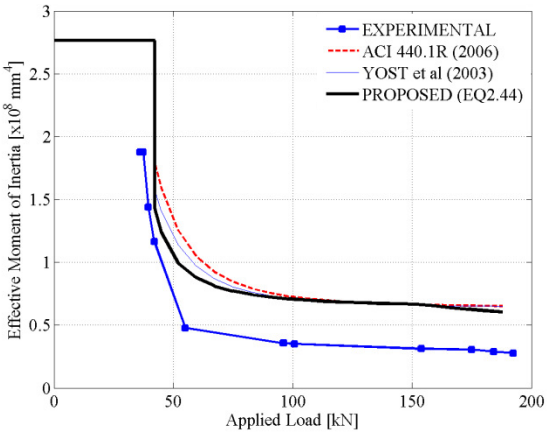

(b) Inertia: BA1

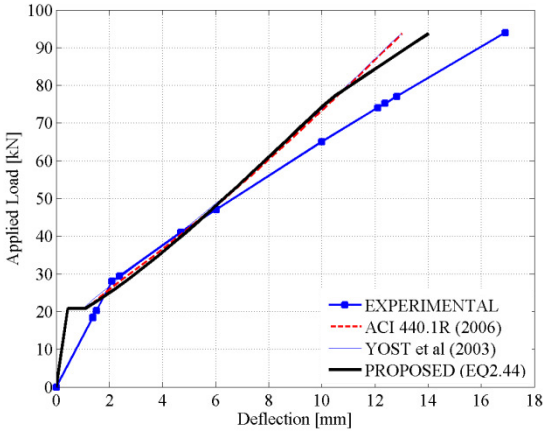

(c) Load-Deflection: BA3

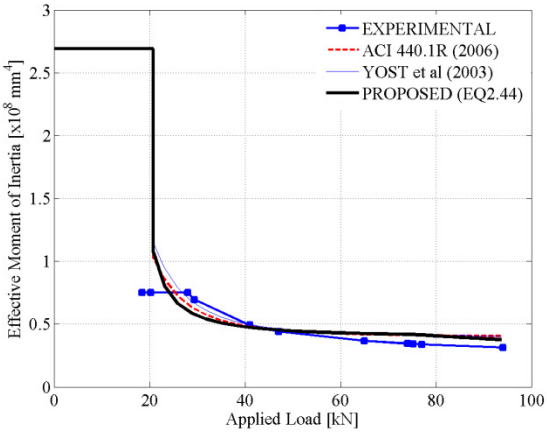

(d) Inertia: BA3

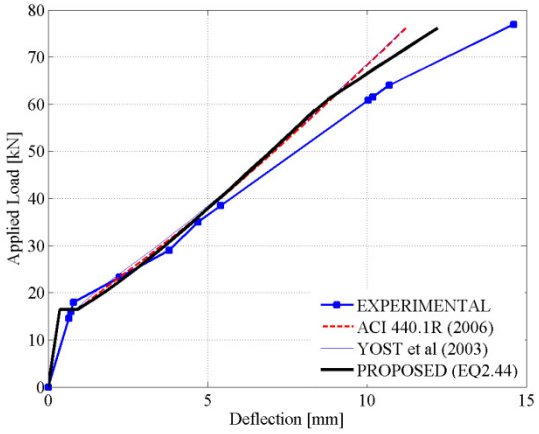

(e) Load-Deflection: BA4

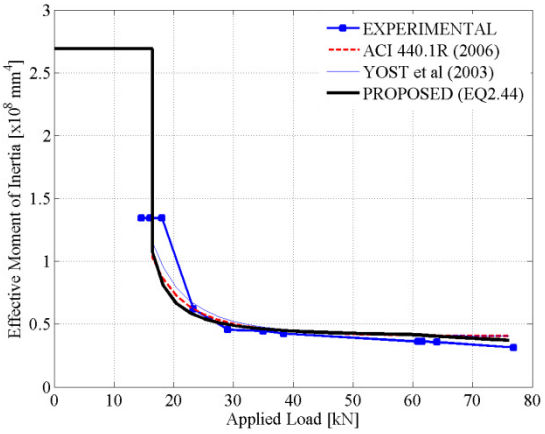

(f) Inertia: BA4

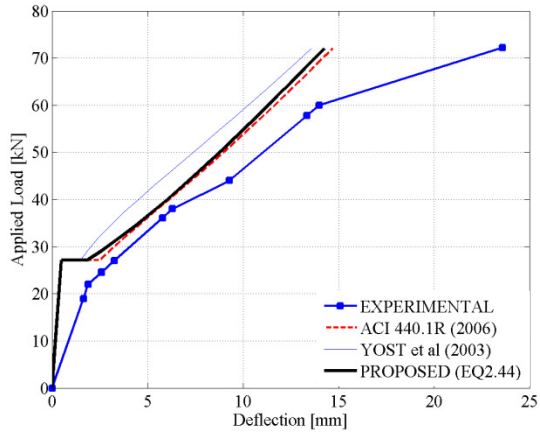

(g) Load-Deflection: BR1

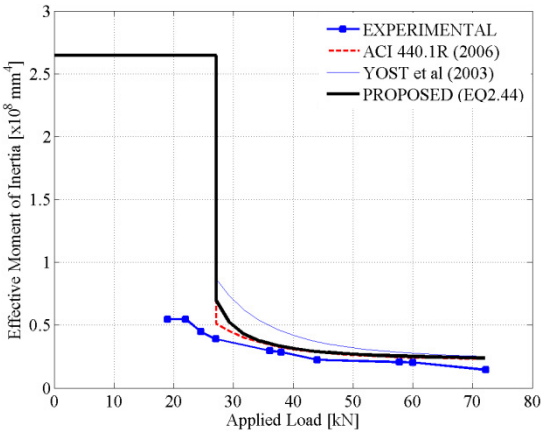

(h) Inertia: BR1

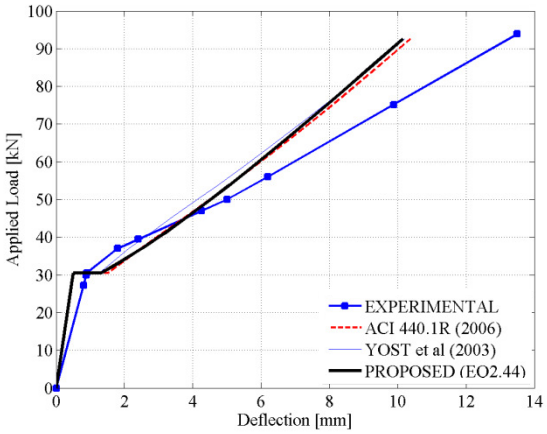

(i) Load-Deflection: BR2

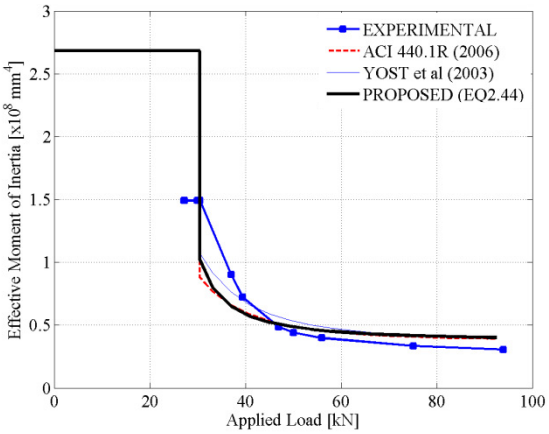

(j) Inertia: BR2

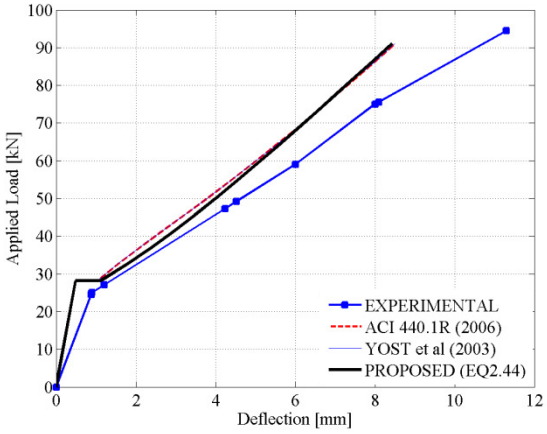

(k) Load-Deflection: BR3

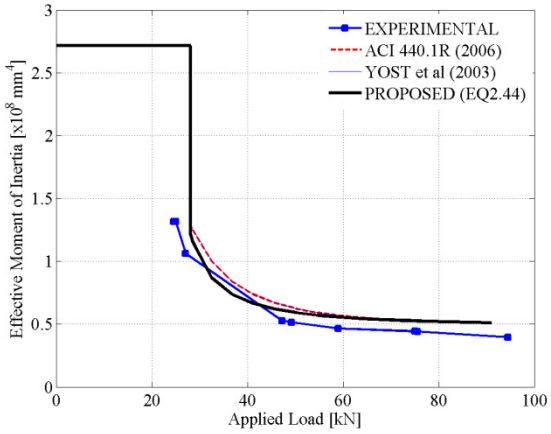

(l) Inertia: BR3

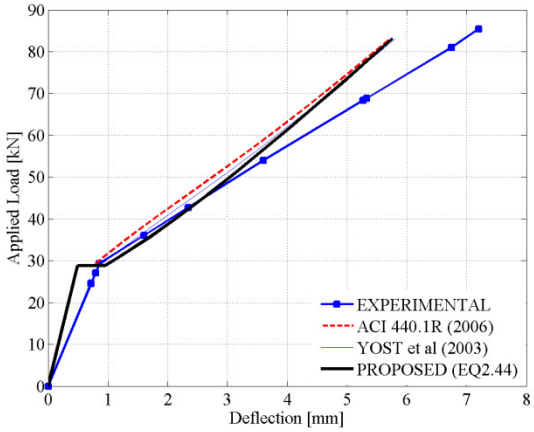

(m) Load-Deflection: BR4

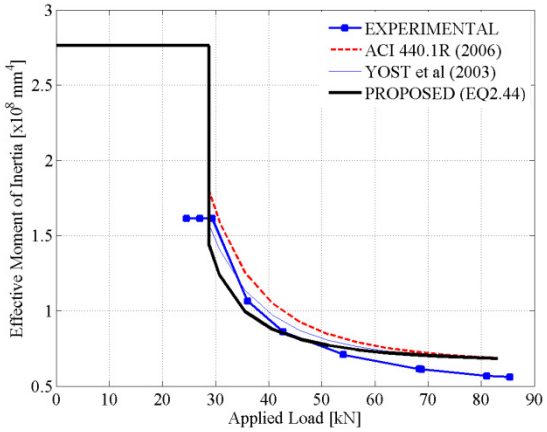

(n) Inertia: BR4

Figure A.28 **– Load-Deflection Estimates** [Razaqpur et al. 2004]

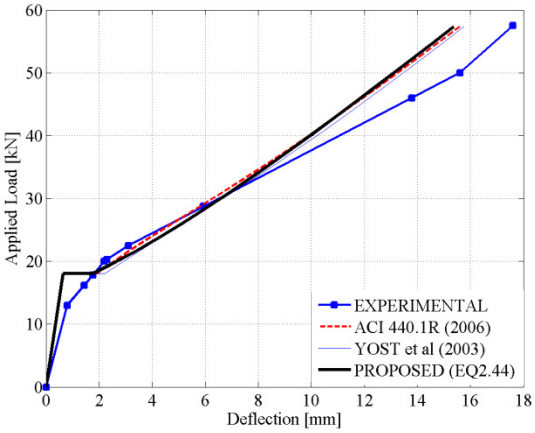

(a) Load-Deflection: GB43

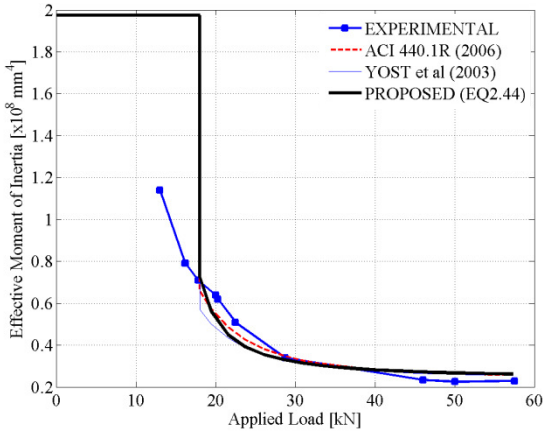

(b) Inertia: GB43

Figure A.29 **– Load-Deflection Estimates** [Guadagnini et al. 2001]

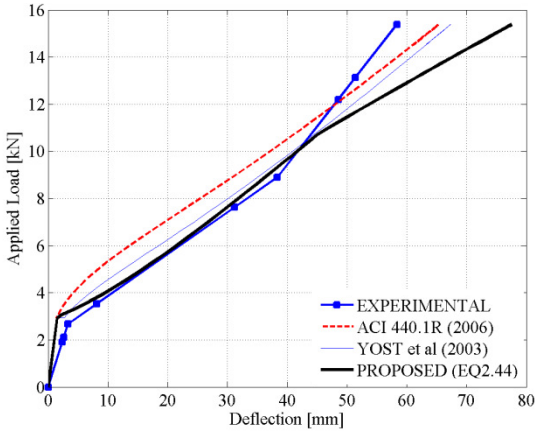

(a) Load-Deflection: SB1

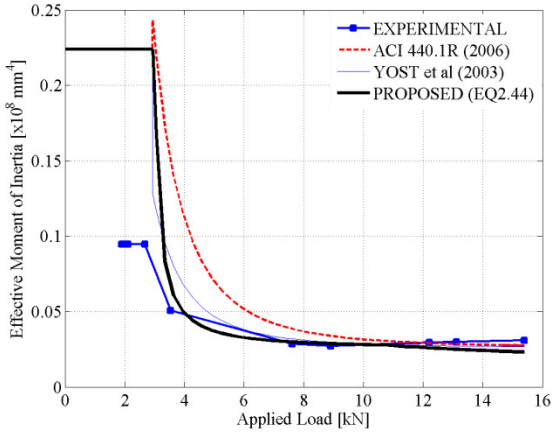

(b) Inertia: SB1

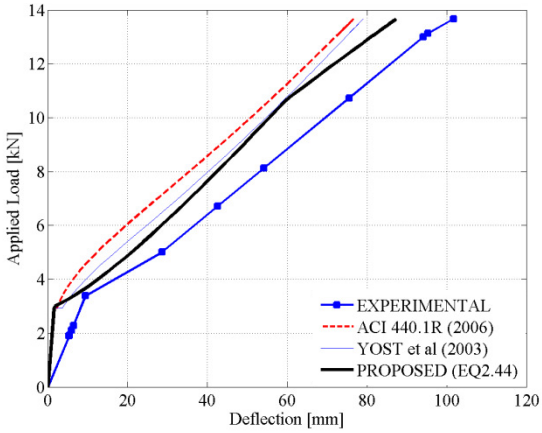

(c) Load-Deflection: SB3

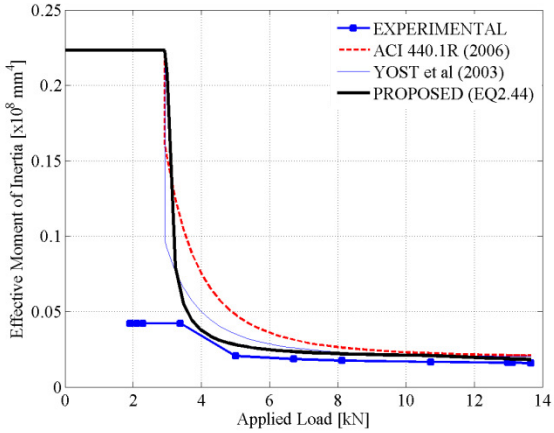

(d) Inertia: SB3

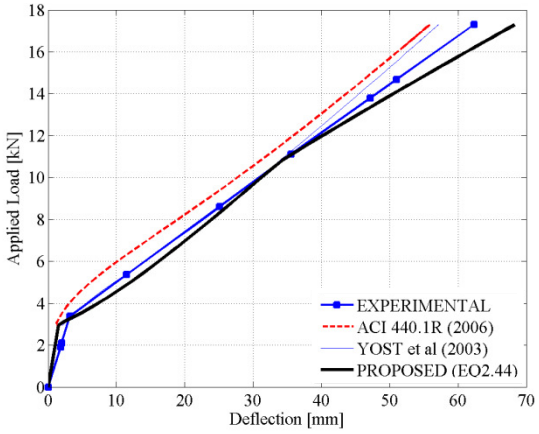

(e) Load-Deflection: SB5

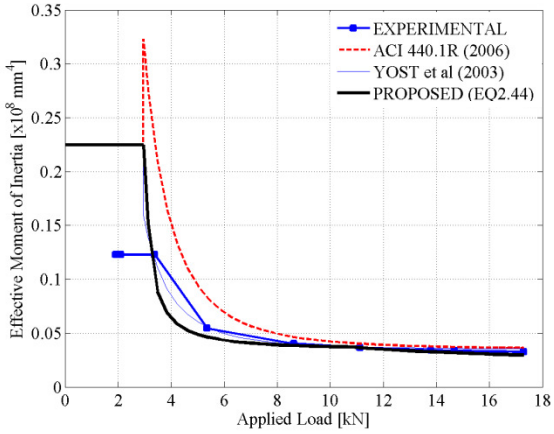

(f) Inertia: SB5

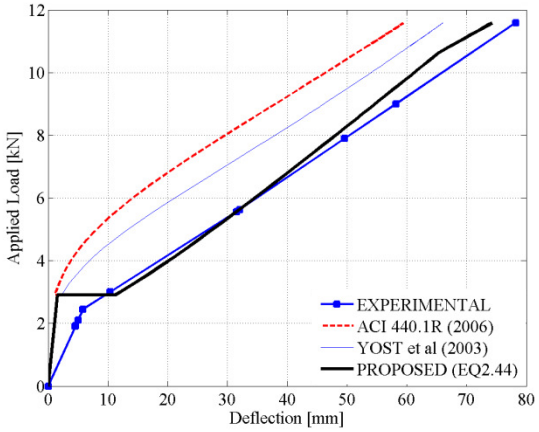

(g) Load-Deflection: SB6

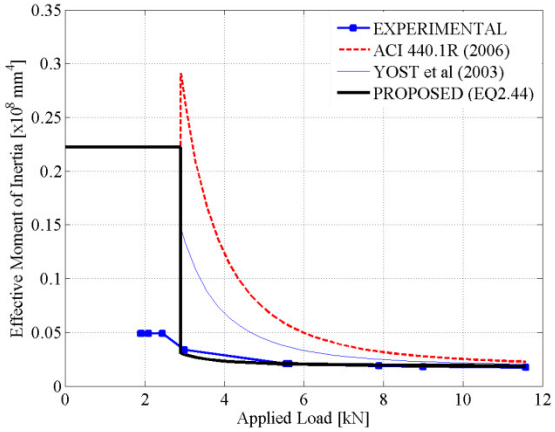

(h) Inertia: SB6

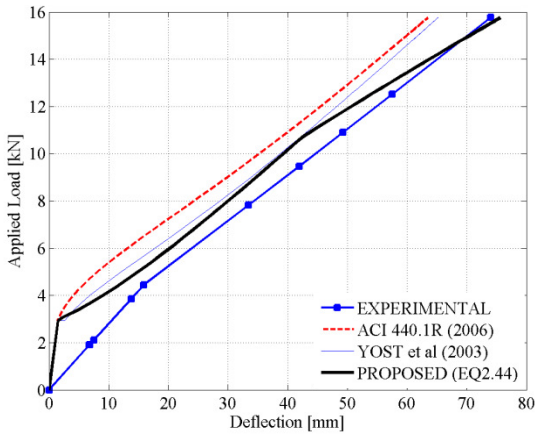

(i) Load-Deflection: SB7

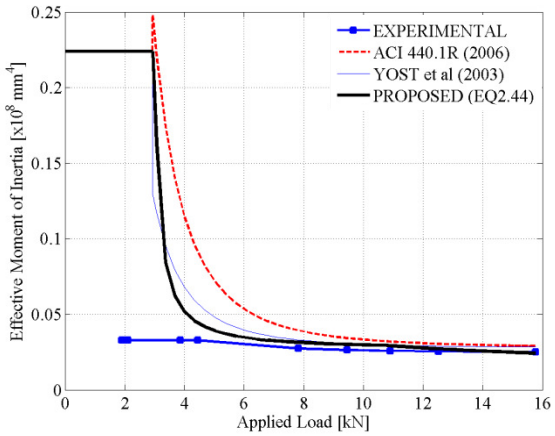

(j) Inertia: SB7

Figure A.30 **– Load-Deflection Estimates** [Alkradji et al. 2000]

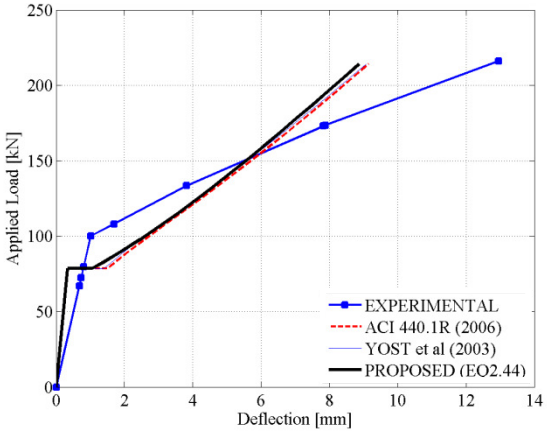

(a) Load-Deflection: V-G1-1

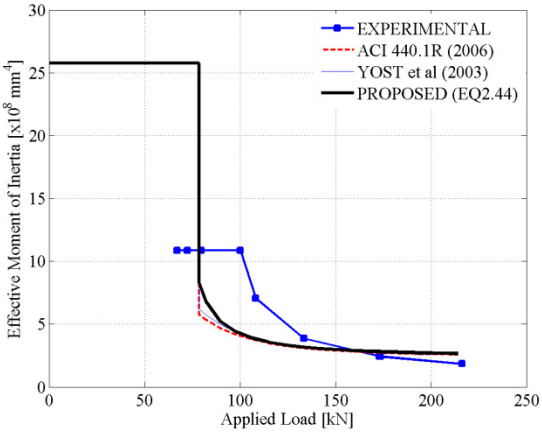

(b) Inertia: V-G1-1

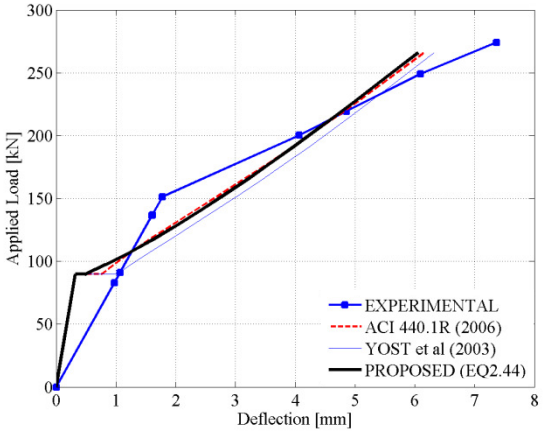

(c) Load-Deflection: V-G1-2

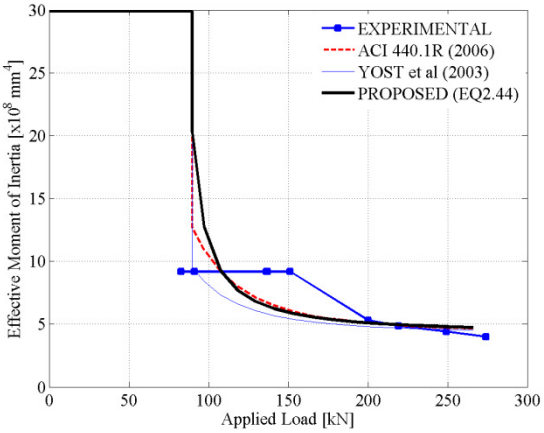

(d) Inertia: V-G1-2

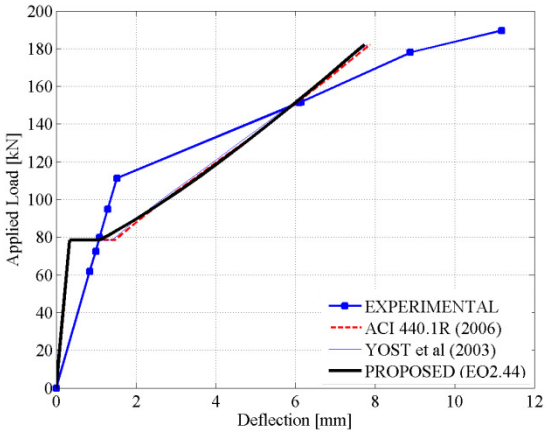

(e) Load-Deflection: V-G2-1

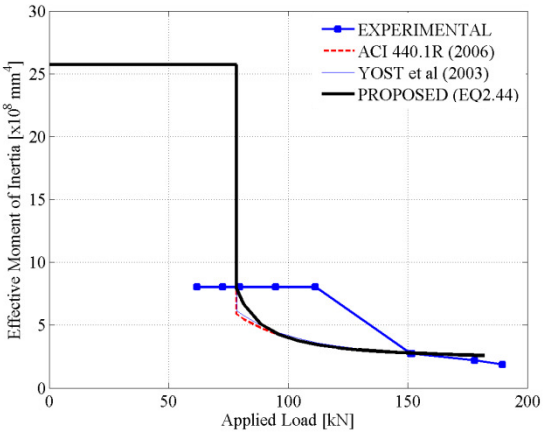

(f) Inertia: V-G2-1

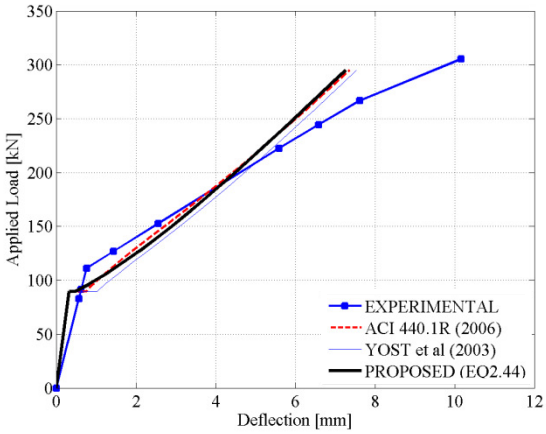

(g) Load-Deflection: V-G2-2

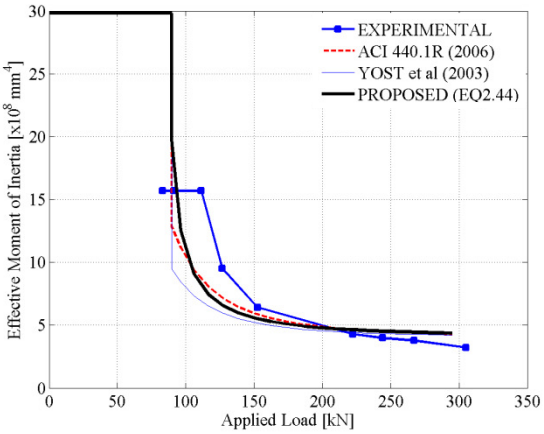

(h) Inertia: V-G2-2

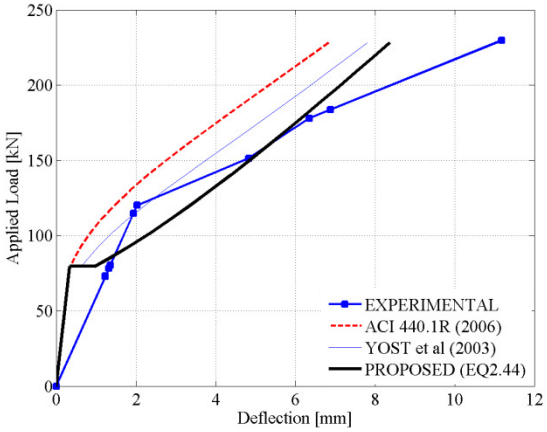

(i) Load-Deflection: V-A1

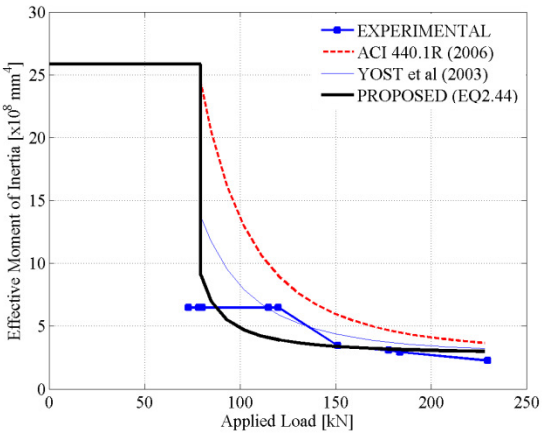

(j) Inertia: V-A1

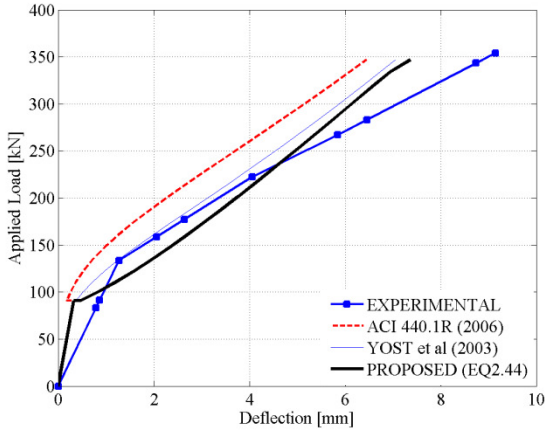

(k) Load-Deflection: V-A2

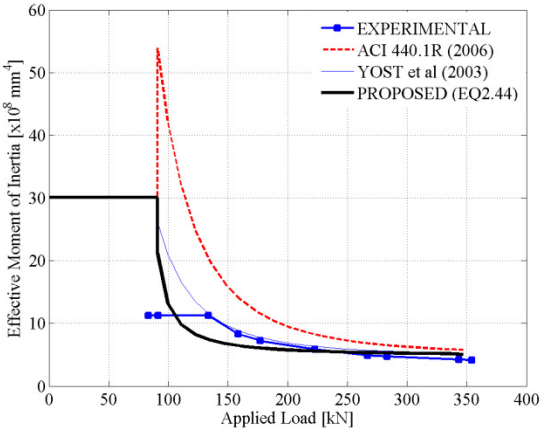

(l) Inertia: V-A2

Figure A.31 **– Load-Deflection Estimates** [Tureyen and Frosch 2002]

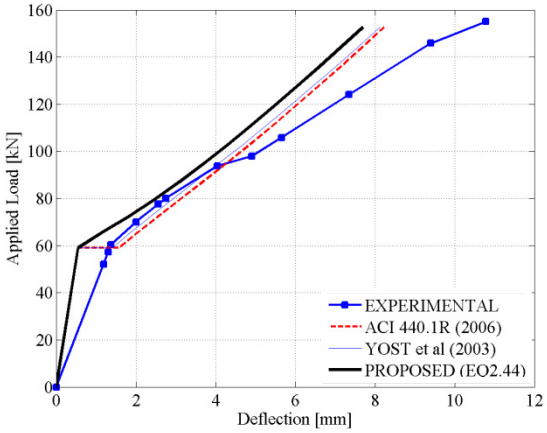

(a) Load-Deflection: CN-1

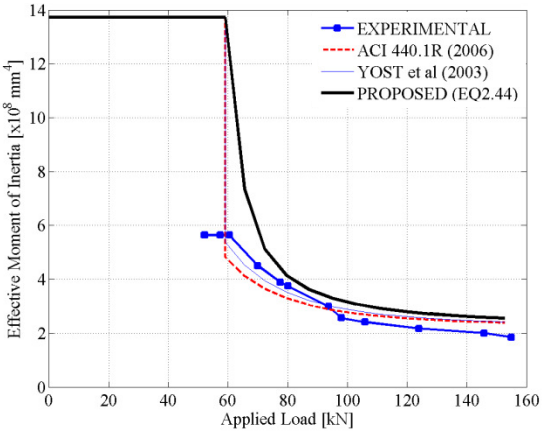

(b) Inertia: CN-1

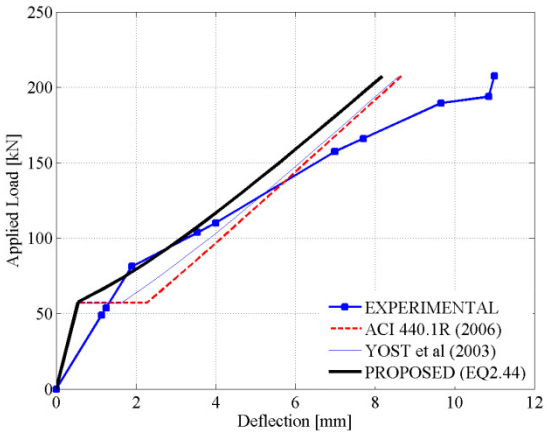

(c) Load-Deflection: CN-2

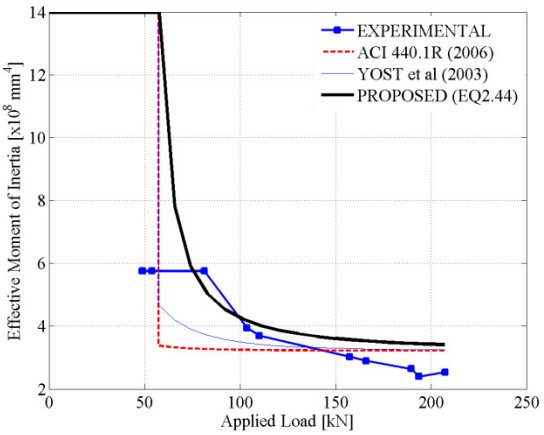

(d) Inertia: CN-2

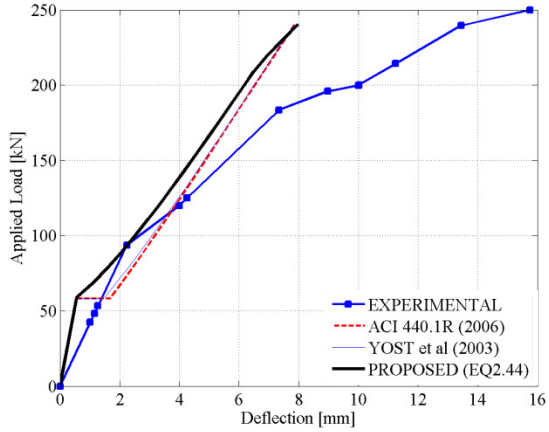

(e) Load-Deflection: CN-3

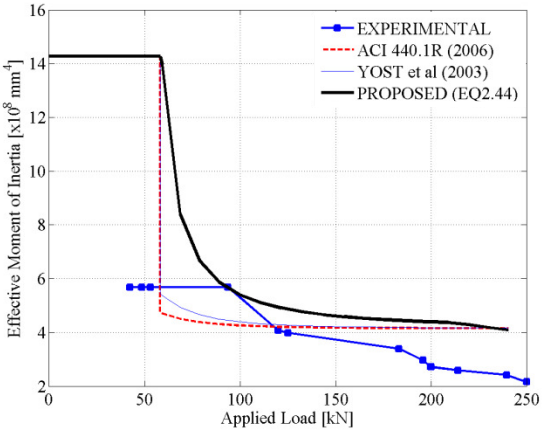

(f) Inertia: CN-3

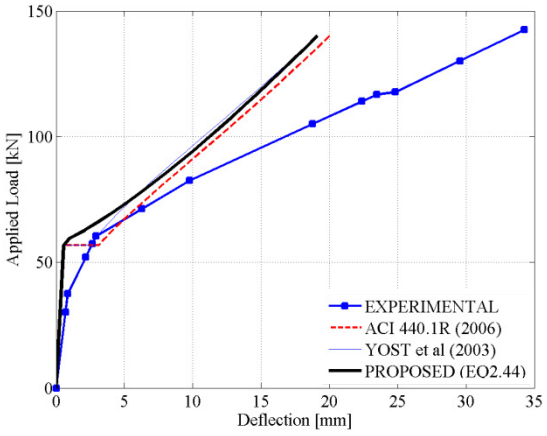

(g) Load-Deflection: GN-1

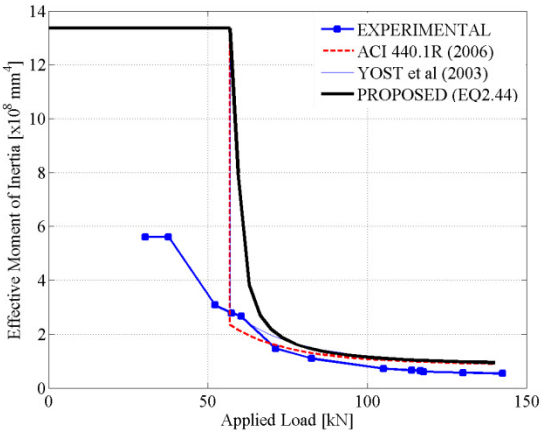

(h) Inertia: GN-1

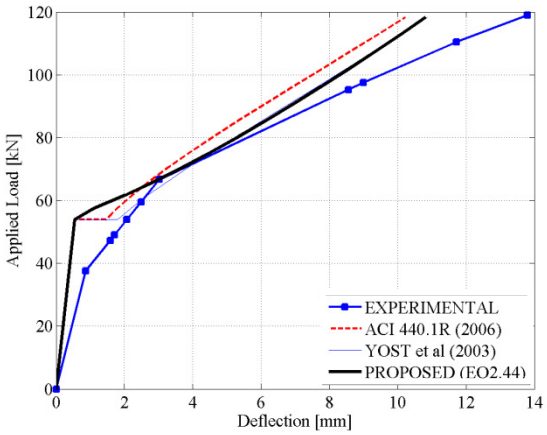

(i) Load-Deflection: GN-2

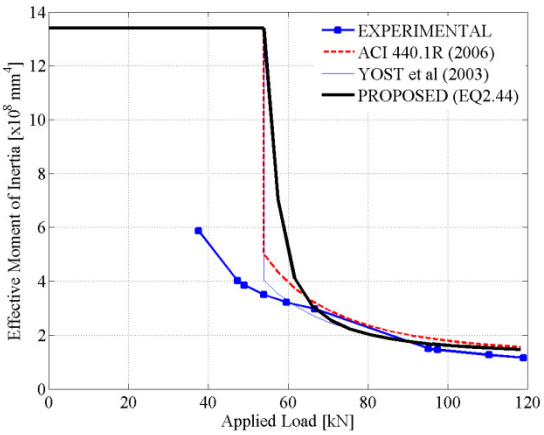

(j) Inertia: GN-2

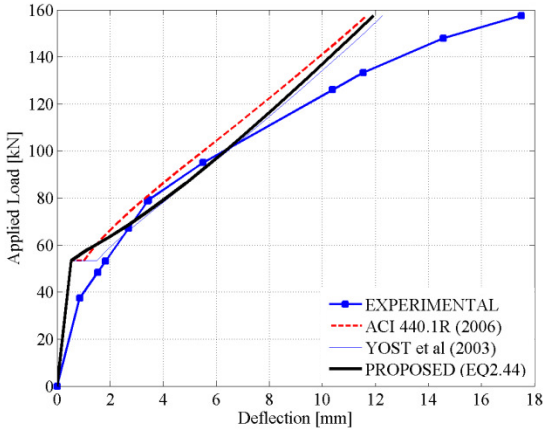

(k) Load-Deflection: GN-3

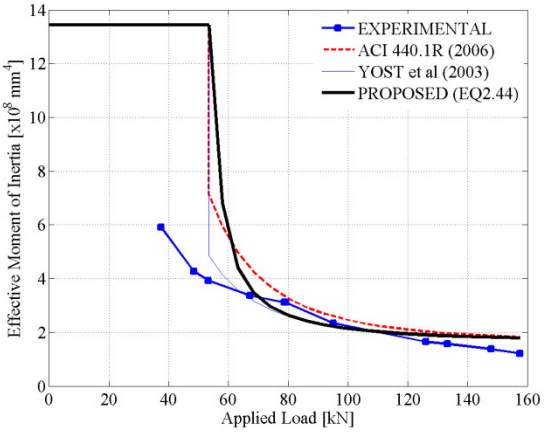

(l) Inertia: GN-3

Figure A.32 **– Load-Deflection Estimates** [El-Sayed et al. 2004]

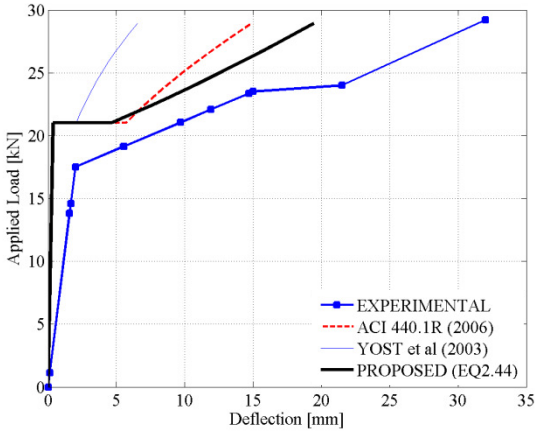

(a) Load-Deflection: Lab1FRP1

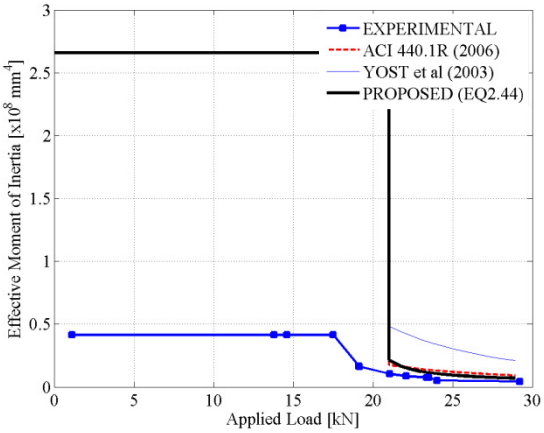

(b) Inertia: Lab1FRP1

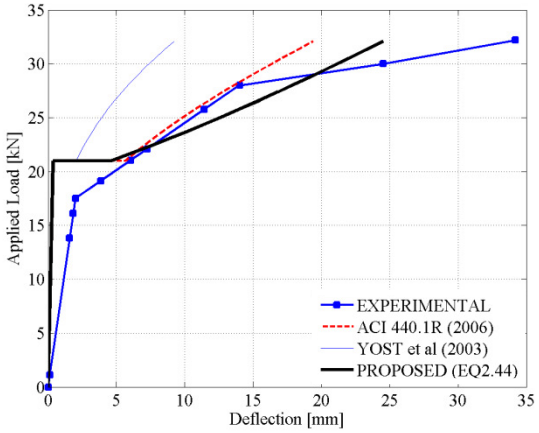

(c) Load-Deflection: Lab1FRP2

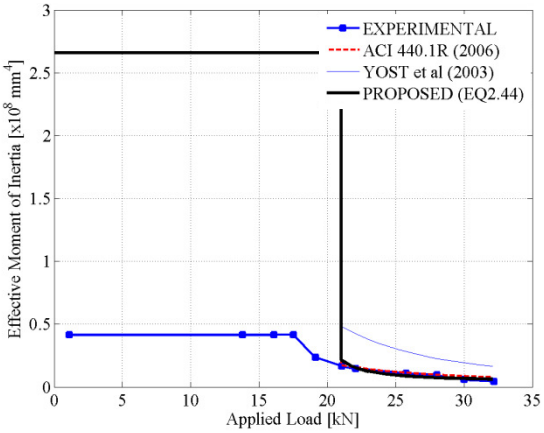

(d) Inertia: Lab1FRP2

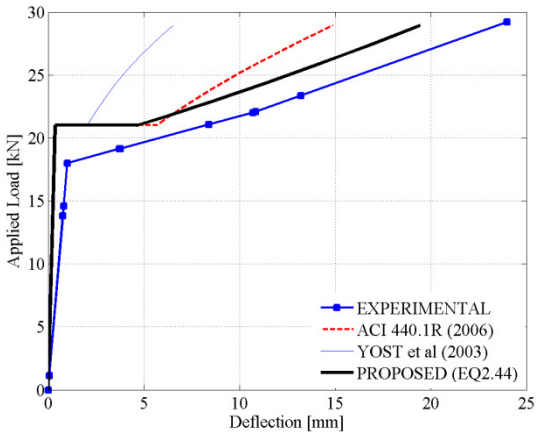

(e) Load-Deflection: Lab1FRP3

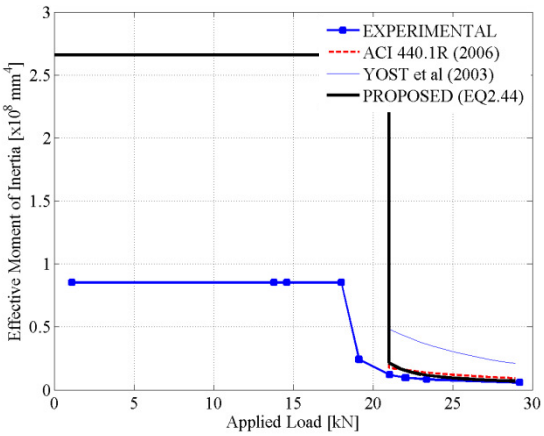

(f) Inertia: Lab1FRP3

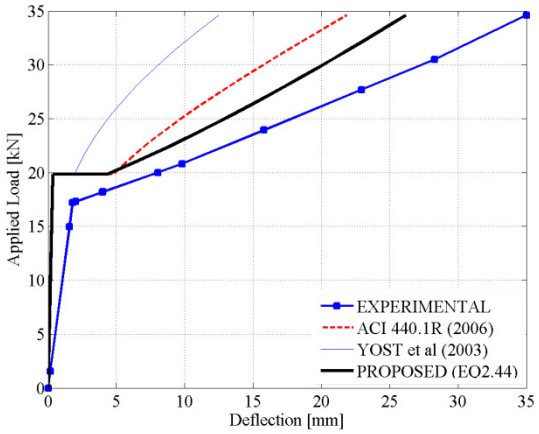

(g) Load-Deflection: Lab2FRP1

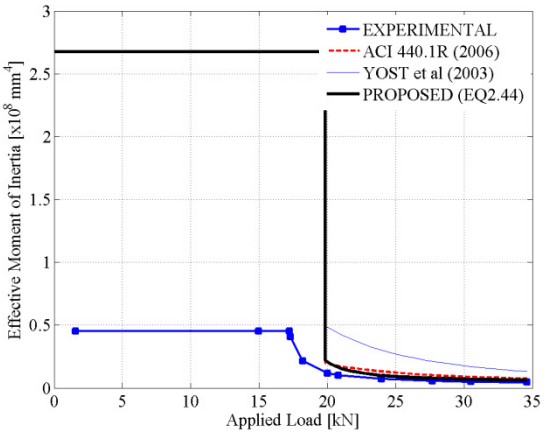

(h) Inertia: Lab2FRP1

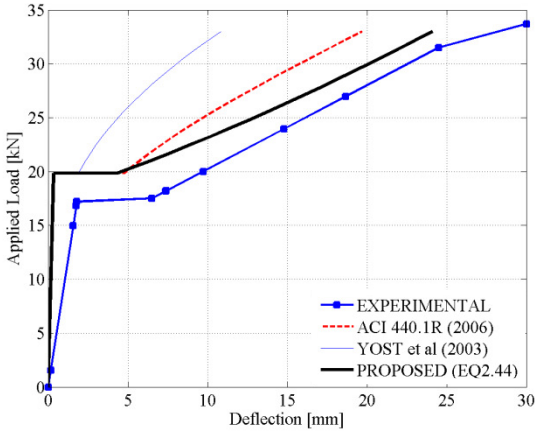

(i) Load-Deflection: Lab2FRP2

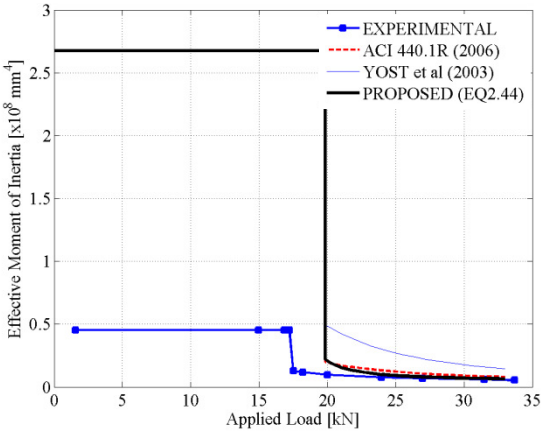

(j) Inertia: Lab2FRP2

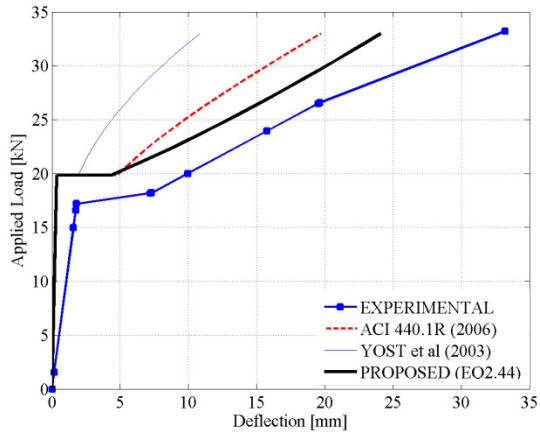

(k) Load-Deflection: Lab2FRP3

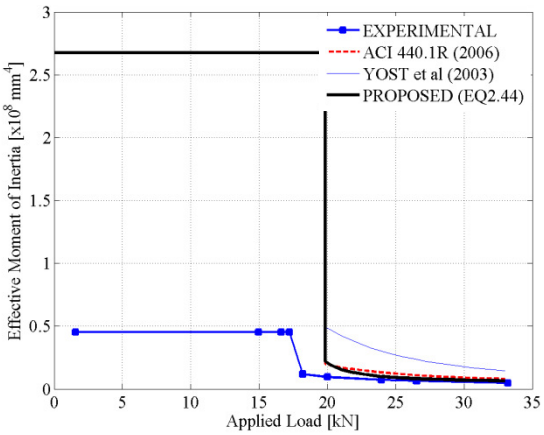

(l) Inertia: Lab2FRP3

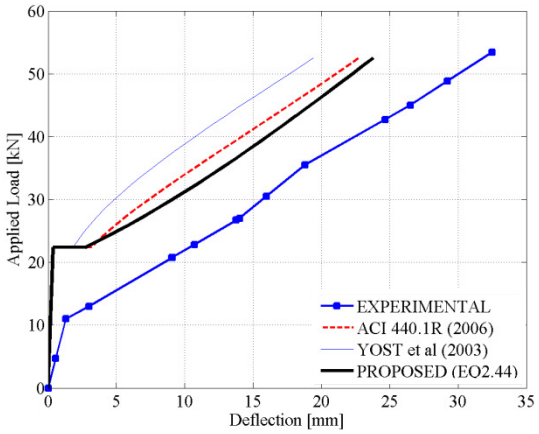

(a) Load-Deflection: Lab3FRP

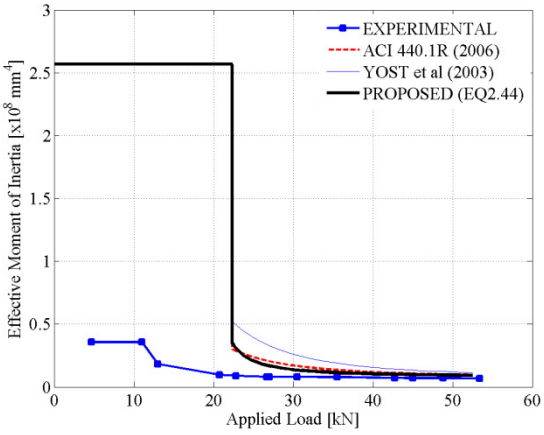

(b) Inertia: Lab3FRP

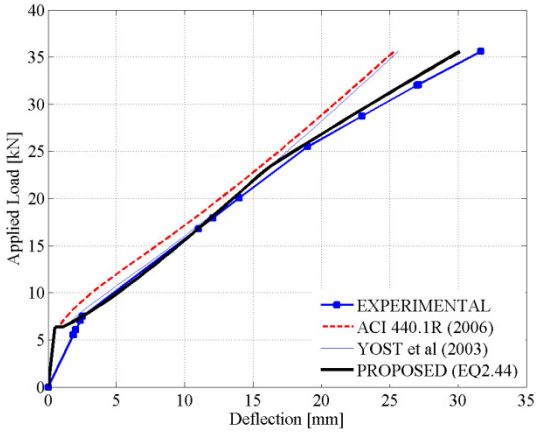

(c) Load-Deflection: Lab4FRP

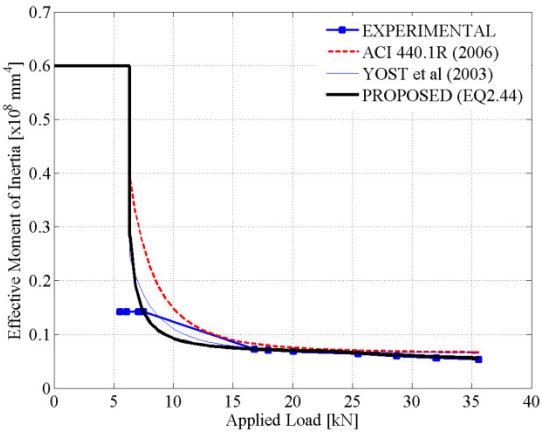

(d) Inertia: Lab4FRP

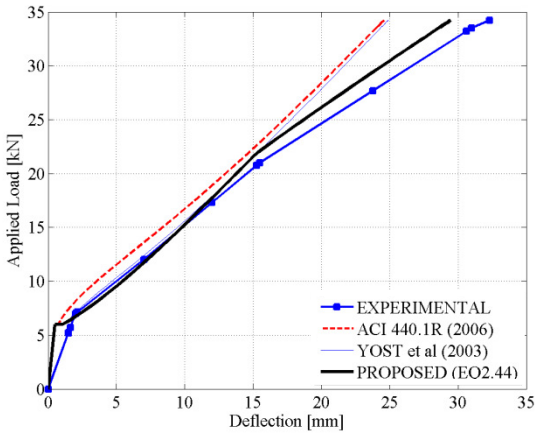

(e) Load-Deflection: Lab5FRP

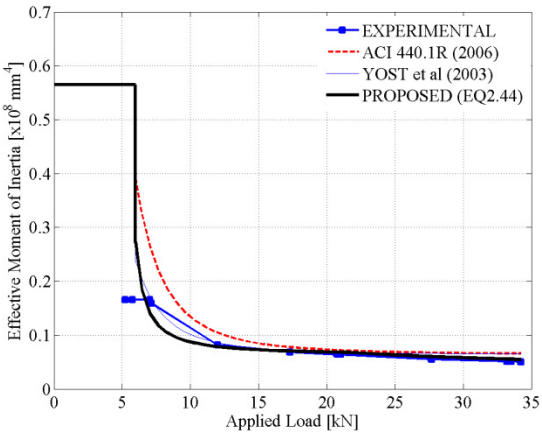

(f) Inertia: Lab5FRP

Figure A.33 **– Load-Deflection Estimates** [Yost et al. 2001]

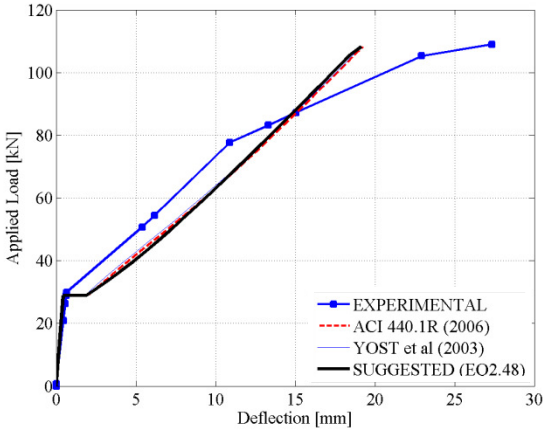

(a) Load-Deflection: R-G007Na

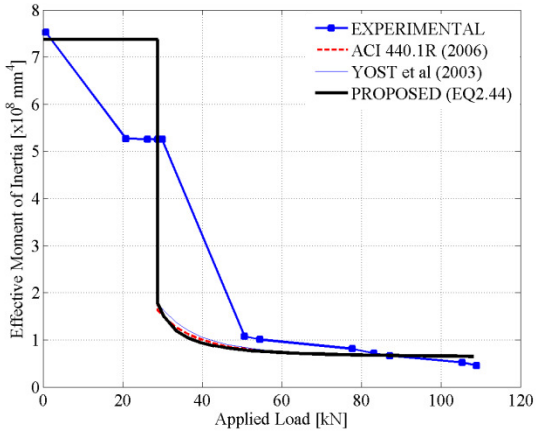

(b) Inertia: R-G007Na

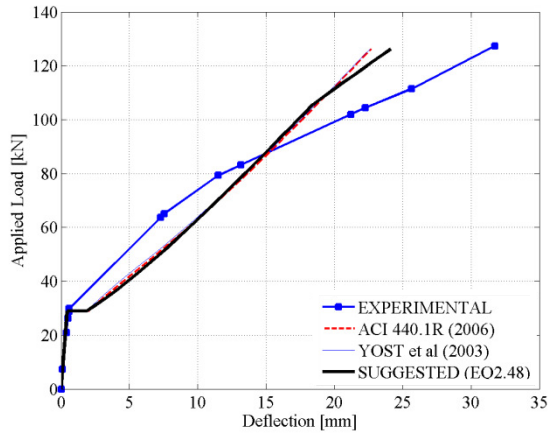

(c) Load-Deflection: R-G007Nb

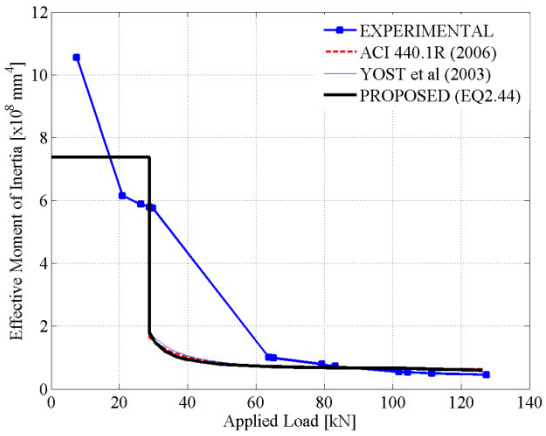

(d) Inertia: R-G007Nb

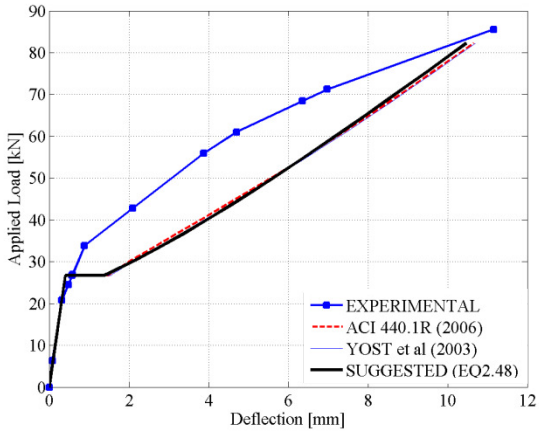

(e) Load-Deflection: R-G010Na

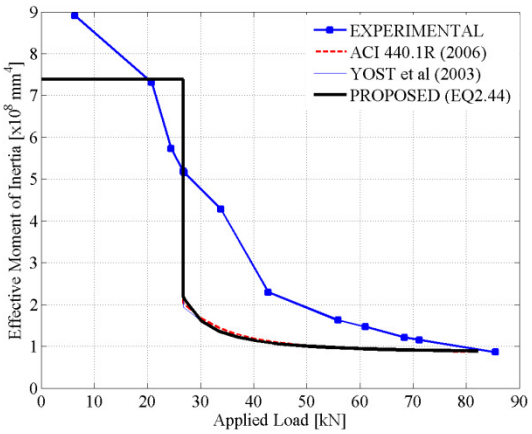

(f) Inertia: R-G010Na

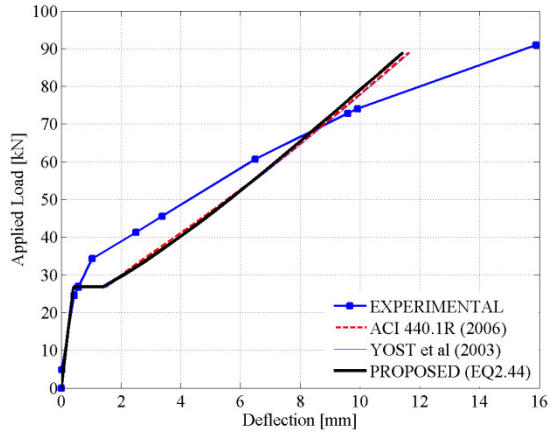

(g) Load-Deflection: R-G010Nb

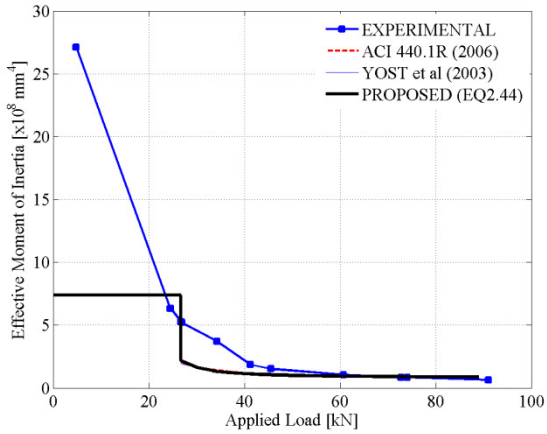

(h) Inertia: R-G010Nb

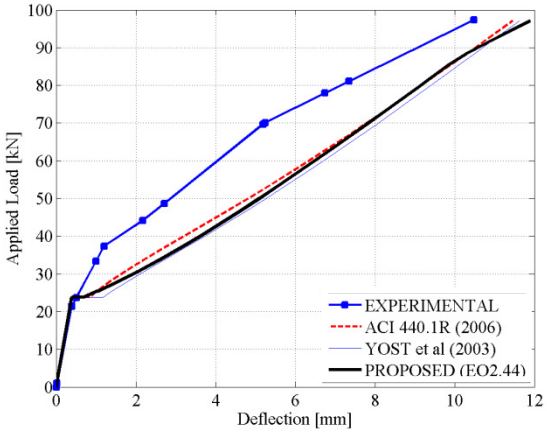

(i) Load-Deflection: R-G015Na

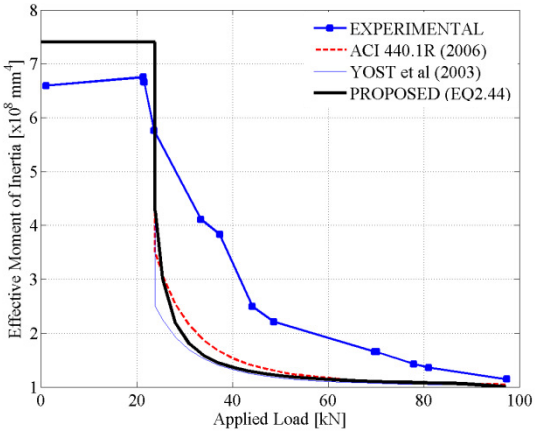

(j) Inertia: R-G015Na

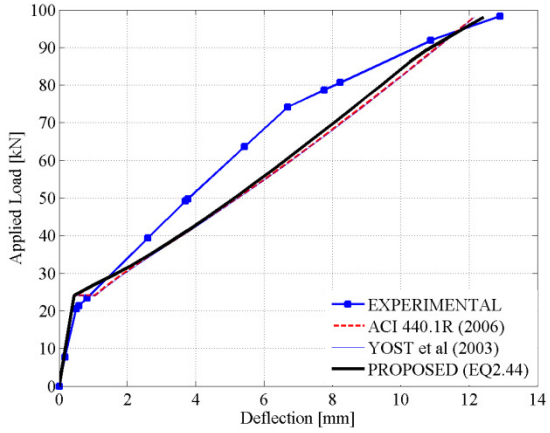

(k) Load-Deflection: R-C007Na

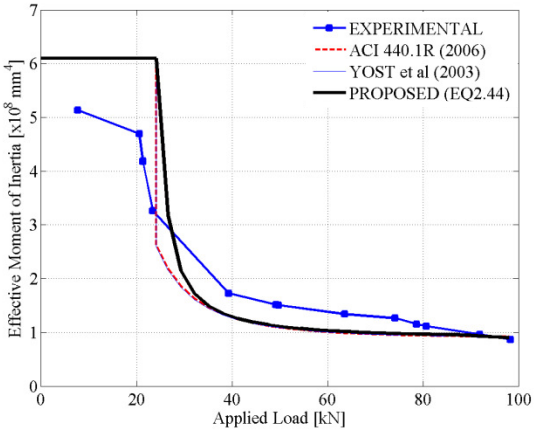

(l) Inertia: R-C007Na

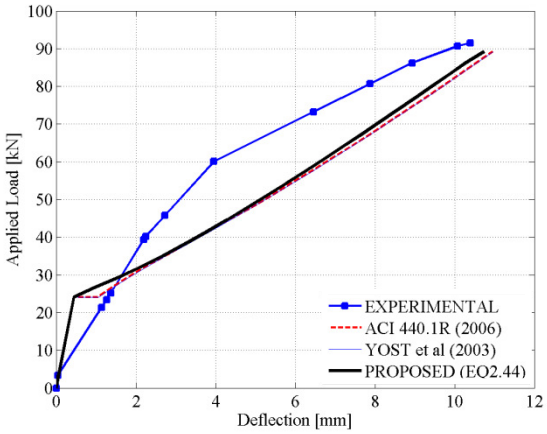

(m) Load-Deflection: R-C007Nb

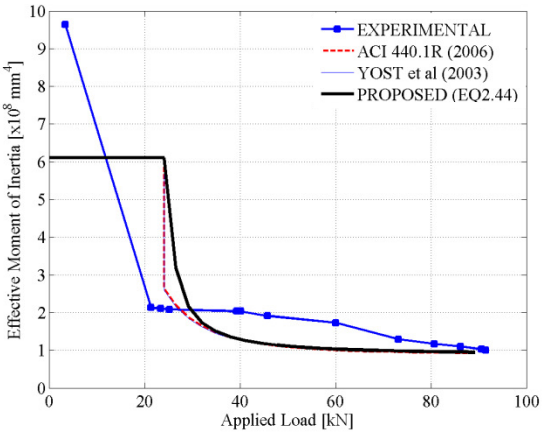

(n) Inertia: R-C007Nb

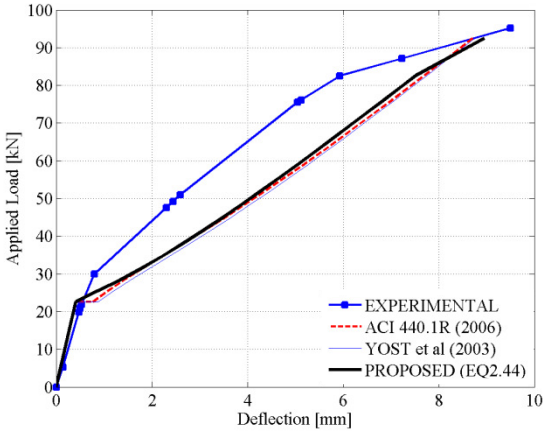

(o) Load-Deflection: R-C010Na

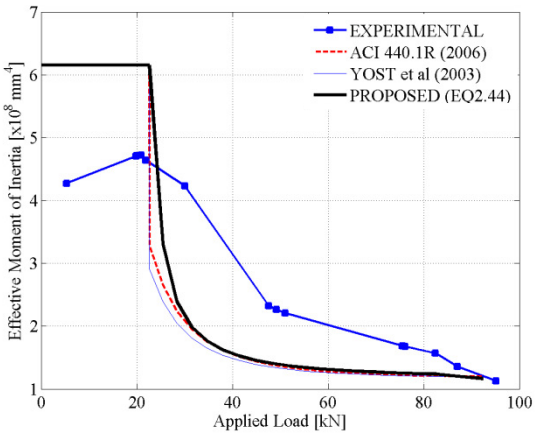

(p) Inertia: R-C010Na

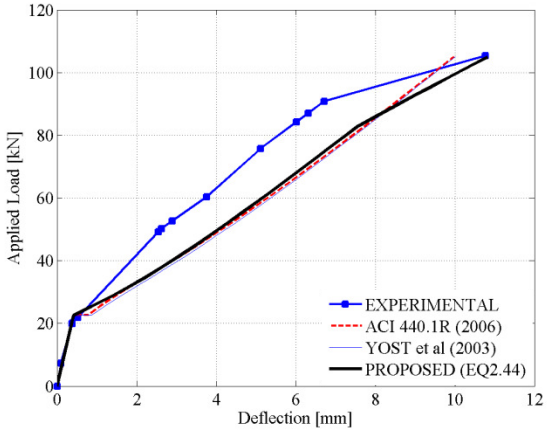

(q) Load-Deflection: R-C010Nb

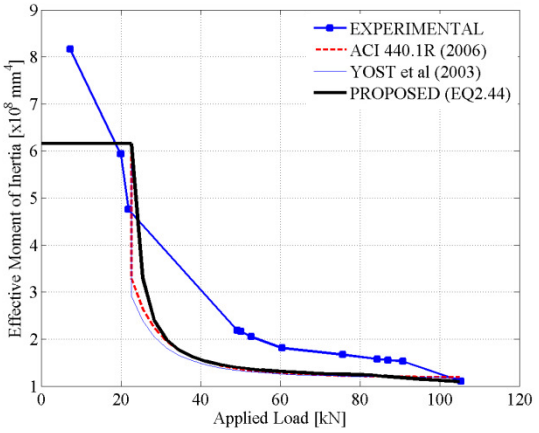

(r) Inertia: R-C010Nb

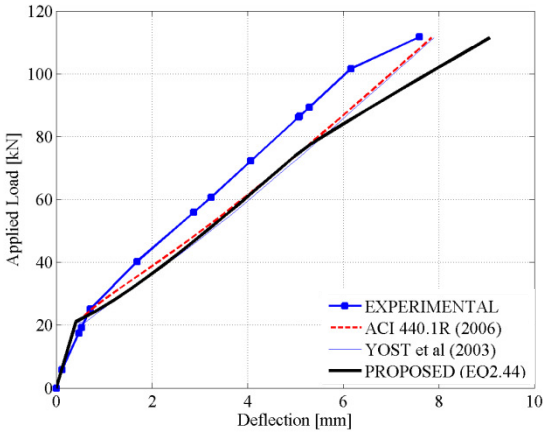

(s) Load-Deflection: R-C015Na

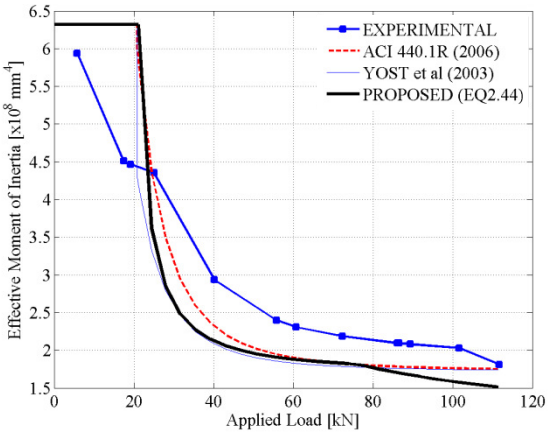

(t) Inertia: R-C015Na

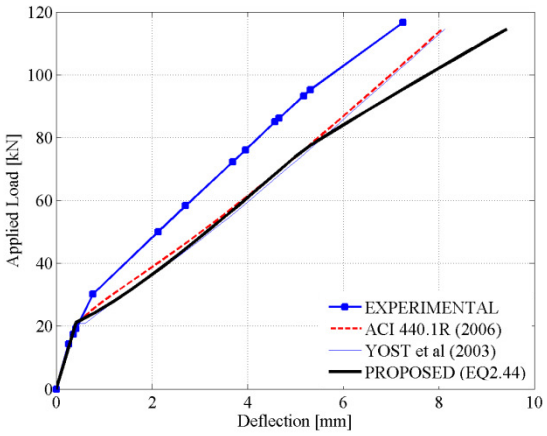

(u) Load-Deflection: R-C015Nb

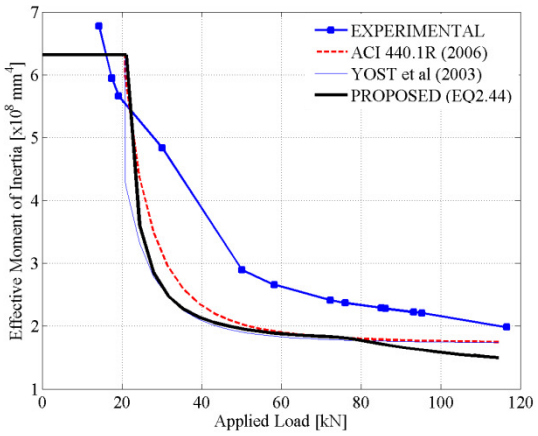

(v) Inertia: R-C015Nb

Figure A.34 **– Load-Deflection Estimates** [Tariq 2003]

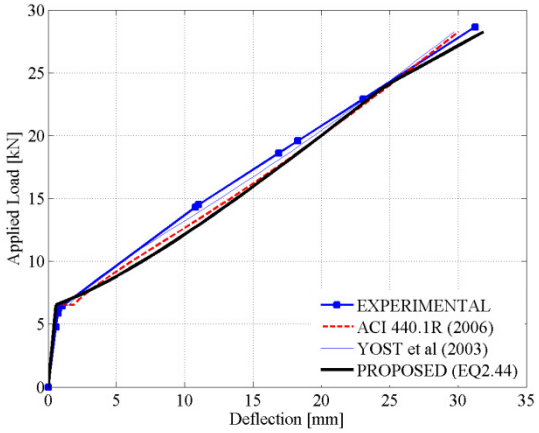

(a) Load-Deflection: S#1

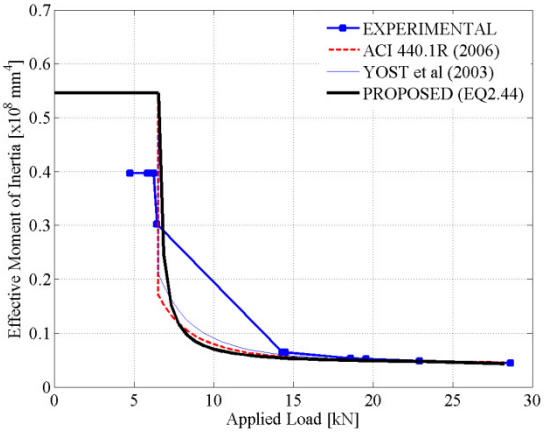

(b) Inertia: S#1

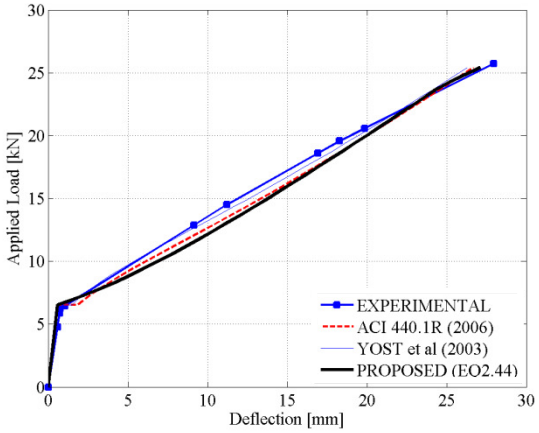

(c) Load-Deflection: S#2

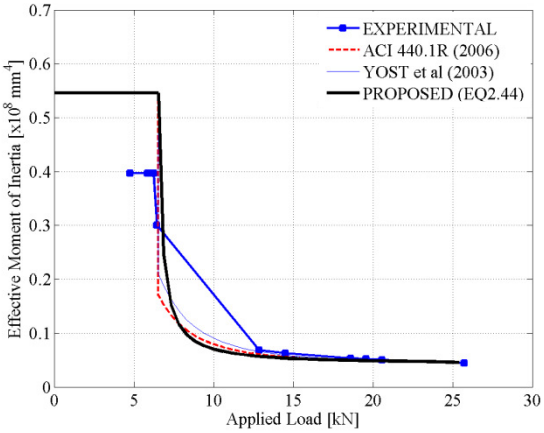

(d) Inertia: S#2

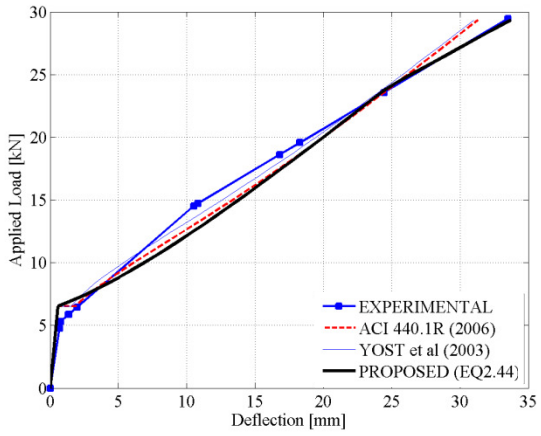

(e) Load-Deflection: S#3

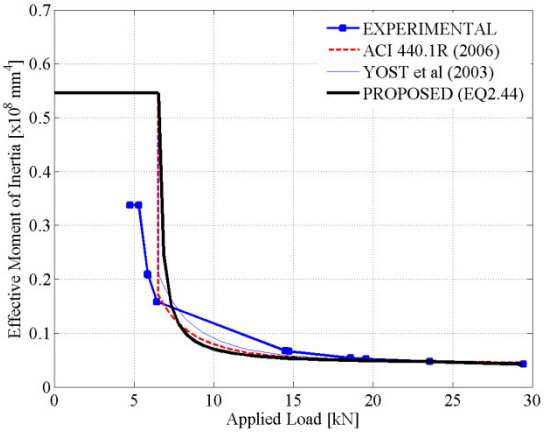

(f) Inertia: S#3

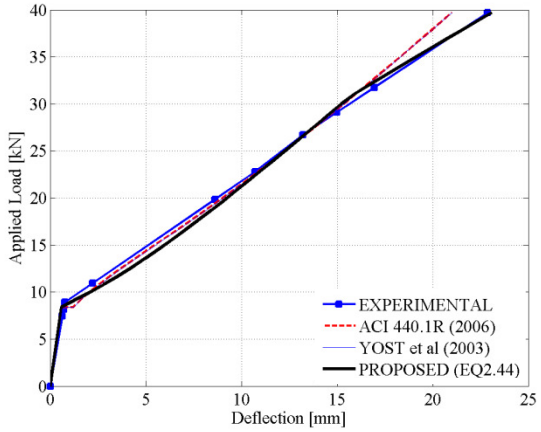

(g) Load-Deflection: S#4

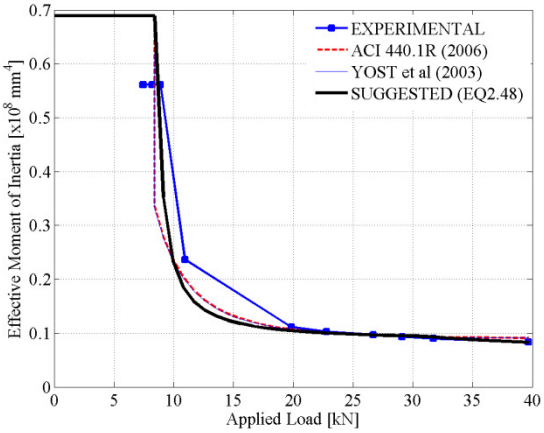

(h) Inertia: S#4

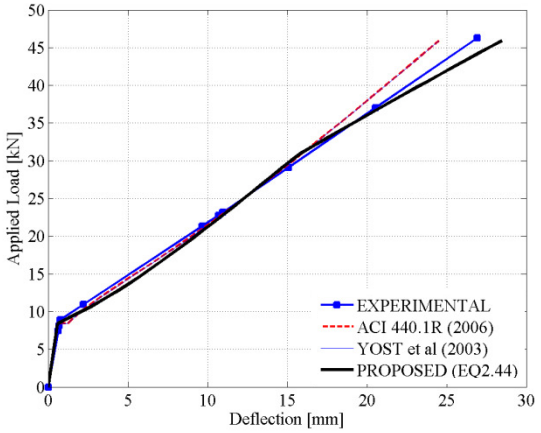

(i) Load-Deflection: S#5

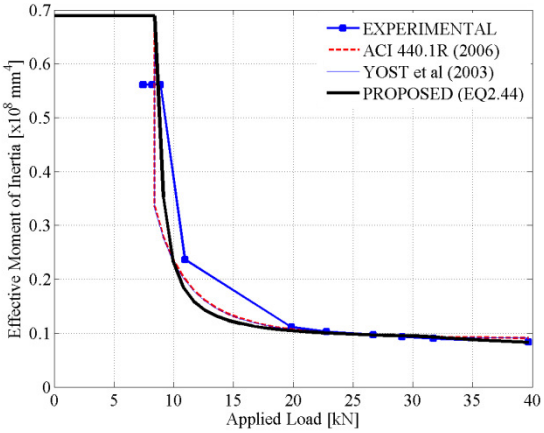

(j) Inertia: S#5

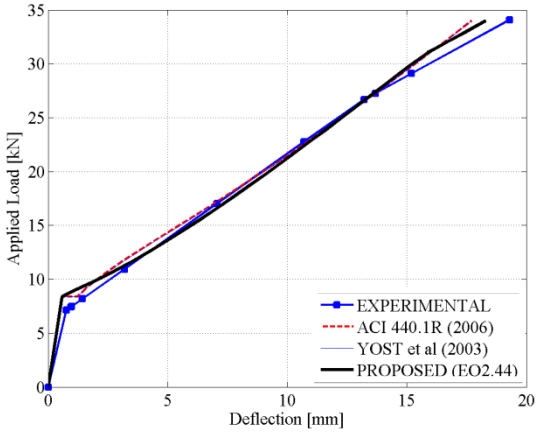

(k) Load-Deflection: S#6

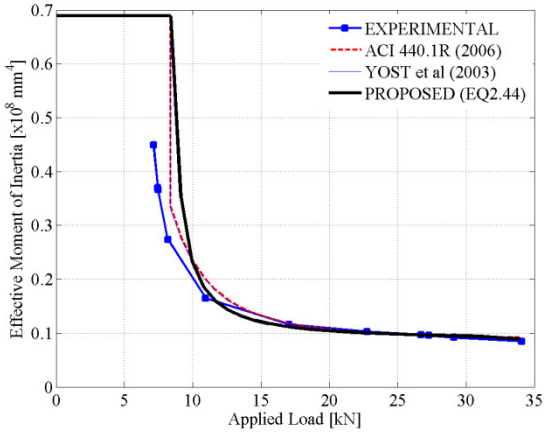

(l) Inertia: S#6

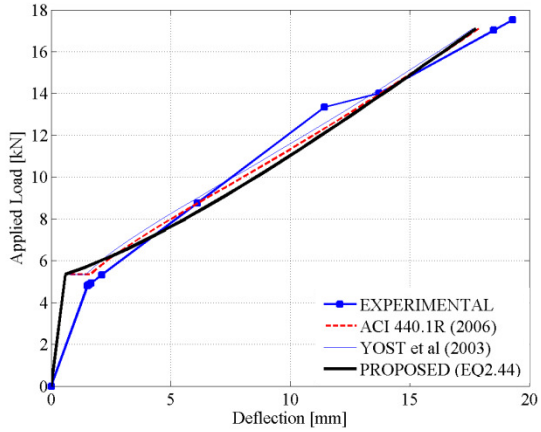

(m) Load-Deflection: S#7

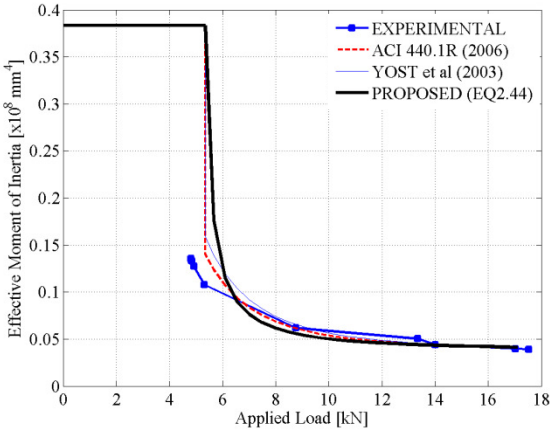

(n) Inertia: S#7

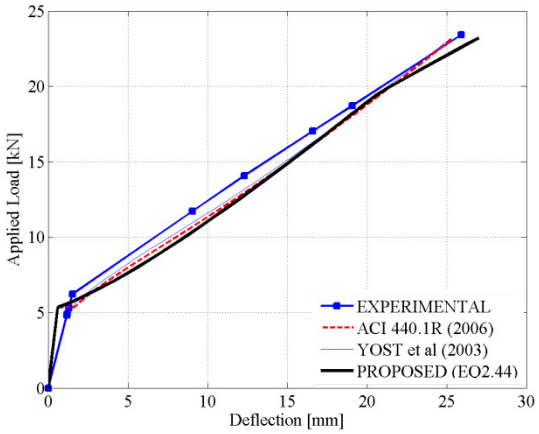

(o) Load-Deflection: S#8

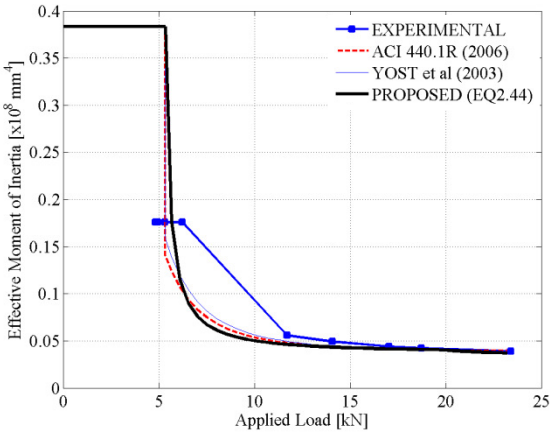

(p) Inertia: S#8

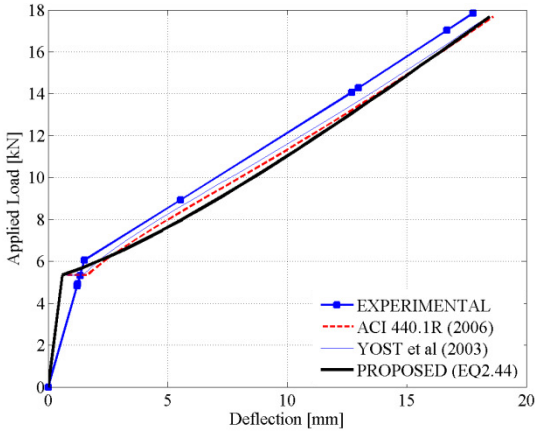

(q) Load-Deflection: S#9

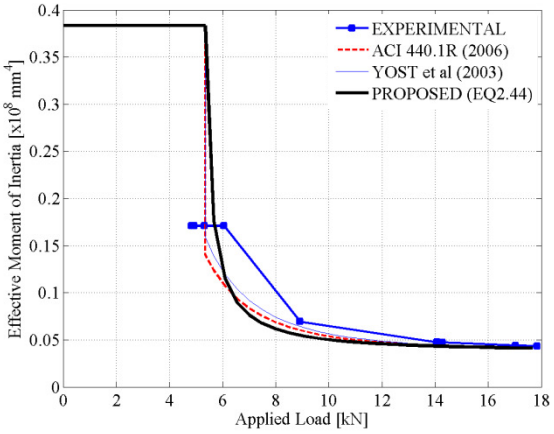

(r) Inertia: S#9

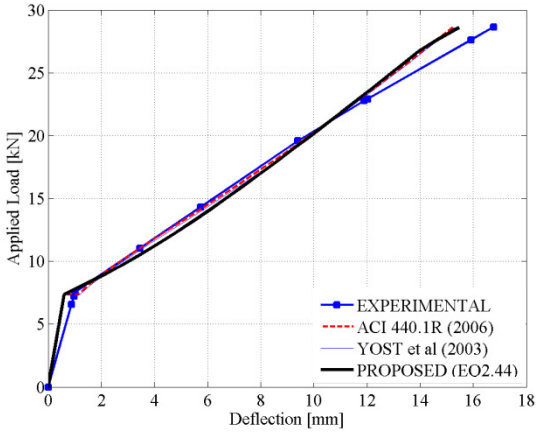

(s) Load-Deflection: S#10

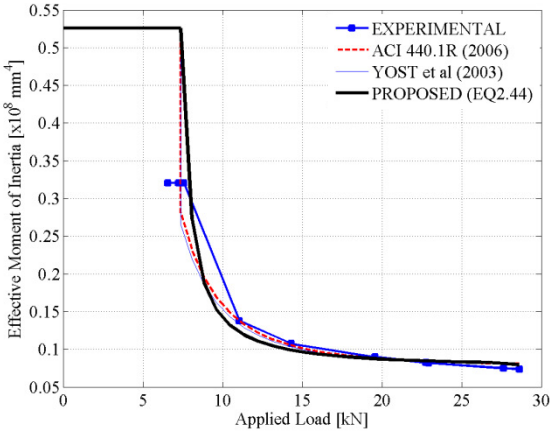

(t) Inertia: S#10

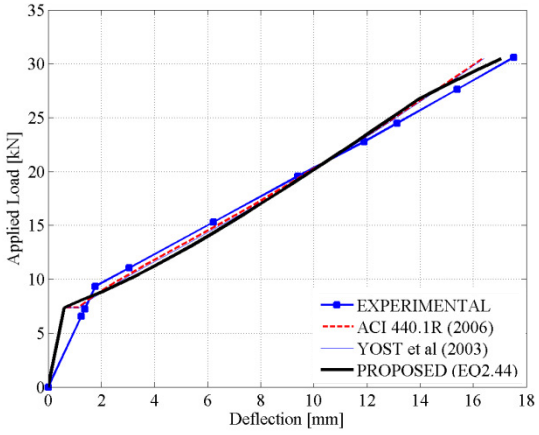

(u) Load-Deflection: S#11

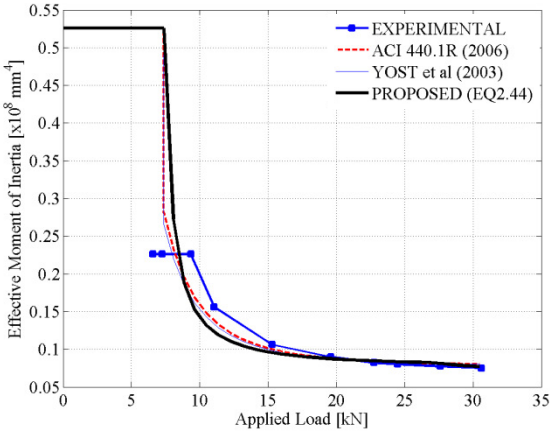

(v) Inertia: S#11

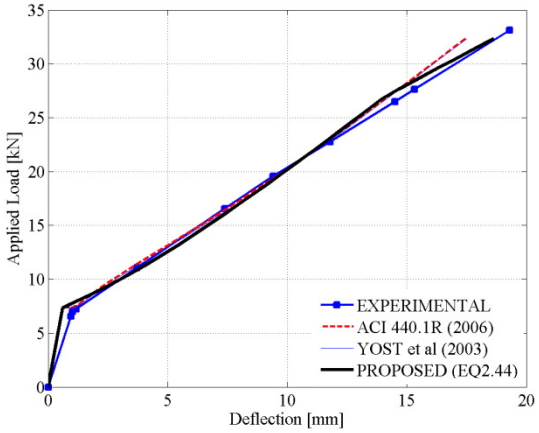

(w) Load-Deflection: S#12

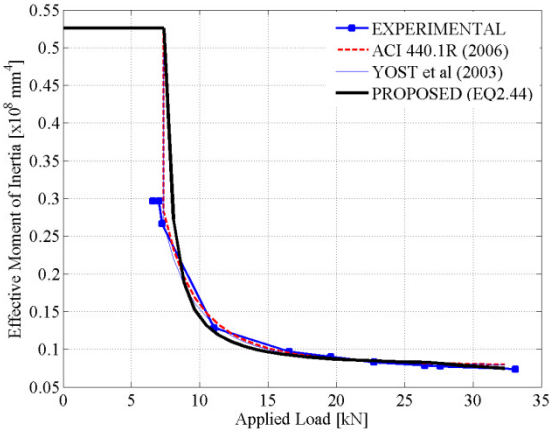

(x) Inertia: S#12

Figure A.35 **– Load-Deflection Estimates** [Gross et al. 2004]

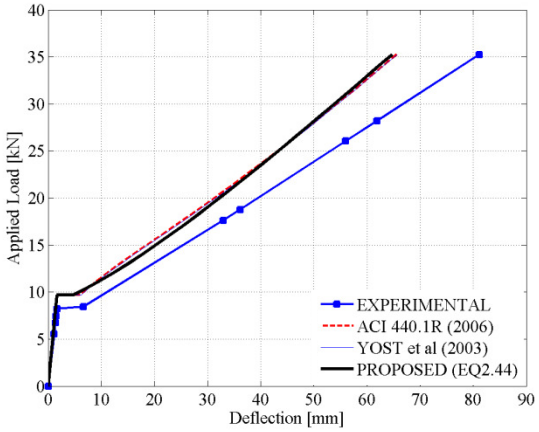

(a) Load-Deflection: Sh-G-2-S

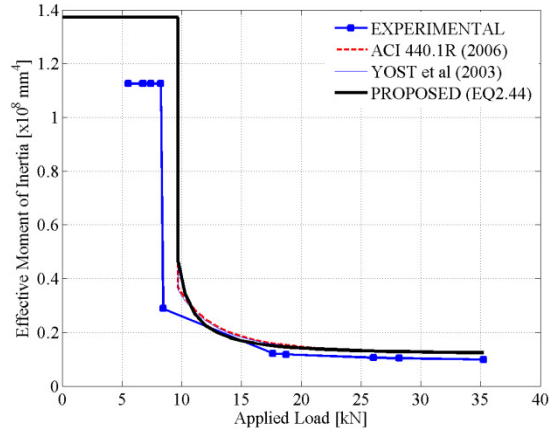

(b) Inertia: Sh-G-2-S

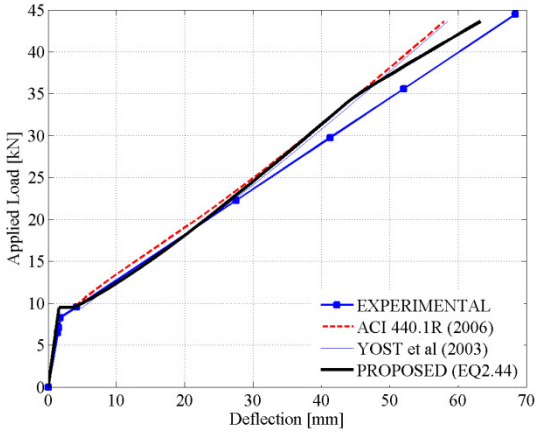

(c) Load-Deflection: Sh-G-3-S

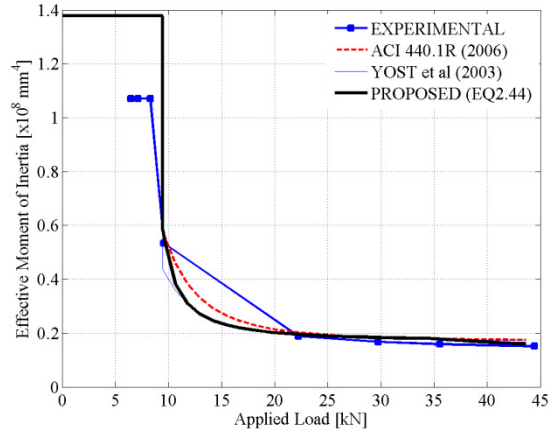

(d) Inertia: Sh-G-3-S

Figure A.36 **– Load-Deflection Estimates** [Hall 2000]

APPENDIX B

EXPERIMENTAL RESULTS

STRAIN PROFILES

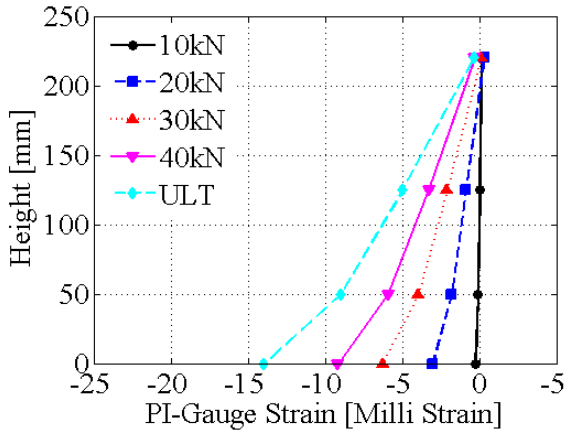

(a) PCPB1-1

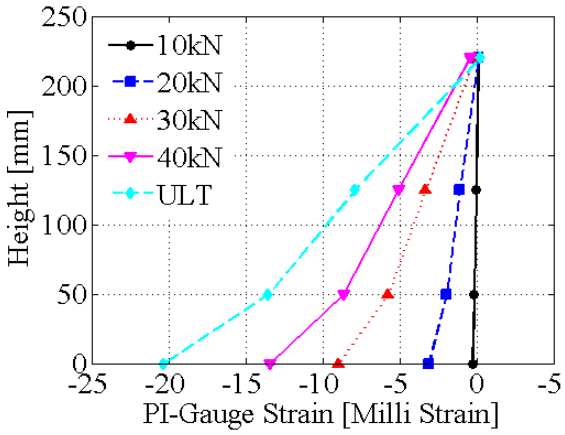

(b) PCPB1-2

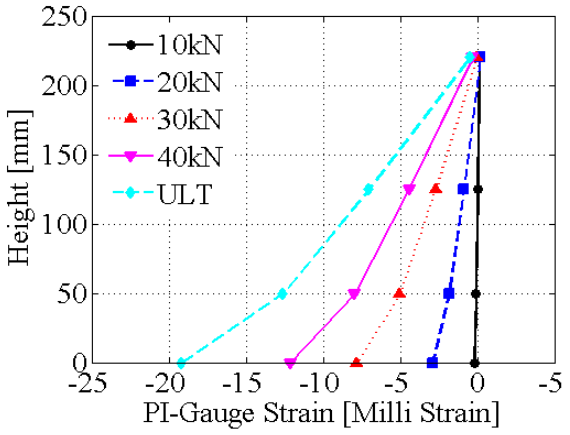

(c) PCPB1-3

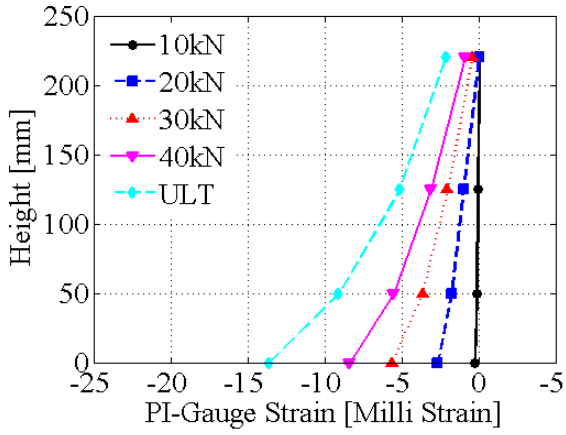

(d) PCPB1-4

Figure B.1 – **Strain Profiles** [First Batch PCP Reinforced Beams]

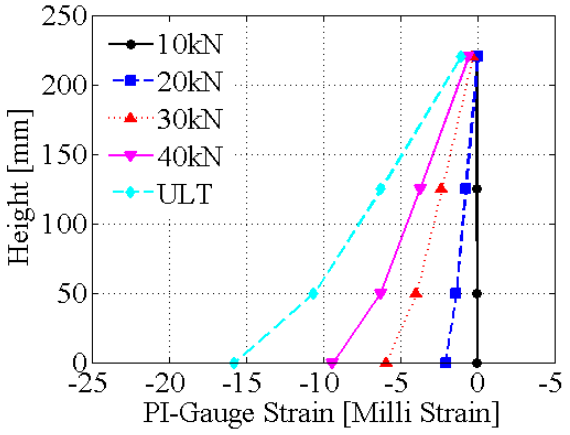

(a) PCB1-1

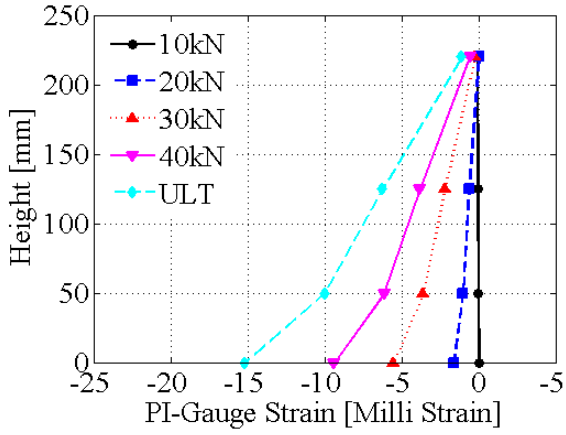

(b) PCB1-2

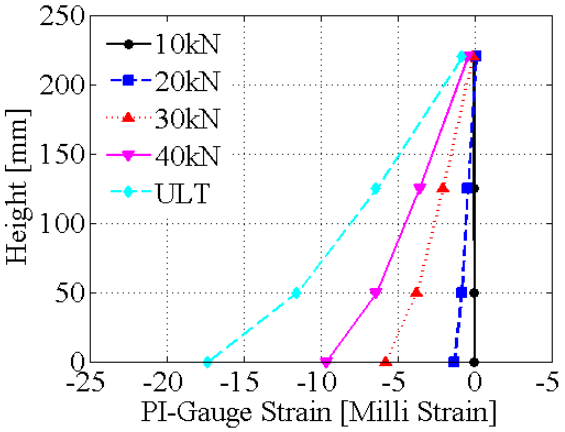

(c) PCB1-3

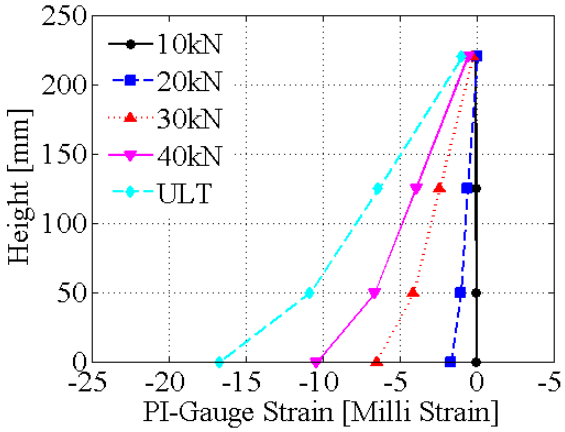

(d) PCB1-4

Figure B.2 – **Strain Profiles** [First Batch Prestressed Beams]

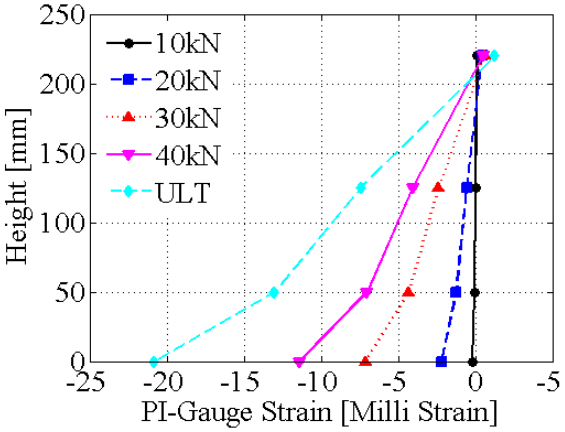

(a) PCPB2-1T

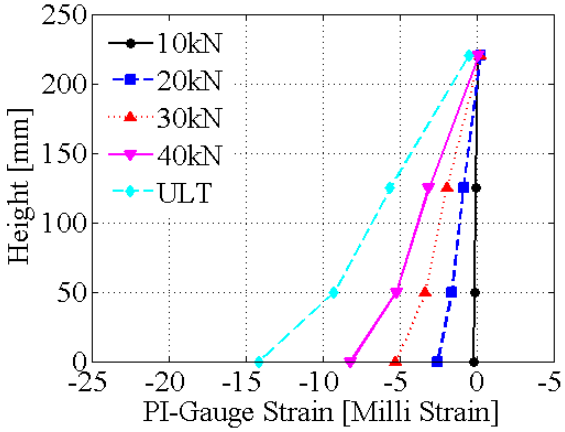

(b) PCPB2-2

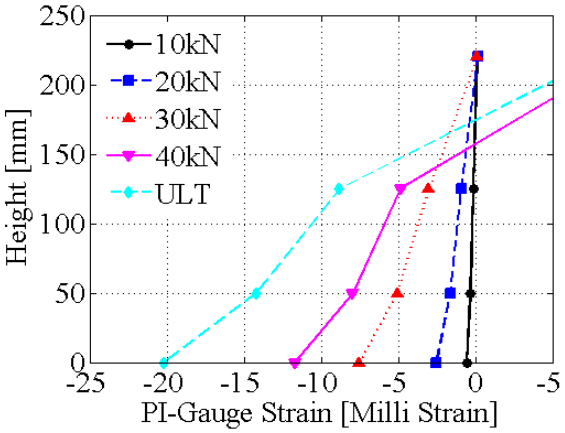

(a) PCPB2-3TF

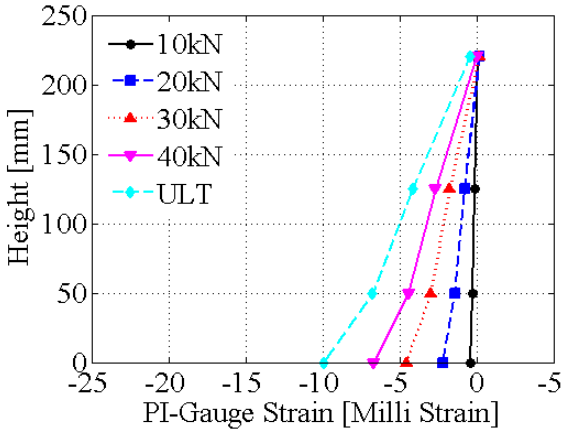

(b) PCPB2-4F

Figure B.3 – **Strain Profiles** [Second Batch PCP Reinforced Beams]

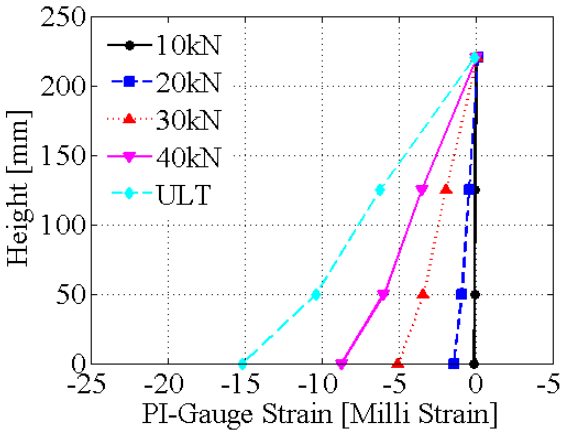

(a) PCB2-1T

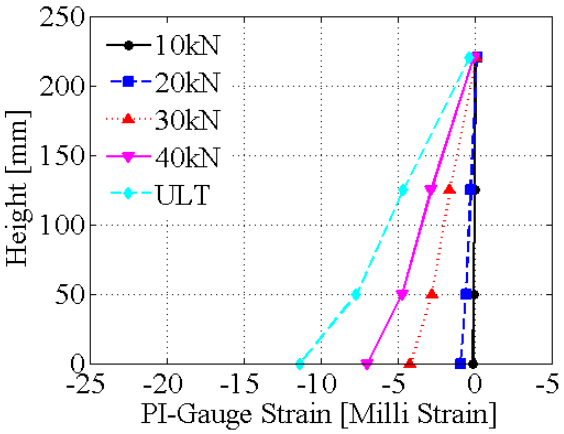

(b) PCB2-2

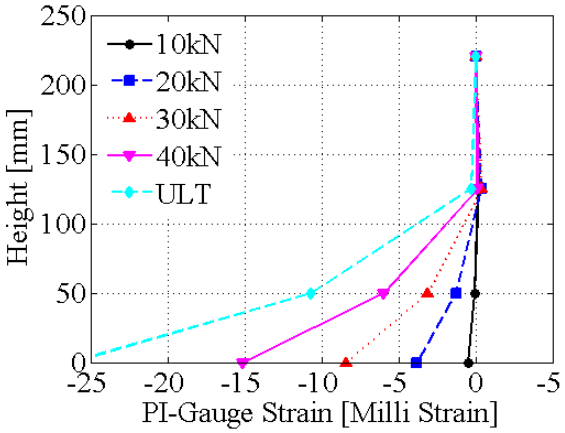

(a) PCB2-3TF

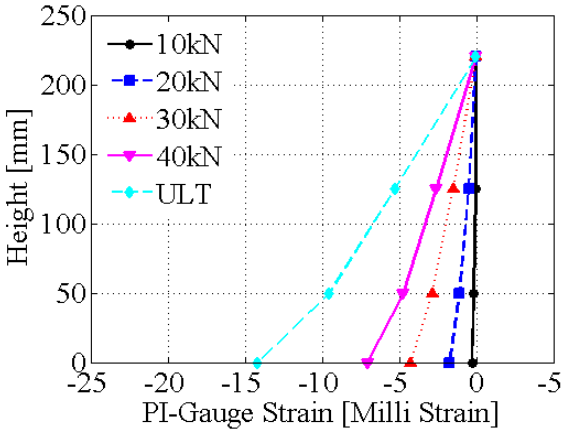

(b) PCB2-4F

Figure B.4 – **Strain Profiles** [Second Batch Prestressed Beams]

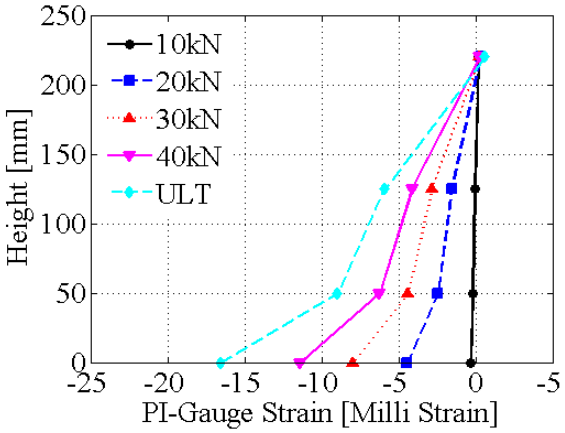

(a) PCPB3-1N

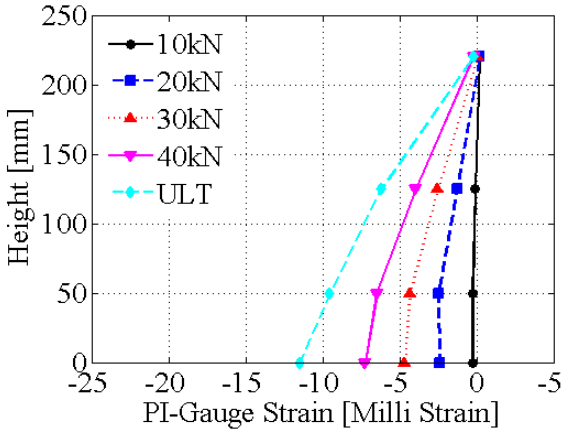

(b) PCPB3-2N

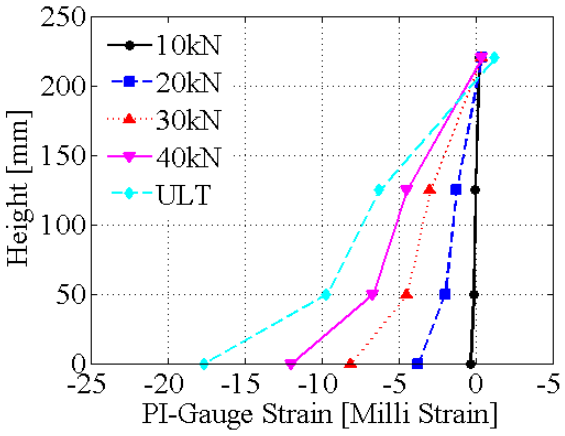

(a) PCPB3-3N

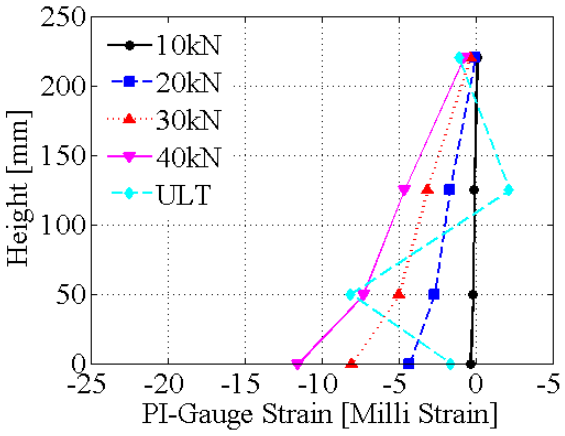

(b) PCPB3-4N

Figure B.5 – **Strain Profiles** [Third Batch PCP Reinforced Beams / Notches]

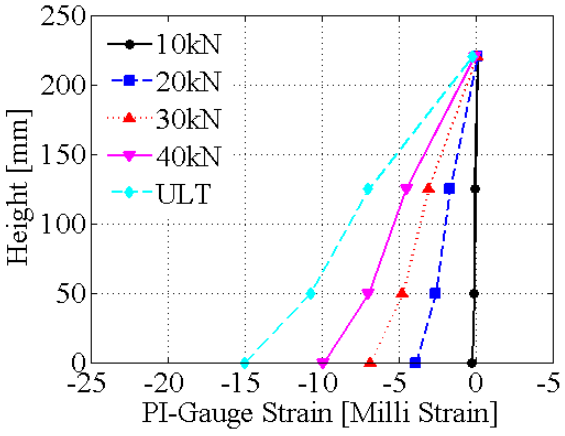

(a) PCPB3-1F50

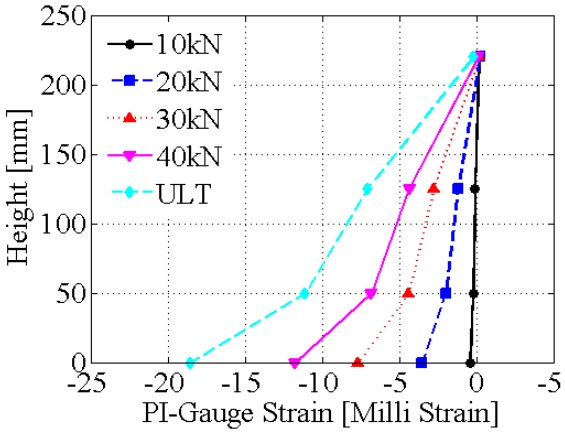

(b) PCPB3-2F50

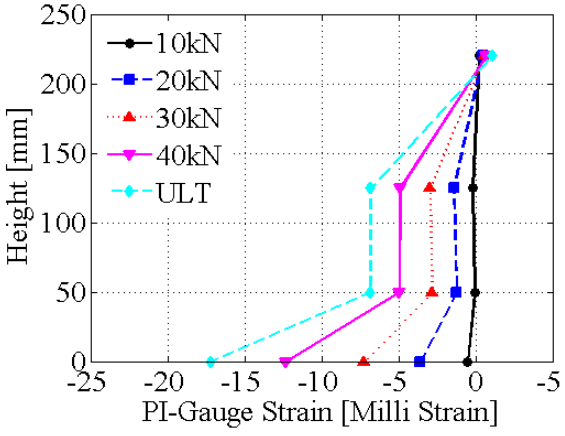

(a) PCPB3-3F50

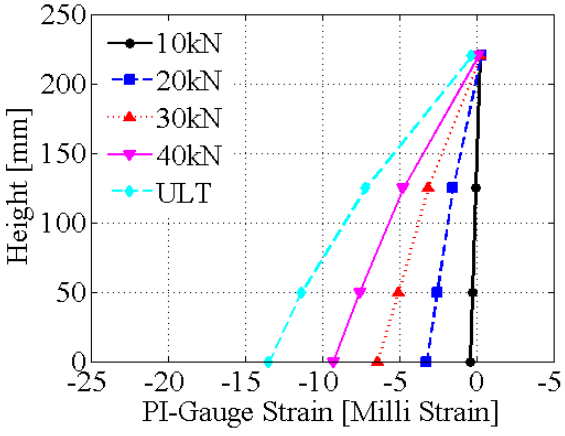

(b) PCPB3-4F50

Figure B.6 – **Strain Readings** [Third Batch PCP Reinforced Beams / Fibres]

PI-GAUGE READINGS

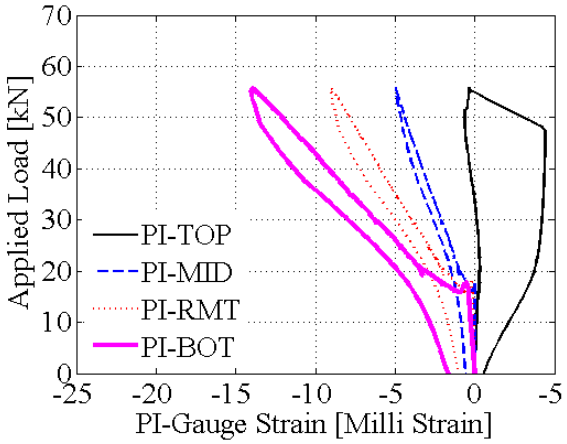

(a) PCPB1-1

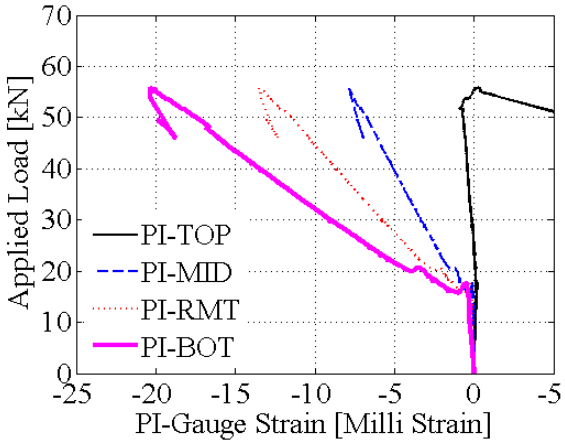

(b) PCPB1-2

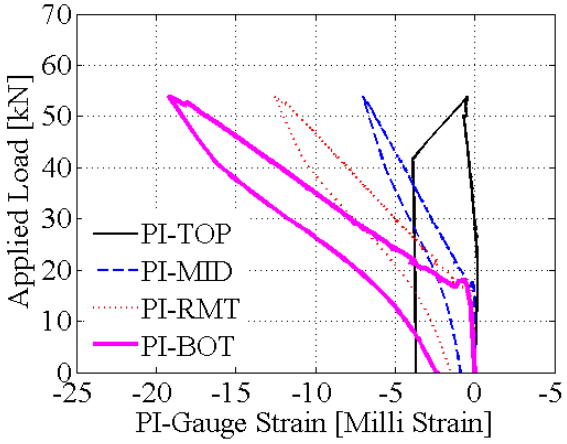

(c) PCPB1-3

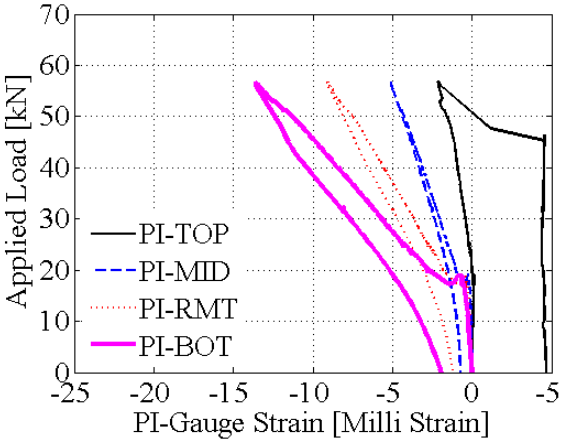

(d) PCPB1-4

Figure B.7 **– PI-Gauge Readings** [First Batch PCP Reinforced Beams]

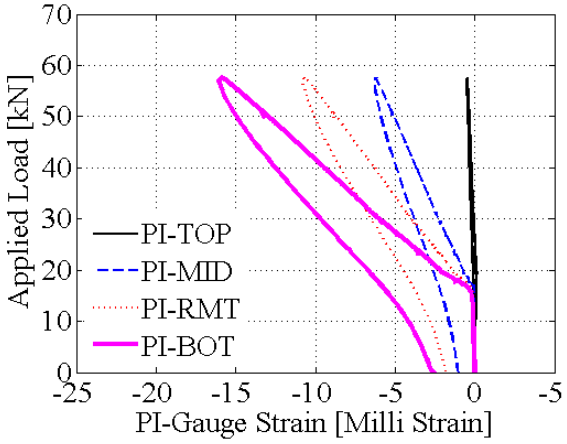

(a) PCB1-1

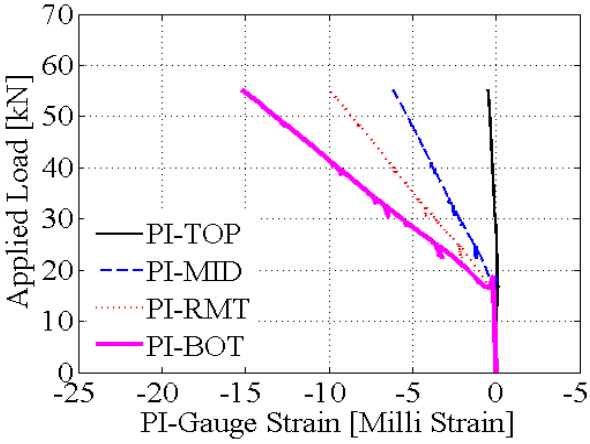

(b) PCB1-2

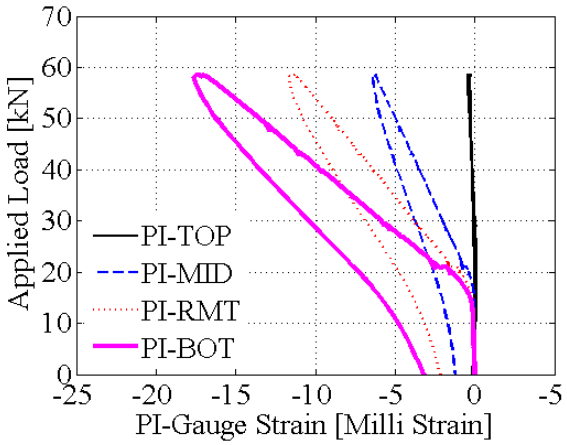

(c) PCB1-3

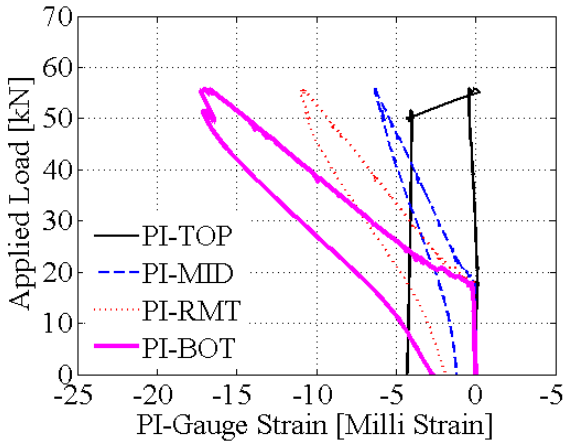

(d) PCB1-4

Figure B.8 – **PI-Gauge Readings** [First Batch Prestressed Beams]

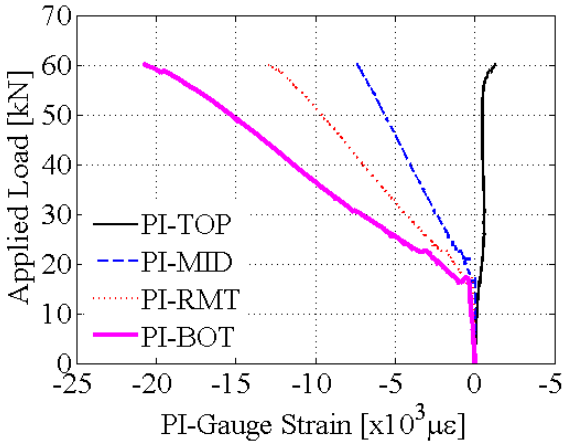

(a) PCPB2-1T

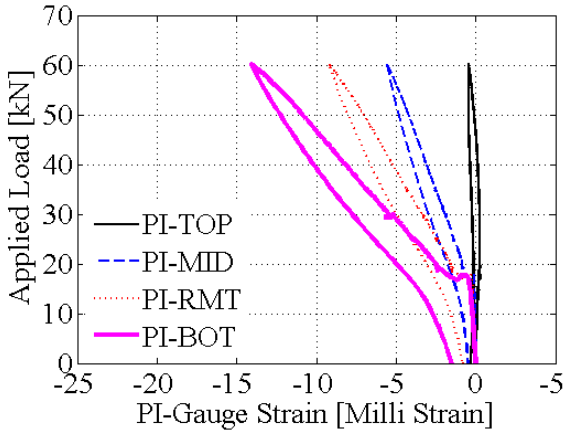

(b) PCPB2-2

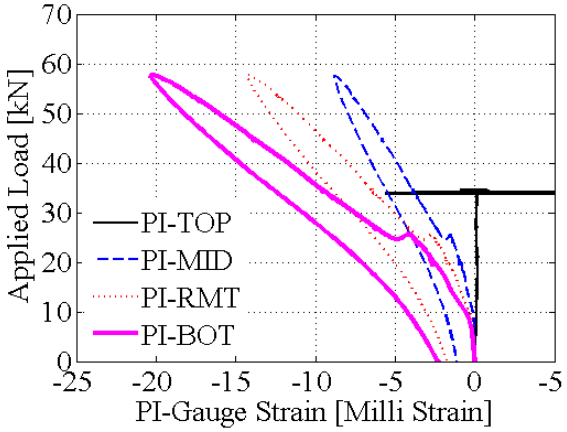

(c) PCPB2-3T

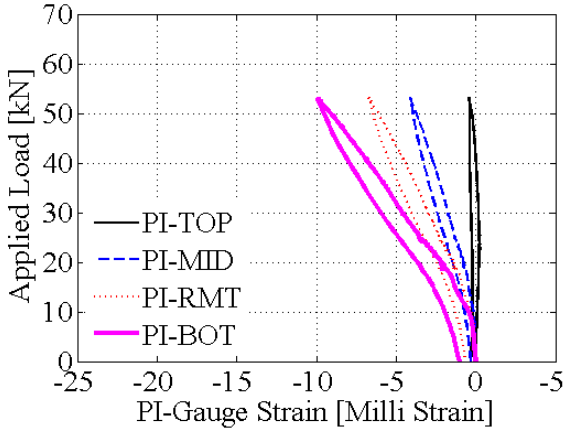

(d) PCPB2-4

Figure B.9 **– PI-Gauge Readings** [Second Batch PCP Reinforced Beams]

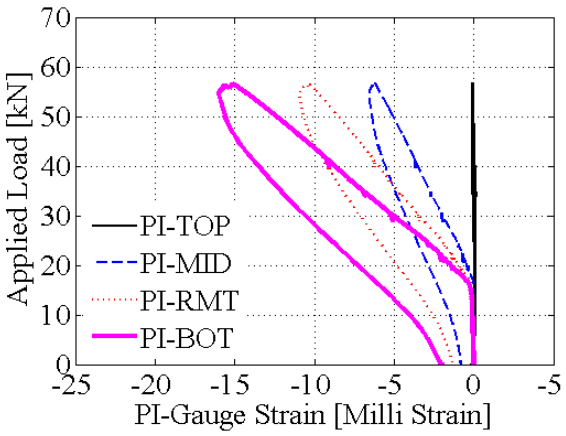

(a) PCB2-1T

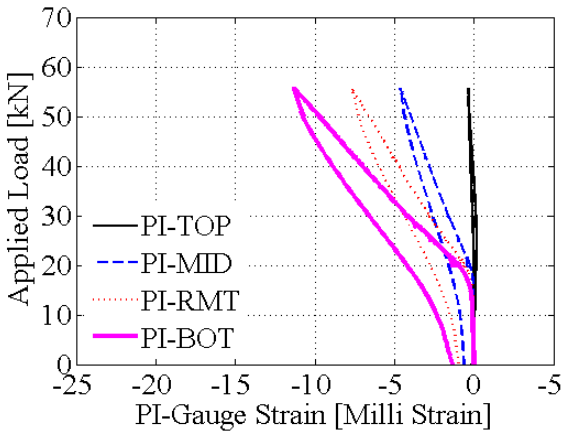

(b) PCB2-2

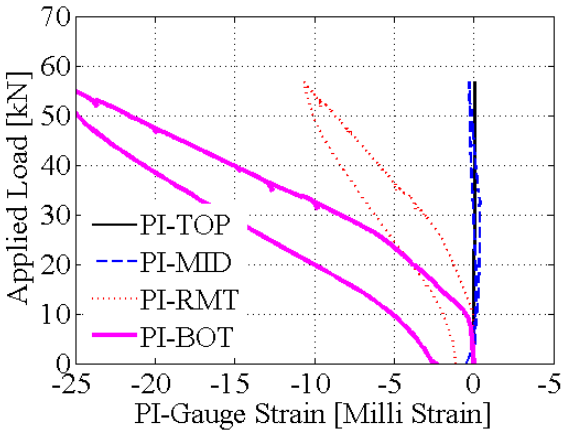

(c) PCB2-3T

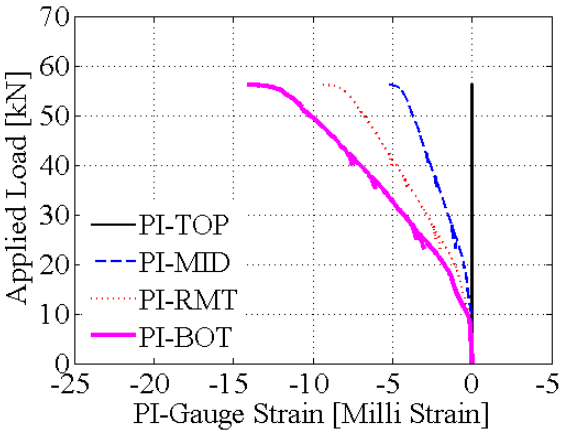

(d) PCB2-4

Figure B.10 – **PI-Gauge Readings** [Second Batch Prestressed Beams]

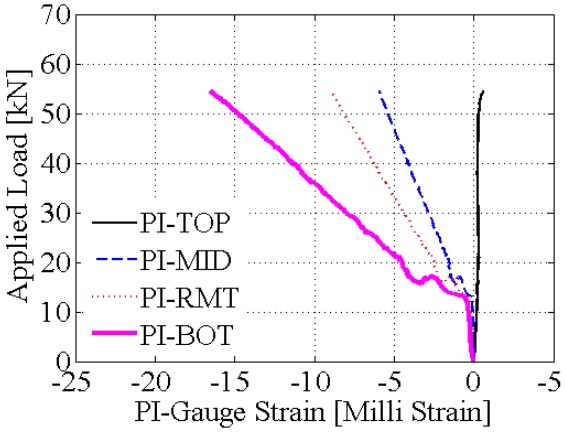

(a) PCPB3-1N

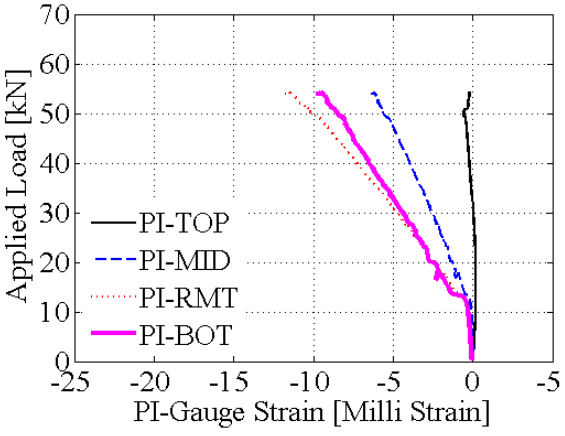

(b) PCPB3-2N

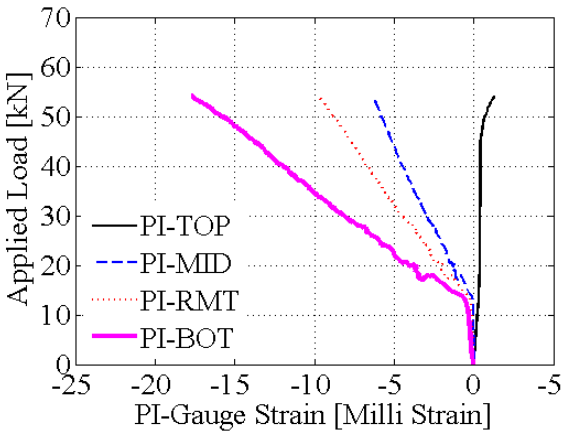

(c) PCPB3-3N

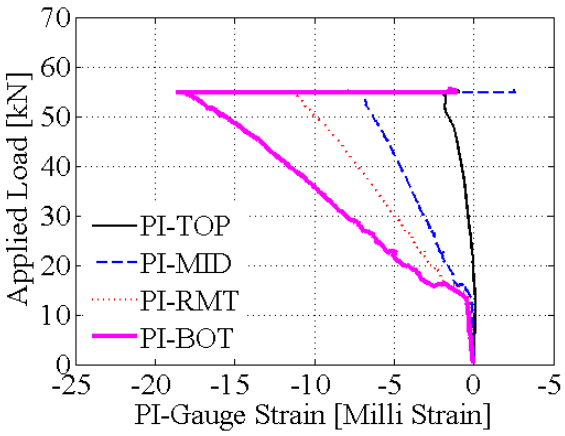

(d) PCPB3-4N

Figure B.11 **– PI-Gauge Readings** [Third Batch PCP Reinforced Beams / Notches]

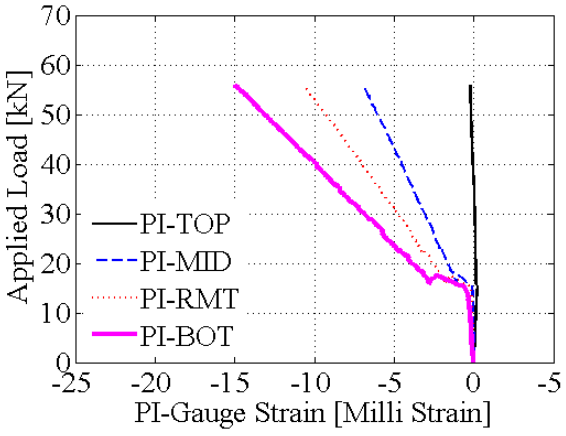

(a) PCPB3-1F50

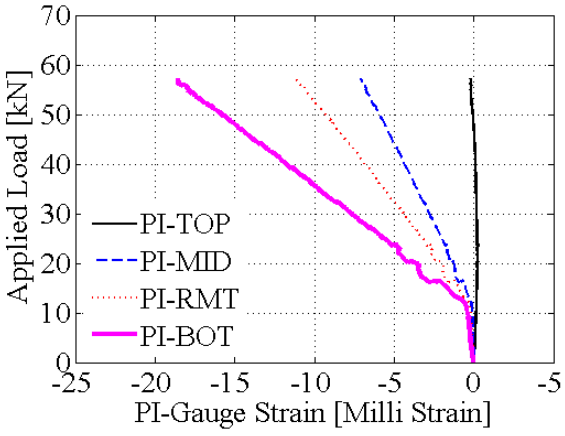

(b) PCPB3-2F50

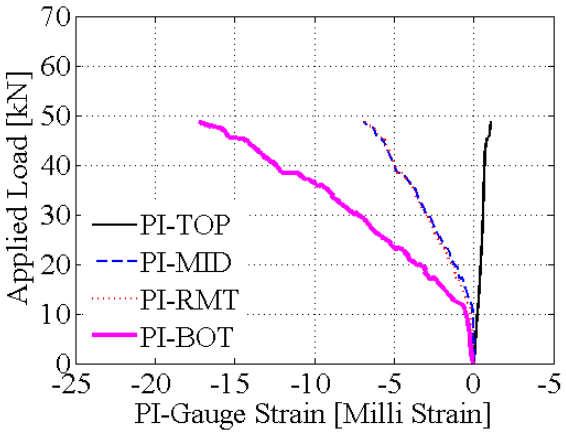

(c) PCPB3-3F50

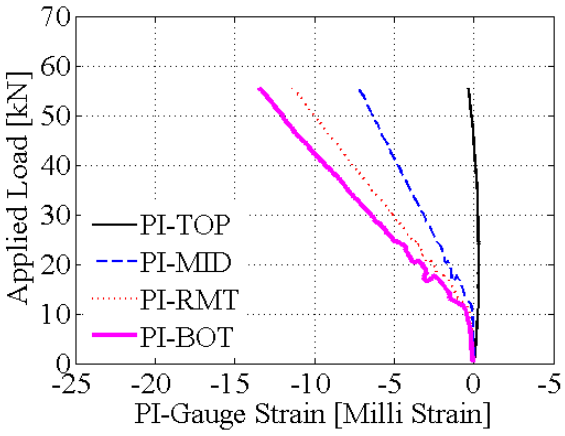

(d) PCPB3-4F50

Figure B.12 **– PI-Gauge Readings** [Third Batch PCP Reinforced Beams / Fibres]

EFFECTIVE MOMENT OF INERTIA

Experimental Response and Theoretical Estimates

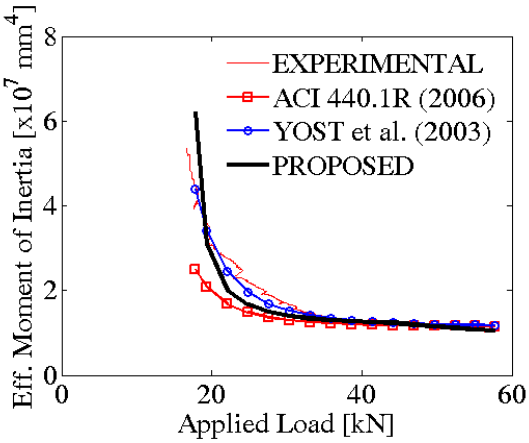

(a) PCB1-1T

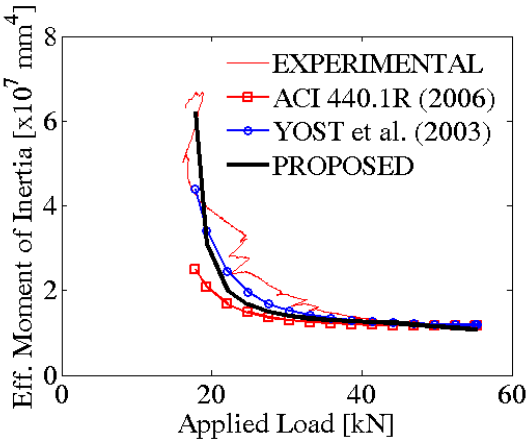

(b) PCB1-2

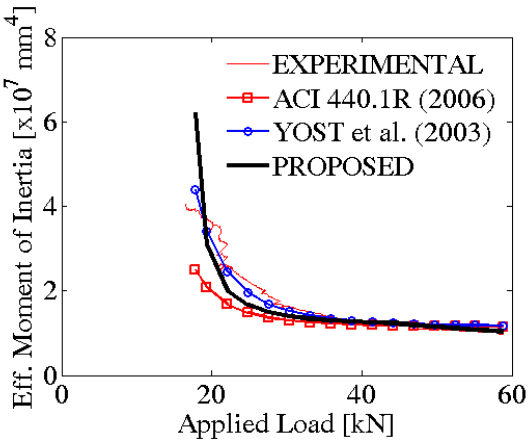

(c) PCB1-3T

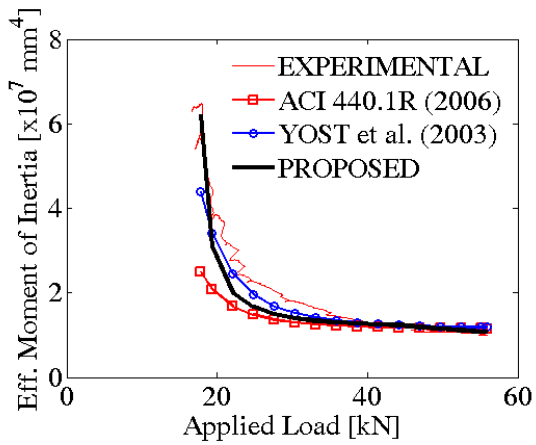

(d) PCB1-4

Figure B.13 – **Effective Moment of Inertia** [First Batch Prestressed Beams]

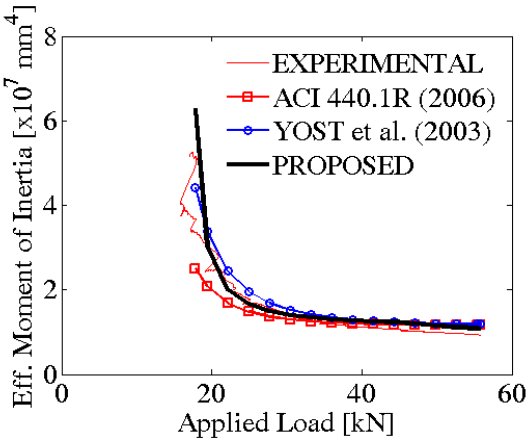

(a) PCPB1-1T

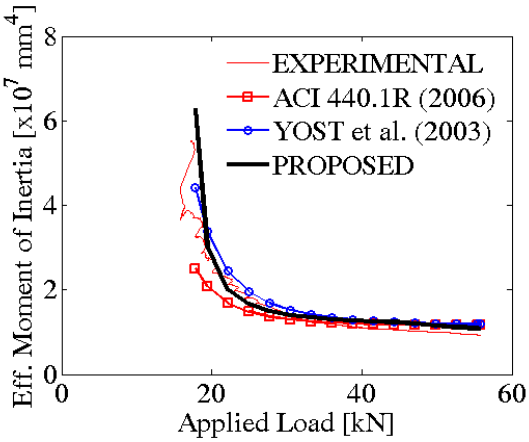

(b) PCPB1-2

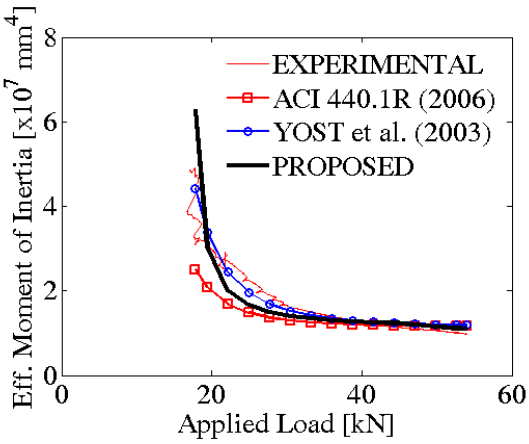

(c) PCPB1-3T

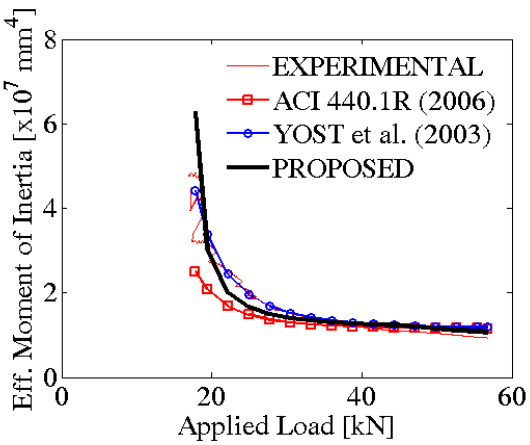

(d) PCPB1-4

Figure B.14 – **Effective Moment of Inertia** [First Batch PCP Reinforced Beams]

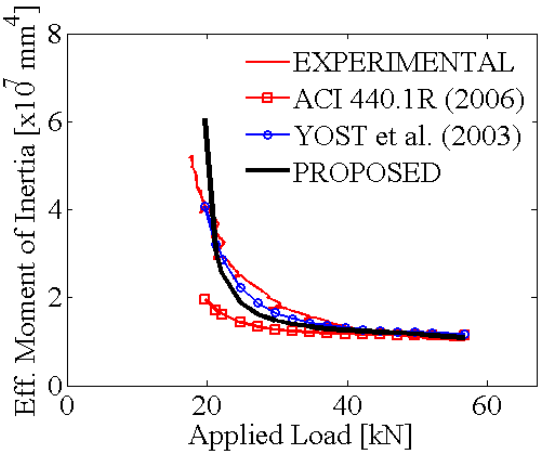

(a) PCB2-1T

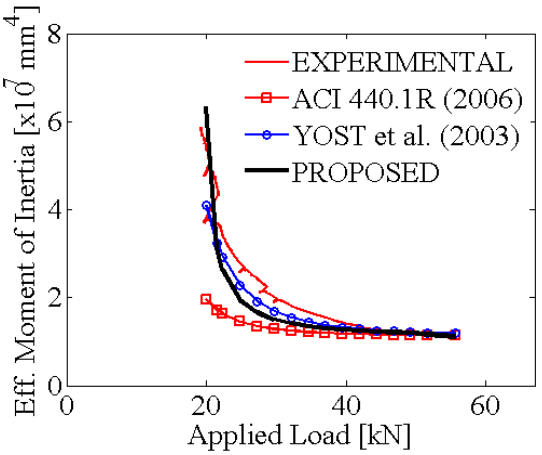

(b) PCB2-2

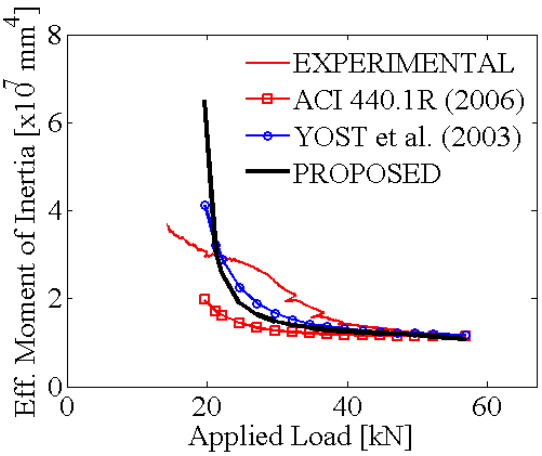

(c) PCB2-3TF

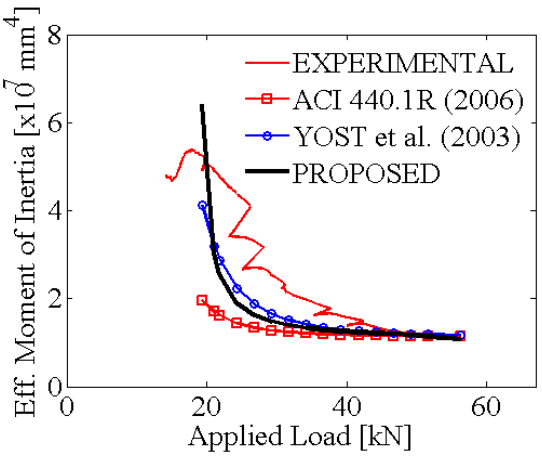

(d) PCB2-4F

Figure B.15 – **Effective Moment of Inertia** [Second Batch Prestressed Beams]

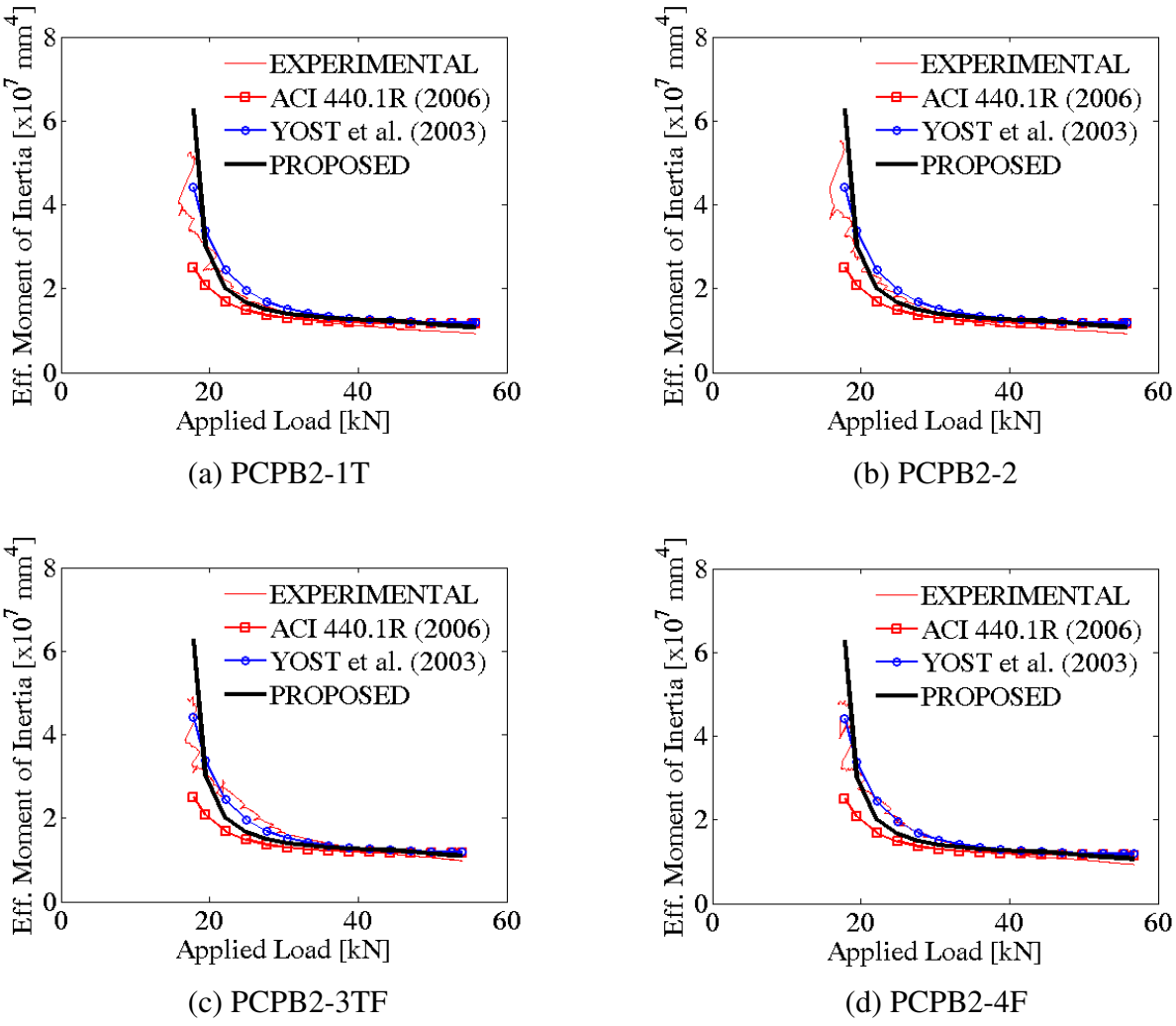

(a) PCPB2-1T (b) PCPB2-2

(c) PCPB2-3TF (d) PCPB2-4F

Figure B.16 **– Effective Moment of Inertia** [Second Batch PCP Reinforced Beams]

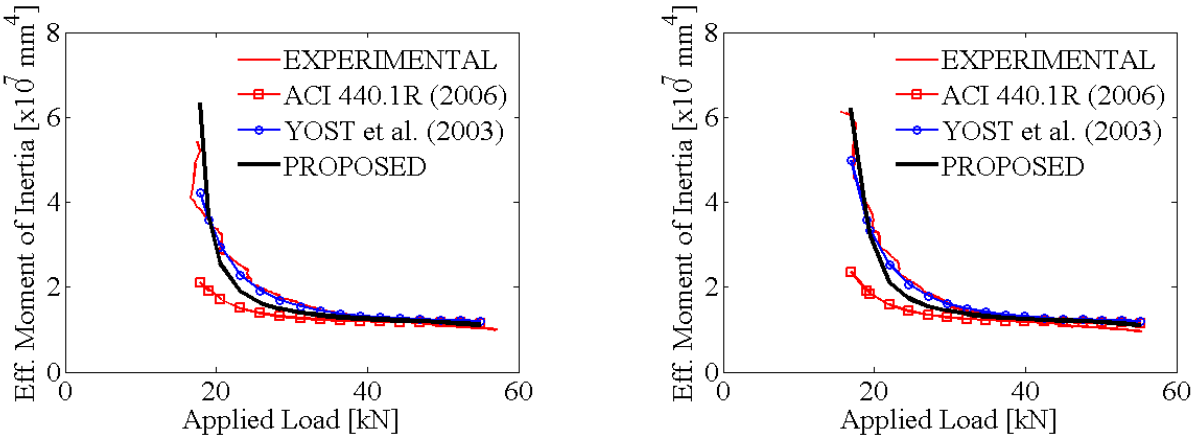

(a) PCPB3-1N (b) PCPB3-2N

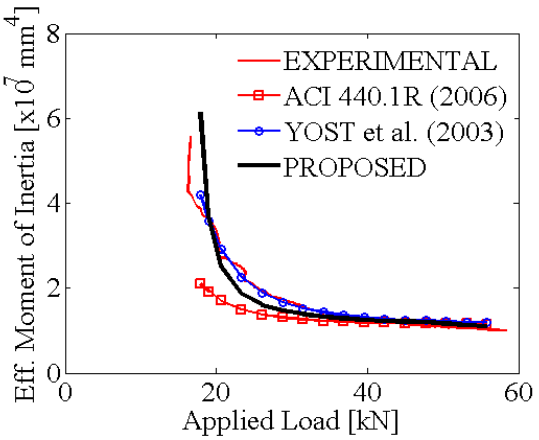

(c) PCPB3-3N

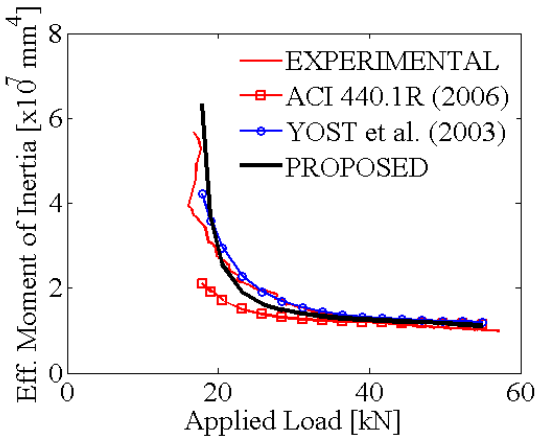

(d) PCPB3-4N

Figure B.17 – **Effective Moment of Inertia** [Third Batch PCP Reinforced Beams / Notches]

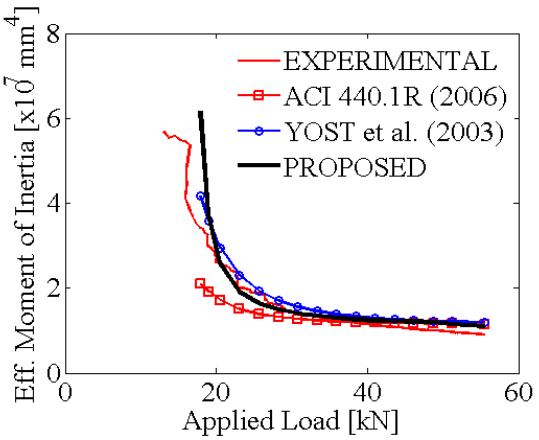

(a) PCPB3-1f50

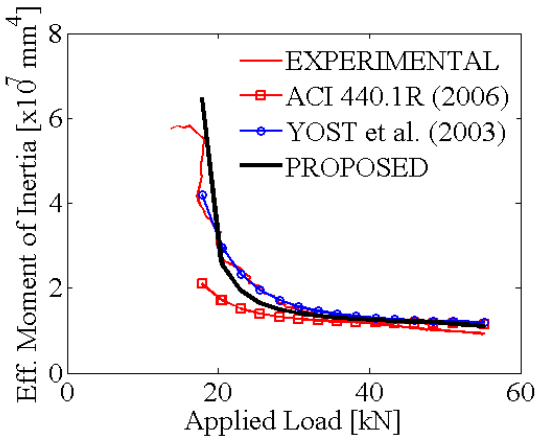

(b) PCPB3-2f50

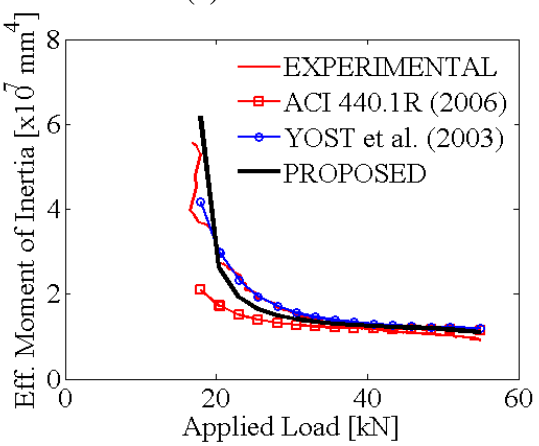

(c) PCPB3-3f50

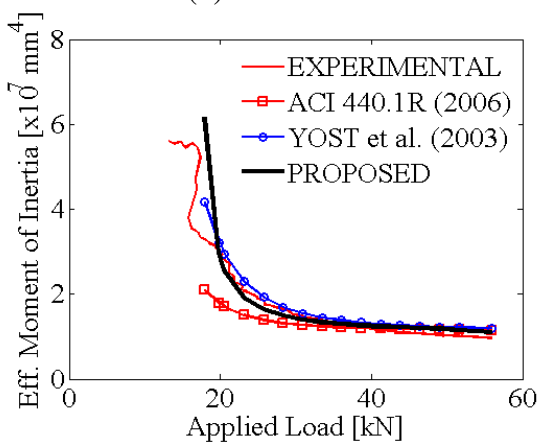

(d) PCPB3-4f50

Figure B.18 – **Effective Moment of Inertia** [Third Batch PCP Reinforced Beams / Fibres]

REFERENCES

[1] Abdalla, H. And El-Badry, M.M. (1996). "Deflection of Concrete Slabs Reinforced with Advanced Composite Materials." *Proceedings of the Second ACMBS Conference* (ACMBS 2), Montreal, Quebec, Canada, 201-208.

[2] Abrishami, H.H. and Mitchell, D. (1996). "Influence of Splitting Cracks on Tension Stiffening." *ACI Structural Journal*, 93(6), 703-710.

[3] Aiello, M.A. (1999). "Concrete Cover Failure in FRP Reinforced Beams Under Thermal Loading." *Journal of Composites for Construction*, 3(1), 46-52.

[4] Aiello, M.A. (2003). "Modeling of the Behavior of Concrete Tension Members Reinforced with FRP Rods." *Journal for the Mechanics of Composite Materials*, 39(4), 283-292.

[5] Aïtcin, P.-C. and Mehta, P. K. (1990). ''Effect of Coarse Aggregate Characteristics on Mechanical Properties of High-Strength Concrete.'' *ACI Materials Journal,* v87, n2, 103–107.

[6] Alkhrdaji, T., Ombres, L. and Nanni, A. (1996). "Flexural Behaviour of One-Way Concrete Slabs Reinforced with Deformed GFRP Bars." *Proceedings of the Second ACMBS Conference* (ACMBS 2), Montreal, Quebec, Canada, 217-224.

[7] Al-Salloum, Y.A., Almusallam, T.H., Alsayed, S.H. and Amjad, M.A. (1997). "Behaviour of Concrete Beams Doubly Reinforced by FRP Bars." *Third International Symposium on Non-Metallic (FRP) Reinforcement for Concrete Structures* (FRPRCS 3), Sapporo, Japan, p471-478, 14-16.

[8] Al-Salloum, Y.A., Alsayed, S.H. and Almusallam, T.H. (1996). "Evaluation of Service Load Deflection for Beams Reinforced by GFRP Bars." *Proceedings of the Second ACMBS Conference* (ACMBS 2), Montreal, Quebec, Canada, 165-172.

[9] Alsayad, S.H., Al-Salloum, Y.A. and Almusallam, T.H. (1996). "Evaluation of Shear Stresses in Concrete Beams Reinforced by FRP Bars." *Proceedings of the Second ACMBS Conference* (ACMBS 2), Montreal, Quebec, Canada, 173-179.

[10] American Concrete Institute (ACI). (1965). "ACI Committee 317—Reinforced Concrete Design Handbook: Working Stress Method." *ACI 317-65*, American Concrete Institute, Detroit, Michigan, USA.

[11] American Concrete Institute (ACI). (1966). "ACI Committee 318 report—Building Code Requirements for Reinforced Concrete." *ACI 318-66*, American Concrete Institute, Detroit, Michigan, USA.

[12] American Concrete Institute (ACI). (1967). "ACI Committee 340—Ultimate Strength Design Handbook." *ACI 340-67*, American Concrete Institute, Detroit, Michigan, USA.

[13] American Concrete Institute (ACI). (1986). "ACI Committee 224 report—Cracking of Members in Direct Tension." *ACI 224.2R-86*, American Concrete Institute, Detroit, Michigan, USA.

[14] American Concrete Institute (ACI). (1992). "ACI Committee 363 report—State-of-the-Art Report on High-Strength Concrete." *ACI 363R-92*, American Concrete Institute, Detroit, Michigan, USA.

[15] American Concrete Institute (ACI). (2001). "ACI Committee 440 report—Guide for the design and construction of structural concrete reinforced with FRP bars." *ACI 440.1R-01*, American Concrete Institute, Farmington Hills, Michigan, USA.

[16] American Concrete Institute (ACI). (2006). "ACI Committee 440 report—Guide for the design and construction of structural concrete reinforced with FRP bars." *ACI 440.1R-06*, American Concrete Institute, Farmington Hills, Michigan, USA.

[17] ASTM C33-03. (2004). "Standard Specification for Concrete Aggregates." *Annual Book of ASTM Standards*, Vol.04.02, Easton, MD, USA, 10-20.

[18] ASTM C39/C39M-04a. (2004). "Standard Test Method for Compressive Strength of Cylindrical Concrete Specimens." *Annual Book of ASTM Standards*, Vol.04.02, Easton, MD, USA, 18-22.

[19] ASTM C127-04. (2004). "Standard Test Method for Density, Relative Density (Specific Gravity), and Absorption of Coarse Aggregates." *Annual Book of ASTM Standards*, American Standards for Testing and Materials, v09.02, Easton, MD, USA, 72-83.

[20] ASTM C469-02. (2002). "Standard Test Method for Static Modulus of Elasticity and Poisson's Ratio of Concrete in Compression." *Annual Book of ASTM Standards*, Vol.04.02, Easton, MD, USA, 242-250.

[21] ASTM C496/496M-04. (2004), "Standard Test Method for Splitting Tensile Strength of Cylindrical Concrete Specimens." *Annual Book of ASTM Standards*, American Standards for Testing and Materials, v09.02, Easton, MD, USA, 268-271.

[22] ASTM E1512-01. (2001). "Testing Bond Performance of Adhesive-Bonded Anchors." *Annual Book of ASTM Standards*, Vol.04.11, Easton, MD, USA, 664-668.

[23] Baalbaki, W., Aïtcin, P.-C. and Ballivy, G. (1992), ‘‘On Predicting Modulus of Elasticity in High-Strength Concrete.’’ *ACI Materials Journal*, v89, n5, 517-520.

[24] Baalbaki, W. (1996), “Contribution to the Prediction of Elastic Modulus of High-Performance Concrete.” Ph.D. Thesis, *Université de Sherbrooke*, Department of Civil Engineering, Sherbrooke, Québec, Canada.

[25] Banthai, N. (1997). “Fiber Reinforced Concrete: Present and Future.” *Proceedings of the Asia-Pacific Special Conference on Fiber Reinforced Concrete*, CI-Premier Singapore, 1-10.

[26] Belarbi, A. and Hsu, T.T.C. (1994). “Constitutive Laws of Concrete in Tension and Reinforcing Bars Stiffened by Concrete.” ACI Structural Journal, 91(4), 465-474.

[27] Bencardino, F., Rizzuti, L., Spadea, G. and Swamy, R.N. (2008). “Stress-Strain Behavior of Steel Fiber-Reinforced Concrete in Compression.” *ASCE Journal of Materials in Construction*, 20(3), 255-263.

[28] Benmokrane, B., Chaallal, O., and Masmoudi, R. (1996). “Flexural Response of Concrete Beams Reinforced with FRP Reinforcing Bars.” *ACI Structural Journal*, 93(1), 46–55.

[29] Benmokrane, B. and Masmoudi, R. (1996). “FRP C-Bar Reinforcing Rod for Concrete Structures.” *Proceedings of the Second ACMBS Conference* (ACMBS 2), Montreal, Quebec, Canada, 181-188.

[30] Bischoff, P.H. and Paixao, R. (2004), “Tension Stiffening and Cracking of Concrete Reinforced with GFRP bars”, *Canadian Journal of Civil Engineering*, 31, 579-588.

[31] Branson, D.E. (1963). “Instantaneous and Time-Dependent Deflection of Simple and Continuous Reinforced Concrete Beams.” *Alabama Highway Research Report No.7*, Bureau of Public Roads, Alabama, United States.

[32] Branson, D.E. (1968). “Design Procedures for Computing Deflections.” *ACI Journal Proceedings*, 65(9), 730-742.

[33] Branson, D.E. and Trost, H. (1982). “Application of the I-Effective Method in Calculating Deflections of Partially Prestressed Members.” *PCI Journal*, September-October, 62-77.

[34] Brown, V.L. and Bartholomew, C.L. (1996). “Long-Term Deflections of GFRP-Reinforced Concrete Beams.” *Proceedings of the ICCI Conference*, Tucsan, Arizona, 389-400.

[35] Burg, R.G. and Ost, B.W. (1992), “Engineering Properties of Commercially Available High-Strength Concretes.” *PCA Research & Development Bulletin RD104T*, Portland Cement Association, Skokie, Illinois, USA.

[36] Canadian Standards Association (CSA). (2002). "Design and Construction of Building Components with Fiber-Reinforced Polymers." *S806-02*, Canadian Standards Association, Toronto, Ontario, Canada.

[37] Canadian Standards Association (CSA). (2004). "Design of Concrete Structures." *A23.3-04*, Canadian Standards Association, Toronto, Ontario, Canada.

[38] Carasquillo, R.L., Nilson, A.H. and Slate, F.O. (1981), "Properties of High-Strength Concrete Subject to Short-Term Loads." *ACI Journal Proceedings*, v78, n3, 171-178.

[39] Chen, W.F. (1970). "Double Punch Test for Tensile Strength of Concrete." *ACI Journal*, v67, n12, 993-995.

[40] Chen, B. and Nawy, E.G. (1994). "Structural Behavior Evaluation of High Strength Concrete Beams Reinforced with Prestressed Prisms Using Fiber Optic Sensors." *ACI Structural Journal*, 91(6), 708-718.

[41] Clark, L.A. and Speirs, D.M. (1978). "Tension Stiffening Model for Reinforced Concrete Members." *Technical Report 42.521*, Cement and Concrete Association, London, UK.

[42] Collins, M.P. and Mitchell, D. (1997) *Prestressed Concrete Structures*, Response Publications, ON, Canada, 766 pp.

[43] Comité Euro-International du Béton (CEB). (1978). "CEB-FIP model code for concrete structures." *MC78*, Paris, France.

[44] Considère, A. (1899) *Experimental Researches on Reinforced Concrete*, Translation Arranged by Moisseiff, L.S., McGraw-Hill, New York, New York, USA, 188 pp.

[45] Cosenza, E., Manfredi, G., Realfonzo, R. (1997). "Behaviour and Modelling of Bond of FRP Rebars to Concrete." *Journal of Composites for Construction*, v1, n2, 40-51.

[46] Cosenza, E., Manfredi, G., Realfonzo, R.(1997). "Crack Width Prediction for NEFMAC-Reinforced Flexural Members." *Third International Symposium on Non-Metallic (FRP) Reinforcement for Concrete Structures* (FRPRCS 3), 14-16 October, 447-454, Sapporo, Japan

[47] Damjanic, F. and Owen, D.R.J. (1984). "Practical Considerations for Modelling of Post-Cracking Concrete Behavior for Finite Element Analysis of Reinforced Concrete." *Proceedings of the International Conference on Computer-Aided Analysis and Design of Concrete Structures*, 693-706.

[48] Davoudi, S. (2009). "CFRP prestressed concrete prisms as reinforcement in continuous concrete T-beams." Ph.D. Thesis, *University of Manitoba*, Department of Civil Engineering, Winnipeg, Manitoba, Canada.

[49] Davoudi, S. and Svecova, D. (2008). "Carbon Fiber-Reinforced Polymer Prestressed Prisms as Reinforcement in Continuous Concrete T-Beams." *ACI Structural Journal*, 105(3), 368-374.

[50] Duranovic, N., Pilakoutas, K. And Waldron, P. (1997). "Tests on Concrete Beams Reinforced with Glass Fiber-Reinforced Plastic Bars." *Third International Symposium on Non-Metallic (FRP) Reinforcement for Concrete Structures* (FRPRCS 3), Sapporo, Japan, 479-485, 14-16 October.

[51] El-Salakawy, E., Kassem, C. and Benmokrane, B. (2003). "Flexural Behaviour of Bridge Deck Slabs Reinforced with FRP Composite Bars." *Proceedings of the FRPRCS-6 Conference*, Singapore, 1291-1300.

[52] El-Sayad, A., El-Salakawy, E. and Benmokrane, B. (2004). "Evaluation of Concrete Shear Strength for Beams Reinforced with FRP Bars." *Proceedings of the Fifth SSP of the CSCE Conference*, Canadian Society of Civil Engineers, Saskatoon, Saskatchewan, Canada.

[53] Evans, R.H. and Parker, A.S. (1955). "Behavior of Prestressed Concrete Composite Beams." *ACI Journal Proceedings*, 26(9), 861-878.

[54] Fernando, L. (2001). "The Serviceability of Concrete Beams Reinforced with FRP." *BSc. Thesis*, University of Manitoba, Winnipeg, Manitoba, Canada.

[55] Gao, D., Benmokrane, B. and Masmoudi, R. (1998), "A Calculating Method of Flexural Properties of FRP-Reinforced Concrete Beam: Part 1: Crack Width and Deflection." *Technical Report*, Department of Civil Engineering, Université de Sherbrooke, Sherbrooke, Québec, Cananda.

[56] Gentry, R.T. and Hussain, M., "Thermal Compatibility of Concrete and Composite Reinforcement." *Journal of Composites for Construction*, Vol.3, No.2, 1999, 82-86.

[57] Giaccio, G., Rocco, C., Violini, D., Sappitelli, J. and Zerbino, R. (1992), "High-Strength Concretes Incorporating Different Coarse Aggregates." *ACI Materials Journal*, v89, n3, 242-246.

[58] Gilbert, I. (1981). "Deflections of reinforced concrete beams—a design approach." *UNICIV Rep. No. R-201*, School of Civil Engineering, Univ. of New South Wales, Kensington, New South Wales, Australia.

[59] Gilbert, R.I. (1983), "Deflection Calculations for Reinforced Concrete Beams", *Institution of Engineers from Australia*, 25(2), 128-134.

[60] Gross, S.P., Dinehart, D.W. and Yost, J.R. (2004). "Experimental Tests on High Strength Concrete Beams Reinforced with CFRP Bars." *Proceedings of the Fourth ACMBS Conference* (ACMBS 4), Calgary, Alberta, Canada.

[61] Guadagnini, M., Pilakoutas, K. and Waldron, P. (2001). "Investigation on Shear Carrying Mechanisms in FRP RC Beams." *Proceedings of the FRPRCS-5 Conference*, London, England, 949-958.

[62] Hall, T.S. (2000). "Deflections of Concrete Members Reinforced with Fiber Reinforced Polymer (FRP) Bars." *MSc. Thesis*, University of Calgary, Calgary, Alberta, Canada.

[63] Hannant, D.J. (1978). *Fiber Cements and Fiber Concrete*, Wiley, New York, New York, USA.

[64] Hansen, T.C. (1965). "Influence of Aggregate and Voids on Modulus of Elasticity of Concrete, Cement and Mortar Cement Paste." *American Concrete Institute Journal*, v62, n2, 193-216.

[65] Hanson, N.W. (1969). "Prestressed Concrete Prisms as Reinforcement for Crack Control." *PCI Journal*, 14(4), 14-31.

[66] Hirsch, T.J. (1962). "Modulus of Elasticity of Concrete Affected by Elastic Moduli of Cement Paste Matrix and Aggregate." *ACI Journal*, v59, 427-451.

[67] Hoppe, A. (1963). "The Mass Production of Prestressed Auxiliary Members." *PCI Journal*, October, 44-46.

[68] Illston, J.M., Dinwoodie, J.M. and Smith, A.A. (1987), "Concrete, Timber and Metals." *Von Nostrand Reinhold*, ISBN 0-442-30145-6, New York, New York, USA.

[69] Iravani, S. (1996). ''Mechanical Properties of High-Performance Concrete.'' *ACI Materials Journal,* v93, n5, 416-426.

[70] ISIS Canada (2001). *Reinforcing concrete structures with FRP*, Design Manual III, University of Manitoba, Winnipeg, Manitoba, Canada.

[71] Jawara, A. (1999). "Low Heat High Performance Concrete for Glass Fiber Reinforced Polymer Reinforcement." *MSc. Thesis*, University of Manitoba, Winnipeg, Manitoba, Canada.

[72] Kassem, C., El-Salakawy, E. and Benmokrane, B. (2003). "Deflection Behaviour of Concrete Beams Reinforced with Carbon FRP Composite Bars." *ACI Special Publication SP-210*, Gardner, J.Ed., American Concrete Institute, Michigan, 65-92.

[73] Katz, A. and Berman, N. (2000). "Modelling the Effect of High Temperature on the Bond Strength of FRP Reinforcing Bars to Concrete." *Journal of Cement and Concrete Composites*, 22, 433-443.

[74] Khayat, K.H., Bickley (1995). J.A. and Hooton, R.D., "High-Strength Concrete Properties Derived from Compressive Strength Values." *Cement, Concrete and Aggregates*, CCAGDP, v17, n2, 126-133.

[75] Kommandigesellschaft, D. and Kommandigesellschaft, W. (1963), "Concrete Pavement with Prestressed Concrete Bars as Reinforcement." *PCA Foreign Literature Study No.442*, Munich Germany, 19 pp.

[76] Kupfer, H., Hilsdorf, H.K. and Rusch, H. (1969). "Behavior of Concrete under Biaxial Stresses." *ACI Journal Proceedings*, 66(8), 656-666.

[77] de Larrard, F. and Belloc, A. (1997). "The Influence of Aggregate on the Compressive Strength of Normal and High-Strength Concrete." *ACI Materials Journal*, v94, n5, 417-426.

[78] Li, G. (2004). "The Effect of Moisture Content on the Tensile Strength Properties of Concrete." *Master of Civil Engineering Thesis*, University of Florida, Florida, USA.

[79] Lok, T.S. and Pei, J.S. (1988). "Flexural Behavior of Steel-Reinforced Concrete." *ASCE Journal of Materials in Construction*, 10(2), 88-97.

[80] Lok, T.S. and Xiao, J.R. (1999). "Flexural Strength Assessment of Steel Fiber Reinforced Concrete." *ASCE Journal of Materials in Civil Engineering*, 11(3), 188-196.

[81] Lutz, L.A., Sharma, N.K. and Gergely, P. (1968). "Increase in Crack Width in Reinforced Concrete Beams under Sustained Loading." *ACI Journal Proceedings*, v64, n9, 538-546.

[82] MacGregor, J.G., Bartlett, F.M. (2000) *Reinforced Concrete Mechanics and Design*, First Canadian Edition, Prentice Hall, Scarborough, ON, Canada, 1042 pp.

[83] Mansur, M.A., Wee, T.H. and Chin, M.S. (1995). "Derivation of the Complete Stress-Strain Curves for Concrete in Compression." *Magazine of Concrete Research*, v47, n173, 285-290.

[84] Matthys, S.; Taerwe, L. (1995). "Loading Tests on Concrete Slabs Reinforced with FRP Grids." *Second International Symposium on Non-Metalic (FRP) Reinforcement for Concrete Structures* (FRPRCS 2), Ghent, Belgium.

[85] Marti, P. (1990). "Size Effect in Double-Punch Tests on Concrete Cylinders." *ACI Materials Journal*, 86(6), 597-601.

[86] Michaluk, C., Rizkalla, S., Tadros, C. And Benmokrane, B. (1998). "Flexural Behaviour of One-Way Concrete Slabs Reinforced by Fiber Plastic Reinforcements." *ACI Structural Journal*, v95, n3, 353-365.

[87] Mikhailov (1958). "Recent Research on the Action of Unstressed Concrete in Composite Structures." *Third Congress of FIP*, Berlin, Germany, 51-65.

[88] Mirza, J.F., Zia, P. and Bhargava, J.R. (1971). "Static and Fatigue Strength of Beams Containing Prestressed Concrete Tension Elements." *Final Report NCSU Project FRD-110-69-2*, North Carolina State University, North Carolina, United States.

[89] Mostofinejad, D. and Nozhati, M. (2005). "Prediction of the Modulus of Elasticity of High Strength Concrete." *Iranian Journal of Science & Technology*, v29, nB3, 311-321.

[90] Mota, C. (2005). *MSc. Thesis*, University of Manitoba, Winnipeg, Manitoba, Canada, 2005

[91] Maruyama, K. and Zhao, W. (1996). "Size Effect in Shear Behaviour of FRP Reinforced Concrete Beams." *Proceedings of the Second ACMBS Conference* (ACMBS 2), Montreal, Quebec, Canada.

[92] Najjar, S., Pilakoutas, K. and Waldron, P. (1997). "Finite Element Analysis of GFRP Reinforced Concrete Beams." *Third International Symposium on Non-Metallic (FRP) Reinforcement for Concrete Structures* (FRPRCS 3), 14-16 October, 519-526, Sapporo, Japan.

[93] Nanni, A. (1993b). "Flexural Behavior and Design of RC Members Using FRP Reinforcement." *ASCE Journal of Structural Engineering*, 119(11), 3344-3359.

[94] Nawy, E.G. and Chen, B. (1998). "Deformational Behavior of High Performance Concrete Continuous Composite Beams Reinforced with Prestressed Prisms and Instrumented with Bragg Grating Fiber Optic Sensors." *ACI Structural Journal*, 95(1), 51-60.

[95] Nawy, E.G. and Neuwerth, A.M. (1977). "Fiberglass Reinforced Concrete Slabs and Beams." *ACI Structural Journal*, v103, n2, 421-439.

[96] Pecce, M., Manfredi, G. And Cosenza, E. (2000). "Experimental Response and Code Models of GFRP RC Beams in Bending." *Journal of Composites for Construction*, v4, American Society of Civil Engineers, 182-190.

[97] Pillai, S.U. (1999) *Reinforced Concrete Design*, McGraw-Hill, New York, New York, USA.

[98] Popovics, S. and Erdey, M. (1970), "Estimation of the Modulus of Elasticity of Concrete-Like Composite Materials." *Materials and Structures, Research and Testing*, v3, n16, 253-260.

[99] Portland Cement Association (PCA). (1992). "Engineering Properties of Commercially Available High-Strength concretes." *Research and Development Bulletin RD104T*, Portland Cement Association, Skokie, Illinois, USA.

[100] Rahman, A.H., Kingsley, C.Y., and Taylor, D.A. (1995). "Thermal Stress in FRP-Reinforced Concrete." *Proceedings of the Canadian Society for Civil Engineering Annual Conference*, Canadian Society for Civil Engineering, Montreal, Canada, 2, 605-614.

[101] Rao, P.S. (1966). Die Grundlagen zur Berechnung der bei statisch unbestimmten Stahlbetonkonstruktionen im plastichen Bereich aufttretenden Umlagerungen der Schnittkräfte (Basic laws governing moment redistribution in statically indeterminate reinforced concrete strucutures). Ernst & Sohn, Berlin, Germany.

[102] Rao, P.S. and Subrahmanyam, B.V. (1973). "Trisegmental Moment-Curvature Relations for Reinforced Concrete Members." *ACI Journal Proceedings*, 70(5), 346-351.

[103] Rashid, M.A., Mansur, M.A. and Paramasivam, P. (2002), ''Correlations between Mechanical Properties of High-Strength Concrete.'' *Journal of Materials in Civil Engineering,* v14, n3, 230-238.

[104] Razaqpur, A., Isgor, B., Greenway, S. And Selley, A. (2004). "Concrete Contribution to the Shear Resistance of FRP Reinforced Concrete Members." *Journal of Composites in Construction*, 452-460, September/October.

[105] de Schutter, G., Matthys, S. and Taerwe, L. (1997). "Two-Dimensional Analysis of Thermal Incompatibility Between FRP Reinforcement and Concrete." *Proceedings of the Second International DIANA Conference on Finite Elements in Engineering and Science*, Amsterdam, Netherlands.

[106] Sooriyaarachchi, H., Pilakoutas and K., Byars, E. (2005). "Tension Stiffening Behavior of GFRP-Reinforced Concrete", *7th International Symposium on Fiber Reinforced Polymer Reinforcement for Concrete Structures (FRPRCS-7)*, Kansas City, USA, 975-989.

[107] Soroushian, P. and Lee, C.D. (1990). "Distribution and Orientation of Fibers in Steel Fiber Reinforced Concrete." *ACI Materials Journal*, 87(5), 433-439.

[108] Svecova, D. and Razaqpur, A.G. (2000). "Flexural Behavior of Concrete Beams Reinforced with Carbon Fiber-Reinforced Polymer (CFRP) Prestressed Prisms." *ACI Structural Journal*, 97(5), 731-738.

[109] Swamy N., Aburawi M. (University of Sheffield, UK). (1997). "Structural Implications of Using GFRP Bars as Concrete Reinforcement." *Third International Symposium on Non-Metallic (FRP) Reinforcement for Concrete Structures* (FRPRCS 3), 14-16 October, Sapporo, Japan.

[110] Swamy, R.N. and Al-Ta'an, S.A. (1981). "Deformation and Ultimate Strength in Flexural Reinforced Concrete Beams made with Steel Fiber Concrete." *ACI Structural Journal*, 78(5), 395-405.

[111] Tariq, M. (2003). "Effects of Flexural Reinforcement Properties on shear Strength of Concrete Beams." *MSc. Thesis*, Dalhousie University, Halifax, Nova Scotia, Canada.

[112] Tasuji, M.E., Slate, F.O. and Nilson, A.H. (1978). "Stress-Strain Response and Fracture of Concrete in Biaxial Loading." *ACI Journal Proceedings*, 75(7), 306-312.

[113] Thériault, M. and Benmokrane, B. (1997). "Theoretical and Experimental Investigation on Crack Width, Deflection and Deformability of Concrete Beams Reinforced with FRP Rebars." *Proceedings of the Annual CSCE Conference,* Canadian Society for Civil Engineering, v6, 151-160

[114] Tighiouart, B., Benmokrane, B. and Baalbaki, W. (1994). ''Caractéristiques Mécaniques et Elastiques de Bétons a Haute Performance Confectionnés avec Différents Types de Gros Granulats.'' *Journal of Materials and Structures*, v27, 211-221.

[115] Tighiouart, B., Benmokrane, B. and Gao, D. (1998). "Investigation of Bond in Concrete Members with Fiber Reinforced Polymer (FRP) Bars." *Construction and Building Materials*, 12, 453-462.

[116] Timoshenko, S.P. and Goodier, J.N. (1970). *Theory of Elasticity*, McGraw-Hill, New York, USA.

[117] Toutanji, H.A. and Saafi, M. (2000). ''Flexural Behviour of Concrete Beams Reinforced with Glass Fiber-Reinforced Polymer (GFRP) Bars." *ACI Structural Journal*, v97, n5, 712-719.

[118] Tureyen, A.K. and Frosch, R.J. (2002). "Shear Tests of FRP-Reinforced Concrete Beams without Stirrups." *ACI Structural Journal*, v99, n4, 427-434.

[119] Vogel, H. and Svecova, D. (2009). "Effective Moment of Inertia Expression for Concrete Beams Reinforced with Fiber Reinforced Polymer (FRP)" *ACI Convention*, San Antonio, Texas, USA.

[120] Vogel, H. and Svecova, D. (2008). "Effective Moment of Inertia for Concrete Beams Reinforced with Fiber Reinforced Polymer (FRP)" *International Conference for Advanced Composite Materials for Bridges and Structures* (ACMBS-V), Winnipeg, Manitoba, Canada.

[121] Vogel, H., Davoudi, S., Noël, M. and Svecova, D. (2008). "Evaluation of Properties of High Strength Concrete for Prestressed Concrete Prisms" *Proceedings of the Second International Symposium on Ultra High Performance Concrete*, Kassel, Germany.

[122] Vogel, H. (2005). "Thermal Compatibility and Bond Strength of FRP Reinforcement in Prestressed Concrete Applications." M.Sc. Thesis, *University of Manitoba*, Department of Civil Engineering, Winnipeg, Manitoba, Canada.

[123] Warner, R.F. and Pulmano, V.A. (1980). "Post-Cracking Behaviour and Deflections of Partially-Prestressed Concrete Beams." *7th Australian Conference on the Mechanics of Structures and Materials*, University of Western Australia, May, 110-115.

[124] Wee, T.H., Chin, M.S. and Mansur, M.A. (1996). ''Stress-Strain Relationship of High-Strength Concrete in Compression'' *Journal of Materials in Civil Engineering,* v8, n2, 70-76.

[125] Yost, J. R., Gross, S. P., and Dinehart, D. W. (2003). "Effective moment of inertia for GFRP reinforced concrete beams." *ACI Structural Journal*, 100(6), 732-739.

[126] Yost, J. R. and Goodspeed, C.H. (2001). "Strength and Deflection Prediction of Concrete Beams Reinforced with 2-Dimensional FRP Grids." *Proceedings of the 10th Annual Congress on Polymers in Concrete*, Honolulu, Hawaii, USA, Paper No.58.

[127] Yost, J.R., Goodspeed, H. And Schmeckpeper, R. (2001). "Flexural Performance of Concrete Beams Reinforced with FRP Grids." *Journal of Composites for Construction,* American Society of Civil Engineers, 18-25.

[128] Zhao, W., Pilakoutas, K., and Waldron, P. (1997). "FRP reinforced concrete: Calculations for deflections." *Non-Metallic (FRP) Reinforcement for Concrete Structures*, 2, 511–518.

[129] Zia, P., Mirza, S. and Rizkalla, S. (1976). "Static and Fatigue Tests of Composite T-beams Containing Prestressed Tension Elements." *PCI Journal*, 21(6), 76-93.